Discrete Dynamics in Nature and Society

Analysis, Control and Applications of Passivity in Complex Networks 2022

Lead Guest Editor: Jin-Liang Wang
Guest Editors: Guoguang Wen and Zi-Peng Wang

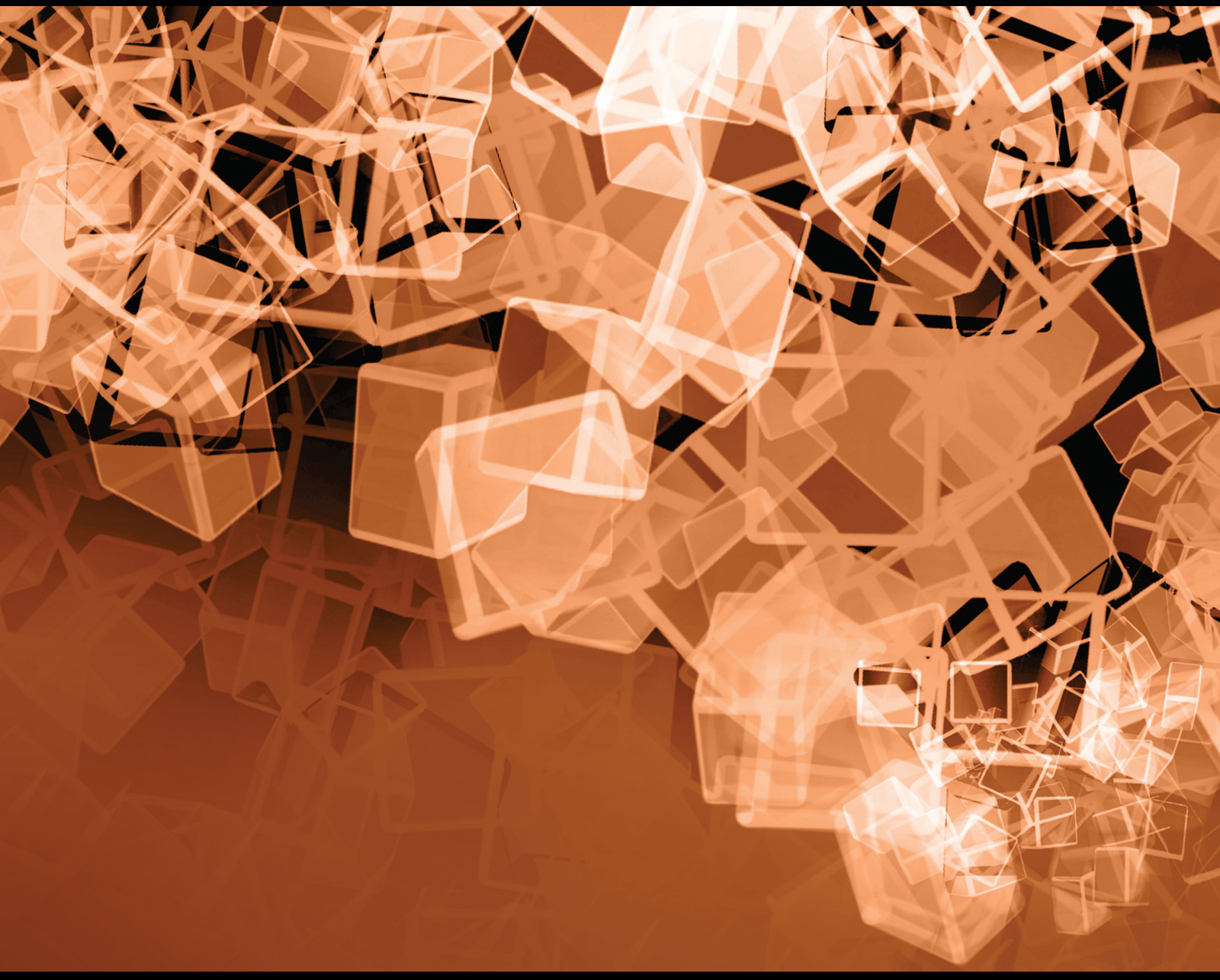

Analysis, Control and Applications of Passivity in Complex Networks 2022

Discrete Dynamics in Nature and Society

Analysis, Control and Applications of Passivity in Complex Networks 2022

Lead Guest Editor: Jin-Liang Wang
Guest Editors: Guoguang Wen and Zi-Peng Wang

Contents

Hindawi
Discrete Dynamics in Nature and Society
Volume 2023, Article ID 5220356, 20 pages
https://doi.org/10.1155/2023/5220356

Research Article

Antisynchronization and Generalized Pinning Control of Multiweighted Coupled Complex-Valued Delayed Memristive Neural Networks

Limei Su and Yanli Huang

Tianjin Key Laboratory Autonomous Intelligence Technology and Systems, School of Computer Science and Technology, Tiangong University, Tianjin 300387, China

Correspondence should be addressed to Yanli Huang; huangyanli@tiangong.edu.cn

Received 27 May 2022; Accepted 19 August 2022; Published 28 February 2023

Academic Editor: A. E. Matouk

In this article, antisynchronization problem of multiweighted coupled complex-valued delayed memristive neural networks (MWCCVDMNNs) with and without coupling delays are investigated. First, via devising a suitable controller and constructing an appropriate Lyapunov functional, a criterion for ensuring antisynchronization of MWCCVDMNNs is derived. Second, we research the generalized pinning antisynchronization of MWCCVDMNNs by creating a generalized pinning controller to guarantee that the considered networks can accomplish antisynchronization. Similarly, several sufficient conditions guaranteeing the antisynchronization and generalized pinning antisynchronization of MWCCVDMNNs with coupling delays are also presented. Third, two numerical examples are provided to verify the correctness of the obtained antisynchronization results.

1. Introduction

In recent decades, the applications of neural networks (NNs) in automatic control [1], pattern recognition [2], associative memory [3], and many other fields have attracted much attention. As a particular case of complex networks, coupled NNs (CNNs) are generated from a large number of single NN through complex interactions between different NNs. Enormous practical problems such as target recognition, edge detection, and image segmentation can be described and studied with the help of CNNs. Therefore, increasing interest has been dedicated to exploring the dynamic behaviors of CNNs, such as the passivity and synchronization of CNNs [4–8]. The authors in [4] obtained the global exponential synchronization and passivity conditions of CNNs under impulse control. Wang et al. [5] derived some adequate conditions to ensure the finite-time passivity of directed and undirected CNNs.

Chua [9] first presented the concept of memristor in 1971. Numerous studies have shown that memristor shows the characteristic of pinched hysteresis, that is to say, there is a lag between the application and removal of a field and its succeeding effect, just like neurons in the human brain have [10, 11]. Due to this feature, the past dynamic history of memristor can be remembered, with a substantial similarity to the function of synapses. For this reason, many scholars have been trying to use memristors to simulate neurons to achieve brain-like computation, which leads to the development of memristive neural networks (MNNs) [12, 13]. An increasing number of scholars have recently investigated the dynamical behaviors of coupled MNNs (CMNNs) [14–16]. In [14], a distributed impulsive control strategy is employed to explore the multisynchronization problem of CMNNs. As discussed in [15], several synchronization conditions in finite-time and fixed-time for CMNNs were derived. Wu and Zeng [16] investigated a class of memristive recurrent NNs (MRNNs) and realized the exponential antisynchronization of the drive-response-based coupled MRNNs (CMRNNs).

As a generalization of the real-valued NNs (RVNNs), the state, activation function, connection weight matrix, and

external input of the complex-valued NNs (CVNNs) are all defined in the range of complex numbers. The CVNNs can solve many practical problems which cannot be solved by RVNNs. Thus, it is urgent to explore the dynamic properties of CVNNs, and some achievements have been made in recent years [17–19]. As discussed by Wei et al. [17], the antisynchronization and synchronization problems of complex-valued inertial NNs were studied, and some corresponding adequate conditions for synchronization and antisynchronization of complex-valued inertial NNs were established. The authors in [18] researched the multistability and robustness of CVNNs with delays and input perturbation. Moreover, Wei et al. [19] analyzed the matter of antisynchronization for CVNNs with time-varying delays and leakage delay and proposed several corresponding antisynchronization criteria. Furthermore, a large number of researchers have discussed the synchronization and passivity of complex-valued MNNs (CVMNNs) [20, 21]. In [20], the model of delayed CVMNNs is established for the first time, and some sufficient criteria for the passivity of the given CVMNNs are derived. Zhang et al. [21] discussed the global asymptotical synchronization of fractional-order CVMNNs with both parameter uncertainties and multiple time delays. To the best of the authors' knowledge, there is no research result on the coupled CVMNNs (CCVMNNs) except that some conditions for ensuring passivity and synchronization of CCVMNNs were established in [22].

In the works as mentioned above, the network models about CCVMNNs are coupled by single-weight. As a matter of fact, in the real world, it is more intuitive and convenient to describe some large-scale networks with multiweighted complex dynamical networks (MWCDNs), such as social networks, bus line networks, and communication networks. Hence, the multiweighted coupled neural networks (MWCNNs) as a special type of MWCDNs have received extensive attention [23, 24]. Wang et al. [23] obtained several novel criteria for ensuring finite-time passivity and synchronization of MWCNNs without and with coupling delays by proposing several novel concepts about passivity in finite-time and designing appropriate controllers. The authors derived some passivity and synchronization of MWCNNs by means of designing proportional-integral-derivative controllers [24]. As is known to all, stability is an essential theoretical problem in studying NNs. The introduction of time delays may lead to oscillations or instability or even chaos in the neural network system. Thus, multiweighted coupled complex-valued delayed MNNs (MWCCVDMNNs) is more worthy of being studied. Moreover, it is also important to discuss the MWCCVDMNNs with coupling delays. In [25, 26], the authors studied the multiweighted coupled delayed MNNs (MWCDMNNs) for event-triggered passivity and passivity-based synchronization, but the networks considered in these publications are all real-valued.

It is generally known that antisynchronization of chaotic oscillators is a fascinating phenomenon. Antisynchronization is basically the same type of synchronization that Pecora and Carroll [27] first studied. The only discrepancy is that antisynchronization allows mutually symmetrical chaotic attractors to coexist. More precisely, antisynchronization refers to a phenomenon that the state vectors of the slave systems have the opposite signs but the same amplitude as those of the master system. Hence, the sum of two signals is anticipated to converge to 0 when antisynchronization occurs. So far, a wide range of methods have been proposed for the antisynchronization of chaotic systems, such as adaptive control, direct linear coupling, and nonlinear control. In [28], Ren et al. investigated the antisynchronization of chaotic systems and deduced some sufficient conditions for the given chaotic system to realize antisynchronization.

In many practical situations, antisynchronization has gained widespread use in many areas including image processing, communication systems, and laser. Hence, antisynchronization, like synchronization, also plays a critical role in the study of the dynamic behaviors of CNNs [29, 30]. In [29], some finite-time antisynchronization conditions were derived for the MWCNNs. By integrating the definition of lag synchronization into the definition of decay synchronization, the concept of general decay lag antisynchronization was proposed and obtained several criteria for guaranteeing that multiweighted delayed CNNs with reaction-diffusion terms achieve decay lag antisynchronization [30].

Different from other control methods, pinning control is a very effective control scheme in which only a small fraction of nodes are chosen to be controlled. So far, some scholars have investigated pinning synchronization control problem of the coupled delayed NNs (CDNNs) [31] and CMNNs [32]. In [31], several criteria were proposed to ensure the cluster synchronization of nonlinear CDNNs in both finite-time and fixed-time aspects based on the pinning control strategy. In a previous study [32], Yue et al. addressed the passivity and synchronization of CMNNs by making use of two effective pinning control strategies. However, the investigation on pinning antisynchronization of MWCNNs is very rare [33]. Hou et al. [33] analyzed the pinning antisynchronization of the MWCNNs. To the best of the authors' knowledge, antisynchronization and pinning antisynchronization problems of MWCCVDMNNs have not been researched yet which motivates the study in this paper. Different from the classical pinning control method, what we study in this paper is the networks with discontinuous neurons; in this case, we develop the generalized antisynchronization pinning scheme for this kind of network.

From what has been discussed above, this paper studies two classes of NNs: MWCCVDMNNs and MWCCVDMNNs with coupling delays. The main novelties of our work can be outlined as follows. (1) The network model of CCVDMNNs with multiweights is presented for the first time. (2) By virtue of employing appropriate Lyapunov functional and several inequality techniques, several adequate conditions are proposed to ensure the antisynchronization of MWCCVDMNNs with and without coupling delays. (3) Considering that MWCCVDMNNs are discontinuous neural networks, a novel pinning controller for this type of network is designed to realize the generalized pinning antisynchronization.

2. Preliminaries

2.1. Notations. Let $\mathbb{R}^N$ and $\mathbb{C}^N$ be the N-dimensional real and complex vector space, respectively. The smallest and largest eigenvalue of the corresponding matrix are denoted by $\lambda_m(\cdot)$ and $\lambda_M(\cdot)$, respectively. $\otimes$ represents the Kronecker product. For any complex number $a = a^R + ia^I$, in which $i = \sqrt{-1}$ is the imaginary unit, $a^I, a^R \in \mathbb{R}$ are the imaginary part and real part of a, respectively. For any vector $a(t) \in \mathbb{C}^N$, $\|a(t)\| = \sqrt{a^H(t)a(t)}$, where $a^H(t)$ represents the conjugate transposition of $a(t)$. If the real and imaginary parts of $a(t) \in \mathbb{C}^N$ are denoted by $a^R(t), a^I(t) \in \mathbb{R}^N$, then one has $\|a(t)\| = \sqrt{(a^R(t))^T a^R(t) + (a^I(t))^T a^I(t)}$. Obviously, the vector norm in our paper is Euclidean norm, i.e., L_2 norm. Note that the vector $a(t)$ is a complex vector, and the norm of $a(t)$ is the square of $a^H(t)a(t) = (a^R(t))^T a^R(t) + (a^I(t))^T a^I(t)$.

2.2. Lemmas

Lemma 1 (see [34]). *For any real vectors $\alpha_1, \alpha_2 \in \mathbb{R}^n$ and matrix $0 < \Xi \in \mathbb{R}^{n\times n}$,*

$$2\alpha_1^T\alpha_2 \le \alpha_1^T\Xi\alpha_1 + \alpha_2^T\Xi^{-1}\alpha_2. \tag{1}$$

Lemma 2 (see [35]). *Let A, B, C, and D be matrices with compatible dimensions and $a \in \mathbb{R}$. Then,*

$$\begin{aligned}
&(1)\,(aA)\otimes B = A\otimes(aB);\\
&(2)\,(A\otimes B)^T = A^T\otimes B^T;\\
&(3)\,(A\otimes B)(C\otimes D) = (AC)\otimes(B\ D);\\
&(4)\,(A+B)\otimes C = A\otimes C + B\otimes C.
\end{aligned} \tag{2}$$

3. Antisynchronization and Generalized Pinning Antisynchronization of MWCCVDMNNs

3.1. Antisynchronization of MWCCVDMNNs. In this paper, a single model of CVDMNN is presented as follows:

$$\begin{aligned}
\dot{a}_s(t) &= -d_s a_s(t) + \sum_{h=1}^{n} p_{sh}(a_s(t))\, y_h(a_h(t-u_h(t))),\\
s &= 1,2,\ldots,n,
\end{aligned} \tag{3}$$

where the complex-valued $a_s(t)$ indicates the state variable associated with the s-th neuron; $d_s > 0$ represents the self-feedback coefficient; $p_{sh}(a_s(t))$ stands for the weight of the synaptic connection of complex-valued memristor; the complex-valued nonlinear function $y_h(\cdot)$ denotes the activation function of the h-th neuron; $u_h(t)$ is the time-varying delay with $0 \le u_h(t) \le u_h \le u = \max_{h=1,2,\ldots,n}\{u_h\}$ and $\dot{u}_h(t) \le \varrho_h < 1$.

Let

$$\begin{aligned}
a_s(t) &= a_s^R(t) + ia_s^I(t),\ p_{sh}(a_s(t))\\
&= p_{sh}^R\big(a_s^R(t)\big) + ip_{sh}^I\big(a_s^I(t)\big),\ y_h(a_h(t-u_h(t))\\
&= y_h^R\big(a_h^R(t-u_h(t))\big) + iy_h^I a_h^I(t-u_h(t))\big),
\end{aligned} \tag{4}$$

where $a_s^I(t), p_{sh}^I(a_s^I(t)), y_h^I(a_h^I(t-u_h(t)))$ are the imaginary parts of $a_s(t), p_{sh}(a_s(t)), y_h(a_h(t-u_h(t)))$ and $a_s^R(t)$, $p_{sh}^R(a_s^R(t)), y_h^R(a_h^R(t-u_h(t)))$ are the real parts of $a_s(t), p_{sh}(a_s(t)), y_h(a_h(t-u_h(t)))$.

According to the characteristics of memristor's current and voltage, one has

$$\begin{aligned}
p_{sh}^R\big(a_s^R(t)\big) &= \begin{cases} \widehat{p}_{sh}^R, & \left|a_s^R(t)\right| \le \Lambda_s,\\ \check{p}_{sh}^R, & \left|a_s^R(t)\right| > \Lambda_s,\end{cases}\\
p_{sh}^I\big(a_s^I(t)\big) &= \begin{cases} \widehat{p}_{sh}^I, & \left|a_s^I(t)\right| \le \Lambda_s,\\ \check{p}_{sh}^I, & \left|a_s^I(t)\right| > \Lambda_s,\end{cases}
\end{aligned} \tag{5}$$

where $s, h \in \{1,2,\ldots,n\}$; $\widehat{p}_{sh}^R, \check{p}_{sh}^R, \widehat{p}_{sh}^I, \check{p}_{sh}^I$ are constants; $\Gamma_s > 0$ represents the threshold level. Let $\widetilde{p}_{sh}^R = \max\{|\widehat{p}_{sh}^R|, |\check{p}_{sh}^R|\}$, $\widetilde{p}_{sh}^I = \max\{|\widehat{p}_{sh}^I|, |\check{p}_{sh}^I|\}$, $\overline{p}_{sh}^R = |\widehat{p}_{sh}^R - \check{p}_{sh}^R|$, $\overline{p}_{sh}^I = |\widehat{p}_{sh}^I - \check{p}_{sh}^I|$, $\overline{P}^R = (\overline{p}_{sh}^R)_{n\times n}$, $\overline{P}^I = (\overline{p}_{sh}^I)_{n\times n}$, $\widetilde{P}^R = \mathrm{diag}(\sum_{h=1}^n (\widetilde{p}_{1h}^R)^2, \sum_{h=1}^n (\widetilde{p}_{2h}^R)^2, \ldots, \sum_{h=1}^n (\widetilde{p}_{nh}^R)^2)$, and $\widetilde{P}^I = \mathrm{diag}(\sum_{h=1}^n (\widetilde{p}_{1h}^I)^2, \sum_{h=1}^n (\widetilde{p}_{2h}^I)^2, \ldots, \sum_{h=1}^n (\widetilde{p}_{nh}^I)^2)$.

In the following, we consider the MWCCVDMNNs made up of N CVDMNNs as (3)

$$\begin{aligned}
\dot{A}_\delta(t) &= -DA_\delta(t) + P(A_\delta(t))\, y\big(\overline{A_\delta(t)}\big) + c_\delta(t)\\
&\quad + \sum_{\epsilon=1}^{\eta}\sum_{\kappa=1}^{N} l_\epsilon K_{\delta\kappa}^\epsilon H_\epsilon A_\kappa(t),\ \delta = 1,2,\ldots,N,
\end{aligned} \tag{6}$$

in which the complex-valued vector $A_\delta(t) = (A_{\delta1}(t), A_{\delta2}(t), \ldots, A_{\delta n}(t))^T \in \mathbb{C}^n$ denotes the state vector for the δ-th node; $0 < D = \mathrm{diag}(d_1, d_2, \ldots, d_n) \in \mathbb{R}^{n\times n}$, $\overline{A_\delta(t)} = (A_{\delta1}(t-u_1(t)), A_{\delta2}(t-u_2(t)), \ldots, A_{\delta n}(t-u_n(t)))^T \in \mathbb{C}^n$, $y(\overline{A_\delta(t)}) = (y_1(A_{\delta1}(t-u_1(t))), y_2(A_{\delta2}(t-u_2(t))), \cdots, y_n(A_{\delta n}(t-u_n(t))))^T \in \mathbb{C}^n$, and $H_\epsilon \in \mathbb{R}^{n\times n}(\epsilon = 1,2,\ldots,\eta)$ is an internally coupled matrix; $P(A_\delta(t)) = (p_{sh}(A_{\delta s}(t)))_{n\times n} \in \mathbb{C}^{n\times n}$; $c_\delta(t) = c_\delta^R(t) + ic_\delta^I(t) = (c_{\delta1}(t), c_{\delta2}(t), \ldots, c_{\delta n}(t))^T \in \mathbb{C}^n$ represents the controller; $\mathbb{R} \ni l_\epsilon > 0\,(\epsilon = 1,2,\ldots,\eta)$ symbols coupling strength for the ϵ-th coupling form; $K^\epsilon = (K_{\delta\kappa}^\epsilon)_{N\times N} \in \mathbb{R}^{N\times N}(\epsilon = 1,2,\ldots,\eta)$ describes the outer coupling matrix, where $\mathbb{R} \ni K_{\delta\kappa}^\epsilon > 0$, if there is a connection from node ι to node $\kappa(\delta \ne \kappa)$; otherwise, $\mathbb{R} \ni K_{\delta\kappa}^\epsilon = 0$.

$$K_{\delta\delta}^\epsilon = -\sum_{\substack{k=1\\ k\ne\delta}}^{N} K_{\delta\kappa}^\epsilon,\ \delta = 1,2,\ldots,N. \tag{7}$$

Remark 1. CVNNs, as an extension of RVNNs, can solve some problems which cannot be dealt by RVNNs because their states, activation functions, and connection weights are

all complex-valued. For instance, the detection of symmetric problem and the XOR problem cannot be modelled by a single real-valued neuron, but they can be achieved by a single complex-valued neuron with the orthogonal decision boundaries [36]. Moreover, it is more suitable to describe various physical phenomena (e.g., the phase progression and retardation, the superposition of fields, and the wave propagation) through complex numbers in reality, all of which can be drawn as the applications of CVNNs. Naturally, CVNNs have found widespread practical applications in physical systems dealing with quantum waves, ultrasonic, and electromagnetic waves. Therefore, it is very meaningful to consider the characteristic of complex-value when studying CMNNs.

Then, separating network (6) into the following imaginary and real parts:

$$\begin{aligned}\dot{A}_\delta^R(t) &= -DA_\delta^R(t) + P^R\left(A_\delta^R(t)\right)y^R\left(\overline{A_t^R(t)}\right) + \sum_{\epsilon=1}^{\eta}\sum_{\kappa=1}^{N} l_\epsilon K_{\delta\kappa}^\epsilon H_\epsilon A_\kappa^R(t)\\ &\quad -P^I\left(A_\delta^I(t)\right)y^I\left(\overline{A_\delta^I(t)}\right) + c_\delta^R(t),\\ \dot{A}_\delta^I(t) &= -DA_\delta^I(t) + P^R\left(A_\delta^R(t)\right)y^I\left(\overline{A_\delta^I(t)}\right) + \sum_{i=1}^{\eta}\sum_{\kappa=1}^{N} l_\epsilon K_{\iota\kappa}^\epsilon H_\epsilon A_\kappa^I(t)\\ &\quad +P^I\left(A_\delta^I(t)\right)y^R\left(\overline{A_\delta^R(t)}\right) + c_\delta^I(t),\end{aligned} \tag{8}$$

where $y^R(\overline{A_\delta^R(t)}) = (y_1^R(A_{\delta1}^R(t-u_1(t))),\ y_2^R(A_{\delta2}^R(t-u_2(t))),\ldots,y_n^R(A_{\delta n}^R(t-u_n(t))))^T$, $y^I(\overline{A_\delta^I(t)}) = (y_1^I(A_{\delta1}^I(t-u_1(t))), y_2^I(A_{\delta2}^I(t-u_2(t))),\ldots,y_n^I(A_{\delta n}^I(t-u_n(t))))^T$, $A_\delta^R(t) = (A_{\delta1}^R(t), A_{\delta2}^R(t),\ldots,A_{\delta n}^R(t))^T$, $P^R(\cdot) = (p_{sh}^R(\cdot))_{n\times n}$, $A_\delta^I(t) = (A_{\delta1}^I(t), A_{\delta2}^I(t),\ldots,A_{\delta n}^I(t))^T$, $c_\delta^R(t) = (c_{\delta1}^R(t), c_{\delta2}^R(t),\ldots,c_{\delta n}^R(t))^T$, and $P^I(\cdot) = (p_{sh}^I(\cdot))_{n\times n}$, $c_\delta^I(t) = (c_{\delta1}^I(t), c_{\delta2}^I(t),\ldots,c_{\delta n}^I(t))^T$.

Assumption 1. For all $\beta_1, \beta_2 \in \mathbb{R}$, there exist real numbers $Y_\delta^R, Y_\delta^I, j_\delta^R, j_\delta^R > 0$ such that

$$\begin{gathered}\left|y_\delta^R(\cdot)\right| \le Y_\delta^R, \left|y_\delta^I(\cdot)\right| \le Y_\delta^I,\\ \left|y_\delta^R(\beta_1) + y_\delta^R(\beta_2)\right| \le j_\delta^R\left|\beta_1 + \beta_2\right|,\\ \left|y_\delta^I(\beta_1) + y_\delta^I(\beta_2)\right| \le j_\delta^I\left|\beta_1 + \beta_2\right|.\end{gathered} \tag{9}$$

For the network (6), assume that $A_*(t) = (A_{*1}(t), A_{*2}(t),\ldots,A_{*n}(t))^T \in \mathbb{C}^n \in \mathbb{C}^n$ is an arbitrary solution, then

$$\dot{A}_*(t) = -DA_*(t) + P\left(A_*(t)\right)y\left(A_*(t)\right). \tag{10}$$

Here, $A_*(t) = A_*^R(t) + iA_*^I(t)$. Then, (10) can be expressed by separating it into the following two real systems:

$$\begin{aligned}\dot{A}_*^R(t) &= -DA_*^R(t) + P^R\left(A_*^R(t)\right)y^R\left(A_*^R(t)\right)\\ &\quad - P^I\left(A_*^I(t)\right)y^I\left(A_*^I(t)\right),\\ \dot{A}_*^I(t) &= -DA_*^I(t) + P^R\left(A_*^R(t)\right)y^I\left(A_*^I(t)\right)\\ &\quad + P^I\left(A_*^I(t)\right)y^R\left(A_*^R(t)\right).\end{aligned} \tag{11}$$

Let $z_\delta(t) = A_\delta(t) + A_*(t)$, then

$$\begin{aligned}\dot{z}_\delta(t) &= -Dz_\delta(t) + P\left(A_\delta(t)\right)y\left(\overline{A_\delta(t)}\right)\\ &\quad + c_\delta(t) + P\left(A_*(t)\right)y\left(A_*(t)\right)\\ &\quad + \sum_{\epsilon=1}^{\eta}\sum_{\kappa=1}^{N} l_\epsilon K_{\delta\kappa}^\epsilon H_\epsilon z_\kappa(t),\end{aligned} \tag{12}$$

where $z_\delta(t) = (z_{\delta1}(t), z_{\delta2}(t),\ldots,z_{\delta n}(t))^T$, $\delta = 1,2,\ldots,N$.

Then, the decomposition form of (12) can be expressed as

$$\begin{aligned}\dot{z}_\delta^R(t) &= -Dz_\delta^R(t) + P^R\left(A_\delta^R(t)\right)G^R\left(\overline{z_\delta^R(t)}\right)\\ &\quad - P^I\left(A_\delta^I(t)\right)G^I\left(\overline{z_\delta^I(t)}\right)\\ &\quad -\left(P^R\left(A_\delta^R(t)\right) - P^R\left(A_*^R(t)\right)\right)y^R\left(A_*^R(t)\right) + c_\delta^R(t)\\ &\quad + \left(P^I\left(A_\delta^I(t)\right) - P^I\left(A_*^I(t)\right)\right)y^I\left(A_*^I(t)\right)\\ &\quad + \sum_{\epsilon=1}^{\eta}\sum_{\kappa=1}^{N} l_\epsilon K_{\iota\kappa}^\epsilon H_\epsilon z_\kappa^R(t),\\ \dot{z}_\delta^I(t) &= -Dz_\delta^I(t) + P^R\left(A_\delta^R(t)\right)G^I\left(\overline{z_\delta^I(t)}\right)\\ &\quad + P^I\left(A_\delta^I(t)\right)G^R\left(\overline{z_\delta^R(t)}\right)\\ &\quad -\left(P^R\left(A_\delta^R(t)\right) - P^R\left(A_*^R(t)\right)\right)y^I\left(A_*^I(t)\right) + c_\delta^I(t)\\ &\quad -\left(P^I\left(A_\delta^I(t)\right) - P^I\left(A_*^I(t)\right)\right)y^R\left(A_*^R(t)\right)\\ &\quad + \sum_{\epsilon=1}^{\eta}\sum_{\kappa=1}^{N} l_\epsilon K_{\epsilon\kappa}^\epsilon H_\epsilon z_\kappa^I(t),\end{aligned} \tag{13}$$

where $z_\delta^R(t) = (z_{\delta1}^R(t), z_{\delta2}^R(t),\ldots,z_{\delta n}^R(t))^T$, $z_\delta^I(t) = (z_{\delta1}^I(t), z_{\delta2}^I(t),\ldots,z_{\delta n}^I(t))^T$, $\overline{z_\delta^R(t)} = (z_{\delta1}^R(t-u_1(t)), z_{\delta2}^R(t-u_2(t)),\ldots,z_{\delta n}^R(t-u_n(t)))^T$, $\overline{z_\delta^I(t)} = (z_{\delta1}^I(t-u_1(t)), z_{\delta2}^I(t-u_2(t)),\ldots,z_{\delta n}^I(t-u_n(t)))^T$, $G^R(\overline{z_\delta^R(t)}) = y^R(\overline{A_\delta^R(t)}) + y^R(A_*^R(t))$, and $G^I(\overline{z_\delta^I(t)}) = y^I(\overline{A_\delta^I(t)}) + y^I(A_*^I(t))$.

Definition 1. The network (6) is said to be antisynchronized if

$$\lim_{t\longrightarrow+\infty}\left\|A_\delta(t) + A_*(t)\right\| = 0, \text{for all } \delta = 1,2,\ldots,N. \tag{14}$$

In this paper, the authors construct the following controller for the MWCCVDMNNs (6):

$$\begin{aligned} c_\delta^R(t) &= -\Theta_\delta^R z_\delta^R(t) - \operatorname{sign}\left(z_\delta^R(t)\right)\left(\overline{P}^R\overline{Y}^R + \overline{P}^I\overline{Y}^I\right), \\ c_\delta^I(t) &= -\Theta_\delta^I z_\delta^I(t) - \operatorname{sign}\left(z_\delta^I(t)\right)\left(\overline{P}^R\overline{Y}^I + \overline{P}^I\overline{Y}^R\right), \end{aligned} \tag{15}$$

where $\delta = 1, 2, \ldots, N$; $\mathbb{R} \ni v_\delta^R > 0$ and $\mathbb{R} \ni v_\delta^I > 0$; $\overline{Y}^R = (Y_1^R, Y_2^R, \ldots, Y_n^R)^T$; $\Theta_\delta^R = \operatorname{diag}(v_{\delta 1}^R, v_{\delta 2}^R, \ldots, v_{\delta n}^R) \in \mathbb{R}^{n\times n}$ and $\Theta_\delta^I = \operatorname{diag}(v_{\delta 1}^I, v_{\delta 2}^I, \ldots, v_{\delta n}^I) \in \mathbb{R}^{n\times n}$ are the positive definite control gain matrices; sign $(z_\delta^R(t)) = \operatorname{diag}$ (sign $(z_{\delta 1}^R(t))$, sign $(z_{\delta 2}^R(t)), \ldots,$ sign $(z_{\delta n}^R(t)))$; $\overline{Y}^I = (Y_1^I, Y_2^I, \ldots, Y_n^I)^T$; and sign $(z_\delta^I(t)) = \operatorname{diag}$ (sign $(z_{\delta 1}^I(t))$, sign $(z_{\delta 2}^I(t)), \ldots,$ sign $(z_{\delta n}^I(t)))$.

For convenience, some symbols are denoted as follows:

$$\begin{aligned} z^R(t) &= \left(\left(z_1^R(t)\right)^T, \left(z_2^R(t)\right)^T, \ldots, \left(z_N^R(t)\right)^T\right)^T, \\ z^I(t) &= \left(\left(z_1^I(t)\right)^T, \left(z_2^I(t)\right)^T, \ldots, \left(z_N^I(t)\right)^T\right)^T, \\ \overline{z^R(t)} &= \left(\left(\overline{z_1^R(t)}\right)^T, \left(\overline{z_2^R(t)}\right)^T, \ldots, \left(\overline{z_N^R(t)}\right)^T\right)^T, \\ \overline{z^I(t)} &= \left(\left(\overline{z_1^I(t)}\right)^T, \left(\overline{z_2^I(t)}\right)^T, \ldots, \left(\overline{z_N^I(t)}\right)^T\right)^T, \\ J^R &= \operatorname{diag}\left(\left(j_1^R\right)^2, \left(j_2^R\right)^2, \ldots, \left(j_n^R\right)^2\right), \\ J^I &= \operatorname{diag}\left(\left(j_1^I\right)^2, \left(j_2^I\right)^2, \ldots, \left(j_n^I\right)^2\right), \\ \Lambda &= \operatorname{diag}\left(\frac{1}{1-\varrho_1}, \frac{1}{1-\varrho_2}, \ldots, \frac{1}{1-\varrho_n}\right). \end{aligned} \tag{16}$$

Theorem 1. *The antisynchronization of network (6) can be realized under the controller (15) if the following conditions hold:*

$$\Phi_1^R < 0 \text{and} \Phi_1^I < 0, \tag{17}$$

where $\Phi_1^R = I_N \otimes (-2D + \widetilde{P}^R + \widetilde{P}^I + 2J^R\Lambda) - 2\Theta^R + \sum_{\epsilon=1}^{\eta} l_\epsilon [K^\epsilon \otimes H_\epsilon + (K^\epsilon)^T \otimes H_\epsilon^T]$, $\Phi_1^I = I_N \otimes (-2D + \widetilde{P}^R + \widetilde{P}^I + 2J^I\Lambda) - 2\Theta^I + \sum_{\epsilon=1}^{\eta} l_\epsilon [K^\epsilon \otimes H_\epsilon + (K^\epsilon)^T \otimes H_\epsilon^T]$; $\Theta^R = diag(\Theta_1^R, \Theta_2^R, \ldots, \Theta_N^R) \in \mathbb{R}^{nN\times nN}$, *and* $\Theta^I = diag(\Theta_1^I, \Theta_2^I, \ldots, \Theta_N^I) \in \mathbb{R}^{nN\times nN}$.

Proof. Consider the Lyapunov function as

$$\begin{aligned} V_1(t) = &\sum_{\delta=1}^{N} \left(z_\delta^R(t)\right)^T z_\delta^R(t) + 2\sum_{\delta=1}^{N}\sum_{h=1}^{n} \int_{t-u_h(t)}^{t} \frac{\left(j_h^R z_{\delta h}^R(\varepsilon)\right)^2}{1-\varrho_h} d\varepsilon \\ &+ 2\sum_{\delta=1}^{N}\sum_{h=1}^{n} \int_{t-u_h(t)}^{t} \frac{\left(j_h^I z_{\delta h}^I(\varepsilon)\right)^2}{1-\varrho_h} d\varepsilon + \sum_{\delta=1}^{N} \left(z_\delta^I(t)\right)^T z_\delta^I(t). \end{aligned} \tag{18}$$

Then, one can yield

$$\begin{aligned} \dot{V}_1(t) \le 2\sum_{\delta=1}^{N} \left(z_\delta^R(t)\right)^T \Bigg\{ &-Dz_\delta^R(t) + P^R\left(A_\delta^R(t)\right)G^R\left(\overline{z_\delta^R(t)}\right) - P^I\left(A_\delta^I(t)\right)G^I\left(\overline{z_\delta^I(t)}\right) + \sum_{\epsilon=1}^{\eta}\sum_{\kappa=1}^{N} l_\epsilon K_{\iota\kappa}^\epsilon H_\epsilon z_\kappa^R(t) \\ &-\Theta_\delta^R z_\delta^R(t) - \operatorname{sign}\left(z_\delta^R(t)\right)\left(\overline{P}^R\overline{Y}^R \right. \\ &\left. + \overline{P}^I\overline{Y}^I\right) - \left[P^R\left(A_\delta^R(t)\right) - P^R\left(A_*^R(t)\right)\right]y^R\left(A_*^R(t)\right) + \left[P^I\left(A_\delta^I(t)\right) - P^I\left(A_*^I(t)\right)\right]y^I\left(A_*^I(t)\right)\Bigg\} + 2\sum_{\delta=1}^{N}\left(z_\delta^I(t)\right)^T\Big\{-Dz_\delta^I(t) \\ &+ P^R\left(A_\delta^R(t)\right)G^I\left(\overline{z_\delta^I(t)}\right) + P^I\left(A_\delta^I(t)\right)G^R\left(\overline{z_\delta^R(t)}\right) + \sum_{\epsilon=1}^{\eta}\sum_{\kappa=1}^{N} l_\epsilon K_{\iota\kappa}^\epsilon H_\epsilon z_\kappa^I(t) - \Theta_\delta^I z_\delta^I(t) - \operatorname{sign}\left(z_\delta^I(t)\right)\left(\overline{P}^R\overline{Y}^I + \overline{P}^I\overline{Y}^R\right) - \left[P^R\left(A_\delta^R(t)\right)\right. \\ &\left. - P^R\left(A_*^R(t)\right)\right]y^I\left(A_*^I(t)\right) - \left[P^I\left(A_\delta^I(t)\right) - P^I\left(A_*^I(t)\right)\right]y^R\left(A_*^R(t)\right)\Big\} + 2\left(z^R(t)\right)^T\left(I_N \otimes \left(J^R\Lambda\right)\right)z^R(t) \\ &- 2\left(\overline{z^R(t)}\right)^T\left(I_N \otimes J^R\right)\overline{z^R(t)} + 2\left(z^I(t)\right)^T\left(I_N \otimes \left(J^I\Lambda\right)\right)z^I(t) - 2\left(\overline{z^I(t)}\right)^T\left(I_N \otimes J^I\right)\overline{z^I(t)}. \end{aligned} \tag{19}$$

From Assumption 1, we can deduce

$$\begin{aligned}
&2\sum_{\delta=1}^{N}\left(z_{\delta}^{R}(t)\right)^{T}P^{R}\left(A_{\delta}^{R}(t)\right)G^{R}\left(\overline{z_{\delta}^{R}(t)}\right)\\
&\leq 2\sum_{\delta=1}^{N}\sum_{s=1}^{n}\sum_{h=1}^{n}\left|z_{\delta s}^{R}(t)\left|\widetilde{p}_{sh}^{R}\right|y_{h}^{R}\left(\overline{A_{\delta h}^{R}(t)}\right)+y_{h}^{R}\left(A_{*h}^{R}(t)\right)\right|\\
&\leq \sum_{\delta=1}^{N}\sum_{s=1}^{n}\sum_{h=1}^{n}\left(z_{\delta s}^{R}(t)\right)^{2}\left(\widetilde{p}_{sh}^{R}\right)^{2}+\sum_{\delta=1}^{N}\sum_{h=1}^{n}\left(j_{h}^{R}\right)^{2}\left(\overline{z_{\delta h}^{R}(t)}\right)^{2}\\
&=\left(z^{R}(t)\right)^{T}\left(I_{N}\otimes\widetilde{P}^{R}\right)z^{R}(t)+\left(\overline{z^{R}(t)}\right)^{T}\left(I_{N}\otimes J^{R}\right)\overline{z^{R}(t)}
\end{aligned}\tag{20}$$

and

$$\begin{aligned}
&-2\sum_{\delta=1}^{N}\left(z_{\delta}^{R}(t)\right)^{T}P^{I}\left(A_{\delta}^{I}(t)\right)G^{I}\left(\overline{z_{\delta}^{I}(t)}\right)\\
&\quad\leq\left(z^{R}(t)\right)^{T}\left(I_{N}\otimes\widetilde{P}^{I}\right)z^{R}(t)+\left(\overline{z^{I}(t)}\right)^{T}\left(I_{N}\otimes J^{I}\right)\overline{z^{I}(t)},
\end{aligned}\tag{21}$$

$$\begin{aligned}
&2\sum_{\delta=1}^{N}\left(z_{\delta}^{I}(t)\right)^{T}P^{R}\left(A_{\delta}^{R}(t)\right)G^{I}\left(\overline{z_{\delta}^{I}(t)}\right)\\
&\quad\leq\left(z^{I}(t)\right)^{T}\left(I_{N}\otimes\widetilde{P}^{R}\right)z^{I}(t)+\left(\overline{z^{I}(t)}\right)^{T}\left(I_{N}\otimes J^{I}\right)\overline{z^{I}(t)},
\end{aligned}\tag{22}$$

$$\begin{aligned}
&2\sum_{\delta=1}^{N}\left(z_{\delta}^{I}(t)\right)^{T}P^{I}\left(A_{\delta}^{I}(t)\right)G^{R}\left(\overline{z_{\delta}^{R}(t)}\right)\\
&\quad\leq\left(z^{I}(t)\right)^{T}\left(I_{N}\otimes\widetilde{P}^{I}\right)z^{I}(t)+\left(\overline{z^{R}(t)}\right)^{T}\left(I_{N}\otimes J^{R}\right)\overline{z^{R}(t)}.
\end{aligned}\tag{23}$$

In addition,

$$\begin{aligned}
&2\sum_{\epsilon=1}^{\eta}\sum_{\delta=1}^{N}\sum_{\kappa=1}^{N}l_{\epsilon}K_{\delta\kappa}^{\epsilon}\left(z_{\delta}^{R}(t)\right)^{T}H_{\epsilon}z_{\kappa}^{R}(t)\\
&\quad=\left(z^{R}(t)\right)^{T}\left[\sum_{\epsilon=1}^{\eta}l_{\epsilon}\left(K^{\epsilon}\otimes H_{\epsilon}+\left(K^{\epsilon}\right)^{T}\otimes H_{\epsilon}^{T}\right)\right]z^{R}(t).
\end{aligned}\tag{24}$$

Similarly,

$$\begin{aligned}
&2\sum_{\epsilon=1}^{\eta}\sum_{\delta=1}^{N}\sum_{\kappa=1}^{N}l_{\epsilon}K_{\iota\kappa}^{\epsilon}\left(z_{\delta}^{I}(t)\right)^{T}H_{\delta}z_{\kappa}^{I}(t)\\
&\quad=\left(z^{I}(t)\right)^{T}\left[\sum_{\epsilon=1}^{\eta}l_{\epsilon}\left(K^{\epsilon}\otimes H_{\epsilon}+\left(K^{\epsilon}\right)^{T}\otimes H_{\epsilon}^{T}\right)\right]z^{I}(t).
\end{aligned}\tag{25}$$

Furthermore,

$$\begin{aligned}
&2\sum_{\delta=1}^{N}\left(z_{\delta}^{R}(t)\right)^{T}\left[P^{R}\left(A_{\delta}^{R}(t)\right)-P^{R}\left(A_{*}^{R}(t)\right)\right]y^{R}\left(A_{*}^{R}(t)\right)\\
&\quad=2\sum_{\delta=1}^{N}\sum_{h=1}^{n}\sum_{s=1}^{n}\left|z_{\delta s}^{R}(t)\right|\left[p_{sh}^{R}\left(A_{\delta s}^{R}(t)\right)-p_{sh}^{R}\left(A_{*s}^{R}(t)\right)\right]y_{h}^{R}\left(A_{*h}^{R}(t)\right)\\
&\quad\leq 2\sum_{\delta=1}^{N}\sum_{h=1}^{n}\sum_{s=1}^{n}\left|z_{\delta s}^{R}(t)\right|\left\|\widetilde{p}_{sh}^{R}-\breve{p}_{sh}^{R}\right|Y_{h}^{R}\\
&\quad=2\sum_{\delta=1}^{N}\left|\left(z_{\delta}^{R}(t)\right)^{T}\right|\overline{P}^{R}\overline{Y}^{R}.
\end{aligned}\tag{26}$$

Likewise,

$$\begin{aligned}
&2\sum_{\delta=1}^{N}\left(z_{\delta}^{R}(t)\right)^{T}\left[P^{I}\left(A_{\delta}^{I}(t)\right)-P^{I}\left(A_{*}^{I}(t)\right)\right]y^{I}\left(A_{*}^{I}(t)\right)\\
&\quad\leq 2\sum_{\delta=1}^{N}\left|\left(z_{\delta}^{R}(t)\right)^{T}\right|\overline{P}^{I}\overline{Y}^{I},
\end{aligned}\tag{27}$$

$$\begin{aligned}
&2\sum_{\delta=1}^{N}\left(z_{\delta}^{I}(t)\right)^{T}\left[P^{R}\left(A_{\delta}^{R}(t)\right)-P^{R}\left(A_{*}^{R}(t)\right)\right]y^{I}\left(A_{*}^{I}(t)\right)\\
&\quad\leq 2\sum_{\delta=1}^{N}\left|\left(z_{\delta}^{I}(t)\right)^{T}\right|\overline{P}^{R}\overline{Y}^{I},
\end{aligned}\tag{28}$$

$$\begin{aligned}
&2\sum_{\delta=1}^{N}\left(z_{\delta}^{I}(t)\right)^{T}\left[P^{I}\left(A_{\delta}^{I}(t)\right)-P^{I}\left(A_{*}^{I}(t)\right)\right]y^{R}\left(A_{*}^{R}(t)\right)\\
&\quad\leq 2\sum_{\delta=1}^{N}\left|\left(z_{\delta}^{I}(t)\right)^{T}\right|\overline{P}^{I}\overline{Y}^{R}.
\end{aligned}\tag{29}$$

It then follows from (19)–(29) that

$$\begin{aligned}
\dot{V}_{1}(t)\leq&\left(z^{R}(t)\right)^{T}\left\{I_{N}\otimes\left(-2D+\widetilde{P}^{R}+\widetilde{P}^{I}+2J^{R}\Lambda\right)-2\Theta^{R}+\sum_{\epsilon=1}^{\eta}l_{\epsilon}\left[K^{\epsilon}\otimes H_{\epsilon}+\left(K^{\epsilon}\right)^{T}\otimes H_{\epsilon}^{T}\right]\right\}z^{R}(t)\\
&+\left(z^{I}(t)\right)^{T}\left\{I_{N}\otimes\left(-2D+\widetilde{P}^{R}+\widetilde{P}^{I}+2J^{I}\Lambda\right)-2\Theta^{I}+\sum_{\epsilon=1}^{\eta}l_{\epsilon}\left[K^{\epsilon}\otimes H_{\epsilon}+\left(K^{\epsilon}\right)^{T}\otimes H_{\epsilon}^{T}\right]\right\}z^{I}(t)\\
\leq&\,\alpha_{1}\|z(t)\|^{2},
\end{aligned}\tag{30}$$

where $\alpha_1=\max\{\lambda_M(\Phi_1^R),\lambda_M(\Phi_1^I)\}<0$.

From (30) and the construction of $V_1(t)$, one can obtain that $V_1(t)$ is a bounded function that does not increase. Therefore, $V_1(t)$ converges to a nonnegative constant when $t\longrightarrow+\infty$. In addition, according to (30), we can get

$$\|z(t)\|^{2}\leq\frac{\dot{V}_{1}(t)}{\alpha_{1}}.\tag{31}$$

From (31), one can infer that $\lim_{t\longrightarrow+\infty}\int_0^t\|z(\varepsilon)\|^2d\varepsilon$ exists and is a nonnegative real number. Furthermore,

$$\begin{aligned}0 &\le \lim_{t\longrightarrow+\infty}\sum_{\delta=1}^{N}\sum_{h=1}^{n}\int_{t-u_h(t)}^{t}\frac{2\left(j_h^R z_{\delta h}^R(\varepsilon)\right)^2}{1-\varrho_h}d\varepsilon\\ &\le \lim_{t\longrightarrow+\infty}\int_{t-u}^{t}\left(z^R(\varepsilon)\right)^T\left[I_N\otimes\left(2J^R\Lambda\right)\right]z^R(\varepsilon)d\varepsilon\\ &\le \lambda_M\left(I_N\otimes\left(2J^R\Lambda\right)\right)\lim_{t\longrightarrow+\infty}\int_{t-u}^{t}\|z(\varepsilon)\|^2 d\varepsilon\\ &= 0.\end{aligned} \tag{32}$$

Similarly,

$$0 \le \lim_{t\longrightarrow+\infty}\sum_{\delta=1}^{N}\sum_{h=1}^{n}\int_{t-u_h(t)}^{t}\frac{2\left(j_h^I z_{\delta h}^I(\varepsilon)\right)^2}{1-\varrho_h}d\varepsilon = 0. \tag{33}$$

From (32) and (33), we know that $\lim_{t\longrightarrow+\infty}\sum_{\delta=1}^{N}[(z_\delta^R(t))^T z_\delta^R(t)+(z_\delta^I(t))^T(z_\delta^I(t))]$ exists and is a nonnegative real number. In the next, we will prove $\lim_{t\longrightarrow+\infty}\sum_{\delta=1}^{N}[(z_\delta^R(t))^T z_\delta^R(t)+(z_\delta^I(t))^T z_\delta^I(t)]=0$. If this is not true, we have

$$\lim_{t\longrightarrow+\infty}\sum_{\delta=1}^{N}\left[\left(z_\delta^R(t)\right)^T z_\delta^R(t)+\left(z_\delta^I(t)\right)^T z_\delta^I(t)\right]=\theta>0. \tag{34}$$

In other words, there exists a positive real constant $\widehat{\omega}$ such that

$$\sum_{\delta=1}^{N}\left[\left(z_\delta^R(t)\right)^T z_\delta^R(t)+\left(z_\delta^I(t)\right)^T z_\delta^I(t)\right]>\frac{\theta}{2}\text{for } t\ge\widehat{\omega}. \tag{35}$$

Hence,

$$\|z(t)\|^2>\frac{\theta}{2},\text{when } t\ge\widehat{\omega}. \tag{36}$$

From (30) and (36), we can obtain

$$\dot{V}_1(t)<\frac{\alpha_1\theta}{2}, t\ge\widehat{\omega}. \tag{37}$$

Then, according to (37), one gets

$$\begin{aligned}-V_1(\widehat{\omega}) &\le V_1(+\infty)-V_1(\widehat{\omega})\\ &= \int_{\widehat{\omega}}^{+\infty}\dot{V}_1(t)dt < \int_{\widehat{\omega}}^{+\infty}\frac{\alpha_1\theta}{2}dt=-\infty,\end{aligned} \tag{38}$$

which leads to contradiction. Therefore,

$$\lim_{t\longrightarrow+\infty}\sum_{\delta=1}^{N}\left[\left(z_\delta^R(t)\right)^T z_\delta^R(t)+\left(z_\delta^I(t)\right)^T z_\delta^I(t)\right]=0. \tag{39}$$

Then, we have

$$\lim_{t\longrightarrow+\infty}\|z(t)\|=0, \tag{40}$$

which means that the network (6) achieves antisynchronization. □

3.2. Generalized Pinning Antisynchronization of MWCCVDMNNs. In the following, we generalize the traditional pinning control method. One part of the controller we designed controls all the nodes, and the other part controls the first m nodes of network (6). Then, the MWCCVDMNNs with corresponding pinning controller is described by

$$\begin{aligned}\dot{A}_\delta(t) &= -DA_\delta(t)+P\left(A_\delta(t)\right)y\left(\overline{A_\delta(t)}\right)\\ &\quad+v_\delta(t)+\sum_{\epsilon=1}^{\eta}\sum_{\kappa=1}^{N}l_\epsilon K_{\iota\kappa}^{\epsilon}H_\epsilon A_\kappa(t), \delta=1,2,\ldots,N,\end{aligned} \tag{41}$$

where $v_\delta(t)=v_\delta^R(t)+iv_\delta^I(t)\in\mathbb{C}^n$ is the generalized pinning adaptive controller and $0<D\in\mathbb{R}^{n\times n}$, $A_\delta(t)\in\mathbb{C}^n$, $P(A_\delta(t))\in\mathbb{C}^{n\times n}$, $y(\overline{A_\delta(t)})\in\mathbb{C}^n$, $\mathbb{R}\ni l_\epsilon>0$, $K^\epsilon\in\mathbb{R}^{N\times N}$, and $H_\epsilon\in\mathbb{R}^{n\times n}$ have the same meanings as in Section 3.1. Without loss of generality, we select the first m nodes and pin them with the following generalized pinning adaptive controller designed as

$$v_\delta(t)=c_\delta(t)+\widehat{c}_\delta(t), \delta=1,2,\ldots,N, \tag{42}$$

where $c_\delta(t)=c_\delta^R(t)+ic_\delta^I(t)$, $\widehat{c}_\delta(t)=\widehat{c}_\delta^R(t)+i\widehat{c}_\delta^I(t)$, in which $c_\delta^R(t)$ and $c_\delta^I(t)$ are given as in (15) for $\delta=1,2,\ldots,N$, and

$$\begin{aligned}\widehat{c}_\delta^R(t) &= -\sum_{\epsilon=1}^{\eta}l_\epsilon\left(\rho_\delta^\epsilon(t)\right)^R H_\epsilon z_\delta^R(t), \delta=1,2,\ldots,m,\\ &\quad 0, \delta=m+1,m+2,\ldots,N,\\ \widehat{c}_\delta^I(t) &= -\sum_{\epsilon=1}^{\eta}l_\epsilon\left(\rho_\delta^\epsilon(t)\right)^I H_\epsilon z_\delta^I(t), \delta=1,2,\ldots,m,\\ &\quad 0, \delta=m+1,m+2,\ldots,N,\end{aligned} \tag{43}$$

with

$$\begin{aligned}\left(\dot{\rho}_\delta^\epsilon(t)\right)^R &= \zeta_\delta^\epsilon\left(z_\delta^R(t)\right)^T\frac{H_\epsilon+H_\epsilon^T}{2}z_\delta^R(t),\\ \left(\dot{\rho}_\delta^\epsilon(t)\right)^I &= \zeta_\delta^\epsilon\left(z_\delta^I(t)\right)^T\frac{H_\epsilon+H_\epsilon^T}{2}z_\delta^I(t),\end{aligned} \tag{44}$$

when $\delta=1,2,\ldots,m$, where $\mathbb{R}\ni l_\epsilon>0$, $z_\delta^R(t)=A_\delta^R(t)+A_*^R(t)$, $z_\delta^I(t)=A_\delta^I(t)+A_*^I(t)$, $z_\delta^R(t)=(z_{\delta1}^R(t),z_{\delta2}^R(t),\ldots,z_{\delta n}^R(t))^T$, $z_\delta^I(t)=(z_{\delta1}^I(t),z_{\delta2}^I(t),\ldots,z_{\delta n}^I(t))^T$, $H_\epsilon\in\mathbb{R}^{n\times n}$, $H_\epsilon+H_\epsilon^T>0$, $1\le m<N$, and $\mathbb{R}\ni\zeta_\delta^\epsilon>0$; $\mathbb{R}\ni(\rho_\delta^\epsilon(0))^R>0$; and $\mathbb{R}\ni(\rho_\delta^\epsilon(0))^I>0$ for $\delta=1,2,\ldots,m$.

Similar to Section 3.1, the error vector $z_\delta(t)=A_\delta(t)+A_*(t)$ can be governed by

$$\begin{aligned}\dot{z}_\delta(t) &= -Dz_\delta(t)+P\left(A_\delta(t)\right)f\left(\overline{A_\delta(t)}\right)+v_\delta(t)\\ &\quad+P\left(A_*(t)\right)y\left(A_*(t)\right)\\ &\quad+\sum_{\epsilon=1}^{\eta}\sum_{\kappa=1}^{N}l_\epsilon K_{\delta\kappa}^{\epsilon}H_\epsilon z_\kappa(t), \delta=1,2,\ldots,N.\end{aligned} \tag{45}$$

In order to get the desired result, we separate networks (45) into the following equivalent imaginary and real parts:

$$\begin{aligned}
\dot{z}_\delta^R(t) &= -Dz_\delta^R(t) + P^R\left(A_\delta^R(t)\right)G^R\left(\overline{z_\delta^R(t)}\right) \\
&\quad - P^I\left(A_\delta^I(t)\right)G^I\left(\overline{z_\delta^I(t)}\right) \\
&\quad - \left[P^R\left(A_\delta^R(t)\right) - P^R\left(A_*^R(t)\right)\right]y^R\left(A_*^R(t)\right) \\
&\quad + \sum_{\epsilon=1}^{\eta}\sum_{\kappa=1}^{N} l_\epsilon K_{\delta\kappa}^\epsilon H_\epsilon z_\kappa^R(t) \\
&\quad + \left[P^I\left(A_\delta^I(t)\right) - P^I\left(A_*^I(t)\right)\right]y^I\left(A_*^I(t)\right) + v_\delta^R(t), \\
\dot{z}_\delta^I(t) &= -Dz_\delta^I(t) + P^R\left(A_\delta^R(t)\right)G^I\left(\overline{z_\delta^I(t)}\right) \\
&\quad + P^I\left(A_\delta^I(t)\right)G^R\left(\overline{z_\delta^R(t)}\right) \\
&\quad - \left[P^R\left(A_\delta^R(t)\right) - P^R\left(A_*^R(t)\right)\right]y^I\left(A_*^I(t)\right) \\
&\quad + \sum_{\epsilon=1}^{\eta}\sum_{\kappa=1}^{N} l_\epsilon K_{\delta\kappa}^\epsilon H_\epsilon z_\kappa^I(t) \\
&\quad - \left[P^I\left(A_\delta^I(t)\right) - P^I\left(A_*^I(t)\right)\right]y^R\left(A_*^R(t)\right) + v_\delta^I(t),
\end{aligned} \tag{46}$$

where

$$\begin{aligned}
v_\delta^R(t) &= -\Theta_\delta^R z_\delta^R(t) - \operatorname{sign}\left(z_\delta^R(t)\right)\left(\overline{P}^R\overline{Y}^R + \overline{P}^I\overline{Y}^I\right) \\
&\quad - \sum_{\epsilon=1}^{\eta} l_\epsilon\left(\rho_\delta^\epsilon(t)\right)^R H_\epsilon z_\delta^R(t), \\
v_\delta^I(t) &= -\Theta_\delta^I z_\delta^I(t) - \operatorname{sign}\left(z_\delta^I(t)\right)\left(\overline{P}^R\overline{Y}^I + \overline{P}^I\overline{Y}^R\right) \\
&\quad - \sum_{\epsilon=1}^{\eta} l_\epsilon\left(\rho_\delta^\epsilon(t)\right)^I H_\epsilon z_\delta^I(t),
\end{aligned} \tag{47}$$

in which $(\dot{\rho}_\delta^\varepsilon(t))^R = \zeta_\delta^\varepsilon(z_\delta^R(t))^T(H_\varepsilon + H_\varepsilon^T)/2z_\delta^R(t)$, $(\dot{\rho}_\delta^\varepsilon(t))^I = \zeta_\delta^\varepsilon(z_\delta^I(t))^T(H_\varepsilon + H_\varepsilon^T)/2z_\delta^I(t)$ for $\delta = 1, 2, \ldots, m$, and $(\rho_\delta^\epsilon(t))^R = (\rho_\delta^\epsilon(t))^I \equiv 0$ for $\delta = m+1, m+2, \ldots, N$.

Theorem 2. *If there are matrices* $0 < (\widehat{\rho}^\epsilon)^R = diag\left((\widehat{\rho}_1^\epsilon)^R, (\widehat{\rho}_2^\epsilon)^R, \ldots, (\widehat{\rho}_m^\epsilon)^R, 0, \ldots, 0\right) \in \mathbb{R}^{N\times N}$ *and* $0 < (\widehat{\rho}^\epsilon)^I = diag\left((\widehat{\rho}_1^\epsilon)^I, (\widehat{\rho}_2^\epsilon)^I, \ldots, (\widehat{\rho}_m^\epsilon)^I, 0, \ldots, 0\right) \in \mathbb{R}^{N\times N}$, $\epsilon = 1, 2, \ldots, u$, *such that*

$$\Phi_2^R < 0 \text{and} \Phi_2^I < 0, \tag{48}$$

where $\Phi_2^R = I_N \otimes (-2\ D + \widetilde{P}^R + \widetilde{P}\ \ ^I + 2J^R\Lambda) - 2\Theta^R + \sum_{\epsilon=1}^{\eta} l_\epsilon[(K^\epsilon - (\widehat{\rho}^\epsilon)^R) \otimes H_\epsilon + ((K^\epsilon)^T - (\widehat{\rho}^\epsilon)^R) \otimes H_\epsilon^T]$, $\Phi_2^I = I_N \otimes (-2D + \widetilde{P}^R + \widetilde{P}^I + 2J^I\Lambda) - 2\Theta^I + \sum_{\varepsilon=1}^{\eta} l_\varepsilon[(K^\varepsilon - (\widehat{\rho}^\varepsilon)^I) \otimes H_\varepsilon + (K^\varepsilon)^T - (\widehat{\rho}^\varepsilon)^I \otimes H_\varepsilon^T]$; $\Theta^R = diag(\Theta_1^R, \Theta_2^R, \ldots, \Theta_N^R) \in \mathbb{R}^{nN\times nN}$, $\Theta^I = diag(\Theta_1^I, \Theta_2^I, \ldots, \Theta_N^I) \in \mathbb{R}^{nN\times nN}$; $(\widehat{\rho}_\delta^\epsilon)^R > 0$ *and* $(\widehat{\rho}_\delta^\epsilon)^I > 0$ *for* $\delta = 1, 2, \ldots, m$, *then the network (41) is pinning adaptive antisynchronized.*

Proof. Take the Lyapunov functional for network (45) as follows:

$$\begin{aligned}
V_2(t) &= \sum_{\epsilon=1}^{\eta}\sum_{\delta=1}^{N}\frac{l_\epsilon}{\zeta_\delta^\epsilon}\left(\left(\rho_\delta^\epsilon(t)\right)^R - \left(\widehat{\rho}_\delta^\epsilon\right)^R\right)^2 \\
&\quad + \sum_{\epsilon=1}^{\eta}\sum_{\delta=1}^{N}\frac{l_\epsilon}{\zeta_\delta^\epsilon}\left(\left(\rho_\delta^\epsilon(t)\right)^I - \left(\widehat{\rho}_\delta^\epsilon\right)^I\right)^2 + \sum_{\delta=1}^{N}\left(z_\delta^R(t)\right)^T z_\delta^R(t) \\
&\quad + \sum_{\delta=1}^{N}\left(z_\delta^I(t)\right)^T z_\delta^I(t) \\
&\quad + 2\sum_{\delta=1}^{N}\sum_{h=1}^{\eta}\int_{t-u_h(t)}^{t}\frac{\left(j_h^R z_{\delta h}^R(\varepsilon)\right)^2}{1-\varrho_h}d\varepsilon \\
&\quad + 2\sum_{\delta=1}^{N}\sum_{h=1}^{\eta}\int_{t-u_h(t)}^{t}\frac{\left(j_h^I z_{\delta h}^I(\varepsilon)\right)^2}{1-\varrho_h}d\varepsilon.
\end{aligned} \tag{49}$$

Then, we have

$$\begin{aligned}
\dot{V}_2(t) \le{}& 2\sum_{\delta=1}^{N}\left(z_\delta^R(t)\right)^T\Big\{-Dz_\delta^R(t) + P^R\left(A_\delta^R(t)\right)G^R\left(\overline{z_\delta^R(t)}\right) - P^I\left(A_\delta^I(t)\right)G^I\left(\overline{z_\delta^I(t)}\right) - \left[P^R\left(A_\delta^R(t)\right) - P^R\left(A_*^R(t)\right)\right]y^R\left(A_*^R(t)\right) \\
&+ \sum_{\epsilon=1}^{\eta}\sum_{\kappa=1}^{N} l_\epsilon K_{\delta\kappa}^\epsilon H_\epsilon z_\kappa^R(t) - \Theta_\delta^R z_\delta^R(t) - \operatorname{sign}\left(z_\delta^R(t)\right)\left(\overline{P}^R\overline{Y}^R + \overline{P}^I\overline{Y}^I\right) - \sum_{\epsilon=1}^{\eta} l_\epsilon\left(\rho_\delta^\epsilon(t)\right)^R H_\epsilon z_\delta^R(t) + \Big[P^I\left(A_\delta^I(t)\right) \\
&- P^I\left(A_*^I(t)\right)\Big]y^I\left(A_*^I(t)\right)\Big\} + 2\sum_{\delta=1}^{N}\left(z_\delta^I(t)\right)^T\Big\{-Dz_\delta^I(t) + P^R\left(A_\delta^R(t)\right)G^I\left(\overline{z_\delta^I(t)}\right) + P^I\left(A_\delta^I(t)\right)G^R\left(\overline{z_\delta^R(t)}\right) - \Big[P^R\left(A_\delta^R(t)\right) \\
&- P^R\left(A_*^R(t)\right)\Big]y^I\left(A_*^I(t)\right) + \sum_{\epsilon=1}^{\eta}\sum_{\kappa=1}^{N} l_\epsilon K_{\delta\kappa}^\epsilon H_\epsilon z_\kappa^I(t) - \Theta_\delta^I z_\delta^I(t) - \operatorname{sign}\left(z_\delta^I(t)\right)\left(\overline{P}^R\overline{Y}^I + \overline{P}^I\overline{Y}^R\right) - \sum_{\epsilon=1}^{\eta} l_\epsilon\left(\rho_\delta^\epsilon(t)\right)^I H_\epsilon z_\delta^I(t) \\
&- \left[P^I\left(A_\delta^I(t)\right) - P^I\left(A_*^I(t)\right)\right]y^R\left(A_*^R(t)\right)\Big\} + \sum_{\epsilon=1}^{\eta}\sum_{\delta=1}^{m} l_\epsilon\left[\left(\rho_\delta^\epsilon(t)\right)^R - \left(\widehat{\rho}_\delta^\epsilon\right)^R\right]\left(z_\delta^R(t)\right)^T\left(H_\epsilon + H_\epsilon^T\right)z_\delta^R(t) + \sum_{\epsilon=1}^{\eta}\sum_{\delta=1}^{m} l_\epsilon\Big[\left(\rho_\delta^\epsilon(t)\right)^I \\
&- \left(\widehat{\rho}_\delta^\epsilon\right)^I\Big]\left(z_\delta^I(t)\right)^T\left(H_\epsilon + H_\epsilon^T\right)z_\delta^I(t) + 2\left(z^R(t)\right)^T\left(I_N \otimes \left(J^R\Lambda\right)\right)z^R(t) - 2\left(\overline{z^R(t)}\right)^T\left(I_N \otimes J^R\right)\overline{z^R(t)} \\
&+ 2\left(z^I(t)\right)^T\left(I_N \otimes \left(J^I\Lambda\right)\right)z^I(t) - 2\left(\overline{z^I(t)}\right)^T\left(I_N \otimes J^I\right)\overline{z^I(t)}.
\end{aligned} \tag{50}$$

Moreover, we can derive that

$$
\begin{aligned}
&-2\sum_{\delta=1}^{N}\sum_{\epsilon=1}^{\eta} l_\epsilon\left(\rho_\delta^\epsilon(t)\right)^R\left(z_\delta^R(t)\right)^T H_\epsilon z_\delta^R(t)+\sum_{\epsilon=1}^{\eta}\sum_{\delta=1}^{m} l_\epsilon\left[\left(\rho_\delta^\epsilon(t)\right)^R-\left(\widehat{\rho}_\delta^\epsilon\right)^R\right]\left(z_\delta^R(t)\right)^T\left(H_\epsilon+H_\epsilon^T\right)z_\delta^R(t)\\
&=-2\sum_{\delta=1}^{N}\sum_{\epsilon=1}^{\eta} l_\epsilon\left(\rho_\delta^\epsilon(t)\right)^R\left(z_\delta^R(t)\right)^T H_\epsilon z_\delta^R(t)+\sum_{\epsilon=1}^{\eta}\sum_{\delta=1}^{m} l_\epsilon\left(\rho_\delta^\epsilon(t)\right)^R\left(z_\delta^R(t)\right)^T\left(H_\epsilon+H_\epsilon^T\right)z_\delta^R(t)-\sum_{\epsilon=1}^{\eta}\sum_{\delta=1}^{m} l_\epsilon\left(\widehat{\rho}_\delta^\epsilon\right)^R\left(z_\delta^R(t)\right)^T\left(H_\epsilon+H_\epsilon^T\right)z_\delta^R(t)\\
&=-\sum_{\epsilon=1}^{\eta}\sum_{\delta=1}^{m} l_\epsilon\left(\widehat{\rho}_\delta^\epsilon\right)^R\left(z_\delta^R(t)\right)^T\left(H_\epsilon+H_\epsilon^T\right)z_\delta^R(t)\\
&=-\left(z^R(t)\right)^T\left[\sum_{\epsilon=1}^{\eta} l_\epsilon\left(\widehat{\rho}^\epsilon\right)^R\otimes\left(H_\epsilon+H_\epsilon^T\right)\right]z^R(t).
\end{aligned}
\tag{51}
$$

Similarly,

$$
\begin{aligned}
&-2\sum_{\delta=1}^{N}\sum_{\epsilon=1}^{\eta} l_\epsilon\left(\rho_\delta^\epsilon(t)\right)^I\left(z_\delta^I(t)\right)^T H_\epsilon z_\delta^I(t)+\sum_{\epsilon=1}^{\eta}\sum_{\delta=1}^{m} l_\epsilon\left[\left(\rho_\delta^\epsilon(t)\right)^I-\left(\widehat{\rho}_\delta^\epsilon\right)^I\right]\left(z_\delta^I(t)\right)^T\left(H_\epsilon+H_\epsilon^T\right)z_\delta^I(t)\\
&=-\sum_{\epsilon=1}^{\eta}\sum_{\delta=1}^{m} l_\epsilon\left(\widehat{\rho}_\delta^\epsilon\right)^I\left(z_\delta^I(t)\right)^T\left(H_\epsilon+H_\epsilon^T\right)z_\delta^I(t)\\
&=-\left(z^I(t)\right)^T\left[\sum_{\epsilon=1}^{\eta} l_\epsilon\left(\widehat{\rho}^\epsilon\right)^I\otimes\left(H_\epsilon+H_\epsilon^T\right)\right]z^I(t).
\end{aligned}
\tag{52}
$$

Thus, it is easy to get that by (20)–(29) and (50)–(52)

$$
\begin{aligned}
\dot{V}_2(t)\le&\left(z^R(t)\right)^T\left\{I_N\otimes\left(-2\ D+\widetilde{P}^R+\widetilde{P}^I+2J^R\Lambda\right)-2\Theta^R+\sum_{\epsilon=1}^{\eta} l_\epsilon\left[\left(K^\epsilon-\left(\widehat{\rho}^\epsilon\right)^R\right)\otimes H_\epsilon+\left(\left(K^\epsilon\right)^T-\left(\widehat{\rho}^\epsilon\right)^R\right)\otimes H_\epsilon^T\right]\right\}z^R(t)\\
&+\left(z^I(t)\right)^T\left\{I_N\otimes\left(-2\ D+\widetilde{P}^R+\widetilde{P}^I+2J^I\Lambda\right)-2\Theta^I+\sum_{\epsilon=1}^{\eta} l_\epsilon\left[\left(K^\epsilon-\left(\widehat{\rho}^\epsilon\right)^I\right)\otimes H_\epsilon+\left(\left(K^\epsilon\right)^T-\left(\widehat{\rho}^\epsilon\right)^I\right)\otimes H_\epsilon^T\right]\right\}z^I(t)\\
&\le\alpha_2\|z(t)\|^2,
\end{aligned}
\tag{53}
$$

where $\alpha_2=\max\{\lambda_M(\Phi_2^R),\lambda_M(\Phi_2^I)\}<0$.

From (49) and (53), we can get $V_2(t)$ is nonincreasing, and any term of $V_2(t)$ is bounded. Therefore, $\lim_{t\longrightarrow+\infty}V_2(t)\ge 0$, $(\rho_\delta^\epsilon(t))^R$ and $(\rho_\delta^\epsilon(t))^I$ are bounded. According to (44), we can get $(\rho_\gamma^\epsilon(t))^R$ and $(\rho_\delta^\epsilon(t))^I$ are monotonically increasing; thus, $(\rho_\delta^\epsilon(t))^R$ and $(\rho_\delta^\epsilon(t))^I$ converge to a finite nonnegative value, which means both the limitation of $\sum_{\epsilon=1}^{\eta}\sum_{\delta=1}^{m} l_\epsilon/\zeta_\delta^\epsilon((\rho_\delta^\epsilon(t))^R-\widehat{\rho}_\delta^\epsilon)^2$ and $\sum_{\epsilon=1}^{\eta}\sum_{\delta=1}^{m} l_\epsilon/\zeta_\delta^\epsilon((\rho_\delta^\epsilon(t))^I-\widehat{\rho}_\delta^\epsilon)^2$ exist as well as $\lim_{t\longrightarrow+\infty}\sum_{\epsilon=1}^{\eta}\sum_{\delta=1}^{m} l_\epsilon/\zeta_\delta^\epsilon((\rho_\delta^\epsilon(t))^R-\widehat{\rho}_\delta^r)^2\ge 0$ and $\lim_{t\longrightarrow+\infty}\sum_{\epsilon=1}^{\eta}\sum_{\delta=1}^{m} l_\epsilon/\zeta_\delta^r((\rho_\delta^\epsilon(t))^I-\widehat{\rho}_\delta^\epsilon)^2\ge 0$. Thus, we have $\lim_{t\to+\infty}\left\{\sum_{\delta=1}^{N}\sum_{h=1}^{n}[\int_{t-u_h(t)}^{t}(2(j_h^R x_{\delta h}^R(\varepsilon))^2/1-\varrho_h)\mathrm{d}\varepsilon+\int_{t-u_h(t)}^{t}2(j_h^I z_{\delta h}^I(\varepsilon))^2/(1-\varrho_h)\mathrm{d}\varepsilon]+\sum_{\delta=1}^{N}[(z_\delta^R(t))^T z_\delta^R(t)+(z_\delta^I(t))^T z_\delta^I(t)]\right\}$exist and is a nonnegative real number. Then, by virtue of the similar proof method as in Theorem 1, we can obtain that $\lim_{t\longrightarrow+\infty}\|z(t)\|=0$. Therefore, the network (41) achieves antisynchronization under the generalized pinning adaptive controller (47). □

4. Antisynchronization and Pinning Antisynchronization of MWCCVDMNNs with Coupling Delays

4.1. Antisynchronization of MWCCVDMNNs with Coupling Delays. In this section, the MWCCVDMNNs with coupling delays is considered as follows:

$$
\begin{aligned}
\dot{A}_\delta(t)=&-DA_\delta(t)+P\left(A_\delta(t)\right)y\left(\overline{A_\delta(t)}\right)+c_\delta(t)\\
&+\sum_{\epsilon=1}^{\eta}\sum_{\kappa=1}^{N} l_\epsilon K_{\delta\kappa}^\epsilon H_\epsilon\widehat{A_\kappa(t)},\ \delta=1,2,\ldots,N,
\end{aligned}
\tag{54}
$$

where $D, A_\delta(t)$, $P(A_\delta(t)), y(\overline{A_\delta(t)})$, $c_\delta(t), l_\epsilon, K^\epsilon, H_\epsilon$ have the similar meanings as in Section 3.1; $\widehat{A_\kappa(t)}=(A_{\kappa1}(t-w_1(t)),A_{\kappa2}(t-w_2(t)),\ldots,A_{\kappa n}(t-w_n(t)))^T\in\mathbb{R}^n$; $w_\epsilon(t)(\epsilon=1,2,\ldots,\eta)$ denote the coupling delay with $0\le w_\epsilon(t)\le w_\epsilon\le w=\max_{\epsilon=1,2,\ldots,n}\{w_\epsilon\}$ and $\dot{w}_\epsilon(t)\le\overline{\varrho}_\epsilon<1$.

Let $z_\delta(t)=A_\delta(t)+A_*(t)$, then

$$\begin{aligned}\dot{z}_\delta(t) &= -Dz_\delta(t) + P\left(A_\delta(t)\right)y\left(\overline{A_\delta(t)}\right) + c_\delta(t)\\ &\quad + P\left(A_*(t)\right)y\left(Y_*(t)\right)\\ &\quad + \sum_{\epsilon=1}^{\eta}\sum_{\kappa=1}^{N} l_\epsilon K_{\delta\kappa}^{\epsilon} H_\epsilon \widehat{z_\kappa(t)}, \delta = 1, 2, \ldots, N.\end{aligned} \tag{55}$$

Then, by separating the imaginary and real parts, system (55) can be shown as

$$\begin{aligned}\dot{z}_\delta^R(t) &= -Dz_\delta^R(t) + P^R A_\delta^R(t) G^R\left(\overline{z_\delta^R(t)}\right) - P^I\left(A_\delta^I(t)\right)G^I\left(\overline{z_\delta^I(t)}\right) - \left[P^R\left(A_\delta^R(t)\right) - P^R\left(A_*^R(t)\right)\right]y^R\left(A_*^R(t)\right) + \sum_{\epsilon=1}^{\eta}\sum_{\kappa=1}^{N} l_\epsilon K_{\delta\kappa}^{\epsilon} H_\epsilon \widehat{z_\kappa^R(t)}\\ &\quad + \left[P^I\left(A_\delta^I(t)\right) - P^I\left(A_*^I(t)\right)\right]y^I\left(A_*^I(t)\right) + c_\delta^R(t),\\ \dot{z}_\delta^I(t) &= -Dz_\delta^I + P^R\left(A_\delta^R(t)\right)G^I\left(\overline{z_\delta^I(t)}\right) + P^I\left(A_\delta^I(t)\right)G^R\left(\overline{z_\delta^R(t)}\right) - \left[P^R\left(A_\delta^R(t)\right) - P^R\left(A_*^R(t)\right)\right]y^I\left(A_*^I(t)\right) + \sum_{\epsilon=1}^{\eta}\sum_{\kappa=1}^{N} l_\epsilon K_{\delta\kappa}^{\epsilon} H_\epsilon \widehat{z_\kappa^I(t)}\\ &\quad - \left[P^I\left(A_\delta^I(t)\right) - P^I\left(A_*^I(t)\right)\right]y^R\left(A_*^R(t)\right) + c_\delta^I(t),\end{aligned} \tag{56}$$

where $z_\delta^R(t)$, $z_\delta^I(t)$, $\overline{z_\delta^R(t)}$, $\overline{z_\delta^I(t)}$, $G^R(\overline{z_\delta^R(t)})$, and $G^I(\overline{z_\delta^I(t)})$ have the same definitions as in Section 3.1; $\widehat{z_\kappa^R(t)} = (z_{\kappa1}^R(t-w_1(t)), z_{\kappa2}^R(t-w_2(t)), \ldots, z_{\kappa n}^R \quad (t-w_n(t)))^T$ and $\widehat{z_\kappa^I(t)} = (z_{\kappa1}^I(t-w_{\ 1}(t)), z_{\kappa2}^I(t-w_2(t)), \ldots, z_{\kappa n}^I(t-w_n(t)))^T$.

Theorem 3. *If there are some matrices $0 < \Psi_\epsilon = diag(b_1^\epsilon, b_2^\epsilon, \ldots, b_{nN}^\epsilon) \in \mathbb{R}^{nN\times nN}$, $\epsilon = 1, 2, \ldots, \eta$, such that*

$$\Phi_3^R < 0 \text{ and } \Phi_3^I < 0, \tag{57}$$

where $\Phi_3^R = I_N \otimes (-2D + \widetilde{P}^R + \widetilde{P}^I + 2J^R\Lambda) - 2\Theta^R + \sum_{\varepsilon=1}^{\eta} l_\varepsilon[(K^\varepsilon \otimes H_\varepsilon)\Psi_\varepsilon^{-1}((K^\varepsilon)^T \otimes H_\varepsilon^T) + 1/(1-\overline{\varrho}_\varepsilon)\Psi_\varepsilon]$; $\Phi_3^I = I_N \otimes (-2D + \widetilde{P}^R + \widetilde{P}^I + 2J^R\Lambda) - 2\Theta^I + \sum_{\varepsilon=1}^{\eta} l_\varepsilon[(K^\varepsilon \otimes H_\varepsilon)\Psi_\varepsilon^{-1}((K^\varepsilon)^T \otimes H_\varepsilon^T) + 1/(1-\overline{\varrho}_\varepsilon)\Psi_\varepsilon]$; $\Theta^R = diag(\Theta_1^R, \Theta_2^R, \ldots, \Theta_N^R) \in \mathbb{R}^{nN\times nN}$; and $\Theta^I = diag(\Theta_1^I, \Theta_2^I, \ldots, \Theta_N^I) \in \mathbb{R}^{nN\times nN}$. Then, the network (54) achieves antisynchronized under the controller (15).

Proof. The Lyapunov function is chosen as

$$\begin{aligned}V_3(t) &= \sum_{\delta=1}^{N}\left(z_\delta^R(t)\right)^T z_\delta^R(t) + 2\sum_{\delta=1}^{N}\sum_{h=1}^{n}\int_{t-u_h(t)}^{t}\frac{\left(j_h^R z_{\delta h}^R(\varepsilon)\right)^2}{1-\varrho_h}d\varepsilon\\ &\quad + 2\sum_{\delta=1}^{N}\sum_{h=1}^{n}\int_{t-u_h(t)}^{t}\frac{\left(j_h^I z_{\delta h}^I(\varepsilon)\right)^2}{1-\varrho_h}d\varepsilon + \sum_{\delta=1}^{N}\left(z_\delta^I(t)\right)^T z_\delta^I(t)\\ &\quad + \sum_{\epsilon=1}^{\eta}\frac{l_\epsilon}{1-\overline{\varrho}_\epsilon}\int_{t-w_\epsilon(t)}^{t} z^R(\varepsilon)^T\Psi_\epsilon z^R(\varepsilon)d\varepsilon\\ &\quad + \sum_{\epsilon=1}^{\eta}\frac{l_\epsilon}{1-\overline{\varrho}_\epsilon}\int_{t-w_\epsilon(t)}^{t} z^I(\varepsilon)^T\Psi_\epsilon z^I(\varepsilon)d\varepsilon.\end{aligned} \tag{58}$$

Then, we have

$$\begin{aligned}\dot{V}_3(t) &\le 2\sum_{\delta=1}^{N}\left(z_\delta^R(t)\right)^T\left\{\begin{array}{c}-Dz_\delta^R(t) + P^R\left(A_\delta^R(t)\right)G^R\left(\overline{z_\delta^R(t)}\right) - P^I\left(A_\delta^I(t)\right)G^I\left(\overline{z_\delta^I(t)}\right) + \sum_{\epsilon=1}^{\eta}\sum_{\kappa=1}^{N} l_\epsilon K_{\iota\kappa}^{\epsilon} H_\epsilon \widehat{z_\kappa^R(t)} - \Theta_\delta^R z_\delta^R(t)\\ -\text{sign}\left(z_\delta^R(t)\right)\left(\overline{P}^R\overline{Y}^R + \overline{P}^I\overline{Y}^I\right) - \left[P^R\left(A_\delta^R(t)\right) - P^R\left(A_*^R(t)\right)\right]y^R\left(A_*^R(t)\right) + \left[P^I\left(A_\delta^I(t)\right) - P^I\left(A_*^I(t)\right)\right]y^I\left(A_*^I(t)\right)\end{array}\right\}\\ &\quad + 2\sum_{\delta=1}^{N}\left(z_\delta^I(t)\right)^T\left\{\begin{array}{c}-Az_\delta^I(t) + P^R\left(A_\delta^R(t)\right)G^I\left(\overline{z_\delta^I(t)}\right) + P^I\left(A_\delta^I(t)\right)G^R\left(\overline{z_\delta^R(t)}\right) + \sum_{\epsilon=1}^{\eta}\sum_{\kappa=1}^{N} l_\epsilon K_{\delta\kappa}^{\epsilon} H_\epsilon \widehat{z_\kappa^I(t)} - \Theta_\delta^I z_\delta^I(t)\\ -\text{sign}\left(z_\delta^I(t)\right)\left(\overline{P}^R\overline{Y}^I + \overline{P}^I\overline{Y}^R\right) - \left[P^R\left(A_\delta^R(t)\right) - P^R\left(A_*^R(t)\right)\right]y^I\left(A_*^I(t)\right) - \left[P^I\left(A_\delta^I(t)\right) - P^I\left(A_*^I(t)\right)\right]y^R\left(A_*^R(t)\right)\end{array}\right\}\\ &\quad + 2\left(z^R(t)\right)^T\left(I_N \otimes \left(J^R\Lambda\right)\right)z^R(t) - 2\left(\overline{z^R(t)}\right)^T\left(I_N \otimes J^R\right)\overline{z^R(t)} + 2\left(z^I(t)\right)^T\left(I_N \otimes \left(J^I\Lambda\right)\right)z^I(t) - 2\left(\overline{z^I(t)}\right)^T\left(I_N \otimes J^I\right)\overline{z^I(t)}\\ &\quad + \sum_{\epsilon=1}^{\eta}\frac{l_\epsilon}{1-\overline{\varrho}_\epsilon}\left(z^R(t)\right)^T\Psi_\epsilon z^R(t) - \sum_{\epsilon=1}^{\eta} l_\epsilon\left(\widehat{z^R(t)}\right)^T\Psi_r\widehat{z^R(t)} + \sum_{\epsilon=1}^{\eta}\frac{l_\epsilon}{1-\overline{\varrho}_\epsilon}\left(z^I(t)\right)^T\Psi_\epsilon z^I(t)\\ &\quad - \sum_{\epsilon=1}^{\eta} l_\epsilon\left(\widehat{z^I(t)}\right)^T\Psi_\epsilon\widehat{z^I(t)}.\end{aligned} \tag{59}$$

Obviously,

$$\begin{aligned}
&2\sum_{\delta=1}^{N}\sum_{\epsilon=1}^{\eta}\sum_{\kappa=1}^{N} l_\epsilon K_{\iota\kappa}^{\epsilon}\left(z_\delta^R(t)\right)^T H_\epsilon \widehat{z_\kappa^R(t)} \\
&= 2\sum_{\epsilon=1}^{\eta} l_\epsilon\left(z^R(t)\right)^T\left(K^\epsilon\otimes H_\epsilon\right)\widehat{z^R(t)} \\
&\le \sum_{\epsilon=1}^{\eta} l_\epsilon\left(z^R(t)\right)^T\left(K^\epsilon\otimes H_\epsilon\right)\Psi_\epsilon^{-1}\left(\left(K^\epsilon\right)^T\otimes H_\epsilon^T\right)z^R(t) \\
&\quad+\sum_{\epsilon=1}^{\eta} l_\epsilon\left(\widehat{z^R(t)}\right)^T\Psi_\epsilon\widehat{z^R(t)}.
\end{aligned} \tag{60}$$

Similarly,

$$\begin{aligned}
&2\sum_{\delta=1}^{N}\sum_{\epsilon=1}^{\eta}\sum_{\kappa=1}^{N} l_\epsilon K_{\iota\kappa}^{\epsilon}\left(z_\delta^I(t)\right)^T H_\epsilon \widehat{z_\kappa^I(t)} \\
&\le \sum_{\epsilon=1}^{\eta} l_\epsilon\left(z^I(t)\right)^T\left(K^\epsilon\otimes H_\epsilon\right)\Psi_\epsilon^{-1}\left(\left(K^\epsilon\right)^T\otimes H_\epsilon^T\right)z^I(t) \\
&\quad+\sum_{\epsilon=1}^{\eta} l_\epsilon\left(\widehat{z^I(t)}\right)^T\Psi_\epsilon\widehat{z^I(t)}.
\end{aligned} \tag{61}$$

By (20)–(30), (26)–(29), and (60)-(61), one obtains

$$\begin{aligned}
\dot{V}_3(t) \le{}& \left(z^R(t)\right)^T\left\{I_N\otimes\left(-2D+\widetilde{P}^R+\widetilde{P}^I+2J^R\Lambda\right)-2\Theta^R+\sum_{\epsilon=1}^{\eta} l_\epsilon\left[\left(K^\epsilon\otimes H_\epsilon\right)\Psi_\epsilon^{-1}\left(\left(K^\epsilon\right)^T\otimes H_\epsilon^T\right)+\frac{1}{1-\overline{\varrho}_\epsilon}\Psi_\epsilon\right]\right\}z^R(t) \\
&+\left(z^I(t)\right)^T\left\{I_N\otimes\left(-2D+\widetilde{P}^R+\widetilde{P}^I+2J^I\Lambda\right)-2\Theta^I+\sum_{\epsilon=1}^{\eta} l_\epsilon\left[\left(K^\epsilon\otimes H_\epsilon\right)\Psi_\epsilon^{-1}\left(\left(K^\epsilon\right)^T\otimes H_\epsilon^T\right)+\frac{1}{1-\overline{\varrho}_\epsilon}\Psi_\epsilon\right]\right\}z^I(t) \\
&\le \alpha_3\|z(t)\|^2,
\end{aligned} \tag{62}$$

where $\alpha_3 = \max\{\lambda_M(\Phi_3^R), \lambda_M(\Phi_3^I)\} < 0$. Similar to the deduction of (31), we can obtain that $\lim_{t\longrightarrow+\infty}\int_0^t \|x(\varepsilon)\|^2 d\varepsilon$ exists and is a real nonnegative number. In addition,

$$\begin{aligned}
0 &\le \sum_{\epsilon=1}^{\eta}\frac{l_\epsilon}{1-\overline{\varrho}_\epsilon}\int_{t-w_\epsilon(t)}^{t}\left(z^R(\varepsilon)\right)^T\Psi_\epsilon z^R(\varepsilon)d\varepsilon \\
&\le \sum_{\epsilon=1}^{\eta}\frac{l_\epsilon}{1-\overline{\varrho}_\epsilon}\int_{t-w}^{t}\left(z^R(\varepsilon)\right)^T\Psi_\epsilon z^R(\varepsilon)d\varepsilon \\
&\le \sum_{\epsilon=1}^{\eta}\frac{l_\epsilon}{1-\overline{\varrho}_\epsilon}\lambda_M(\Psi_\epsilon)\int_{t-w}^{t}\|z(\varepsilon)\|^2 d\varepsilon \\
&= 0.
\end{aligned} \tag{63}$$

Similarly,

$$0 \le \sum_{\epsilon=1}^{\eta}\frac{l_\epsilon}{1-\overline{\varrho}_\epsilon}\int_{t-w_\epsilon(t)}^{t}\left(z^I(\varepsilon)\right)^T\Psi_\epsilon z^I(\varepsilon)d\varepsilon = 0. \tag{64}$$

From (32)-(33) and (63)-(64), one can obtain that $\lim_{t\longrightarrow+\infty}\sum_{\delta=1}^{N}[(z_\delta^R(t))^T z_\delta^R(t) + (z_\delta^I(t))^T z_\delta^I(t)]$ exists and is a nonnegative real number. Then, based on the method for proving Theorem 1, one can easily obtain $\lim_{t\longrightarrow+\infty}\|z(t)\| = 0$. Thus, under the controller (15), the network (54) is antisynchronized. □

4.2. Generalized Pinning Antisynchronization of MWCCVDMNNs with Coupling Delays. In this section, we add generalized pinning adaptive controller as in Section 3.2 to the MWCCVDMNNs with coupling delays, then the network (54) under the pinning adaptive controller can be expressed as follows:

$$\begin{aligned}
\dot{A}_\delta(t) &= -DA_\delta(t) + P\left(A_\delta(t)\right)y\left(\overline{A_\delta(t)}\right) + v_\delta(t) \\
&\quad+\sum_{\epsilon=1}^{\eta}\sum_{\kappa=1}^{N} l_\epsilon K_{\delta\kappa}^{\epsilon} H_\epsilon \widehat{A_\kappa(t)}, \delta = 1, 2, \ldots, N,
\end{aligned} \tag{65}$$

where $v_\delta(t) = v_\delta^R(t) + iv_\delta^I(t) \in \mathbb{C}^n$ is the generalized pinning adaptive controller as given in (42), $0 < D \in \mathbb{R}^{n\times n}$, $A_\delta(t) \in \mathbb{C}^n$, $P(A_\delta(t)) \in \mathbb{C}^{n\times n}$, $y(\overline{A_\delta(t)}) \in \mathbb{C}^n$, $\mathbb{R} \ni l_\epsilon > 0$, $K^\epsilon \in \mathbb{R}^{N\times N}$, $H_\epsilon \in \mathbb{R}^{n\times n}$, and $\widehat{A_\kappa(t)} \in \mathbb{R}^n$ have the same meanings as in Section 4.1.

Similarly, the error vector $z_\delta(t) = A_\delta(t) + A_*(t)$ can be governed by equations as follows:

$$\begin{aligned}
\dot{z}_\delta(t) &= -Dz_\delta(t) + P\left(A_\delta(t)\right)y\left(\overline{A_\delta(t)}\right) + v_\delta(t) \\
&\quad+ P\left(A_*(t)\right)y\left(A_*(t)\right) \\
&\quad+\sum_{\epsilon=1}^{\eta}\sum_{\kappa=1}^{N} l_\epsilon K_{\delta\kappa}^{\epsilon} H_\epsilon \widehat{z_\kappa(t)}, \delta = 1, 2, \ldots, N.
\end{aligned} \tag{66}$$

Separating (66) into the following imaginary and real parts:

$$\begin{aligned}
\dot{z}_\delta^R(t) &= -Dz_\delta^R(t) + P^R\left(A_\delta^R(t)\right)G^R\left(\overline{z_\delta^R(t)}\right) - P^I\left(A_\delta^I(t)\right)G^I\left(\overline{z_\delta^I(t)}\right) - \left[P^R\left(A_\delta^R(t)\right) - P^R\left(A_*^R(t)\right)\right]y^R\left(A_*^R(t)\right) + v_\delta^R(t) \\
&\quad + \left[P^I\left(A_\delta^I(t)\right) - P^I\left(A_*^I(t)\right)\right]y^I\left(A_*^I(t)\right) + \sum_{\epsilon=1}^{\eta}\sum_{\kappa=1}^{N} l_\epsilon K_{\delta\kappa}^\epsilon H_\epsilon \widehat{z_\kappa^R(t)}, \\
\dot{z}_\delta^I(t) &= -Dz_\delta^I(t) + P^R\left(A_\delta^R(t)\right)G^I\left(\overline{z_\delta^I(t)}\right) + P^I\left(A_\delta^I(t)\right)G^R\left(\overline{z_\delta^R(t)}\right) - \left[P^R\left(A_\delta^R(t)\right) - P^R\left(A_*^R(t)\right)\right]y^I\left(A_*^I(t)\right) + v_\delta^I(t) \\
&\quad - \left[P^I\left(A_\delta^I(t)\right) - P^I\left(A_*^I(t)\right)\right]y^R\left(A_*^R(t)\right) + \sum_{\epsilon=1}^{\eta}\sum_{\kappa=1}^{N} l_\epsilon K_{\delta\kappa}^\epsilon H_\epsilon \widehat{z_\kappa^I(t)},
\end{aligned} \tag{67}$$

where $v_\delta^R(t)$ and $v_\delta^I(t)$ are given as in (47).

Theorem 4. *The network (65) is pinning adaptive anti-synchronization if there are matrices* $0 < (\widehat{\rho}^\epsilon)^R = diag\left((\widehat{\rho}_1^\epsilon)^R, (\widehat{\rho}_2^\epsilon)^R, \ldots, (\widehat{\rho}_m^\epsilon)^R, 0, \ldots, 0\right) \in \mathbb{R}^{N\times N}$, $0 < (\widehat{\rho}^\epsilon)^I = diag\left((\widehat{\rho}_1^\epsilon)^I, (\widehat{\rho}_2^\epsilon)^I, \ldots, (\widehat{\rho}_m^\epsilon)^I, 0, \ldots, 0\right) \in \mathbb{R}^{N\times N}$, *and* $0 < \Psi_\epsilon = diag\left(b_1^\epsilon, b_2^\epsilon, \ldots, b_{nN}^\epsilon\right) \in \mathbb{R}^{nN\times nN}$, $\epsilon = 1, 2, \ldots, \eta$, *satisfying*

$$\Phi_4^R < 0 \text{ and } \Phi_4^I < 0, \tag{68}$$

where $\Phi_4^R = I_N \otimes (-2\ D + \widetilde{P}\quad{}^R + \widetilde{P}^I + 2J^R\Lambda) - 2\Upsilon^R + \sum_{\epsilon=1}^{\eta} l_\epsilon[(K^\epsilon \otimes H_\epsilon)\ \ \Psi_\epsilon^{-1}((K^\epsilon)^T \otimes H_\epsilon^T) - (\widehat{\rho}^\epsilon)^R \otimes (H_\epsilon\ \ + H_\epsilon^T) + 1/(1-\overline{\varrho}_\epsilon)\Psi_\epsilon]$; $\Phi_4^I = I_N \otimes (-2\ D + \widetilde{P}^R + \widetilde{P}^I + 2J^I\Lambda) - 2\Upsilon^I + \sum_{\epsilon=1}^{\eta} l_\epsilon\ \ [(K^\epsilon \otimes H_\epsilon)\Psi_\epsilon^{-1}\ \ ((K^\epsilon)^T \otimes H_\epsilon^T) - (\widehat{\rho}^\epsilon)^R \otimes (H_\epsilon + H_\epsilon^T) + 1/(1-\overline{\varrho}_\epsilon)\Psi_\epsilon]$; $\Theta^R = diag\left(\Theta_1^R, \Theta_2^R, \ldots, \Theta_N^R\right) \in \mathbb{R}^{nN\times nN}$, $\Theta^I = diag\left(\Theta_1^I, \Theta_2^I, \ldots, \Theta_N^I\right) \in \mathbb{R}^{nN\times nN}$; $(\widehat{\rho}_\delta^r)^R > 0$ *and* $(\widehat{\rho}_\delta^r)^I > 0$ *for* $\delta = 1, 2, \ldots, m$.

Proof. A proper Lyapunov functional for (66) is constructed as follows:

$$\begin{aligned}
V_4(t) &= \sum_{\epsilon=1}^{\eta} \frac{l_\epsilon}{1-\overline{\varrho}_\epsilon} \int_{t-w_\epsilon(t)}^{t} \left(z^R(\varepsilon)\right)^T \Psi_\epsilon z^R(\varepsilon) d\varepsilon \\
&\quad + \sum_{\epsilon=1}^{\eta} \frac{l_\epsilon}{1-\overline{\varrho}_\epsilon} \int_{t-w_\epsilon(t)}^{t} \left(z^I(\varepsilon)\right)^T \Psi_\epsilon z^I(\varepsilon) d\varepsilon \\
&\quad + \sum_{\epsilon=1}^{\eta}\sum_{\delta=1}^{N} \frac{l_\epsilon}{\zeta_\delta^\epsilon}\left(\left(\rho_\delta^\epsilon(t)\right)^R - \left(\widehat{\rho}_\delta^\epsilon\right)^R\right)^2 \\
&\quad + \sum_{\epsilon=1}^{\eta}\sum_{\delta=1}^{N} \frac{l_\epsilon}{\zeta_\delta^\epsilon}\left(\left(\rho_\delta^\epsilon(t)\right)^I - \left(\widehat{\rho}_\delta^r\right)^I\right)^2 \\
&\quad + 2\sum_{\delta=1}^{N}\sum_{h=1}^{n} \int_{t-u_h(t)}^{t} \frac{\left(j_h^R z_{\delta h}^R(\varepsilon)\right)^2}{1-\varrho_h} d\varepsilon \\
&\quad + 2\sum_{\delta=1}^{N}\sum_{h=1}^{n} \int_{t-u_h(t)}^{t} \frac{\left(j_h^I z_{\delta h}^I(\varepsilon)\right)^2}{1-\varrho_h} d\varepsilon \\
&\quad + \sum_{\delta=1}^{N}\left(z_\delta^R(t)\right)^T z_\delta^R(t) + \sum_{\delta=1}^{N}\left(z_\delta^I(t)\right)^T z_\delta^I(t).
\end{aligned} \tag{69}$$

Taking the derivative of $V_4(t)$, we have

$$\begin{aligned}\dot{V}_4(t) \le{}& 2\sum_{\delta=1}^{N}\left(z_\delta^R(t)\right)^T\Big\{-Dz_\delta^R(t)+P^R\left(A_\delta^R(t)\right)G^R\left(\overline{z_\delta^R(t)}\right)-P^I\left(A_\delta^I(t)\right)G^I\left(\overline{z_\delta^I(t)}\right)-\left[P^R\left(A_\delta^R(t)\right)-P^R\left(A_*^R(t)\right)\right]y^R\left(A_*^R(t)\right)\\&+\sum_{\epsilon=1}^{\eta}\sum_{\kappa=1}^{N}l_\epsilon K_{\iota\kappa}^\epsilon H_\epsilon\widehat{z_\kappa^R(t)}-\Theta_\delta^R z_\delta^R(t)-\operatorname{sign}\left(z_\delta^R(t)\right)\left(\overline{P}^R\overline{Y}^R+\overline{P}^I\overline{Y}^I\right)-\sum_{\epsilon=1}^{\eta}l_\epsilon\left(\rho_\delta^\epsilon(t)\right)^R H_\epsilon z_\delta^R(t)+\Big[P^I\left(A_\delta^I(t)\right)\\&-P^I\left(A_*^I(t)\right)\Big]y^I\left(A_*^I(t)\right)\Big\}+2\sum_{\delta=1}^{N}\left(z_\delta^I(t)\right)^T\Big\{-Dz_\delta^I(t)+P^R\left(A_\delta^R(t)\right)G^I\left(\overline{z_\delta^I(t)}\right)+P^I\left(A_\delta^I(t)\right)G^R\left(\overline{z_\delta^R(t)}\right)-\Big[P^R\left(A_\delta^R(t)\right)\\&-P^R\left(A_*^R(t)\right)\Big]y^I\left(A_*^I(t)\right)+\sum_{\epsilon=1}^{\eta}\sum_{\kappa=1}^{N}l_\epsilon K_{\iota\kappa}^\epsilon H_\epsilon\widehat{z_\kappa^I(t)}-\Theta_\delta^I z_\delta^I(t)-\operatorname{sign}\left(z_\delta^I(t)\right)\left(\overline{P}^R\overline{Y}^I+\overline{P}^I\overline{Y}^R\right)-\sum_{\epsilon=1}^{\eta}l_r\left(\rho_\delta^\epsilon(t)\right)^I H_\epsilon z_\delta^I(t)\\&-\left[P^I\left(A_\delta^I(t)\right)-P^I\left(A_*^I(t)\right)\right]y^R\left(A_*^R(t)\right)\Big\}+\sum_{\epsilon=1}^{\eta}\sum_{\delta=1}^{m}l_\epsilon\left(\left(\rho_\delta^\epsilon(t)\right)^R-\left(\widehat{\rho}_\delta^\epsilon\right)^R\right)\left(z_\delta^R(t)\right)^T\left(H_\epsilon+H_\epsilon^T\right)z_\delta^R(t)+\sum_{\epsilon=1}^{\eta}\sum_{\delta=1}^{m}l_\epsilon\left(\rho_\delta^\epsilon(t)\right)^I\\&-\left(\widehat{\rho}_\delta^\epsilon\right)^I\left(z_\delta^I(t)\right)^T\left(H_\epsilon+H_\epsilon^T\right)z_\delta^I(t)+2\left(z^R(t)\right)^T\left(I_N\otimes\left(J^R\Lambda\right)\right)z^R(t)-2\left(\overline{z^R(t)}\right)^T\left(I_N\otimes J^R\right)\overline{z^R(t)}+2\left(z^I(t)\right)^T\Big(I_N\\&\otimes\left(J^I\Lambda\right)z^I(t)-2\left(\overline{z^I(t)}\right)^T\left(I_N\otimes J^I\right)\overline{z^I(t)}+\sum_{\epsilon=1}^{\eta}\frac{l_\epsilon}{1-\overline{\varrho}_\epsilon}\left(z^R(t)\right)^T\Psi_\epsilon z^R(t)-\sum_{\epsilon=1}^{\eta}l_\epsilon\left(\widehat{z^R(t)}\right)^T\Psi_\epsilon\widehat{z^R(t)}\\&+\sum_{\epsilon=1}^{\eta}\frac{l_\epsilon}{1-\overline{\varrho}_\epsilon}\left(z^I(t)\right)^T\Psi_\epsilon z^I(t)-\sum_{\epsilon=1}^{\eta}l_\epsilon\left(\widehat{z^I(t)}\right)^T\Psi_\epsilon\widehat{z^I(t)}.\end{aligned}\tag{70}$$

By (20)–(23), (26)–(29), (51)-(52), (60)-(61), and (70), we have

$$\begin{aligned}\dot{V}_4(t)\le{}&\left(z^R(t)\right)^T\left\{I_N\otimes\left(-2\,D+\widetilde{P}^R+\widetilde{P}^I+2J^R\Lambda\right)-2\Theta^R+\sum_{\epsilon=1}^{\eta}l_\epsilon\left[\left(K^\epsilon\otimes H_\epsilon\right)\Psi_\epsilon^{-1}\left(\left(K^\epsilon\right)^T\otimes H_\epsilon^T\right)-\left(\widehat{\rho}^\epsilon\right)^R\otimes\left(H_\epsilon+H_\epsilon^T\right)+\frac{1}{1-\overline{\varrho}_\epsilon}\Psi_\epsilon\right]\right\}z^R(t)\\&+\left(z^I(t)\right)^T\left\{I_N\otimes\left(-2\,D+\widetilde{P}^R+\widetilde{P}^I+2J^I\Lambda\right)-2\Theta^I+\sum_{\epsilon=1}^{\eta}l_\epsilon\left[\left(K^\epsilon\otimes H_\epsilon\right)\Psi_\epsilon^{-1}\left(\left(K^\epsilon\right)^T\otimes H_\epsilon^T\right)-\left(\widehat{\rho}^\epsilon\right)^I\otimes\left(H_\epsilon+H_\epsilon^T\right)+\frac{1}{1-\overline{\varrho}_\epsilon}\Psi_\epsilon\right]\right\}z^I(t)\\&\le\alpha_4\|z(t)\|^2,\end{aligned}\tag{71}$$

where $\alpha_4=\max\{\lambda_M(\Phi_4^R),\lambda_M(\Phi_4^I)\}<0$. By combining the proofs of Theorems 2 with 3, we can obtain $\lim_{t\longrightarrow+\infty}\|z(t)\|=0$. Thus, the network (65) is anti-synchronized under the controller (47). □ □

5. Numerical Examples

Example 1. Consider the MWCCVDMNNs illustrated by

$$\begin{aligned}\dot{A}_\delta(t)={}&-DA_\delta(t)+P\left(A_\delta(t)\right)y\left(\overline{A_\delta(t)}\right)+c_\delta(t)\\&+l_1\sum_{\kappa=1}^{6}K_{\delta\kappa}^1H_1A_\kappa(t)+l_2\sum_{\kappa=1}^{6}K_{\delta\kappa}^2H_2A_\kappa(t)+l_3\sum_{\kappa=1}^{6}K_{\delta\kappa}^3H_3A_\kappa(t),\end{aligned}\tag{72}$$

where$\delta=1,2,\ldots,6$, $y_i^R(\mu)=y_i^I(\mu)=(|\mu+1|-|\mu-1|)/5\,(i=1,2,3)$, $D=\operatorname{diag}(0.4,0.8,0.5)$, $l_1=0.1$, $l_2=0.2$, $l_3=0.4$, $u_h(t)=1-1/(2+h)x^{-t}$, $u=1$, $\varrho_h=1/(2+h)$, $h=1,2,3$, and the matricesH_ϵ, $K^\epsilon=(K_{\iota\kappa}^\epsilon)_{6\times6}\,(\epsilon=1,2,3)$, and the elements in the matrices $P(A_\delta(t))\,(\delta=1,2,\ldots,6)$ are selected as follows:

$$H_1 = \begin{pmatrix} 0.4 & 0.1 & 0.2 \\ 0.1 & 0.4 & 0.2 \\ 0.4 & 0.2 & 0.5 \end{pmatrix}, H_2 = \begin{pmatrix} 0.4 & 0.3 & 0.4 \\ 0.2 & 0.7 & 0.3 \\ 0.4 & 0.9 & 0.6 \end{pmatrix}, H_3 = \begin{pmatrix} 0.4 & 0.3 & 0.2 \\ 0.2 & 0.8 & 0.4 \\ 0.2 & 1.1 & 0.7 \end{pmatrix},$$

$$\begin{aligned}
p_{11}^R\left(a_{\delta 1}^R(t)\right) &= \begin{matrix} 0.42, & \left|a_{\delta 1}^R(t)\right| \leqslant 1.7, \\ -0.32, & \left|a_{\delta 1}^R(t)\right| > 1.7, \end{matrix} & p_{12}^R\left(a_{\delta 1}^R(t)\right) &= \begin{matrix} -0.32, & \left|a_{\delta 1}^R(t)\right| \leqslant 1.7, \\ -0.36, & \left|a_{\delta 1}^R(t)\right| > 1.7, \end{matrix} \\
p_{13}^R\left(a_{\delta 1}^R(t)\right) &= \begin{matrix} -0.28, & \left|a_{\delta 1}^R(t)\right| \leqslant 1.7, \\ -0.40, & \left|a_{\delta 1}^R(t)\right| > 1.7, \end{matrix} & p_{21}^R\left(a_{\delta 2}^R(t)\right) &= \begin{matrix} 0.33, & \left|a_{\delta 2}^R(t)\right| \leqslant 1.7, \\ -0.28, & \left|a_{\delta 2}^R(t)\right| > 1.7, \end{matrix} \\
p_{22}^R\left(a_{\delta 2}^R(t)\right) &= \begin{matrix} -0.29, & \left|a_{\delta 2}^R(t)\right| \leqslant 1.7, \\ 0.36, & \left|a_{\delta 2}^R(t)\right| > 1.7, \end{matrix} & p_{23}^R\left(a_{\delta 2}^R(t)\right) &= \begin{matrix} 0.20, & \left|a_{\delta 2}^R(t)\right| \leqslant 1.7, \\ -0.19, & \left|a_{\delta 2}^R(t)\right| > 1.7, \end{matrix} \\
p_{31}^R\left(a_{\delta 3}^R(t)\right) &= \begin{matrix} 0.24, & \left|a_{\delta 3}^R(t)\right| \leqslant 1.7, \\ -0.13, & \left|a_{\delta 3}^R(t)\right| > 1.7, \end{matrix} & p_{32}^R\left(a_{\delta 3}^R(t)\right) &= \begin{matrix} 0.39, & \left|a_{\delta 3}^R(t)\right| \leqslant 1.7, \\ 0.26, & \left|a_{\delta 3}^R(t)\right| > 1.7, \end{matrix} \\
p_{33}^R\left(a_{\delta 3}^R(t)\right) &= \begin{matrix} -0.34, & \left|a_{\delta 3}^R(t)\right| \leqslant 1.7, \\ -0.27, & \left|a_{\delta 3}^R(t)\right| > 1.7, \end{matrix} & p_{11}^I\left(a_{\delta 1}^I(t)\right) &= \begin{matrix} -0.34, & \left|a_{\delta 1}^I(t)\right| \leqslant 1.7, \\ 0.25, & \left|a_{\delta 1}^I(t)\right| > 1.7, \end{matrix} \\
p_{12}^I\left(a_{\delta 1}^I(t)\right) &= \begin{matrix} 0.24, & \left|a_{\delta 1}^I(t)\right| \leqslant 1.7, \\ 0.17, & \left|a_{\delta 1}^I(t)\right| > 1.7, \end{matrix} & p_{13}^I\left(a_{\delta 1}^I(t)\right) &= \begin{matrix} -0.42, & \left|a_{\delta 1}^I(t)\right| \leqslant 1.7, \\ 0.36, & \left|a_{\delta 1}^I(t)\right| > 1.7, \end{matrix} \\
p_{21}^I\left(a_{\delta 2}^I(t)\right) &= \begin{matrix} 0.27, & \left|a_{\delta 2}^I(t)\right| \leqslant 1.7, \\ -0.14, & \left|a_{\delta 2}^I(t)\right| > 1.7, \end{matrix} & p_{22}^I\left(a_{\delta 2}^I(t)\right) &= \begin{matrix} 0.26, & \left|a_{\delta 2}^I(t)\right| \leqslant 1.7, \\ 0.17, & \left|a_{\delta 2}^I(t)\right| > 1.7, \end{matrix} \\
p_{23}^I\left(a_{\delta 2}^I(t)\right) &= \begin{matrix} -0.19, & \left|a_{\delta 2}^I(t)\right| \leqslant 1.7, \\ -0.21, & \left|a_{\delta 2}^I(t)\right| > 1.7, \end{matrix} & p_{31}^I\left(a_{\delta 3}^I(t)\right) &= \begin{matrix} -0.25, & \left|a_{\delta 3}^I(t)\right| \leqslant 1.7, \\ 0.31, & \left|a_{\delta 3}^I(t)\right| > 1.7, \end{matrix} \\
p_{32}^I\left(a_{\delta 3}^I(t)\right) &= \begin{matrix} 0.27, & \left|a_{\delta 3}^I(t)\right| \leqslant 1.7, \\ 0.26, & \left|a_{\delta 3}^I(t)\right| > 1.7, \end{matrix} & p_{33}^I\left(a_{\delta 3}^I(t)\right) &= \begin{matrix} -0.38, & \left|a_{\delta 3}^I(t)\right| \leqslant 1.7, \\ 0.40, & \left|a_{\delta 3}^I(t)\right| > 1.7, \end{matrix}
\end{aligned} \tag{73}$$

$$K^1 = \begin{pmatrix} -0.6 & 0.2 & 0.1 & 0.1 & 0 & 0.2 \\ 0.3 & -0.7 & 0.1 & 0.1 & 0.1 & 0.1 \\ 0.1 & 0.2 & -0.8 & 0.1 & 0.3 & 0.1 \\ 0.2 & 0.1 & 0.3 & -1.1 & 0.4 & 0.1 \\ 0.1 & 0.1 & 0.2 & 0.2 & -0.9 & 0.3 \\ 0.2 & 0.5 & 0 & 0 & 0.3 & -1.0 \end{pmatrix},$$

$$K^2 = \begin{pmatrix} -0.7 & 0.1 & 0.2 & 0.3 & 0.1 & 0 \\ 0.2 & -0.9 & 0 & 0.3 & 0.3 & 0.1 \\ 0.2 & 0.2 & -0.9 & 0 & 0.3 & 0.2 \\ 0 & 0.4 & 0.2 & -0.8 & 0.1 & 0.1 \\ 0.3 & 0.1 & 0.4 & 0.1 & -1.1 & 0.2 \\ 0.1 & 0.1 & 0.2 & 0.2 & 0 & -0.6 \end{pmatrix},$$

$$K^3 = \begin{pmatrix} -0.8 & 0.3 & 0 & 0.2 & 0.1 & 0.2 \\ 0.4 & -0.8 & 0.1 & 0.2 & 0 & 0.1 \\ 0 & 0 & -1.0 & 0.5 & 0.2 & 0.3 \\ 0.3 & 0.1 & 0.4 & -1.2 & 0.2 & 0.2 \\ 0.2 & 0.1 & 0 & 0.3 & -0.9 & 0.3 \\ 0.2 & 0.4 & 0 & 0.2 & 0.3 & -1.1 \end{pmatrix}.$$

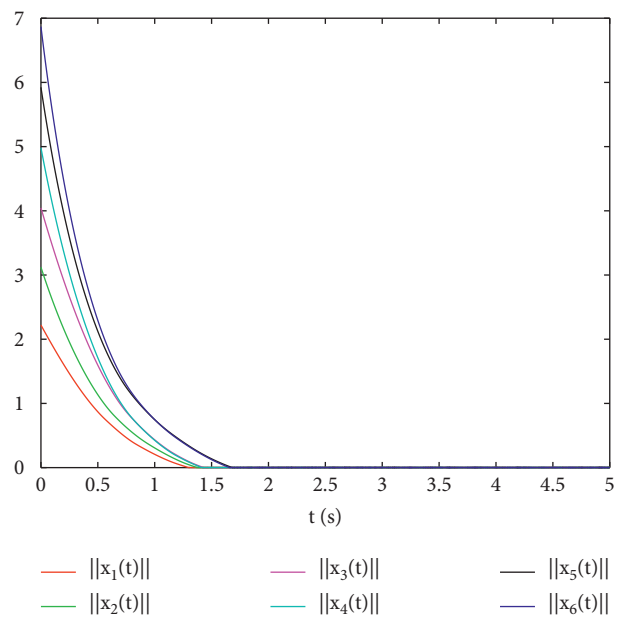

Figure 1: Time evolution of $\|z_\iota(t)\|$, $\iota = 1, 2, \ldots, 6$.

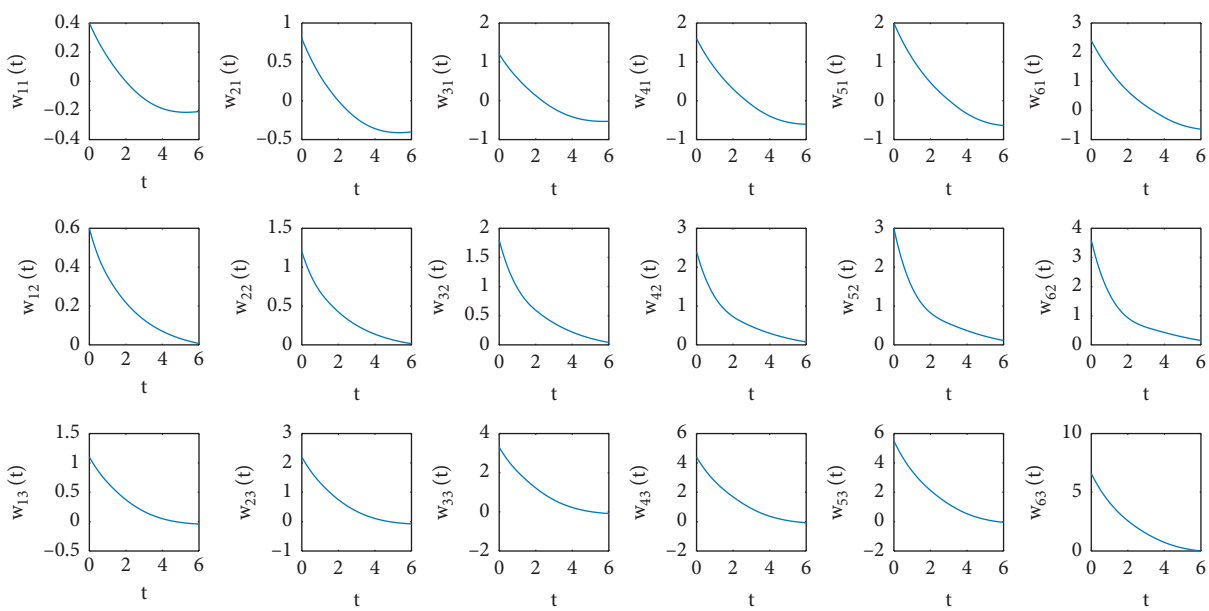

Figure 2: The single dynamical change process of uncoupled NN in (72).

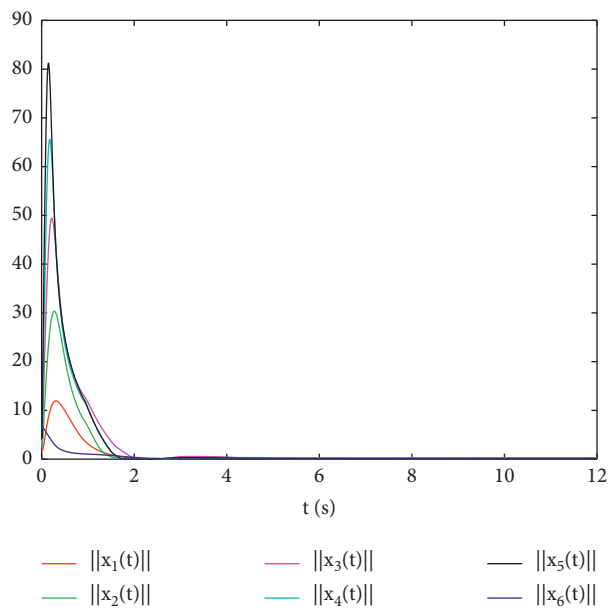

Figure 3: Time evolution of $\|z_\iota(t)\|$ under pinning controller (47), where $\iota = 1, 2, \ldots, 6$.

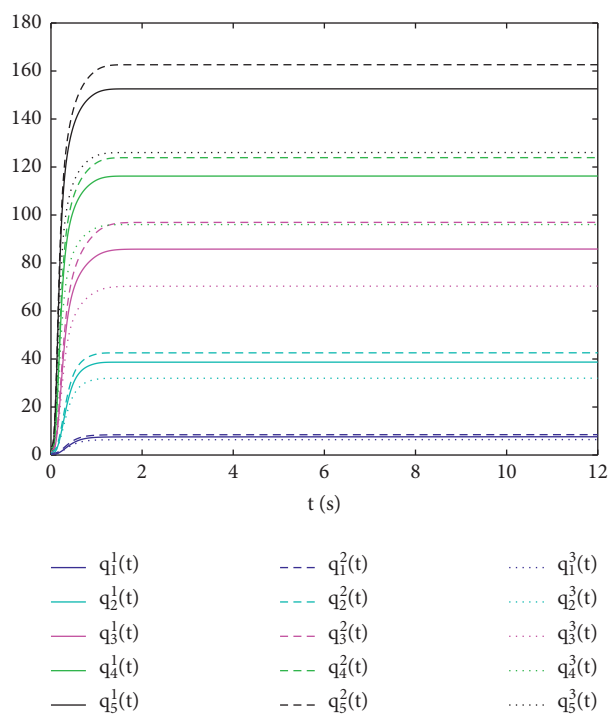

Figure 4: $\rho_\iota^r(t)$ when $\zeta_\iota^r = 0.5$, $\iota = 1, 2, \ldots, 5$, $r = 1, 2, 3$.

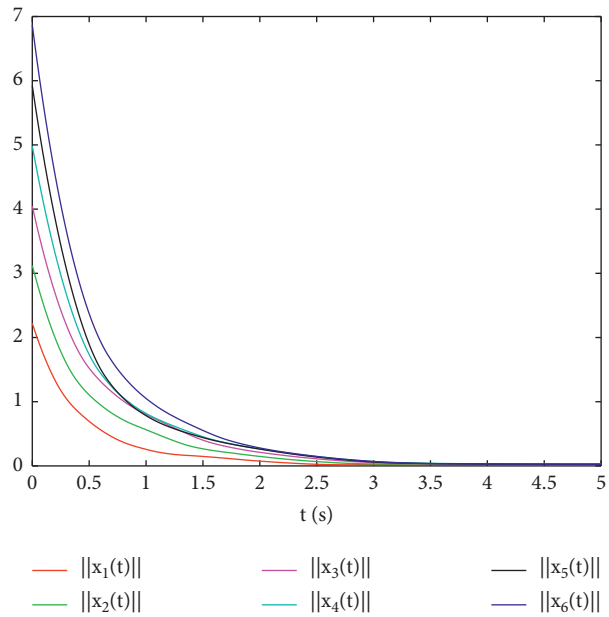

Figure 5: Time evolution of $\|z_\iota(t)\|$ without pinned nodes, where $\iota = 1, 2, \ldots, 6$.

It is readily seen that Assumption 1 is satisfied with $Y_\delta^R = Y_\delta^I = 0.4$ and $j_\delta^R = j_\delta^I = 0.4$. Choose the parameters in the controller (15) as follows: $\Theta^R = \mathrm{diag}(\Theta_1^R, \Theta_2^R, \ldots, \Theta_6^R) = \mathrm{diag}$ $(1.01, 0.98, 0.76, 0.69, 1.10, 1.05, 0.86, 0.79, 0.91,$ $1.23, 1.54, 1.71, 1.82, 1.79, 1.79, 1.06, 0.86, 0.78)$, $\Theta^I = \mathrm{diag}(\Theta_1^I, \Theta_2^I, \ldots, \Theta_6^I) = \mathrm{diag}(0.92,$ $0.76, 0.87, 0.92, 0.71, 0.78, 0.86, 0.99, 0.94, 0.85,$ $0.69, 0.76, 0.59, 0.71, 0.77, 0.89, 0.83, 0.90)$.

By making use of the YALMIP Toolbox in MATLAB, we can obtain

$$\begin{aligned}
&\lambda\left(\Phi_1^R\right) = \{-6.2147, -5.8330, -4.5881, -4.2615, -3.9606, -3.8739, -3.6252, -3.5277, -2.7759, -2.5151, -2.3761, -2.1608, -2.0750, -1.9064, -1.8040, -1.6740, -1.5948, -1.1972\},\\
&\lambda\left(\Phi_1^I\right) = \{-4.7743, -4.3922, -4.0962, -4.0088, -3.5890, -2.3394, -2.1504, -2.0480, -1.9877, -1.9329, -1.8667, -1.7628, -1.7475, -1.7018, -1.5975, -1.5615, -1.4166, -1.0108\},
\end{aligned} \tag{74}$$

which meet condition (17). By Theorem 1, it implies that the network (72) has the capability of realizing anti-synchronization under the pinning adaptive controller (15). Figure 1 depicts the antisynchronization simulation result of network (72). In order to display the effect of multiple coupling matrices, Figure 2 depicts the single dynamical change process of uncoupled NN in (72).

Example 2. Take into account the following MWCCVDMNNs with coupling delays:

$$\begin{aligned}
\dot{A}_\delta(t) = {} & -DA_\delta(t) + P(A_\delta(t))y\left(\overline{A_\delta(t)}\right) + c_\delta(t)\\
& + l_1 \sum_{\kappa=1}^{N} K_{\iota\kappa}^1 H_1 \widehat{A_\kappa(t)} + l_2 \sum_{\kappa=1}^{N} K_{\iota\kappa}^2 H_2 \widehat{A_\kappa(t)}\\
& + l_3 \sum_{\kappa=1}^{N} K_{\iota\kappa}^3 H_3 \widehat{A_\kappa(t)},
\end{aligned} \tag{75}$$

where $\delta = 1, 2, \ldots, 6$, $y_i^R(\mu) = y_i^I(\mu) = (|\mu + 1| - |\mu - 1|)/4\,(i = 1, 2, 3)$, $D = \mathrm{diag}(0.8, 1.0, 0.7)$, $l_1 = 0.4$, $l_2 = 0.3$, $l_3 = 0.1$, $u_h(t) = 1 - 1/(2 + h)z^{-t}$, $u = 1$, $\varrho_h = 1/(2 + h)$, $w_h(t) = (1/20) - (1/10(h + 4))z^{-t}$, $\overline{\varrho}_h$

$= (1/10(h+4))$, $h = 1, 2, 3$, and the matrices H_r, $K^r = (K^r_{\delta\kappa})_{6\times 6}$ $(r = 1, 2, 3)$ and the elements in the matrices $P(A_\delta(t))$ $(\delta = 1, 2, \ldots, 6)$ are selected as follows:

$$H_1 = \begin{pmatrix} 0.18 & 0 & 0 \\ 0.04 & 0.19 & 0.06 \\ 0 & 0 & 0.18 \end{pmatrix}, H_2 = \begin{pmatrix} 0.27 & 0 & 0.09 \\ 0 & 0.07 & 0 \\ 0.04 & 0 & 0.12 \end{pmatrix}, H_3 = \begin{pmatrix} 0.13 & 0 & 0 \\ 0.04 & 0.15 & 0.06 \\ 0 & 0 & 0.15 \end{pmatrix},$$

$$p^R_{11}(a^R_{\delta 1}(t)) = \begin{matrix} 0.53, & |a^R_{\delta 1}(t)| \leqslant 1.5, \\ 0.47, & |a^R_{\delta 1}(t)| > 1.5, \end{matrix} \quad p^R_{12}(a^R_{\delta 1}(t)) = \begin{matrix} 0.23, & |a^R_{\delta 1}(t)| \leqslant 1.5, \\ -0.53, & |a^R_{\delta 1}(t)| > 1.5, \end{matrix}$$

$$p^R_{13}(a^R_{\delta 1}(t)) = \begin{matrix} 0.32, & |a^R_{\delta 1}(t)| \leqslant 1.5, \\ 0.42, & |a^R_{\delta 1}(t)| > 1.5, \end{matrix} \quad p^R_{21}(a^R_{\delta 2}(t)) = \begin{matrix} -0.47, & |a^R_{\delta 2}(t)| \leqslant 1.5, \\ -0.53, & |a^R_{\delta 2}(t)| > 1.5, \end{matrix}$$

$$p^R_{22}(a^R_{\delta 2}(t)) = \begin{matrix} 0.31, & |a^R_{\delta 2}(t)| \leqslant 1.5, \\ 0.24, & |a^R_{\delta 2}(t)| > 1.5, \end{matrix} \quad p^R_{23}(a^R_{\delta 2}(t)) = \begin{matrix} -0.41, & |a^R_{\delta 2}(t)| \leqslant 1.5, \\ 0.51, & |a^R_{\delta 2}(t)| > 1.5, \end{matrix}$$

$$p^R_{31}(a^R_{\delta 3}(t)) = \begin{matrix} -0.27, & |a^R_{\delta 3}(t)| \leqslant 1.5, \\ -0.43, & |a^R_{\delta 3}(t)| > 1.5, \end{matrix} \quad p^R_{32}(a^R_{\delta 3}(t)) = \begin{matrix} 0.37, & |a^R_{\delta 3}(t)| \leqslant 1.5, \\ 0.25, & |a^R_{\delta 3}(t)| > 1.5, \end{matrix}$$

$$p^R_{33}(a^R_{\delta 3}(t)) = \begin{matrix} -0.38, & |a^R_{\delta 3}(t)| \leqslant 1.5, \\ 0.29, & |a^R_{\delta 3}(t)| > 1.5, \end{matrix} \quad p^I_{11}(a^I_{\delta 1}(t)) = \begin{matrix} -0.43, & |a^R_{\delta 1}(t)| \leqslant 1.5, \\ 0.32, & |a^R_{\delta 1}(t)| > 1.5, \end{matrix}$$

$$p^I_{12}(a^I_{\delta 1}(t)) = \begin{matrix} 0.35, & |a^R_{\delta 1}(t)| \leqslant 1.5, \\ -0.27, & |a^R_{\delta 1}(t)| > 1.5, \end{matrix} \quad p^I_{13}(a^I_{\delta 1}(t)) = \begin{matrix} 0.41, & |a^R_{\delta 1}(t)| \leqslant 1.5, \\ 0.40, & |a^R_{\delta 1}(t)| > 1.5, \end{matrix}$$

$$p^I_{21}(a^I_{\delta 2}(t)) = \begin{matrix} 0.32, & |a^R_{\delta 2}(t)| \leqslant 1.5, \\ -0.38, & |a^R_{\delta 2}(t)| > 1.5, \end{matrix} \quad p^I_{22}(a^I_{\delta 2}(t)) = \begin{matrix} 0.42, & |a^R_{\delta 2}(t)| \leqslant 1.5, \\ 0.45, & |a^R_{\delta 2}(t)| > 1.5, \end{matrix}$$

$$p^I_{23}(a^I_{\delta 2}(t)) = \begin{matrix} -0.52, & |a^R_{\delta 2}(t)| \leqslant 1.5, \\ -0.71, & |a^R_{\delta 2}(t)| > 1.5, \end{matrix} \quad p^I_{31}(a^I_{\delta 3}(t)) = \begin{matrix} -0.32, & |a^R_{\delta 3}(t)| \leqslant 1.5, \\ 0.41, & |a^R_{\delta 3}(t)| > 1.5, \end{matrix}$$

$$p^I_{32}(a^I_{\delta 3}(t)) = \begin{matrix} 0.71, & |a^R_{\delta 3}(t)| \leqslant 1.5, \\ 0.54, & |a^R_{\delta 3}(t)| > 1.5, \end{matrix} \quad p^I_{33}(a^I_{\delta 3}(t)) = \begin{matrix} 0.60, & |a^R_{\delta 3}(t)| \leqslant 1.5, \\ 0.57, & |a^R_{\delta 3}(t)| > 1.5, \end{matrix}$$

$$K^1 = \begin{pmatrix} -0.7 & 0.1 & 0.3 & 0 & 0.1 & 0.2 \\ 0.3 & -0.8 & 0.1 & 0.2 & 0.1 & 0.1 \\ 0.1 & 0.2 & -1.1 & 0.5 & 0.1 & 0.2 \\ 0 & 0.2 & 0.4 & -1.1 & 0.2 & 0.3 \\ 0.2 & 0.1 & 0 & 0.2 & -1.0 & 0.5 \\ 0.1 & 0.2 & 0.4 & 0.1 & 0 & -0.8 \end{pmatrix},$$

$$K^2 = \begin{pmatrix} -0.8 & 0.2 & 0.2 & 0.3 & 0.1 & 0 \\ 0.1 & -1.0 & 0.2 & 0.2 & 0.3 & 0.2 \\ 0.3 & 0 & -0.9 & 0 & 0.3 & 0.3 \\ 0.2 & 0.1 & 0.1 & -0.8 & 0.3 & 0.1 \\ 0 & 0.3 & 0.4 & 0.2 & -1.1 & 0.2 \\ 0.2 & 0.1 & 0.3 & 0.1 & 0.2 & -0.9 \end{pmatrix}, \tag{76}$$

$$K^3 = \begin{pmatrix} -0.9 & 0.3 & 0.1 & 0.1 & 0.2 & 0.2 \\ 0.2 & -0.8 & 0 & 0.4 & 0.1 & 0.1 \\ 0 & 0 & -1.0 & 0.5 & 0.2 & 0.3 \\ 0.2 & 0.1 & 0.2 & -0.7 & 0 & 0.2 \\ 0.1 & 0.1 & 0.2 & 0.2 & -0.9 & 0.3 \\ 0.3 & 0 & 0.1 & 0.2 & 0.4 & -1.0 \end{pmatrix}.$$

It is readily seen that Assumption 1 is satisfied with $Y^R_\delta = Y^I_\delta = 0.5$ and $j^R_\delta = j^I_\delta = 0.5$. Select the parameters in the controller (47) as follows: $\Theta^R = \mathrm{diag}(\Theta^R_1, \Theta^R_2, \ldots, \Theta^R_6) = \mathrm{diag}(0.89, 0.78, 0.81, 0.64, 0.71, 0.90, 0.89, 0.65, 0.71, 0.67, 0.74, 0.57, 0.73, 0.77, 0.89, 0.75, 0.88, 0.73)$ and $\Theta^I = \mathrm{diag}(\Theta^I_1, \Theta^I_2, \ldots, \Theta^I_6) = \mathrm{diag}(0.74, 0.65, 0.54, 0.71, 0.93, 0.73, 0.89, 0.65, 0.52, 0.67, 0.51, 0.49, 0.81, 0.60, 0.83, 0.77, 0.81, 0.74)$.

We select the first 5 nodes as pinned nodes. Choose $(\widehat{\rho}^1)^R = \mathrm{diag}((\widehat{\rho}^1_1)^R, (\widehat{\rho}^1_2)^R, \ldots, (\widehat{\rho}^1_5)^R, 0) = \mathrm{diag}(0.1, 0.2, 0.3, 0.4, 0.5, 0)$, $(\widehat{\rho}^2)^R = \mathrm{diag}((\widehat{\rho}^2_1)^R, (\widehat{\rho}^2_2)^R, \ldots, (\widehat{\rho}^2_5)^R, 0) = \mathrm{diag}(0.3, 0.6, 0.9, 1.2, 1.5, 0)$, $(\widehat{\rho}^3)^R = \mathrm{diag}((\widehat{\rho}^3_1)^R, (\widehat{\rho}^3_2)^R, \ldots, (\widehat{\rho}^3_5)^R, 0) = \mathrm{diag}(0.2, 0.4, 0.6, 0.8, 1.0, 0)$, $(\widehat{\rho}^1)^I = \mathrm{diag}((\widehat{\rho}^1_1)^I, (\widehat{\rho}^1_2)^I, \ldots, (\widehat{\rho}^1_5)^I, 0) = \mathrm{diag}(0.2, 0.4, 0.6, 0.8, 1.0, 0)$, $(\widehat{\rho}^2)^I = \mathrm{diag}((\widehat{\rho}^2_1)^I, (\widehat{\rho}^2_2)^I, \cdots, (\widehat{\rho}^2_5)^I, 0) = \mathrm{diag}(0.4, 0.8, 1.2, 1.6, 2.0, 0)$, and $(\widehat{\rho}^3)^I = \mathrm{diag}((\widehat{\rho}^3_1)^I, (\widehat{\rho}^3_2)^I, \ldots, (\widehat{\rho}^3_5)^I, 0) = \mathrm{diag}(0.3, 0.6, 0.9, 1.2, 1.5, 0)$.

By making use of the YALMIP Toolbox of MATLAB, the following Ψ_ϵ $(\epsilon = 1, 2, 3)$ satisfying (68) can be computed: $\Psi_1 = \mathrm{diag}(0.5033, 0.5033, 0.4082, 0.4840, 0.5203, 0.4739, 0.5319, 0.5095, 0.4281, 0.5077, 0.5072, 0.4086, 0.5230, 0.5148, 0.5041, 0.4876, 0.5213, 0.4381)$, $\Psi_2 = \mathrm{diag}(0.3954, 0.3820, 0.3388, 0.3965, 0.3908, 0.3726, 0.4044, 0.3796, 0.3394, 0.3947, 0.3783, 0.3282, 0.4068, 0.3867, 0.3864, 0.3933, 0.3897, 0.3518)$, and $\Psi_3 = \mathrm{diag}(0.1188, 0.1191, 0.1194, 0.1181, 0.1184, 0.1190, 0.1186, 0.1195, 0.1200, 0.1186, 0.1190, 0.1190, 0.1187, 0.1191, 0.1201, 0.1192, 0.1194, 0.1209)$.

Based on Theorem 4, we conclude that the pinning antisynchronization of network (75) is realized with the controller (47). Figures 3 and 4 show the simulation results. For comparison, Figure 5 shows the variation trajectory of error variables $x_i(t)$ without pinned nodes.

6. Conclusions

This paper has investigated the antisynchronization of MWCCVDMNNs without and with coupling delays. On the one hand, we have presented some sufficient conditions for reaching antisynchronization of the proposed network models. On the other hand, some generalized pinning antisynchronization criteria on the basis of the designed pinning control strategy have been established to ensure that the considered MWCCVDMNNs with and without coupling delays realize generalized pinning antisynchronization, respectively. Furthermore, two numerical examples have been shown to verify the correctness of the derived results. This paper is an extended version of our previous work published in [37]. Based on the derived antisynchronization results of MWCCVDMNNs with and without coupling delays in [37], we have further investigated the generalized pinning antisynchronization of the considered networks by designing a novel generalized pinning adaptive controller in this paper. More specifically, the pinning controller we designed in this paper consists of two parts, one part controls all the nodes, and the other part controls the first m nodes of the considered network, which is different from the classical pinning control. To the best of the authors' knowledge, this is the first paper toward to researching the pinning antisynchronization of the MWCCVDMNNs. However, there are several interesting problems for further study. On the one hand, some scholars have investigated the dynamical behavior of a new type of coupled complex-valued networks with intermittent coupling recently [38]. In contrast to the common continuous coupling in this paper, intermittent coupling is a discontinuous form of communication which has greater flexibility for nodes because they are not constrained by communication requirements in decoupling time, which unavoidably result in the difference of dynamics of nodes between the coupling time and decoupling period. Therefore, it would be very interesting to take the intermittent coupling into consideration when studying the pinning antisynchronization of MWCCVDMNNs in our

future work. On the other hand, it is known to all that fractional calculus is a theory that generalizes the concept of calculus from the integer order to arbitrary order. Up to now, fractional-order systems have been applied in some new mechanical models due to their non-Markovian and non-Gaussian properties during the studying of dynamical systems. In [39], a novel criterion for achieving synchronization of fractional-order chaotic and hyperchaotic systems was proposed. Motivated by this work, it would be also a very interesting problem of research to insert fractional operators into the proposed MWCCVDMNNs in this paper and study the antisynchronization of this kind of the fractional-order network model.

Data Availability

No data were used to support this study.

Conflicts of Interest

The authors declare that there are no conflicts of interest.

Acknowledgments

This work was supported in part by the National Natural Science Foundation of China under Grants 62173016 and 62173244 and in part by the Beijing Natural Science Foundation (P.R. China) under Grant 4202038.

References

[1] M. Lungu and R. Lungu, "Automatic control of aircraft lateral-directional motion during landing using neural networks and radio-technical subsystems," *Neurocomputing*, vol. 171, pp. 471–481, 2016.

[2] V. A. Demin, D. V. Nekhaev, I. A. Surazhevsky et al., "Necessary conditions for STDP-based pattern recognition learning in a memristive spiking neural network," *Neural Networks*, vol. 134, pp. 64–75, 2021.

[3] G. Yang and F. Ding, *Associative memory optimized method on deep neural networks for image classification Information Sciences*, vol. 533, pp. 108–119, 2020.

[4] H. A. Tang, S. Duan, X. Hu, and L. Wang, "Passivity and synchronization of coupled reaction-diffusion neural networks with multiple time-varying delays via impulsive control," *Neurocomputing*, vol. 318, pp. 30–42, 2018.

[5] J. L. Wang, X. X. Zhang, H. N. Wu, T. Huang, and Q. Wang, "Finite-time passivity of adaptive coupled neural networks with undirected and directed topologies," *IEEE Transactions on Cybernetics*, vol. 50, no. 5, pp. 2014–2025, 2020.

[6] C. Hu and H. Jiang, "Special functions-based fixed-time estimation and stabilization for dynamic systems," *IEEE Transactions on Systems, Man, and Cybernetics: Systems*, vol. 52, no. 5, pp. 3251–3262, 2022.

[7] C. Hu, H. He, and H. Jiang, "Fixed/Preassigned-time synchronization of complex networks via improving fixed-time stability," *IEEE Transactions on Cybernetics*, vol. 51, no. 6, pp. 2882–2892, 2021.

[8] C. Hu, H. He, and H. Jiang, "Edge-based adaptive distributed method for synchronization of intermittently coupled spatiotemporal networks," *IEEE Transactions on Automatic Control*, vol. 67, no. 5, pp. 2597–2604, 2022.

[9] L. Chua, "Memristor-the missing circuit element," *IEEE Transactions on Circuit Theory*, vol. 18, no. 5, pp. 507–519, 1971.

[10] Y. V. Pershin and M. D. Ventra, "Experimental demonstration of associative memory with memristive neural networks," *Neural Networks*, vol. 23, no. 7, pp. 881–886, 2010.

[11] J. Hu and J. Wang, "Global uniform asymptotic stability of memristor-based recurrent neural networks with time delays," *International Joint Conference on Neural Networks (IJCNN)*, pp. 1–8, 2010.

[12] X. Lv, J. Cao, and L. Rutkowski, "Dynamical and static multisynchronization analysis for coupled multistable memristive neural networks with hybrid control," *Neural Networks*, vol. 143, pp. 515–524, 2021.

[13] R. Li and J. Cao, "Passivity and dissipativity of fractional-order quaternion-valued fuzzy memristive neural networks: nonlinear scalarization approach," *IEEE Transactions on Cybernetics*, vol. 52, no. 5, pp. 2821–2832, 2022.

[14] L. Peng, X. Li, D. Bi, X. Xie, and Y. Xie, "Multiple m-stable synchronization control for coupled memristive neural networks with unbounded time delays," *IEEE Transactions on Systems, Man, and Cybernetics: Systems*, vol. 52, no. 2, pp. 990–1002, 2020.

[15] J. Chen, B. Chen, and Z. Zeng, "Exponential quasi-synchronization of coupled delayed memristive neural networks via intermittent event-triggered control," *Neural Networks*, vol. 141, pp. 98–106, 2021.

[16] A. Wu and Z. Zeng, "Anti-synchronization control of a class of memristive recurrent neural networks," *Communications in Nonlinear Science and Numerical Simulation*, vol. 18, no. 2, pp. 373–385, 2013.

[17] X. Wei, Z. Zhang, C. Lin, and J. Chen, "Synchronization and anti-synchronization for complex-valued inertial neural networks with time-varying delays," *Applied Mathematics and Computation*, vol. 403, Article ID 126194, 2021.

[18] F. Zhang, T. Huang, D. Feng, and Z. Zeng, "Multistability and robustness of complex-valued neural networks with delays and input perturbation," *Neurocomputing*, vol. 447, pp. 319–328, 2021.

[19] X. Wei, Z. Zhang, M. Liu, Z. Wang, and J. Chen, "Anti-synchronization for complex-valued neural networks with leakage delay and time-varying delays," *Neurocomputing*, vol. 412, pp. 312–319, 2020.

[20] G. Velmurugan, R. Rakkiyappan, and S. Lakshmanan, "Passivity analysis of memristor-based complex-valued neural networks with time-varying delays," *Neural Processing Letters*, vol. 42, no. 3, pp. 517–540, 2015.

[21] W. Zhang, H. Zhang, J. Cao, F. E. Alsaadi, and D. Chen, "Synchronization in uncertain fractional-order memristive complex-valued neural networks with multiple time delays," *Neural Networks*, vol. 110, pp. 186–198, 2019.

[22] Y. Huang, J. Hou, S. Ren, and E. Yang, "Passivity and Synchronization of Coupled Complex-Valued Memristive Neural Networks," in *Proceedings of the IEEE Symposium Series on Computational Intelligence (SSCI)*, pp. 2152–2159, Xiamen, China, December 2019.

[23] J. L. Wang, M. Xu, H. N. Wu, and T. Huang, "Finite-time passivity of coupled neural networks with multiple weights," *IEEE Transactions on Network Science and Engineering*, vol. 5, no. 3, pp. 184–197, 2018.

[24] J. L. Wang and L. H. Zhao, "PD and PI control for passivity and synchronization of coupled neural networks with multi-weights," *IEEE Transactions on Network Science and Engineering*, vol. 8, no. 1, pp. 790–802, 2021.

[25] Y. Huang, S. Lin, and E. Yang, "Event-triggered passivity of multi-weighted coupled delayed reaction-diffusion memristive neural networks with fixed and switching topologies," *Communications in Nonlinear Science and Numerical Simulation*, vol. 89, Article ID 105292, 2020.

[26] S. Lin, Y. Huang, and S. Ren, "Event-triggered passivity and synchronization of delayed multiple-weighted coupled reaction-diffusion neural networks with non-identical nodes," *Neural Networks*, vol. 121, pp. 259–275, 2020.

[27] L. M. Pecora and T. L. Carroll, "Synchronization in chaotic systems," *Physical Review Letters*, vol. 64, no. 8, pp. 821–824, 1990.

[28] L. Ren, R. Guo, and U. E. Vincent, "A necessary and sufficient condition for anti-synchronization of a class of chaotic systems," *International Journal of Dynamics and Control*, vol. 5, no. 4, pp. 1252–1261, 2017.

[29] J. Hou, Y. Huang, and E. Yang, "Finite-time anti-synchronization of multi-weighted coupled neural networks with and without coupling delays," *Neural Processing Letters*, vol. 50, no. 3, pp. 2871–2898, 2019.

[30] Y. Huang, J. Hou, and E. Yang, "General decay lag anti-synchronization of multi-weighted delayed coupled neural networks with reaction-diffusion terms," *Information Sciences*, vol. 511, pp. 36–57, 2020.

[31] X. Zhang, W. Zhou, H. R. Karimi, and Y. Sun, "Finite- and fixed-time cluster synchronization of nonlinearly coupled delayed neural networks via pinning control," *IEEE Transactions on Neural Networks and Learning Systems*, vol. 32, no. 11, pp. 5222–5231, 2021.

[32] C. X. Yue, L. Wang, X. Hu, H. A. Tang, and S. Duan, "Pinning control for passivity and synchronization of coupled memristive reaction-diffusion neural networks with time-varying delay," *Neurocomputing*, vol. 381, pp. 113–129, 2020.

[33] J. Hou, Y. Huang, and S. Ren, "Anti-synchronization analysis and pinning control of multi-weighted coupled neural networks with and without reaction-diffusion terms," *Neurocomputing*, vol. 330, pp. 78–93, 2019.

[34] J. Lu and J. Cao, "Synchronization-based approach for parameters identification in delayed chaotic neural networks," *Physica A: Statistical Mechanics and Its Applications*, vol. 382, no. 2, pp. 672–682, 2007.

[35] J. L. Wang and H. N. Wu, "Local and global exponential output synchronization of complex delayed dynamical networks," *Nonlinear Dynamics*, vol. 67, no. 1, pp. 497–504, 2012.

[36] A. Hirose, "Dynamics of fully complex-valued neural networks," *Electronics Letters*, vol. 28, no. 16, pp. 1492–1494, 1992.

[37] L. Su, Y. Huang, and J. Wang, "Anti-synchronization of multi-weighted coupled complex-valued delayed memristive neural networks with coupling delays," in *Proceedings of the 1st International Conference on Neuromorphic Computing (ICNC 2021)*, Wuhan, China, October 2021.

[38] C. Hu, H. He, and H. Jiang, "Synchronization of complex-valued dynamic networks with intermittently adaptive coupling: a direct error method," *Automatica*, vol. 112, Article ID 108675, 2020.

[39] A. Al-Khedhairi, A. E. Matouk, and S. S. Askar, "Computations of synchronisation conditions in some fractional-order chaotic and hyperchaotic systems," *Pramana*, vol. 92, no. 5, pp. 72–82, 2019.

Hindawi
Discrete Dynamics in Nature and Society
Volume 2022, Article ID 6260916, 7 pages
https://doi.org/10.1155/2022/6260916

Research Article

Miniaturized Multiband Bandpass Filters Based on a Single Multimode Resonator Loading Branches

Jie Luo,[1] **Kaibo Shi**,[1] **and Shanshan Gao**[1,2]

[1]*School of Information Science and Engineering, Chengdu University, Chengdu, Sichuan 610106, China*
[2]*State Key Laboratory of Millimeter Waves, Nanjing 210096, China*

Correspondence should be addressed to Jie Luo; luojie01@cdu.edu.cn

Received 28 July 2022; Accepted 27 September 2022; Published 10 October 2022

Academic Editor: Zi-Peng Wang

In this paper, the operating mechanism of proposed bandpass filters with a single multimode resonator loaded with branches is introduced. Based on the design procedure, the center frequencies of the proposed bandpass filters can be controlled due to the design freedom. Meanwhile, the proposed bandpass filters (BPFs) feature compact sizes and small insertion loss. To validate the design and analysis, a prototype was fabricated and measured with six passbands centered at 1.23/1.76/2.38/4.24/5.23/6.75 GHz. The measured result of the fabricated filter agrees well with the simulation, which indicates that the proposed structure can serve as a potential candidate for multiband BPF designs.

1. Introduction

In the modern multiservice wireless communication system, developments in microwave multiband bandpass filters (BPFs) have been gaining much attention for such as GPS, WLAN, WiMAX, and RFID applications.

In the past, some research was conducted for the design of multiband BPFs. In [1–6], different quad-band BPFs were realized based on different approaches, Yan et al. used two sets of short-stub-loaded E-Type resonators in [1], Bukuru et al. investigated quad-mode stepped impedance resonator (QMSIR) in [2], Li et al. realized novel quad-band bandpass filters on a basis of the multimode resonator (MMR) using SIRs loaded tapered-line (SIRTL) in [3], Kamma et al. used T-shaped stubs loaded with a modified ring resonator (MRR) in [4], Zhang et al. investigated three-layer stacked structures in [5], Li et al. used two-/tri-section SIRs and stepped impedance inverters in [6]. And in [7–9], some quint-band BPFs were achieved using different structures, in [7], W.Yang used multimode resonators, Liu et al. investigated uniform impedance resonators (UIRs) in [8], Hsu et al. realized a quint-band BPF using five tri-mode stub-loaded SIRs in [9]. It is noted that some works were reported for the case of sext-band application in [10–12], Chen used six pairs of semilumped resonators to achieve a sext-band BPF in [10], Hsu et al. used stepped-impedance resonators in [11], and Ai et al. used a single multimode resonator in [12]. Besides, it is still a challenge to achieve high-performance multiband BPFs with compact size, closely spaced passbands, low insertion loss, high return loss, and sharp skirt to satisfy the whole wireless communication system application demands.

In this paper, miniaturized multiband bandpass filters using a single multimode resonator loaded with branches are proposed. To validate the design and analysis, a prototype filter has been fabricated with six passbands centered at 1.23 GHz for GPS, 1.76 GHz for GSM, 2.38/5.23 GHz for WiFi, 4.23 GHz for digital relay system, and 6.75 GHz for RF. The proposed filter has a compact size, low insertion loss, and adjustable frequency response.

2. Filter, Design, and Procedure

What is shown in Figure 1 should be given here. As shown in Figure 1, θ_j ($j = 1$, p_1, p_2) corresponds to the equivalent electrical length of the microstrip line, while the characteristic impedance of the microstrip line is represented by Z_i ($i = 1$, p_1, p_2). Explain first the reason, then, give the

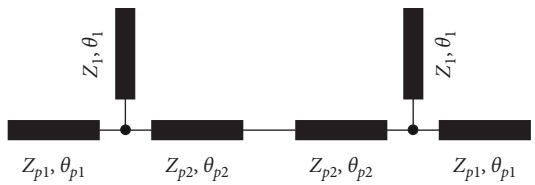

Figure 1: The proposed symmetrical branch loaded resonator.

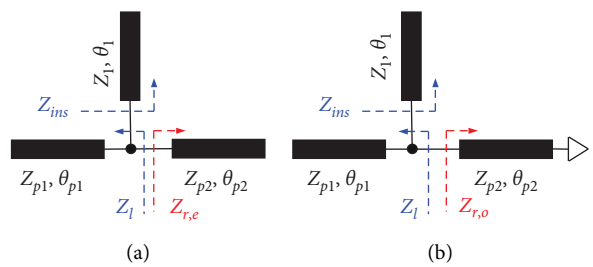

Figure 2: Symmetrical branch resonator equivalent circuit. (a) Even mode circuit; (b) odd mode circuit.

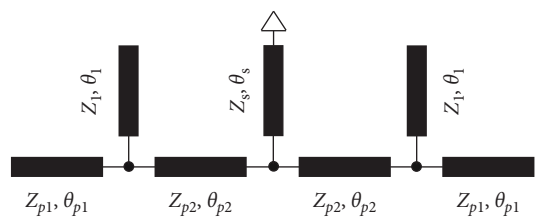

Figure 3: The proposed equivalent model of symmetrical branch loaded resonator.

conclusion ⟶ By increasing the length of the open branch (Z_1, θ_1), more transmission zeros can be obtained within the specified frequency range, and these transmission zeros can be used to realize the multifrequency response of the BPFs.

The characteristics of multimode resonators are analyzed by the odd and even mode method. Figure 2(a) shows the even mode equivalent circuit of symmetrical branch loaded resonators, while the odd mode equivalent circuit of symmetrical branch loaded resonators is shown in Figure 2(b). Since the transmission zeros are produced when the resonance frequencies satisfy the transverse resonance condition, the symmetrical branch-loaded resonator needs to satisfy the following formula:

$$\begin{aligned} &\mathrm{Im}\left(Z_l + Z_{r,e}\right) = 0, \\ &\mathrm{Im}\left(Z_l + Z_{r,o}\right) = 0, \\ &Z_l = \frac{Z_{\mathrm{p1}} Z_{\mathrm{ins}} \cot\theta_{\mathrm{p1}}}{jZ_{\mathrm{ins}} + Z_{p1}\cot\theta_{p1}}, Z_{\mathrm{ins}} = -jZ_1 \cot\theta_1, \\ &Z_{r,e} = -jZ_{p2}\cot\left(\theta_{p2}\right), Z_{r,o} = jZ_{p2}\tan\left(\theta_{p2}\right). \end{aligned} \tag{1}$$

When the open branch (Z_1, θ_1) port produces a virtual ground effect, the input impedance can meet the condition $Z_{\mathrm{ins}} = 0$. As a result, a set of out-of-band transmission zeros can be obtained because the signals at the input end cannot be directly transmitted to the output port and the signals are all reflected. The positions of these transmission zeros can be calculated by (2). By adjusting the out-of-band transmission zeros f_{zs} of the BPF, the required number of passbands can be obtained within a specified frequency range.

$$\begin{aligned} &\cot\theta_1 = 0, \\ &f_{zs} = \frac{n\pi f_0}{2\theta_1}, n = 1, 3, 5.... \end{aligned} \tag{2}$$

Figure 3 presents the equivalent model of the symmetrical branch loaded resonator proposed in this paper. Compared with Figure 1, a short-circuit branch (Z_s, θ_s) is introduced in the middle of the resonator with the purpose of improving the S parameter of the multiband BPFs.

By adjusting the characteristic impedance and electrical length of the microstrip line, three passbands of the BPF are generated in the range of [0, 7 GHz] through three groups of resonance points of even mode and odd mode: the first passband is composed of the fundamental resonance frequency f_{o1} and f_{e1}, the second passband is composed of the first harmonic resonance frequency f_{o2} and f_{e2}, and the third passband is composed of the first harmonic resonance frequency f_{o3} and f_{e3}.

Figure 4 shows the based tri-band equivalent transmission line model for the proposed BPF. It consists of transmission branches (Z_{p1}, θ_{p1}) (Z_{p2}, θ_{p2}), an open branch (Z_1, θ_1), and a short branch (Z_s, θ_s). The proposed BPF shown in Figure 4 can generate three passbands. The center frequencies of the three passbands are represented by f_1, f_2, and f_3, respectively. L_s represent the length of the short branch (Z_s, θ_s). It can be seen in Figure 5 that f_{e1}, f_{e2}, and f_{e3} all move to the lower frequency band with the increase of parameter L_s, while the positions of f_{o1}, f_{o2}, and f_{o3} remain unchanged, the passband bandwidth can be changed by adjusting parameter L_s.

Similarly, in Figure 5(b), L_1 represents the length of the open branch (Z_1, θ_1). L_1 is adjusted to get the center frequency variation shown in Figure 5(b). With the increase of L_1, f_{o1}, f_{o2}, f_{o3}, f_{e1}, f_{e2}, and f_{e3} all move to the lower frequency. The f_{o3} and f_{e3} in the higher frequency move to the lower frequency faster than other resonance frequencies. The center frequency can be adjusted by the fact that the resonance frequency moves at different rates with the change of L_1. To validate the proposed design flow, an example tri-band BPF is fabricated. As shown in Figure 6, the measured performances show good agreement with the simulated ones.

By increasing the number of symmetric open branches, multiple sets of fundamental and higher harmonics can be superimposed. The proposed quad-band multimode resonator based on the asymmetric tree structure is composed of an open branch (Z_2, θ_2) cascaded in the previous tri-band multimode resonator filter, as shown in Figure 7.

As shown in Figure 8, when the multimode resonator has only the open stub1, the length of the open stub1 can be adjusted to obtain a fundamental resonance at

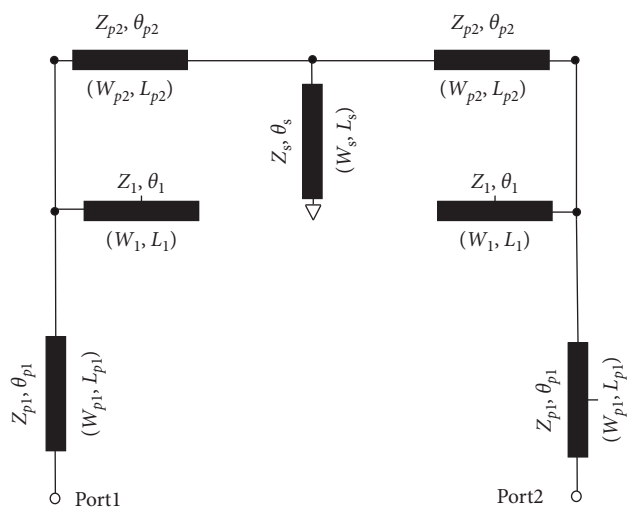

Figure 4: The based tri-band equivalent transmission line model for the proposed BPF.

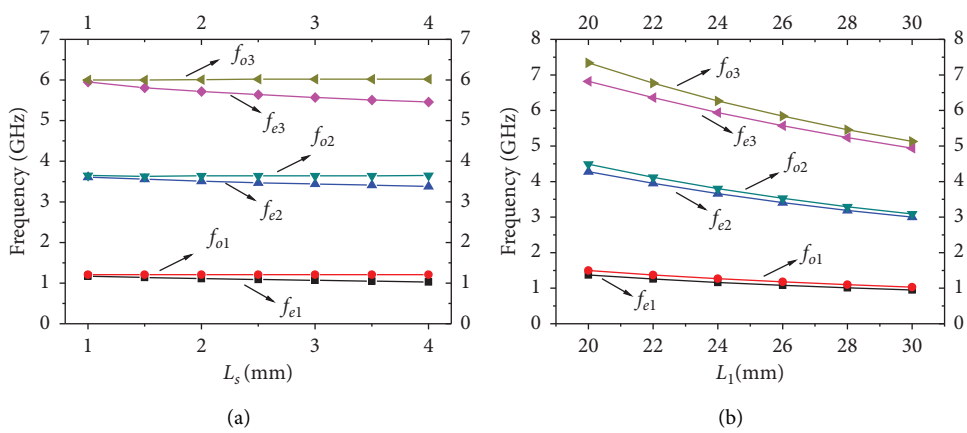

Figure 5: Variation of frequency with different L_s and L_1.

1.71 GHz and the center frequency of the first harmonic passband at 5.14 GHz. When the multimode resonator has only the open stub2, the length of the open stub2 can be adjusted to obtain a fundamental resonance at 2.19 GHz and the center frequency of the first harmonic passband at 6.44 GHz. When the multimode resonator includes both the stub1 and the stub2, the four passband center frequencies are 1.61 GHz, 2.37 GHz, 5.15 GHz, and 6.87 GHz.

To validate the proposed design flow, an example quad-band BPF is fabricated. As shown in Figure 9, good agreements between the measured and simulated performances are also observed.

From the previous theoretical analysis, it can be concluded that the obtained design method of the multiband BPFs is based on the coupling of fundamental and high-order harmonics of different branches. For example, the quad-band BPF is realized by the dual-band generated by stub1 and the other dual-band generated by stub2. If stub1 is used to realize tri-band and stub2 is used to realize dual-band, the quint-band multimode resonator can be obtained as the model shown in Figure 10.

Similarly, as shown in Figure 11, when the multimode resonator has only stub1, adjusting the length of stub1 can achieve the fundamental passband centered at 1.32 GHz, the first harmonic passband centered at 4.01 GHz, and the second harmonic passband centered at 6.54 GHz. If there is only stub2 in the multimode resonator, adjusting the length of stub2 can obtain the fundamental passband centered at 1.71 GHz and the first harmonic passband centered at 5.14 GHz. When the multimode resonator includes both stub1 and stub2, the center frequencies of the five passbands are 1.27 GHz, 1.80 GHz, 4.01 GHz, 5.31 GHz, and 6.82 GHz.

As shown in Figure 12, an example quint- band BPF is fabricated, the measurement performances show good agreements with the simulation.

Finally, the sext-band multimode resonator based on the proposed asymmetric tree structure is composed of an

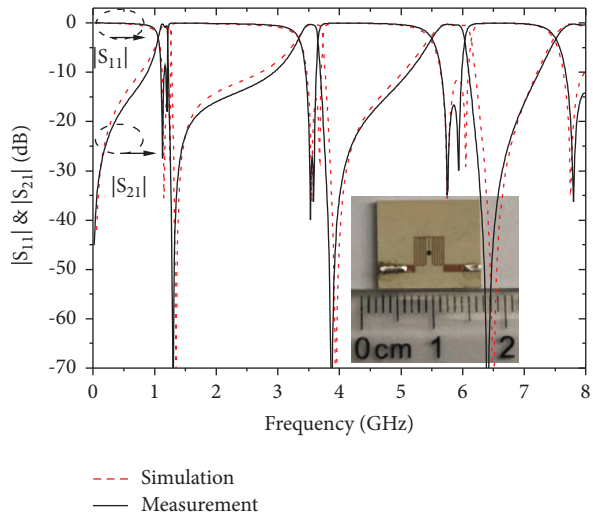

Figure 6: Simulated and measured results of tri-band BPF.

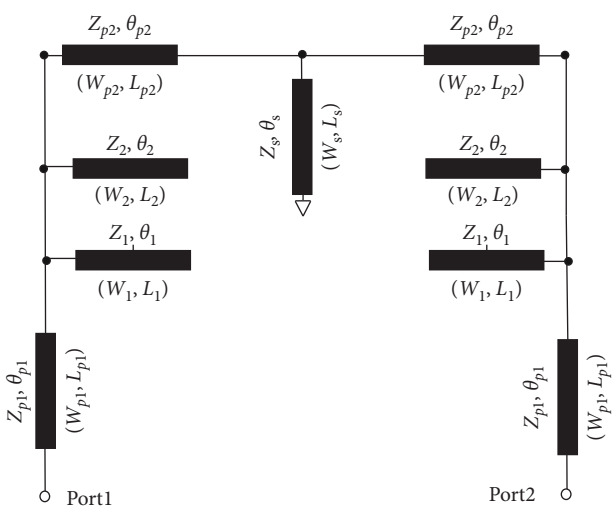

Figure 7: The quad-band equivalent transmission line model for the proposed BPF.

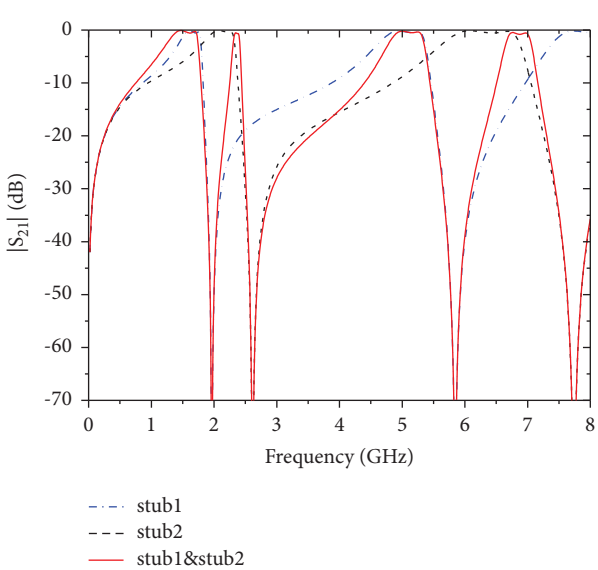

Figure 8: The $|S_{11}|$ of the proposed BPF composed of stub1 and stub2.

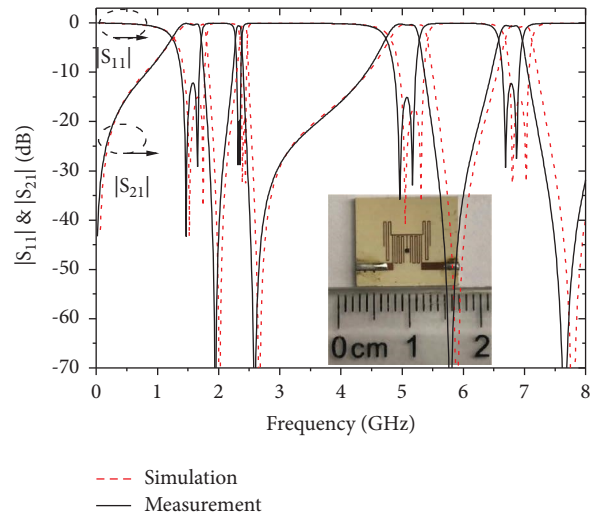

Figure 9: Simulated and measured results of quad-band BPF.

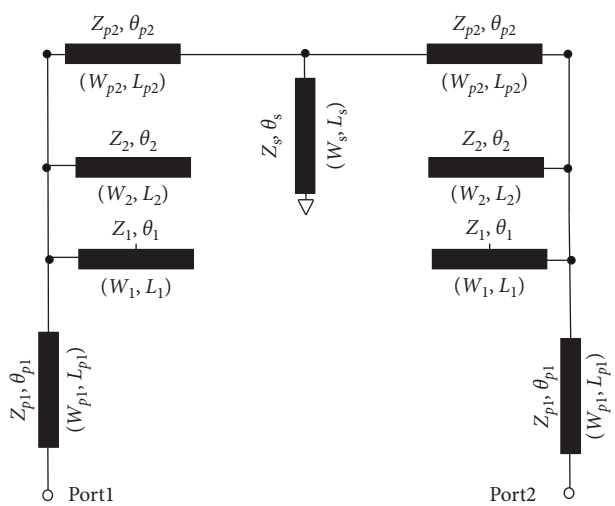

Figure 10: The quint-band equivalent transmission line model for the proposed BPF.

open branch (Z_3, θ_3) cascaded in the previous quint-band multimode resonator filter, as shown in Figure 13.

3. Results and Comparisons

The structure of the proposed sext-band BPF is shown in Figure 14. An example sext-band BPF is fabricated on a Rogers TMM10 (relative dielectric constant $\varepsilon_r = 9.20$, loss tangent $\tan\delta = 0.0022$) substrate with a thickness of 1.00 mm, as shown in the inset of Figure 12. The dimension values are summarized as follows (all in mm): $L_1 = 16.73$, $L_2 = 12.57$, $L_3 = 21.10$, $L_{p1} = 4.01$, $L_{p2} = 1.99$, $L_s = 2.01$, $W = 0.10$ mm. The overall size of the circuit is approximately $0.08\lambda_g \times 0.07\lambda_g$, where λ_g represents the guided wavelength at the first passband.

Measurement of the fabricated filter is performed using an Agilent E8363 B network analyzer. Figure 15 shows the simulated and measured S-parameters of the sext-band BPF,

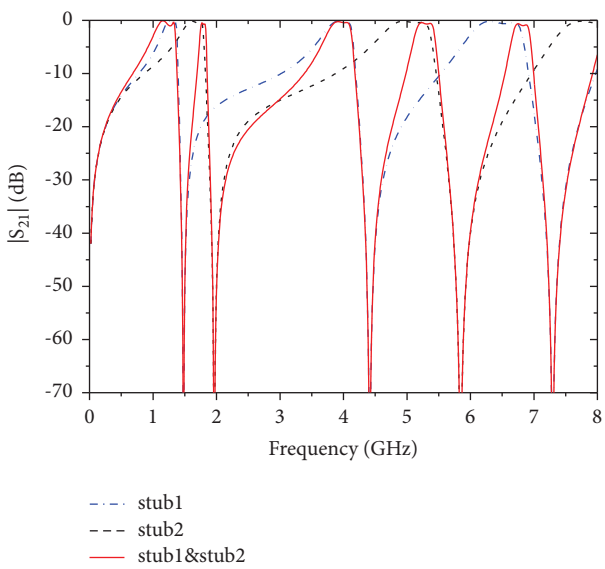

Figure 11: The $|S_{11}|$ of the proposed BPF composed of stub1 and stub2.

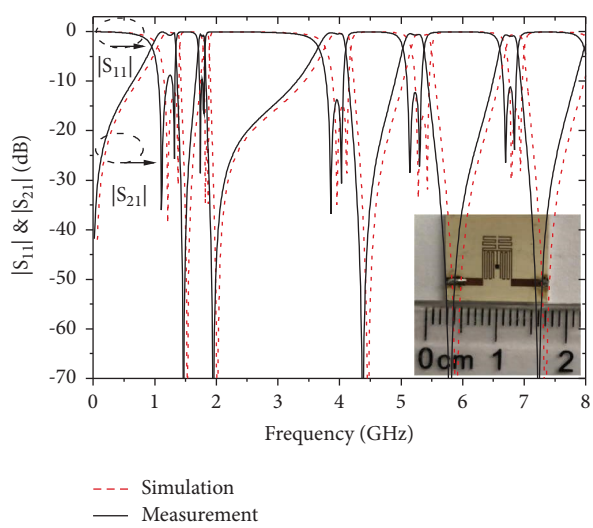

Figure 12: Simulated and measured results of quint-band BPF.

and the photograph of the fabricated BPF is also demonstrated in the inset of Figure 15. The measured six passbands are centered at 1.23/1.76/2.38/4.24/5.23/6.75 GHz with 3 dB fractional bandwidth of 29.27%/3.41%/3.78%/5.19%/3.06%/4.45%. The minimum insertion losses of each band are 1.52/1.61/1.43/0.79/0.68/0.87dB.

The band-to-band isolations are above 70 dB, which generates sharp and deep rejections between the adjacent passbands.

The slight difference between the measured and simulated results may result from the nonuniformity of the relative permittivity of the substrate, the fabrication tolerance, and SMA connectors.

In order to better evaluate the achieved performance, Table 1 presents a performance comparison of the proposed sext-band BPF with some previously reported works. The

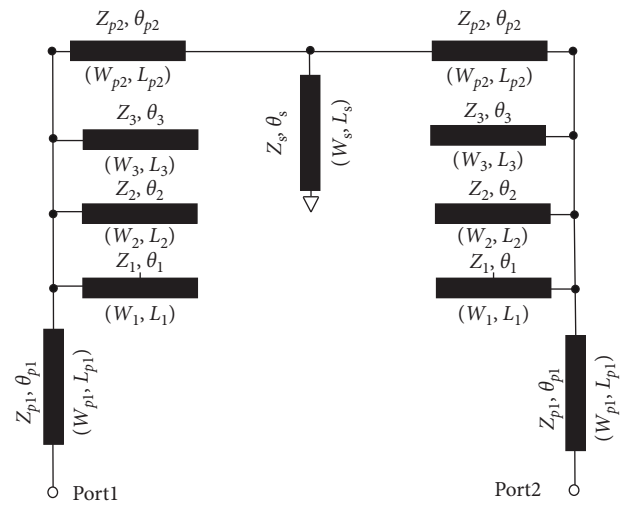

Figure 13: The equivalent transmission line model for the proposed sext-band BPF.

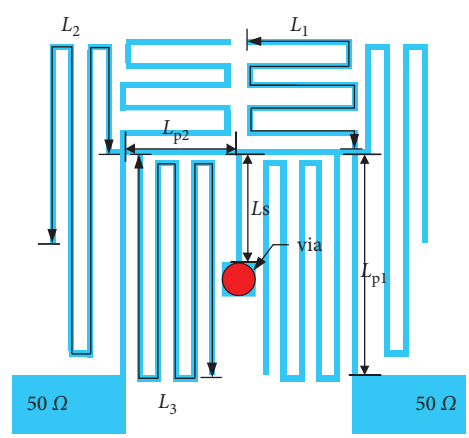

Figure 14: Structure of the proposed sext-band BPF.

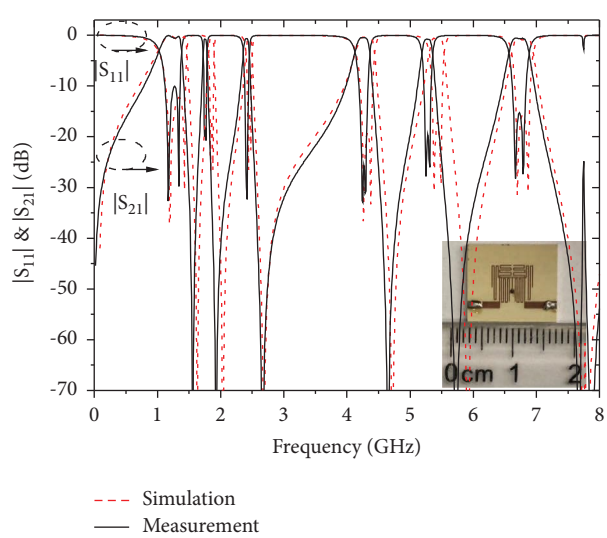

Figure 15: Simulated and measured results of sext-band BPF.

Table 1: Comparison with some previous multi-band BPFs.

Ref.	Frequency (GHz)	Insertion loss (dB)	Isolation (dB)	Size ($\lambda_g \times \lambda_g$)
[5]	1.48/2.49/3.47/4.49/5.78	1.49/1.78/0.89/1.18/2.47	ISO_{12}>34.77 ISO_{23}>27.91 ISO_{34}>32.98 ISO_{45}>30.88	0.24×0.17 (0.0408)
[6]	0.59/0.88/1.17/1.48/1.79	2.79/2.88/2.87/2.58/2.27	ISO_{12}>27.89 ISO_{23}>29.97 ISO_{34}>35.78 ISO_{45}>26.90	0.51×0.05 (0.0255)
[7]	0.88/1.19/1.37/1.66/1.97/2.39	2.28/1.99/2.27/2.68/2.19/1.97	ISO_{12}>37.98 ISO_{23}>19.87 ISO_{34}>29.80 ISO_{45}>21.92 ISO_{56}>14.85	0.26×0.15 (0.039)
[8]	0.69/1.98/3.18/4.49/5.77/6.95	1.29/0.58/0.79/1.06/1.37/2.16	ISO_{12}>52.83 ISO_{23}>44.95 ISO_{34}>51.72 ISO_{45}>41.92 ISO_{56}>37.88	0.16×0.09 (0.0144)
This work	**1.23/1.76/2.38/4.24/5.23/6.75**	**1.52/1.61/1.43/0.79/0.68/0.87**	**ISO_{12}>70.00** **ISO_{23}>70.00** **ISO_{34}>70.00** **ISO_{45}>70.00** **ISO_{56}>70.00**	**0.08×0.07 (0.0056)**

proposed sext -band BPF in this paper exhibits compact size, high selectivity, and a conveniently adjustable frequency response.

4. Conclusions

This paper presents miniaturized multiband BPFs by using a single multimode resonator loaded with branches. The proposed multiband BPFs feature very high design freedom for every single passband. The simulated and measured results have good agreement, which shows that the proposed filters feature compact size and high selectivity. Owing to these merits, the proposed structure could be a good candidate for multiband BPF design.

Data Availability

The data used in this study can be obtained free of charge form https://pan.baidu.com/s/1CbroDDVOh8nv4Y8uiUGlWQ?pwd=5axh.

Conflicts of Interest

The authors declare that they have no conflicts of interest.

Acknowledgments

This work was supported by the "Design of compact high performance MEMS filter," Chengdu Songyuan Photoelectric Technology Co., Ltd, China and the State Key Laboratory of Millimeter Waves (K202121), Southeast University, China.

References

[1] T. F. Yan, X. H. Tang, and J. Wang, "A novel quad-band bandpass filter using short stub loaded E-shaped resonators," *IEEE Microwave and Wireless Components Letters*, vol. 25, no. 8, pp. 508–510, 2015.

[2] D. Bukuru, K. Song, F. Zhang, Y. Zhu, and M. Fan, "Compact quad-band band pass filter using quad-mode stepped impedance resonator and multiple coupling circuits," *IEEE Transactions on Microwave Theory and Techniques*, vol. 65, no. 3, pp. 783–791, 2017.

[3] X. Li, Y. Zhang, Y. Tian, Y. Yang, and Y. Fan, "Quad- and sext-band bandpass filter based on multimode resonator utilizing SIRs loaded tapered line," *Microwave and Optical Technology Letters*, vol. 60, no. 3, pp. 650–654, 2018.

[4] A. Kamma, R. Das, and J. Mukherjee, "Spurious free independently controllable compact quad-band filter using folded T-shaped stub loaded modified ring resonator," *IET Microwaves, Antennas & Propagation*, vol. 11, no. 8, pp. 1156–1161, 2017.

[5] Y. Zhang, F. Ling, R. Huang, Z. Zhong, and B Zhang, "The characteristics of a terahertz filter with three-layer stacked structure," *Optik*, vol. 168, pp. 847–852, 2018.

[6] D. Li, Y. Yu, R. Song, M. Tang, J. Ai, and Y. Liao, "Design of compact quad-band bandpass filter with good selectivity using two-/tri-section SIRs and stepped impedance inverters," *IET Microwaves, Antennas & Propagation*, vol. 13, no. 5, pp. 675–682, 2019.

[7] W. Yang, L. Wang, and L. Wang, "Design of a quint-band bandpass filter based on multi-mode resonator," in *Proceedings of the 2021 IEEE International Conference on Power Electronics, Computer Applications (ICPECA)*, January 2021.

[8] H. Liu, R. Wang, and C. Lai, "A Compact Quint-Band Bandpass Filter with High Selectivity Using Uniform

Impedance Resonators (UIRs)," in *Proceedings of the 2020 IEEE MTT-S International Microwave Workshop Series on Advanced Materials and Processes for RF and THz Applications (IMWS-AMP)*, July 2020.

[9] K. W. Hsu, W. C. Hung, and W. H. Tu, "Compact quint-band microstrip bandpass fifilter using double-layered substrate," *IEEE International Microwave Symposium*, vol. 6, pp. 1–3, 2014.

[10] C. F. Chen, "Design of a compact microstrip quint-band fifilter based on the tri-mode stub-loaded stepped-impedance resonators," *IEEE Microwave and Wireless Components Letters*, vol. 22, pp. 357–359, 2012.

[11] K. W. Hsu, J. H. Lin, and W. H. Tu, "Compact sext-band bandpass filter with sharp rejection response," *IEEE Microwave and Wireless Components Letters*, vol. 24, no. 9, pp. 593–595, 2014.

[12] J. Ai, Y. H. Zhang, K. D. Xu, Y. J. Guo, W. T. Joines, and Q. H. Liu, "Compact sext-band bandpass filter based on single multimode resonator with high band-to-band isolations," *Electronics Letters*, vol. 52, no. 9, pp. 729–731, 2016.

Hindawi
Discrete Dynamics in Nature and Society
Volume 2022, Article ID 6257658, 12 pages
https://doi.org/10.1155/2022/6257658

Research Article

Rumor Detection Based on Knowledge Enhancement and Graph Attention Network

Wanru Wang,[1,2] **Yuwei Lv**,[3] **Yonggang Wen**,[4] **and Xuemei Sun**[2,3]

[1]*School of Software, Tiangong University, Tianjin 300387, China*
[2]*Tianjin Key Laboratory of Autonomous Intelligence Technology and Systems, Tianjin 300387, China*
[3]*School of Computer Science and Technology, Tiangong University, Tianjin 300387, China*
[4]*Tianjin University of Commerce Boustead College, Tianjin 300384, China*

Correspondence should be addressed to Wanru Wang; tjpuwwr@126.com

Received 17 April 2022; Revised 11 July 2022; Accepted 17 September 2022; Published 6 October 2022

Academic Editor: Akbar Ali

Presently, most of the existing rumor detection methods focus on learning and integrating various features for detection, but due to the complexity of the language, these models often rarely consider the relationship between the parts of speech. For the first time, this paper integrated a knowledge graphs and graph attention networks to solve this problem through attention mechanisms. A knowledge graphs can be the most effective and intuitive expression of relationships between entities, providing problem analysis from the perspective of "relationships". This paper used knowledge graphs to enhance topics and learn the text features by using self-attention. Furthermore, this paper defined a common dependent tree structure, and then the ordinary dependency trees were reshaped to make it generate a motif-dependent tree. A graph attention network was adopted to collect feature representations derived from the corresponding syntax-dependent tree production. The attention mechanism was an allocation mechanism of weight parameters that could help the model capture important information. Rumors were then detected accordingly by using the attention mechanism to combine text representations learned from self-attention and graph representations learned from the graph attention network. Finally, numerous experiments were performed on the standard dataset Twitter, and the proposed model here had achieved a 7.7% improved accuracy rate compared with the benchmark model.

1. Introduction

In recent years, with the rapid development of social media platforms, various social media have been widely used, such as Sina Weibo and Twitter. The popularity of social media platforms has brought great convenience for people to collect information and news, but the development of social media platforms has also led to the spread of rumors. Rumors in social media have the characteristics of fast spread, wide influence range, large cost, and low efficiency of manual refuting. Therefore, rumor detection has become an extremely challenging research topic in the field of text classification, which has attracted close attention from academia and industry.

In recent studies, Ma et al. [1] used recurrent neural network and attention mechanisms to perform rumor detection, improving the most sophisticated detection effects at the time. However, attention mechanisms may sometimes fail due to the complexity of linguistic morphology and syntax. To this end, Wang et al. [2] proposed syntax tree-based structure information for text. As knowledge is refined into a structured form, many domains of knowledge graph (KG) have been constructed. Comet [3] used triples in KG as a corpus to train generative pretraining for common sense learning. But this knowledge embedding fails to account for the impacts of the introduced knowledge on sentences. Recently, Zhang et al. [4] used graph neural networks to process representations of graphs learned from the dependency tree. Lv et al. [5] proposed rumor detection based on a time graph attention network. The method first aggregated the spread structure and text features of rumors through the graph attention neural network, then, recorded the historical state of the spread structure using the time attention

mechanism, and then, captured the features of the spread structure changing with time through the gated loop unit. This method innovatively proposes the concept of time for rumor detection but does not consider the deep connection between words as the characteristics of the text itself. Although these models have improved in some ways, their disadvantages cannot be ignored. The dependency trees constructed first ignore the connection between subjects and viewpoint words; second, introduced knowledge graphs also inevitably bring noise; and finally, only a small fraction of the dependent trees are associated with rumor detection, which does not require encoding the entire dependency trees.

To address these problems, for the first time, this paper proposed a method of rumor detection based on knowledge enhancement and graph attention network models.

First, motif of knowledge graph triples was injected for thematic enhancement, modifying the effects of mask mechanisms for noise reduction. Second, the syntax-dependent trees were reshaped so that the motif was dependent and pruning for the syntax-dependent trees, only retaining edges that had a direct dependence on the motif. This unified tree structure was able to focus not only on the connection between topics and potential opinion words, but also facilitated batch processing and parallel operation. Finally, our study fused the text representations learned by self-attention with the representation of the graphs learned by graph attention network. The Twitter dataset was extensively evaluated, and the experimental results demonstrated that our model outperformed the benchmark method.

Main contributions of the research:

(1) For the first time, this paper proposed that knowledge graphs and syntactic-dependent trees could be used to reshape sentences to detect rumors, which has improved the effects of rumor detection.

(2) In this paper, we improved the traditional graph neural network by using a graph attention network model based on text-classification and a dual attention mechanism, where node attention and edge attention could enhance each other.

(3) The attention mechanism was adopted to integrate the text representation and the graph representation, and the fusion feature representation was used to enhance the text representation learned from the attention and the graph representation learned by the graph attention network, respectively.

(4) Comparing the proposed model with the current benchmark model, we experimentally demonstrated that the proposed model could improve detection accuracy by 7.7%.

2. Related Work

The earliest study of rumor detection was based on traditional machine learning, which transformed the rumor detection into a second classification problem for processing. First, the rumor features were extracted, then, the machine learning model was applied for modeling, and finally, the rumor characteristics were input into the model for training to realize the rumor detection. Zhao et al. [6] presented a model based on the decision tree classifier that had clustered the questioned and corrected phrases that were extracted from messages, and then a decision tree based on statistical features was built for rumor detection. Yang et al. [7] added content-based subject features, semantic bias, and comment information to the rumor detection model. Guo et al. [8] proposed that emotional features had an important role in rumor detection. With the development of information technology, deep learning has been successfully applied in information processing, mode recognition and artificial intelligence, and has achieved fruitful research results. Kwon et al. [9] used text structure information and linguistic features to capture the multimodal phenomena of rumor propagation by applying three classification models: support vector machine, random forest classifier, and decision tree. Ma et al. [1] first proposed using circular neural networks to realize rumor detection, considering the comment information and timing characteristics of the message in the transmission process. A circular neural network can automatically capture the changes of time signals in the process of rumor transmission, modeling the long-time context information on the time axis, thus, realizing the time series-based event representation and achieving good results in rumor prediction. Chen et al. [10] took advantage of the characteristics of the constantly changing importance of words during message transmission and the replication of rumors to introduce attention mechanisms in recurrent neural networks. Yu et al. [11] first applied the convolutional neural network to detect rumors, using the paragraph vectors to model the rumor information, taking the obtained paragraph vectors as the input to the convolutional neural network, and generating high-order abstract features through the underlying combination of the features to achieve the purpose of improving the rumor detection accuracy.

The knowledge graph can automatically make use of massive unstructured text data and information to assist with manual analysis, research, understanding the big data, and provide an accurate, reliable, and efficient factual basis for rumor detection. Rospocher et al. [12] presented an event-centered knowledge graph that drew events from news reports, which included time, place, and participants established causal and coexisting relationships between events, and reconstructed the historical development and temporal evolution of events. Gottschalks et al. [13] resented a knowledge graph with event-centered multilingual temporal that drew 690,000 contemporary historical events and over 2.3 million temporal relationships from existing large knowledge graphs like DBpedia, YAGO, and Wikidata and integrated the extracted events, entities, and relationships. Hemes et al. [14] proposed a semantic representation of financial events that automatically processed and analyzed financial events to assist decision-making. Entities from the rumor dataset are extracted to connect these entities to the open knowledge graph DBpedia, based on which relationships and entities connected are obtained. The knowledge graph needed in this paper is formed by using these relationships and entities.

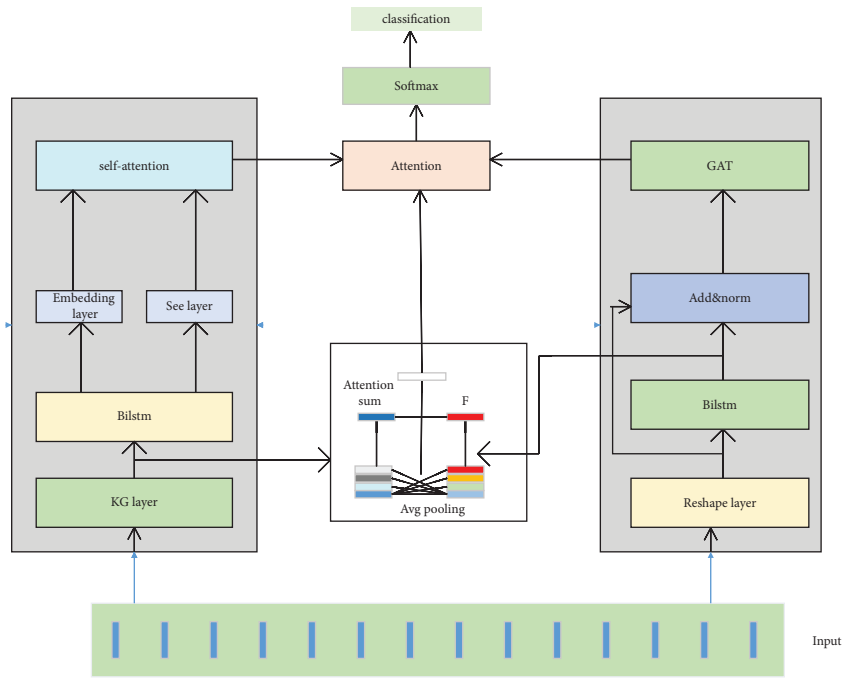

Figure 1: The overall framework of rumor detection based on knowledge enhancement and Graph Attention Network.

The attention mechanism was an allocation mechanism of weight parameters that could help the model capture important information. Some works provide the visualization of the learned attention, such as: Xu et al. [15] proposed a novel X-invariant Contrastive Augmentation and Representation learning framework to thoroughly obtain rotate-shear-scale invariant features. Shu et al. [16] proposed a novel Expansion-Squeeze-Excitation-Fusion Network to learn modal and channel-wise Expansion-Squeeze-Excitation attentions for attentively fusing the multimodal features in the modal and channel-wise ways. Shu et al. [17] present a Spatio-Temporal Context Coherence constraint and a Global Context Coherence constraint to capture the relevant motions and quantify their contributions to the group activity, an attention mechanism is employed to quantify the contribution of a certain motion by measuring the consistency between itself and the whole activity at each time step. Tang et al. [18] proposed a novel Skeleton-joint Co-Attention Recurrent Neural Network to capture the spatial coherence among joints and the temporal evolution among skeletons simultaneously on a skeleton-joint co-attention feature map in spatiotemporal space.

Since the first introduction of graph neural networks in Kipf et al. [19], Graph Neural Network (GNN) has recently shown its strong power in processing graphical structural representations in the context of natural language processing. Marcheggiani and Ivan [20] in 2017 proposed a semantic Graph Convolution Network (GCN) based role labeling model, at the word level; it effectively combined syntactic information and skillfully combined sequence model and graph representation, which alleviated the defects of the sequence model to a certain extent. Shu et al. [21] propose a novel graph LSTM-in-LSTM (GLIL) for group activity recognition by modeling the person-level actions and the group-level activity simultaneously. Zhang et al. [22] used the GNN in the documentation and relational classification. The Graph Attention Network (GAN) was first introduced into the text classification task under document-word and word-word relations by Yao et al. For similar purposes, Huang and Carley [23] in 2019 explicitly established the dependence between words by using a graph attention network. However, these methods often ignore dependencies, which may determine the connection between words.

3. Model

In the model, we integrated the text representation learned by self-attention with the graph representation of syntactic dependency trees learned by the Graph Attention Network. Figure 1 shows the overall framework of the rumor detection model, which contains 3 main modules, the knowledge embedding module, dependency tree module based on the graph attention network, and the attention module.

In this section, the task of rumor detection is expressed as follows: In each document D contains sentences $\{s_1, s_2, \ldots, s_i\}$, given a sentence s_i, i {1,2, . . ., i} and his subject a_k, k {1,2, . . ., k}, the purpose of rumor detection is to predict whether an a_k event is a rumor or not by automatically learning the sentences related to a_k.

3.1. Dependency Tree Modules Based on Graph Attention Network. A Graph Neural Network (GNN) model for text classification was first introduced, and then a syntax dependency tree was used to model the text for rumor detection. Finally, a graph attention network model based on text classification with a novel dual attention mechanism was

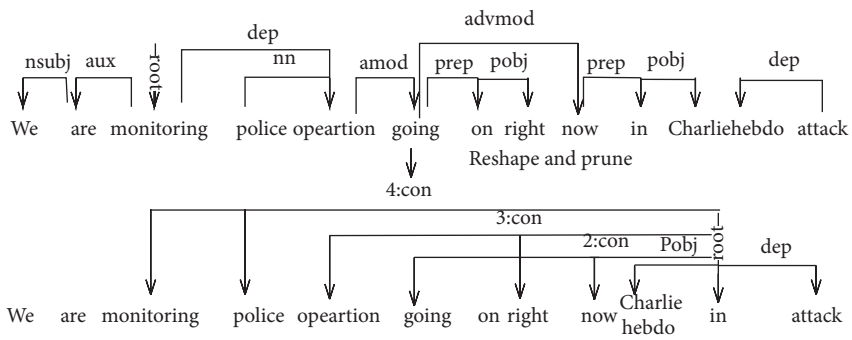

Figure 2: Schematic diagram of common dependency tree and modified and deleted topic dependency tree.

also applied in the research. Node attention was used to enhance edge attention and edge attention was used to enhance node attention.

3.1.1. Introduction of the GNN Model. With the proliferation of deep learning techniques, GNN has achieved great success in representation learning of graph structure data. In general, most of the existing GNN models follow a neighborhood aggregation strategy, and a GNN layer can be defined as shown in the following equation :

$$h_i^l = \mathrm{AGGR}\left(h_i^{l-1}, \left\{h_j^{l-1} | \forall j \int N_i\right\}\right), \tag{1}$$

where h_i^l was the node representation of node i at the l-layer (usually using x_i as h_0^i), and N_i was the local domain set of node i. AGGR was the aggregation function of GNN, and there were many ways to implement it. GNN, which was with excellent performance in text classification, had the ability to capture long-distance interactions between entities. Most of the current methods are to build corpus-level document graphs and try to classify documents through semisupervised node classification. Despite of its success, most existing methods are computational flawed. Meanwhile, these methods are largely influenced by the use of simple graphs for modeling word interactions, which could limit text expressibility. Therefore, how to improve the computational power of the model expression is an important task to be solved.

3.1.2. Subject-Based Syntax-Dependent Trees. The subject-based dependency trees suggested that dependencies with direct connections to a certain subject could help the model focus more attention on relevant opinion words and, therefore, are more important than others. In addition, as was shown in Figure 2, the dependency trees that contained rich syntactic information were not usually rooted in the subject. However, the subject was the key target rather than the roots of the trees, while some relationships appeared somewhat redundant.

Based on the above observations, a novel subject-oriented dependent tree structure was adopted to reshape the original dependent trees to be subject-dependent. Algorithm 1 described the process, for the input statement, first, the dependent tree parser was applied to obtain its dependency trees; secondly, the subject was placed at the root, considered as an entity. Finally, the node with a direct connection to the subject was set to subnode, for which the original node dependency was retained.

Table 1: Dependence.

Label	Relationship type
Advmod	Adverbial modifier
Aux	Auxiliary
Conj	Conjunct
det	Determiner
Nsubj	Nominal subject
Prep	Prepositional modifier
Amod	Adjectival modifier
cc	Coordination
dep	Dependent
Nn	Noun compound modifier
Pobj	Object of a preposition

There are many dependencies in sentences, such as: juxtaposition, dependencies, preposition modification, noun combination forms, correlations, and so on. The existence of these relationships may increase distance and computation. In order to shorten the distance between words and increase the calculation rate, we entered a character in the coordination(CC), which was unable to determine a more precise dependency between two words(DEP), determiner(DET), noun clause adjunct(ACL), nominal modifier(NMOD), etc. relationships remained stable after putting two characters in the dictionary. The distance was still equal after removing the edge in the dependency. Figure 2 shows the motif-oriented dependent trees constructed from the ordinary dependency trees. This subject-oriented structure has at least two advantages. First, each aspect has its own dependency trees and is less affected by joint-free points and relationships. Second, a motif contains a distance greater than 2, setting $n = \infty$ if the distance is greater than 4. This paper uses the natural language processing tool Stanford core NLP to construct the syntactic dependency tree of the rumor text. The common dependencies of this tool are shown in Table 1.

The dependency tree was defined as $G = (V, E)$, where $V = \{v_1, ..., v_n\}$ represented the set of nodes in the graph, where each node represented a word in the sentence, $E = \{e_1, \ldots, e_m\}$ represented the dependency, and the neighborhood information of the node ei, v_i can be represented by N_i.

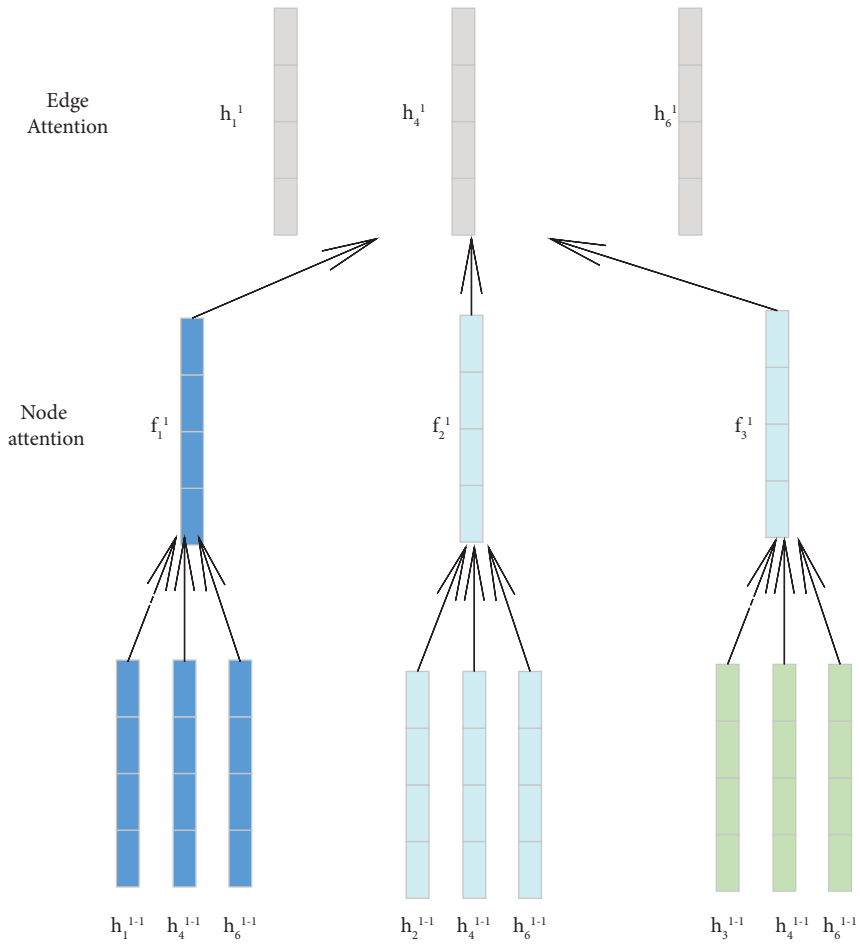

Figure 3: The overall architecture of Graph Attention Network information aggregation.

The topology of the syntax-dependent tree G was represented by the matrix $A \in R^{n\times m}$, as defined in the following equation :

$$A_{ij} = \begin{cases} 1 \text{ if } v_i \in e_j \\ 0 \text{ if } v_i \notin e_j \end{cases}. \tag{2}$$

Each node in the syntax-dependent trees had a d-dimensional attribute vector. Thus, all node properties could be expressed as $X = [x_1 x2 \ldots\ldots x_n]^T$, and we could further use G= (A, X) to represent the entire syntax-dependent trees. For syntax-dependent trees, nodes represented words in a document, and the node attribute could be a thermal vector or pretrained word embeddings (e. g., word2vec, GloVe).

Syntax-dependent trees, that described grammatical relations among words, had been shown for its effectiveness in text representation learning. To exploit the syntax information for each word, a syntax dependency tree was first constructed for each text in the corpus. Inspired by the success of the hierarchical attention network, each syntactic information was viewed as an edge that could connect all the words in the sentence.

3.1.3. Graph Attention Network(GAT). Graph neural networks aggregate representations of neighborhood nodes along the dependent path. However, this process failed to account for the dependencies, which may result in some important dependency information. Intuitively, there should be different effects for neighborhood nodes with different dependencies. This model used additional relational headers to extend the original GAT, which served as relational-level gates to control the flow of information from the neighborhood nodes. Figure 3 shows the overall architecture of the proposed method. So as to support the representation learning of the constructed dependent trees, this paper used the GAT model to aggregate the neighborhood node representation by using two different aggregation functions, iteratively updating each node representation, such as equations (3) and (5).

$$f^{l+1}_{\text{node}\,i} = \|_{k=1}^{K} \sum_{j\varepsilon Ni} a^{lk}_{ij} W^l_k h^l_j, \tag{3}$$

$^{K}_{k=1}$ represented the concatenation of vectors from x_1 to x_k, and W^l_k was a trainable weight matrix. The a_{ij} represented the attention coefficient of the $node_j$, use the same method as literature [24] calculated as in the following formula:

$$a_{ij} = \text{attention}\left(\text{node}_i, \text{node}_j\right). \tag{4}$$

This model used edge attention to highlight the next layer representation of the learning node $node_i$. This procedure can be represented in the following form as:

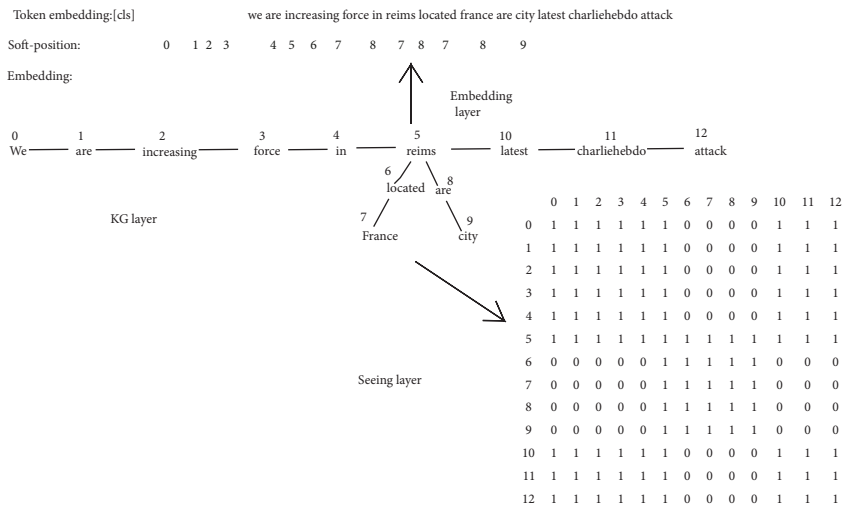

	0	1	2	3	4	5	6	7	8	9	10	11	12
0	1	1	1	1	1	1	0	0	0	0	1	1	1
1	1	1	1	1	1	1	0	0	0	0	1	1	1
2	1	1	1	1	1	1	0	0	0	0	1	1	1
3	1	1	1	1	1	1	0	0	0	0	1	1	1
4	1	1	1	1	1	1	0	0	0	0	1	1	1
5	1	1	1	1	1	1	1	1	1	1	1	1	1
6	0	0	0	0	0	1	1	1	1	1	0	0	0
7	0	0	0	0	0	1	1	1	1	1	0	0	0
8	0	0	0	0	0	1	1	1	1	1	0	0	0
9	0	0	0	0	0	1	1	1	1	1	0	0	0
10	1	1	1	1	1	1	0	0	0	0	1	1	1
11	1	1	1	1	1	1	0	0	0	0	1	1	1
12	1	1	1	1	1	1	0	0	0	0	1	1	1

Figure 4: Schematic diagram of knowledge embedding layer, the upper left corner is embedding, and the lower right corner is the visible matrix.

$$h_{\text{edge}\,i}^{l+1} = \|_{m=1}^{M} \sum_{j\varepsilon Ni} B_{ij}^{lk} W_k^l f_j^l. \tag{5}$$

W_k^l was a weight matrix. B_{ij}^{lk} represented the attention coefficient of the edge e_j on the node v_i, which can be calculated by (6) and (7).

$$B_{ij}^{lm} = \frac{\exp\left(a^T v_i^{lm}\right)}{\sum_j \int Ni\left(a^T v_j^{lm}\right)}, \tag{6}$$

$$v_j = \text{Leak Re}lu\left(\left[w_2 f_j^{l+1} w1hlj\right]\right). \tag{7}$$

Among these, a^T was a weight vector for computational dependencies, while || was a connection operation. This model could not only capture higher-order word interactions, but also learn dependencies of dependent trees.

3.2. Knowledge Embedded Module. The knowledge embedding module consisted of four modules, namely, knowledge layer, embedding layer, seeing layer, and mask-self-attention. For the sentence input, the knowledge layer, first, injected the relevant triples into the sentence from the KG, and then, transformed the original sentence into knowledgeable sentence trees. The sentence tree was then input into both embedding layer and seeing layer and then converted to token-level embedding representations and visible matrices. A visible matrix was used to determine the visible region of each subject word, preventing changes in the original meaning of the sentence due to excessive knowledge edges injected. A simple example:"We are increasing our force in reims latest on charliehebdo attack". For reims, triples "reims country France" were used and noise occurred when injecting triples into the sentence, the effect of the introduced sentences on the original sentence was reduced through the seeing layer.

Lastly, input the embedding layer and seeing layer to learn feature representation from self-attention, as shown in Figure 4. Among them, at the knowledge layer, for traditional knowledge graphs, such as SNOMED-CT, HowNet, were not suitable for rumor detection, so that triples of the grasped data from the DBpedia were injected into the sentence. Given the input sentence $S = \{w_0, w_1, w_2, \ldots, w_n\}$, and KG, the output sentence tree $t = \{w_0, w_1, \ldots, w_i\{(r_i^0, w_i^0), \ldots, (r_i^k, w_i^k)\}, \ldots, w_n\}$. From input to output, it can be divided into two steps: knowledge query and knowledge injection. In the knowledge query, the motifs in the sentence were selected to query their corresponding triples from the KG. The knowledge injection could be expressed as E = K-Query (S, K), where $E = \{(w_i^0, r_i^0, w_i^0), \ldots, (w_i^k, r_i^k, w_i^k)\}$ is the set of the corresponding triples.

Next, K-Inject generated the sentence tree T by injecting the triples into sentence by adding the triples in E to its corresponding location. K-Inject could be represented as $T = K\text{-}Inject\ (S, E)$. Self-attention was adopted to prevent K-Inject changes from taking advantage of the sentence structure information in N. The formula was as follows: (8), (9), (10):

$$Q^{i+1}, K^{i+1}, V^{i+1} = h^i W_q, h^i W_k, h^i W_v, \tag{8}$$

$$G^{i+1} = \text{soft max}\left(\frac{Q^{i+1} K^{i+1} + M}{\sqrt{\mathrm{d}_k}}\right) V, \tag{9}$$

$$G^{i+1} = G^{i+1} V^{i+1}. \tag{10}$$

Where W_q, W_k and W_v are trainable model parameters. h^i is the hidden state of the i-th self-attention blocks. d_k is the scaling factor. N is the visible matrix calculated by the seeing layer. if w_k is invisible to w_j, the M_{jk} will mask the attention score G^{i+1}, which means w_k make no contribution to the hidden state of w_j.

```
Input: aspect a = {|w_i^a, w_{i+1}^a, ...w_k^a}, sentence = {w_1^s, w_2^s, ...w_n^s} dependency tree T, and dependency relations r.
Output: subject dependency tree T1^. 1:
Construct the root R for T1^;
for x to k do
    for y = 1 to n do
        if b_y^s ⟶ b_x^a then,
            b_y^s ⟶ R
        else if b_y^s ← b_x^a then,
            b_y^s ← R
        else
            b_y^s = change word((b_y^s))
            n = distance(x,y)
        b_y^s ⟶ n: con R
        end if
    end for
end for
return T1^
```

Algorithm 1: subject Dependency Tree.

3.3. Attention Module. The Attention Module is an interaction between the knowledge-embedding module and the subject-dependent tree module. The graph-based representations that guided the updates learned by self-attention could also guide the graph-based representations learned by the graph neural network.

Assuming the existence of three input matrices: $Q \in R_n \times D_k$, $K \in Rm \times Dk$, $V \in R_m \times D_v$, which, respectively. represented query matrix, key matrix, and value matrix. n and m are the length of two inputs; text representations learned by self-attention guide the updates of graph neural network. Text representations were converted to key and value, namely, K and V, and graph representation was converted to queries, namely, Q. The calculation procedure was shown in the following formula:

$$\begin{aligned} Q' &= \text{Attention}(Q, K, V) \\ &= \text{soft max}\left(\frac{QK^T}{\sqrt{\text{d}_k}}\right)V. \end{aligned} \tag{11}$$

The updated graph representation was then spliced with the original graph representation, and finally, converted to the original dimension via the full connection layer without the activation function. The calculation procedure of Q is shown in the following formula formula.

$$Q = \text{Linear}([Q', Q]). \tag{12}$$

The graph representation Q was averagely pooled to obtain the final graph representation Q'. The update of text representations learned by graph-based representation via graph neural networks was similar to the update flow of text representations. Graph representations were transformed to key and value, text representations were transformed to query, and text features were updated to H' via an attention mechanism.

Finally, the attention weights of the modes after each update were calculated through a two-layer feedforward neural network, and both the updated graph representation and the text representation were fused by the attention weights, with the calculation process shown in the following formula.

$$\begin{aligned} \text{attention} &= \text{soft max}\left(w_2 \tanh\left(w_1\left[Q', H'\right] + b_1\right) + b_2\right), \\ F &= \text{Rule}\left(\text{Linear}\left(\text{attention}\left[Q', H'\right]\right)\right). \end{aligned} \tag{13}$$

4. Simulation Experiment

4.1. Dataset. This experiment used the standard Twitter dataset publicly available proposed by Ma et al. The Twitter dataset, presented in 2016, was quickly recognized by academics and researchers, are now widely used for text classification tasks, is a classic dataset on text classification issues. The model used the Twitter ID of the Twitter dataset, texts, and entities, where the specific data information was shown in Table 1. The original dataset is divided into two mutually exclusive datasets, namely, training set and testing set by calling the function, the training set and the test set account for three and seven parts of the dataset, respectively, with 4061 events as the training set, 1741 events as testing set to test the model in this paper. As shown in Table 2.

Knowledge graphs in many fields have been constructed, such as SNOMED-CT in the medical field and HowNet in the Chinese concept, the knowledge graph used in this paper is based on Wikipedia. Since Wikidata has more than 24.7 million knowledge entities, the search is very time-consuming, so we manually search out the entities used in the dataset to establish the knowledge graph.

4.2. Parameters and Environment. A Biaffine Parser was used for the dependency solution, and the dimension of the dependency embedding was set to 300. The batch was set at 32, and the number of training rounds was 30. This model was trained on the GPU of python3.6, pytorch1.2.0; specific superparameters are shown in the following Table 3:

Table 2: Data information of Twitter.

Statistics	Twitter
User#	49,345
Posts#	103,212
Events#	5,802
Rumors#	1,972
Nonrumors	3,830
Avg.hours per event	33.4
Avg.# of posts per event	17
Max # of posts per event	346
Min # of post per event	1

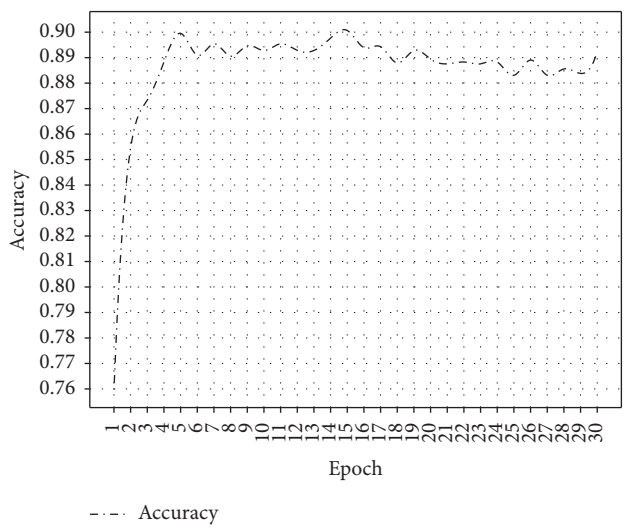

Figure 5: Schematic diagram of evaluation index accuracy changes.

4.3. An Introduction of the Comparison Model. Some mainstream models of rumor detection were used for comparison, including:

Circulating Neural Network (CNN): Considering the comment information re-transmitted and the timing characteristics of messages in the propagation process, the long-term context information was modeled on the timeline to realize the time-series-based representation of events.

Long and Short-Term Memory (LSTM): LSTM can learn long-distance dependencies through gate structure and memory units to capture text features from local continuous word sequences.

Gated Recurrent Unit (GRU): The GRU improved the LSTM to integrate forgetting date and the input gate as a single update gate. It also mixed cell and hidden states, thus increasing the speed of the model processing data.

Transformer [25]: The transformer used an attention mechanism to model the dependence of the input-output sequences without consideration of their distance in the sequence.

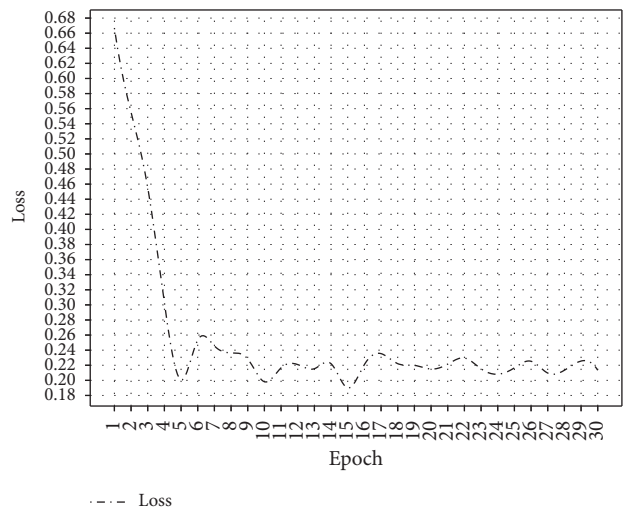

Figure 6: Schematic diagram of evaluation index loss changes.

Table 3: Hyperparametric table.

Hyperparametric	Numerical value
num_heads	6
Dropout	0.2
learning_rate	$5e-5$
Epsilon for adam optimizer	$1e-8$
num_train_epochs	30
hidden_size	200
batch_size	32
embedding_dim	300

BERT [26]: A language model that trained text bidirectional by using the encoder part of self-attention could capture longer-distance dependencies more efficiently.

Bi-GCN [27]: The GCN was based on the rumor detection model to model the text by using the two-way propagation structure.

5. Experimental Analysis and the Results Analysis

5.1. Training Loss and Accuracy. During the training of the model, we set up 30 rounds of training, and the indicators obtained by the model became stabilized as the number of training rounds increased. A schematic diagram of the evaluation index accuracy changes was shown in Figure 5. Schematic diagram of evaluation index loss change was shown in Figure 6. In the first four rounds, the accuracy value obtained by the model was relatively low; the rumor detection effect of this model was poor, and in the fifth round, the accuracy value of the model increased rapidly. As the number of training rounds increased, the results of the model on the three metrics, finally, floated around the optimal value.

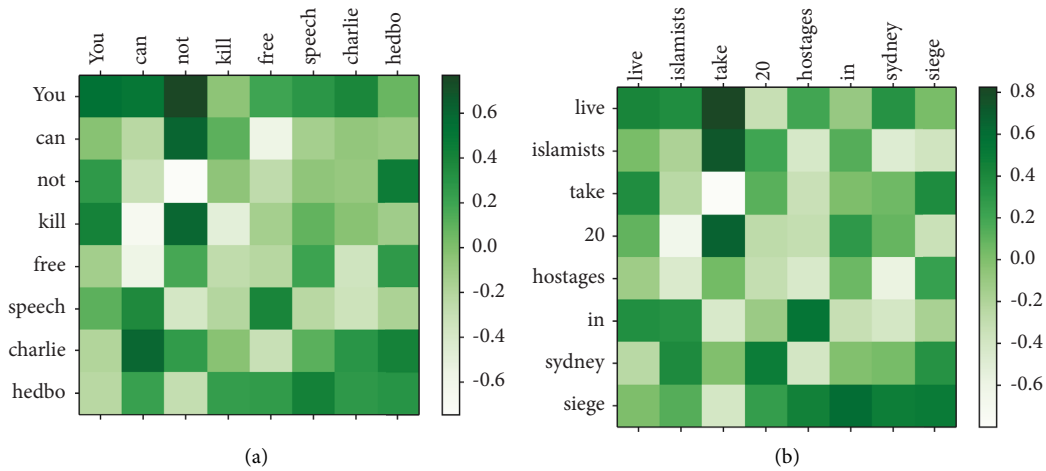

Figure 7: Case Study: a testing example demonstrates that the information of dependency tree contributes to the classification performance; our model generated a proper attention distribution with the assistance of dependency tree. Darker cell color indicates higher attention value.(a) The attention matrix of nonrumor by our method. (b) The attention matrix of rumor by our method.

In conclusion, the number of rounds trained had an important impact on the experimental results. As the number of training rounds increased, the accuracy of this model in rumor detection continuously improved and stabilized after a certain number of rounds. The model presented in this paper showed good detection effects after its stability.

5.2. Comparison Models. The overall performance of all the models was listed in Table 4, from the observation of Table 4, it can be concluded that the accuracy and F1 value of the traditional machine learning baseline model are relatively low, because the traditional machine learning manual feature extraction is cumbersome, so in the direction of rumor detection, deep learning is more effective than traditional machine learning. The deep learning models CNN, RNN, LSTM, and GRU in the table all belong to the simple recurrent neural network model, with accuracy and F1 above 60%. In terms of constructing and mining rumor features, the simple recurrent neural network model does not consider the characteristics of important spatial levels among objects. The performance of the method of modeling rumors based on graph and tree structure is better than that of the method of baseline time series. The effect of graph neural network model in identifying rumors should reach more than 80%, but the correlation between Bi-GCN and computing vertices is weak. The GAT model can fully consider the correlation between vertices and pay attention to the relationship between words. From which some observations could be noted. First, the GAT model outperformed most benchmark models. Second, in a subject-based dependent tree structure, GAT performance was significantly improved when combined with text word embedding representations. It also outperformed most of the baseline models, demonstrating that our GAT encodes the grammatical information better. After self-attention + GAT, this powerful model had further improved and achieved better detection results. These results demonstrated the effectiveness of our self-attention + GAT in terms of the syntactic structure of rumor detection.

5.3. Case Study and Attention Distribution Exploration. In order to observe the effect of attention on the model, a nonrumor and rumor were selected for the study. As shown in Figure 7(a), our method predicted that the post you can not kill free speech Charlie Hebdo was positive. In order to find out the reason, we studied the attention matrix and found that the model paid more attention to negative words and verbs, the common dependency tree was reconstructed to make it dependent on Charlie Hebdo. According to the dependency tree, not and kill form a dependency relationship, kill and free speech form a dependency relationship, and finally, free kill and Charlie Hebdo form a dependency relationship. Finally, it was identified as nonrumor. As shown in Figure 7(b), our method predicted that the post "live Islam take 20 hostages in Sydney College" was a rumor. In order to find out the reason, we studied its attention matrix. This model paid more attention to verbs and the words around them. Islam and in form a prep relationship, and in and Sydney College form a pobj, which was finally determined as a rumor.

5.4. Effects of the Different Parsers. Dependent analysis played a crucial role in this model. To assess the impact of the different parsers, we conducted a study based on GAT models by using two well-known dependency parsers.

After using the comparison, the better the Biaffine parser was, the higher the classification accuracy would be, as shown in Table 5. Furthermore, it further implied that our approach had the potential to be further improved with analytic techniques while existing parsers could correctly capture syntactic structure information.

Table 4: Comparison of detection accuracy on Twitter.

Method	accuracy	Twitter Rumors Precision	Twitter Rumors F1	Twitter Nonrumors Precision	Twitter Nonrumors F1
Baseline	0.548	0.581	0.558	0.577	0.548
CNN	0.653	0.655	0.643	0.663	0.653
LSTM	0.796	0.706	0.723	0.724	0.697
RNN	0.785	0.712	0.692	0.701	0.679
GRU	0.736	0.729	0.734	0.745	0.729
BERT	0.752	0.792	0.819	0.782	0.733
Bi-GCN	0.880	0.924	0.930	0.853	0.847
Ours	**0.885**	0.937	0.942	0.856	0.852

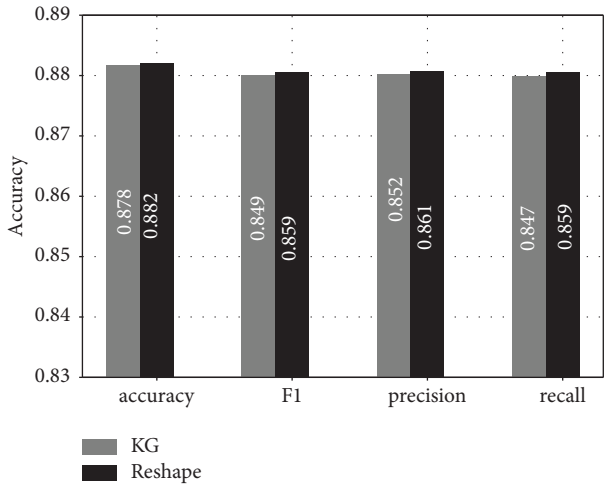

Figure 8: Schematic diagram of comparative analysis of knowledge graph and reshaped dependency tree.

Table 5: GAT results based on two different parsers, unlabeled attachment score, and labeled attachment score are indicators for evaluating parsers. The higher the score, the better the performance.

Parser	Performance UAS	Performance LAS	Dataset twitter
Stanford	94.10	91.49	0.885
Biaffine	95.74	94.08	0.853

5.5. Knowledge Graph & Comparative Analysis of the Remodeling-Dependent Trees. In this paper, two methods of a graph neural network-based rumor detection model were testified through subject enhancement. KG represented the application of the common dependency trees. Reshape represented the application of text unprocessed. The experimental results are shown in Figure 6. Rumor detection results were testified by using text and ordinary dependent tree methods, respectively, by comparison of four evaluation measures, accuracy, F1, precision, and recall. The effect of rumor detection by using the remodeling dependent trees was 0.004, 0.04, 0.01, 0.009, and 0.012 higher than those under the common dependency trees, respectively. It proved that the remodeling structure of the dependent trees had improved the accuracy of the model, as shown in Figure 8.

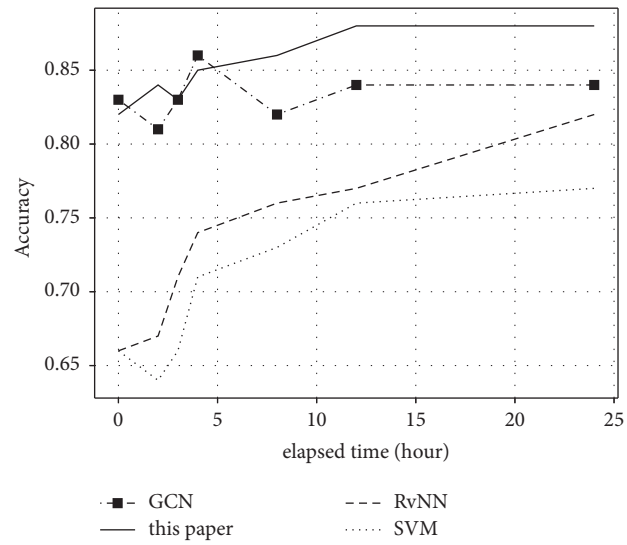

Figure 9: Early detection accuracy of rumors, accuracy obtained from Twitter datasets sent by posts and test posts scanned incrementally.

Table 6: accuracy and F1 obtained after adding five typical ablation conditions.

Ablation	Twitter Accuracy (%)	Twitter F1 (%)
Transformer + GAT	88.5	85.7
(i) Mask	88.3	85.4
(ii) Reshape	87.8	84.9
(iii) BiAffine	87.1	84.3
(iv) KG	88.2	84.1
(v) Attention	88.1	85.2

5.6. Ablation Experiments. As was shown in Table 6, we investigated and reported five typical ablation conditions. "-Mask" indicated that we had removed the mask mechanism of self-attention," Reshape "indicated that we had only used a common syntactic dependent tree by removing the sentence reconstruction trees. "-BiAffine" represented that we had removed the BiAffine process and used the output of the BiLSTM structure. So we could conclude that the BiAffine process was critical for our model. "-KG" means the removal of knowledge embedding without processing the text. "-attention" represented the representation of the removed middle graph and the interaction module of text representation.

5.7. Early Rumor Detection. In order to take precautions to prevent the spread in time, it is important to expose them in the early stages of spread. In the early detection task, we compared different detection methods to assess performance with the accuracy obtained for Twitter datasets being sent from posts and testing posts scanned incrementally.

Figure 9 shows the comparison of the method of this model with the GCN, RNN, and SVM models. It could be observed that a phenomenon that the early performance of

all methods fluctuated more or less. This was because as the postspread, there was more semantic and structural information. Meanwhile, the amount of noise information increased correspondingly. The method of this model could achieve better results in the Twitter dataset after its publication 4 hours later, indicating the superior performance of this model in the early detection of rumors.

6. Conclusions

This paper presented a graph-based neural network model under topic enhancement. First, the topic of news text was injected into the knowledge graph for topic enhancement, which could modify the effect of the mask mechanism to achieve noise reduction. Second, reshaping of the dependent trees enabled it to be subject-dependent. We only retained edges that had a direct dependence on the motif by pruning the trees. Finally, this paper integrated the text representations learned by self-attention with the graph-based representations learned by the graph attention network.

Dependency graphs can guide and facilitate text representation learning. The final text representations derived by self-attention could be used for perceptual classification together with the motif-based dependency plots. The Twitter dataset was extensively evaluated, the accuracy of this model had outperformed many previous mature models, and on various other metrics, the present model also outperformed the benchmark model, and the experimental results showed that our model outperformed the baseline method. It is a promising direction to apply graph neural networks to rumor detection in the following research [28–37].

Data Availability

The data used to support the findings of this study are openly available at https://figshare.com/articles/PHEME_dataset_of_rumours_and_non-rumours/4010619. The code implementation of this paper is placed on Gitee (https://gitee.com/wertr/rumor-detection-based-on-knowledge-enhancement-and-graph-attention-network/tree/master/).

Conflicts of Interest

The authors declare that they have no conflicts of interest.

Acknowledgments

The authors would like to thank the anonymous reviews for their helpful suggestions. And the work was supported by the Technical Innovation Guidance Special Fundation of Tianjin (Grant No. 21YDTPJC00130).

References

[1] A. Ma, W. Gao, P. Mitra et al., "Detection rumors from microblogs with recurrent neural networks," *Proceedings of the 25th International Joint Conference on Artificial Intelligence*, vol. 16, pp. 3818–3824, 2016.

[2] S. Wang, S. Mazumder, and B. Liu, "Target-sensitive memory networks for aspect sentiment classifification," *Proceedings of the 56th Annual Meeting of the Association for Computational Linguistics*, vol. 1, pp. 957–967, 2018.

[3] A. Bosselut, H. Rashkin, and M. Sap, "COMET: commonsense transformers for automatic knowledge graph construction," *Proceedings of the 57th Annual Meeting of the Association for Computational Linguistics*, vol. 57, pp. 4762–4779, 2019.

[4] C. zhang, Q. Li, and D. A. Song, "Aspect-based sentiment classifification with aspectspecifific graph convolutional networks," *Proceedings of the 2019 Conference on Empirical Methods in Natural Language Processing and the 9th International Joint Conference on Natural Language Processing*, vol. 9, pp. 4560–4570, 2019.

[5] Y. Lv, M. Sun, Y. Wen, and W. Wang, "Rumor detection based on time graph attention network," in *Proceedings of the 2022 4th International Conference on Advances in Computer Technology*, Suzhou, China, April 2022.

[6] Z. Zhao, P. Rensnick, and Q. Mei, "Enquairing minds:Early detection of rumors in social media from enquiry posts," *Processdings of the 24th international conference on world wide web*, vol. 24, pp. 1395–1405, 2015.

[7] F. Yang, Y. Liu, X. Yu, and M. Yang, "Automatic detection of rumor on sina weibo," *Processdings of the ACM SIGKDD workshop on Mining Data Semantics*, vol. 12, pp. 1–7, 2012.

[8] C. Guo, J. Cao, X. Zhang, K. Shu, and M. Yu, "Exploiting Emotions for Fake news detection on social media," 2019, https://arxiv.org/abs/1903.01728.

[9] S. Kwon, M. Cha, K. Jung, W. Chen, and W. Wang, "Prominent featurea of rumor propagation in online social media," *IEEE 12th international conference on Data Mining*, vol. 12, pp. 1103–1108, 2013.

[10] T. Chen, L. Wu, X. Li, H. Yin, and J. Zhang, "Call attention to rumors:deep attention based recurrent neural networks for early rumor detection," Article ID 059735, 2017, https://arxiv.org/abs/1704.05973.

[11] F. Yu, Q. Liu, S. Wu, L. Wang, and T. Tan, "A convolutional approachfor misinformation identification," *Proceedings of the Twenty-Sixth International Joint Conference on Artificial Intelligence*, vol. 17, pp. 3901–3907, 2017.

[12] M. Rospocher, M. Vanerp, P. Vossen et al., "Building event-centric knowledge graphs from news," *Journal of Web Semantics*, vol. 37-38, pp. 132–151, 2016.

[13] S. Gottschalks and E. Demidovae, "Event KG:A multilin-gual event-centric temporal knowledge graph," in *Proceedings of the European Semantic Web Conference*, vol. 15, pp. 272–287, Hersonissos, Greece, June, 2018.

[14] M. Hernes and A. Bytniewski, "Knoeledge representation of cognitive agents processing the economy events," *Asian Conference on Intelligent Information and Database Systems*, vol. 1, pp. 392–401, 2018.

[15] B. Xu, X. Shu, and Y. Song, "X-Invariant contrastive augmentation and representation learning for semi-supervised skeleton-based action recognition," *IEEE Transactions on Image Processing*, vol. 31, no. 5, pp. 3852–3867, 2022.

[16] X. Shu, J. Yang, R. Yan, and Y. Song, "Expansion-squeeze-excitation fusion network for elderly activity recognition," *IEEE Transactions on Circuits and Systems for Video Technology*, vol. 32, 2022.

[17] X. Shu, L. Zhang, G. J. Qi, W. Liu, and J. Tang, "Spatio-temporal co-attention recurrent neural networks for human-skeleton motion prediction," *IEEE Transactions on Pattern Analysis and Machine Intelligence*, vol. 44, no. 6, pp. 3300–3315, 2022.

[18] J. Tang, X. Shu, R. Yan, and L. Zhang, "Coherence constrained graph LSTM for group Activity recognition," *IEEE*

Transactions on Pattern Analysis and Machine Intelligence, vol. 44, no. 2, pp. 636–647, 2022.

[19] T. N. Kipf and M. W. Thomas, "Semi-supervised classication with graph convolutional networks," *International Conference on Learning Representations*, vol. 2016, Article ID 02907, 2016 https://arxiv.org/abs/1609.02907.

[20] D. Marcheggiani and D. Ivan, "Encoding sentences with graph convolutional networks for semantic role labeling," *Conference on Empirical Methods in Natural Language Processing*, vol. 17, pp. 1506–1515, 2017.

[21] X. Shu, L. Zhang, Y. Sun, and J. Tang, "Host–parasite: graph LSTM-in-LSTM for group activity recognition," *IEEE Transactions on Neural Networks and Learning Systems*, vol. 32, pp. 663–674, 2021.

[22] Z. Zhang, F. Zhuang, H. Zhu, Z. Shi, H. Xiong, and Q. He, "Relational graph neural network with hierarchical attention for knowledge graph completion," *Proceedings of the AAAI Conference on Artificial Intelligence*, vol. 34, no. 5, pp. 9612–9619, 2020.

[23] B. Huang and K. Carley, "Parameterized convolutional neural networks for aspect level sentiment classifi-cation," *Proceedings of the 2018 Conference on Empirical Methods in Natural Language Processing*, vol. 18, pp. 1091–1096, 2018.

[24] X. Yang, H. Ma, and M. Wang, "Rumor detection with bi-directional graph attention networks," *Security and Communication Networks*, vol. 2022, Article ID 4840997, 2022.

[25] A. Vaswani, N. Shazeer, and N. Parmar, "Attention is all you need," *Proceedings of the 31st International Conference on Neural Information Processing Systems*, vol. 31, pp. 6000–6010, 2017.

[26] J. Devlin, M. Chang, and K. Lee, "BERT: pre-training of deep bidirectional transformers for language understanding," 2018, https://arxiv.org/abs/1810.04805.

[27] T. Bian, X. Xiao, T. Xu et al., "Rumor detection on social media with Bi-directional graph convolutional networks," *Proceedings of the AAAI Conference on Artificial Intelligence*, vol. 34, no. 1, pp. 549–556, 2020.

[28] S. Ai, S. Hong, X. Zheng, Y. Wang, and X. Liu, "CSRT rumor spreading model based on complex network," *International Journal of Intelligent Systems*, vol. 36, no. 5, pp. 1903–1913, 2021.

[29] X. Chen, F. Zhou, F. Zhang, and M. Bonsangue, "Modeling microscopic and macroscopic information diffusion for rumor detection," *International Journal of Intelligent Systems*, vol. 36, no. 10, pp. 5449–5471, 2021.

[30] R. Zhang and D. Li, "Identifying influential rumor spreader in social network," *Discrete Dynamics in Nature and Society*, vol. 2019, Article ID 8938195, 2019.

[31] J. Borge-Holthoefer and Y. Moreno, "Absence of influential spreaders in rumor dynamics," *Physical Review*, vol. 85, no. 2, Article ID 026116, 2012.

[32] S. Srinivasan and B. Dhinesh, "A social immunity based approach to suppress rumors in online social networks," *International Journal of Machine Learning and Cybernetics*, vol. 12, no. 5, pp. 1281–1296, 2021.

[33] F. Liu and M. Li, "A game theory-based network rumor spreading model: based on game experiments," *International Journal of Machine Learning and Cybernetics*, vol. 10, no. 6, pp. 1449–1457, 2019.

[34] Q. Huang, C. Zhou, J. Wu, L. Liu, and B. Wang, "Deep spatial–temporal structure learning for rumor detection on twitter," *Neural Computing & Applications*, vol. 32, 2020.

[35] M. T. Rashid and D. Wang, "CovidSens: a vision on reliable social sensing for COVID-19," *Artificial Intelligence Review*, vol. 54, pp. 1–25, 2021.

[36] S. Raza and C. Ding, "News recommender system: a review of recent progress, challenges, and opportunities," *Artificial Intelligence Review*, vol. 55, no. 1, pp. 749–800, 2022.

[37] Q. Li, C. Zeng, W. Xu, and Y. Xiao, "A social rumor and anti-rumor game diffusion model based on sparse representation and tensor completion," *Journal of Network and Computer Applications*, vol. 201, Article ID 103343, 2022.

Hindawi
Discrete Dynamics in Nature and Society
Volume 2022, Article ID 3414493, 15 pages
https://doi.org/10.1155/2022/3414493

Research Article

Research on Partial Ordered Sets That Can Be Constructed as Effect Algebras

Hai-feng Zhang and Meng Zhou

School of Mathematics and Systems Science, Beihang University, Xueyuan Road No. 37, Haidian District, Beijing 100191, China

Correspondence should be addressed to Hai-feng Zhang; zhfcun@163.com

Received 30 June 2022; Accepted 29 July 2022; Published 26 September 2022

Academic Editor: Jinliang Wang

In this paper, we study effect algebra-induced partial ordered sets. All possible cases of effect algebras generated by bounded partial ordered set M_I of height 2 are given. In addition, the structure of chain effect algebra is studied carefully and the corresponding results are obtained.

1. Introduction

In the past few decades, algebraic structure *models* used to describe objective things have emerged in large numbers, providing effective tools for our scientific research. In the field of quantum mechanics and quantum logic, there are effects algebra [1], mv-algebra and bck-algebra [2]. In particular, effect algebra greatly promotes the rapid development of quantum theory and quantum logic.

Effect algebra is an important concept introduced by Foulis and Bennett through algebraic abstraction when they studied quantum logic. Since 1994, the study of effect algebra has been favored by scholars.First, Foulis and Bennett gave a series of basic properties of effect algebra [1]. In 1996, Gudder proposed the concept of accurately measurable elements and pivot elements [3], and proved that the effect algebra in which all elements are pivot elements is an orthogonal modular lattice. In 1999, Riecanova removed the condition of existence of identity elements in the effect algebra and obtained the generalized effect algebra [4]. In 2002, Gudder and Greechie extracted some properties of sequence product operation in Hilbert space and proposed sequence effect algebra [5]. In 2019, Wu et al. proposed L-algebras in [6], which is a generalization of homogeneous effect algebra. The relationship between effect algebras and other algebraic structures has also been studied extensively.

Generally speaking, effects algebra is an algebraic structure with a binary partial operation and a unary operation, and contains elements 0,1. The elements of effects algebra are events that are not sharp or clear, such as fuzzy events, quantum effects. Therefore, we can think of effect algebra as fuzzy and ambiguous quantum logic [7]. Effects algebra, of course, is also an algebraic abstraction of the various physical models of quantum mechanics. At the same time, effect algebra is in the category of partial order structure, it is MV-algebra.

As we all know, effect algebra has been applied to quantum theory and quantum logic with great success. However, because effect algebra is a defect of partial algebra, its algebraic structure is not perfect, which brings inconvenience to the application research. The partial binary operation + of effect algebra are fully embodied in the partial order relation introduced. Therefore, it is a good idea to study effect algebra from the perspective of partial ordered sets.

To avoid the difficulty of partial algebras, starting from the concept of effect algebras, we use effect algebras to induce the unique partial order and make it a partial order set. We study effect algebras from this perspective. The types, quantities and structures of partial ordered sets are discussed in effect algebras. The results show that this method can give some interesting theorems describing the structure of effect algebras perfectly.

Below, we first give the basic definition and some properties used in the paper.

2. Preliminaries

First we introduce the concept of effects algebra and some properties that will be used.

Definition 1. [1] *An* ***effect algebra*** *(**EA** for short) is a system* $\mathcal{X} = (X, +, 0, 1)$ *where* $0, 1 \in X$ *and* $+$ *is a partial binary operation on* X *satisfying the conditions*:

(E1) for all $u, v \in X$, $u + v$ is defined $\Rightarrow v + u$ is defined, and $u + v = v + u$;

(E2) for all $u, v, w \in X$, $(u + v) + w$ is defined $\Rightarrow u + (v + w)$ is defined, and $(u + v) + w = u + (v + w)$;

(E3) for all $u \in X$ there is a unique $u' \in E$ such that $u + u' = 1$;

(E4) for all $u \in X$, if $1 + u$ is defined then $u = 0$.

The mapping $x \mapsto x'$ is a total unary operation on X We can define the so-called **induced order** $\leq_{\mathcal{X}}$ on X by stipulation

$$\leq_{\mathcal{X}} = \{(a, b) \in X \times X \mid \exists r \in X \, s.t. \, a + r = b\}. \tag{1}$$

Since $0 \leq_{\mathcal{X}} u \leq_{\mathcal{X}} 1$ is true for any $u \in X$, $(X, \leq_{\mathcal{X}})$ is a bounded poset, denoted by $P(\mathcal{X})$. When $\leq_{\mathcal{X}}$ is a lattice-order relation, we call the effect algebra $\mathcal{X}$ a **lattice-order effect algebra** (**LEA** for short). When $\leq_{\mathcal{X}}$ is a total-order relation, we call the effect algebra $\mathcal{X}$ a **chain effect algebra** (**CEA** for short).

Definition 2. Two effect algebras $\mathcal{X} = (X, +, ', 0_X, 1_X)$ *and* $\mathcal{Y} = (Y, \oplus, ^{\dagger}, 0_Y, 1_Y)$ *are* ***isomorphic*** *if there is a bijection* φ *from* X *to* Y *such that for every* u, v *in* X *the following four equations hold*:

(I1) $u + v$ is defined $\Leftrightarrow \varphi(u) \oplus \varphi(v)$ is defined and then $\varphi(u + v) = \varphi(u) \oplus \varphi(v)$;

(I2) $\varphi(0_X) = 0_Y$;

(I3) $\varphi(1_X) = 1_Y$;

(I4) $\varphi(u') = (\varphi(u))^{\dagger}$.

Such a φ *is called an* ***isomorphism*** *, denoted by* $\mathcal{X} \overset{\varphi}{\simeq} \mathcal{Y}$ *(*$\mathcal{X} \simeq \mathcal{Y}$ *for short).*

Definition 3. (see[8]). *Let* $(F, \leq)$ *be a poset, and* $f, g \in P$.

(1) g ***covers*** f *in* F, *denoted by* $f \prec g$, *iff* $f < g$ *and* $\forall t \in P, f \leq t \leq g \Rightarrow f = t$ or $g = t$.

In a poset $(F, \leq)$ with a smallest element 0, the element covering the 0 is called an **atom**. Let $A(F) = \{a \in F | a \text{ is an atom }\}$.

(2) $f, g \in F$ are called ***comparable*** *iff* $f \leq g$ *or* $g \leq f$. *Otherwise* f *and* g *are* ***incomparable****, which denoted by* $f \| g$.

The following are the basic properties of effect algebra given by Foulis and Bennett in 1994, which we will use.

Lemma 1 (see[1]). *Let* $\mathcal{X} = (X, +, 0, 1)$ *be an EA and* $g_1, g_2, k, l \in X$ *. Then*

(1) $g_1 + g_2$ *is defined* $\Leftrightarrow g_2 \leq_{\mathcal{X}} g_1' \Leftrightarrow g_1 \leq_{\mathcal{X}} g_2'$ *;*

(2) if $g_1 + g_2$ *is defined then* $k + l$ *is defined for all* $k \leq_{\mathcal{X}} g_1$ *and* $l \leq_{\mathcal{X}} g_2$ *;*

(3) $g_1 \leq_{\mathcal{X}} g_2 \Leftrightarrow g_2' \leq_{\mathcal{X}} g_1'$ *;*

(4) $k'' = k$ *;*

(5) if $g_1 \leq_{\mathcal{X}} g_2$ *and* $g_2 + k$ *is defined then* $g_1 + k$ *is defined and* $g_1 + k \leq_{\mathcal{X}} g_2 + k$*;*

(6) $g_1 + g_2 = k \Leftrightarrow g_1' = g_2 + k' \Leftrightarrow g_1 = (g_2 + k')'$.

Theorem 1. *The necessary and sufficient condition for the EA* $\mathcal{X} = (X, +, ', 0_E, 1_E)$ *and* $\mathcal{Y} = (Y, \oplus, ^{\dagger}, 0_F, 1_F)$ *to be isomorphic is that there exists a bijective* φ *from* X *to* Y *such that* $\forall g, h \in X$ *the following condition (I1) is true.*

(I1) $g + h$ *is defined* $\Leftrightarrow \varphi(g) \oplus \varphi(h)$ *is defined and* $\varphi(g + h) = \varphi(g) \oplus \varphi(h)$*,*

Proof. ($\Leftarrow$): Since φ: $X \longrightarrow Y$ is a bijection, then $\exists j \in X$, such that $\varphi(j) = 1_Y$. Hence

$$\varphi(1_X) = \varphi(j + j') = \varphi(j) \oplus \varphi(j') = 1_Y \oplus \varphi(j'). \tag{2}$$

By (E3), we have $\varphi(j') = 0_Y$. Therefore, $\varphi(1_X) = 1_Y$, $j = 1_X$ and $j' = 0_X$, which shows that (I2) and (I3) holds.

For every $l \in X$, Since $l + l' = 1_X$, we have

$$\varphi(l) \oplus \varphi(l') = \varphi(l + l') = \varphi(1_X) = 1_Y. \tag{3}$$

Hence $\varphi(l') = (\varphi(l))^{\dagger}$, i.e. (I4) holds. Therefore, $\mathcal{X} \overset{\varphi}{\simeq} \mathcal{Y}$.

($\Rightarrow$): By Definition 2, it is trivial. □

Definition 4. By an ***isomorphism*** *between two posets* $(S, \leq)$ *and* $(T, \leq)$ *, is meant a one-one correspondence* ψ *between* S *and* T *such that*

$$s \leq t \Leftrightarrow \psi(s) \leq \psi(t). \tag{4}$$

Two posets are called **isomorphic** iff there exists an isomorphism between them, we write ψ: $S \overset{\psi}{\simeq}_{po} T$ *or just* $S \simeq T$; an isomorphism of a partly ordered set with itself is called an automorphism. A many-one corregiondence satisfying (4) is called **isotone** .

By the **converse** of a relation R is meant the relation R^c such that $xR^c y$ if and only if yRx.

Definition 5. By the ***dual*** P^c *of a poset* P *is meant that poset defined by the converse relation on the same elements.*

According to Definitions 2 and 4, we can obtain the following lemma. It gives the conclusion that the

isomorphism of EA isomorphism can imply the order isomorphism.

Lemma 2. *Let* $\mathscr{X} = (X, +, ', 0_X, 1_X)$ *and* $\mathscr{Y} = (Y, \oplus, ^{\dagger}, 0_Y, 1_Y)$ *be EAs,* $\mathscr{X} \overset{\varphi}{\simeq} \mathscr{Y}$ *. Then* $(X, \leq_{\mathscr{X}}) \overset{\varphi}{\simeq}_{po} (Y, \leq_{\mathscr{Y}})$.

The condition (I1) can be further simplified by the following theorem.

Theorem 2. *Two effect algebras* $\mathscr{X} = (X, +, ', 0_X, 1_X)$ *and* $\mathscr{Y} = (Y, \oplus, ^{\dagger}, 0_Y, 1_Y)$ *are isomorphic iff* $\exists \varphi$: $X \longrightarrow Y$, *and for all* $w, v \in X$

(I1) $'$ *if* $w + v$ *is defined then* $\varphi(w) \oplus \varphi(v)$ *is defined and* $\varphi(w + v) = \varphi(w) \oplus \varphi(v)$,

(Ii) $(X, \leq_{\mathscr{X}}) \overset{\varphi}{\simeq}_{po} (Y, \leq_{\mathscr{Y}})$

Proof. ($\Leftarrow$): First of all, since $(X, \leq_{\mathscr{X}}) \overset{\varphi}{\simeq}_{po} (Y, \leq_{\mathscr{Y}})$, φ is bijective.

For all $u \in Y$, $0_X + \varphi^{-1}(u)$ is defined, then so does $\varphi(0_X) \oplus \varphi(\varphi^{-1}(u))$ and

$$\varphi(0_X) \oplus \varphi\left(\varphi^{-1}(u)\right) = \varphi\left(0_X + \varphi^{-1}(u)\right) = \varphi\left(\varphi^{-1}(u)\right) = u. \tag{5}$$

Thus $\varphi(0_X) = 0_Y$.

Since φ: $X \longrightarrow Y$ is a bijection, then $\exists h \in X$, such that $\varphi(h) = 1_Y$. Hence

$$\varphi(1_X) = \varphi(h + h') = \varphi(h) \oplus \varphi(h') = 1_Y \oplus \varphi(h'). \tag{6}$$

By (E3), we have $\varphi(h') = 0_Y$. Thus $h' = 0_X$ and $h = 1_Y$.Therefore, which shows that (I2) and (I3) holds.

For every $w \in X$, Since $w + w' = 1_X$, we have

$$\varphi(w) \oplus \varphi(w') = \varphi(w + w') = \varphi(1_X) = 1_Y. \tag{7}$$

Hence $\varphi(w') = (\varphi(w))^{\dagger}$, i.e. (I4) holds.

The following is the proof of condition $(I1)'$ and (Ii) implication condition (I1).

Let $k, l, r \in X$ and $\varphi(k) \oplus \varphi(l)$ is defined, $\varphi(k) \oplus \varphi(l) = \varphi(r)$ in $\mathscr{Y}$. Then

$$\varphi(k) \leq_{\mathscr{Y}} \varphi(r). \tag{8}$$

therefore

$$k \leq_{\mathscr{X}} r. \tag{9}$$

$\exists o \in X$, such that $k + o = r$. By (I1), we have $\varphi(k) \oplus \varphi(o) = \varphi(r)$. Then $\varphi(l) = \varphi(o)$ and $l = o$. i.e. (I1) holds.

Therefore, $\mathscr{X} \overset{f}{\simeq} \mathscr{Y}$.

($\Rightarrow$):By Definition 2 and Lemma 2, it is trivial. □

Remark 1. The condition (I1)$'$ *in* Theorem 1 *does not imply the condition (I1), see* Example 1.

Example 1. Let $X_1 = \{0_1, 1_1, p_1, q_1,\}, X_2 = \{0_2, 1_2, p_2, q_2,\}$ *. It is easy to verify that* $\mathscr{X}_1 = (X_1, +, ', 0_1, 1_1)$ *and* $\mathscr{X}_2 = (X_2, \oplus, ^{\dagger}, 0_2, I_2)$ *are effect algebras, where*$+, ', \oplus, ^{\dagger}$ *see the follows.*

$+$	0_1	p_1	q_1	1_1
0	0_1	p_1	q_1	1_1
p_1	p_1	$-$	1_1	$-$
q_1	q_1	1_1	$-$	$-$
1_1	1_1	$-$	$-$	$-$

$0_1' = 1_1$,
$p_1' = q_1$,
$q_1' = p_1$,
$1_1' = 0_1$,

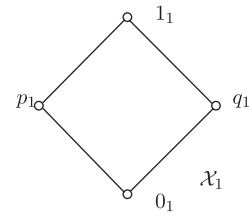

$\oplus$	0_2	p_2	q_2	1_2
0_2	0_2	p_2	q_2	1_2
p_2	p_2	q_2	1_2	$-$
q_2	q_2	1_2	$-$	$-$
1_2	1_2	$-$	$-$	$-$

$0_2' = 1_2$,
$p_2' = q_2$,
$q_2' = p_2$,
$1_2' = 0_2$,

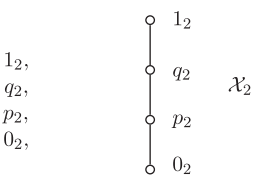

Let f: $X_1 \longrightarrow X_2, 0_1 \mapsto 0_2, 1_1 \mapsto 1_2, p_1 \mapsto p_2, q_1 \mapsto q_2$. Then f is a bijection from X_1 to X_2, and satisfies condition $(I1)'$. But the effect algebras $\mathscr{X}_1$ and $\mathscr{X}_2$ are not isomorphic.

For each effect algebra $\mathscr{E}$, a unique partially ordered set $P(\mathscr{E})$ can be obtained under (1). Then, for a given bounded poset $(P, \leq)$, can we introduce partial binary operation $+$ and unary operation$'$such that $(P, +, ', 0, 1)$ is an EA and the induced order relation on P is exactly $\leq$?

The following counterexamples answers this question.

Example 2. Let $V_5 = \{0, 1, v_1, v_2, r\}, 0 < r < v_1 < 1, 0 < r < v_2 < 1$, *(see* Figure 1*).*

If $E(V_5) = (V_5, +, ', 0, 1)$ is an EA. Since $0 < r < v_1 < 1$, we have $r + r = v_1$. Similarly, since $0 < r < v_2 < 1$, we have $r + r = v_2$, hence $v_1 = v_2$. This is a contradiction. Thus, $(V_5, \leq)$ cannot be constructed as an EA.

Example 3. Let$V_4 = \{0, 1, v_1, v_2\}$*and partial binary operations* $+$, $\oplus$ *and unary*operations$'^{,\dagger}$ *are defined by*

$+$	0	v_1	v_2	1
0	0	v_1	v_2	1
v_1	v_1	1	-	-
v_2	v_2	-	1	-
1	1	-	-	-

$\oplus$	0	v_1	v_2	1
0	0	v_1	v_2	1
v_1	v_1	-	1	-
v_2	v_2	1	-	-
1	1	-	-	-

x	x'
0	1
v_1	v_1
v_2	v_2
1	0

x	$x^{\dagger}$
0	1
v_1	v_2
v_2	v_1
1	0

It is easy to prove that $\mathscr{E}_1(V_4) = (V_4, +, ', 0, 1)$ and $\mathscr{E}_2(V_4) = (V_4, \oplus, ^{\dagger}, 0, 1)$ are two completely different effect algebras, but they both induce partial ordered sets of V_4 (see Figure 2). In face, We have more general examples.

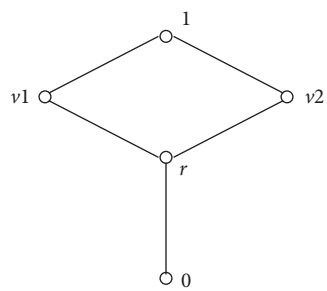

Figure 1: Lattice V_5.

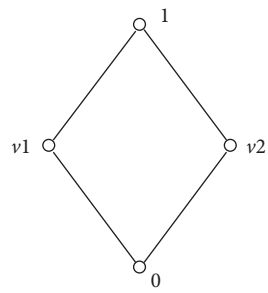

Figure 2: Lattice V_4.

Example 4. Let $E_0 = [0,1] \subseteq \mathbb{R}$ ($\mathbb{R}$ is a set of real numbers) and define $\oplus_n$ and $'_n$ as follows:

$$x \oplus_n y = \begin{cases} (x^n + y^n)^{1/n} & x^n + y^n \leq 1 \\ - & x^n + y^n > 1 \end{cases} \quad x'_n = (1 - x^n)^{1/n}. (n \in Z^+). \tag{10}$$

Then $\mathscr{E}_n = (E_0, \oplus_n, '_n, 0, 1)$ is a LEA with the induced order $\leq_n$. For all $u_1, u_2 \in [0,1]$, since

$$u_1 \leq_n u_2 \Leftrightarrow \exists h \in [0,1]\, s.t.\, u_1 \oplus_n d = u_2. \tag{11}$$

Thus, if $(u_1, u_2) \in \leq_n$, then $u_2 = u_1 \oplus_n d = \sqrt[n]{u_1^n + d^n} \geqslant u_1$, i.e. $(u_1, u_2) \in \leqslant$, where $\leqslant$ is usual orders on $\mathbb{R}$. Hence $\leq_n \subseteq \leqslant$.

Conversely, let $(s,t) \in \leqslant$, i.e. $0 \leqslant s \leqslant t \leqslant 1$, then we have $0 \leqslant s^n \leqslant t^n \leqslant 1$ and $\sqrt[n]{t^n - s^n} \in [0,1]$, $s \oplus_n (\sqrt[n]{t^n - s^n}) = t$, hence $s \leq_n t$, i.e. $\leq \subseteq \leq_n$. Thus $\leq_n = \leqslant (n = 1, 2, \cdots)$.

Theorem 3. *Let $(X, \leq)$ be a bounded poset with $|X| = n$ ($n \in \mathbb{Z}^+$). If $n \leq 4$, then poset $(X, \leq)$ can be used to construct an EA.*

Proof

(1) When $n = 1$, the statement is clearly true.

(2) If $n = 2$, then $X = \{0, 1\}$, $0 + 0 = 0, 0 + 1 = 1 + 0 = 1$, $0' = 1, 1' = 0$, and $\mathscr{X} = (X, +, 0, 1)$ is an EA.

(3) Since $(X, \leq)$ is a bounded poset, when $n = 3$, we have $X = \{0, a, 1\}$, and $0 < a < 1$, i.e. poset $(X, \leq)$ is a 3-element chain. Define + and $'$ as follows:

$+$	0	a	1
0	0	a	1
a	a	1	$-$
1	1	$-$	$-$

x	x'
0	1
a	a
1	0

therefor, $\mathscr{X} = (X, +, 0, 1)$ is an EA.

(4) For a bounded poset $(X, \leq)$, there are two cases when $n = 4$, one is a chain of four elements and the other is V_4 (see Example 1). So by Theorem 2 and Example 1, we get $(X, +)$, which can be converted into EA. The proof is complete. □

Remark 2. These results can be summarized in the following table.

n	P	$(P,\leq)$	$+$ and $'$	Uniqueness
1	$\{0\}$		$0+0=0,\ 0'=0$	Yes
2	$\{0,1\}$		$0+0=0,\ 0'=1$ $0+1=1,\ 1'=0$	Yes
3	$\{0,c_0,1\}$		$\begin{array}{c\|ccc} + & 0 & c_0 & 1 \\ \hline 0 & 0 & c_0 & 1 \\ c_0 & c_0 & 1 & - \\ 1 & 1 & - & - \end{array}$ $0'=1,$ $c_0'=c_0,$ $1'=0,$	Yes
4	$\{0,c_0,c_1,1\}$	1)  2) 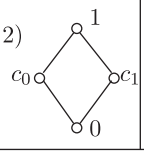	1) $\begin{array}{c\|cccc} + & 0 & c_0 & c_1 & 1 \\ \hline 0 & 0 & c_0 & c_1 & 1 \\ c_0 & c_0 & c_1 & 1 & - \\ c_1 & c_1 & 1 & - & - \\ 1 & 1 & - & - & - \end{array}$ $0'=1,$ $c_0'=c_1,$ $c_1'=c_0,$ $1'=0,$ 2) see Example 3	1) Yes 2) No

We use $\mathscr{E}(n)$ to denote n-element effect algebras $(n=1,2,3)$.

Remark 3. Example 2 *shows lattice V_5 with the least number of elements in non-effect algebra.*

Lemma 3. *Let $\mathscr{K}=(K,+,0,1)$ be an EA. Then $'$: $K\simeq K^c$, that is. $(K,\leq_{\mathscr{K}})$ is automorphic.*

Proof. for all $k_1,k_2\in K$, if $k_1\leq k_2$, then $k_2'\geq k_1'$ by Lemma 1 (3). And if $k_2'\geq k_1'$, then

$$k_1=k_1''=(k_1')\leq(k_2'),=k_2''=k_2. \tag{12}$$

by Lemma 1 (4). Thus $'$: $K\simeq K^c$. □

Theorem 4. *In the isomorphism sense, there are only four types of effect algebra for five elements, which are:*

(1) $C_5=\{0,u,v,w,1\}$. Define $+$ and $'$ as follows:

$$\begin{array}{c|ccccc} + & 0 & v & w & u & 1 \\ \hline 0 & 0 & v & w & u & 1 \\ v & v & w & u & 1 & - \\ w & w & u & 1 & - & - \\ u & u & 1 & - & - & - \\ 1 & 1 & - & - & - & - \end{array} \qquad \begin{array}{l} 0'=1, \\ u'=v, \\ v'=u, \\ w'=w, \\ 1'=0, \end{array}$$

$(C_5,\leq)$.

(2) $N_5=\{0,u,v,w,1\}$. Define $+$ and $'$ as follows:

$$\begin{array}{c|ccccc} + & 0 & v & w & u & 1 \\ \hline 0 & 0 & v & w & u & 1 \\ v & v & 1 & - & - & - \\ w & w & - & - & 1 & - \\ u & u & - & 1 & - & - \\ 1 & 1 & - & - & - & - \end{array} \qquad \begin{array}{l} 0'=1, \\ u'=w, \\ v'=v, \\ w'=u, \\ 1'=0, \end{array}$$

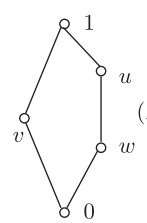

$(N_5,\leq)$.

(3) $M_3 = \{0, u, v, w, 1\}$. *Define* $+$ *and* $'$ *as follows:*

$+$	0	v	w	u	1
0	0	v	w	u	1
v	v	$-$	1	$-$	$-$
w	w	1	$-$	$-$	$-$
u	u	$-$	$-$	1	$-$
1	1	$-$	$-$	$-$	$-$

$0' = 1,$
$u' = u,$
$v' = w,$
$w' = v,$
$1' = 0,$

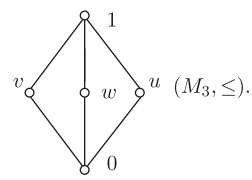

Proof. Since there are only three kinds of automorphic bounded five-element partial ordered sets: C_5, N_5, and M_3, the theorem holds. □

Remark 4. The five-element effect algebras whose induced poset isM_3 *are not unique. There are altogether four of them. We'll look at this in the next section.*

Corollary 1. *Let* $\mathscr{L} = (L, +, ', 0, 1)$ *be an EA with* $|E| = n$ *(* $n \in \mathbb{Z}^+$ *). If* $n < 6$ *, then* $\mathscr{L} = (L, +, ', 0, 1)$ *is a LEA.*

Example 5. [6] *The*$\mathscr{P}_6 = (P_6, +, ', 0, 1)$*is an EA, where*$+, '$*see the follows.*

$+$	0	l	k	s	t	1
0	0	l	k	s	t	1
l	l	t	s	1	$-$	$-$
k	k	s	t	$-$	1	$-$
s	s	1	$-$	$-$	$-$	$-$
t	t	$-$	1	$-$	$-$	$-$
1	1	$-$	$-$	$-$	$-$	$-$

$0' = 1,$
$l' = s,$
$k' = t,$
$s' = l,$
$t' = k,$
$1' = 0,$

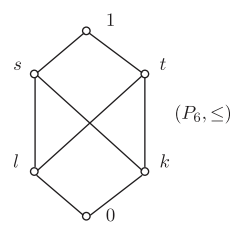

Let $(F, \leq)$ be a poset, $r, s \in F$ and $r < s$. Here are the definitions of the intervals:

$$[r, s] = \{d \in F | r \leq d \leq s\}, \ (r, s) = \{d \in F | r < d < s\}. \tag{13}$$

Note that P_6 is not a lattice, next, we will consider lattice-ordered effect algebras.

3. Homo-Ordered Effect Algebras

Next we will study the poset induced by the effect algebra with the same property, and first give the definition of the same order effect algebra.

Definition 6. Two effect algebras $\mathscr{X} = (X, +, 0_X, 1_X)$ *and* $\mathscr{Y} = (Y, +, 0_Y, 1_Y)$ *are called***Homo-ordered** *if the posets* $(X, \leq_X)$ *and* $(Y, \leq_Y)$ *are isomorphic, denoted by* $\mathscr{X} \overset{po}{\cong} \mathscr{Y}$.

In Example 3, $\mathscr{E}_1(V_4) \overset{po}{\cong} \mathscr{E}_2(V_4)$ and in Example 4, $\mathscr{E}_n \overset{po}{\cong} \mathscr{E}_1, n = 1, 2, \cdots$ holds. Below, we have more general results.

Theorem 5. *Let* $\mathscr{Z} = (Z, +, 0_Z, 1_Z)$ *be an EA,* $(K, \leq)$ *be a poset. If*$P(\mathscr{Z}) \overset{h}{\cong} (K, \leq)$*, then* $\mathscr{Z} \overset{po}{\cong} \mathscr{K}$*, where* $\mathscr{K} = (K, \oplus, ^\dagger, 0_K, 1_K)$*,* $\forall l_1, l_2 \in K$*:*

$$l_1 \oplus l_2 = \begin{cases} h\left(h^{-1}(l_1) + h^{-1}(l_2)\right) & h^{-1}(l_1) + h^{-1}(l_2) \text{is defined,} \\ - & \text{otherwise,} \end{cases} \quad l_1^\dagger = h\left(h^{-1}(l_1)\right). \tag{14}$$

Proof. First, we prove that $\mathscr{K} = (K, \oplus, ^\dagger, 0_K, 1_K)$ is an EA.

For all $l_1, l_2 \in K$, if $l_1 \oplus l_2$ is defined, then $h^{-1}(l_1) + h^{-1}(l_2)$ is defined, and $h^{-1}(l_1) + h^{-1}(l_2) = h^{-1}(l_2) + h^{-1}(l_1)$ is defined, hence $l_2 \oplus l_1$ is defined and

$$\begin{aligned} l_2 \oplus l_1 &= h\left(h^{-1}(l_2) + h^{-1}(l_1)\right) \\ &= h\left(h^{-1}(l_1) + h^{-1}(l_2)\right) = l_1 \oplus l_2. \end{aligned} \tag{15}$$

i.e. (E1) holds. Similarly, we can prove that (E2) holds as well.

$$\begin{aligned} l_1 \oplus l_1^{\dagger} &= l_1 \oplus \left(h\left(\left(h^{-1}(l_1)\right)'\right)\right) \\ &= h\left(h^{-1}(l_1) + h^{-1}\left(h\left(\left(h^{-1}(l_1)\right)'\right)\right)\right), \\ &= h\left(h^{-1}(l_1) + \left(\left(h^{-1}(l_1)\right)'\right)\right) \\ &= h(1_Z) = 1_K. \end{aligned} \tag{16}$$

Then (E3) holds.

Let $1_K \oplus l$ is defined $(l \in K)$, then $h^{-1}(1_K) + h^{-1}(l) = 1_Z + h^{-1}(l)$ is defined. Thus, $h^{-1}(l) = 0_Z$,

$$l = h\left(h^{-1}(l)\right) = h(0_Z) = 0_K. \tag{17}$$

i.e. (E4) holds. Hence $\mathscr{K} = (K, \oplus, \dagger, 0_K, 1_K)$ is an EA.

Next, we show that $P(\mathscr{K}) = (K, \leq)$. i.e. $\leq_{\mathscr{K}} = \leq$.

Let $k_1, k_2 \in K$ and $k_1 \leq k_2$. Then we have $h^{-1}(k_1) \leq h^{-1}(k_2)$ and $\exists y \in Z$, $h^{-1}(k_1) + y = h^{-1}(k_2)$.i.e.

$$h^{-1}(k_1) + h^{-1}(h(y)) = h^{-1}(k_2). \tag{18}$$

Therefore $k_1 \oplus h(y) = h(h^{-1}(k_1) + h^{-1}(h(y))) = h(h^{-1}(k_2)) = k_2$, i.e. $k_1 \leq_{\mathscr{K}} k_2$.

Since $k_1 \leq_{\mathscr{K}} k_2$, then $\exists r \in K$, $k_1 \oplus r = k_2$. therefore we have $h^{-1}(k_1) + h^{-1}(r) = h^{-1}(k_2)$. Hence $h^{-1}(k_1) \leq_{\mathscr{Z}} h^{-1}(k_2)$. Since $P(\mathscr{Z}) \overset{h}{\simeq} (K, \leq)$, we have $k_1 \leq k_2$. Thus, we conclude that $P(\mathscr{K}) = (K, \leq)$ holds as well. Therefore, $P(\mathscr{Z})$ and $P(\mathscr{K})$ are isomorphic.

Thus, $\mathscr{Z} \overset{po}{\cong} \mathscr{K}$, the proof is complete. □

Remark 5

(1) This theorem gives a way to construct a new EA from the poset of an EA.

(2) *This method is not sufficient, see* Example 3, $\mathscr{E}_1(V_4) \overset{po}{\cong} \mathscr{E}_2(V_4)$*holds, but+and* $\oplus$ *do not satisfy the relationship of* Theorem 5.

Definition 7. Let $\mathscr{K}_1 = (K_1, +_{K_1}, {}'^{K_1}, 0, 1)$ *and* $\mathscr{K}_2 = (K_2, +_{K_2}, {}'^{K_2}, 0, 1)$ *are effect algebras and* $K_1 \cap K_2 = \{0, 1\}$, $M = K_1 \cup K_2$. *If we put*

$$\begin{aligned} r + t &:= \begin{cases} r +_{K_1} t, & r +_{K_1} t \text{ is defined } r, t \in K_1, \\ r +_{K_2} t, & r +_{K_2} t \text{ is defined } r, t \in K_2, r' \\ - & \text{otherwise}, \end{cases} \\ &:= \begin{cases} r'^{K_1}, & r \in K_1, \\ r'^{K_2}, & r \in K_2, \end{cases} \end{aligned} \tag{19}$$

for all $r, t \in M$ *then* $\mathscr{M} = (M, +, ', 0, 1)$ *is EA, we call* $\mathscr{M}$ *a* ***union effect algebra*** *of* $\mathscr{K}_1$ *and* $\mathscr{K}_2$, *denoted by* $\mathscr{M} = \mathscr{K}_1 \sqcup \mathscr{K}_2$ *(see* Figure 3.

In Example 3, if we put $G = \{0, a, 1\}, H = \{0, b, 1\}$, then $\mathscr{E}_1(V_4) = \mathscr{G} \sqcup \mathscr{H}$.

Definition 8. Let $\mathscr{K} = (K, +_K, {}'^K, 0_K, 1_K)$ *and* $\mathscr{L} = (L, +_L, {}'^L, 0_L, 1_L)$ *are EA. If we put*

$$\begin{aligned} (k_1, h_1) + (k_2, h_2) &:= \begin{cases} (k_1 +_K k_2, h_1 +_L h_2), & k_1 +_K k_2 \text{ and } h_1 +_L h_2 \text{ are defined}, \\ -, & \text{otherwise}, \end{cases} \\ (k_1, h_1)' &:= \left(k_1'^K, h_1'^L\right). \end{aligned} \tag{20}$$

for all $(k_1, h_1), (k_2, h_2) \in K \times L$, obviously $\mathscr{K} \otimes \mathscr{L} = (K \times L, +, ', (0_K, 0_L), (1_K, 1_L))$ *is EA, we call* $\mathscr{K} \otimes \mathscr{L}$ a **direct product effect algebra** of $\mathscr{K}$ and $\mathscr{L}$.

In Example 3, if we put $G = H = \{0, 1\}$, $\mathscr{G} = (G, +, ', 0, 1)$, $\mathscr{H} = (H, +, ', 0, 1)$ and $0 + 0 = 0, 0 + 1 = 1 + 0 = 1$, $0' = 1, 1' = 0$, then $\mathscr{E}_2(V_4) = \mathscr{G} \otimes \mathscr{H} \cong \mathscr{E}(2) \otimes \mathscr{E}(2)$.

If all sub-chains in a poset $P = (P, \leq)$ contain at most $m + 1$ element $(m \in N)$, then we say that the **height** of the poset $P = (P, \leq)$ is m, denoted by $h(P) = m$.

Lemma 4. *Let* $H = (H, \leq)$ *be a bounded poset with* $h(H) = 2$, *then* $H = M_I$, *where* $M_I = (M_I, \leq_M)$, $M_I = \{0, 1\} \cup I, I \neq \varnothing, 0 \leq_M a \leq_M 1$, *for all* $a \in I$ *(see Figure 4).*

Proof. The proof can be obtained directly from the boundedness and height of the poset $(H, \leq)$. □

Theorem 6. *Let* $H = (H, \leq)$*be a bounded poset with* $h(H) = 2$, *then there is an EA* $\mathscr{X} = (H, +, ', 0, 1)$ *such that* $P(\mathscr{X}) = (H, \leq)$.

Proof. Let $0, 1$ be the smallest and largest element of a bounded poset $(H, \leq)$, that is: $0 \leq x \leq 1$, for any $x \in H$.

Since $h(H) = 2$, $H = I \cup \{0, 1\}, I = \{x, y, \cdots\}$ by Lemma 4 (see Figure 4). Obviously, $\mathscr{X} = (H, +, ', 0, 1)$ is an EA and $P(\mathscr{X}) = (H, \leq)$, where $+, '$ see the follows.

$$\begin{aligned} &0 + j = j + 0 := j, j + j := 1; j' = j, \text{for all } j \in I, \\ &0 + 1 = 1 + 0 = 1, 0 + 0 = 0; 0' = 1, 1' = 0. \end{aligned} \tag{21}$$

□

Theorem 7. *Let* $\mathscr{X} = (X, +, ', 0, 1)$*be an EA and* $I = X/\{0, 1\}$. *Then the following are equivalent:*

(1) $P(\mathscr{X}) = M_I$;

(2) For all $u, v \in I$, *if* $u + v$ *is defined then* $u + v = 1$.

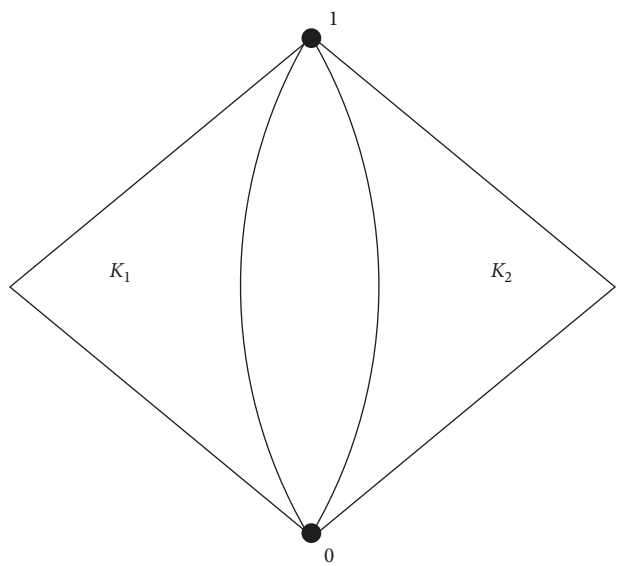

Figure 3: Union effect algebra $\mathscr{K}_1 \sqcup \mathscr{K}_2$.

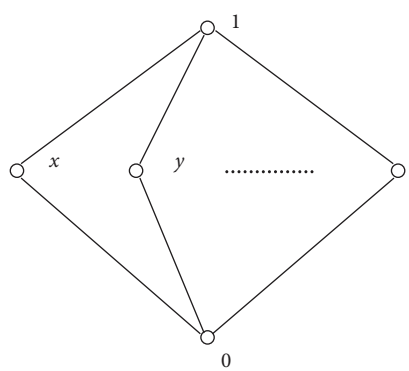

Figure 4: Bounded poset M_I.

Proof

(1) $\Rightarrow$ (2). For all $u, v \in I$, if $u + v$ is defined, then $u, v \leq u + v$ and $u \vee v \leq u + v$. In M_I, $u \vee v = 1$ for all $u, v \in I$. Thus we have $u + v = 1$.

(2)$\Rightarrow$ (1). For all $u, v \in I$, when $u \neq v$, we have $u < u \vee v$ or $v < u \vee v$. Then $\exists s, t \in I$, such that

$$u \vee v = u + s, \text{or } u \vee v = v + t. \tag{22}$$

and $u \vee v = 1$ by (2).

Since $X \simeq X^c$ by Lemma 3, $u \wedge v = 0$ for all $u, v \in I$. Hence $P(\mathscr{X}) = M_I$, the proof is complete. □

Theorem 8. *Let $\mathscr{Z} = (Z, +, ', 0, 1)$ be an EA with $P(\mathscr{Z}) = M_I$, $I = Z/\{0, 1\}$. Then*

$$\mathscr{Z} = \sqcup\{\mathscr{Z}_a | a \in I\}, \tag{23}$$

where $\mathscr{Z}_a = (Z_a, +, ', 0, 1)$, $Z_a = \{0, a, a', 1\}, a \in I$.

Proof. For all $a \in I$, $\mathscr{Z}_a = (\{0, a, a', 1\}, +, ', 0, 1)$ and

$$Z_a = \{0, a, a', 1\} = \begin{cases} \{0, a, 1\}, & a = a'; \\ \{0, a, a', 1\}, & a \neq a'. \end{cases} \tag{24}$$

It is easy to verify that $\mathscr{Z}_a$ is an EA and

$$\mathscr{Z}_r \cap \mathscr{Z}_s = \begin{cases} \{0, 1\}, & r \neq s \text{ and } r \neq s'; \\ \mathscr{Z}_r = \mathscr{Z}_s, & r = s \text{ or } r = s'. \end{cases} \tag{25}$$

for all $r, s \in I$. Thus, $\sqcup\{\mathscr{Z}_a | a \in I\}$ is defined and $\cup_{a \in I} Z_a = Z$, therefore, $u + v$ is defined iff $v \in \mathscr{Z}_u$ by Theorem 7. Hence $\mathscr{Z} = \sqcup\{\mathscr{Z}_a | a \in I\}$, the proof is complete. □

Corollary 2. *Let $|I| = n \in \mathbb{Z}^+$. In the isomorphism sense, there are altogether $[n/2] + 1$ different homo-ordered effect algebras with M_I as the induced partial ordered set.*

Remark 6

(1) In Theorem 8, when $a \neq a'$, $\mathscr{E}_a \simeq \mathscr{E}(2) \otimes \mathscr{E}(2)$. Therefore, the effect algebra $\mathscr{E}$ with $P(\mathscr{E}) = M_I$ is

obtained by some 2-element effect algebras and 3-element effect algebras through $\otimes$ and $\sqcup$ operations.

(2) We find out the structure of the EA of height 2 of its partial ordered set.

The structure of the EA of height 3 of its partial ordered set. Here are some examples.

(1) $+,'$ of $\mathscr{C}_1 = \mathscr{E}(2) \otimes \mathscr{E}(2) \otimes \mathscr{E}(2)$:

$+$	0	s_1	r_1	k_1	s_2	r_2	k_2	1	
0	0	s_1	r_1	k_1	s_2	r_2	k_2	1	$0' = 1,$
s_1	s_1	$-$	s_2	r_2	$-$	$-$	1	$-$	$s_1' = k_2,$
r_1	r_1	s_2	$-$	k_2	$-$	1	$-$	$-$	$r_1' = r_2,$
k_1	k_1	r_2	k_2	$-$	1	$-$	$-$	$-$	$k_1' = s_2,$
s_2	s_2	$-$	$-$	1	$-$	$-$	$-$	$-$	$s_2' = k_1,$
r_2	r_2	$-$	1	$-$	$-$	$-$	$-$	$-$	$r_2' = r_1,$
k_2	k_2	1	$-$	$-$	$-$	$-$	$-$	$-$	$k_2' = s_1,$
1	1	$-$	$-$	$-$	$-$	$-$	$-$	$-$	$1' = 0,$

(2) $+,'$ of $\mathscr{C}_2 = (\mathscr{E}(2) \sqcup \mathscr{E}(2)) \otimes \mathscr{E}(2)$:

$+$	0	s_1	r_1	k_1	s_2	r_2	k_2	1	
0	0	s_1	r_1	k_1	s_2	r_2	k_2	1	$0' = 1,$
s_1	s_1	s_2	$-$	r_2	$-$	1	$-$	$-$	$s_1' = r_2,$
r_1	r_1	$-$	s_2	k_2	$-$	$-$	1	$-$	$r_1' = k_2,$
k_1	k_1	r_2	k_2	$-$	1	$-$	$-$	$-$	$k_1' = s_2,$
s_2	s_2	$-$	$-$	1	$-$	$-$	$-$	$-$	$s_2' = k_1,$
r_2	r_2	1	$-$	$-$	$-$	$-$	$-$	$-$	$r_2' = s_1,$
k_2	k_2	$-$	1	$-$	$-$	$-$	$-$	$-$	$k_2' = r_1,$
1	1	$-$	$-$	$-$	$-$	$-$	$-$	$-$	$1' = 0,$

Example 6. $\mathscr{P}_6$, $\mathscr{C}_1 = \mathscr{E}(2) \otimes \mathscr{E}(2) \otimes \mathscr{E}(2)$ and $\mathscr{C}_2 = (\mathscr{E}(2) \sqcup \mathscr{E}(2)) \otimes \mathscr{E}(2)$ are effect algebras whose partial ordered sets have height 3. But the poset $P(\mathscr{P}_6)$ of $\mathscr{P}_6$ is not a lattice, and $\mathscr{C}_1 \overset{po}{\cong} \mathscr{C}_2$, $P(\mathscr{C}_1) = P(\mathscr{C}_2)$ is a cube $C_2 \times C_2 \times C_2$ (see Figure 5(a)*).*

Here is another example of an EA $\mathscr{X}$ whose poset $P(\mathscr{X})$ is not a lattice.

Example 7. It is easy to verify that $\mathscr{P}_8 = (P_8, +,', 0, 1)$ is an EA, where $+,'$ see the follows.

$+$	0	s_1	r_1	k_1	s_2	r_2	k_2	1	
0	0	s_1	r_1	k_1	s_2	r_2	k_2	1	$0' = 1,$
s_1	s_1	$-$	s_2	r_2	$-$	$-$	1	$-$	$s_1' = r_2,$
r_1	r_1	s_2	r_2	k_2	$-$	1	$-$	$-$	$r_1' = k_2,$
k_1	k_1	r_2	k_2	$-$	1	$-$	$-$	$-$	$k_1' = s_2,$
s_2	s_2	$-$	$-$	1	$-$	$-$	$-$	$-$	$s_2' = k_1,$
r_2	r_2	$-$	1	$-$	$-$	$-$	$-$	$-$	$r_2' = s_1,$
k_2	k_2	1	$-$	$-$	$-$	$-$	$-$	$-$	$k_2' = r_1,$
1	1	$-$	$-$	$-$	$-$	$-$	$-$	$-$	$1' = 0,$

$(P_8, \leq)$ is not a lattice (see Figure 5(b)).

Example 8. The poset in Figure 6*is not an induced poset of any lattice effect algebra $(n \geq 4)$. At the same time, we notice that at $n \neq 2$, Z_n is all lattice, and we call Z_n crown lattice.*

Figure 7 below shows the crown lattice Z_1, Z_2, Z_3, and Z_4 with $n = 1, 2, 3$, and 4.

4. Chain Effect Algebra (CEA)

In the previous section we obtained the complete structure of a class of effect algebras.They are constructed from 2-element and 3-element effect algebra by $\otimes$ and $\sqcup$ operations. Since both 2-element and 3-element effect algebras are chain effect algebras, we will discuss chain effect algebras in this section.

Lemma 5. *Let $\mathscr{X} = (X, +,', 0, 1)$ be an EA and $u, v, p, q \in X$. Then*

(1) if $u + p = u + q$ then $p = q$;

(2) if $u + p = p$ then $u = 0$;

(3) $u \prec v$ iff there exists a atom $p \in X$ such that $u + p = v$;

(4) if $u \prec v$ then $v' \prec u'$.

Proof

(1) Let $w = u + p = u + q$, then $p' = u + w', q' = u + w'$ by Lemma 1 (4). Thus $p' = q'$, that is $p = q$.

(2) Since $u + p = p = 0 + p$, Hence $p = 0$ by (1).

(3) If $u \prec v$, then $\exists d \in X$, $u + d = v$. Let $y \in X, 0 \leq y < d$, since $u + d = v$, we have $u + y$ is defined and $u \leq u + y < u + d = b$ by (1), then $u = u + y$ and $y = 0$ by (2).

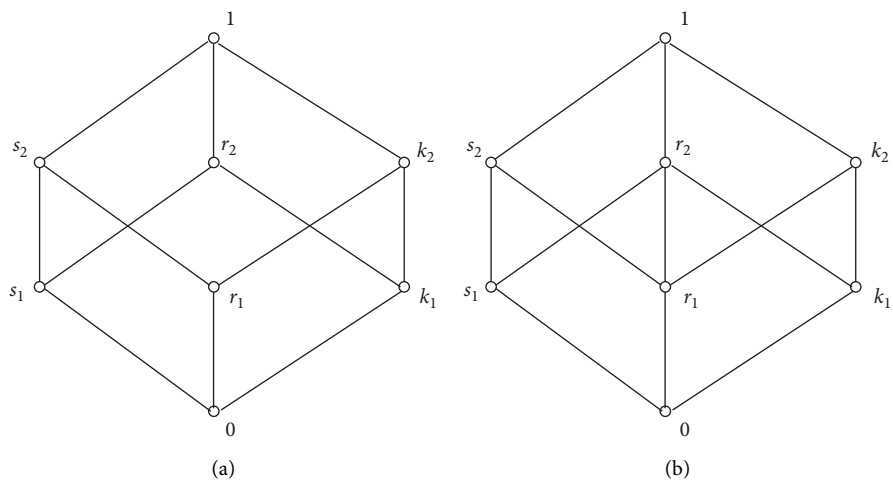

Figure 5: Lattice $C_2 \times C_2 \times C_2$ and poset P_8. (a) $C_2 \times C_2 \times C_2$ (b) P_8.

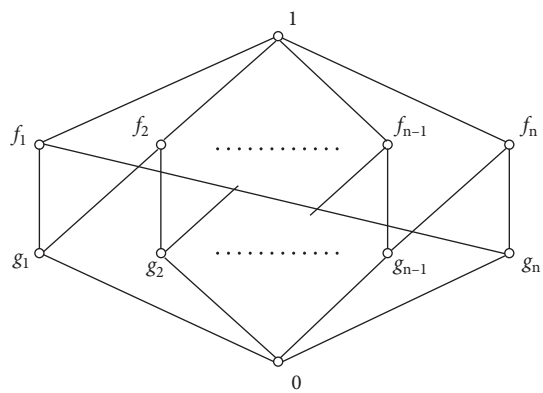

Figure 6: The crown lattice Z_n.

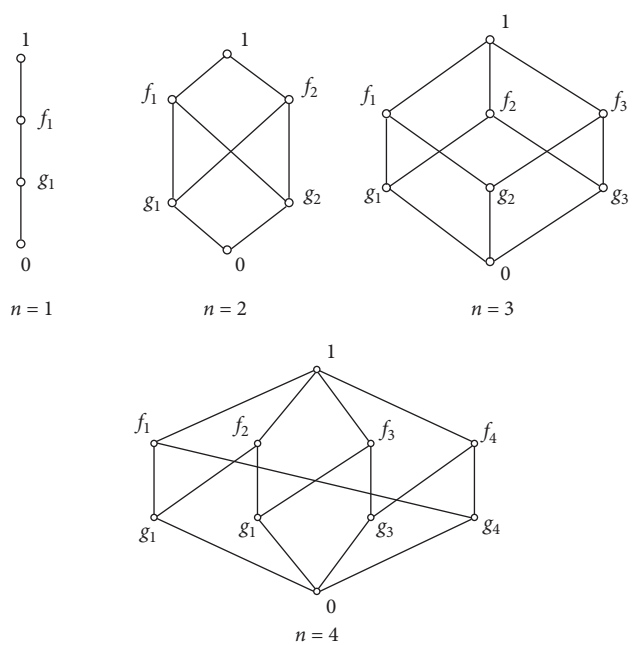

Figure 7: The crown lattices Z_1, Z_2, Z_3, Z_4.

Hence d is atom of $(X, \leq)$. Conversely, let d be an atom of X, and $u + d = v$, then $u \leq v$. If there $\exists e \in X$ $u \leq e < v$. that is $e = u + y < v = u + d$ for some $y \in X$. Then $0 \leq y < d$, Since d is an atom, we have $y = 0$, i.e. $u = e$. Hence $u \prec v$.

(4) Since $u \prec v$, then $\exists w \in X$, $u + w = v$ and w is atom of X by (3). We have $u' + w = v'$ by Lemma 1 (4), Then $v' \prec u'$, the proof is complete. □

Theorem 9. *If $(L, \leq)$ is an n-element chain $\{0 = l_1 < l_2 < \cdots < l_{n-1} < l_n = 1\}$, there is and only one effect algebra constructed by poset $(P, \leq)$, and its+and′operations are as follows:*

Proof. Obviously, the + and ′ operations given in the theorem satisfy the condition (E1) – (E4), that is, $\mathscr{L} = (L, +, ', 0, 1)$ is an EA. The order relation induced on $\mathscr{L}$ is $\leq$.

The following shows that the effect algebra constructed by $(L, \leq)$ is unique.

Let $(L, \oplus, ^\dagger, 0, 1)$ be an EA and the induced poset is the $(L, \leq)$. Since $l_1 = 0$, we have

$$l_1 \oplus l_r = l_r, r = 1, 2, \ldots, n. \tag{26}$$

Since $l_r \prec l_{r+1}$, then $\exists x \in L$, $l_r \oplus x = l_{r+1}$ $(r = 1, 2, \cdot n - 1)$, then $x = l_2$ by Lemma 5 (1). Hence

$$l_2 \oplus l_r = l_{r+1} \ (r = 1, 2, \ldots, n-1), \text{ and } l_2 \oplus l_n \text{ is not defined.} \tag{27}$$

Therefore, $l_{r+2} = l_2 \oplus l_{r+1} = l_2 \oplus (l_2 \oplus l_r) = (l_2 \oplus l_2) \oplus l_r = l_3 \oplus l_r$, that is

$$l_3 \oplus l_r = \begin{cases} l_{r+2} & (r = 1, \ldots, n-2), \\ - & (r = n-1, n). \end{cases} \tag{28}$$

Similarly, we can show that

$$\begin{aligned} l_4 \oplus l_r &= \begin{cases} l_{r+3} & (r = 1, \ldots, n-3), \\ - & (r = n-2, n-1, n), \end{cases} \\ &\cdots\cdots\cdots\cdots\cdots\cdots, \\ l_i \oplus l_r &= \begin{cases} l_{r+(i-1)} & (r = 1, \ldots, n+1-i), \\ - & (r = n+2-i, \ldots, n-1, n), \end{cases} \\ & i = 1, 2, 3, \ldots, n-1. \end{aligned} \tag{29}$$

Considering the above mentioned, we can get: $\oplus = +$. And, according to the above equation, $l_k \oplus l_{n-k+1} = 1$, hence $l_k^\dagger = l_{n-k+1}$, $(k = 1, 2, \ldots, n)$, i.e. $\dagger = '$.

Thus, the effect algebra constructed by poset $(L, \leq)$ is unique, the proof is complete. □

Definition 9 (see[9]). *Let $(P, \leq)$ be a partial ordered set.*

(1) *$(P, \leq)$ has the **ascending chain condition** (**ACC**) if it has no infinite strictly ascending sequences, that is, for any ascending sequence*

$$a_1 \leq a_2 \leq a_3 \leq \cdots. \tag{30}$$

$\exists m \in N$, $a_{m+r} = a_m$ for all $r \geq 0$.

(2) *$(P, \leq)$ has the **descending chain condition** (**DCC**) if it has no infinite strictly descending sequences, that is, for any descending sequence*

$$a_1 \geq a_2 \geq a_3 \geq \cdots. \tag{31}$$

$\exists m \in N$, $a_{m+r} = a_m$ for all $r \geq 0$.

(3) An effect algebra $\mathscr{X} = (X, +, ', 0, 1)$ has the ***ACC*** (***DCC***) *if* $(X, \leq)$ has the ***ACC (DCC)***.

where $\leq$ is induced order of X.

Definition 10 (see[9]). *A poset $(P, \leq)$ is said to have a **maximal condition** if each non-empty subset of $(P, \leq)$ contains a maximal element. Dually, the poset $(P, \leq)$ can be defined to have **minimal conditions**.*

Lemma 6 (see[9]). *Let $(X, \leq)$ be a poset, then*

(1) The sufficient and necessary condition for $(X, \leq)$ to satisfy ACC is that $(X, \leq)$ has the maximum condition.

(2) The sufficient and necessary condition for $(X, \leq)$ to satisfy DCC is that $(X, \leq)$ has the minimal condition.

Theorem 10. *Let $\mathscr{X} = (X, +, 0, 1)$ be an EA, then $\mathscr{X}$ has the ACC iff it has the DCC.*

Proof. If $\mathscr{X}$ has the ACC and let $\{p_1, p_2, p_3, \cdots\} \subseteq X$ be descending sequence, i.e.

$$p_1 \geq p_2 \geq p_3 \geq \cdots. \tag{32}$$

Then $p_1' \leq p_2' \leq p_3' \leq \cdots$, therefor, $\exists m \in N$, $a_{m+k}' = a_m'$ for all $k \geq 0$ by ACC. Thus $a_{n+k} = a_n$ for all $k \geq 0$, and $\mathscr{X} = (X, +, ', 0, 1)$ has the DCC, i.e. ACC ⇒ DCC and vice versa. The proof is complete.

Using the above two theorems, we get the following result. □

Theorem 11. *A chain effect algebra $\mathscr{C} = (C, +, ', 0, 1)$ must is one of the following:*

(1) Cis a finite set $\{0 = p_1, p_2, \ldots, p_{n-1}, p_n = 1\}$ and

$$0 = p_1 < p_2 < \cdots < p_{n-1} < p_n = 1. \tag{33}$$

(2) Chave an infinite strictly ascending chain

$$1 > q_1 > q_2 > q_3 > \cdots, \tag{34}$$

and an infinite strictly descending chain

$$0 < q_1' < q_2' < q_3' < \cdots. \tag{35}$$

Proof. If C is a finite set. Obviously, (1) is true.

Now let's assume that C is an infinite set, and let's prove that C can only be (2). In face, C fails to have the DCC and ACC (if not, C has the ACC, then C has the DCC by Theorem 10, hence C is a finite set. This is a contradiction.). Hence $(C, \leq)$ have an infinite strictly ascending chain

$$1 > q_1 > q_2 > q_3 > \cdots. \tag{36}$$

Obviously,

$$0 < q_1' < q_2' < q_3' < \cdots. \tag{37}$$

is an infinite strictly descending chain in $(C, \leq)$. The proof is complete.

Here is the simplest example of an infinite chain effect algebra. □

Example 9. Let $C_0 = \{0 = a_0, a_1, \ldots, a_n, \ldots, b_n, b_{n-1}, \ldots, b_1, b_0 = 1\}$ *, and define +and ′ as follows*:

$$\begin{aligned} a_s + a_t &= a_{s+t}, b_s + b_t = -, a_s + b_t \\ &= \begin{cases} b_{t-s} & (s \leq t), \\ - & (s > t), \end{cases} \left(\forall s, t = 0, 1, 2, \cdots\right), \\ a_s' &= b_s, b_s' = a_s \left(\forall s = 0, 1, 2, \cdots\right). \end{aligned} \tag{38}$$

Then $\mathscr{C}_0 = (C_0, +, ', 0, 1)$ is an infinite CEA. And

$$0 = a_0 < a_1 < \cdots < a_n < \cdots < b_n < b_{n-1} < \cdots < b_1 < b_0 = 1. \tag{39}$$

Theorem 12. *Let* $\mathscr{X} = (X, +, 0, 1)$ *be an EA,* $\leq$ *its induced order,* $t, u, w \in X$ *. If* $t < u$ *and* $u + w$ *is defined then* $([t, u], \leq) \simeq ([t + w, u + w], \leq)$.

Proof. Since $u + w$ is defined, $t < u$, we have $z + w$ is defined and $z + w \in [t + w, u + w]$ $(\forall w \in [t, u])$ by Lemma 1 (2) and (5).

Let $f\colon ([t, u], \leq) \longrightarrow ([t + w, u + w], \leq), z \mapsto z + w$, $(\forall z \in [t, u])$.

For every $l, k \in [t, u]$

$$l \leq k \Leftrightarrow l + w \leq k + w \Leftrightarrow f(l) \leq f(k). \tag{40}$$

Thus, $([t, u], \leq) \simeq ([t + w, u + w], \leq)$. □

Corollary 3. *Let* $\mathscr{L} = (L, +, 0, 1)$ *be a CEA,* $p \in C$. *If* $np = \overset{n}{\frown} p + p + \cdots + p$ *is defined then we have:*

$$\begin{aligned} ([0, p], \leq) &\simeq ([p, 2p], \leq) \simeq ([2p, 3p], \leq) \\ &\simeq \cdots \simeq ([(n-1)p, np], \leq). \end{aligned} \tag{41}$$

Theorem 13. *Let* $\mathscr{X} = (X, +, 0, 1)$ *be an EA with* $(X, \leq)$ *has no atoms. If* $l < k, l, k \in X$ *then* $\exists w \in X$ *such that* $l < w < k$.

Proof. Consider $l, k \in X, l < k$. So $\exists s \in X, s \neq 0$ such that $l + s = k$ by Definition 1 (E1). Since $(X, \leq)$ has no atoms, we have: $\exists y \in X$ such that $0 < y < s$, therefore $l < l + y < l + s = k$, the result holds. □

Corollary 4. *Let* $\mathscr{M} = (M, +, 0, 1)$ *be a finite EA. If* $(M, \leq)$ *has a atom* $p \in M$, *such that* $\forall t \in M/\{0\}$, $p \leq t$, *then* $(M, \leq)$ *is a chain.*

Proof. For the sequence $d, 2d, 3d, \cdots$ in $(M, \leq)$, since M is finite, we have: $\exists k \in N$, $kd \in M$ but $(k + 1)d$ is undefined.

Since $k\ d \leq 1$, we have $k\ d + m = 1$ for some $m \in M$. If $m \neq 0$, then $d \leq b$ and $(k + 1)d = kd + d$ is defined by Lemma 1 (2). This is a contradiction, hence $m = 0$. Thus $kd = 1$. Now let's drove that M is equal to $\{0, d, 2d, \ldots, (k-1)d, 1\}$.

Assume that $c \in M$ and $c \notin \{0, d, 2d, \ldots, (k-1)d, 1\}$. Since $d < c$ and $0 \prec d \prec 2d \prec \cdots \prec (k-1)d \prec 1$, then $\exists t\,(1 \leq t < k)$, $td < c$, but $(t + 1)d < c$. Hence

$$c = t\ d + y\,(\exists\, y \in M). \tag{42}$$

Obvious, $y \neq 0$, and $y \geq d$, thus $c = td + y \geq td + d$. This is a contradiction. Hence

$$M = \{0, d, 2\ d, \ldots, (k-1)d, 1\},\ |M| = k + 1, \tag{43}$$

and $(M, \leq)$ is a chain.

The following example shows that Corollary 4 fails when L is an infinite EA. □

Example 10. Let $K = \{0, 1, kp, (kp)' | k = 1, 2, \cdots\} \cup \{a_t | t = 0, \pm\ 1, \cdots\} \cup \{b_t | t = 0, \pm 1, \cdots\}$, *and*

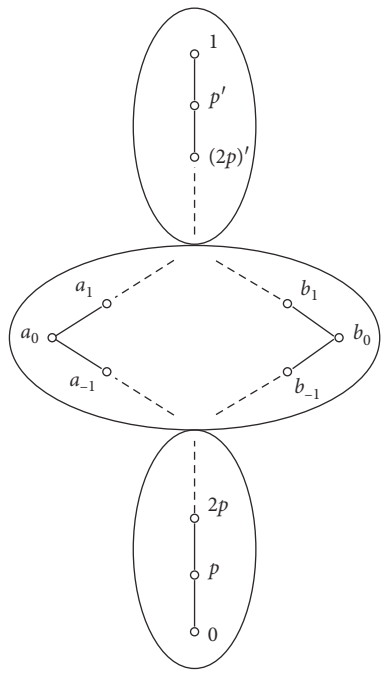

Figure 8: Poset $(K, \leq)$.

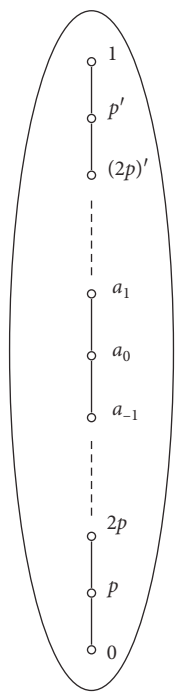

Figure 9: Chain $(K, \leq)$.

$$sp + tp = (s+t)p, sp + (tp)' = \begin{cases} ((t-s)p)' & s < t, \\ 1 & s = t, (s, t \in Z^+), \\ - & s > t, \end{cases}$$
$$np + a_i = a_{n+i}, a_i + a_j = \begin{cases} 1 & i + j = 0, \\ ((-i-j)p)' & i + j < 0, (i, j \in Z), \\ - & i + j > 0, \end{cases} \tag{44}$$
$$np + b_i = b_{n+i}, b_i + b_j = \begin{cases} 1 & i + j = 0, \\ ((-i-j)p)' & i + j < 0, \\ - & i + j > 0, \end{cases} (i, j \in Z).$$

then $\mathscr{K} = (K, +, 0, 1)$ is an EA, but $(K, \leq)$ is not chain (See Figure 8). In face, $(K, \leq)$ is not even a lattice ($\{a_0, b_0\}$ has no least upper bound in $(k, \leq)$).

Example 11. Let

$$K_0 = \{0, p, 2p, \ldots, np, \ldots, (np)', \ldots, (2p)', p', 1\} \cup \{a_0, a_1, a_{-1}, \cdots\}, \tag{45}$$

$$\begin{aligned} sp + tp &= (s+t)p, sp + (tp)' \\ &= \begin{cases} ((t-s)p)' & s < t, \\ 1 & s = t, (s, t \in Z^+), \\ - & s > t, \end{cases} \\ np + a_i &= a_{n+i}, a_i + a_j \\ &= \begin{cases} 1 & i + j = 0, \\ ((-i-j)p)' & i + j < 0, (i, j \in Z). \\ - & i + j > 0, \end{cases} \end{aligned} \tag{46}$$

then $\mathscr{K}_0 = (K_0, +, 0, 1)$ is an EA, and $(K_0, \leq)$ is a chain (See Figure 9).

We naturally ask the question: in Corollary 4, if $\mathscr{L} = (L, +, 0, 1)$ is a LEA must $(L, \leq)$ be a chain?

The following theorem answers this question.

Theorem 14. *Let $\mathscr{L} = (L, +, 0, 1)$ be a LEA. If $(L, \leq)$ has a atom $p \in L$, such that $\forall l \in L/\{0\}$, $p \leq l$, then $(L, \leq)$ is a chain.*

Proof. If $\exists m \in N$ such that $mp \in L$ but $(m+1)p$ is undefined. Then by Corollary 4, we know that the theorem is true. The theorem will be proved in the case where np is defined $(\forall n \in N)$.

Obvious, for all $k \in N$, $0 < kp < 1$. According to the proof of Corollary 4, similarly, we can get

$$\{x \in L | x \leq np\} = \{0, p, 2p, \ldots, (n-1)p, np\}, \quad 0 < p < 2p < \cdots < np, \tag{47}$$

and its dual

$$\{x \in L | x \geq (np')\} = \{1, p', (2p)', \ldots, (np)'\}, \quad (np)' < \cdots < (2p)' < p' < 1. \tag{48}$$

Since $p < p'$, we have $np < (np)'$ $(n \in N)$.

Next, we will prove that L is a chain. Since

$$\{0, p, 2p, \ldots, np, \ldots, (np)', \ldots, (2p)', p', 1\} \subseteq C. \tag{49}$$

Assume that $u, v \in L$ are incomparable. Then

$$w, v \notin \{0, p, 2p, \ldots, np, \ldots, (np)', \ldots, (2p)', p', 1\}, \tag{50}$$

and, $\forall s, t \in N$, $sp < w, v < (tp)'$. Since $(L, \leq)$ is a lattice, we have $w \wedge v \in L$, let $d = w \wedge v$. Since $d < w, v$, we have $\exists x, y \in L, x, y \geq p$ such that $d + x = w, d + y = v$. Then

$$d = w \wedge v = (d + x) \wedge (d + y) = d + (x \wedge y), \tag{51}$$

hence $x \wedge y = 0$, This is a contradiction, thus $(L, \leq)$ is a chain. □

Definition 11. Let Lbe a lattice, $j, m \in L$,

(1) *j is join-irreducible if $j = u \vee v \Rightarrow j = u$ or $j = v$, $(u, v \in L)$.*

(2) *m is meet-irreducible if $m = s \wedge t \Rightarrow m = s$ or $m = t$, $(s, t \in L)$.*

$J(L) = \{j \in L | j$ is join-irreducible$\}$ and $M(L) = \{m \in L | m$ is meet-irreducible$\}$.

Theorem 15. *Let $\mathscr{C} = (C, +, 0, 1)$ be a LEA. Then the following conditions are equivalent:*

(1) $(C, \leq)$is a chain.

(2) 1is join-irreducible element of$(C, \leq)$.

(3) 0is meet-irreducible element of$(C, \leq)$.

Proof

(1) ⇒ (2): Let $s \vee t = 1, s, t \in C$. Since $(C, \leq)$ is a chain, we have: x and y are comparable. Hence $s \vee t = s$ or $s \vee t = t$, that is. $1 = s$ or $1 = t$. Thus, 1 is join-irreducible.

(2) ⇒ (3): By Lemma 2.

(3) $\Rightarrow$ (1): Let $\mathscr{C} = (C, +, 0, 1)$ be a LEA. Suppose that $(C, \leq)$ is not a chain. then $\exists p, q \in C$ have $p \| q$ holds.

Since $(C, \leq)$ is a lattice, $p \wedge q \in C$, let $d = p \wedge q$. Since $p \| q$, we have: $d < p, q$, then $\exists x, y \in C, x, y > 0$ such that $d + x = p, d + y = q$. Hence

$$d = p \wedge q = (d + x) \wedge (d + y) = d + (x \wedge y), \tag{52}$$

that is. $x \wedge y = 0$, That contradicts the fact that 0 is meet-irreducible element. Thus $(C, \leq)$ is a chain. □

Corollary 5. *Let $\mathscr{L} = (L, +, 0, 1)$ be a LEA. If 0 is meet-irreducible element of $(L, \leq)$, then $L = J(L) = M(L)$.*

5. Conclusion

The main content of this paper is to study the properties and structures of LEAs from the perspective of partial ordered sets. We study the characterization of original effect algebras by partial ordered sets induced by EAs. The structure and number of effect algebras generated by M_I bounded partially ordered sets of height 2 are solved.

We study the chain effect algebra and give some necessary and sufficient conditions for determining the LEA as a CEA. It is proved that a finite EA is a CEA if and only if it has only one atom, and some counterexamples are given.

Data Availability

All data from this study are included in the article.

Conflicts of Interest

The authors declare that they have no conflicts of interest.

Acknowledgments

The research was supported by the National Natural Science Foundation of China (Grant nos. 19801016, 10261003).

References

[1] D. J. Foulis and M. K. Bennett, "Effect algebras and unsharp quantum logics," *Foundations of Physics*, vol. 24, no. 10, pp. 1331–1352, 1994.

[2] T. Vetterlein, "Pseudo-BCK algebras as partial algebras," *Information Science*, vol. 180, no. 24, pp. 5101–5114, 2010.

[3] S. Gudder, "Examples, Problems, and results in effect algebras," *International Journal of Theoretical Physics*, vol. 35, no. 11, pp. 2365–2376, 1996.

[4] Z. Riecanova, "Subalgebras,Intervals,and central elements of generalized effect algebras," *International Journal of Theoretical Physics*, vol. 38, no. 12, pp. 3209–3220, 1999.

[5] S. Gudder and R. Greechie, "Sequential products on effect algebras," *Reports on Mathematical Physics*, vol. 49, pp. 87–111, 2002.

[6] Y. Wu, J. Wang, and Y. Yang, "Lattice-ordered effect algebras and L-algebras," *Fuzzy Sets and Systems*, vol. 369, no. 15, pp. 103–113, 2019.

[7] I. Chajda and H. Lnger, *Unsharp Residuation in Effect Algebras*, 2019.

[8] G. Birkhoff, *Lattice Theory*, AMS Colloquium Publications, vol. 25, 3rd edition, 1967.

[9] P. Crawley and R. Dilworth, *Algebraic Theory of Lattices*, Prentice-Hall, 1973.

Hindawi
Discrete Dynamics in Nature and Society
Volume 2022, Article ID 4677680, 10 pages
https://doi.org/10.1155/2022/4677680

Research Article

Bipartite Containment Control for Multiagent Systems with Adaptive Quantization Information

Jie Wu,[1] **Heng Lei**,[2] **and Xisheng Zhan**[2]

[1]*College of Arts and Sciences of Hubei Normal University, Huangshi 435002, China*
[2]*Hubei Normal University, Huangshi 435002, China*

Correspondence should be addressed to Jie Wu; jiewu@hbnu.edu.cn

Received 10 July 2022; Accepted 12 August 2022; Published 19 September 2022

Academic Editor: Guoguang Wen

In this study, bipartite containment control for multiagent systems (MASs) with quantitative information is investigated. Communication topology is structurally balanced, and the follower's trajectory is within the area surrounded by the leader by designing distributed error terms. The leader is an external system, and the matrix information of the leader cannot be accessed by followers. Based on an adaptive quantization information distributed observer, the authors introduce an output feedback protocol to study bipartite containment control. Finally, simulations demonstrate the effectiveness of proposed control algorithms.

1. Introduction

In recent years, collaborative control has attracted a lot of attention. It is widely used in vehicle formation [1–3], complex dynamic networks [4, 5], and sensor networks [6–8]. With the development of MASs, many interesting results have been obtained, which makes many control problems become hot issues, including consensus of multiagent problem [9], the output regulation problem [10, 11], contains the problem [12, 13], and an adaptive parameter problem [14]. In the field of control, the MASs are a topical research object. It is composed of a group of single multiagent, and the information transmission between them constitutes the communication topology. The consensus of MASs can be divided into two types by whether there is a leader or not, that is, the MASs without leaders who cannot accept the information of other agents and the leader tracking systems with leaders. In [15], the leaderless continuous and discrete time consistency problem of the first-order MASs is studied by the frequency domain method. Based on the leaderless fixed communication topology [16], the finite-time consensus for MASs with external disturbance is studied. In addition, it is also important to consider the existence of leaders in multiagent research. Tang et al. [17] studied the tracking consistency problem, Hong et al. designed a distributed observer for leading tracking MASs [18], and Ni and Cheng solved leader-following consensus of the MASs through switching topology [19]. This study considers multiple leaders, and the leaders are considered to be the exogenous systems, and the leaders' information cannot be received by the followers.

Inspired by the biological behavior of nature, containment control is adopted for systems with multiple leaders in most cases, and the containment control problem is widely used in practice. In containment control, there is more than one leader. The area surrounded by the leader is called the convex shell, and followers will only move within the boundaries defined by the leader. For example, several robots carry equipment through a dangerous stretch of road. Robots without equipment act as leaders. Other robots transmit a safe travel route range to them through sensors or artificial information, while robots with equipment act as followers to enter the movement area surrounded by the leaders so as to avoid dangerous areas in the path. In [20], authors studied the necessary and sufficient conditions to achieve containment control. This paper studies bipartite output containment; that is, some follower curves converge to the region surrounded by the leader and others converge to the region of symmetry. In [21], the authors solved containment control with an

output feedback method. In real life, the state is probabilistically unmeasurable, and external disturbance also affects the stability of the system. In [22, 23], by using the output feedback method, containment control of the MASs with exogenous disturbance is solved. This study also considers the influence of quantitative information on information transmission between agents to meet the practical challenges.

In the existing distributed controller, the information exchange between agent and neighbor is very accurate, but the accurate information exchange is a simplification, which is unreasonable. In practical applications, agents exchange information through digital communication channels. Due to the limitation of their own information storage capacity and communication width, the quantization effect must be considered [24–26], which is also meaningful and interesting for the study of consensus problems. Therefore, many articles on the consensus issue take into account the quantitative impact. In [27], the problem of quantization information consistency with Markov chains for the first-order MASs is solved. Control input problem: in [28], the author uses the distributed variable adjacency matrix method to deal with the quantized second-order consensus problem. In addition, the problem of the digital digraph of MASs is solved by designing an observer, and the consensus of the system in [29] is realized by using the probabilistic quantization method.

Each follower can get the leader's information, which is not realistic in practical application. Therefore, researchers introduced an adaptive algorithm. In [30], the asymptotic output regulation problem was studied by using the Luenberger observer and introducing an adaptive regulation method. In [31], an adaptive controller was proposed to cope with finite-time bipartite consensus for output feedback in the unknown state information. In [21], containment control for the linear MASs was solved. In addition, multiagent networks with competition and cooperation among agents are more common. Such problems can be called bipartite control problems [32, 33]. In topology graphs, the collar matrix has positive and negative weights. A special example of bipartite control is the control that is only cooperative between agents. The bipartite consensus of the MASs is restudied in [34] by means of output feedback and state feedback. In [35], the leader matrix information is obtained by using an adaptive observer, the solution of the mediation equation is obtained by designing an algorithm, and the consensus of the MASs is solved by output feedback. The bipartite containment problem of the MASs is studied in [36]. To solve some problems in actual life, an adaptive quantization information distributed observer is designed to estimate the leader's state, and then, a feedback controller is used to reach output bipartite containment.

The remaining four sections are as follows. Section 2 is the formulation and preliminary work of the problem. Section 3 is the main theoretical results. Numerical simulation results are shown in Section 4 to verify the effectiveness of theoretical results. In the end, Section 5 gives the conclusion.

2. Preliminaries and Model Statement

2.1. Algebraic Graph Theory. To achieve the bipartite output containment, communication topology is described in a topology diagram [37]. Let $G(V, E, A)$ be weighted directed graph and consist of node set $V = \{V_1, V_2, \ldots, V_N\}$ which denotes finite nonempty set of N nodes and edge set $E \subseteq V \times V$ describing transfer of information between nodes. We define $A = (a_{ij}) \in R^{N\times N}$ as weighted adjacency matrix. Let $d_i = \sum_{j=1}^{N} a_{ij}$ be in-degree of vertex i and $D = \mathrm{diag}\{d_1, d_2, \ldots, d_N\}$ be in-degree matrix of G. Laplace matrix $L = [l_{ij}]$ of weighted directed graph G is defined as $L = D - A$. The point set is divided into two subgroups, v_1 and v_2, and $v_1 \cup v_2 = V$ and $v_1 \cap v_2 = \varnothing$, which is different from the general graph theory. Define $N_i = \{V_j | (V_j, V_i) \in E, i \neq j.\}$ to represent neighbor points of V_i. If there is an edge $(V_i, V_j) \in E$ and V_i and V_j are in the same subgroup, it represents cooperative relationship; then, there is $a_{ij} > 0$; if V_i and V_j are in different subgroups, it represents antagonistic relationship; then, there is $a_{ij} < 0$, otherwise, $a_{ij} = 0$. Define τ_i as a symbolic parameter, where $\tau_i = 1$ is used if $V_i \in v_1$ and $\tau_i = -1$ is used if $V_i \in v_2$.

2.2. Quantizer. Quantizer has been added to many literature studies on multiagent research. In this study, we use the quantizer q: $R \longrightarrow R$ as

$$q(x) = \begin{cases} \mu_i, & if \dfrac{1}{1+\gamma}\mu_i < x \leq \dfrac{1}{1-\gamma}\mu_i, x > 0, \\ 0, & if\ x = 0, \\ -q(-x), & if\ x < 0, \end{cases} \tag{1}$$

where μ_i is the quantization level and $\gamma \in (0, 1)$ is the quantization accuracy parameter. For the quantization level, one has a set $\overline{\mu} = \{\pm\mu_i\colon \mu_i = (1-\gamma/\ 1+\gamma)^i\mu_0, i = 0, \pm 1, \pm 2, \ldots, \pm n\} \cup \{0\}$, where $\mu_0 > 0$ is the initial quantization level. $|q(m) - m| \leq \gamma|m|, \quad \forall m \in R$can be obtained through the definition of quantizer. It is worth noting that, for any set of vectors$y = [y_1, y_2, \ldots, y_N]^T \in R^n$, we can write$q(y) = [q(y_1), q(y_2), \ldots, q(y_N)]^T \in R^n$. So, obviously there is $q(y) - y = \Gamma y$, where $\Gamma = \mathrm{diag}\{\Gamma_1, \Gamma_2, \ldots, \Gamma_N\}$ and $\Gamma_i \in [-\gamma, +\gamma]$.

2.3. Problem Formulation. In this study, we study the bipartite containment control for a group of MASs composed of Z leaders and N followers. In addition, $Z = \{N+1, N+2, \ldots, N+Z\}$ and $N = \{1, 2, \ldots, N\}$ are defined as leaders' set and followers' set, respectively. The kinetic equation for N followers is as follows:

$$\begin{cases} \dot{x}_i = A_i x_i + B_i u_i + \displaystyle\sum_{k=N+1}^{N+Z} Q_{ik} V_k, \\ y_i = C_i x_i, i = 1, 2, \ldots, N, \end{cases} \tag{2}$$

where $x_i \in R^l, u_i \in R^l$, and $y_i \in R^l$ are state quantity of i th agent, control input quantity of the system, and the control output quantity of the system, respectively. A_i, B_i, C_i, and Q_{ik} are parameter matrix with suitable dimensions. Then, the kinetic equation of leaders is in the following form:

$$\begin{cases} \dot{V}_k = A_0 V_k, \\ y_k = F V_k, k \in Z, \end{cases} \tag{3}$$

where $V_k \in R^l$ represents the state of the exogenous system, that is, disturbance quantity or reference input of the system.

Definition 1. In this study, a reasonable controller is designed to solve the problem of bipartite containment control, which makes the followers converge to the positive and negative region defined by the leader, namely, the convex hull. So, for follower systems and leader systems (1) and (2), the following features can be used to solve their bipartite containment problem.

(1) Define the convex hull $co(X)$ belonging to set $X = \{x_1, x_2, \ldots, x_N\}$ of the form

$$co(X) = \left\{ \sum_{i=1}^{N} \beta_i x_i x_i \in R, \beta_i \geq 0, \sum_{i=1}^{N} \beta_i = 1 \right\}. \tag{4}$$

(2) For followers and leaders with any initial value, the follower can only enter the positive and negative convex hull defined by the leader:

$$\begin{aligned} &\lim_{t \longrightarrow \infty} \operatorname{dist}(x_i, co(V_k, k \in Z)) = 0, i \in N_1, \\ &\lim_{t \longrightarrow \infty} \operatorname{dist}(x_j, -co(V_k, k \in Z)) = 0, j \in N_2, \end{aligned} \tag{5}$$

in which $N_1 \cup N_2 = N$ and $N_1 \cap N_2 = \varnothing$.

When $e_i = 0$ is used, (2) can be displayed by the following containment error:

$$\begin{aligned} e_i = &\sum_{j \in N_i} |a_{ij}| (y_i - \operatorname{sgn}(a_{ij}) y_j) \\ &+ \sum_{k=N+1}^{N+Z} |a_{ik}| (y_i - \tau_i y_k), i \in N. \end{aligned} \tag{6}$$

Let $e = \operatorname{col}(e_1, e_2, \ldots, e_N)$ and $x = \operatorname{col}(x_1, x_2, \ldots, x_N)$; then,

$$e = (H \otimes I_N) Cx - \sum_{k=N+1}^{N+Z} (A_{0k} \otimes F) \widetilde{V}_k, \tag{7}$$

where $\widetilde{V}_k = G 1_N \otimes V_k N$ with $G = \operatorname{diag}\{\tau_1, \tau_2, \ldots, \tau_N\}$ and 1_N is an N-dimensional column vector, $H = \sum_{k=N+1}^{N+Z} (1/Z) L + A_{0k}$, and $A_{0k} = \operatorname{diag}\{|a_{1k}|, |a_{2k}|, \ldots, |a_{Nk}|\}$. Then, if $\lim_{t \longrightarrow \infty} e_i = 0$, we can get the following formula:

$$\lim_{t \longrightarrow \infty} C_i x_i = \lim_{t \longrightarrow \infty} \sum_{k=N+1}^{N+Z} \zeta_{ik} F \tau_i V_k, i \in N, \tag{8}$$

where $\zeta_{ik} \in R^l$ is ith row vector of $H^{-1} A_{0k} 1_N$.

Assumption 1. Graph G is a signed graph with a balanced structure and a spanning tree.

Assumption 2. Eigenvalues of A_0 are in the right half plane.

Assumption 3. (C_i, A_i) is observable and (A_i, B_i) is stabilizable.

3. Main Results

In this section, an adaptive quantitative information observer is designed to observe the information of the leader matrix A_0 so as to solve the problem that followers are unknowable of the information of the leader matrix. The Sylvester equation is presented, and an algorithm for solving it is presented. The bipartite containment control is realized by designing an observer and by using the output feedback method.

3.1. Bipartite Adaptive Quantization Information Observer. The adaptive quantization information distributed observer of the bipartite containment control is as follows:

$$\dot{A}_{0i} = \chi_1 \left(\sum_{j \in N_i} |a_{ij}| (A_{0i} - \operatorname{sgn}(a_{ij}) A_{0j}) + \sum_{k=N+1}^{N+Z} |a_{ik}| (A_{0i} - \tau_i A_0) \right), \tag{9}$$

$$\begin{aligned} \dot{\eta}_i = &\tau_i A_{0i} \eta_i + c_1 \chi_2 \left(\sum_{j \in N_i} |a_{ij}| q((\eta_i - \operatorname{sgn}(a_{ij}) \eta_j)) \right. \\ &\left. + \sum_{k=N+1}^{N+Z} |a_{ij}| q((\eta_i - \tau_i V_k)) \right), \end{aligned} \tag{10}$$

where $\eta_i \in R^n, i \in N$, and $\chi_1, \chi_2 < 0$. $c_1 > 0$ is the compensator parameter.

Lemma 1. *Consider external systems (2) and adaptive quantized information distributed observer (6) and (7). Let* $\widetilde{A}_{0i} = A_{0i} - \tau_i A_0$ *and* $\widetilde{\eta}_i = \eta_i - \sum_{k=N+1}^{N+Z} \zeta_{ik} \tau_i V_k$. *Then, for* $\chi_1, \chi_2 < 0$ *and* $i \in N$, $\lim_{t \longrightarrow \infty} \widetilde{A}_{0i}(t) = 0$ *and* $\lim_{t \longrightarrow \infty} \widetilde{\eta}_i(t) = 0$.

Proof. According to (6), the derivative of $\widetilde{A}_{0i}(t)$ can be obtained as follows:

$$\begin{aligned}\dot{\widetilde{A}}_{0i} &= \dot{A}_{0i} - \tau_i \dot{A}_0 \\ &= \chi_1\left(\sum_{j\in N_i}\left|a_{ij}\right|\left(A_{0i} - \operatorname{sgn}\left(a_{ij}\right)A_{0j}\right) + \sum_{k=N+1}^{N+Z}\left|a_{ik}\right|\left(A_{0i} - \tau_i A_0\right)\right) \\ &= \chi_1\left(\sum_{j\in N_i}\left|a_{ij}\right|\left(A_{0i} - \tau_i A_0 + \tau_i A_0 - \operatorname{sgn}\left(a_{ij}\right)\left(A_{0j} - \tau_j A_0 + \tau_j A_0\right)\right) + \sum_{k=N+1}^{N+Z}\left|a_{ik}\right|\left(A_{0i} - \tau_i A_0\right)\right) \\ &= \chi_1\left(\sum_{j\in N_i}\left|a_{ij}\right|\left(\widetilde{A}_{0i} - \operatorname{sgn}\left(a_{ij}\right)\widetilde{A}_{0j}\right) + \sum_{j\in N_i}\left|a_{ij}\right|\left(\tau_i A_0 - \operatorname{sgn}\left(a_{ij}\right)\tau_i A_0\right) + \sum_{k=N+1}^{N+Z}\left|a_{ik}\right|\widetilde{A}_{0i}\right).\end{aligned} \tag{11}$$

Notice if i and j are in the same subset $i, j \in N_1$ or $i, j \in N_2$, there are $a_{ij} > 0, \tau_i = \tau_j$. So, it is easy to get $\tau_i = \operatorname{sgn}(a_{ij})\tau_j$. In another case, i and j in different subgroups, we can get $a_{ij} < 0, \tau_i = -\tau_j\ \tau_i = \operatorname{sgn}(a_{ij})\tau_j$. Through the above discussion, $\tau_i A_0 - \operatorname{sgn}(a_{ij})\tau_j A_0 = 0$ can be obtained. Then, (8) can be written as

$$\dot{\widetilde{A}}_{0i} = \chi_1\left(\sum_{j\in N_i}\left|a_{ij}\right|\left(\widetilde{A}_{0i} - \operatorname{sgn}\left(a_{ij}\right)\widetilde{A}_{0j}\right) + \sum_{k=N+1}^{N+Z}\left|a_{ik}\right|\widetilde{A}_{0i}\right). \tag{12}$$

Let $\widetilde{A}_{0I} = \operatorname{block\,diag}(\widetilde{A}_{01}, \widetilde{A}_{02}, \ldots, \widetilde{A}_{0N})$; (9) can be written in concise form:

$$\dot{\widetilde{A}}_{0I} = \chi_1 (H \otimes I_n)\widetilde{A}_{0I}, \tag{13}$$

where $H = \sum_{k=N+1}^{N+Z} 1/ZL + A_{0k}$. By assumption 1 and Lemma 2of[29], eigenvalues of matrix L have only positive real part and $1/ZL + A_{0k}$ is nonsingular. Since A_{0k} has no negative eigenvalues, $H = \sum_{k=N+1}^{N+Z}(1/Z)L + A_{0k}$ also has only nonzero positive eigenvalues. That is to say, $\lambda(H) > 0$. $\chi_1(H \otimes I_n) < 0$ can be obtained by setting the parameter $\chi_1 < 0$, and $\lambda(\chi_1(H \otimes I_n)) < 0$ with all negative eigenvalues can be obtained. And then, we get $\lim_{t\longrightarrow\infty}\widetilde{A}_{0I}(t) = 0$, which means we get $\lim_{t\longrightarrow\infty}\widetilde{A}_{0i}(t) = 0$. Thus, the following formula can be obtained:

$$\begin{aligned}\dot{\widetilde{\eta}}_i &= \dot{\eta}_i - \sum_{k=N+1}^{N+Z}\zeta_{ik}\tau_i\dot{V}_k = \tau_i A_{0i}\eta_i \\ &\quad + c_1\chi_2\left(\sum_{j\in N_i}\left|a_{ij}\right|q\left(\left(\eta_i - \operatorname{sgn}\left(a_{ij}\right)\eta_j\right)\right) + \sum_{k=N+1}^{N+}\left|a_{ij}\right|q\left(\left(\eta_i - \tau_i V_k\right)\right)\right) \\ &\quad - \sum_{k=N+1}^{N+Z}\zeta_{ik}\tau_i A_0 V_k.\end{aligned} \tag{14}$$

Since the signature parameter $\tau_i = 1$ or $\tau_i = -1$, multiply both sides of $\widetilde{A}_{0i} = A_{0i} - \tau_i A_0$ by τ_i to obtain $\tau_i\widetilde{A}_{0i} = \tau_i A_{0i} - A_0$. Then, formula can be written as

$$\begin{aligned}\dot{\widetilde{\eta}}_i &= \left(\tau_i\widetilde{A}_{0i} + A_0\right)\eta_i \\ &\quad + c_1\chi_2\left(\sum_{j\in N_i}\left|a_{ij}\right|q\left(\left(\eta_i - \operatorname{sgn}\left(a_{ij}\right)\eta_j\right)\right) + \sum_{k=N+1}^{N+Z}\left|a_{ij}\right|q\left(\left(\eta_i - \tau_i V_k\right)\right)\right) \\ &\quad - \sum_{k=N+1}^{N+Z}\zeta_{ik}\tau_i A_0 V_k,\end{aligned} \tag{15}$$

and (11); from Section 2.2, quantizer definition can be written in the following concise form as

$$\begin{aligned}\dot{\widetilde{\eta}} &= \left((G \otimes I_n)\widetilde{A}_{0I} + I_N \otimes A_0\right)\eta \\ &\quad + c_1(1-\gamma)\chi_2(H \otimes I_n)\left(\eta - \sum_{k=N+1}^{N+Z}\left(H^{-1}A_{0k} \otimes I_n\right)\widetilde{V}_k\right) \\ &\quad - \sum_{k=N+1}^{N+Z}\left(H^{-1}A_{0k} \otimes I_n\right)(I_N \otimes A_0)\widetilde{V}_k \\ &= (G \otimes I_n)\widetilde{A}_{0I}\eta + (I_N \otimes A_0)\widetilde{\eta} \\ &= (G \otimes I_n)\widetilde{A}_{0I}\left(\widetilde{\eta} + \sum_{k=N+1}^{N+Z}\left(H^{-1}A_{0k} \otimes I_n\right)\widetilde{V}_k\right) \\ &\quad + (I_N \otimes A_0)\widetilde{\eta} + c_1(1-\gamma)\chi_2(H \otimes I_n)\widetilde{\eta} \\ &= (I_N \otimes A_0 + c_1(1-\gamma)\chi_2(H \otimes I_n))\widetilde{\eta} \\ &\quad + (G \otimes I_n)\widetilde{A}_{0I}\widetilde{\eta} + (G \otimes I_n)\widetilde{A}_{0I}\sum_{k=N+1}^{N+Z}\left(H^{-1}A_{0k} \otimes I_n\right)\widetilde{V}_k.\end{aligned} \tag{16}$$

Under the condition of assumption 3, χ_2 is negative and small enough; that is, $\chi_2 \ll 0$. So, $I_N \otimes A_0 + \chi_2(H \otimes I_n)$ is Hurwitz. We can get $\lim_{t\longrightarrow\infty}\widetilde{\eta}(t) = 0$ and $\lim_{t\longrightarrow\infty}\widetilde{\eta}_i(t) = 0$ through Lemma 1of[30]. The proof is completed. □

3.2. Solution of Sylvester Equations. In this study, some followers cannot get information from the leader's matrix A_0. A_0 is estimated by A_{0i}, and the generalized Lyapunov equation of the Sylvester equation is used to prove the stability of MASs. Therefore, in this section, the Sylvester equations in this paper are solved by the method in [30]. The Sylvester equations are as follows

$$X_k\left(I_N \otimes A_0\right) = \widehat{A}X_k + \widehat{B}_k, \tag{17}$$

$$0 = \widehat{C}X_k + \widehat{D}, \tag{18}$$

where X_k is solution to the above equation and $\widehat{A}$, $\widehat{B}_k$, $\widehat{C}$, and $\widehat{D}$ are given in the simulation examples in Section 4.

Lemma 2. *By Lemma 3in[30], we give a matrix $P(t)$; $\lim_{t\longrightarrow\infty}(P(t)-p)=0$ can be obtained. For any $\varepsilon>0$,*

$$\dot{X} = -\varepsilon P^T(t)P(t)X, \tag{19}$$

has and only has a unique solution $X(t)$. There are several X^* that make $pX^*=0$ and $\lim_{t\longrightarrow\infty}(X(t)-X^*)=0$.

Proof. The orthogonal matrix M guarantees $pM = (\overline{p}0)$ and

$$M^T p^T pM = \begin{pmatrix} \overline{p}^T\overline{p} & 0 \\ 0 & 0 \end{pmatrix}, \tag{20}$$

$$M^T p^T = \begin{pmatrix} \overline{p} \\ 0 \end{pmatrix}. \tag{21}$$

Let $X^* = M\begin{pmatrix} \overline{X}_1^* \\ \overline{X}_2^* \end{pmatrix}$ and $\overline{p}\overline{X}_1^* = 0$. Then, the formula is established as follows:

$$pX^* = pMM^TX^* = (\overline{p}0)\begin{pmatrix} \overline{X}_1^* \\ \overline{X}_2^* \end{pmatrix} = 0. \tag{22}$$

Let $\overline{X} = M^TX$; it yields

$$\begin{aligned} \dot{\overline{X}} &= -M^T\varepsilon P^T(t)P(t)X \\ &= -\varepsilon M^Tp^TpX + \varepsilon M^Tp^TpX - \varepsilon M^TP^T(t)P(t)X \\ &= -\varepsilon M^Tp^TpX + \varepsilon M^T\left(p^Tp - P^T(t)P(t)\right)X \\ &= -\varepsilon M^Tp^TpM\overline{X} + f(t), \end{aligned} \tag{23}$$

in which $f(t) = \varepsilon M^T(p^Tp - P^T(t)P(t))M\overline{X}$. Let $\overline{X} = \begin{pmatrix} \overline{X}_1 \\ \overline{X}_2 \end{pmatrix}$ and $f(t) = \begin{pmatrix} f_1(t) \\ f_2(t) \end{pmatrix}$. By Lemma 3 and Remark 2 in [30], $\lim_{t\longrightarrow\infty}f(t)=0$ and $\lim_{t\longrightarrow\infty}f_1(t)=0$. Then, from (18), we can get the following formula:

$$\begin{pmatrix} \dot{\overline{X}}_1 \\ \dot{\overline{X}}_2 \end{pmatrix} = -\varepsilon\begin{pmatrix} \overline{p}^T\overline{p} & 0 \\ 0 & 0 \end{pmatrix}\begin{pmatrix} \overline{X}_1 \\ \overline{X}_2 \end{pmatrix} + \begin{pmatrix} f_1(t) \\ f_2(t) \end{pmatrix}, \tag{24}$$

and it is concluded that

$$\begin{aligned} \dot{\overline{X}}_1 &= -\varepsilon\overline{p}^T\overline{p}\overline{X}_1 + f_1(t), \\ \dot{\overline{X}}_2 &= f_2(t), \end{aligned} \tag{25}$$

and there is $\overline{X}_2^*$ to make $\lim_{t\longrightarrow\infty}(\overline{X}_2 - \overline{X}_2^*) = 0$. Let $\widetilde{X}_2 = \overline{X}_1 - \overline{X}_1^*$; derivative of $\widetilde{X}_2$ is

$$\begin{aligned} \dot{\overline{X}}_1 &= f_1(t) - \varepsilon\overline{p}^T\overline{p}\overline{X}_1 \\ &= f_1(t) - \varepsilon\overline{p}^T\overline{p}\overline{X}_1^* - \varepsilon\overline{p}^T\overline{p}\widetilde{X}_1 \\ &= f_1(t) - \varepsilon\overline{p}^T\overline{p}\widetilde{X}_1. \end{aligned} \tag{26}$$

By Lemma 1in[30], $\lim_{t\longrightarrow\infty}\widetilde{X}_1 = 0$ because $\overline{X} = M^TX$ has

$$\begin{aligned} \lim_{t\longrightarrow\infty}(X(t)-X^*) &= \lim_{t\longrightarrow\infty}\left(M\overline{X} - M\begin{pmatrix} \overline{X}_1^* \\ \overline{X}_2^* \end{pmatrix}\right) \\ &= \lim_{t\longrightarrow\infty}M\begin{pmatrix} \overline{X}_1 - \overline{X}_1^* \\ \overline{X}_2 - \overline{X}_2^* \end{pmatrix} = 0. \end{aligned} \tag{27}$$

Proof is done.

Now, the feedback protocol is designed:

$$\begin{aligned} \dot{\xi}_i &= A_i\xi_i + B_iu_i + \sum_{k=N+1}^{N+Z}E_{ik}V_k + L_i\left(C_i\xi_i - y_i\right), \\ u_i &= K_{1i}\xi_i + \eta_i \end{aligned} \tag{28}$$

in which K_{1i} is gain matrix. (1), (2), and (19) give us the following formula:

$$\begin{aligned} \dot{x}_i &= A_ix_i + B_iK_{1i}\xi_i + B_i\eta_i + \sum_{k=N+1}^{N+Z}E_{ik}V_k, \\ \dot{\xi}_i &= A_i\xi_i + B_iK_{1i}\xi_i + B_i\eta_i + \sum_{k=N+1}^{N+Z}E_{ik}V_k + L_i\left(C_i\xi_i - C_ix_i\right), \end{aligned} \tag{29}$$

Let $X = \begin{pmatrix} x \\ \xi \end{pmatrix}$ and $V_k = \begin{pmatrix} \overline{V}_k \\ \eta \end{pmatrix}$, where

$$\begin{aligned} x &= \mathrm{col}\left(x_1, x_2, \ldots, x_N\right), \\ \xi &= \mathrm{col}\left(\xi_1, \xi_2, \ldots, \xi_N\right), \\ \overline{V}_k &= \mathrm{col}\left(V_k, V_k, \ldots, V_k\right) \in R^{Nn}, \\ \eta &= \mathrm{col}\left(\eta_1, \eta_2, \ldots, \eta_N\right). \end{aligned} \tag{30}$$

So, (20) can be changed as

$$\dot{X} = \widehat{A}X + \sum_{k=N+1}^{N+Z}\widehat{B}_kV_k, \tag{31}$$

where

$$\begin{aligned} \widehat{A} &= \begin{pmatrix} A & BK_1 \\ -LC & A + BK_1 + LC \end{pmatrix}, \\ \widehat{B}_k &= \begin{pmatrix} E_k & \frac{1}{Z}B \\ E_k & \frac{1}{Z}B \end{pmatrix}, \end{aligned} \tag{32}$$

and

$$\begin{aligned} A &= \text{block diag}\{A_1, A_2, \ldots, A_N\}, \\ B &= \text{block diag}\{B_1, B_2, \ldots, B_N\}, \\ C &= \text{block diag}\{C_1, C_2, \ldots, B_N\}, \\ E_k &= \text{block diag}\{E_{1k}, E_{2k}, \ldots, E_{3k}\}, \\ K_1 &= \text{block diag}\{K_{11}, K_{12}, \ldots, K_{1N}\}, \\ K_2 &= \text{block diag}\{K_{21}, K_{22}, \ldots, K_{2N}\}. \end{aligned} \tag{33}$$

Through (13) and (14), where $\widehat{D} = (0 - I_N \otimes 1/ZF)$ and $\widehat{C} = (C\,0)$. And then, we solve (13) and (14) through the lemma derived from [30]. □

Lemma 3. *Consider equation as*

$$\dot{Y} = -\varepsilon\psi^T(t)\psi(t)Y, \tag{34}$$

where $\varepsilon > 0$ is large enough and $\psi(t) = (I_{2N} \otimes A_{0i}(t))^T \otimes \begin{pmatrix} I_{2Nn} & 0 \\ 0 & 0 \end{pmatrix} - I_{2Nn} \otimes \begin{pmatrix} \widehat{A} & \widehat{B}_k \\ \widehat{C} & \widehat{D} \end{pmatrix}$. Let $\Xi(t) = m_{3Nn}^{2Nn}(Y) = \begin{pmatrix} X_k(t) \\ I_{2Nn} \end{pmatrix}$. Then, X_k^* is the solution of (13) and (14):

$$\lim_{t \longrightarrow \infty} \left(\Xi(t) - \begin{pmatrix} X_k^* \\ I_{2Nn} \end{pmatrix} \right) = 0, \tag{35}$$

which goes to zero no slower than $\widetilde{A}_{0I}$.

Proof. (13) and (14) can be written as follows:

$$\begin{pmatrix} I_{2Nn} & 0 \\ 0 & 0 \end{pmatrix} \begin{pmatrix} X_k \\ I_{2Nn} \end{pmatrix} (I_{2N} \otimes A_0) - \begin{pmatrix} \widehat{A} & \widehat{B}_k \\ \widehat{C} & \widehat{D} \end{pmatrix} \begin{pmatrix} X_k^* \\ I_{2Nn} \end{pmatrix} = 0. \tag{36}$$

Then, we have

$$\psi\Theta = 0, \tag{37}$$

in which

$$\begin{aligned} \psi &= (I_{2N} \otimes A_0)^T \otimes \begin{pmatrix} I_{2Nn} & 0 \\ 0 & 0 \end{pmatrix} - I_{2Nn} \otimes \begin{pmatrix} \widehat{A} & \widehat{B}_k \\ \widehat{C} & \widehat{D} \end{pmatrix}. \\ \Theta &= \begin{pmatrix} X_k^* \\ I_{2Nn} \end{pmatrix} \end{aligned} \tag{38}$$

$\lim_{t \longrightarrow \infty} (\psi(t) - \psi) = 0$ goes to zero no slower than $\widetilde{A}_{0I}$. Based on Lemma 2, $\lim_{t \longrightarrow \infty} (\Xi(t) - \Theta) = 0$ can be obtained, where there is a X_k^* satisfying (21). The proof is completed. □

3.3. Collaborative Analysis. By the above lemma and proof, we prove (4) and solve the problem of the bipartite containment control. In addition, $X_k^* = \begin{pmatrix} X_{k11}^* & X_{k12}^* \\ X_{k21}^* & X_{k22}^* \end{pmatrix}$ is the solution of equations (13) and (14), where $X_{k11}^*, X_{k12}^*, X_{k21}^*, X_{k22}^* \in R^{Nn \times Nn}$.

Theorem 1. *For (1) and (2), the MASs composed of the follower and the leader are described, respectively. Under assumption two, the existence of K_{1i} and L_i makes $A_i + B_i K_{1i}$ and $A_i + L_i C_i$ are Hurwitz. Then, a matrix $T = \begin{pmatrix} I_{Nn} & 0 \\ -I_{Nn} & I_{Nn} \end{pmatrix}$ controller (20) can be used to achieve the bipartite containment and the distributed error (4) converges to zero.*

Proof. Let $\overline{A} = T\widehat{A}T^{-1}$; we obtain

$$\overline{A} = \begin{pmatrix} A_i + BK_1 & BK_1 \\ 0 & A + LC \end{pmatrix}. \tag{39}$$

In assumption 2, we can see that $\overline{A}$ is Hurwitz. Then, we know $\widehat{A}$ is Hurwitz. If $\widetilde{X} = X - \sum_{k=N+1}^{N+Z} X_k^* V_k$ is set, the derivative of $\widetilde{X}$ can be obtained:

$$\begin{aligned} \dot{\widetilde{X}} &= \dot{X} - \sum_{k=N+1}^{N+Z} X_k^* \dot{V}_k = \widehat{A}X + \sum_{k=N+1}^{N+Z} \widehat{B}_k V_k - \sum_{k=N+1}^{N+Z} X_k^* \begin{pmatrix} \dot{\overline{V}}_k \\ \dot{\eta} \end{pmatrix} \\ &= \widehat{A}X + \sum_{k=N+1}^{N+Z} \widehat{B}_k V_k \\ &\quad - \left(\sum_{k=N+1}^{N+Z} X_k^* \begin{pmatrix} (I_N \otimes A_0)V_k \\ (I_N \otimes A_0)\eta \end{pmatrix} + \sum_{k=N+1}^{N+Z} X_k^* \begin{pmatrix} 0 \\ (G \otimes I_N)\widetilde{A}_{0I}\,\eta \end{pmatrix} + \sum_{k=N+1}^{N+Z} X_k^* \begin{pmatrix} 0 \\ c_1(1-\gamma)\chi_2(H \otimes I_N) \end{pmatrix} \widetilde{\eta} \right) \\ &= \widehat{A}X + \sum_{k=N+1}^{N+Z} \widehat{B}_k V_k - \sum_{k=N+1}^{N+Z} X_k^* (I_{2N} \otimes A_0) V_k \\ &\quad - \left(\sum_{k=N+1}^{N+Z} X_k^* \begin{pmatrix} 0 \\ (G \otimes I_N)\widetilde{A}_{0I}\,\eta \end{pmatrix} + \sum_{k=N+1}^{N+Z} X_k^* \begin{pmatrix} 0 \\ c_1(1-\gamma)\chi_2(H \otimes I_N) \end{pmatrix} \widetilde{\eta} \right). \end{aligned} \tag{40}$$

Then, formula (13) is used to rewrite (23) into the following form:

$$\dot{\widetilde{X}} = \widehat{A}X - \sum_{k=N+1}^{N+Z} \widehat{A}X_k^* V_k - \left(\sum_{k=N+1}^{N+Z} X_k^* \begin{pmatrix} 0 \\ (G \otimes I_N)\widetilde{A}_{0I}\eta \end{pmatrix} + \sum_{k=N+1}^{N+Z} X_k^* \begin{pmatrix} 0 \\ c_1(1-\gamma)\chi_2(H \otimes I_N) \end{pmatrix} \widetilde{\eta} \right) = \widehat{A}\widetilde{X} + \Lambda_1 \widetilde{\eta} + \Lambda_2, \tag{41}$$

in which

$$\begin{aligned} \Lambda_1 &= -\sum_{k=N+1}^{N+Z} X_k^* \begin{pmatrix} 0 \\ c_1((1-\gamma))\chi_2(H \otimes I_N) \end{pmatrix}, \\ \Lambda_2 &= -\sum_{k=N+1}^{N+Z} X_k^* \begin{pmatrix} 0 \\ (G \otimes I_N)\widetilde{A}_{0I}\eta \end{pmatrix}, \end{aligned} \tag{42}$$

and $\lim_{t\longrightarrow\infty}\Lambda_2 = 0$ exponentially at least as fast as $\lim_{t\longrightarrow\infty}\widetilde{A}_{0I} = 0$. Therefore, through Lemma 1in[30] and Lemma 1 of this paper, we get $\lim_{t\longrightarrow\infty}\widetilde{X} = 0$. Now, consider distributed error (4), which has the following form:

$$\begin{aligned} e &= (H \otimes I_N)Cx - (H \otimes I_N)(I_N \otimes F)\eta \\ &\quad + (H \otimes I_N)(I_N \otimes F)\eta - \sum_{k=N+1}^{N+Z} (A_{0k} \otimes F)\widetilde{V}_k \\ &= (H \otimes I_n)\sigma + (H \otimes F)\widetilde{\eta}, \end{aligned} \tag{43}$$

where $\sigma = Cx - (I_N \otimes F)\eta$, and σ has this

$$\begin{aligned} \sigma &= Cx - (I_N \otimes F)\eta \\ &= (C \quad 0)X + \sum_{k=N+1}^{N+Z} \left(0 - I_N \otimes \frac{1}{Z}F\right) \begin{pmatrix} \overline{V}_k \\ \eta \end{pmatrix} \\ &= \widehat{C}X + \sum_{k=N+1}^{N+Z} \widehat{D}V_k \\ &= \widehat{C}\overline{X} + \sum_{k=N+1}^{N+Z} \widehat{C}XV_k + \sum_{k=N+1}^{N+Z} \widehat{D}V_k. \end{aligned} \tag{44}$$

Through (14), we have

$$\sigma = \widehat{C}\widetilde{X}. \tag{45}$$

Because of $\lim_{t\longrightarrow\infty}\widetilde{X} = 0$, we can get $\lim_{t\longrightarrow\infty}\sigma = 0$. Under Lemma 1, $\lim_{t\longrightarrow\infty}\widetilde{\eta} = 0$. So, bipartite containment error converges to zero, that is, $\lim_{t\longrightarrow\infty}e = 0$.

The proof is completed. □

4. Numerical Simulations

In this section, a numerical example is used to illustrate the effectiveness of the bipartite containment control. Figure 1 can be viewed as a topology of (1) and (2), showing the communication relationship between six agents. Since the symbolic graph is considered in this study, we select 5 and 6 as the leader and the other agents as the followers and then divide 1 and 3, 2, and 4 into two different subgroups N_1, N_2, including $N_1 \cup N_2 = N$ and $N_1 \cap N_2 = \varnothing$. It can be concluded from Figure 1 that the Laplace matrix L and matrix A have the following forms:

$$\begin{aligned} A &= \begin{pmatrix} 0 & 0 & 0 & -1 \\ 0 & 0 & 0 & 1 \\ 1 & 0 & 0 & 0 \\ 0 & 0 & -1 & 0 \end{pmatrix}, \\ L &= \begin{pmatrix} 1 & 0 & 0 & 1 \\ 0 & 1 & 0 & -1 \\ -1 & 0 & 1 & 0 \\ 0 & 0 & 1 & 1 \end{pmatrix}. \end{aligned} \tag{46}$$

In addition, $A_{0k} = \mathrm{diag}\{|a_{1k}|, |a_{2k}|, \ldots, |a_{Nk}|\}$ and $H = \sum_{k=N+1}^{N+Z}(1/Z)L + A_{0k}$ have the following forms:

$$A_{05} = \begin{pmatrix} 1 & 0 & 0 & 0 \\ 0 & 1 & 0 & 0 \\ 0 & 0 & 0 & 0 \\ 0 & 0 & 0 & 0 \end{pmatrix}, A_{06} = \begin{pmatrix} 0 & 0 & 0 & 0 \\ 0 & 0 & 0 & 0 \\ 0 & 0 & 1 & 0 \\ 0 & 0 & 0 & 1 \end{pmatrix}, \tag{47}$$

$$H = L + A_{05} + A_{06} = \begin{pmatrix} 2 & 0 & 0 & 1 \\ 0 & 2 & 0 & -1 \\ -1 & 0 & 2 & 0 \\ 0 & 0 & 0 & 2 \end{pmatrix}. \tag{48}$$

Considering the follower and leader systems (1) and (2), the correlation matrix is given as follows:

$$\begin{aligned} A_0 &= \begin{pmatrix} 1 & -2 \\ 1.5 & -1 \end{pmatrix}, F = \begin{pmatrix} 4 & 0 \\ 0 & 0 \end{pmatrix}, \\ A_i &= \begin{pmatrix} 0 & 0.5 * i \\ 0 & 0 \end{pmatrix}, B_i = \begin{pmatrix} 0 & 1 \\ 0.5 * i & 0 \end{pmatrix}, \\ C_1 &= \begin{pmatrix} 8 & -10.5 \\ 2 & -7 \end{pmatrix}, C_2 = \begin{pmatrix} 2 & -6 \\ -3 & -5.5 \end{pmatrix}, \\ C_3 &= \begin{pmatrix} 1.5 & -8 \\ -3 & -3.8 \end{pmatrix}, C_4 = \begin{pmatrix} -4 & -15 \\ -4 & -2 \end{pmatrix}, \\ E_{i5} &= \begin{pmatrix} 0 & 0 \\ 0 & 0.1 \end{pmatrix}, E_{i6} = \begin{pmatrix} 0 & 0 \\ 0.0 & 50 \end{pmatrix}. \end{aligned} \tag{49}$$

Based on Section 3.3, it can be known that $A_i + B_iK_{1i}$ and $A_i + L_iC_i$ are Hurwitz, and then, K_{1i} and L_i can be calculated according to the above matrix. $c_1 = 3.6$ is also given:

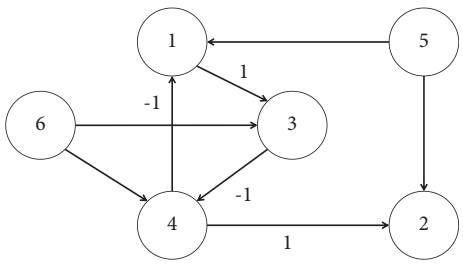

Figure 1: Communication topology of 2 leaders and 4 followers.

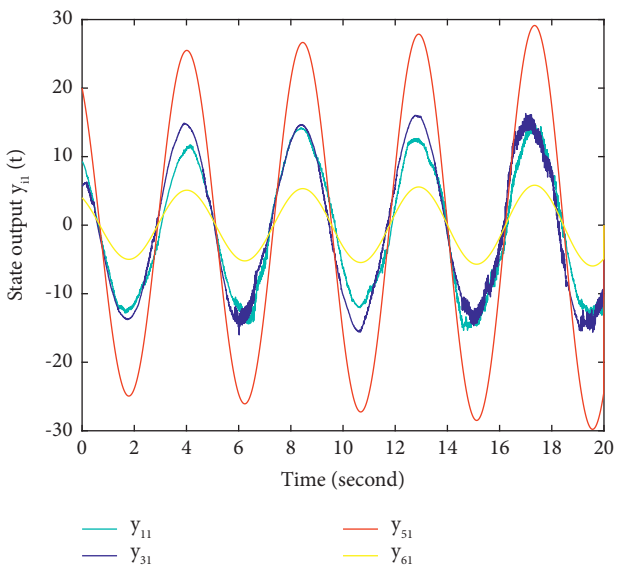

Figure 2: Output curves of leader 51 and 61 and follower 11 and 31.

$$
\begin{aligned}
K_{11} &= \begin{pmatrix} -0.1604 & -1.1036 \\ -0.9871 & -0.3207 \end{pmatrix}, \\
K_{12} &= \begin{pmatrix} -0.4142 & -1.2872 \\ -0.9102 & -0.4142 \end{pmatrix}, \\
K_{13} &= \begin{pmatrix} -0.6074 & -1.4321 \\ -0.7944 & -0.4049 \end{pmatrix}, \\
K_{14} &= \begin{pmatrix} -0.7310 & -1.5259 \\ -0.6824 & -0.3655 \end{pmatrix}, \\
L_1 &= \begin{pmatrix} -0.9321 & 0.5586 \\ 0.4413 & 0.8974 \end{pmatrix}, \\
L_2 &= \begin{pmatrix} -0.5706 & 0.8181 \\ 0.7434 & 0.6689 \end{pmatrix}, \\
L_3 &= \begin{pmatrix} -0.3307 & 0.9681 \\ 0.8798 & 0.4754 \end{pmatrix}, \\
L_4 &= \begin{pmatrix} 0.1999 & 0.8685 \\ 0.9989 & -0.0451 \end{pmatrix}.
\end{aligned}
\tag{50}
$$

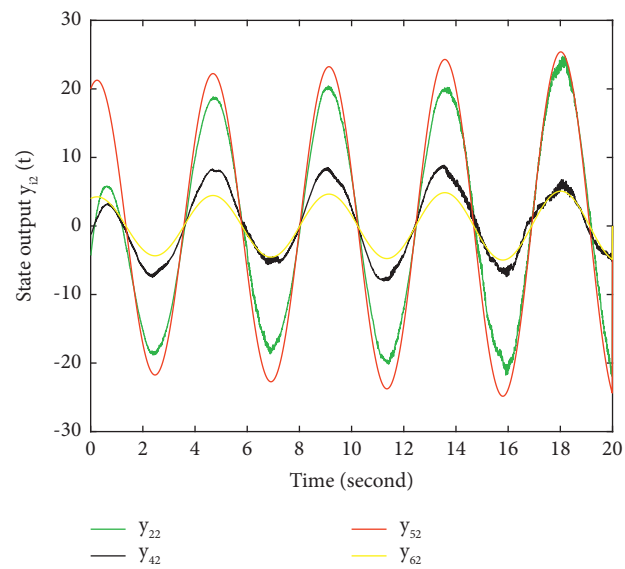

Figure 3: Output curves of leader 52 and 62 and follower 22 and 42.

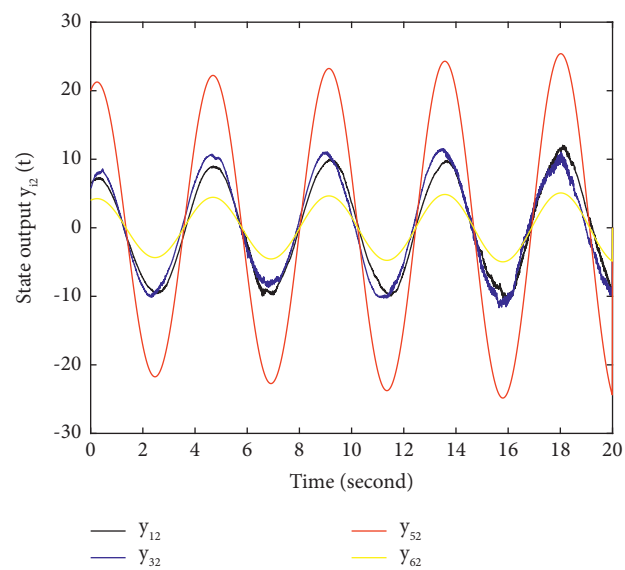

Figure 4: Output curves of leader 52 and 62 and follower 12 and 32.

Based on the above matrix, Figures 2–5 show the bilateral output curve of the agent. The red line represents leader 5, the yellow line represents leader 6, and the remaining colors are followers. Figures 2 and 5 show the first row contained in the leader bilateral output with 5 and 6. Specifically, y_{51} is the first line of $y_5 = FV_5$ and y_{61} is the first line of $y_6 = FV_6$. y_{11} is the first line of $y_1 = C_1x_1$, y_{21} is the first line of $y_2 = C_2x_2$, y_{31} is the first line of $y_3 = C_3x_3$, and y_{41} is the first line of $y_4 = C_4x_4$. Similarly, Figures 3 and 4 show the output containing the second row, the second component. To sum up, it can be observed that some followers converge to the region bounded by leaders 5 and 6, while the rest converge to the opposite region. Moreover, follower information transmission takes into account the

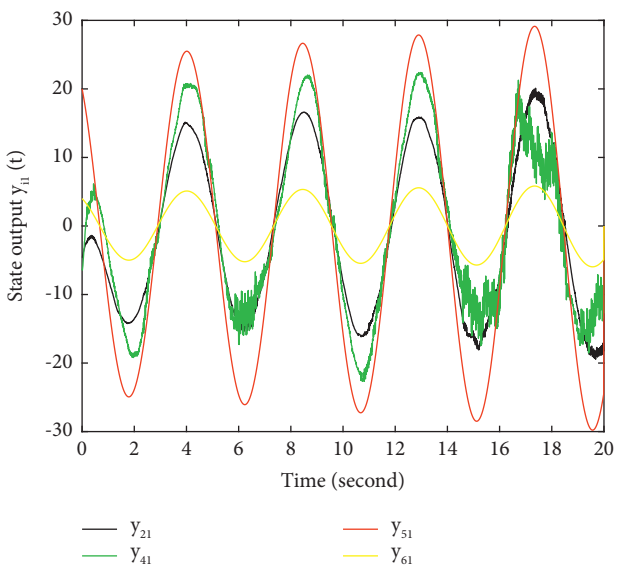

Figure 5: Output curves of leader 51 and 61 and follower 21 and 41.

influence of quantification, which is more interesting and challenging.

5. Conclusions

In this study, bipartite containment control is discussed. The matrix A_0 of the external leader system is observed by using an adaptive quantization observer, and the adaptive quantization information observer is proved to be effective by the eigenvalue analysis method without M-matrix. A controller with only one gain matrix and an appropriate protocol for the control evolution algorithm is designed. At the same time, considering the influence of quantization on follower information transmission, a quantizer is added. Finally, the bipartite containment control is realized by using the feedback method.

In the future, we will further study the bipartite containment control with adaptive quantization information distributed observer under switched topology or in finite time.

Data Availability

The data that support the findings of this study can be obtained from the corresponding author upon reasonable request.

Conflicts of Interest

The authors declare that they have no conflicts of interest.

Acknowledgments

This work was partially supported by the National Natural Science Foundation of China, under Grants 61971181 and 62072164.

References

[1] J. A. Fax and R. M. Murray, "Information flow and cooperative control of vehicle formations," *IEEE Transactions on Automatic Control*, vol. 49, no. 9, pp. 1465–1476, 2004.

[2] X. K. Liu, Y. W. Wang, P. Lin, and P. Wang, "Distributed supervisory secondary control for a DC microgrid," *IEEE Transactions on Energy Conversion*, vol. 35, no. 4, pp. 1736–1746, 2020.

[3] M. Li, G. Xu, Q. Lai, and J. Chen, "A chaotic strategy-based quadratic opposition-based learning adaptive variable-speed whale optimization algorithm," *Mathematics and Computers in Simulation*, vol. 193, no. 5, pp. 71–99, 2022.

[4] T. H. Lee, Q. Ma, S. Xu, and J. H. Park, "Pinning control for cluster synchronisation of complex dynamical networks with semi-Markovian jump topology," *International Journal of Control*, vol. 88, no. 6, pp. 1223–1235, 2015.

[5] M. Lu, J. Wu, X. S. Zhan, T. Han, and H. Yan, "Consensus of second-order heterogeneous multi-agent systems with and without input saturation," *ISA Transactions*, vol. 126, no. 12, pp. 14–20, 2022.

[6] X. S. Zhan, J. Wu, T. Jiang, and X. W. Jiang, "Optimal performance of networked control systems under the packet dropouts and channel noise," *ISA Transactions*, vol. 58, no. 5, pp. 214–221, 2015.

[7] J. Wu, Q. Deng, T. Han, and H. Yan, "Bipartite output regulation for singular heterogeneous multi-agent systems on signed graph," *Asian Journal of Control*, 2021.

[8] F. Deng, S. Guan, X. Yue et al., "Energy-based sound source localization with low power consumption in wireless sensor networks," *IEEE Transactions on Industrial Electronics*, vol. 64, no. 6, pp. 4894–4902, 2017.

[9] A. Nedic and A. Ozdaglar, "Distributed subgradient methods for multi-agent optimization," *IEEE Transactions on Automatic Control*, vol. 54, no. 1, pp. 48–61, 2009.

[10] Y. Jiang, J. Fan, W. Gao, T. Chai, and F. L. Lewis, "Cooperative adaptive optimal output regulation of nonlinear discrete-time multi-agent systems," *Automatica*, vol. 121, Article ID 109149, 2020.

[11] T. Han, Z. H. Guan, B. Xiao, J. Wu, and X. Chen, "Distributed output consensus of heterogeneous multi-agent systems via an output regulation approach," *Neurocomputing*, vol. 360, pp. 131–137, 2019.

[12] W. Wang, H. Liang, Y. Pan, and T. Li, "Prescribed performance adaptive fuzzy containment control for nonlinear multiagent systems using disturbance observer," *IEEE Transactions on Cybernetics*, vol. 50, no. 9, pp. 3879–3891, 2020.

[13] Y. M. Li, F. Y. Qu, and S. C. Tong, "Observer-based fuzzy adaptive finite-time containment control of nonlinear multiagent systems with input delay," *IEEE Transactions on Cybernetics*, vol. 51, no. 1, pp. 126–137, 2021.

[14] H. G. Zhang, Y. Zhou, Y. Liu, and J Sun, "Cooperative bipartite containment control for multiagent systems based on adaptive distributed observer," *IEEE Transactions on Cybernetics*, vol. 52, no. 6, pp. 5432–5440, 2022.

[15] R. Olfati-Saber and R. M. Murray, "Consensus problems in networks of agents with switching topology and time-delays," *IEEE Transactions on Automatic Control*, vol. 49, no. 9, pp. 1520–1533, 2004.

[16] X. He and Q. Wang, "Distributed finite-time leaderless consensus control for double-integrator multi-agent systems with external disturbances," *Applied Mathematics and Computation*, vol. 295, pp. 65–76, 2017.

[17] Y. Tang, H. Gao, W. Zhang, and J. Kurths, "Leader-following consensus of a class of stochastic delayed multi-agent systems with partial mixed impulses," *Automatica*, vol. 53, pp. 346–354, 2015.

[18] Y. Hong, G. Chen, and L. Bushnell, "Distributed observers design for leader-following control of multi-agent networks," *Automatica*, vol. 44, no. 3, pp. 846–850, 2008.

[19] W. Ni and D. Cheng, "Leader-following consensus of multi-agent systems under fixed and switching topologies," *Systems & Control Letters*, vol. 59, no. 3-4, pp. 209–217, 2010.

[20] H. Liu, G. Xie, and L. Wang, "Necessary and sufficient conditions for containment control of networked multi-agent systems," *Automatica*, vol. 48, no. 7, pp. 1415–1422, 2012.

[21] H. Haghshenas, M. A. Badamchizadeh, and M. Baradarannia, "Containment control of heterogeneous linear multi-agent systems," *Automatica*, vol. 54, no. Apr, pp. 210–216, 2015.

[22] H. Liang, H. Li, Z. Yu, P. Li, and W. Wang, "Cooperative robust containment control for general discrete-time multi-agent systems with external disturbance," *IET Control Theory & Applications*, vol. 11, no. 12, pp. 1928–1937, 2017.

[23] H. Liang, Y. Zhou, H. Ma, and Q. Zhou, "Adaptive distributed observer approach for cooperative containment control of nonidentical networks," *IEEE Trans. Syst. Man Cybern. Syst.* vol. 49, no. 2, pp. 299–307, 2019.

[24] X. S. Zhan, L. Hao, T. Han, and H. Yan, "Adaptive bipartite output consensus for heterogeneous multi-agent systems with quantized information: a fixed-time approach," *Journal of the Franklin Institute*, vol. 358, no. 14, pp. 7221–7236, 2021.

[25] Y. R. Zhu, S. Li, J. Ma, and Y. Zheng, "Bipartite consensus in networks of agents with antagonistic interactions and quantization," *IEEE Transactions on Circuits and Systems II: Express Briefs*, vol. 65, no. 12, pp. 2012–2016, 2018.

[26] Z. G. Wu, Y. Xu, Y. J. Pan, P. Shi, and Q. Wang, "Event-triggered pinning control for consensus of multiagent systems with quantized information," *IEEE Trans. Syst. Man Cybern. Syst.*vol. 48, no. 11, pp. 1929–1938, 2018.

[27] X. X. Li, M. Z. Q. Chen, and H. S. Su, "Quantized consensus of multi-agent networks with sampled data and Markovian interaction links," *IEEE Transactions on Cybernetics*, vol. 49, no. 5, pp. 1816–1825, 2019.

[28] A. Ahmadi, H. Atrianfar, and F. Abdollahi, "Distributed accelerating of quantized second-order consensus with bounded input," *Asian Journal of Control*, vol. 23, no. 1, pp. 399–411, 2021.

[29] L. Rong, S. Wang, G. P. Jiang, and S. Xu, "Distributed observer-based consensus over directed networks with limited communication bandwidth constraints," *IEEE Trans. Syst. Man Cybern. Syst.*vol. 50, no. 12, pp. 5361–5368, 2020.

[30] P. Bernard, M. Bin, and L. Marconi, "Adaptive output regulation via nonlinear Luenberger observer-based internal models and continuous-time identifiers," *Automatica*, vol. 122, Article ID 109261, 2020.

[31] M. Shahvali, M.-B. Naghibi-Sistani, and J. Askari, "Adaptive output-feedback bipartite consensus for nonstrict-feedback nonlinear multi-agent systems: a finite-time approach," *Neurocomputing*, vol. 318, pp. 7–17, 2018.

[32] Y. Liu, H. Zhang, Z. Shi, and Z. Gao, "Neural-network-based finite-time bipartite containment control for fractional-order multi-agent systems," *IEEE Transactions on Neural Networks and Learning Systems*, pp. 1–12, 2022.

[33] Y. X. Wu, D. Meng, and Z. G. Wu, "Bipartite containment fluctuation behaviors of cooperative-antagonistic networks with time-varying topologies," *IEEE Trans. Syst. Man Cybern. Syst*, pp. 1–10, 2022.

[34] H. Zhang and J. Chen, "Bipartite consensus of multi-agent systems over signed graphs: state feedback and output feedback control approaches," *International Journal of Robust and Nonlinear Control*, vol. 27, no. 1, pp. 3–14, 2017.

[35] H. Cai, F. L. Lewis, G. Hu, and J. Huang, "The adaptive distributed observer approach to the cooperative output regulation of linear multi-agent systems," *Automatica*, vol. 75, pp. 299–305, 2017.

[36] D. Meng, "Bipartite containment tracking of signed networks," *Automatica*, vol. 79, no. Sep, pp. 282–289, 2017.

[37] C. Godsil and G. Royle, *Algebraic Graph Theory*, pp. 151–181, Algebraic Graph Theory, 1974.

Hindawi
Discrete Dynamics in Nature and Society
Volume 2022, Article ID 9308923, 11 pages
https://doi.org/10.1155/2022/9308923

Research Article

Delayed Impulsive Control for Lag Synchronization of Neural Networks with Time-Varying Delays and Partial Unmeasured States

Jiarui Ye and Jin-E Zhang

College of Mathematics and Statistics, Hubei Normal University, Huangshi 435002, China

Correspondence should be addressed to Jin-E Zhang; zhang86021205@163.com

Received 12 June 2022; Accepted 5 July 2022; Published 16 September 2022

Academic Editor: Guoguang Wen

In this article, a controller with delay impulse is applied to a neural network (NN) with time-varying delays. Firstly, the lag synchronization of the system is discussed. In addition, a sufficient condition for guaranteed lag synchronization requiring all state information is derived by using linear matrix inequality (LMI). In particular, the main results of neural networks (NNs) with time-varying delays and partial unmeasured states are studied by using the delay impulsive control gain matrix derived from dimension expansion. Finally, we will give two examples, both of which can confirm the validity of the results.

1. Introduction

As the most important branch system in modern artificial intelligence, the neural network (NN) [1–3] has always been an important object of scholars' research. In recent decades, NN has made great progress in control systems, signal analysis and processing, traffic safety, pattern recognition, and other fields. However, when using NN to solve practical problems, many scholars have found that the information transmission mode between neurons is not continuous, and the transmission of neurotransmitters may be delayed. Thus, it is necessary to discuss NNs with a time delay.

Time delay is a common phenomenon in many practical NNs and a key factor that directly affects and determines the synchronization of NNs. In [4], the lag synchronization of NNs with time delays is studied by establishing appropriate controllers. In [5], the asymptotic control of nonlinear NNs with time delays is discussed by using adaptive mechanisms and projection operators to estimate unknown time delays. In [6], fixed time synchronization for delayed complex dynamic NNs is studied. At present, the synchronization analysis of linear systems with a constant delay has been widely studied, but there are still many problems in the study of time-varying delay cases. For example, it is difficult to establish sufficient and necessary conditions for the synchronization of time-varying delay NNs, so it is particularly important to seek synchronization conditions with minimum conservatism.

As a branch of time-delay NNs, NNs with time-varying delays have wide application prospects in pattern recognition, optimization calculation, and image processing. Over the past three decades, it has been proved that linear matrix inequality (LMI) methods can be used to obtain more concise ideas and their interrelationships, such as the feasibility of solutions, reversibility, and controller specification form. In [7], some sufficient conditions for the global exponential stability (GES) of high-order Cohen–Grossberg NNs are derived by using induction and the properties of nonsingular M-matrices. In [8], the synchronization problem of complex dynamic neural networks (CDNNs) with time-varying delays is studied by using an impulse distributed control scheme. In [9], exponential adaptive synchronization of time-varying delay NNs is discussed by establishing the Lyapunov functional. It is not hard to find that the synchronization of NNs in material transportation, adaptive control, psychology, and transportation is still

worth studying, in addition to the stability problems of a large number of differential NNs with time-varying delays directly proposed in engineering practice. Therefore, the research on synchronization theory of NNs with time-varying delays has an extensive practical engineering background and profound theoretical value.

As one of the most important dynamic behaviors of NNs, synchronization can be divided into quasi-synchronization [10], lag synchronization [11], exponential synchronization [12], and coupling synchronization [13] according to different synchronization behaviors. In [14], a new method of high-order NNs based on time delays and impulses discrete is studied. In [15], an adaptive controller is designed to study the adaptive synchronization problem of NNs with time delays. In [16], the synchronization problem of complex NNs with unknown bounded time-varying delays using LMI is discussed. It is not hard to see that the lag synchronization result of delayed impulsive control has attracted the attention of many scholars. Current research results concentrate on the complete state of information. In other words, when the state of the NN is partial and immeasurable, the above results do not apply to the case of the NN with impulsive action. Therefore, it is a key problem to realize lag synchronization of NNs, which refers to partial unmeasured states under the delayed impulse of NNs with time-varying delays. However, we find that the analysis of lag synchronization of delayed impulses is still in its infancy.

Motivated by the above discussions, the purpose of this article is to discuss the lag synchronization of time-varying NNs with partial unmeasured states under the control of delayed impulse. By increasing the unmeasurable state dimension and extending the measurable state dimension, the unmeasurable state dimension and measurable state dimension can be unified. The results show that some sufficient conditions for lag synchronization of NNs with time-varying delays can be obtained. The main contributions to this article include the following:

(1) A new time-varying delay differential NN is established.

(2) The state transition matrix is used to separate the measurable state and the unmeasurable state, and the dimensions of the two states obtained are consistent through dimension expansion.

(3) The result of lag synchronization is obtained by LMI inequality. At the same time, compared with the general nonlinear system, because of the complexity of time-varying delay NNs, the design of impulsive control gain is more difficult. Appropriate delay impulsive gain can be obtained by using LMI.

The remainder of the article is as follows: Section 2 provides an NN model with a time-varying delay, a definition, a hypothesis, and two useful lemmas. In Section 3, some conditions for satisfying LMI are given, and some theorems satisfying the main results are obtained. In Section 4, two numerical examples are discussed to illustrate the feasibility of the conclusions. Finally, Section 5 is the conclusion of the article.

Notations: in the whole article, R signifies real number set, R^n, and $R^{n\times q}$ stand, respectively, the set of real numbers and all n-dimensional and $n\times q$-dimensional real spaces equipped. $A<0\,(A>0)$ denotes a negative (positive) definite matrix. $\lambda_{\min}(A)\,(\lambda_{\max}(A))$, A^T and A^{-1} denote the minimum (maximum) eigenvalue, the transpose and the inverse of matrix A, respectively. Set $\alpha\vee\beta$ be the maximum value of α and β and $\alpha\wedge\beta$ denotes the minimum value. For any interval $I\subseteq R$, set $S\subseteq R^k\,(1\le k\le n)$, $PC(I,S)=\{\theta\colon I\longrightarrow S\}$, where θ is a continuous point except at the finite point t, exist $\theta(t^+)$, $\theta(t^-)$, and $\theta(t^+)=\theta(t)$. $\tau(t)$ denotes time-varying delay, $\tau>0$ is time delay, $PC([-\tau,0],R^n)$ represents the collection of piecewise right-hand functions $h\colon[-\tau,0]\longrightarrow R^n$ with the norm defined by $\|h\|_\tau=\sup_{-\tau\le s\le 0}\|h(s)\|$. $\Lambda=\{1,2,\ldots,n\}$ and the symbol $\bigstar$ denote a symmetric block in a symmetric matrix.

2. Preliminaries

2.1. Model. First, time-varying delay NN can be considered as

$$\begin{cases}\dot z(t)=-Az(t)+Bz(t-\tau(t))+Cf(z(t))+Df(z(t-\tau(t)))+I, & t>0,\\ z(s)=\phi(s), & s\in[-\tau,0],\end{cases}\tag{1}$$

where $z(t)=(z_1,\ldots,z_n)^T\in R^n$ denotes neuron state vector; $A=\mathrm{diag}\{a_1,\ldots,a_n\}$ and $B=\mathrm{diag}\{b_1,\ldots,b_n\}$ are diagonal matrices with $a_i,b_i>0$, $i\in\Lambda$; C and D correspond to the constant connection weight matrix; $f(z(t))=(f_1(z_1(t)),\ldots,f_n(z_n(t)))^T$ denote the neuron activation functions; assume that $0\le\tau(t)\le\tau$, $\tau\le\infty$; I is an external input signal; $\phi(\cdot)\in PC([-\tau,0],R^n)$ represents the initial state.

Consider a time-varying delay NNs (1), its response NN is as follows:

$$\begin{cases}\dot w(t)=-Aw(t)+Bw(t-\tau(t))+Cf(w(t))+Df(w(t-\tau(t)))+I+u(t), & t>d\\ w(s)=\theta(s), s\in[-\tau+d,d],\end{cases}\tag{2}$$

where the number of measurable states in the state part of the response NN is q and $\theta(\cdot) \in PC([-\tau+d, d], R^n)$ is the initial state. Let $H = \{r_1, \ldots, r_q\} \subset \{1, \ldots, n\}$ and $G = \{r_{q+1}, \ldots, r_n\} \subset \{1, \ldots, n\}$ represent the collection of measurable and unmeasurable states, respectively. The lag synchronization characteristic of the NN is $w(t) \longrightarrow z(t-d)$ for exist $d > 0$. Assume that the error variable is $e(t) = w(t) - z(t-d)$. Thus, the error dynamics NN of drive and response NN is as follows:

$$\begin{cases} \dot{e}(t) = -Ae(t) + Be(t-\tau(t)) + Cg(e(t)) + Dg(e(t-\tau(t))) + u(t), & t > d \\ e(s) = \theta(s) - \phi(s-d), & s \in [-\tau+d, d], \end{cases} \tag{3}$$

where $g(e) = f(e(\cdot) + z(\cdot)) - f(z(\cdot))$. Let $u(t) \in R^n$ be a controller and

$$u(t) = \sum_{k \in Z_+} (Ke(t-\eta_k) - e(t))\delta(t-t_k), \tag{4}$$

where $\{t_k\}$ denotes the impulse sequence, and it satisfies $\inf\{t_k - t_{k-1}, k \in Z_+\} > 0$. Assume Θ_d is the impulse sequences, and it satisfies $t_k - t_{k-1} \le \rho$ (ρ is any positive constant), $K \in R^{n\times n}$ denotes the control gain matrix. $\delta(\cdot)$ denotes the Dirac delta function, when $t = t_k$, $\delta(t) = 1$; otherwise, $\delta(t) = 0$. η_k is delayed in the impulse, and it satisfies $0 \le \eta_k \le \eta, \eta > 0$.

Define e_i $(i \in H)$ as the measurable state, we shift the e_i in front of e. It is not hard to find a matrix that T satisfies $\vartheta(t) = Te(t)$, where T is a transition matrix; then, we can get

$$\begin{cases} \dot{\vartheta}(t) = -A_\vartheta \vartheta(t) + B_\vartheta \vartheta(t-\tau(t)) + C_\vartheta g(\vartheta(t)) + D_\vartheta g(\vartheta(t-\tau(t))), & t \ne t_k, \\ \vartheta(t) = K_\vartheta \vartheta(t^- - \eta_k), & t = t_k, \\ \vartheta(s) = \theta_\vartheta(s) - \phi_\vartheta(s-d), & s \in [(-\tau+d)\wedge(-\eta+d), d], \end{cases} \tag{5}$$

where $\vartheta = (e_{r_1}, \ldots, e_{r_q}, e_{r_{q+1}}, \ldots, e_{r_n})^T$, $D_\vartheta = \mathrm{TDT}^{-1}$, $C_\vartheta = \mathrm{TCT}^{-1}$, $g(\vartheta) = g(Te)$, $A_\vartheta = \mathrm{TAT}^{-1}$, $B_\vartheta = \mathrm{TBT}^{-1}$, $\phi_\vartheta = T\phi$, $\theta_\vartheta = T\theta$, $K_\vartheta = \mathrm{TKT}^{-1}$. After obtaining the transformed error system, we will discuss two different cases of error state information.

Remark 1. During the past period, lag synchronization of NNs has been investigated in the literature [8, 14, 15]. In [15], lag synchronization of BAM NNs with impulses is discussed. However, few studies consider the existence of unmeasured states of time-varying delay NNs, so the above results for lag synchronization are not applicable. Thus, we improve the known results and study the lag synchronization problem of time-varying delay NNs in both measurable and unmeasurable states. Therefore, we divide impulsive control into two situations: the first is that the number of set H is greater than the number of set G, namely, $q > n - q$; the second is that the number of sets. H is less than or equal to the number of sets G, namely, $q \le n - q$.

Hypothesis 1. The neuron activation function $f_i(\cdot)$ satisfies

$$|f_i(u) - f_i(v)| \le l_i |u - v|, \tag{6}$$

where $u, v \in R$, l_i is a positive constant and $i \in \Lambda$.

Definition 1. For any initial conditions $z(s) = \phi(s)$ and $w(s) = \theta(s)$ satisfies

$$|z(t) - w(t-d)| \longrightarrow 0. \tag{7}$$

As $t \longrightarrow +\infty$, then it is said that the drive NN (1) and response NN (2) achieve lag synchronization with the time lag d.

Lemma 1 (see [16]). *Assume that $h(t) \in PC(R, R_+)$ satisfies*

$$\begin{cases} \dfrac{dh(t)}{dt} \le \lambda h(t) + \delta h(t-\tau(t)), & t \ne t_k, \\ h(t) \le \theta_k h(t-\eta_k), & t = t_k, k \in Z_+, \end{cases} \tag{8}$$

where $\lambda \in R, \delta \in R_+$, and $\theta_k \in R_+$. If there exist α, β, p are constants, and $\alpha > 0, \beta > 0, p > 0$, such that

$$\begin{aligned} &\alpha + |\lambda| + \beta\delta e^{\alpha\tau} < \ln\beta/p, \\ &\beta e^{\alpha\eta}\theta_k \le 1, \quad k \in Z_+. \end{aligned} \tag{9}$$

Then the solution of (5) satisfies the following:

$$h(t) \le \beta \overline{h}(0) e^{-\alpha t}, \tag{10}$$

in Θ_d, where $\overline{h}(0) = sup_{-(\tau\vee\eta)\le s\le 0} h(s)$.

Proof. Similar to Lemma 2 proof in [16], setting $T = p, \mu_1 = \exp(\alpha T), \mu_2 = \exp(\alpha\tau), \mu_3 = \exp(\alpha\eta)$, one may derive Lemma 1. □

Lemma 2. *For any real vectors $z, \zeta \in R^n$ and real matrix $P \in R^{n\times n}$, there exists an $n \times n$ real matrix $M > 0$ satisfies the following:*

$$2z^T P\zeta \le z^T PM^{-1}P^T z + \zeta^T M\zeta. \tag{11}$$

3. Main Results

This section presents the main theoretical results of the article; that is, the lag synchronization problem of time-varying delay NNs is proved by delayed impulse. To better demonstrate the comprehensiveness of the results, two cases will be considered, i.e., $q > n - q$ and $q \le n - q$, respectively.

Case 1. The number of set H is greater than the number of set G, namely, $q > n - q$.

First of all, we think about the lag synchronization of time-varying delay NNs via delayed impulsive control, when $q > n - q$. Considering the error states $\vartheta(t)$, $\vartheta = (\vartheta_1^T, \vartheta_2^T)^T$, $\vartheta_1 = (\vartheta_1^{1T}, \vartheta_1^{2T})^T$, $\vartheta_1^1 = (e_{r_1}, \ldots, e_{r_{n-q}})^T$, $\vartheta_1^2 = (e_{r_{n-q+1}}, \ldots, e_{r_q})^T$, $\vartheta_2 = (e_{r_{q+1}}, \ldots, e_{r_n})^T$, $g(\vartheta_1^1) = (g_{r_1}(e_{r_1}(\cdot)), \ldots, g_{r_{n-q}}(e_{r_{n-q}}(\cdot)))^T$, $g(\vartheta_1^2) = (g_{r_{n-q+1}}(e_{r_{n-q+1}}(\cdot)), \ldots, g_{r_q}(e_{r_q}(\cdot)))^T$, and $g(\vartheta_2) = (g_{r_{q+1}}(e_{r_{q+1}}(\cdot)), \ldots, g_{r_n}(e_{r_n}(\cdot)))^T$. After expanding the error state, NN (4) can be rewritten as

$$\begin{cases} \dot{\vartheta}(t) = -\begin{pmatrix} A_{11} & A_{12} & A_{13} \\ A_{21} & A_{22} & A_{23} \\ A_{31} & A_{32} & A_{33} \end{pmatrix} \begin{pmatrix} \vartheta_1^1(t) \\ \vartheta_1^2(t) \\ \vartheta_2(t) \end{pmatrix} + \begin{pmatrix} B_{11} & B_{12} & B_{13} \\ B_{21} & B_{22} & B_{23} \\ B_{31} & B_{32} & B_{33} \end{pmatrix} \begin{pmatrix} \vartheta_1^1(t-\tau(t)) \\ \vartheta_1^2(t-\tau(t)) \\ \vartheta_2(t-\tau(t)) \end{pmatrix} \\ + \begin{pmatrix} C_{11} & C_{12} & C_{13} \\ C_{21} & C_{22} & C_{23} \\ C_{31} & C_{32} & C_{33} \end{pmatrix} \begin{pmatrix} g\left(\vartheta_1^1(t)\right) \\ g\left(\vartheta_1^2(t)\right) \\ g(\vartheta_2(t)) \end{pmatrix} + \begin{pmatrix} D_{11} & D_{12} & D_{13} \\ D_{21} & D_{22} & D_{23} \\ D_{31} & D_{32} & D_{33} \end{pmatrix} \begin{pmatrix} g\left(\vartheta_1^1(t-\tau(t))\right) \\ g\left(\vartheta_1^2(t-\tau(t))\right) \\ g(\vartheta_2 = (t-\tau(t))) \end{pmatrix}, \\ \vartheta(t) = K_\vartheta \vartheta(t^- - \eta_k), \quad t = t_k, \\ \vartheta(s) = \theta_\vartheta(s) - \phi_\vartheta(s-d), \quad s \in [(-\tau+d)\wedge(-\eta+d), d], \end{cases} \tag{12}$$

where $\vartheta_1^1, \vartheta_1^2 \in \vartheta_1$ and ϑ_1 denote measurable state of the neuron and ϑ_2 denote unmeasurable state of the neuron. Compared with the traditional impulsive controller, in this article, unmeasurable and measurable state information are discussed. In other words, state information can be divided into unmeasurable state and measurable state information by transformation matrix. Therefore, we can obtain the control gain matrix as below:

$$K_\wp = \begin{pmatrix} k_1^1 & 0 & 0 \\ 0 & k_1^2 & 0 \\ k_2 & 0 & 0 \end{pmatrix}, \tag{13}$$

where k_1^1, k_1^2, and k_2 are real matrices. When $q > n - q$, this means that the dimension of the measurable state may be greater than that of the unmeasurable state. When $q > n - q$, extend the dimension of ϑ_1^2 to the dimension of unmeasurable state ϑ_2, then we get $\overline{\vartheta}_2 = (\vartheta_2^T, \vartheta_1^{2T})^T$. Redefine variables after dimension expansion, then one has $\overline{\vartheta} = (\overline{\vartheta}_1^T, \overline{\vartheta}_2^T)^T$, $\overline{\vartheta}_1 = \vartheta_1$, $g(\overline{\vartheta}_1(\cdot)) = (g(\vartheta_1^1(\cdot))^T, g(\vartheta_1^2(\cdot))^T)$, $g(\overline{\vartheta}_2(\cdot)) = (g(\vartheta_2(\cdot))^T, g(\vartheta_1^2(\cdot))^T)$, which means that $\overline{\vartheta}_1$, $\overline{\vartheta}_2$ have the same dimension. Hence, NN (6) can be indicated as follows:

$$\begin{cases} \overline{\vartheta} = -\overline{A}\overline{\vartheta}(t) + \overline{B}\overline{\vartheta}(t-\tau(t)) + \overline{C}g(\overline{\vartheta}(t)) + \overline{D}g(\overline{\vartheta}(t-\tau(t))), \quad t \ne t_k, \\ \overline{\vartheta}(t) = \overline{K}\overline{\vartheta}(t^- - \eta_k), \quad t = t_k, \\ \overline{\vartheta}(s) = \overline{\varphi}(s) - \overline{\phi}(s-d), \quad s \in [(-\tau+d)\wedge(-\eta+d), d], \end{cases} \tag{14}$$

where

$$\begin{aligned}
&\overline{A}=\begin{pmatrix}\overline{A}_{11} & \overline{A}_{12}\\ \overline{A}_{21} & \overline{A}_{22}\end{pmatrix},\overline{B}=\begin{pmatrix}\overline{B}_{11} & \overline{B}_{12}\\ \overline{B}_{21} & \overline{B}_{22}\end{pmatrix},\overline{C}=\begin{pmatrix}\overline{C}_{11} & \overline{C}_{12}\\ \overline{C}_{21} & \overline{C}_{22}\end{pmatrix},\overline{D}=\begin{pmatrix}\overline{D}_{11} & \overline{D}_{12}\\ \overline{D}_{21} & \overline{D}_{22}\end{pmatrix},\\
&\overline{A}_{11}=\begin{pmatrix}A_{11} & A_{12}\\ A_{21} & A_{22}\end{pmatrix},\overline{A}_{12}=\begin{pmatrix}A_{13} & 0\\ A_{23} & 0\end{pmatrix},\overline{A}_{21}=\begin{pmatrix}A_{31} & A_{32}\\ A_{21} & A_{22}\end{pmatrix},\overline{A}_{22}=\begin{pmatrix}A_{33} & 0\\ A_{23} & 0\end{pmatrix},\\
&\overline{B}_{11}=\begin{pmatrix}B_{11} & B_{12}\\ B_{21} & B_{22}\end{pmatrix},\overline{B}_{12}=\begin{pmatrix}B_{13} & 0\\ B_{23} & 0\end{pmatrix},\overline{B}_{21}=\begin{pmatrix}B_{31} & B_{32}\\ B_{21} & B_{22}\end{pmatrix},\overline{B}_{22}=\begin{pmatrix}B_{33} & 0\\ B_{23} & 0\end{pmatrix},\\
&\overline{C}_{11}=\begin{pmatrix}C_{11} & C_{12}\\ C_{21} & C_{22}\end{pmatrix},\overline{C}_{12}=\begin{pmatrix}C_{13} & 0\\ C_{23} & 0\end{pmatrix},\overline{C}_{21}=\begin{pmatrix}C_{31} & C_{32}\\ C_{21} & C_{22}\end{pmatrix},\overline{C}_{22}=\begin{pmatrix}C_{33} & 0\\ C_{23} & 0\end{pmatrix},\\
&\overline{D}_{11}=\begin{pmatrix}D_{11} & D_{12}\\ D_{21} & D_{22}\end{pmatrix},\overline{D}_{12}=\begin{pmatrix}D_{13} & 0\\ D_{23} & 0\end{pmatrix},\overline{D}_{21}=\begin{pmatrix}D_{31} & D_{32}\\ D_{21} & D_{22}\end{pmatrix},\overline{D}_{22}=\begin{pmatrix}D_{33} & 0\\ D_{23} & 0\end{pmatrix}.
\end{aligned} \tag{15}$$

It can be seen that measurable state $\overline{\vartheta}_1$ and unmeasurable state $\overline{\vartheta}_2$ of NN (12) have the same dimension. Therefore, the lag synchronization problem of partial unmeasured time-varying delay NNs can be studied under delayed impulsive control, and control gain matrix $\overline{K}\in R^{2q\times 2q}$ is shown below:

$$\overline{K}=\begin{pmatrix}K_1 & 0\\ K_2 & 0\end{pmatrix}, \tag{16}$$

where $K_1=\begin{pmatrix}k_1^1 & 0\\ 0 & k_1^2\end{pmatrix}, K_2=\begin{pmatrix}k_2 & 0\\ 0 & k_1^2\end{pmatrix}$. Then, the error dynamical system is given as

$$\begin{cases}\overline{\vartheta}=-\overline{A}\overline{\vartheta}(t)+\overline{B}\overline{\vartheta}(t-\tau(t))+\overline{C}g(\overline{\vartheta}(t))+\overline{D}g(\overline{\vartheta}(t-\tau(t))), & t\neq t_k,\\ \overline{\vartheta}_1(t)=K_1\overline{\vartheta}_1(t^- -\eta_k), & t=t_k,\\ \overline{\vartheta}_2(t)=K_2\overline{\vartheta}_1(t^- -\eta_k), & t=t_k,\\ \overline{\vartheta}(s)=\overline{\theta}(s)-\overline{\phi}(s-d), & s\in[(-\tau+d)\wedge(-\eta+d),d].\end{cases} \tag{17}$$

Theorem 1. *Assume that Hypothesis 1 is satisfied, there exist $(n-q)\times(n-q)$ real matrices $N_1>0,\Phi_1>0,\Psi_{11},\Psi_{21}$, $(2q-n)\times(2q-n)$ real matrices $N_2>0,\Phi_2>0,\Psi_{12},\Psi_{22}, 2q\times 2q$ diagonal matrices $U_1>0,U_2>0$, and $\gamma>0,\delta>0,\beta>1,p>0,\alpha>0$ are constants sufficing*

$$\begin{aligned}
&\alpha+|\lambda|+\beta\delta e^{\alpha\tau}<\frac{\ln\beta}{p},\\
&\begin{pmatrix}\Omega & \Upsilon\overline{C} & \Upsilon\overline{D}\\ \star & -U_1 & 0\\ \star & \star & -U_2\end{pmatrix}\leq 0,\\
&\overline{B}^T\Upsilon+\Upsilon\overline{B}+LU_2L-\delta\Upsilon\leq 0,\\
&\begin{pmatrix}-\overline{\beta}N & \Psi_1 & \Psi_2\\ \star & -N & 0\\ \star & \star & -\Phi\end{pmatrix}\leq 0,
\end{aligned} \tag{18}$$

where $\overline{\beta}=\beta^{-1}e^{-\alpha\eta}$ and

$$\begin{aligned}
&N=\mathrm{diag}\{N_1,N_2\},\Omega\\
&L=\mathrm{diag}\left\{l_{r_1},\ldots,l_{r_q},l_{r_{q+1}},\ldots,l_{r_n},l_{r_{n-q+1}},\ldots,l_{r_q}\right\},\\
&\Phi=\mathrm{diag}\{\Phi_1,\Phi_2\},\Upsilon\\
&\Psi_1=\mathrm{diag}\{\Psi_{11},\Psi_{12}\},\Psi_2
\end{aligned} \tag{19}$$

This signifies that NN (2) is globally lag synchronized with the drive NN (1) for

$$K=T^{-1}\begin{pmatrix}N_1^{-1}\Psi_{11}^T & 0 & 0\\ 0 & N_2^{-1}\Psi_{12}^T & 0\\ \Phi_1^{-1}\Psi_{21}^T+N_1^{-1}\Psi_{11}^T & 0 & 0\end{pmatrix}T, \tag{20}$$

in Θ_d, where real matrix T is $n\times n$.

Proof. Consider Lyapunov functions

$$\begin{aligned}
V(t)&=\overline{\vartheta}_1^T(t)N\overline{\vartheta}_1(t)+\left(\overline{\vartheta}_2(t)-\overline{\vartheta}_1(t)\right)^T\Phi\left(\overline{\vartheta}_2(t)-\overline{\vartheta}_1(t)\right)\\
&=\overline{\vartheta}(t)Y\overline{\vartheta}(t).
\end{aligned} \tag{21}$$

When $t\in[t_{k-1},t_k)$, taking the derivative of $V(t)$ in NN (14), we can get

$$\begin{aligned}\dot{V}(t) &= \dot{\overline{\vartheta}}(t)^T \Upsilon \overline{\vartheta}(t) + \overline{\vartheta}(t)^T \Upsilon \dot{\overline{\vartheta}}(t) \\ &= \overline{\vartheta}(t)^T \left(-\overline{A}^T \Upsilon - \Upsilon \overline{A}\right) \overline{\vartheta}(t) + \overline{\vartheta}(t-\tau(t))^T \\ &\quad \left(\overline{B}^T \Upsilon + \Upsilon \overline{B}\right) \overline{\vartheta}(t-\tau(t)) \\ &\quad + 2\overline{\vartheta}(t)^T \Upsilon \overline{C} g(\overline{\vartheta}(t)) + 2\overline{\vartheta}(t)^T \Upsilon \overline{D} g(\overline{\vartheta}(t-\tau(t))).\end{aligned} \tag{22}$$

According to Hypothesis 1 and Lemma 2, we can get

$$\begin{aligned}&2\overline{\vartheta}(t)^T \Upsilon \overline{C} g(\overline{\vartheta}(t)) \\ &\le \overline{\vartheta}(t)^T \Upsilon \overline{C} U_1^{-1} \overline{C}^T \Upsilon \overline{\vartheta}(t) + g^T(\overline{\vartheta}(t)) U_1 g(\overline{\vartheta}(t)) \\ &\le \overline{\vartheta}(t)^T \Upsilon \overline{C} U_1^{-1} \overline{C}^T \Upsilon \overline{\vartheta}(t) + \overline{\vartheta}^T(t) L U_1 L \overline{\vartheta}(t), \\ &2\overline{\vartheta}(t)^T \Upsilon \overline{D} g(\overline{\vartheta}(t-\tau(t))) \\ &\le \overline{\vartheta}^T(t) \Upsilon \overline{D} U_2^{-1} \overline{D}^T \Upsilon \overline{\vartheta}(t) + g^T(\overline{\vartheta}(t-\tau(t))) U_2 g(\overline{\vartheta}(t-\tau(t))) \\ &\le \overline{\vartheta}(t)^T \Upsilon \overline{D} U_2^{-1} \overline{D}^T \Upsilon g(\overline{\vartheta}(t)) + \overline{\vartheta}^T(t-\tau(t)) L U_2 L \overline{\vartheta}(t-\tau(t)).\end{aligned} \tag{23}$$

Substituting the above inequality into (19), considering inequalities (16) and (17), we obtain

$$\begin{aligned}\dot{V}(t) &\le \dot{\overline{\vartheta}}(t)^T \left(-A^T \Upsilon - \Upsilon A + L U_1 L + \Upsilon \overline{C} U_1^{-1} \overline{C}^T \Upsilon + \Upsilon \overline{D} U_2^{-1} \overline{D}^T \Upsilon\right) \overline{\vartheta}(t) \\ &\quad + \overline{\vartheta}^T(t-\tau(t)) \left(\overline{B}^T \Upsilon + \Upsilon \overline{B} + L U_2 L\right) \overline{\vartheta}(t-\tau(t)) \\ &\le \lambda \overline{\vartheta}^T(t) \Upsilon \overline{\varpi}(t) + \delta \overline{\vartheta}^T(t-\tau(t)) \Upsilon \overline{\vartheta}(t-\tau(t)).\end{aligned} \tag{24}$$

When $t = t_k$, by (11), we can get

$$\begin{aligned}V(t_k^+) &= \overline{\vartheta}_1(t_k - \eta_k)^T K_1^T N K_1 \overline{\vartheta}_1(t_k - \eta_k) \\ &\quad + \overline{\vartheta}_1(t_k - \eta_k)^T (K_2 - K_1)^T \Phi (K_2 - K_1) \overline{\vartheta}_1(t_k - \eta_k) \\ &\le (\beta e^{\alpha\eta})^{-1} V(t_k^- - \eta_k).\end{aligned} \tag{25}$$

Considering the inequality in the condition, and using Lemma 1, we can get

$$V(t) \le \beta \sup_{\overline{s} \le s \le d} V(s) e^{-\alpha t}, \tag{26}$$

which implies that

$$|\vartheta(t)| \le \sqrt{\frac{\beta \lambda_{\max}(Y)}{\lambda_{\min}(Y)}} \vartheta(d) \exp\left(-\frac{\alpha}{2} t\right), \quad t \ge t_0, \tag{27}$$

where $\vartheta(d) = \sup_{\overline{s} \le s \le d} \vartheta(s), \overline{s} = (-\tau + d) \wedge (-\eta + d)$. From the above proof, it follows that error NN (17) converges exponentially to zero. That is, the coupled NN with time-varying delay achieves lag synchronization. The proof has been completed. □

Case 2. The number of set H is less than or equal the number of set G; i.e., $q \le n - q$.

Then we consider the lag synchronization of NNs with time-varying delayed impulsive control, under the $q \le n - q$. Considering error sates ϑ, set $\vartheta = (\vartheta_1^T, \vartheta_2^T)^T$, $\vartheta_1 = (e_{r_1}, \ldots, e_{r_q})^T, \vartheta_2 = (\vartheta_2^{1T}, \vartheta_2^{2T})^T, \vartheta_2^1 = (e_{r_{n-q+1}}, \ldots, e_{r_{2q}})^T$, $\vartheta_2^2 = (e_{r_{2q+1}}, \ldots, e_{r_n})^T$, $g(\vartheta_1(\cdot)) = (g_{r_1}(e_{r_1}(\cdot)), \ldots, g_{r_q}(e_{r_q}(\cdot)))^T$, $g(\vartheta_2^1) = (g_{r_{q+1}}(e_{r_{q+1}}(\cdot)), \ldots, g_{r_{2q}}(e_{r_{2q}}(\cdot)))^T$, and $g(\vartheta_2^2) = (g_{r_{2q+1}}(e_{r_{2q+1}}(\cdot)), \ldots, g_{r_n}(e_{r_n}(\cdot)))^T ss$. After expanding the error state, NN (4) can be rewritten as

$$\begin{cases}\dot{\vartheta}(t) = -\begin{pmatrix} A_{11} & A_{12} & A_{13} \\ A_{21} & A_{22} & A_{23} \\ A_{31} & A_{32} & A_{33} \end{pmatrix} \begin{pmatrix} \vartheta_1(t) \\ \vartheta_2^1(t) \\ \vartheta_2^2(t) \end{pmatrix} + \begin{pmatrix} B_{11} & B_{12} & B_{13} \\ B_{21} & B_{22} & B_{23} \\ B_{31} & B_{32} & B_{33} \end{pmatrix} \begin{pmatrix} \vartheta_1(t-\tau(t)) \\ \vartheta_2^1(t-\tau(t)) \\ \vartheta_2^2(t-\tau(t)) \end{pmatrix} \\ + \begin{pmatrix} C_{11} & C_{12} & C_{13} \\ C_{21} & C_{22} & C_{23} \\ C_{31} & C_{32} & C_{33} \end{pmatrix} \begin{pmatrix} g(\vartheta_1(t)) \\ g(\vartheta_2^1(t)) \\ g(\vartheta_2^2(t)) \end{pmatrix} + \begin{pmatrix} D_{11} & D_{12} & D_{13} \\ D_{21} & D_{22} & D_{23} \\ D_{31} & D_{32} & D_{33} \end{pmatrix} \begin{pmatrix} g(\vartheta_1(t-\tau(t))) \\ g(\vartheta_2^1(t-\tau(t))) \\ g(\vartheta_2^2(t-\tau(t))) \end{pmatrix}, \\ \vartheta(t) = K_\vartheta \vartheta(t^- - \eta_k), \quad t = t_{k,} \\ \vartheta(s) = \theta_\vartheta(s) - \phi_\vartheta(s-d), \quad s \in [(-\tau + d) \wedge (-\eta + d), d],\end{cases} \tag{28}$$

where $\vartheta_2^1, \vartheta_2^2 \in \vartheta_2$, since $q \le n-q$, and the control gain matrix is shown below:

$$K_\vartheta = \begin{pmatrix} k_1 & 0 & 0 \\ k_2^1 & 0 & 0 \\ 0 & k_2^2 & 0 \end{pmatrix}, \tag{29}$$

where k_1, k_2^1, and k_2^2 are real matrices. When $q \le n-q$, this means that the dimension of measurable state may be smaller than the value of unmeasurable state. For the sake of easy, the dimension of measurable state is extended to ϑ_1 part of measurable state e_{r_q}, and then we get $\tilde{\vartheta}_1 = (\vartheta_1^T, \hat{\vartheta}_1^T)^T$, where $\hat{\vartheta}_1 = (e_{r_q}, e_{r_q}, \ldots, e_{r_q})^T$. So, we can get $\tilde{\vartheta} = (\tilde{\vartheta}_1^T, \tilde{\vartheta}_2^T)^T, \tilde{\vartheta}_2 = \vartheta_2, g(\tilde{\vartheta}_1(\cdot)) = s(g(\vartheta_1(\cdot))^T, g(\hat{\vartheta}_1(\cdot))^T)^T$, $g(\tilde{\vartheta}_2(\cdot)) = g(\vartheta_2(\cdot))$, which means that $\tilde{\vartheta}_1$ and $\tilde{\vartheta}_2$ have the same dimension. When $q = n-q$, that is, H has the same dimension as G, $\tilde{\vartheta}_1 = \vartheta_1$ and $\tilde{\vartheta}_2 = \vartheta_2$. Hence, NN (26) can be indicated as follows:

$$\begin{cases} \dot{\tilde{\vartheta}} = -\tilde{A}\tilde{\vartheta}(t) + \tilde{B}\tilde{\vartheta}(t-\tau(t)) + \tilde{C}g(\tilde{\vartheta}(t)) + \tilde{D}g(\tilde{\vartheta}(t-\tau(t))), & t \ne t_k, \\ \tilde{\vartheta}(t) = \tilde{K}\tilde{\vartheta}(t^- - \eta_k), & t = t_k, \\ \tilde{\vartheta}(s) = \tilde{\theta}(s) - \tilde{\phi}(s-d), & s \in = [(-\tau+d)\wedge(-\eta+d), d], \end{cases} \tag{30}$$

where

$$\begin{aligned} &\tilde{A} = \begin{pmatrix} \tilde{A}_{11} & \tilde{A}_{12} \\ \tilde{A}_{21} & \tilde{A}_{22} \end{pmatrix}, \tilde{B} = \begin{pmatrix} \tilde{B}_{11} & \tilde{B}_{12} \\ \tilde{B}_{21} & \tilde{B}_{22} \end{pmatrix}, \tilde{C} = \begin{pmatrix} \tilde{C}_{11} & \tilde{C}_{12} \\ \tilde{C}_{21} & \tilde{C}_{22} \end{pmatrix}, \tilde{D} = \begin{pmatrix} \tilde{D}_{11} & \tilde{D}_{12} \\ \tilde{D}_{21} & \tilde{D}_{22} \end{pmatrix}, \\ &\tilde{A}_{11} = \begin{pmatrix} A_{11} & 0 \\ \hat{A}_1 & 0 \end{pmatrix}, \tilde{A}_{12} = \begin{pmatrix} A_{12} & A_{13} \\ \hat{A}_2 & \hat{A}_3 \end{pmatrix}, \tilde{A}_{21} = \begin{pmatrix} A_{21} & 0 \\ A_{31} & 0 \end{pmatrix}, \tilde{A}_{22} = \begin{pmatrix} A_{22} & A_{23} \\ A_{32} & A_{33} \end{pmatrix}, \\ &\tilde{B}_{11} = \begin{pmatrix} B_{11} & 0 \\ \hat{B}_1 & 0 \end{pmatrix}, \tilde{B}_{12} = \begin{pmatrix} B_{12} & B_{13} \\ \hat{B}_2 & \hat{B}_3 \end{pmatrix}, \tilde{B}_{21} = \begin{pmatrix} B_{21} & 0 \\ B_{31} & 0 \end{pmatrix}, \tilde{B}_{22} = \begin{pmatrix} B_{22} & B_{23} \\ B_{32} & B_{33} \end{pmatrix}, \\ &\tilde{C}_{11} = \begin{pmatrix} C_{11} & 0 \\ \hat{C}_1 & 0 \end{pmatrix}, \tilde{C}_{12} = \begin{pmatrix} C_{12} & C_{13} \\ \hat{C}_2 & \hat{C}_3 \end{pmatrix}, \tilde{C}_{21} = \begin{pmatrix} C_{21} & 0 \\ C_{31} & 0 \end{pmatrix}, \tilde{C}_{22} = \begin{pmatrix} C_{22} & C_{23} \\ C_{32} & C_{33} \end{pmatrix}, \\ &\tilde{D}_{11} = \begin{pmatrix} D_{11} & 0 \\ \hat{D}_1 & 0 \end{pmatrix}, \tilde{D}_{12} = \begin{pmatrix} D_{12} & D_{13} \\ \hat{D}_2 & \hat{D}_3 \end{pmatrix}, \tilde{D}_{21} = \begin{pmatrix} D_{21} & 0 \\ D_{31} & 0 \end{pmatrix}, \tilde{D}_{22} = \begin{pmatrix} D_{22} & D_{23} \\ D_{32} & D_{33} \end{pmatrix}, \\ &\hat{A}_1 = \begin{pmatrix} a_{r_{q,1}} & \cdots & a_{r_{q,q}} \\ \vdots & \vdots & \vdots \\ a_{r_{q,1}} & \cdots & a_{r_{q,q}} \end{pmatrix}, \hat{A}_2 = \begin{pmatrix} a_{r_{q,q+1}} & \cdots & a_{r_{q,2q}} \\ \vdots & \vdots & \vdots \\ a_{r_{q,q+1}} & \cdots & a_{r_{q,2q}} \end{pmatrix}, \hat{A}_3 = \begin{pmatrix} a_{r_{q,2q+1}} & \cdots & a_{r_{q,n}} \\ \vdots & \vdots & \vdots \\ a_{r_{q,2q+1}} & \cdots & a_{r_{q,n}} \end{pmatrix}, \end{aligned} \tag{31}$$

and $\hat{B}_i, \hat{C}_i, \hat{D}_i, i = 1, 2, 3$, similar to $\hat{A}_1, \hat{A}_2, \hat{A}_3$.

The control gain matrix $\tilde{K}$ is shown below:

$$\tilde{K} = \begin{pmatrix} K_1 & 0 \\ K_2 & 0 \end{pmatrix}, \tag{32}$$

where $\hat{k}_1$ is a real matrix, $K_1 = \begin{pmatrix} k_1 & 0 \\ 0 & \hat{k}_1 \end{pmatrix}$, and $K_2 = \begin{pmatrix} k_2^1 & 0 \\ 0 & k_2^2 \end{pmatrix}$.

Then, the error dynamical system is given as

$$\begin{cases} \dot{\tilde{\vartheta}} = -\tilde{A}\tilde{\vartheta}(t) + \tilde{B}\tilde{\vartheta}(t-\tau(t)) + \tilde{C}g(\tilde{\vartheta}(t)) + \tilde{D}g(\tilde{\vartheta}(t-\tau(t))), & t \ne t_k, \\ \tilde{\vartheta}_1(t) = K_1\tilde{\vartheta}_1(t^- - \eta_k), & t = t_k, \\ \tilde{\vartheta}_2(t) = K_2\tilde{\vartheta}_1(t^- - \eta_k), & t = t_k, \\ \tilde{\vartheta}(s) = \tilde{\varphi}(s) - \tilde{\phi}(s-d), & s \in [(-\tau+d)\wedge(-\eta+d), d]. \end{cases} \tag{33}$$

Theorem 2. *Assume that Hypothesis 1 is satisfied, there exist $q \times q$ real matrices $N_1 > 0, \Phi_1 > 0, \Psi_{11}, \Psi_{21}$, $(n-2q) \times (n-2q)$ real matrices $N_2 > 0, \Phi_2 > 0, \Psi_{12}, \Psi_{22}, 2(n-q) \times 2(n-q)$ diagonal matrices $U_1 > 0, U_2 > 0$, and $\gamma > 0, \delta > 0, \beta > 1, p > 0, \alpha > 0$ are constants sufficing*

$$\alpha + |\lambda| + \beta\delta e^{\alpha\tau} < \frac{\ln\beta}{p},$$

$$\begin{pmatrix} \Omega & \Upsilon\overline{C} & \Upsilon\overline{D} \\ \star & -U_1 & 0 \\ \star & \star & -U_2 \end{pmatrix} \leq 0,$$

$$\overline{B}^T\Upsilon + \Upsilon\overline{B} + LU_2L - \delta\Upsilon \leq 0, \tag{34}$$

$$\begin{pmatrix} -\overline{\beta}N & \Psi_1 & \Psi_2 \\ \star & -N & 0 \\ \star & \star & -\Phi \end{pmatrix} \leq 0,$$

where $\overline{\beta} = \beta^{-1}e^{-\alpha\eta}$, and

$$\begin{aligned} &N = \operatorname{diag}\{N_1, N_2\}, \Omega = -A^T\Upsilon - \Upsilon A - \lambda\Upsilon + LU_1L, \\ &L = \operatorname{diag}\left\{1_{r_1}, \ldots, 1_{r_q}, 1_{r_q}, \ldots, 1_{r_q}, 1_{r_{n-q+1}}, \ldots, 1_{r_n}\right\}, \\ &\Phi = \operatorname{diag}\{\Phi_1, \Phi_2\}, \Upsilon = \begin{pmatrix} N+\Phi & -\Phi \\ -\Phi & \Phi \end{pmatrix}, \\ &\Psi_1 = \operatorname{diag}\{\Psi_{11}, \Psi_{12}\}, \Psi_2 = \operatorname{diag}\{\Psi_{21}, \Psi_{22}\}. \end{aligned} \tag{35}$$

Then, it signifies that NN (2) is globally lag synchronized with the drive NN (1) for

$$K = T^{-1}\begin{pmatrix} N_1^{-1}\Psi_{11}^T & 0 & 0 \\ \Phi_1^{-1}\Psi_{21}^T + N_1^{-1}\Psi_{11}^T & 0 & 0 \\ 0 & \Phi_2^{-1}\Psi_{22}^T + N_2^{-1}\Psi_{12}^T & 0 \end{pmatrix}T, \tag{36}$$

over the class Θ_d, where real matrix T is $n \times n$.

Proof. Similarly, the proof of Theorem 2 is similar to Theorem 1. □

Remark 2. Compared with the general time delay NN, due to the complex structure of NN, it is particularly difficult to design delayed impulsive control for time-varying delay NNs, so in order to overcome this problem, this article designs two controllers, which make it easier to monitor the measurable status of the impulsive time information. In other words, when the state of the NN is not measurable, the information of the instantaneous measurable state can also be adopted through impulsive control.

Remark 3. Throughout the article, we solve the global lag synchronization problem on different dimensions of measurable and unmeasurable states using Theorems 1 and 2. It can be seen from this article that, in Theorem 1, when the dimension of the measurable state is greater than that of the unmeasurable state, we extend the dimension of the unmeasurable state and get lag synchronization; in Theorem 2, the dimension of the measurable state is less than the unmeasurable state, and we obtain the lag synchronization result by extending the dimension of the measurable state.

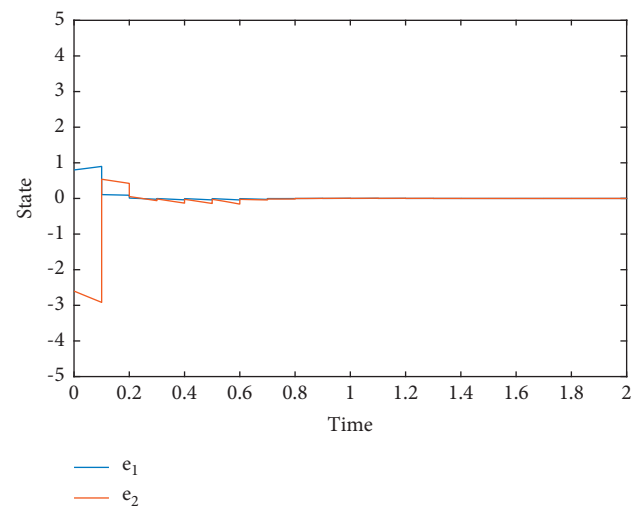

Figure 1: The trajectory of an error NN (12) with control inputs.

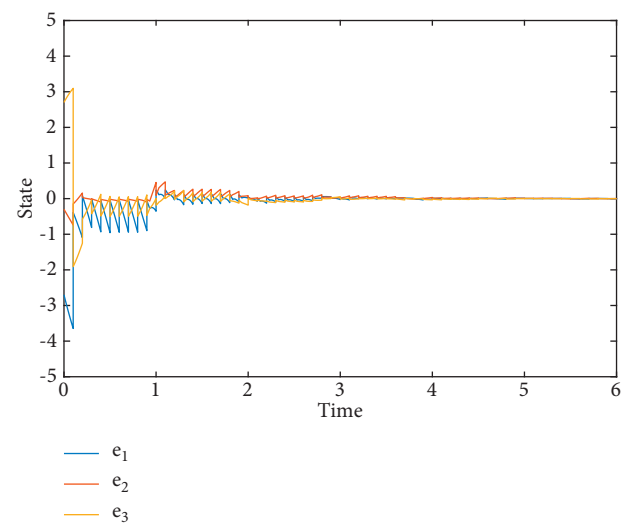

Figure 2: The trajectory of an error NN (26) with control inputs.

Remark 4. In [11], LMI is used to derive some sufficient conditions for lag synchronization of NNs with time-delayed. However, studies on NNs with time-varying delays are excluded. Our results not only study the lag synchronization of NNs with time-varying delays but also relax the restrictions on upper and lower bounds, which greatly reduces the time to reach the lag synchronization.

4. Examples

At last, a 2D and a 3D example are used to verify the main results of this article.

Example 1. Consider the 2D autonomous time-varying delay NNs

$$\begin{cases} \dot{z}(t) = -Az(t) + Bz(t-\tau(t)) + Cf(z(t)) + Df(z(t-\tau(t))) + J, \quad t > 0 \\ z(s) = \phi(s), \quad s \in [-\tau, 0], \end{cases} \tag{37}$$

where $A = B = I, f_1 = f_2 = \tanh(s), \tau(t) = 1/2|\cos(t)|$ and

$$C = \begin{pmatrix} 3.0 & -0.1 \\ -4.0 & 2.0 \end{pmatrix}, \quad D = \begin{pmatrix} -2.0 & -0.2 \\ -0.1 & 1.5 \end{pmatrix}. \tag{38}$$

In the simulation, the initial values of NN (36) are set as $\phi = (0.5, 0.8)^T$. The response NN is as follows:

$$\begin{cases} \dot{w}(t) = -Aw(t) + Bw(t-\tau(t)) + Cf(w(t)) \\ +Df(w(t-\tau(t))) + I + u(t), \quad t > d, \\ w(s) = \theta(s), \quad s \in [-\tau + d, d], \end{cases} \tag{39}$$

where the initial conditions of NN (37) are set as $\theta(s) = (1.3, -1.8)^T, d = 1$. The error dynamical system is given as

$$\begin{cases} \dot{e}(t) = -Ae(t) + Be(t-\tau(t)) + Cg(e(t)) + Dg(e(t-\tau(t))) + u(t), \quad t > d \\ e(t) = Ke(t^- - \eta_k), \quad t = t_k, \\ e(s) = \theta(s) - \phi(s-d), \quad s \in [(-\tau + d) \wedge (-\eta + d), d], \end{cases} \tag{40}$$

where $K = \begin{pmatrix} 0.1286 & 0 \\ 0.678 & 0 \end{pmatrix}, \sup_{k \in Z_+}\{t_k - t_{k-1}\} = 0.1, \eta_k = 0.03$.

Let $\alpha = 0.02, \lambda = 11, \delta = 1, \beta = 15$. According to Theorem 3.1, via solving the LMI matrix, we can get

$$\begin{aligned} \Upsilon &= \begin{pmatrix} 7.7063 & -0.0799 \\ -0.0799 & 0.0799 \end{pmatrix}, \\ U_1 &= \begin{pmatrix} 39.2851 & 0 \\ 0 & 39.2851 \end{pmatrix} \\ U_2 &= \begin{pmatrix} 21.3584 & 0 \\ 0 & 21.3584 \end{pmatrix}, \\ \Psi_1 &= 1.0714, \\ \Psi_2 &= 0.0954. \end{aligned} \tag{41}$$

In the example, the condition in Theorem 1 holds, so on the basis of Theorem 1, NNs with time-varying delays are lag synchronization.

Then the numerical simulation is shown in Figure 1.

Example 2. Consider the 3D autonomous time-varying delayed NNs involving unmeasurable states w_1 and w_3 with

$$C = \begin{pmatrix} 1.3 & -3 & -3 \\ -3 & 1.2 & -4.5 \\ -3 & 4.5 & 1.5 \end{pmatrix}, \quad D = \begin{pmatrix} 6.5 & -8 & -3 \\ -2.8 & 1.4 & -5 \\ -3 & -4.6 & -2.5 \end{pmatrix}. \tag{42}$$

According to Theorem 2, it can be known that the number of measurable states is less than or equal to that of unmeasurable states. In order to get same dimensions, the impulsive control gain matrix is designed by

$$K = \begin{pmatrix} 0 & 0.5236 & 0 \\ 0 & 0.1997 & 0 \\ 0.5236 & 0 & 0 \end{pmatrix}, \tag{43}$$

where $A = B = I, \tau(t) = 1/2|\sin t| + 1/3, f_1 = f_2 = f_3 = \tanh(s), \phi = (0.2, 0.2, -0.4)^T, \theta = (-0.5, 0.5, 0.3)^T$, and Θ_d: $t_{2n-1} = 0.04n + 0.4, t_{2n} = 0.04n + 0.5$. So, we can easily get

$$T = \begin{pmatrix} 0 & 1 & 0 \\ 1 & 0 & 0 \\ 0 & 0 & 1 \end{pmatrix}. \tag{44}$$

The error system is transformed to

$$\begin{cases} \dot{\vartheta}(t) = -A_\vartheta \vartheta(t) + B_\vartheta \vartheta(t-\tau(t)) + C_\vartheta g(\vartheta(t)) + D_\vartheta g(\vartheta(t-\tau(t))), \quad t \neq t_k, \\ \vartheta(t) = K_\vartheta \vartheta(t^- - \eta_k), \quad t = t_k, \\ \vartheta(s) = \theta_\vartheta(s) - \phi_\vartheta(s-d), \quad s \in [(-\tau + d) \wedge (-\eta + d), d], \end{cases} \tag{45}$$

where $\vartheta = (\vartheta_1, \vartheta_2)^T, \vartheta_1 = x_2,$ and $\vartheta_2 = (\vartheta_2^1, \vartheta_2^1)^T = (x_1, x_3)^T,$

$$C_\vartheta = \begin{pmatrix} 1.2 & -3.0 & -4.5 \\ -3.0 & 1.3 & -3.0 \\ 4.5 & -3.0 & 1.5 \end{pmatrix}, D_\vartheta = \begin{pmatrix} 1.4 & -2.8 & -5 \\ -8 & 6.5 & -3 \\ 4.6 & -3 & -2.5 \end{pmatrix}, K_\vartheta = \begin{pmatrix} 0.1997 & 0 & 0 \\ 0.5236 & 0 & 0 \\ 0 & 0.5236 & 0 \end{pmatrix}. \tag{46}$$

Therefore, a new error system can be obtained

$$\begin{cases} \overline{\vartheta} = -\overline{A}\overline{\vartheta}(t) + \overline{B}\overline{\vartheta}(t-\tau(t)) + \overline{C}g(\overline{\vartheta}(t)) + \overline{D}g(\overline{\vartheta}(t-\tau(t))), & t \neq t_k, \\ \overline{\vartheta}_1(t) = K_1\overline{\vartheta}_1(t^- - \eta_k), & t = t_k, \\ \overline{\vartheta}_2(t) = K_2\overline{\vartheta}_1(t^- - \eta_k), & t = t_k, \\ \overline{\vartheta}(s) = \overline{\theta}(s) - \overline{\phi}(s-d), & s \in [(-\tau+d)\wedge(-\eta+d), d], \end{cases} \tag{47}$$

where

$$K_1 = \begin{pmatrix} 0.1997 & 0 \\ 0 & 0.1997 \end{pmatrix}, K_2 = \begin{pmatrix} 0.5236 & 0 \\ 0 & 0.5236 \end{pmatrix},$$
$$\widetilde{C} = \begin{pmatrix} 1.2 & 0 & -3.0 & -4.5 \\ 1.2 & 0 & -3.0 & -4.5 \\ -3 & 0 & 1.3 & -3.0 \\ 4.5 & 0 & -3.0 & 1.5 \end{pmatrix}, \widetilde{D} = \begin{pmatrix} 1.4 & 0 & -2.8 & -5 \\ 1.4 & 0 & -2.8 & -5 \\ -8 & 0 & 6.5 & -3 \\ 4.6 & 0 & -3 & -2.5 \end{pmatrix}. \tag{48}$$

Set $\alpha = 0.01, \lambda = 82, \delta = 7,$ and $\beta = 8$. From Example 1, similarly, we can see that it is not hard to check that LMI in Theorem 3 holds.

In the example, the condition in Theorem 2 holds, so on the basis of Theorem 2, NNs with time-varying delays are lag synchronization.

Then the numerical simulation is shown in Figure 2.

5. Concluding Remarks

Looking through the article, we study the synchronization problem of delay impulsive control for time-varying delay NNs. In this article, the measurable state and the unmeasurable state are separated by a transformation matrix. In Theorems 1 and 2, we use different methods to extend the dimension to obtain sufficient conditions for lag synchronization of NNs with time-varying delays derived from the control gain matrix. Finally, we also give two examples to confirm the validity of the theoretical results.

Data Availability

No data were used to support this study.

Conflicts of Interest

The authors declare that they have no conflicts of interest.

References

[1] L. K. Hansen and P. Salamon, "Neural network ensembles," *IEEE Transactions on Pattern Analysis and Machine Intelligence*, vol. 12, no. 10, pp. 993–1001, 1990.

[2] D. Psaltis and A. Sideris, "A multilayered neural network controller," *IEEE Control Systems Magazine*, vol. 8, no. 2, pp. 17–21, 1988.

[3] M. Shanker, M. Y. Hu, and M. S. Hung, "Effect of data standardization on neural network training," *Omega*, vol. 24, no. 4, pp. 385–397, 1996.

[4] W. Yu and J. Cao, "Adaptive synchronization and lag synchronization of uncertain dynamical system with time delay based on parameter identification," *Physica A: Statistical Mechanics and Its Applications*, vol. 375, no. 2, pp. 467–482, 2007.

[5] C. Xi and J. Dong, "Adaptive asymptotic tracking control of uncertain nonlinear time-delay systems depended on delay estimation information," *Applied Mathematics and Computation*, vol. 391, no. 15, Article ID 125662, 2021.

[6] H. Ren, P. Shi, F. Deng, and Y. Peng, "Fixed-time synchronization of delayed complex dynamical systems with stochastic perturbation via impulsive pinning control," *Journal of the Franklin Institute*, vol. 357, no. 17, pp. 12308–12325, 2020.

[7] Z. Dong, X. Zhang, and X. Wang, "Global exponential stability of discrete-time higher-order Cohen-Grossberg neural networks with time-varying delays, connection weights and impulses," *Journal of the Franklin Institute*, vol. 358, no. 11, pp. 5931–5950, 2021.

[8] Z. H. Guan, Z. W. Liu, G. Gang Feng, and Y. W. Wang, "Synchronization of complex dynamical networks with time-varying delays via impulsive distributed control," *IEEE Transactions on Circuits and Systems I: Regular Papers*, vol. 57, no. 8, pp. 2182–2195, 2010.

[9] X. Li, J. Fang, and H. Li, "Exponential adaptive synchronization of stochastic memristive chaotic recurrent neural networks with time-varying delays," *Neurocomputing*, vol. 267, no. 6, pp. 396–405, Dec. 2017.

[10] J. Chen, B. Chen, and Z. Zeng, "Exponential quasi-synchronization of coupled delayed memristive neural networks via intermittent event-triggered control," *Neural Networks*, vol. 141, pp. 98–106, Sep. 2021.

[11] M. Li, X. Yang, and X. Li, "Delayed impulsive control for lag synchronization of delayed neural networks involving partial unmeasurable states," *IEEE Transactions on Neural Networks and Learning Systems*, pp. 1–9, 2022.

[12] J. Lu, D. W. C. Ho, J. Cao, and J. Kurths, "Exponential synchronization of linearly coupled neural networks with impulsive disturbances," *IEEE Transactions on Neural Networks*, vol. 22, no. 2, pp. 329–336, 2011.

[13] J. Wang, C. Xu, M. Z. Q. Chen, J. Feng, and G. Chen, "Stochastic feedback coupling synchronization of networked harmonic oscillators," *Automatica*, vol. 87, pp. 404–411, 2018.

[14] J. Wang, H. Jiang, T. Ma, and C. Hu, "A new approach based on discrete-time high-order neural networks with delays and impulses," *Journal of the Franklin Institute*, vol. 355, no. 11, pp. 4708–4726, 2018.

[15] X. Yang, J. Cao, Y. Long, and W. Rui, "Adaptive lag synchronization for competitive neural networks with mixed delays and uncertain hybrid perturbations," *IEEE Transactions on Neural Networks*, vol. 21, no. 10, pp. 1656–1667, 2010.

[16] Z. Xu, X. Li, and P. Duan, "Synchronization of complex networks with time-varying delay of unknown bound via delayed impulsive control," *Neural Networks*, vol. 125, pp. 224–232, May 2020.

Hindawi
Discrete Dynamics in Nature and Society
Volume 2022, Article ID 2033708, 14 pages
https://doi.org/10.1155/2022/2033708

Research Article

Robustness Analysis of Control Laws in Complex Dynamical Networks Evoked by Deviating Argument

Biwen Lia, Jingjing Huang, and Donglun Wang

College of Mathematics and Statistics, Hubei Normal University, Huangshi 435002, China

Correspondence should be addressed to Biwen Lia; lbw20200320@163.com, Jingjing Huang; 1170823018@qq.com, and Donglun Wang; 2511393083@qq.com

Received 27 May 2022; Accepted 10 August 2022; Published 15 September 2022

Academic Editor: Guoguang Wen

In recent years, robust performance of the system has been broadly studied as a trending topic among a vast array of scholars. This paper discusses the robustness of control laws for complex dynamic networks (CDNs) with a deviation argument. We design two categories of control laws (linear control law and nonlinear control law) for the undisturbed CDNs to achieve exponential synchronization. It is intractable to ascertain the range of the deviation function exactly. Hence, some corresponding sufficient criteria are put forward to ensure exponential synchronization of CDNs with deviation argument when control laws are not changed. By adopting the Gronwall–Bellman lemma and solving the transcendental equation, we can obtain the admissible upper limits of the deviating function, to keep the corresponding control laws. In comparison with previous research findings, robustness, deviating argument, and control laws are all considered in this study, which enhances the previous findings. Finally, two emulation examples verify the validity of the analysis.

1. Introduction

More recently, as a vital component of the nonlinear system, CDNs have been broadly investigated and have found many potential applications in various domains, including biology, sociology, physics, network science, engineering, automatic control, and so on [1–3]. In particular, the dynamical behavior of complex systems has flourished vigorously in the field of control engineering, which has aroused tremendous interest among scholars [4].

Synchronization is a fairly vital nonlinear phenomenon widely existing in nature. It has wide-ranging implications for numerous applications, such as secret communication, facial recognition, artificial intelligence, and associative memory. Recently, the synchronization of CDNs has been extensively studied, for instance, quasi-synchronization [5], cluster synchronization [6], master-slave synchronization [7], exponential synchronization [8, 9], and so on.

At present, the control law is indispensable in achieving the synchronization of CDNs. To guarantee synchronization, many effective synchronization control laws have been proposed. On the basis of existing literature [10–12], there are two main categories of control laws of the systems: linear control law and nonlinear control law. As we all know, linear control law is the basis of the control strategy, and the structure of the controller is relatively uncomplicated. Compared with linear control law, nonlinear control law has become an increasingly interesting research topic for researchers from diverse backgrounds. In [8], the exponential synchronization for a kind of CDN with stochastic perturbations and delays was well investigated by utilizing the time-delayed impulsive controller. In [4], based on the event-triggered strategy, quasi-synchronization of CDNs was obtained. In [12], the author addressed robust synchronization between fractional-order CDNs involving parameter uncertainty and applying the nonlinear control law. By means of a sliding mode control scheme, global asymptotical synchronization for CDNs was discussed in [13].

As a result of imperfect measurements as well as the finite switching frequency of amplifiers, delays are always inherent in real applications of machine learning, which can

exacerbate performance and derail the stability of the models. Generally speaking, time delays are inevitable, and we can never be too concerned about them. Especially, deviation argument can have substantial consequences in the running process of the dynamical system model. As a matter of fact, numerous biomedical models are inscribed by differential equations with a deviation argument. In the process of motion, the deviation function alters the relevant deviation characteristics, so the differential equation with deviation argument unites delay and advanced equation. More precisely, with respect to the study of economics, biology, and physics, past and future events are crucial to current decisions. Therefore, it is of great significance to discuss the models of retarded and advanced alternating differential equations. A system with a deviation argument is a mixture of retarded and advanced systems. Sufficient conditions on the globally exponentially stable for recursive systems containing deviating functions were obtained by virtue of Lyapunov functions in [14]. The author utilized algebraic inequalities to present novel analytical findings from Mittag-Leffler stability about the fractional-order model involving deviating arguments in [15]. On the basis of the comparison principle, valuable theoretic results on the stability and robustness of interval fuzzy Cohen-Grossberg networks were presented in [16]. Additionally, a useful impulsive control law was considered to accomplish the synchronization in the presence of the deviating argument of CDN in [9]. In order to elaborate on the convenience and completeness of CDNs, we will analyze CDNs with deviating arguments here. Among the above studies, only one investigated the synchronization of CDNs with deviating arguments. At present, there are few research studies on robust synchronization control schemes for CDNs with deviating arguments. The objective of our research is to fill the gap.

To our knowledge, some work has been performed on the stabilization of dynamical systems equipped with deviating arguments [14, 17]. Some work has been conducted on stabilization and synchronization from the perspective of control [13, 18, 19]. Others have also studied research on complex dynamic networks with deviating arguments [9], but their purpose was to study stability rather than robustness. However, the robustness of control laws in complex dynamic networks is rarely studied by setting appropriate parameters for deviation argument.

Motivated by the above-mentioned discussion, we will find that the presence of deviating arguments will exacerbate difficulties in achieving synchronization of controlled complex dynamical networks (CDNs). In view of the literature [20, 21], it is worth considering the influence of the deviation argument on the control method. A new issue arises: can linear control law (nonlinear law) still be kept if a deviation function occurs in the system? As the deviation function involves information about the past and future, it is worthwhile to investigate: under the constraints of linear or nonlinear control laws, how much is the deviation argument intensity to allow CDNs to maintain exponential synchronization?

Therefore, the following is concretely scheduled for this paper. Some mathematical preliminaries are provided in Section 2. In view of the two categories of control laws, several crucial lemmas and theorems are further elaborated in Section 3. Two emulation examples are mentioned to validate the feasibility of the analytical results in Section 4. Finally, Section 5 of this paper carries a concise summary and outlook for the future research direction.

2. Preliminaries

2.1. Notation. On the basis of this paper, $\mathbb{N}$ represents the sets of natural numbers. $\mathbb{R}^n$ and $\mathbb{R}^{n\times m}$ be made up of all n real vectors, all $n\times m$ real matrices, respectively. I_n is denoted as the n-order identity matrix. Moreover, 0_n refers to $n\times n$ zero matrix. $\|\cdot\|$ means the Euclidean vector norm or the induced matrix norm. Denote $E\otimes F$ as the Kronecker product of matrices E and F.

Generally, a graph $G=(\nu,\varepsilon,\widetilde{A})$ has three basic elements. $\nu=\{1,\ldots,N\}$ signifies the set of nodes; $\varepsilon=\{e_{ij}\}$, $(i,j\in\nu)$ is the set of edges; and the coupling matrix $\widetilde{A}=(\mathrm{a_{ij}})_{\mathrm{N\times N}}$, where a_{ij} stands for coupling weight between i th CDN and node j th CDN. If the message is delivered from j th CDN to i th $(i\neq j)$ CDN, then $a_{ij}\neq 0$; otherwise, $a_{ij}=0$.

Provide two real-valued sequences $\{\rho_q\}$, $\{\eta_q\}$, $q\in\mathbb{N}$, such that $\rho_q<\rho_{q+1}$, $\rho_q\le\eta_q\le\rho_{q+1}$ for all $\rho_q\longrightarrow\infty$ as $q\longrightarrow\infty$.

2.2. Model. Consider a kind of CDN with a deviating argument consisting of N coupled nodes

$$\begin{aligned}&\dot{y}_i(t)=f(y_i(t))+c\sum_{j=1}^{N}a_{ij}y_j(t)+c\sum_{j=1}^{N}b_{ij}y_j(\delta(t))+u_i(t),\\&y(t_0)=y_0\in\mathbb{R}^n.\end{aligned}\tag{1}$$

where $y_i(t)=(y_{i1},\cdots y_{in})^T\in\mathbb{R}^n$ is the state vector of the i th node; the nonlinear $f\colon\mathbb{R}^n\longrightarrow\mathbb{R}^n$ is called continuous vector-valued function; c stands for the coupling strength; $u_i(t)\in\mathbb{R}^n$ is defined as the control input vectors of node i; and a_{ij} and b_{ij} denote the (i,j)-th term of coupling matrix $\widetilde{A}$ and $\widetilde{B}$ satisfying $a_{ii}=-\sum_{j=1,j\neq i}^{N}a_{ij}$ and $b_{ii}=-\sum_{j=1,j\neq i}^{N}b_{ij}$, respectively. $\delta(t)$ is a deviating argument satisfying $\delta(t)=\eta_q\in[\rho_q,\rho_{q+1}]$, if $t\in(\rho_q,\rho_{q+1}]$.

Remark 1. Obviously, when $t\in(\rho_q,\rho_{q+1}]$, if $\delta(t)>t$, then the coupling term of system (1) is advanced, and if $\delta(t)<t$, then the coupling term of system (1) is retarded. Hence, system (1) is a hybrid CDN, which integrates alternately advanced and retarded argument.

The dynamical equation for the isolated node of CDN (1) is

$$\dot{s}(t)=f(s(t)),\tag{2}$$

where $s(t)$ allows to be defined by an arbitrary desired state, that is, the equilibrium point, the periodic orbit, and so on.

Remark 2. Further, in contrast to (1), in case of $\delta(t)=t$, the CDN (1) turns into the following CDN:

$$\dot{x}_i(t) = f(x_i(t)) + c\sum_{j=1}^{N} a_{ij}x_j(t) + c\sum_{j=1}^{N} b_{ij}x_j(t) + u_i(t),$$
$$x(t_0) = x_0 \in \mathbb{R}^n. \tag{3}$$

Similarly,

$$\dot{s}(t) = f(s(t)), \tag{4}$$

Also referred to as the dynamical equation of the isolated node of CDN (3).

Define the synchronization error as $e_i(t) = x_i(t) - s(t)$, and subtracting (4) from (3) to obtain the following system:

$$\dot{e}_i(t) = f(e_i(t)) + c\sum_{j=1}^{N} a_{ij}e_j(t) + c\sum_{j=1}^{N} b_{ij}e_j(t) + u_i(t),$$
$$e(t_0) = e_0 \in \mathbb{R}^n, \tag{5}$$

where $f(e_i(t)) = f(x_i(t)) - f(s(t))$.

To acquire synchronization, the linear controller is arranged as

$$u_i(t) = \widetilde{W}e_i(t), \quad i = 1, \ldots, N, \tag{6}$$

where $\widetilde{W} \in \mathbb{R}^{n\times n}$ represents the feedback controller gain matrix.

Combining (5) and (6), one has that

$$\dot{e}_i(t) = f(e_i(t)) + c\sum_{j=1}^{N} a_{ij}e_j(t) + c\sum_{j=1}^{N} b_{ij}e_j(t) + \widetilde{W}e_i(t),$$
$$e(t_0) = e_0 \in \mathbb{R}^n. \tag{7}$$

With a view to simplifying writing, the following notations:

$e(t) = (e_1^T(t), \ldots e_N^T(t))^T$, $e(\delta(t)) = (e_1^T(\delta(t)), \ldots e_N^T(\delta(t)))^T$, $f(e(t)) = (f^T(e_1(t)), \ldots, f^T(e_N(t)))^T$, $\widetilde{A} = (a_{ij})_{N\times N}$, $\widetilde{B} = (b_{ij})_{N\times N}$, $A = I_n \otimes \widetilde{A}$, $B = I_n \otimes \widetilde{B}$, $W = I_n \otimes \widetilde{W}$, are put forward to describe the system. Incorporating these simplifications, the error system (7) is further characterized as a compact representation:

$$\dot{e}(t) = f(e(t)) + \mathrm{cAe}(t) + \mathrm{cBe}(t) + We(t),$$
$$e(t_0) = e_0 \in \mathbb{R}^n. \tag{8}$$

In the same way, we can define error $z_i(t) = y_i(t) - s(t)$, and the following error dynamic equation can be obtained by subtracting (2) from (1)

$$\dot{z}(t) = f(z(t)) + cAz(t) + cBz(\delta(t)) + Wz(t),$$
$$z(t_0) = z_0 \in \mathbb{R}^n. \tag{9}$$

As a starting point, we will provide some essential definitions and required assumptions for this paper.

Definition 1. If the error system (8) is exponential stability, then the CDN (3) with (4) is described as exponential synchronization, namely, for any initial value $e_0 \in \mathbb{R}^n$, there exist two scalars $\alpha > 0$ and $\beta > 0$ such that for any $t \in \mathbb{R}^+$, satisfying $\|e(t)\| \le \alpha\|e_0\|e^{-\beta(t-t_0)}$:

(D1) Assume that the existence of nonnegative scalar p, satisfying $\|f(m_i(t)) - f(n_i(t))\| \le p\|m_i(t) - n_i(t)\|$ and $f(0_n) = 0$ for any $m_i(t) \in \mathbb{R}^n$, $n_i(t) \in \mathbb{R}^n$

(D2) There is a positive constant ρ that has the property $\rho_{q+1} - \rho_q \le \rho$, for all $q \in \mathbb{N}$

(D3) $\rho(h_1 + 2h_2)\exp\{h_1\rho\} < 1$

3. Main Results

Under (D1), (D2), and (D3), system (9) has a unique state $z(t; t_0, z_0)$ on $t > t_0$ for any initial state (t_0, z_0). Obviously, $z = 0$ is the equilibrium point of system (9). Synchronization, as a highly representative subject of complex system, has been paid attention to and researched by many academics, for example [5–8, 10, 15]. For now, a fundamental point requires consideration. While keeping the original controller unchanged, if the deviation argument is added to the CDN, can synchronization of the system still hold? Obviously, synchronization is not established. How much is the deviation argument intensity in order to allow the CDNs (1) to maintain exponential synchronization when the control law is as valid as before? On the basis of this fact, we are going to investigate the robustness of the controller of CDNs (1) with a deviating argument when the control scheme of the CDNs (2) is fixed.

As we all know, among all kinds of control laws, the most efficient and concise control law is the linear feedback controller. What should be noted is that the linear control law is the foundation of the control system. Compared with the nonlinear controller, its structure is relatively uncomplicated. However, nonlinear control law has become an increasingly interesting topic of study for researchers from diverse backgrounds. Therefore, it is worthwhile to design two types of controllers for study: the linear feedback controller and the nonlinear feedback controller.

3.1. The Linear Feedback Controller. Before describing the principal theorem of this section, some important lemmas need to be presented here. The following assumptions are also required:

$$\alpha\exp(-\beta T) + 2h_2\alpha\exp\{(2h_1 + 6h_2)T\}/\beta < 1, \tag{10}$$

Remark 3. As can be inferred from Theorem 2 appearing in [6], the existence and uniqueness of the solution of system (1) is collectively ensured by (D1), (D2), and (D3).

Lemma 1. *Let $z(t)$ stands for the current state of error dynamic (9) and conditions (D1), (D2), (D3), and (D4) are all met. So, the following inequality:*

$$\|z(\delta(t))\| \le \lambda\|z(t)\|. \tag{11}$$

It exists for any $t > 0$, where

$$\begin{aligned} \lambda &= 1/(1-u_1), \\ u_1 &= h_2\rho + h_1\rho(1+h_2\rho)\exp\{h_1\rho\}, \\ h_1 &= p + c\|A\| + \|W\|, \\ h_2 &= c\|B\|. \end{aligned} \tag{12}$$

Proof. For the deviation term $\delta(t) = \eta_q$, define a set $\sigma = \{t/t > 0, \rho_q \le t \le \rho_{q+1}\}$, let $t \in \sigma$, $q \in \mathbb{N}$, and then one obtains

$$z(t) = z(\eta_q) + \int_{\eta_q}^{t} (f(z(s))) + cAz(s) + cBz(\eta_q) + Wz(s)ds. \tag{13}$$

Combining (D1) and (13), one has that

$$\begin{aligned} \|z(t)\| &\le \|z(\eta_q)\| + \int_{\eta_q}^{t} \left(\|f(z(s))\| + c\|A\|\|z(s)\| + c\|B\|\|z(\eta_q)\| + \|W\|\|z(s)\| \right) ds \\ &= (1+h_2\rho)\|z(\eta_q)\| + \int_{\eta_q}^{t} h_1\|z(s)\| ds, \end{aligned} \tag{14}$$

where

$$\begin{aligned} h_1 &= p + c\|A\| + \|W\|, \\ h_2 &= c\|B\|. \end{aligned} \tag{15}$$

By virtue of the Gronwall–Bellman's inequality, (14) can evolve into

$$\|z(t)\| \le \left[(1+h_2\rho)\|z(\eta_q)\|\right]\exp\{h_1\rho\}, \tag{16}$$

Otherwise, for $\rho_q \le t \le \rho_{q+1}$, similarly, we have

$$\begin{aligned} \|z(\eta_q)\| &\le \|z(t)\| + \int_{\eta_q}^{t} \left(\|f(z(s))\| + c\|A\|\|z(s)\| + c\|B\|\|z(\eta_q)\| + \|W\|\|z(s)\| \right) ds \\ &\le \|z(t)\| + h_2\rho\|z(\eta_q)\| + \int_{\eta_q}^{t} h_1\|z(s)\| ds \le \|z(t)\| + h_2\rho\|z(\eta_q)\| + h_1\rho\left[(1+h_2\rho)\|z(\eta_q)\|\right]\exp\{h_1\rho\} \\ &\le \|z(t)\| + [h_2\rho + h_1\rho(1+h_2\rho)\exp\{h_1\rho\}]\|z(\eta_q)\| \le \|z(t)\| + u_1\|z(\eta_q)\|, \end{aligned} \tag{17}$$

where $u_1 = [h_2\rho + h_1\rho(1+h_2\rho)\exp\{h_1\rho\}]$, and h_1, h_2 are defined in (15).

Hence, by uniting the aforementioned equation with similar entries, we further get

$$(1-u_1)\|z(\eta_q)\| \le \|z(t)\|. \tag{18}$$

Accordingly, when $\delta(t) = \eta_q$, $u_1 < 1$ for (D4), it follows that

$$\begin{aligned} \|z(\eta_q)\| &\le (1-u_1)^{01}\|z(t)\| \\ &=: \lambda\|z(t)\|, \end{aligned} \tag{19}$$

where $\lambda = 1/(1-u_1)$. By this means, (11) is effective for $t > 0$. □

Remark 4. By virtue of Lemma 1, we establish the link from the deviating argument $z(\delta(t))$ to the state $z(t)$ and provide a strong base to prove the subsequent Theorem 1.

Next, we explore the influence of the deviation argument on the robustness of exponentially stable of error system (9).

Theorem 1. *If assumption (D1) (D2) (D3) (D4) (D5) hold, and error system (8) is exponential stability, then error system (9) is exponential stability, that is, system (1) is said to be exponential synchronization under the linear-type controller (6), if $\rho < \overline{\rho}$, where $\overline{\rho}$ is the only solution of the transcendental equation:*

$$k_2 \exp\{2k_1T\} + \alpha \exp\{-\beta T\} = 1, \tag{20}$$

where $k_1 = h_1 + (2+\lambda)h_2$, $k_2 = h_2(1+\lambda)\alpha/\beta$, $\lambda = (1 - [h_2\rho + h_1\rho(1+h_2\rho)\exp\{h_1\rho\}])^{-1}$ and $T > (\ln \alpha)/\beta$. Here, in addition to h_1, h_2, λ and T, all of them are consistent with those defined in Lemma 1.Proof For convenience, $e(t) = e(t; t_0, e_0)$ and $z(t) = z(t; t_0, z_0)$ are expressed by $e(t)$ and $z(t)$, respectively. According to (8) and (9), as well as the initial value $e_0 = z_0$, one has

$$z(t) - e(t) = \int_{t_0}^{t} [(f(z(s)) - f(e(s))) + cA(z(s) - e(s)) + cB(z(\delta(t)) - e(s)) + W(z(s) - e(s))] ds. \tag{21}$$

Then,

$$\begin{aligned}\|z(t)-e(t)\| &= \left\|\int_{t_0}^{t}[(f(z(s))-f(e(s)))+cA(z(s)-e(s))+cB(z(\delta(t))-e(s))+W(z(s)-e(s))]\mathrm{d}s\right\| \\ &\le \int_{t_0}^{t}[\|f(z(s))-f(e(s))\|+c\|A\|\|z(s)-e(s)\|+c\|B\|\|z(\delta(t))-e(s)\|+\|W\|\|z(s)-e(s)\|]\mathrm{d}s.\end{aligned} \tag{22}$$

In view of (D1) and the norm inequality, for (22), one has

$$\begin{aligned}\|z(t)-e(t)\| &\le \int_{t_0}^{t}[p\|z(s)-e(s)\|+c\|A\|\|z(s)-e(s)\|+c\|B\|\|z(\delta(s))-e(s)\|+\|W\|\|z(s)-e(s)\|]\mathrm{d}s \\ &\le \int_{t_0}^{t}[(p+c\|A\|+\|W\|)\|z(s)-e(s)\|+c\|B\|\|z(\delta(s))-e(s)\|]\mathrm{d}s \\ &\le \int_{t_0}^{t}[(p+c\|A\|+\|W\|)\|z(s)-e(s)\|+c\|B\|\|z(\delta(s))-z(s)+z(s)-e(s)\|]\mathrm{d}s \\ &\le \int_{t_0}^{t}[(p+c\|A\|+\|W\|)\|z(s)-e(s)\|+c\|B\|\|z(\delta(s))-z(s)\|+c\|B\|\|z(s)-e(s)\|]\mathrm{d}s \\ &\le \int_{t_0}^{t}[(p+c\|A\|+c\|B\|+\|W\|)\|z(s)-e(s)\|+c\|B\|\|z(\delta(s))-z(s)\|]\mathrm{d}s \\ &\le \int_{t_0}^{t}[(h_1+h_2)\|z(s)-e(s)\|+h_2\|z(\delta(s))-z(s)\|]\mathrm{d}s.\end{aligned} \tag{23}$$

By Lemma 1, when $0 \le t_0 \le t$, then

$$\begin{aligned}\|z(t)-e(t)\| &\le \int_{t_0}^{t}[(h_1+h_2)\|z(s)-e(s)\|+h_2\|z(\delta(s))\|+h_2\|z(s)\|]\mathrm{d}s \\ &\le \int_{t_0}^{t}[(h_1+h_2)\|z(s)-e(s)\|+h_2(1+\lambda)\|z(s)\|]\mathrm{d}s \\ &= (h_1+h_2)\int_{t_0}^{t}\|z(s)-e(s)\|ds+h_2(1+\lambda)\int_{t_0}^{t}\|z(s)-e(s)+e(s)\|\mathrm{d}s \\ &\le (h_1+h_2)\int_{t_0}^{t}\|z(s)-e(s)\|ds+h_2(1+\lambda)\int_{t_0}^{t}\|z(s)-e(s)\|+\|e(s)\|\mathrm{d}s \\ &\le [h_1+(2+\lambda)h_2]\int_{t_0}^{t}\|z(s)-e(s)\|ds+h_2(1+\lambda)\int_{t_0}^{t}\|e(s)\|\mathrm{d}s.\end{aligned} \tag{24}$$

Due to the error system (8) is exponential stability, according to Definition 1, on the interval $[t_0-\rho, t_0+\rho]$, it comes to the conclusion that

$$\|e(t)\| \le \alpha\|e_0\|e^{-\beta(t-t_0)}. \tag{25}$$

And then,

$$\frac{\int_{t_0}^{t}\|e(t)\|\mathrm{d}s \le \alpha\|e_0\|}{\beta}. \tag{26}$$

Furthermore,

$$\begin{aligned}\|z(t)-e(t)\| &\le [h_1+(2+\lambda)h_2]\int_{t_0}^{t}\|z(s)-e(s)\|\mathrm{d}s \\ &\quad + h_2(1+\lambda)\frac{\|e_0\|\alpha}{\beta} \\ &= k_1\int_{t_0}^{t}\|z(s)-e(s)\|\mathrm{d}s+k_2\|e_0\|,\end{aligned} \tag{27}$$

where

$$k_1 = h_1 + (2+\lambda)h_2,$$
$$k_2 = \alpha h_2 \frac{(1+\lambda)}{\beta}. \tag{28}$$

By the Gronwall–Bellman's inequality, when $t_0 + \rho \le t \le t_0 + 2T$, we can acquire

$$\|z(t) - e(t)\| \le k_2 \|e_0\| \exp\{2k_1 T\}. \tag{29}$$

Since $t_0 - \rho + T \le t \le t_0 - \rho + 2T$, from (27) and (29), one has

$$\begin{aligned}\|z(t)\| &= \|z(t) - e(t) + e(t)\| \le \|z(t) - e(t)\| + \|e(t)\| \\ &\le k_2 \|e_0\| \exp(2k_1 T) + \alpha \|e_0\| \exp(-\beta T) \\ &= \{k_2 \exp(2k_1 T) + \alpha \exp(-\beta T)\} \|e_0\| \\ &\le \widehat{h} \sup_{t_0-\rho \le t \le t_0-\rho+T} \|z(t)\|,\end{aligned} \tag{30}$$

where $\widehat{h} = k_2 \exp\{2k_1 T\} + \alpha \exp(-\beta T)$.

Denote

$$\begin{aligned}H(\lambda) &= k_2 \exp\{2k_1 T\} + \alpha \exp(-\beta T) \\ &= h_2 (1+\lambda)\alpha/\beta \exp\{2[h_1 + (2+\lambda)h_2]T\} \\ &\quad + \alpha \exp(-\beta T).\end{aligned} \tag{31}$$

By substituting $\lambda = 1$ into (31), we can readily get

$$H(1) = \alpha \exp(-\beta T) + 2h_2 \alpha \exp\{(2h_1 + 6h_2)T\}/\beta < 1. \tag{32}$$

Clearly that, $H(+\infty) > 1$. In addition, $H(\lambda)$ is monotonically increasing for λ. Accordingly, there is only one $\overline{\lambda} \in (1, +\infty)$ meeting

$$H(\overline{\lambda}) = 1. \tag{33}$$

Denote

$$\Gamma(\rho) = h_2 \rho + h_1 \rho (1 + h_2 \rho) \exp\{h_1 \rho\}, \tag{34}$$

and identify $\widetilde{\rho}$ as the only one positive solution to $\Gamma(\rho) = 1$.

Apparently,

$$\lambda(\rho) = (1 - \Gamma(\rho))^{-1} \in (1, +\infty), \tag{35}$$

for $\rho \in (0, \widetilde{\rho})$. Furthermore, λ is monotonically increasing for ρ. In this sense, there is the only one positive $\overline{\rho} \in (0, \widetilde{\rho})$ to satisfy

$$\lambda = \overline{\lambda}, \tag{36}$$

and $\overline{\rho}$ is the only one positive solution to (20).

Consequently, for $\rho < \overline{\rho}$,

$$\widehat{h} = k_2 \exp\{2k_1 T\} + \alpha \exp(-\beta T) < 1. \tag{37}$$

Picking out $\xi = -(\ln \widehat{h})/T > 0$, and in consideration of (30), one has

$$\sup_{t_0-\rho+T \le t \le t_0-\rho+2T} \|z(t)\| \le \exp(-\xi T) \sup_{t_0-\rho \le t \le t_0-\rho+T} \|z(t)\|. \tag{38}$$

Considering the existence and uniqueness of the solution $z(t)$ of system (9), when $t \ge t_0 - \rho + (l-1)T$, it holds

$$z(t, t_0, z_0) = z(t, t_0 - \rho + (l-1)T, z(t_0 - \rho + (l-1)T, t_0, z_0)). \tag{39}$$

From (38) and (39), it follows that

$$\begin{aligned}&\sup_{t_0-\rho+lT \le t \le t_0-\rho+(l+1)T} \|z(t, t_0, z_0)\| \\ &= \sup_{t_0-\rho+(l-1)T+T \le t \le t_0-\rho+(l-1)T+2T} \|z(t; t_0 - \rho + (l-1)T, z(t_0 - \rho + (l-1)T; t_0, z_0))\| \\ &\le \exp(-\xi T) \sup_{t_0-\rho+(l-1)T \le t \le t_0-\rho+lT} \|z(t; t_0, z_0)\| \\ &\le \exp(-\xi l T) \sup_{t_0-\rho \le t \le t_0-\rho+T} \|z(t; t_0, z_0)\| \\ &= G \exp(-\xi l T),\end{aligned} \tag{40}$$

where $G = \sup_{t_0-\rho \le t \le t_0-\rho+T} \|z(t; t_0, z_0)\|$.

To go a step further, there is the only scalar $l \in \mathbb{N}$ so that $t_0 - \rho + lT \le t \le t_0 - \rho + (l+1)T$, and one can easily show

$$\begin{aligned}\|z(t; t_0, z_0)\| &\le G \exp(-\xi l T) \le G \exp\{-\xi(t - t_0) + \xi(T - \rho)\} \\ &\le G \exp(\xi T) \exp\{-\xi(t - t_0)\}.\end{aligned} \tag{41}$$

Based on Theorem 1, one can readily find that an error system (9) is exponentially stable, i.e., the system (1) can achieve exponential synchronization under a designed linear-type controller (6).

Remark 5. Theorem 1demonstrates that when an error system (8) is exponentially stable, the perturbed system (9) evoked by the deviation argument can still remain exponentially stable as long as the interval length of the deviating argument $\delta(t)$ is less than the estimated upper bound. So, system (1) involving deviating argument is still exponentially synchronous under a designed linear-type controller (6).

Remark 6. As can be seen in Figure 1, there is a relationship between the interval length of a deviating argument and time in the proof of Theorem 1.

3.2. The Nonlinear Feedback Controller. To acquire synchronization, the nonlinear controller is defined as

$$u_i(t) = -f(x_i(t)) + f(s(t)) + \widetilde{R}e_i(t), \quad i = 1, \ldots, N, \tag{42}$$

where $\widetilde{R} \in \mathbb{R}^{n\times n}$ represents the feedback controller gain matrix.

With the nonlinear control law (42), system (5) is reworded to

$$\begin{aligned} \dot{e}_i(t) &= c\sum_{j=1}^{N} a_{ij}e_j(t) + c\sum_{j=1}^{N} b_{ij}e_j(t) + \widetilde{R}e_i(t), \\ e(t_0) &= e_0 \in \mathbb{R}^n. \end{aligned} \tag{43}$$

That is,

$$\dot{e}(t) = \mathrm{cAe}(t) + \mathrm{cBe}(t) + \mathrm{Re}(t), \quad e(t_0) = e_0 \in \mathbb{R}^n, \tag{44}$$

where $R = I_n \otimes \widetilde{R}$. Here, in addition to R, all of them are consistent with previous notations in (8).

In the same way, error system with mixed coupling terms containing deviation arguments is reformulated as

$$\dot{z}(t) = cAz(t) + cBz(\delta(t)) + Rz(t), \quad z(t_0) = z_0 \in \mathbb{R}^n, \tag{45}$$

where $R = I_n \otimes \widetilde{R}$.

To validate Theorem 2 more expeditiously, we will introduce Lemma 2. In this subsection, the following assumptions are required:

(i) (D6) $\rho(\varepsilon_1 + 2\varepsilon_2)\exp\{\varepsilon_1\rho\} < 1$

(ii) (D7) $\varepsilon_2\rho + \varepsilon_1\rho(1 + \varepsilon_2\rho)\exp\{\varepsilon_1\rho\} < 1$

(D8) The following inequality characterize the parameters of the system (44)

$$\frac{\alpha\exp(-\beta T) + 2\varepsilon_2\alpha\exp\{(2\varepsilon_1 + 6\varepsilon_2)T\}}{\beta < 1}, \tag{46}$$

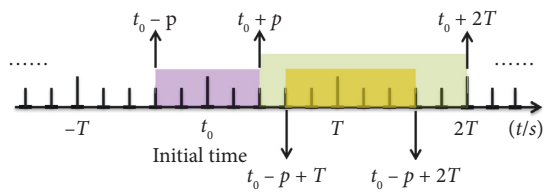

Figure 1: Relationship between interval length of deviating argument and time.

where $T > (\ln\alpha)/\beta$, $\varepsilon_1 = c\|A\| + \|R\|$, $\varepsilon_2 = c\|B\|$.

Lemma 2. *Let $z(t)$ stands for the current state of error system (45) and conditions (D1) (D2) (D6) (D7) are all met. So, we have the following inequality:*

$$\|z(\delta(t))\| \le \kappa\|z(t)\|, \tag{47}$$

This exists for any $t > 0$, where

$$\begin{aligned} \kappa &= \frac{1}{1 - \upsilon_1}, \\ \upsilon_1 &= [\varepsilon_2\rho + \varepsilon_1\rho(1 + \varepsilon_2\rho)\exp\{\varepsilon_1\rho\}], \\ \varepsilon_1 &= c\|A\| + \|R\|, \\ \varepsilon_2 &= c\|B\|. \end{aligned} \tag{48}$$

Proof. For the deviation term $\delta(t) = \eta_q$, define a set $\sigma = \{t > 0, \rho_q \le t \le \rho_{q+1}\}$, let $t \in \sigma$, and $q \in \mathbb{N}$, and then, we have

$$z(t) = z(\eta_q) + \int_{\eta_q}^{t} (cAz(s) + cBz(\eta_q) + Rz(s))ds. \tag{49}$$

Combining (D1), we obtain

$$\begin{aligned} \|z(t)\| &\le \|z(\eta_q)\| + \int_{\eta_q}^{t} \left(c\|A\|z(s) + c\|B\|\|z(\eta_q)\| + \|R\|\|z(s)\|\right)\mathrm{d}s \\ &\le \|z(\eta_q)\| + \int_{\eta_q}^{t} (c\|A\| + \|R\|)\|z(s)\|ds + \int_{\eta_q}^{t} c\|B\|\|z(\eta_q)\|\mathrm{d}s \\ &= (1 + \varepsilon_2\rho)\|z(\eta_q)\| + \int_{\eta_q}^{t} \varepsilon_1\|z(s)\|\mathrm{d}s, \end{aligned} \tag{50}$$

where

$$\begin{aligned} \varepsilon_1 &= c\|A\| + \|R\|, \\ \varepsilon_2 &= c\|B\|. \end{aligned} \tag{51}$$

Therefore, for (50), using the Gronwall–Bellman's inequality, it yields that

$$\|z(t)\| \le \left[(1 + \varepsilon_2\rho)\|z(\eta_q)\|\right]\exp\{\varepsilon_1\rho\}. \tag{52}$$

Otherwise, for $\rho_q \le t \le \rho_{q+1}$, similarly, it follows that

$$\begin{aligned}\left\|z\left(\eta_q\right)\right\| &\le \|z(t)\| + \int_{\eta_q}^{t}\left(c\|A\|z(s) + c\|B\|\left\|z\left(\eta_q\right)\right\| + \|R\|\|z(s)\|\right)\mathrm{d}s \\ &\le \|z(t)\| + \varepsilon_2\rho\left\|z\left(\eta_q\right)\right\| + \int_{\eta_q}^{t}\varepsilon_1\|z(s)\|\mathrm{d}s \le \|z(t)\| + \varepsilon_2\rho\left\|z\left(\eta_q\right)\right\| + \varepsilon_1\rho\left[\left(1+\varepsilon_2\rho\right)\left\|z\left(\eta_q\right)\right\|\right]\exp\{\varepsilon_1\rho\} \\ &\le \|z(t)\| + \left[\varepsilon_2\rho + \varepsilon_1\rho\left(1+\varepsilon_2\rho\right)\exp\{\varepsilon_1\rho\}\right]\left\|z\left(\eta_q\right)\right\| \le \|z(t)\| + \upsilon_1\left\|z\left(\eta_q\right)\right\|,\end{aligned} \tag{53}$$

where $\upsilon_1 = [\varepsilon_2\rho + \varepsilon_1\rho(1+\varepsilon_2\rho)\exp\{\varepsilon_1\rho\}]$ and ε_1 and ε_2 are defined in (51).

Hence, by uniting the aforementioned equation with similar entries, we can further require

$$\left(1-\upsilon_1\right)\left\|z\left(\eta_q\right)\right\| \le \|z(t)\|. \tag{54}$$

Accordingly, when $\delta(t) = \eta_q$, $\upsilon_1 < 1$ for (D7), it further derives

$$\begin{aligned}\left\|z\left(\eta_q\right)\right\| &\le \left(1-\upsilon_1\right)^{01}\|z(t)\| \\ &=: \kappa\|z(t)\|,\end{aligned} \tag{55}$$

where $\kappa = 1/(1-u_1)^{-1}$. By this means, (47) is available for $t \ge 0$. □

Theorem 2. *If assumption (D1) (D2) (D6) (D7) (D8) hold, and error system (44) is exponentially stable, then, error system (45) is exponentially stable, that is, system (1) is said to be exponential synchronization under the nonlinear-type controller (42), if $\rho < \overline{\rho}$, where $\overline{\rho}$ is the only solution of the transcendental equation:*

$$\Lambda_2\exp\{2\Lambda_1 T\} + \alpha\exp\{-\beta T\} = 1, \tag{56}$$

where $\Lambda_2 = \alpha\varepsilon_2(1+\kappa)/\beta$, $\kappa = (1-[\varepsilon_2\rho + \varepsilon_1\rho(1+\varepsilon_2\rho)\exp\{\varepsilon_1\rho\}])^{-1}$ and $T > (\ln\alpha)/\beta$. Here, in addition to $\varepsilon_1, \varepsilon_2, \kappa$ and T, all of them are consistent with those defined in Lemma 2.

Proof. For convenience, $e(t) = e(t; t_0, e_0)$ and $z(t) = z(t; t_0, z_0)$ are expressed by $e(t)$ and $z(t)$, respectively. According to (44) and (45), as well as the initial value $e_0 = z_0$, one has

$$\begin{aligned}z(t) - e(t) = \int_{t_0}^{t}&[cA(z(s)-e(s)) + cB(z(\delta(t)) \\ &- e(s)) + R(z(s)-e(s))]\mathrm{d}s.\end{aligned} \tag{57}$$

Then,

$$\begin{aligned}\|z(t)-e(t)\| &= \left\|\int_{t_0}^{t}[cA(z(s)-e(s)) + cB(z(\delta(t)) - e(s)) + R(z(s)-e(s))]\mathrm{d}s\right\| \\ &\le \int_{t_0}^{t}[c\|A\|\|z(s)-e(s)\| + c\|B\|\|z(\delta(t)) - e(s)\| + \|R\|\|z(s)-e(s)\|]\mathrm{d}s.\end{aligned} \tag{58}$$

In view of the norm inequality, for (58), one has

$$\begin{aligned}\|z(t)-e(t)\| &\le \int_{t_0}^{t}[c\|A\|\|z(s)-e(s)\| + c\|B\|\|z(\delta(s)) - e(s)\| + \|R\|\|z(s)-e(s)\|]\mathrm{d}s \\ &= \int_{t_0}^{t}[(c\|A\| + \|R\|)\|z(s)-e(s)\| + c\|B\|\|z(\delta(s)) - e(s)\|]\mathrm{d}s \\ &= \int_{t_0}^{t}[(c\|A\| + \|R\|)\|z(s)-e(s)\| + c\|B\|\|z(\delta(s)) - z(s) + z(s) - e(s)\|]\mathrm{d}s \\ &\le \int_{t_0}^{t}[(c\|A\| + \|R\|)\|z(s)-e(s)\| + c\|B\|\|z(\delta(s)) - z(s)\| + c\|B\|\|z(s) - e(s)\|]\mathrm{d}s \\ &\le \int_{t_0}^{t}[(c\|A\| + c\|B\| + \|R\|)\|z(s)-e(s)\| + c\|B\|\|z(\delta(s)) - z(s)\|]\mathrm{d}s \\ &\le \int_{t_0}^{t}[(\varepsilon_1 + \varepsilon_2)\|z(s)-e(s)\| + \varepsilon_2\|z(\delta(s)) - z(s)\|]\mathrm{d}s.\end{aligned} \tag{59}$$

By Lemma 2, when $0 \le t_0 \le t$, then

$$\begin{aligned}\|z(t)-e(t)\| &\le \int_{t_0}^{t}\left[(\varepsilon_1+\varepsilon_2)\|z(s)-e(s)\|+\varepsilon_2\|z(\delta(s))\|+\varepsilon_2\|z(s)\|\right]\mathrm{d}s\\ &\le \int_{t_0}^{t}\left[(\varepsilon_1+\varepsilon_2)\|z(s)-e(s)\|+\varepsilon_2(1+\kappa)\|z(s)\|\right]\mathrm{d}s\\ &= (\varepsilon_1+\varepsilon_2)\int_{t_0}^{t}\|z(s)-e(s)\|\mathrm{d}s+\varepsilon_2(1+\kappa)\int_{t_0}^{t}\|z(s)-e(s)+e(s)\|\mathrm{d}s\\ &\le (\varepsilon_1+\varepsilon_2)\int_{t_0}^{t}\|z(s)-e(s)\|\mathrm{d}s+\varepsilon_2(1+\kappa)\int_{t_0}^{t}\|z(s)-e(s)\|+\|e(s)\|\mathrm{d}s\\ &\le \left[\varepsilon_1+(2+\kappa)\varepsilon_2\right]\int_{t_0}^{t}\|z(s)-e(s)\|\mathrm{d}s+\varepsilon_2(1+\kappa)\int_{t_0}^{t}\|e(s)\|\mathrm{d}s.\end{aligned} \tag{60}$$

Due to CDN, (44) is exponential stability, and according to Definition 1, on the interval $[t_0-\rho, t_0+\rho]$, it comes to the conclusion that

$$\|e(t)\| \le \alpha\|e_0\|e^{-\beta(t-t_0)}. \tag{61}$$

And then,

$$\int_{t_0}^{t}\|e(t)\|\mathrm{d}s \le \alpha\|e_0\|/\beta. \tag{62}$$

Furthermore,

$$\begin{aligned}\|z(t)-e(t)\| &\le \left[\varepsilon_1+(2+\kappa)\varepsilon_2\right]\int_{t_0}^{t}\|z(s)-e(s)\|\mathrm{d}s\\ &\quad+\frac{\left(\alpha\varepsilon_2(1+\kappa)\|e_0\|\right)}{\beta}\\ &= \Lambda_1\int_{t_0}^{t}\|z(s)-e(s)\|\mathrm{d}s+\Lambda_2\|e_0\|,\end{aligned} \tag{63}$$

where

$$\begin{aligned}\Lambda_1 &= \varepsilon_1+(2+\kappa)\varepsilon_2,\\ \Lambda_2 &= \alpha\varepsilon_2(1+\kappa)/\beta.\end{aligned} \tag{64}$$

By the Gronwall–Bellman's inequality, when $t_0+\rho \le t \le t_0+2T$, we can expediently acquire

$$\|z(t)-e(t)\| \le \Lambda_2\|e_0\|\exp\{2\Lambda_1 T\}. \tag{65}$$

Since $t_0-\rho+T \le t \le t_0-\rho+2T$, from (65) and (66), further we derive

$$\begin{aligned}\|z(t)\| &= \|z(t)-e(t)+e(t)\|\\ &\le \|z(t)-e(t)\|+\|e(t)\|\\ &\le \Lambda_2\|e_0\|\exp(2\Lambda_1 T)+\alpha\|e_0\|\exp(-\beta T)\\ &= \{\Lambda_2\exp(2\Lambda_1 T)+\alpha\exp(-\beta T)\}\|e_0\|\\ &\le \hat{\iota}\sup_{t_0-\rho\le t\le t_0-\rho+T}\|z(t)\|,\end{aligned} \tag{66}$$

where $\hat{\iota} = \Lambda_2\exp\{2\Lambda_1 T\}+\alpha\exp(-\beta T)$.

Denote

$$\begin{aligned}\Psi(\kappa) &= \Lambda_2\exp\{2\Lambda_1 T\}+\alpha\exp(-\beta T)\\ &= \alpha\varepsilon_2(1+\kappa)\exp\frac{\{2[\varepsilon_1+(2+\kappa)\varepsilon_2]T\}}{\beta}+\alpha\exp(-\beta T).\end{aligned} \tag{67}$$

By substituting $\kappa = 1$ into (74), we can see that

$$\Psi(1) = \alpha\exp(-\beta T)+2\varepsilon_2\alpha\exp\frac{\{(2\varepsilon_1+6\varepsilon_2)T\}}{\beta<1}. \tag{68}$$

Clearly that, $\Psi(+\infty) > 1$. In addition, $\Psi(\kappa)$ is strictly monotonously increasing for κ. Accordingly, there is the only one $\overline{\kappa} \in (1, +\infty)$ make

$$\Psi(\overline{\kappa}) = 1. \tag{69}$$

Denote

$$\mathfrak{I}(\rho) = \varepsilon_2\rho+\varepsilon_1\rho(1+\varepsilon_2\rho)\exp\{\varepsilon_1\rho\}, \tag{70}$$

and identify $\widetilde{\rho}$ as the only one positive solution to $\mathfrak{I}(\rho) = 1$.

Apparently,

$$\kappa = (1-\mathfrak{I}(\rho))^{-1} \in (1, +\infty), \tag{71}$$

for $\rho \in (0, \widetilde{\rho})$. Furthermore, κ is increase strictly monotonically for ρ. In this sense, there is the only one positive scalar $\overline{\rho} \in (0, \widetilde{\rho})$ satisfy

$$\kappa = \overline{\kappa}, \tag{72}$$

and $\overline{\rho}$ is the only one positive solution for (56).

Thus,

$$\hat{\iota} = \Lambda_2\exp\{2\Lambda_1 T\}+\alpha\exp(-\beta T) < 1, \tag{73}$$

for $\rho < \overline{\rho}$.

Picking out $g = -(\ln\hat{\iota})/T > 0$, and by (67), one gets

$$\sup_{t_0-\rho+T\le t\le t_0-\rho+2T}\|z(t)\| \le \exp(-gT)\sup_{t_0-\rho\le t\le t_0-\rho+T}\|z(t)\|. \tag{74}$$

Considering the existence and uniqueness of solution $z(t)$ of the system (45), when $t \geq t_0 - \rho + (l-1)T$, it holds

$$z(t, t_0, z_0) = z(t, t_0 - \rho + (l-1)T, z(t_0 - \rho + (l-1)T, t_0, z_0)). \tag{75}$$

From (75) and (76), we have

$$\begin{aligned}
&\sup_{t_0-\rho+lT \leq t \leq t_0-\rho+(l+1)T} \|z(t, t_0, z_0)\| \\
&= \sup_{t_0-\rho+(l-1)T+T \leq t \leq t_0-\rho+(l-1)T+2T} \|z(t; t_0 - \rho + (l-1)T, z(t_0 - \rho + (l-1)T; t_0, z_0))\| \\
&\leq \exp(-gT) \sup_{t_0-\rho+(l-1)T \leq t \leq t_0-\rho+lT} \|z(t; t_0, z_0)\| \\
&\leq \exp(-glT) \sup_{t_0-\rho \leq t \leq t_0-\rho+T} \|z(t; t_0, z_0)\| \\
&= G\exp(-glT),
\end{aligned} \tag{76}$$

where $G = \sup_{t_0-\rho \leq t \leq t_0-\rho+T} \|z(t; t_0, z_0)\|$.

Furthermore, there is only scalar $l \in \mathbb{N}$, so that $t_0 - \rho + lT \leq t \leq t_0 - \rho + (l+1)T$, and one can easily show that

$$\begin{aligned}
\|z(t; t_0, z_0)\| &\leq G\exp(-glT) \leq G\exp\{-g(t - t_0) + g(T - \rho)\} \\
&\leq G\exp(gT)\exp\{-g(t - t_0)\}.
\end{aligned} \tag{77}$$

By virtue of Theorem 2, one can readily deduce that error system (45) is exponentially stable, i.e., system (1) can achieve exponential synchronization under a designed nonlinear-type controller (42). □

Remark 7. Theorem 2 clearly indicates that when error system (42) is exponentially stable, the corresponding perturbed error system (45) evoked by a deviation argument can still remain exponentially stable as long as the interval length of the deviating argument $\delta(t)$ is less than the estimated upper bound. Furthermore, system (1) involving a deviating argument is still exponentially synchronous under a designed nonlinear-type controller (42).

4. Simulations

Two illustrative examples will be enumerated to show the validity of conclusions obtained above in this section.

Example 1. Here considering a CDN with linear control law, which consists of two nodes:

$$\begin{cases}
\dot{x}_i(t) = f(x_i(t)) + c\sum_{j=1}^{2} a_{ij}x_j(t) + u_i(t), \\
x(t_0) = x_0 \in \mathbb{R}^n, \\
\dot{s}(t) = f(s(t)), \\
u_i(t) = \widetilde{W}e_i(t).
\end{cases} \tag{78}$$

In the case of deviation argument, system (78) turns into

$$\begin{cases}
\dot{x}_i(t) = f(x_i(t)) + c\sum_{j=1}^{2} a_{ij}x_j(t) + c\sum_{j=1}^{2} b_{ij}x_j(\delta(t)) + u_i(t), \\
x(t_0) = x_0 \in \mathbb{R}^n, \\
\dot{s}(t) = f(s(t)), \\
u_i(t) = \widetilde{W}e_i(t),
\end{cases} \tag{79}$$

where $i \in 1, 2$, and $x_i(t) = (x_{i1}(t), x_{i2}(t))^T \in \mathbb{R}^2$ is the state vectors of $i-$th nodes for the CDN. let $e_i(t) = x_i(t) - s(t)$, one can see that error system (78) and error system (79) turns into, respectively,

$$\dot{e}(t) = F(e(t)) + cAe(t) + We(t), \quad e(t_0) = e_0 \in \mathbb{R}^n, \tag{80}$$

$$\begin{aligned}
&\dot{e}(t) = F(e(t)) + cAe(t) + cBe(\delta(t)) + We(t), \\
&e(t_0) = e_0 \in \mathbb{R}^n.
\end{aligned} \tag{81}$$

Let coupling matrices $A = \begin{pmatrix} -5 & 5 \\ 2 & -2 \end{pmatrix}$, $B = \begin{pmatrix} -0.001 & 0.001 \\ 0.002 & -0.002 \end{pmatrix}$, and $K = \begin{pmatrix} -5.5 & 0 \\ 0 & -5.3 \end{pmatrix}$. The coupling strength is designed as $c = 0.1$. The activation function is $f(\cdot) = \tanh(\cdot)$. Two nodes and isolated nodes of the initial value can be designed as $x_1 = (-1.1, 1.2)^T$, $x_2 = (1.7, -1.4)^T$, and $s(t) = (0.2, 0.1)^T$.

As shown in Figure 2, error system (80) is exponentially stable when $\alpha = 1.1$ and $\beta = 0.8$.

Fix two consequences: $\{\rho_q\} = \{q/20\}$, $\{\eta_q\} = \{2q + 1/40\}$, and $q \in \mathbb{N}$. Let $T = 0.2 \geq (\ln 1.1)/0.8 = 0.1191$, $T = 0.2 \geq (\ln 1.1)/0.8 = 0.1191$; then by calculation, we can obtain $h_1 = 7.2616$ and $h_2 = 3.1623 \times 10^{-4}$.

Based on inequality (D4), it is expedient to calculate $\rho = 0.0781$. According to (30), we can obtain $\lambda = 6.8815$ and $\overline{\rho} = 0.0705$.

Selecting $\delta(t) = \rho = 1/20 < \overline{\rho} = 0.0705$, by conducting simple calculations, we can find

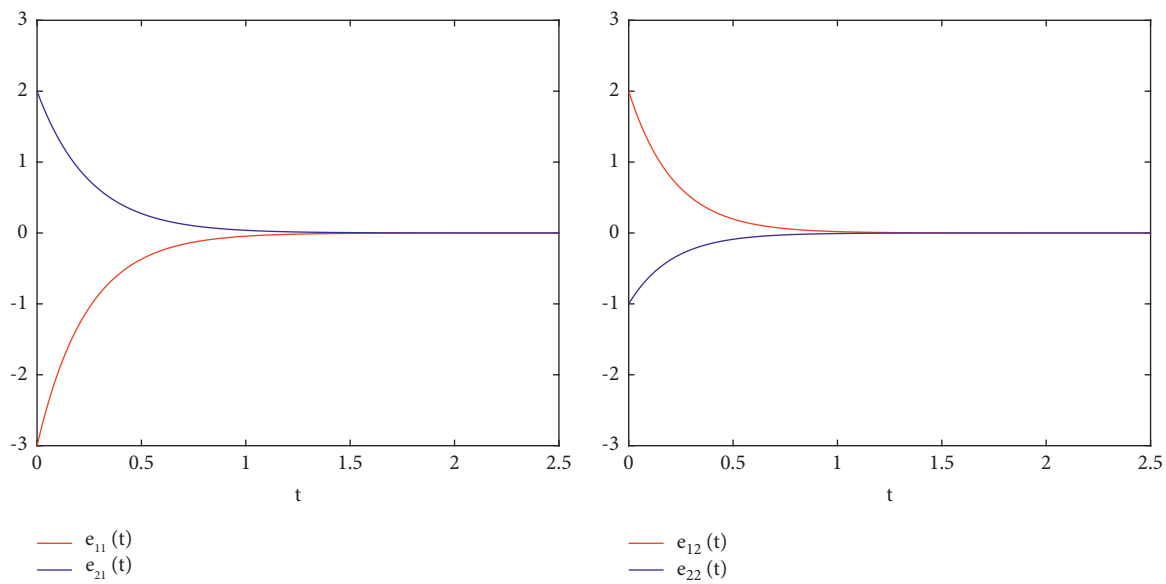

Figure 2: The convergent behavior of the error system under a nonlinear control law.

$$\frac{1}{20}\times\left(7.2616+2\times 3.1623\times 10^{-4}\right)\times\exp\left(7.2616\times\frac{1}{20}\right)=0.5221<1, \tag{82}$$

and (D3) is satisfied.

It is obvious that all the requirements appearing are each fulfilled in Theorem 1. In view of Theorem 1 and Definition 1, we are able to deduce that error system (81) is exponential stability, that is, system (79) is exponential synchronization. As shown in Figure 3, the simulated findings closely match the theory.

Example 2. We discuss a CDN, consisting of two nodes, with nonlinear control law whose dynamics are described as

$$\begin{cases}\dot{x}_i(t)=f(x_i(t))+c\sum_{j=1}^{2}a_{ij}x_j(t)+w_i(t),\\ x(t_0)=x_0\in\mathbb{R}^n,\\ \dot{s}(t)=f(s(t)),\\ u_i(t)=-f(x_i(t))+f(s(t))+e\widetilde{R}_i(t).\end{cases} \tag{83}$$

Subsequently, in the presence of deviating argument, system (83) becomes

$$\begin{cases}\dot{x}_i(t)=f(x_i(t))+c\sum_{j=1}^{2}a_{ij}x_j(t)+c\sum_{j=1}^{2}b_{ij}x_j(\delta(t))+w_i(t),\\ x(t_0)=x_0\in\mathbb{R}^n,\\ \dot{s}(t)=f(s(t)),\\ w_i(t)=-f(x_i(t))+f(s(t))+\widetilde{R}e_i(t),\end{cases}, \tag{84}$$

where $i\in 1,2$, and $x_i(t)=(x_{i1}(t),x_{i2}(t))^T\in\mathbb{R}^2$, is the state vectors.

Let $e_i(t)=x_i(t)-s(t)$, one can see that error system (83) and error system (84) are simplified as, respectively,

$$\dot{e}(t)=cAe(t)+\mathrm{Re}(t),\quad e(t_0)=e_0\in\mathbb{R}^n, \tag{85}$$

$$\dot{e}(t)=cAe(t)+cBe(\delta(t))+\mathrm{Re}(t),\quad e(t_0)=e_0\in\mathbb{R}^n. \tag{86}$$

Let coupling matrices $A=\begin{pmatrix}-2 & 2\\ 4 & -4\end{pmatrix}$, $B=\begin{pmatrix}-0.003 & 0.003\\ 0.002 & -0.002\end{pmatrix}$, and $K=\begin{pmatrix}-4.1 & 0\\ 0 & -4.7\end{pmatrix}$. The coupling strength is designated as $c=0.05$ for $i=1,2$. The activation function is $f(\cdot)=\tanh(\cdot)$. Two nodes and isolated nodes of the initial value can be designed as $x_1=(-2,2)^T$, $x_2=(3,-1)^T$, and $s(t)=(1,0)^T$.

As shown in Figure 4, the error system (85) is exponential stability when $\alpha=1.1$ and $\beta=0.5$.

Fix two consequences: $\{\rho_q\}=\{q/20\}$, $\{\eta_q\}=\{2q+1/40\}$, $q\in\mathbb{N}$. Let $T=0.4\geq(\ln 1.1)/0.5=0.1906$, then by calculation, we can obtain $h_1=5.0162$, $h_2=2.5495\times 10^{-4}$.

Based on inequality (D7), it is expedient to calculate $\rho=0.1131$. According to (56), we can obtain $\lambda=2.2011$, $\overline{\rho}=0.0748$.

Selecting $\delta(t)=\rho=1/20<\overline{\rho}=0.0748$, by conducting simple calculations, we can find

$$\frac{1}{20}\times\left(5.0162+2\times 2.5495\times 10^{-4}\right)\times\exp\left(5.0162\times\frac{1}{20}\right)=0.3223<1, \tag{87}$$

and (D6) is satisfied.

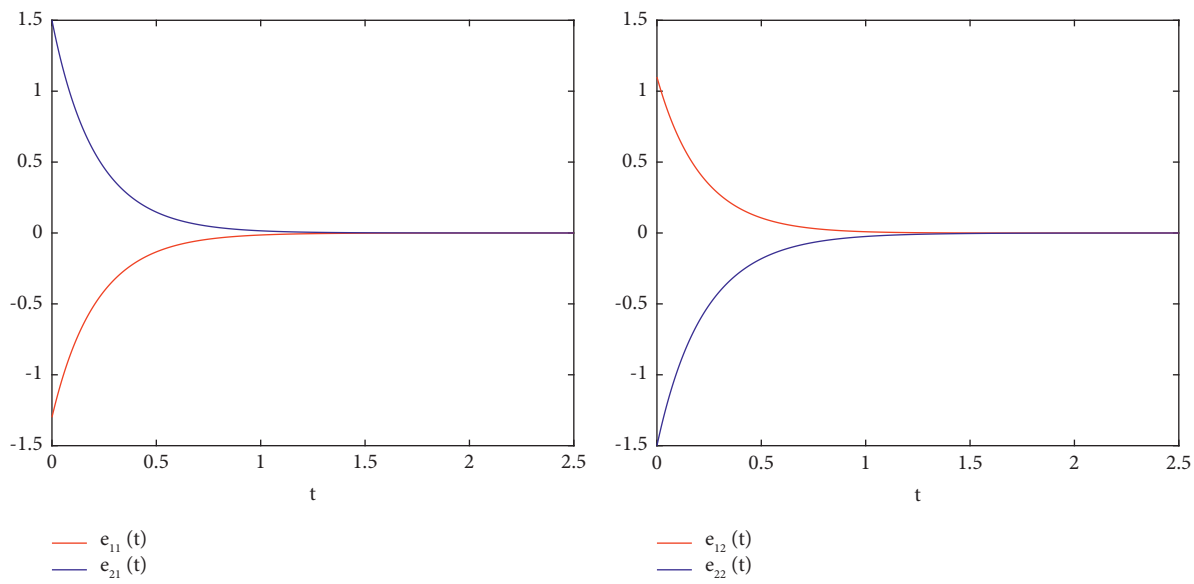

Figure 3: The convergent behavior of error system (80) under a linear control law.

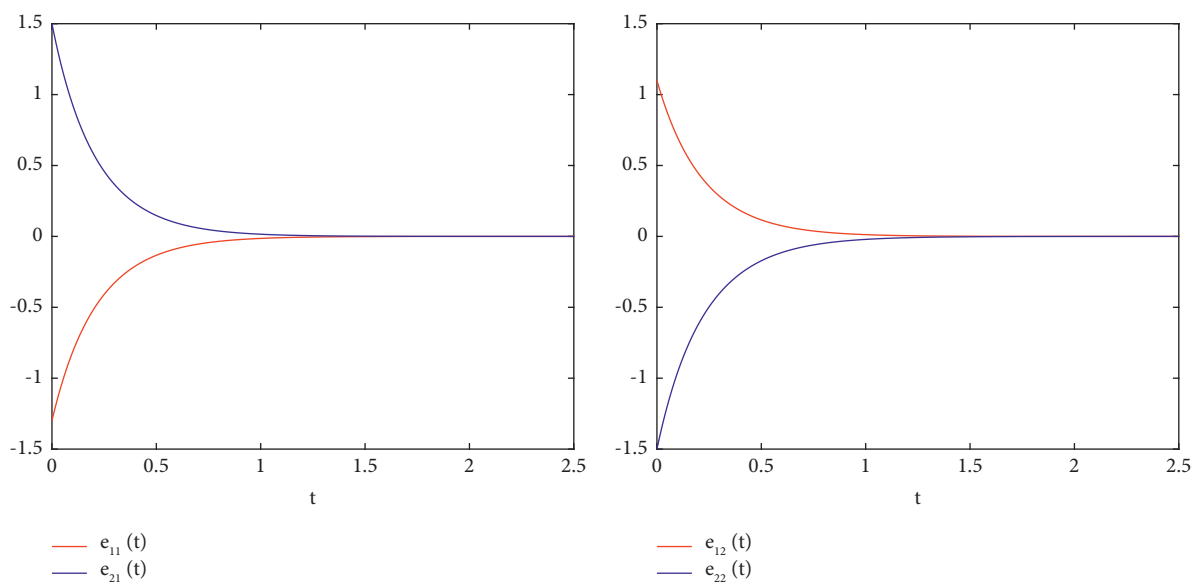

Figure 4: The evolvement behavior of error system (81) under a linear control law.

Clearly, all the requirements outlined in Theorem 2 are each fulfilled. In the light of Theorem 2 and Definition 1, we are able to deduce that error system (86) is exponentially stable, that is to say, system (84) can achieve exponential synchronization when $\rho = 1/20$. As indicated in Figure 5, the simulated findings closely correlate with the theory.

Figure 6 depicts that error system (86) is instable when $\rho = 1/2$. Moreover, in this situation, the parameters are not

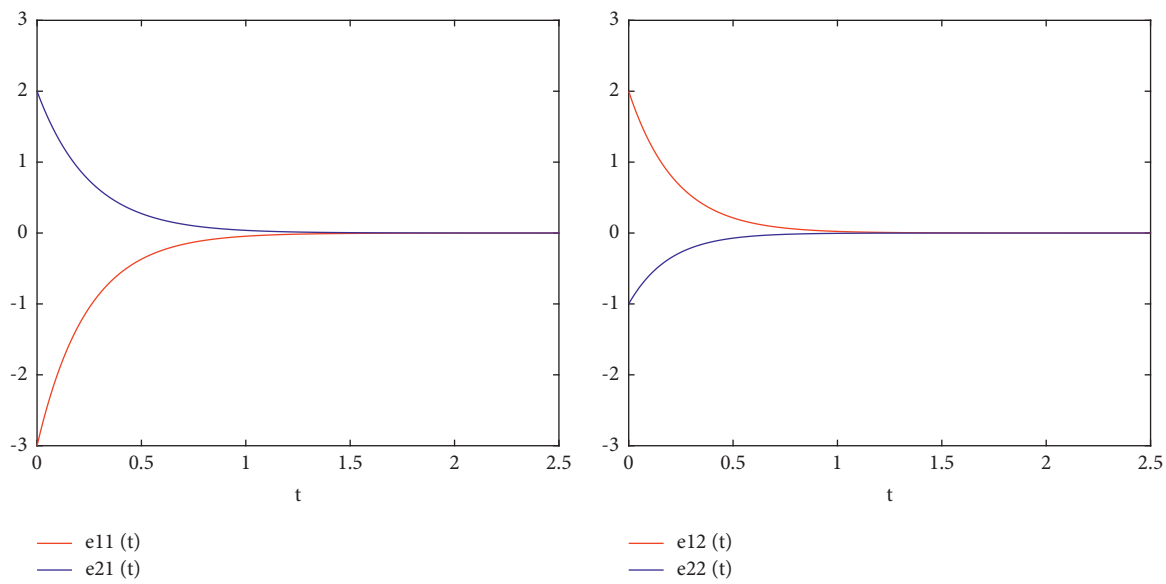

Figure 5: The evolvement behavior of error system (86) under a nonlinear control law.

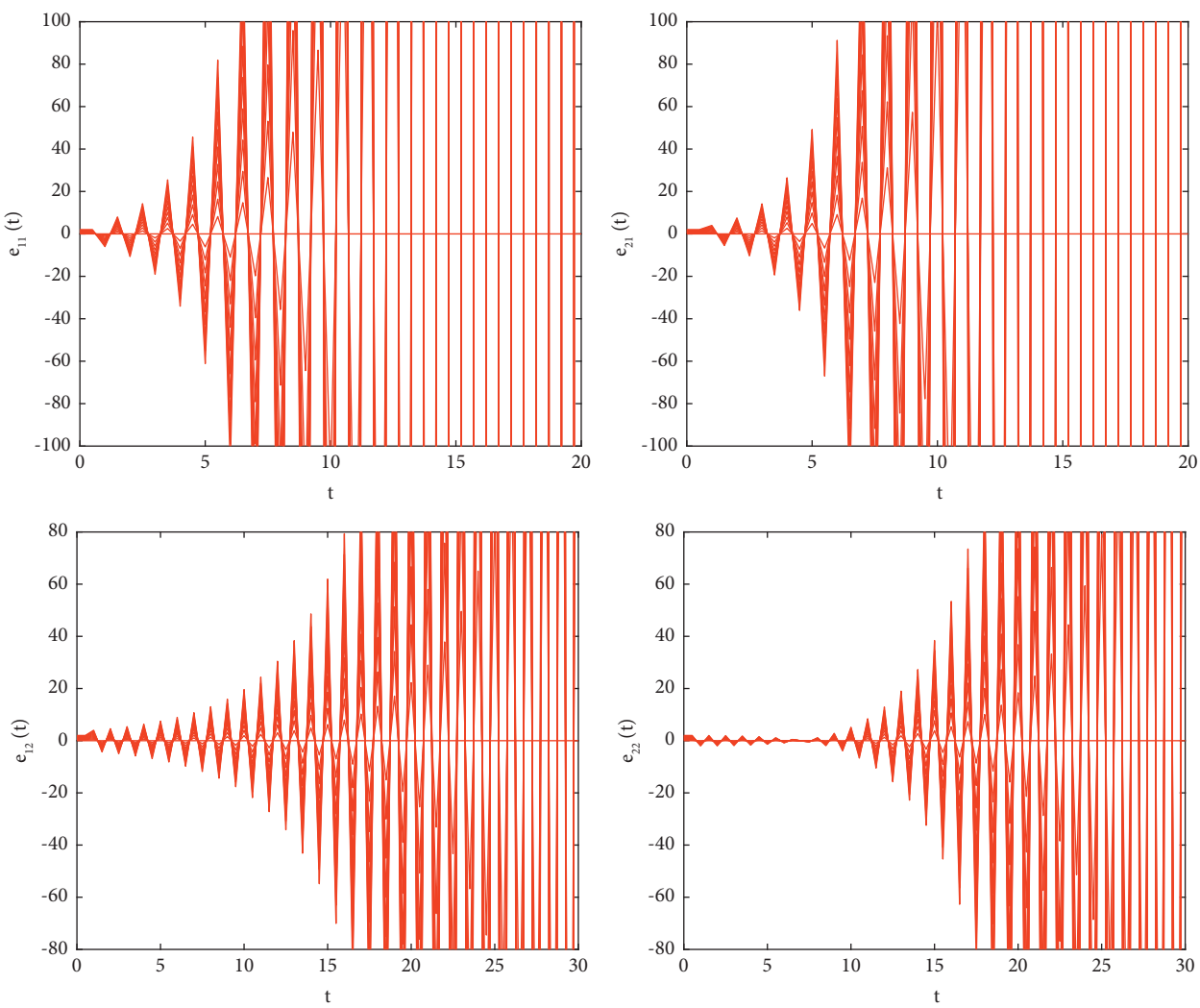

Figure 6: The instable behavior of error system (86) with $\rho = 1/2$ under a nonlinear control law.

appropriate for Theorem 2. Therefore, system (84) is not exponential synchronization.

5. Concluding Remarks

The robustness of the complex system to control laws evoked by deviating arguments is investigated. In this paper, two categories of control laws are provided and some corresponding sufficient criteria are put forward to prove the synchronization of CDNs with deviation argument. The findings show that a complex system containing a deviation function will keep exponential synchronization continuously as long as the interval length of the deviation function is lower than the derived upper limit. In view of the analysis and methodology discussed in this paper, more complex models will be considered for further topics.

Data Availability

No data were used to support this study.

Conflicts of Interest

The authors declare that there are no conflicts of interest regarding the publication of this paper.

Acknowledgments

This work was sponsored by the Natural Science Foundation of China (62072164 and 11704109).

References

[1] D. J. Watts and S. H. Strogatz, "Collective dynamics of "small-world" networks," *Nature*, vol. 393, no. 6684, pp. 440–442, 1998.

[2] J. Chen, B. Chen, and Z. Zeng, "Exponential quasi-synchronization of coupled delayed memristive neural networks via intermittent event-triggered control," *Neural Networks*, vol. 141, pp. 98–106, 2021.

[3] L. Wang and Y. x. Sun, "Robustness of pinning a general complex dynamical network," *Physics Letters A*, vol. 374, no. 15-16, pp. 1699–1703, 2010.

[4] J. Chen, B. Chen, Z. Zeng, and P. Jiang, "Event-triggered synchronization strategy for multiple neural networks with time delay," *IEEE Transactions on Cybernetics*, vol. 50, no. 7, pp. 3271–3280, 2020.

[5] J. Chen, B. Chen, Z. Zeng, and P. Jiang, "Event-based synchronization for multiple neural networks with time delay and switching disconnected topology," *IEEE Transactions on Cybernetics*, vol. 51, no. 12, pp. 5993–6003, 2021.

[6] G. S. Wang, J. W. Xiao, Y. W. Wang, and J. W. Yi, "Adaptive pinning cluster synchronization of fractional-order complex dynamical networks," *Applied Mathematics and Computation*, vol. 231, pp. 347–356, 2014.

[7] Y. Huang and H. Bao, "Master-Slave Synchronization of Complex-Valued Delayed Chaotic Lur'e Systems with Sampled-Data Control," *Applied Mathematics and Computation*, vol. 379, Article ID 125261, 2020.

[8] L. Zhang, X. Yang, C. Xu, and J. Feng, "Exponential synchronization of complex-valued complex networks with time-varying delays and stochastic perturbations via time-delayed impulsive control," *Applied Mathematics and Computation*, vol. 306, pp. 22–30, 2017.

[9] W. Shen, Z. Zeng, and S. Wen, "Synchronization of complex dynamical network with piecewise constant argument of generalized type," *Neurocomputing*, vol. 173, pp. 671–675, 2016.

[10] Y. Cao, S. Wang, Z. Guo, T. Huang, and S. Wen, "Synchronization of memristive neural networks with leakage delay and parameters mismatch via event-triggered control," *Neural Networks*, vol. 119, pp. 178–189, 2019.

[11] B. Houska and M. Diehl, "Robust design of linear control laws for constrained nonlinear dynamic systems," *IFAC Proceedings Volumes*, vol. 44, no. 1, pp. 13438–13443, 2011.

[12] W. Wong, H. Li, and S. Leung, "Robust synchronization of fractional-order complex dynamical networks with parametric uncertainties," *Communications in Nonlinear Science and Numerical Simulation*, vol. 17, no. 12, pp. 4877–4890, 2012.

[13] Y. Zhao, X. Li, and R. Rao, "Synchronization of nonidentical complex dynamical networks with unknown disturbances via observer-based sliding mode control," *Neurocomputing*, vol. 454, pp. 441–447, 2021.

[14] M. U. Akhmet, D. Arağaslan, and E. Yılmaz, "Stability analysis of recurrent neural networks with piecewise constant argument of generalized type," *Neural Networks*, vol. 23, no. 7, pp. 805–811, 2010.

[15] A. Wu, L. Liu, T. Huang, and Z. Zeng, "Mittag-leffler stability of fractional-order neural networks in the presence of generalized piecewise constant arguments," *Neural Networks*, vol. 85, pp. 118–127, 2017.

[16] G. Bao, S. Wen, and Z. Zeng, "Robust stability analysis of interval fuzzy cohen–grossberg neural networks with piecewise constant argument of generalized type," *Neural Networks*, vol. 33, pp. 32–41, 2012.

[17] W. Zhou, B. Li, J. E. Zhang, and B. Ding, "Matrix measure approach for stability and synchronization of complex-valued neural networks with deviating argument," *Mathematical Problems in Engineering*, vol. 2020, pp. 1–16, Article ID 8877129, 2020.

[18] Q. Xi and X. Liu, "Finite-time stability and controller design for a class of hybrid dynamical systems with deviating argument," *Nonlinear Analysis: Hybrid Systems*, vol. 39, Article ID 100952, 2021.

[19] S. Dong, H. Zhu, S. Zhong, K. Shi, and Y. Liu, "New study on fixed-time synchronization control of delayed inertial memristive neural networks," *Applied Mathematics and Computation*, vol. 399, Article ID 126035, 2021.

[20] L. Wan, A. Wu, and J. Chen, "Robustness analysis of global exponential stability in neural networks evoked by deviating argument and stochastic disturbance," *The Journal of Nonlinear Science and Applications*, vol. 10, no. 11, pp. 5646–5667, 2017.

[21] J. E. Zhang, "Robustness analysis of global exponential stability of nonlinear systems with deviating argument and stochastic disturbance," *IEEE Access*, vol. 5, pp. 13446–13454, 2017.

Hindawi
Discrete Dynamics in Nature and Society
Volume 2022, Article ID 1976765, 8 pages
https://doi.org/10.1155/2022/1976765

Research Article

Leaderless Consensus of Semilinear Hyperbolic Multiagent Systems with Semipositive or Seminegative Definite Convection

Jiashu Dai,[1] **Chengdong Yang**,[2] **Dong Xu**,[3] **Shiping Wen**,[4] **Muwei Jian**,[2] **and Dongliang Yang**[5]

[1]*School of Computer and Information, Anhui Polytechnic University, Wuhu 241000, China*
[2]*School of Information Science and Technology, Linyi University, Linyi 276005, China*
[3]*College of Computer Science and Technology, Harbin Engineering University, Harbin 150001, China*
[4]*Australian AI Institute, University of Technology Sydney, Ultimo 2007, NSW, Australia*
[5]*Intelligent Manufacturing Institute, Heilongjiang Academy of Sciences, Harbin 150090, China*

Correspondence should be addressed to Chengdong Yang; yangchengdong@lyu.edu.cn, Dong Xu; xudong@hrbeu.edu.cn, and Shiping Wen; shiping.wen@uts.edu.au

Received 28 April 2022; Accepted 6 July 2022; Published 8 August 2022

Academic Editor: Akbar Ali

This paper deals with a leaderless consensus of semilinear first-order hyperbolic partial differential equation-based multiagent systems (HPDEMASs). A consensus controller under an undirected graph is designed. Dealing with different convection assumptions, two different boundary conditions are presented, one right endpoint and the other left endpoint. Two sufficient conditions for leaderless consensus of HPDEMAS are presented by giving the gain range in the case of the symmetric seminegative definite convection coefficient and the semipositive definite convection coefficient, respectively. Two examples are presented to show the effectiveness of the control methods.

1. Introduction

As one well-known group of dynamical behavior, multiagent systems (MASs) received many researchers' attention in the last few decades [1]. There are a number of applications for MASs in engineering fields, for instance, power engineering [2], artificial intelligence [3], energy optimization [4], security [5, 6], traffic decision [7], and precision agriculture [8].

Consensus control of MASs is to derive agents to do a designated task synchronously[9, 10]. Many meaningful control methods have been presented, such as event-triggered control [11, 12], containment control [13], pinning control [14], impulsive control [15], sampled-data control [16], and adaptive control [17].

To put it another way, the mentioned literature assumed dynamics of MASs depending only on time. In practice, dynamics of all processes depends on both time and space. As a consequence, it is necessary to study spatio-temporal MASs [18]. Qi et al. proposed boundary control for PDE-modeled MASs(PDEMASs) under 3-D space with a control delay [19] and formation control for PDEMASs on a cylindrical surface [20]. An iterative learning algorithm was proposed for the consensus of multiagent system PDEMASs [21]. Yang et al. proposed several control methods for the consensus of semilinear PDEMASs or partial integro-differential equation-based MASs without and with time delays [22–24]. Several iterative learning methods were studied for the consensus of PDEMASs[21, 25–27].

Most of the above references are modeled by parabolic PDE-based MASs, while there are few works considering hyperbolic PDE-based MASs (HPDEMASs). The consensus of HPDEMASs is meaningful and significant, as a result of existence of a number of hyperbolic PDE systems in practice [28, 29], including gas dynamics [30], reactor [31], traffic flow [32], and hyperbolic Hopfield neural networks [33]. There are several important studies about consensus of

HPDEMASs. For example, Fu et al. proposed the containment control method for the consensus of linear parabolic PDEMASs and second-order HPDEMASs [34]. Wang and Huang proposed the boundary control approach for the finite-time consensus of HPDEMASs by assuming the convection coefficient to be 1 [35]. Zhang et al. proposed boundary control for the leader-following consensus of MASs with input delays by assuming the convection coefficient to be a positive definite diagonal matrix[36]. However, there are still technical difficulties in the consensus of semilinear first-order HPDEMASs for the cases of the convection coefficient to be symmetric seminegative definite or semipositive definite, which are motives of this paper.

This paper mainly studies leaderless consensus control of a semilinear HPDEMAS with two sorts of boundary conditions in one-dimensional space. The contribution of this paper contains (1) a class of HPDEMAS models is given, assuming two sorts of conditions, one symmetric seminegative definite convection coefficient and the other semipositive definite convection coefficient. (2) Dealing with different convection assumptions, two different boundary conditions are presented, one right endpoint and the other left endpoint. (3) A consensus controller based on communication is studied to drive HPDEMAS to reach leaderless consensus. (4) Dealing with two sorts of convection coefficients, two sufficient conditions for the consensus of the leaderless HPDEMAS are, respectively, reached.

Notations: Let I denotes the identity matrix with proper order, $\lambda_{\max(\min)}(\cdot)$ denotes the maximum (minimum) eigenvalue of $\cdot$, $\lambda_2(\cdot)$ denotes the smallest nonzero eigenvalue of $\cdot$, and the superscript T denotes the transpose.

2. Problem Formulation

This paper studies a class of semilinear HPDEMASs with time delays

$$\frac{\partial z_i(\zeta,t)}{\partial t} = \Theta\frac{\partial z_i(\zeta,t)}{\partial \zeta} + Az_i(\zeta,t) + f\left(z_i(\zeta,t)\right) + u_i(\zeta,t), \tag{1}$$

where $(\zeta,t) \in t[0,L]n \times q[0,\infty)$ are space and time, respectively. $z_i(\zeta,t), u_i(\zeta,t) \in \mathbb{R}^n$ are the state and control input, respectively. $0 < L \in \mathbb{R}$, $i \in \{1,2,\ldots,N\}$, $A, \Theta \in \mathbb{R}^{n\times n}$, and $f(\cdot)$ are a nonlinear function.

The boundary condition is

$$z_i(0,t) = 0, \tag{2}$$

or

$$z_i(L,t) = 0. \tag{3}$$

The initial condition is

$$z_i(\zeta,t) = z_i^0(\zeta,t). \tag{4}$$

This paper aims to study one controller $u_i(\zeta,t)$ driving HPDEMAS (1) to the leaderless consensus. Let consensus error $e_i(\zeta,t) \triangleq z_i(\zeta,t) - 1/N\sum_{j=1}^N z_j(\zeta,t)$ and the controller is designed as follows:

$$u_i(\zeta,t) = c\sum_{j=1}^N g_{ij}\Gamma\left(z_j(\zeta,t) - z_i(\zeta,t)\right), \tag{5}$$

where c is a control gain to be determined and Γ is symmetric positive definite. Assume that the topological structure $G = (g_{ij})_{N\times N}$ is defined $g_{ii} = 0$; $g_{ij} = g_{ji} > 0\,(i \neq j)$ if the agent i connects to j, otherwise $g_{ij} = 0\,(i \neq j)$.

Remark 1. Compared with papers [35, 36] using the information of only one neighbor, this controller (5) considers the whole communication information among all neighbors and takes full advantage of that.

Definition 1. ([35]) HPDEMAS (1) reaches a consensus, if

$$\lim_{t\longrightarrow\infty}\left\|z_i(\zeta,t) - \overline{z}(\zeta,t)\right\| = 0, i \in \{1,2,\ldots,N\}, \tag{6}$$

where $\overline{z}(\zeta,t) \triangleq 1/N\sum_{j=1}^N z_j(\zeta,t)$.

Lemma 1. *([37]) For the Laplacian matrix $\mathscr{L}$, symmetric positive definite P and $y \in \mathbb{R}^{Nn}$ such that $1_{Nn}^T y = 0$, the following inequality is satisfied:*

$$\lambda_2(\mathscr{L})y^T\left(I_N \otimes P\right)y \leq y^T\left(\mathscr{L}\otimes P\right)y. \tag{7}$$

Assumption 1. ([23]) For any $\zeta_1, \zeta_2 \in \mathbb{R}$, there exists $0 < \mathscr{X} \in \mathbb{R}$ satisfying

$$\left|f(\zeta_1) - f(\zeta_2)\right| \leq \mathscr{X}\left|\zeta_1 - \zeta_2\right|. \tag{8}$$

3. Consensus of HPDEMASs with the Seminegative Definite Convection Coefficient

Assumption 2. Assume Θ is symmetric seminegative definite.

Note that Assumption 2 is sort of classical, which is extensively employed in the practice, see, e.g. [38, 39].

The error system of HPDEMAS (1), (2), and (4) can be obtained as follows

$$\begin{cases} \dfrac{\partial e(\zeta,t)}{\partial t} = \Theta\dfrac{\partial e(\zeta,t)}{\partial \zeta} + \left(I_N \otimes A\right)e(\zeta,t) + F\left(e(\zeta,t)\right) \\ -c\left(\mathscr{L}\otimes\Gamma\right)e(\zeta,t), \\ e(0,t) = 0, \\ e(\zeta,0) = e^0(\zeta), \end{cases} \tag{9}$$

where $e_i^0(\zeta) \triangleq z_i^0(\zeta) - 1/N\sum_{j=1}^N z_j^0(\zeta)$, $e(\zeta,t) \triangleq [e_1^T(\zeta,t), e_2^T(\zeta,t),\ldots,e_N^T(\zeta,t)]^T$, $F(e_i(\zeta,t)) \triangleq f(z_i(\zeta,t)) - 1/N\sum_{j=1}^N f(z_j(\zeta,t))$, $F(e(\zeta,t)) \triangleq [F^T(e_1(\zeta,t)), F^T(e_2(\zeta,t)), \ldots, F^T(e_N(\zeta,t))]^T$, $\mathscr{L} = D - G$, $D = \mathrm{diag}\{d_1, d_2, \ldots, d_N\}$, $d_i = \sum_{j=1}^N g_{ij}$, and so $\mathscr{L}$ is a Laplace matrix [37].

Theorem 1. *Suppose that Assumptions 1 and 2 hold. The leaderless HPDEMAS shown in equations (1), (2), and (4) reaches the consensus under the controller (5), if*

$$c > \frac{\lambda_{\max}\left(I_N \otimes A + A^T/2 + \chi I\right)}{\lambda_2(\mathscr{L})\lambda_{\min}(\Gamma)}. \tag{10}$$

Proof. We choose the Lyapunov functional candidate as shown in the following equation:

$$V(t) = 0.5\int_0^L e^T(\zeta,t)e(\zeta,t)d\zeta. \tag{11}$$

Taking the time derivative of $V(t)$, we obtain

$$\begin{aligned}\dot{V}(t) &= \int_0^L e^T(\zeta,t)\frac{\partial e(\zeta,t)}{\partial t}d\zeta \\ &= \int_0^L e^T(\zeta,t)\left(I_N\otimes\Theta\right)\frac{\partial e(\zeta,t)}{\partial \zeta}d \\ &\quad + \int_0^L e^T(\zeta,t)\left(I_N\otimes A - c\mathscr{L}\otimes\Gamma\right)e(\zeta,t)d\zeta\zeta \\ &\quad + \int_0^L e^T(\zeta,t)F(e(\zeta,t))d\zeta.\end{aligned} \tag{12}$$

Since $\mathscr{L}$ is a Laplace matrix and Γ is a symmetric positive definite matrix, using Lemma 1, one has

$$\begin{aligned}&-c\int_0^L e^T(\zeta,t)(\mathscr{L}\otimes\Gamma)e(\zeta,t)d\zeta \\ &\leqslant -c\lambda_2(\mathscr{L})\int_0^L e^T(\zeta,t)\left(I_N\otimes\Gamma\right)e(\zeta,t)d\zeta \\ &\leqslant -c\lambda_2(\mathscr{L})\lambda_{\min}(\Gamma)\int_0^L e^T(\zeta,t)e(\zeta,t)d\zeta,\end{aligned} \tag{13}$$

where $0 = \lambda_1(\mathscr{L}) < \lambda_2(\mathscr{L}) \leq \mathscr{L} \leq \lambda_N(\mathscr{L})$ [40].

For symmetric seminegative definite Θ, employing integrating by parts, one gets

$$\begin{aligned}&\int_0^L e^T(\zeta,t)\left(I_N\otimes\Theta\right)\frac{\partial e(\zeta,t)}{\partial\zeta}d\zeta \\ &= e^T(\zeta,t)\left(I_N\otimes\Theta\right)e(\zeta,t)\Big|_{\zeta=0}^{\zeta=L} \\ &\quad - \int_0^L \frac{\partial e^T(\zeta,t)}{\partial\zeta}\left(I_N\otimes\Theta\right)e(\zeta,t) \\ &= e^T(L,t)\left(I_N\otimes\Theta\right)e(L,t) \\ &\quad - \int_0^L e^T(\zeta,t)\left(I_N\otimes\Theta\right)\frac{\partial e(\zeta,t)}{\partial\zeta}d\zeta \\ &\leq -\int_0^L e^T(\zeta,t)\left(I_N\otimes\Theta\right)\frac{\partial e(\zeta,t)}{\partial\zeta}d\zeta,\end{aligned} \tag{14}$$

which implies

$$\int_0^L e^T(\zeta,t)\left(I_N\otimes\Theta\right)\frac{\partial e(\zeta,t)}{\partial\zeta}d\zeta \leq 0. \tag{15}$$

Since $\sum_{i=0}^N \int_0^L e_i^T(\zeta,t)[f(\overline{y}(\zeta,t)) - 1/N \sum_{j=0}^N f(y_j(\zeta,t))]\mathrm{d}x = 0$, under Assumption 1, we can get

$$\begin{aligned}&\int_0^L e^T(\zeta,t)F(e(\zeta,t))d\zeta \\ &= \sum_{i=0}^N \int_0^L e_i^T(\zeta,t)\left(f(z_i(\zeta,t)) - \frac{1}{N}\sum_{j=1}^N f\left(z_j(\zeta,t)\right)\right)d\zeta \\ &= \sum_{i=0}^N \int_0^L e_i^T(\zeta,t)\left(f(z_i(\zeta,t)) - f(\overline{z}(\zeta,t))\right)d\zeta \leq \chi\int_0^L e^T(\zeta,t)e(\zeta,t)d\zeta.\end{aligned} \tag{16}$$

Substitution of (12), (14), (15) into (11), we obtain

$$\dot{V}(t) \leqslant \int_0^L e^T(\zeta,t)\Psi e(\zeta,t)d\zeta, \tag{17}$$

where $\Psi \triangleq I_N\otimes A + A^T/2 + \chi I - c\lambda_2(\mathscr{L})\lambda_{\min}(\Gamma)I$.

It is obvious that (9) implies

$$\Psi < 0. \tag{18}$$

Substitution of (17) into (16), we obtain $\dot{V}(t) \leqslant -\lambda\|\tilde{e}(\cdot,t)\| \leqslant -\lambda\|e(\cdot,t)\|$ for all nonzero $e(\zeta,t)$, implying consensus of HPDEMAS (1). □

4. Consensus of HPDEMASs with the Symmetric Semipositive Definite Convection Coefficient

Assumption 3. Assume Θ is symmetric semipositive definite.

Note that Assumption 3 is sort of classical, which is extensively employed in practice, see, e.g. [35, 36].

The error system of the HPDEMAS (1), (3), and (4) can be obtained as follows:

$$\begin{cases}\dfrac{\partial\epsilon(\zeta,t)}{\partial t} = \Theta\dfrac{\partial e(\zeta,t)}{\partial\zeta} + \left(I_N\otimes A\right)e(\zeta,t) \\ +F(e(\zeta,t)) - c(\mathscr{L}\otimes\Gamma)e(\zeta,t), \\ e(L,t) = 0, \\ e(\zeta,0) = e^0(\zeta).\end{cases} \tag{19}$$

Theorem 2. *Suppose that Assumptions 1 and 3 hold. The leaderless HPDEMAS shown in equations (1), (3), and (4) reaches the consensus under controller (5) if (9) holds.*

Proof. We choose the same Lyapunov functional candidate as in (10). Taking the time derivative of $V(t)$, we obtain (11). For the symmetric semipositive definite $\Theta > 0$, employing integrating by parts, one has

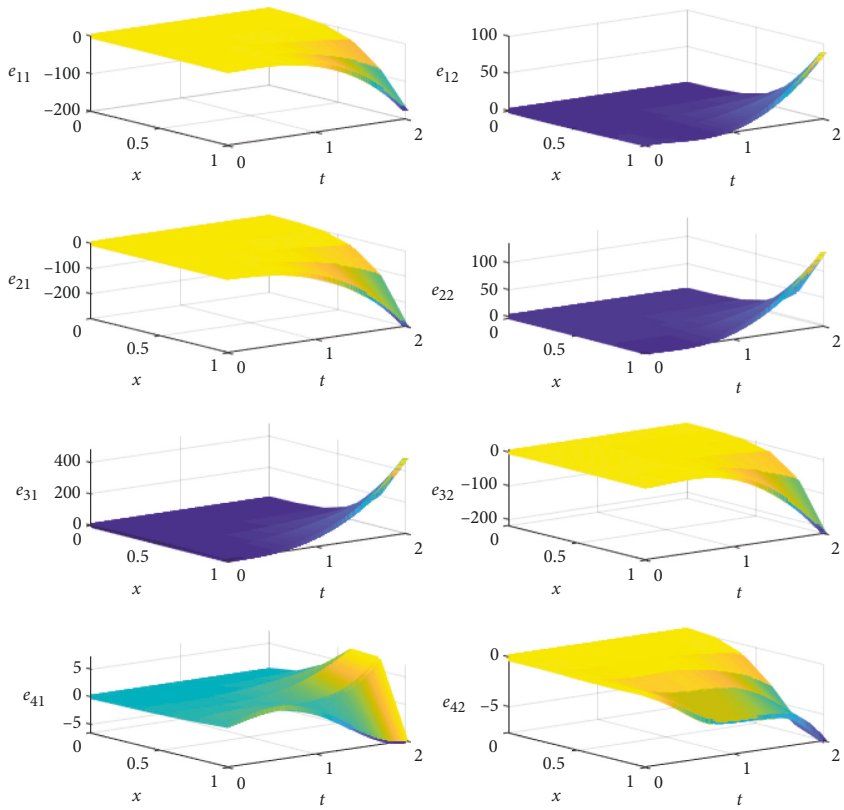

Figure 1: The open-loop profile of $z(\zeta,t)$.

$$\begin{aligned}
&\int_0^L e^T(\zeta,t)(I_N\otimes\Theta)\frac{\partial e(\zeta,t)}{\partial\zeta}d\zeta \\
&= e^T(\zeta,t)(I_N\otimes\Theta)e(\zeta,t)\Big|_{\zeta=0}^{\zeta=L} \\
&\quad -\int_0^L \frac{\partial e^T(\zeta,t)}{\partial\zeta}(I_N\otimes\Theta)e(\zeta,t) \\
&= -e^T(0,t)(I_N\otimes\Theta)e(0,t) \\
&\quad -\int_0^L e^T(\zeta,t)(I_N\otimes\Theta)\frac{\partial e(\zeta,t)}{\partial\zeta}d\zeta \\
&\le -\int_0^L e^T(\zeta,t)(I_N\otimes\Theta)\frac{\partial e(\zeta,t)}{\partial\zeta}d\zeta,
\end{aligned} \tag{20}$$

which implies

$$\int_0^L e^T(\zeta,t)(I_N\otimes\Theta)\frac{\partial e(\zeta,t)}{\partial\zeta}d\zeta \le 0. \tag{21}$$

Substitution of (12), (15), (19) into (11), we obtain (16). It is obvious that (9) implies

$$\Psi < 0. \tag{22}$$

The later part of the proof is similar to that of Theorem 2, and so it is omitted. □

Remark 2. Different from the control design for consensus of parabolic PDEMASs in [41, 42], this paper deals with the consensus of a class of HPDEMASs.

Remark 3. Consensus of HPDEMASs has been studied by assuming the convection coefficient to be 1 in [35] and to be a positive definite diagonal matrix in [36]. Different from these results, this paper assumes the convection coefficient to be symmetric seminegative and semipositive definite.

5. Numerical Simulation

Example 1. This example considers one HPDEMAS (1) as follows:

$$\begin{cases}
\dfrac{\partial z_i(\zeta,t)}{\partial t} = \begin{bmatrix} -0.8 & 0 \\ 0 & -1.6 \end{bmatrix}\dfrac{\partial z_i(\zeta,t)}{\partial\zeta} \\
+\begin{bmatrix} 5 & 2.6 \\ -1.2 & 3.9 \end{bmatrix} z_i(\zeta,t) + \tanh(z_i(\zeta,t)) + u_i(\zeta,t), \\
z_i(0,t) = 0, \\
z_i(\zeta,t) = z_i^0(\zeta,t),
\end{cases} \tag{23}$$

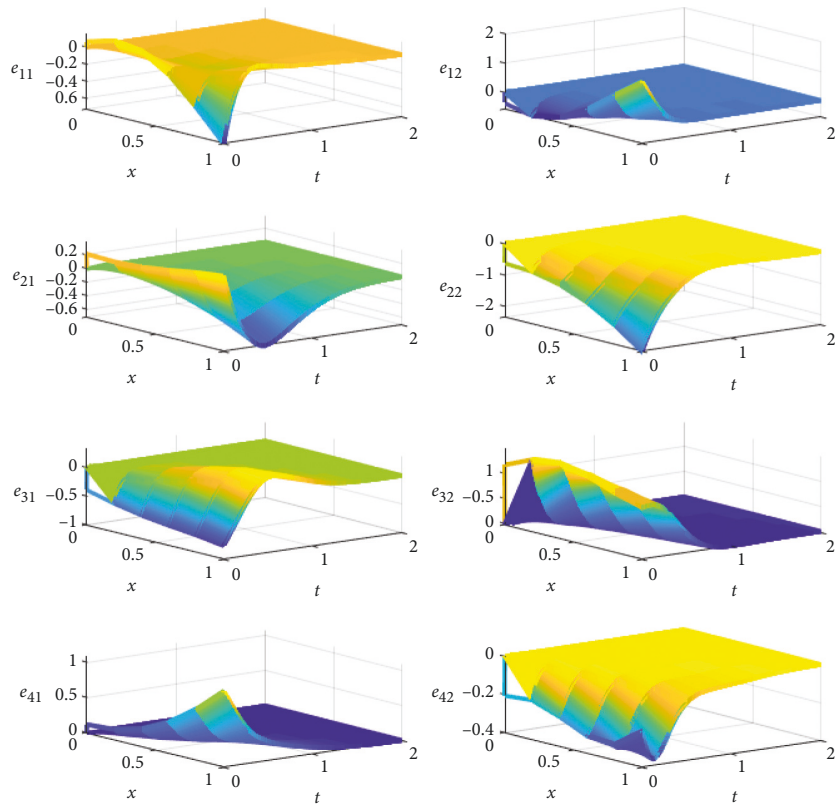

Figure 2: The closed-loop profile of $z(\zeta, t)$.

with random initial conditions. We get the following parameters:

$$\Theta = \begin{bmatrix} -0.8 & 0 \\ 0 & -1.6 \end{bmatrix},$$
$$A = \begin{bmatrix} 5 & 2.6 \\ -1.2 & 3.9 \end{bmatrix}, \tag{24}$$
$$L = 1, f(\cdot) = \tanh(\cdot).$$

The controller (5) is used with the following parameters:

$$\Gamma = \begin{bmatrix} 1 & 0 \\ 0 & 1 \end{bmatrix},$$
$$g_{ij} = 1, \text{for } i, j = 1, 2, 3, 4 \text{ and } i \neq j. \tag{25}$$

From Figure 1, it can be seen that HPDEMAS (1) cannot reach the consensus without control. With Theorem 1, solving (9) by Matlab, $c = 1.59$ is obtained. Figure 2 shows that the HPDEMAS (1) reaches the consensus under controller (5) with $c = 1.59$. Controller (5) with the feedback gain $c = 1.59$ is shown in Figure 3.

Example 2. This example considers one HPDEMAS (1) as follows:

$$\begin{cases} \dfrac{\partial z_i(\zeta, t)}{\partial t} = \begin{bmatrix} 0.2 & 0 \\ 0 & 0.5 \end{bmatrix} \dfrac{\partial z_i(\zeta, t)}{\partial \zeta} + \begin{bmatrix} 5 & 2.6 \\ -1.2 & 3.9 \end{bmatrix} z_i(\zeta, t) \\ +\tanh(z_i(\zeta, t)) + u_i(\zeta, t), \\ z_i(L, t) = 0, \\ z_i(\zeta, t) = z_i^0(\zeta, t), \end{cases} \tag{26}$$

with random initial conditions.

We get $\Theta = \begin{bmatrix} 0.2 & 0 \\ 0 & 0.5 \end{bmatrix}$, and the other parameters are the same as (22). The parameters Γ and g_{ij} of the controller (5) are the same as (23).

From Figure 4, it can be seen that HPDEMAS (1) cannot reach the consensus without control. With Theorem 2, solving (9) by Matlab, $c = 1.59$ is obtained. Figure 5 shows that the HPDEMAS (1) reaches the consensus under controller (5) with $c = 1.59$. The controller (5) with the feedback gain $c = 1.59$ is shown in Figure 6.

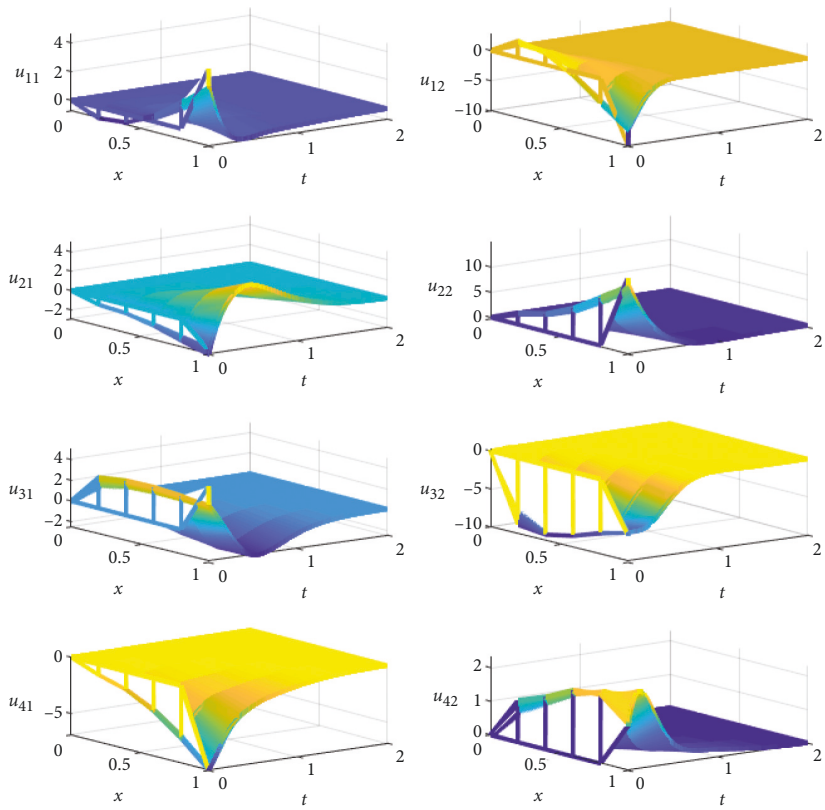

Figure 3: The profile of $u(\zeta, t)$.

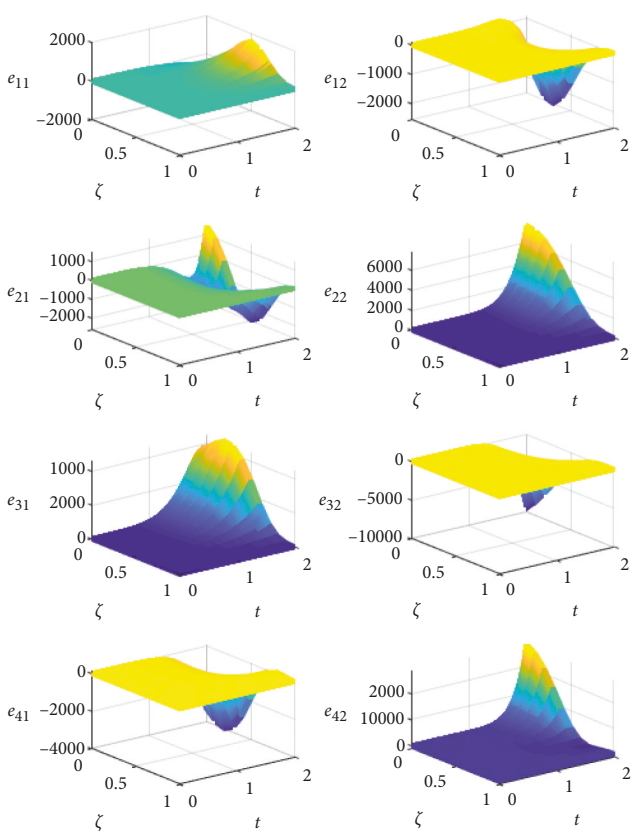

Figure 4: The open-loop profile of $z(\zeta, t)$.

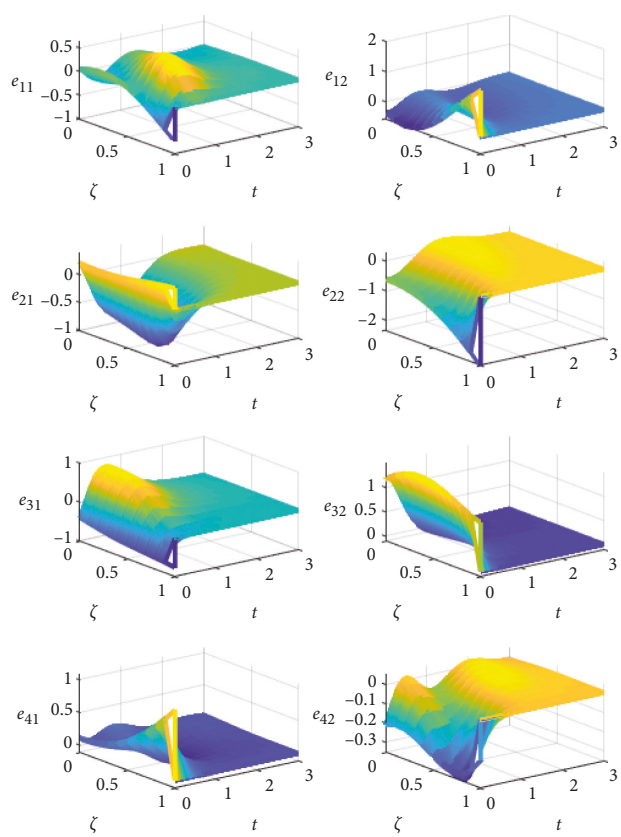

Figure 5: The closed-loop profile of $z(\zeta, t)$.

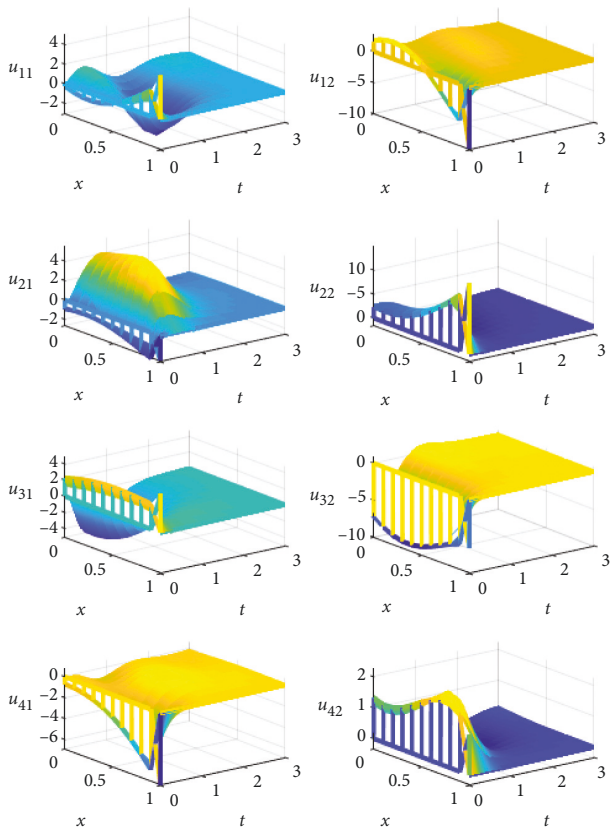

Figure 6: The profile of $u(\zeta, t)$.

6. Conclusion

This paper has dealt with leaderless consensus control of a class of semilinear HPDEMASs. One consensus controller of HPDEMASs under the structure of undirected graphs, making use of communication among agents, was established. Firstly, for the case of the symmetric seminegative definite convection coefficient, the boundary condition of the right endpoint was given. For the case of the symmetric semipositive definite convection coefficient, the boundary condition of the left endpoint was given. Two sufficient conditions for the consensus of HPDEMASs were obtained. Two examples illustrated the effectiveness of developed theoretical results. In future work, containment control, event-triggered control, and many other factors will be studied.

Data Availability

All the data in the simulation are included within this article.

Conflicts of Interest

The authors declare that they have no conflicts of interest.

Acknowledgments

This work was jointly supported by the National Natural Science Foundation of China (Grant no. 61976123), the Natural Science Research in Colleges and Universities of Anhui Province of China (Grant nos. KJ2020A0362, KJ2020A0361, KJ2019ZD15), the Anhui Natural Science Foundation (Grant no. 2108085MF213), the Taishan Young Scholars Program of Shandong Province, the Key Development Program for Basic Research of Shandong Province (Grant No.ZR2020ZD44), and the Natural Science Foundation of Heilongjiang Province (Grant no. LH2020F049).

References

[1] A. Dorri, S. Kanhere, and R. Jurdak, "Multi-agent systems: A survey," *IEEE Access*, vol. 6, Article ID 28573, 2018.

[2] D. J. McArthur, E. M. Davidson, V. M. Catterson et al., "Multi-agent systems for power engineering applications-Part I: Concepts, approaches, and technical challenges," *IEEE Transactions on Power Systems*, vol. 22, no. 4, pp. 1743–1752, 2007.

[3] J. Ferber and G. Weiss, *Multi-agent Systems: An Introduction to Distributed Artificial Intelligence*, Vol. 1, Addison-Wesley, , Boston, Massachusetts, United States, 1999.

[4] A. Briones, F. Prieta, M. Mohamad, S. Mohamad, M. Omatu, and J. Corchado, "Multi-agent systems applications in energy optimization problems: A state-of-the-art review," *Energies*, vol. 11, no. 8, p. 1928, 2018.

[5] W. He, W. Xu, X. Ge, Q.-L. Han, W. Du, and F. Qian, "Secure Control of Multiagent Systems Against Malicious Attacks: A Brief Survey," *IEEE Transactions on Industrial Informatics*, vol. 18, no. 6, pp. 3595–3608, 2022.

[6] W. He, Z. Mo, Q.-L. Han, and F. Qian, "Secure impulsive synchronization in Lipschitz-type multi-agent systems subject to deception attacks," *IEEE/CAA Journal of Automatica Sinica*, vol. 7, no. 5, pp. 1–9, 2020.

[7] M. Zouari, N. Baklouti, M. H. Kammoun, M. Ben Ayed, A. M Alimi, and J. Sanchez-Medina, "A multi-agent system for road traffic decision making based on hierarchical interval type-2 fuzzy knowledge representation system," in *Proceedings of the IEEE International Conference on Fuzzy Systems*, pp. 1–6, IEEE, Luxembourg, Luxembourg, July 11th -14th, 2021.

[8] M. Davoodi, S. Faryadi, and J. M. Velni, "A graph theoretic-based approach for deploying heterogeneous multi-agent systems with application in precision agriculture," *Journal of Intelligent and Robotic Systems*, vol. 101, no. 1, pp. 10–15, 2021.

[9] W. Ren, R. W. Beard, and E. M. Atkins, "A survey of consensus problems in multi-agent coordination," in *Proceedings of the American Control Conference*, pp. 1859–1864, IEEE, Atlanta Ga, June 8-10 2005.

[10] X. Tan, M. Cao, and J. Cao, "Distributed dynamic event-based control for nonlinear multi-agent systems," *IEEE Transactions on Circuits and Systems II: Express Briefs*, vol. 68, no. 2, pp. 687–691, 2021.

[11] Z. Liu, A. Zhang, J. Qiu, and Z. Li, "Event-triggered control of second-order nonlinear multi-agent systems with directed topology," *Neurocomputing*, vol. 452, pp. 820–826, 2021.

[12] W. Xu, W. He, D. W. C. Ho, and J. . Kurths, "Fully distributed observer-based consensus protocol: Adaptive dynamic event-triggered schemes," *Automatica*, vol. 139, Article ID 110188, 2022.

[13] D. Wang and W. Wang, "Necessary and sufficient conditions for containment control of multi-agent systems with time delay," *Automatica*, vol. 103, pp. 418–423, 2019.

[14] X. Li, Z. Yu, Z. Li, and N. Wu, "Group consensus via pinning control for a class of heterogeneous multi-agent systems with

input constraints," *Information Sciences*, vol. 542, pp. 247–262, 2021.

[15] W. He, X. Gao, W. Zhong, and F. Qian, "Secure impulsive synchronization control of multi-agent systems under deception attacks," *Information Sciences*, vol. 459, pp. 354–368, 2018.

[16] X. Ge, Q.-L. Han, D. Ding, X.-M. Zhang, and B. Ning, "A survey on recent advances in distributed sampled-data cooperative control of multi-agent systems," *Neurocomputing*, vol. 275, pp. 1684–1701, 2018.

[17] X. Jin, S. Lü, C. Deng, and M. Chadli, "Distributed adaptive security consensus control for a class of multi-agent systems under network decay and intermittent attacks," *Information Sciences*, vol. 547, pp. 88–102, 2021.

[18] G. Ferrari-Trecate, A. Buffa, and M. Gati, "Analysis of coordination in multi-agent systems through partial difference equations," *IEEE Transactions on Automatic Control*, vol. 51, no. 6, pp. 1058–1063, 2006.

[19] J. Qi, S. Wang, J.-an Fang, and M. Diagne, "Control of multi-agent systems with input delay via PDE-based method," *Automatica*, vol. 106, pp. 91–100, 2019.

[20] J. Qi, S.-X. Tang, and C. Wang, "Parabolic PDE-based multi-agent formation control on a cylindrical surface," *International Journal of Control*, vol. 92, no. 1, pp. 77–99, 2019.

[21] Q. Fu, L. Du, G. Xu, and J. Wu, "Consensus control for multi-agent systems with distributed parameter models via iterative learning algorithm," *Journal of the Franklin Institute*, vol. 355, no. 10, pp. 4453–4472, 2018.

[22] C. Yang, H. He, T. Huang et al., "Consensus for non-linear multi-agent systems modelled by PDEs based on spatial boundary communication," *IET Control Theory & Applications*, vol. 11, no. 17, pp. 3196–3200, 2017.

[23] C. Yang, T. Huang, A. Zhang, J. Qiu, J. Cao, and F. E. Alsaadi, "Output consensus of multiagent systems based on pdes with input constraint: A boundary control approach," *IEEE Transactions on Systems, Man, and Cybernetics: Systems*, vol. 51, no. 1, pp. 370–377, 2021.

[24] J. Dai, C. Yang, X. Yan, J. Wang, K. Zhu, and C. Yang, "Leaderless consensus control of nonlinear PIDE-type multi-agent systems with time delays," *IEEE Access*, vol. 10, pp. 21211–21218, 2022.

[25] X. Dai, C. Wang, S. Tian, and Q. Huang, "Consensus control via iterative learning for distributed parameter models multi-agent systems with time-delay," *Journal of the Franklin Institute*, vol. 356, no. 10, pp. 5240–5259, 2019.

[26] Y.-H. Lan, B. Wu, Y.-X. Shi, and Yi-P. Luo, "Iterative learning based consensus control for distributed parameter multi-agent systems with time-delay," *Neurocomputing*, vol. 357, pp. 77–85, 2019.

[27] Y.-H. Lan, W. Bin, and Y. Zhou, "Iterative learning consensus control with initial state learning for fractional order distributed parameter models multi-agent systems," *Mathematical Methods in the Applied Sciences*, vol. 45, no. 1, pp. 5–20, 2022.

[28] S.-H. Tsai, J.-W. Wang, En-S. Song, and H.-K. Lam, "Robust h_∞ control for nonlinear hyperbolic PDE systems based on the polynomial fuzzy model," *IEEE Transactions on Cybernetics*, vol. 51, no. 7, pp. 3789–3801, 2019.

[29] Ji Krstic and M. Krstic, "Event-triggered output-feedback backstepping control of sandwich hyperbolic PDE systems," *IEEE Transactions on Automatic Control*, vol. 67, no. 1, pp. 220–235, 2022.

[30] S. Benzoni-Gavage and D. Serre, *Multi-dimensional Hyperbolic Partial Differential Equations: First-Order Systems and Applications*, OUP Oxford, England, 2006.

[31] I. Aksikas, "Optimal control and duality-based observer design for a hyperbolic PDEs system with application to fixed-bed reactor," *International Journal of Systems Science*, vol. 52, no. 12, pp. 2493–2504, 2021.

[32] I. Karafyllis, N. Bekiaris-Liberis, and M. Papageorgiou, "Feedback control of nonlinear hyperbolic PDE systems inspired by traffic flow models," *IEEE Transactions on Automatic Control*, vol. 64, no. 9, pp. 3647–3662, 2019.

[33] M. Kobayashi, "Storage capacity of hyperbolic Hopfield neural networks," *Neurocomputing*, vol. 369, pp. 185–190, 2019.

[34] Q. Fu, P. Yu, G. Xu, and J. Wu, "Containment control for partial differential multi-agent systems," *Physica A: Statistical Mechanics and its Applications*, vol. 529, Article ID 121549, 2019.

[35] X. Huang and N. Huang, "Finite-time consensus of multi-agent systems driven by hyperbolic partial differential equations via boundary control," *Applied Mathematics and Mechanics*, vol. 42, no. 12, pp. 1799–1816, 2021.

[36] H. Zhang, T. Wang, and J. Qiu, "PDE-based leader-following consensus of multi-agent systems with input delay under spatial boundary communication," *IFAC-PapersOnLine*, vol. 54, no. 18, pp. 181–185, 2021.

[37] J. Qin, H. Gao, and W. X. Zheng, "Exponential synchronization of complex networks of linear systems and nonlinear oscillators: A unified analysis," *IEEE Transactions on Neural Networks and Learning Systems*, vol. 26, no. 3, pp. 510–521, 2015.

[38] J.-W. Wang, H.-N. Wu, and H.-X. Li, "Distributed fuzzy control design of nonlinear hyperbolic PDE systems with application to nonisothermal plug-flow reactor," *IEEE Transactions on Fuzzy Systems*, vol. 19, no. 3, pp. 514–526, 2011.

[39] I. Aksikas, A. Fuxman, J. F. Forbes, and J. J. Winkin, "LQ control design of a class of hyperbolic PDE systems: Application to fixed-bed reactor," *Automatica*, vol. 45, no. 6, pp. 1542–1548, 2009.

[40] A. Pilloni, A. Pisano, Y. Orlov, and E. Usai, "Consensus-based control for a network of diffusion PDEs with boundary local interaction," *IEEE Transactions on Automatic Control*, vol. 61, no. 9, pp. 2708–2713, 2016.

[41] D. Bahuguna, R. Sakthivel, and A. Chadha, "Asymptotic stability of fractional impulsive neutral stochastic partial integro-differential equations with infinite delay," *Stochastic Analysis and Applications*, vol. 35, no. 1, pp. 63–88, 2017.

[42] H. Long and H. T. P. Thao, "Hyers-Ulam stability for nonlocal fractional partial integro-differential equation with uncertainty," *Journal of Intelligent and Fuzzy Systems*, vol. 34, no. 1, pp. 233–244, 2018.

Hindawi
Discrete Dynamics in Nature and Society
Volume 2022, Article ID 8969903, 14 pages
https://doi.org/10.1155/2022/8969903

Research Article

Model Selection and Parameter Estimation for an Improved Approximate Bayesian Computation Sequential Monte Carlo Algorithm

Yue Deng,[1] Yongzhen Pei,[2] Changguo Li,[3] and Bin Zhu[1]

[1]*School of Software, Tiangong University, Tianjin 300387, China*
[2]*School of Mathematical Science, Tiangong University, Tianjin 300387, China*
[3]*Department of Basic Science, Army Military Transportation University, Tianjin 300161, China*

Correspondence should be addressed to Yongzhen Pei; peiyzh_team@sina.com

Received 24 April 2022; Accepted 12 June 2022; Published 30 June 2022

Academic Editor: Abdellatif Ben Makhlouf

Model selection and parameter estimation are very important in many fields. However, the existing methods have many problems, such as low efficiency in model selection and inaccuracy in parameter estimation. In this study, we proposed a new algorithm named improved approximate Bayesian computation sequential Monte Carlo algorithm (IABC-SMC) based on approximate Bayesian computation sequential Monte Carlo algorithm (ABC-SMC). Using the IABC-SMC algorithm, given data and the set of two models including logistic and Gompertz models of infectious diseases, we obtained the best fitting model and the values of unknown parameters of the corresponding model. The simulation results showed that the IABC-SMC algorithm can quickly and accurately select a model that best matches the corresponding epidemic data among multiple candidate models and estimate the values of unknown parameters of model very accurately. We further compared the effects of IABC-SMC algorithm with that of ABC-SMC algorithm. Simulations showed that the IABC-SMC algorithm can improve the accuracy of estimated parameter values and the speed of model selection and also avoid the shortage of ABC-SMC algorithm. This study suggests that the IABC-SMC algorithm can be seen as a promising method for model selection and parameter estimation.

1. Introduction

In many fields of engineering and science, researchers or engineers are dealing with model selection and comparison problems. The selection of the most suitable model among several competitive models is the necessary basis to determine whether the data can accurately estimate and predict the characteristics of data. In reality, it may be a challenge to choose a model that best matches the real data among some similar models, because it requires a deep understanding of the nature of things, in addition, if the parameters in the similar models are also unknown and the reliability of model selection is questionable. To get a reliable model, it is necessary to estimate the values of unknown parameters in the model. Infectious diseases that have occurred in recent years have significantly affected public health and the economy. Therefore, it is very important to perform model selection and parameter estimation in similar models in the process of infectious disease analysis, prediction, and control.

More attention has been paid to model selection and parameter estimation in recent decades. Given several potential models and one or more sets of data, the model selection should be able to select the best fitting model and estimate the values of unknown parameters in the model, to better fit the data. Several approaches have been applied to model selection, among which the Bayesian method is the most popular. The Bayesian theory is a very comprehensive approach and has universal applicability to the method of inferring models from data. Many different examples illustrated the application of the Bayesian methods [1–6]. When the likelihood function is very complex or difficult to

calculate, the Markov chain Monte Carlo (MCMC) method that can obtain approximate posterior distributions of parameters through sampling is successfully applied in model selection [7]. A practical solution combining particle filter model identification algorithm with real-time measurement system was proposed [8]. Skilling [9, 10] has proposed nested sampling (NS) as an alternative way of handling model selection and parameter estimation. In [11], when the distance between observed data and simulated data is the smallest, the observed data in likelihood are replaced by simulated data in the ABC algorithm. The authors in [12, 13] introduced the application of approximate Bayesian computation based on the sequential Monte Carlo (ABC-SMC) algorithm in model selection and parameter estimation. The advantage of ABC-SMC algorithm is that the prior distributions of parameters are adaptive, so it can study the complex posterior distributions of parameters more effectively. Reference [14] offered a recalibration posterior processing method that satisfies the coverage attribute to improve the quality of posterior distributions of parameters of ABC algorithm. Several criteria have been proposed to deal with the goodness of fit between the candidate model and data when dealing with model selection, such as AIC [15, 16], weighted Bayesian information criterion (BIC) [17], and Bayes factors, but all criteria are an approximation of Bayes factors [18]. These criteria are related to the marginal likelihood approximation and are also commonly used in the Bayesian inference [19, 20]. AIC is still the most widely used information criterion for ranking models among IT methods.

The ABC-SMC algorithm is a classic algorithm that provides the possibility to select the most suitable model among multiple competing models and estimate the values of unknown parameters of the model. However, a tolerance sequence is required as a selection criterion for accepting or rejecting sampling parameters in this algorithm. More seriously, the ABC-SMC algorithm must manually define an appropriate threshold sequence to ensure the accuracy of the algorithm, but choosing an appropriate threshold sequence requires us to try many times, which may be very troublesome and time-consuming. Another problem of the ABC-SMC algorithm is that the algorithm selects an appropriate model at each iteration instead of selecting an optimal model at the end of the algorithm, which results in a longer computation time and lower efficiency of the algorithm. So, is there a better way to solve these problems? Is it possible to choose the best model to fit the corresponding data?

This study is intended to investigate the effects of the proposed algorithm in model selection and parameter estimation. To overcome the drawbacks of classical ABC-SMC algorithm, we propose an IABC-SMC algorithm based on the ABC-SMC algorithm and recalibration postprocessing method. Taking dengue outbreak data and A/H1N1 outbreak data of infectious disease as examples, the IABC-SMC algorithm is used to estimate the values of unknown parameters of classic model including logistic model and Gompertz model, and the model that best matches the corresponding data is selected. The simulations show that the parameter values estimated by the IABC-SMC algorithm are very accurate, and the model that matches the data can be quickly selected from multiple candidate models. By comparing the IABC-SMC algorithm with the ABC-SMC algorithm, we can see many advantages of the IABC-SMC algorithm.

2. Methods

2.1. Background Knowledge. In this section, we reviewed the theory and some details of ABC-SMC algorithm and recalibration postprocessing method, before introducing the IABC-SMC model selection algorithm.

2.1.1. Approximate Bayesian Computation Based on Sequential Monte Carlo Algorithm. The approximate Bayesian computation (ABC) algorithm is a Bayesian inference method developed in recent years based on data simulation. When dealing with complex or computationally tricky likelihood problems, ABC is an improved Bayesian inference algorithm for the purpose of inferring the posterior distributions of parameters. Based on the ABC algorithm, many methods have been extended including the ABC rejection sampler algorithm and ABC MCMC algorithm [21, 22]. ABC rejection algorithm is one of the basic algorithms of ABC. When the prior distributions of parameters are far from the posterior distributions of parameters, it may lead to too long computation time of the ABC rejection algorithm. The potential advantage of ABC MCMC algorithm is that it saves computation time of algorithm due to the introduction of acceptance probability. However, this algorithm can cause sample values of parameters to be trapped in a low probability region for a long time and we may never get a good approximation of parameters. To solve these problems, the concept of particle filtering has been introduced. The ABC algorithm is accelerated using a large pool of candidate objects called particles instead of selecting a candidate particle. In each step of the algorithm, the particles are interfered and filtered by distance metric and weights, and eventually, the particle pool becomes closer and closer to meet the requirement of the posterior estimation of parameters. This method is named ABC-SMC.

The ABC-SMC Algorithm 1 is described as follows [23].

2.1.2. Recalibration Postprocessing Method. A large number of postprocessing methods have been mentioned to correct the deviation between posterior distributions of parameters of the ABC algorithm and the true distributions of parameters. The purpose of the recalibration postprocessing method introduced in [14] is to produce an approximation posterior distribution of parameters that is closer to the true distributions of parameters. Not only does this method improve the accuracy of posterior distributions of parameters but also it avoids some shortcomings of existing posterior processing methods. So, the recalibration method can directly sample from the

S1 Define the threshold values $\varepsilon_1, \ldots, \varepsilon_H$ (larger at the beginning and decrease gradually), start with iteration $h = 1$
S2 Set the particle indicator $j = 1$.
S3 If $h = 1$, sample θ^* from the prior distribution $\pi(\theta)$. A simulated data set $D_{(f)}(\theta^*)$ of F_1 times is generated and the value of $f_h(\theta^*)$ is calculated, where $p(D|\theta)$ is a posterior distribution and $D_{(f)} \sim p(D|\theta)$ for any deterministic parameter θ and F_1, $f_h(\theta^*) = \sum_{f=1}^{F1} I\left\{d(D_0, D_{(f)}(\theta^*)) \leq \epsilon_1\right\}$ represents the approximation degree between θ^* and the true parameter, D_0 is the experimental data set and I is an indicative function.
If $h > 1$, sample a particle from the last generation $\theta_{h-1}^{(j)}$ with weight $v_{h-1}^{(j)}$, $j = 1, 2, \ldots, N$ and use a kernel function K_h to disturb the particle to gain θ^*.
If $\pi(\theta^*) = 0$ or $f_h(\theta^*) = 0$, return to the beginning of $S3$.
S4 Set $\theta_h^j = \theta^*$ and determine the weights of the estimated particle θ_h^j, $v_h^{(j)} = \begin{cases} f_h(\theta_h^j) & \text{if } h = 1 \\ (\pi(\theta_h^j) f_h(\theta_h^j) / \sum_{j=1}^{N} K_h(\theta_{h-1}^j, \theta_h^j)) & \text{if } h > 1 \end{cases}$
If $j < N$, update $j = j + 1$ and go back to $S3$ until all the particles and their distributions are obtained.
S5. Normalize the weights $v_h^{(j)}$, If $h < H$ (number of threshold values), update $h = h + 1$ and go back to $S2$.

Algorithm 1: ABC-SMC algorithm.

approximate posterior distributions of samples or improve the efficiency of other posterior adjustment methods.

Recalibration postprocessing algorithm presents a standard parameter posterior simulation algorithm, which completes the recalibration process of parameters. $\theta^{(i)}$ $(i = 1, \ldots, N)$ sampled from the prior distribution of parameter is substituted into the model $\pi(y|\theta)$ to get the simulation value $y^{(i)}$. Then, the weight of parameters $\omega^{(i)}$ is calculated according to the kernel function; that is, $\omega^{(i)} \propto k_h(\|y^{(i)} - y_{obs}\|)$ and $K_h(u)$ is a smoothing kernel with scale parameter $h > 0$. The marginal distribution function $\widetilde{F}_{j,y_{obs}}(\cdot)$ based on y_{obs} is constructed with the weighted parameters $\left\{\theta^{(i)}, \omega^{(i)}\right\}_{i=1}^{N}$. Marginal distribution function $\widetilde{F}_{j,y_{(i)}}(\cdot)$ based on $y_{(i)}$ is constructed in the same way with $\left\{\theta^{(m)}, v^{(m)}\right\}_{m=1,m\neq i}^{N}$ as samples, where $\left\{\theta^{(m)}, v^{(m)}\right\}_{m=1,m\neq i}^{N}$ is the weighted parameters. It is assumed that $\widetilde{F}_{j,y_{obs}}(\cdot) \approx \widetilde{F}_{j,y_{(i)}}(\cdot)$, and then, the probability of $\theta_j^{(i)}$ is calculated as $p_j^{(i)} = \widetilde{F}_{j,y_i}(\theta_j^{(i)})$. The adjusted parameters can be obtained according to several results in [14], namely $\widehat{\theta}^i = \widetilde{F}_{j,y_{obs}}^{-1}(p_j^{(i)})$.

The recalibration postprocessing method proceeds as follows:

Data simulation and weighting:

For $i = 1, \ldots, N$:

M1.1 Sample $\theta^{(i)}$ from prior distribution $\pi(\theta)$.

M1.2 $y^{(i)}$ is obtained from likelihood $\pi(y|\theta)$.

M1.3 Compute the sample weight $w^{(i)} \propto K_h\|y^{(i)} - y_{obs}\|$, where $K_h(u)$ is a smoothing kernel with scale parameter $h > 0$.

Recalibration:

M2.1 For $j = 1, \ldots, d$, construct the jth marginal distribution function $\widetilde{F}_{j,y_{obs}}(\cdot)$ according to sample $\left\{\theta^{(i)}, w^{(i)}\right\}_{i=1}^{N}$.

M2.2 Construct the jth marginal distribution function $\widetilde{F}_{j,y^{(i)}}(\cdot)$ with $\left\{\theta^{(m)}, v^{(m)}\right\}_{m=1,m\neq i}^{N}$ as samples in the same way of step $M1.3$ and $M2.1$.

M2.3 Calculate the probability of $\theta_j^{(i)}$ in $\widetilde{F}_{j,y^{(i)}}(\cdot)$, $p_j^{(i)} = \widetilde{F}_{j,y^{(i)}}(\theta_j^{(i)})$.

M2.4 (optional) Correct $p_j^{(i)}$ using a regression adjustment.

M2.5 Set $\widehat{\theta}^i = \widetilde{F}_{j,y_{obs}}^{-1}(p_j^{(i)})$.

2.2. Model Selection Algorithm. Mathematical models play an important role in understanding how the disease spread. There is an evidence that mathematical models have the ability to inform policymakers, in particular the feasibility of achieving the ambitious goal of keeping the prevalence of moderate and severe infections below 1% by 2020 [24]. So, model prediction based on appropriate epidemiological data is very important. The goal of ABC algorithm is to obtain approximate posterior distributions of parameters that are easy to calculate the following:

$$\pi(\theta|y_{\text{obs}}, M) \propto L(y_{\text{obs}}|\theta, M)\pi(\theta|M), \tag{1}$$

where M is a model based on a series of parameter θ, $\pi(\theta|M)$ represents the prior distribution of the parameter space, and $L(y_{obs}|\theta, M)$ is the likelihood of the observed data y_{obs} for a given series of parameter θ. To overcome the problem of intractable likelihood function, ABC algorithm compared the observed value with the simulated value and accepted the simulated value when the distance between the observed value and the simulated value is less than the artificial threshold. In the ABC-SMC algorithm, it sampled from a set of parameters and treated each parameter vector set as a particle, instead of having only one parameter vector at a time.

The disadvantage of ABC-SMC algorithm is that an appropriate threshold sequence must be selected to ensure the accuracy of the algorithm, and it is very troublesome and time-consuming to choose an appropriate threshold

sequence. Generally, if the defined tolerance sequence is too long, it will lead to too many simulations of the algorithm and take a long time. On the contrary, the posterior distributions of the estimated parameters are inaccurate if the defined tolerance sequence is too short. The principle of the ABC-SMC algorithm is to find the optimal model and parameters in each iteration of the algorithm, rather than selecting the optimal model and parameters at the end of the algorithm, which is also time-consuming. Therefore, to overcome these shortcomings, we proposed the improved approximate Bayesian computation algorithm (IABC-SMC) based on the ABC-SMC algorithm. The principle of the IABC-SMC algorithm is to calculate the values of unknown parameters of each candidate model separately, then recalibrate the values of unknown parameters in the model, and finally select the model that best matches the data. In each iteration of the algorithm, the particles are selected by the distance between simulated data and observed data to avoid setting the threshold sequence manually. Then, the posterior distributions of unknown parameters can be adjusted through the recalibration postprocessing method to make them closer to the true distributions of unknown parameters in the model. So, the IABC-SMC algorithm also improves the accuracy of estimated unknown parameters.

In the first iteration, the IABC-SMC algorithm calculated the distance between the simulated data and the observed data and selected some particles with an acceptance rate when the distance between the simulated data and the observed data is very close, which means that these particles are selected randomly to avoid setting threshold sequence artificially. The weights of these particles are all 1. In the second iteration, the particles selected randomly from the previous generation were substituted into the model to get the simulated data, and the particles with an acceptance rate were selected through the distance between the simulated data and the observed data. Finally, the particles of the second iteration were obtained by perturbation kernel. The weights of these particles were updated and normalized. After several iterations of this algorithm, preliminary posterior distributions of parameters can be obtained, but these distributions are different from the true distributions of parameters. Then, we adjusted the above distributions by the recalibration postprocessing method to make the adjusted distributions closer to the true distributions of parameters.

The IABC-SMC Algorithm 2 is described as follows.

2.3. Model Evaluation Criteria. Recently, more and more scientists are using novel model selection methods to analyze data. The AIC method is a popular method among these novel methods [25–27]. AIC provides a standard to balance the complexity of estimated model and the goodness of data. This approach allows people to compare multiple competing models and estimate which model is closest to the "real" process behind the epidemiological phenomenon being studied. Accordingly, AIC itself is meaningless, but its significance comes from the comparison of the model and AIC value. The model with the smallest AIC value is the "closest model." The calculation of AIC is not difficult, and it is counted as follows:

$$\mathrm{AIC} = -2 \cdot \ln(L) + 2k, \tag{2}$$

where L is likelihood function and k is number of parameters in the model.

Nevertheless, there are various controversies about the use of AIC [16], and many alternative methods have been proposed. In the meantime, BIC is proposed as a special alternative to AIC, which is superior to AIC in the average method of IT model [17]. BIC is denoted as follows:

$$\mathrm{BIC} = -2 \cdot \ln(L) + k\ln(n), \tag{3}$$

where L is likelihood function, k is number of parameters in the model, and n is the length of observed data.

3. Data and Results

3.1. Data and Models. We employed the data from China's Centers for Disease Control and Prevention website on the number of confirmed cases during the dengue outbreak from 2014 to 2015 and the number of confirmed cases during the A/H1N1 outbreak from 2009 to 2010. The data listed in Tables 1 and 2 represent the monthly cumulative confirmed number of dengue and A/H1N1 reported by hospitals across China, respectively. We considered these data to be observed data.

Logistic model and Gompertz model are widely used single-population models that can be easily used to fit data and estimate the values of unknown parameters. They are also two alternative models of dengue data and A/H1N1 data in this study.

The logistic model is shown as follows [28]:

$$x'(t) = rx(t)\left(1 - \frac{x(t)}{K}\right). \tag{4}$$

The Gompertz model is shown as follows [29]:

$$x'(t) = rx(t)\ln\left(\frac{K}{x(t)}\right). \tag{5}$$

For convenience, the above two models are denoted as M_1 and M_2. $x(t)$ in (4) and (5) represents the number of confirmed cases of dengue and A/H1N1 at time t, respectively. There are two distinct unknown parameters r and K. The positive parameter r represents the intrinsic growth rate, which reflects the propagation capacity of infectious diseases under ideal conditions. K denotes the maximum environmental capacity of infectious diseases.

Our purpose is to select the best model among the above two commonly used models based on the infectious disease data listed in Tables 1 and 2, which will help us to evaluate the characteristics of infectious diseases. Therefore, we need to estimate the values of unknown parameters r and K of each candidate model according to the data, to determine the best fitting model.

The first generation
Q1.1 Define the number of iteration $t = 1$, the number of particles $i\,(i = 1, \ldots, n)$.
Q1.2 Sample $\theta^{(i)}$ from prior distribution $\pi(\theta)$ and get simulated values $y^{(i)}$ from model $\pi(y|\theta)$.
Q1.3 An acceptance rate of particles θ^* is selected from $\pi(\theta)$ and simulated values y^* are selected from y when the simulated value y^* is close to the observed value y_{obs}.
Q1.4 Set $\theta_t^{(i)} = \theta^*$ and fix the weights $w_t^{(i)} = 1\,(i = 1, \ldots, n * \text{acceptance rate})$.
The 2. . .T generation
Q2.1 Define the number of iteration $t\,(t = 2, \ldots, T)$, the number of particles $i\,(i = 1, \ldots, n)$ and the particle dimension $j\,(j = 1, \ldots, m)$.
Q2.2 Select n particles with weights w_{t-1} from previous generation particles randomly and use the kernel function K to perturb those particles, an acceptance rate of particles θ^{**} is selected from $\pi(\theta)$ and simulated values y^{**} are selected from y when the simulated value y^{**} is close to the observed value y_{obs}.
Q2.3 Set $\theta_t^{(i)} = \theta^{**}$ and fix the weight of each particle $w_t^i = (\pi(\theta_t^i)/\sum_{j=1}^n w_{t-1}^j k_t(\theta_{t-1}^j, \theta_t^i))$.
Q2.4 Normalize the weights $w_t^{(i)}$.If $t < T$, update $t = t + 1$ and return to Q2.1.
Recalibration
Q3.1 According to the particles and the simulation values obtained by the Tth iteration, the weight v of each particle is calculated and $v^{(i)} \propto k_h(\|y^{(i)} - y_{obs}\|)$, where $k_h(0)$ is a smooth kernel with scale parameter $h > 0$.
Q3.2 For $j = 1, \ldots, m$, construct the jth marginal distribution function $\widetilde{F}_{j,y_{obs}}(\cdot)$ according to sample $\left\{\theta^{(i)}, v^{(i)}\right\}_{i=1}^Q$, where $v^{(i)} > 0$ and Q is the total number of particles in the marginal distribution function.
Q3.3 Construct the jth marginal distribution function $\widetilde{F}_{j,y_i}(\cdot)$ according to sample $\left\{\theta^{(x)}, v^{(x)}\right\}_{x=1,x\neq i}^Q$ in the same way of Q3.1 and Q3.2.
Q3.4 Calculate the probability of $\theta_j^{(i)}$ in $\widetilde{F}_{j,y_i}(\cdot)$, $p_j^{(i)} = \widetilde{F}_{j,y_{(i)}}(\theta_j^{(i)})$.
Q3.5 Calculate the adjusted particle, $\widehat{\theta}^{(i)} = \widetilde{F}_{j,y_{obs}}^{-1}(p_j^{(i)})$.
Model output
Q4 According to the given model, adjusted parameters and weights, the evaluation criteria of AIC and BIC are obtained, then the most fitting model can be selected.

Algorithm 2: IABC-SMC algorithm.

Table 1: Monthly cumulative confirmed data on dengue outbreaks from April 2014 to March 2015.

Month	4	5	6	7	8	9	10	11	12	1	2	3
Data	5	28	53	208	995	15754	44550	47110	47290	47309	47331	47356

Table 2: Monthly cumulative confirmed data on A/H1N1 outbreaks from May 2009 to April 2010.

Month	5	6	7	8	9	10	11	12	1	2	3	4
Data	22	566	1587	3170	19136	52079	96349	125128	131059	131893	132308	132431

3.2. Numerical Results. Our focus so far has been on the IABC-SMC algorithm, model evaluation criteria, and two alternative models with unknown parameters of the intrinsic growth rate r and maximum environmental capacity K. To simplify the interpretation of our mathematical results, we continued to discuss them by numerical simulation.

3.2.1. Results of Dengue

(1) Simulation 1: Results of IABC-SMC Algorithm. To get the results of model selection and parameter estimation of dengue by the IABC-SMC algorithm, the number of initial infections $x_0 = 5$ according to Table 1, the total number of algorithm iterations $T = 6$, and the total number of parameters $n = 6000$ is used here as the initial condition. The infection time of dengue in China was from April 2014 to March 2015 (12 months). It is proved by practice that the Monte Carlo error is minimal when the acceptance rate is 0.4, so we set the acceptance rate to 0.4.

When applying the IABC-SMC algorithm to estimate unknown parameters of model and make model selection of dengue disease, we assumed that the prior distribution of each estimated parameter is uniformly distributed, $r \sim U(0, 2)$ and $K \sim U(40000, 60000)$. The disturbance added by each sampled particle is uniform, and r and K are 0.1 and 1000, respectively. In this experiment, two particles are sampled simultaneously and the IABC-SMC algorithm ends when the most fitting model is selected for dengue data. The algorithm abstracts the parameter estimation of the above two models and the real data of dengue.

Figure 1 shows the histograms of intrinsic growth rate r (Figure 1(a)) and maximum environmental capacity K (Figure 1(b)) of the logistic model. These parameters are obtained by the IABC-SMC algorithm. X-coordinate indicates the range of estimated parameter, and Y-coordinate indicates the frequency of parameter occurrence. In Figure 1,

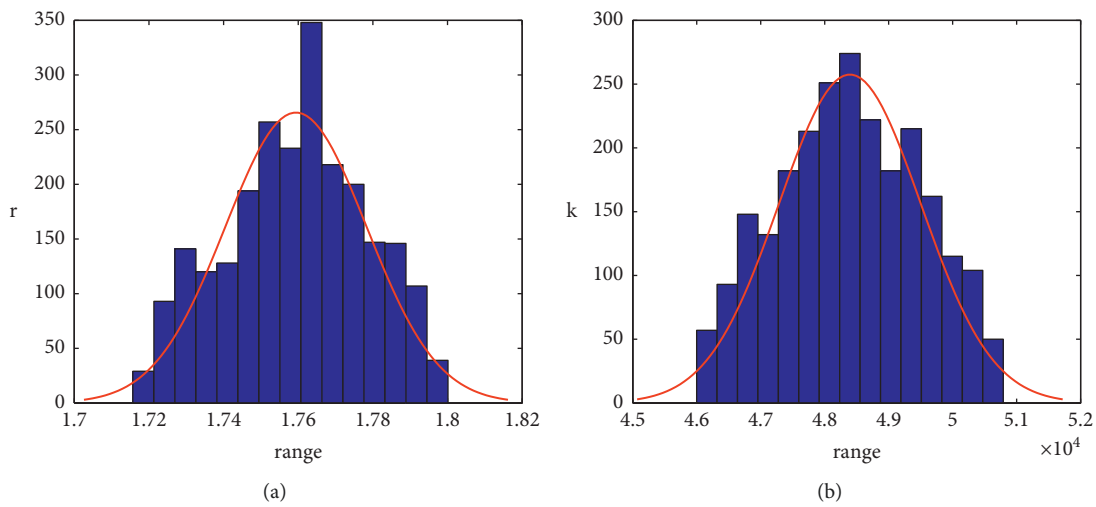

Figure 1: Parameter histograms of logistic model of the IABC-SMC algorithm. (a) Estimation of r. (b) Estimation of K. Here, the initial states are $n = 6000, x_0 = 5, a = 0.4, T = 6$, and $t = 12$.

Table 3: Parameter ranges and statistics of the logistic model.

Parameter	Lower bound	Upper bound	Mean	Std.	[2.5th, 97.5th] percentiles
r	1.7157	1.8001	1.7596	7.2548×10^{-4}	[1.7231, 1.7927]
K	45998	50790	48393	42.6146	[46351, 50413]

the range of parameter r is between 1.72 and 1.8 and the range of parameter K is between 4600 and 5100, which indicates that the range of posterior distributions of these two parameters is very small and concentrated. The distributions of both parameters are all close to normal distributions. When r is about 1.764, the cumulative number of r reaches a peak of about 350 times. When the parameter K is 48500, the cumulative number of K reaches a peak of about 270 times.

The parameter statistics associated with candidate model can be estimated. Table 3 gives the ranges of parameters and parameter statistics of approximate posterior distributions of logistic model. As can be seen from Table 3, the two parameters are estimated precisely and the results of these two parameters are excellent because the most parameter values are within the [2.5th, 97.5th] percentiles.

Figure 2 displays the histograms of intrinsic growth rate r (Figure 2(a)) and maximum environmental capacity K (Figure 2(b)) of the Gompertz model. They are available by the IABC-SMC algorithm, which is the same method as above. X-coordinate indicates the range of estimated parameters, and Y-coordinate indicates the frequency of occurrence of parameters. As can be seen from Figure 2, the distributions of these two parameters are all similar to normal distribution, but both distributions of these parameters in Figures 2(a) and 2(b) have two peaks. When r is 0.5 and 0.53, the peak of cumulative times of r all reaches about 235 times. When the parameter K is 50000 and 54000, the peak of cumulative number of K all reaches about 280 times. So, the estimated parameters are not particularly good.

Table 4 expresses the parameter ranges and the parameter statistics of the Gompertz model of approximate posterior distribution. We can see that the variances of these two parameters in Table 3 are smaller than that in Table 4, which indicates that the parameter range estimated by the logistic model is more accurate.

To further study which model is more credible and verify the posterior distributions of parameters, some calculations and simulations were performed. As mentioned above, the models are sorted by the value of AIC and the best approximation model is the model with the smallest AIC value. Therefore, AIC is an important element to measure the matching degree between model and data. The selection result of the two candidate models is based on the AIC values calculated in Table 5, which confirms the decisive evidence for the existence of the model. That is, they are 7831.8 and 43980 for logistic model ($M1$) and Gompertz model ($M2$), respectively. The AIC value of model $M1$ is the smallest, so the best model is logistic model. To further verify the effect of IABC-SMC algorithm, the BIC value of each model was counted. BIC values of models $M1$ and $M2$ are 7832.7 and 43981, respectively. The results also indicate that the logistic model is the best, which is consistent with the results of AIC. Finally, we verified the above results again by comparing the operation time of model selection, because the operation time of $M1$ is 151.48 seconds, which is less than 163.52 seconds of $M2$. Therefore, the logistic model saves the computation time of IABC-SMC algorithm and is more efficient than the Gompertz model.

Using the mean values of the parameters obtained above, the disease prediction figure can be made. Figure 3 manifests the comparison between the observed data and simulated data calculated from the estimated mean values of the

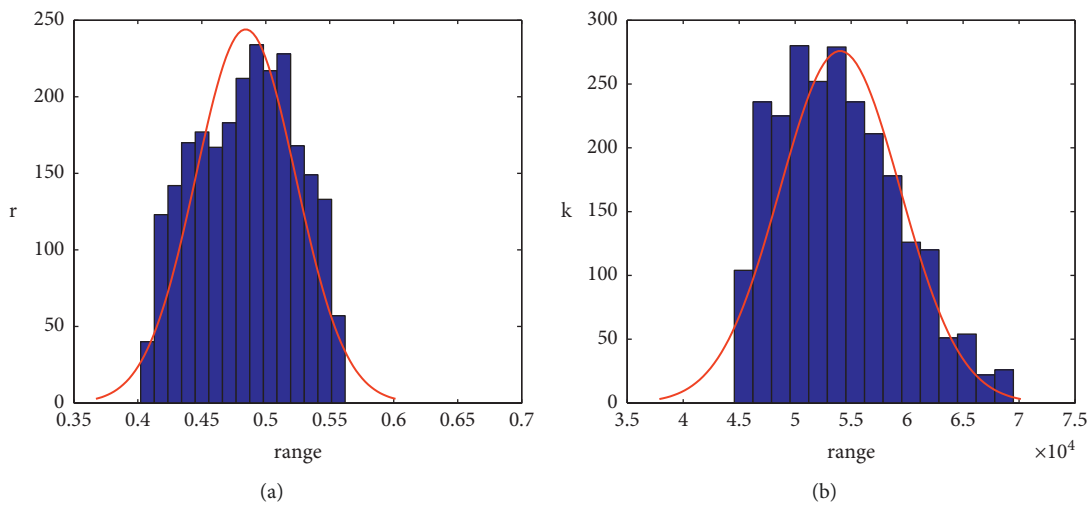

Figure 2: Parameter histograms of the Gompertz model of the IABC-SMC algorithm. (a) Estimation of r. (b) Estimation of K. Here, the initial states are $n = 6000, x_0 = 5, a = 0.4, T = 6$, and $t = 12$.

Table 4: Parameter ranges and statistics of the Gompertz model.

Parameter	Lower bound	Upper bound	Mean	Std.	[2.5th, 97.5th] percentiles
r	0.4022	0.5621	0.4861	6.0838×10^{-4}	[0.4143, 0.5507]
K	44572	69495	53852	44.5627	[45830, 65812]

Table 5: AIC, BIC, and operation time of two models.

Model	Logistic	Gompertz
AIC	7831.8	43980
BIC	7832.7	43981
Operation time (s)	151.48	163.52

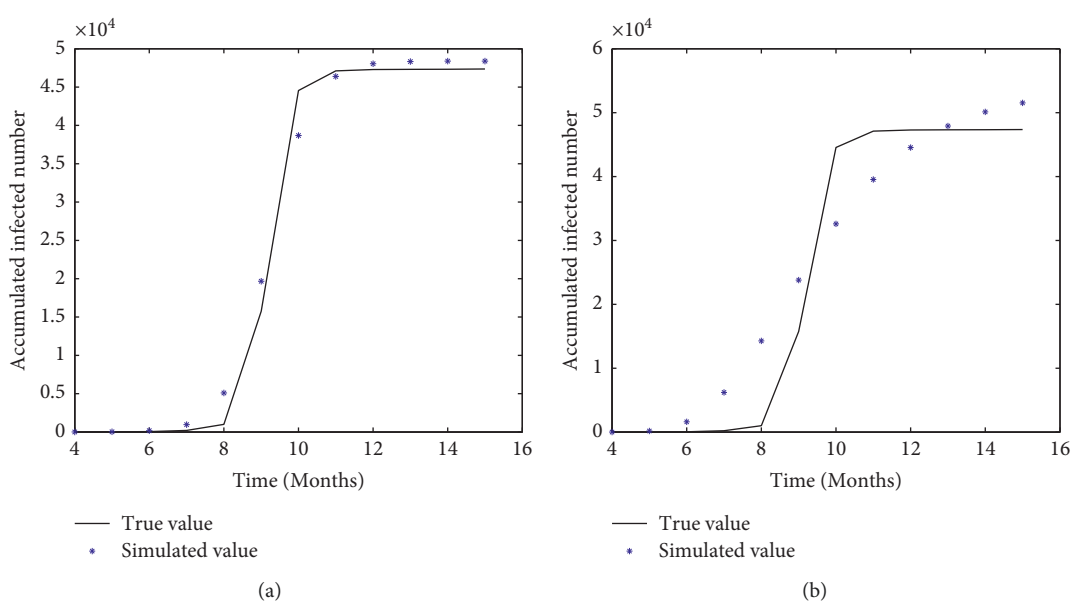

Figure 3: Comparison between the observed data and simulated data of the IABC-SMC algorithm. (a) Logistic model. (b) Gompertz model. Here, the initial states are $n = 6000, x_0 = 5, a = 0.4, T = 6$, and $t = 12$.

parameters. Figure 3(a) is the fitting effect of observed data and simulated data of the logistic model, and Figure 3(b) is the fitting effect of observed data and simulated data of the Gompertz model. The black curve represents the number of confirmed cases of dengue fever from April 2014 to March 2015, and the blue dots represent the simulated data of the model. The trend of Figure 3(a) is that the number of infections rises sharply from August and stabilizes after November. It is clear that the logistic model is very consistent with the data of the outbreak of dengue fever in 2014. The trend of Figure 3(b) is that the number of simulated infections is on the rise, but there is a certain deviation between the simulated data and the observed data. Under the same conditions, the simulated data of the logistic model match the observed data much better than those of the Gompertz model.

From the above results, it can be concluded that the IABC-SMC algorithm can improve the quality of posterior distributions of parameters greatly, obtain more accurate parameter values, and choose the most suitable model. The result of model selection is also consistent with the result of [7].

(2) Simulation 2: Results of ABC-SMC Algorithm. To verify the effects of the IABC-SMC algorithm, we compared the IABC-SMC algorithm, with the ABC-SMC algorithm in [13]. Both algorithms used the same model, experimental data, parameter initial values, and thresholds. The threshold set is selected manually and given as $\varepsilon = 65389, 41043, 33049, 30077, 28770$, and 16433. The prior probability of each model is equal, i.e., $p(M1) = p(M2) = 1/2$. Figure 4 is the fitting effect of the observed data and simulated data obtained by the ABC-SMC algorithm. The black curve represents the number of confirmed cases of dengue fever from April 2014 to March 2015, and the blue dots represent the simulated data of the ABC-SMC algorithm. Compared with the Gompertz model, the simulated data obtained from logistic model are closer to the observed data, which indicates that the logistic model is better than the Gompertz model. The result of model selection is also consistent with the result of the IABC-SMC algorithm, and the results of model selection are all logistic model. However, from the perspective of simulation effect of algorithm, the fitting effect between the simulated data obtained from the ABC-SMC algorithm and the observed data is worse than that of the IABC-SMC algorithm. From the perspective of simulation time of algorithm, the computation time of ABC-SMC algorithm is 40272 seconds, which far exceeds the computation time of IABC-SMC algorithm.

Figure 5 shows the histograms of parameters r (Figure 5(a)) and K (Figure 5(b)) of the model selected by the ABC-SMC algorithm. The X-coordinate is the range of the parameters, and the Y-coordinate is the frequency of parameter. When r is 0.5, parameter r appears most frequently, which is about 2700 times. However, other values of r occur between 1.5 and 2. The parameter K appears between 40000 and 60000. When K is 55000, K appears most frequently and it is about 680 times. Table 6 shows the parameter summary statistics estimated by the ABC-SMC algorithm. It can be seen from Figure 5 and Table 6 that the ABC-SMC algorithm can also estimate the posterior distributions of unknown parameters, but the parameter range is larger and more dispersed than that of the IABC-SMC algorithm.

These results confirm that the IABC-SMC algorithm has the advantages of high computational efficiency, low time complexity, and more accurate parameter values.

3.2.2. Results of A/H1N1

(1) Simulation 1: Results of IABC-SMC Algorithm. To verify the results of model selection and parameter estimation of A/H1N1 by the IABC-SMC algorithm, the number of initial infections $x_0 = 22$ according to Table 2, total number of algorithm iterations $T = 6$, and the total number of parameters $n = 6000$ are used as the initial condition. The infection time of A/H1N1 disease in China was from May 2009 to April 2010, expressed by $t = 5$ to $t = 16$ (12 months) in diagram. As above, the acceptance rate is also set to 0.4.

When applying the IABC-SMC algorithm to estimate model parameters and make model selection, we assumed that the prior distribution of each estimated parameter is uniformly distributed, $r \sim U(0, 2.5)$ and $K \sim U(100000, 150000)$. The disturbance added by each sampled particle is uniform, and r and K are 0.1 and 1000, respectively. When the IABC-SMC algorithm finishes, the model that best matches the A/H1N1 data can be obtained. The algorithm abstracts the parameter estimation of the above two models and the real data of A/H1N1.

Figure 6 shows the histograms of intrinsic growth rate r (Figure 6(a)) and maximum environmental capacity K (Figure 6(b)) of the logistic model. These parameters are available by the IABC-SMC algorithm. X-coordinate indicates the range of estimated parameters, and Y-coordinate indicates the frequency of parameters. As can be seen from Figure 6, the range of parameter r is between 1.6 and 1.68, and the range of parameter K is between 125000 and 139520, which shows that the range of posterior distributions of these two parameters is very small and concentrated. The distributions of both parameters are all close to normal distribution. When r is about 1.64, the peak of cumulative number of r reaches about 290 times. When the parameter K is 131000, the peak of cumulative number of K reaches about 235 times.

The correlation statistics of parameters r and K related to the logistic model can be obtained. Table 7 gives the range of parameters and the unknown parameters statistics of the approximate posterior distributions of logistic model. As can be seen from Table 7, the parameters all can be well estimated. The results of these two parameters are excellent because their parameter values are within the [2.5th, 97.5th] percentiles.

Figures 7(a) and 7(b) show the histograms of intrinsic growth rate r and maximum environmental capacity K of the Gompertz model, respectively. These parameters are obtained by the IABC-SMC algorithm. X-coordinate indicates the range of estimated parameters, and Y-coordinate

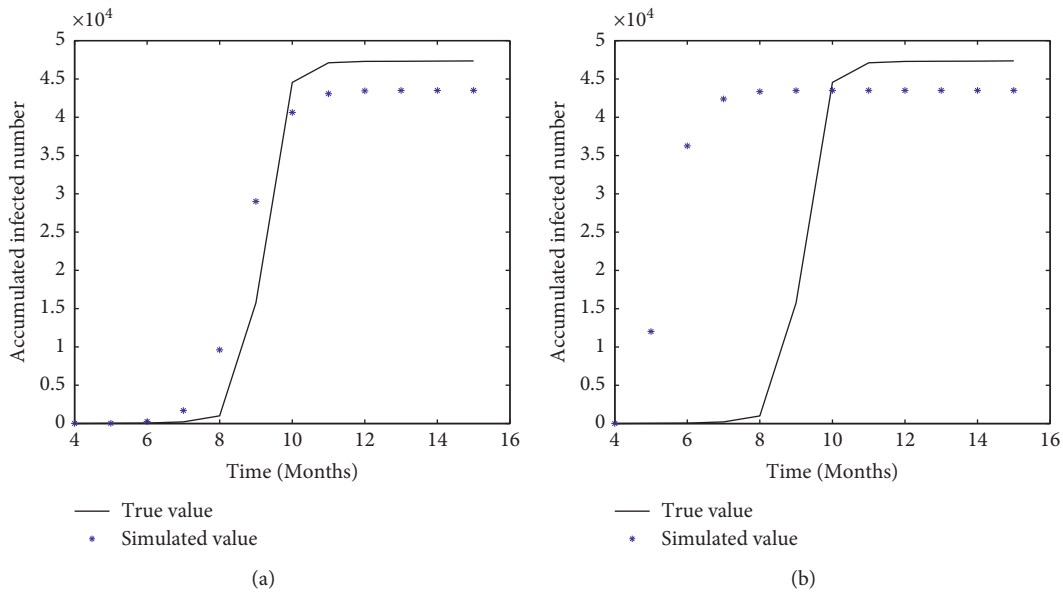

Figure 4: Fitting effect of simulated data and observed data of ABC-SMC algorithm. (a) Logistic model. (b) Gompertz model. Here, the initial states are $n = 6000, x_0 = 5, T = 6, t = 12, \varepsilon = 57453, 22335, 16047, 12872, 11540, 6720$, and $p(M1) = p(M2) = 1/2$.

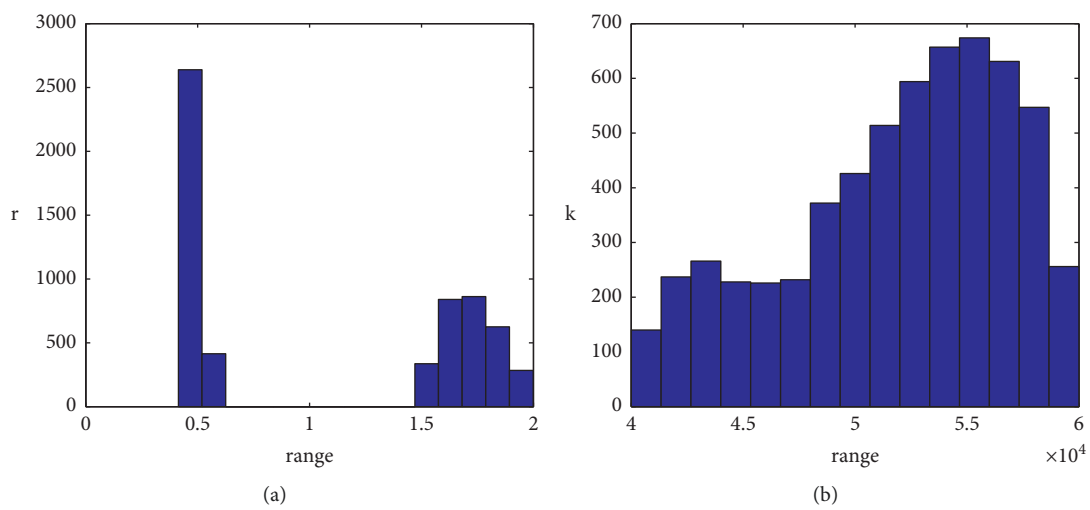

Figure 5: Model parameter histograms of ABC-SMC algorithm. (a) Estimation of r. (b) Estimation of K. Here, the initial states are $n = 6000, x_0 = 5, T = 6, t = 12$, and $\varepsilon = 65389, 41043, 33049, 30077, 28770$, and 16433.

Table 6: Parameter summary statistics of ABC-SMC algorithm.

Parameter	Lower bound	Upper bound	Mean	Std.	[2.5th, 97.5th] percentiles
r	0.4138	1.9986	1.0814	0.8011	[0.4287, 1.9285]
K	40003	60000	52019	1.0596×10^{-4}	[41416, 59042]

indicates the total times of parameters. As can be seen from Figure 7, the distributions of parameters r and K do not follow normal distribution and both parameters have two peaks. When r is 0.5 and 0.53, the peak of cumulative number of r reaches about 235 times. When the parameter K is 50000 and 54000, the peak of cumulative number of K reaches about 280 times. So, the results of estimated parameters are not particularly good.

The posterior estimation results of unknown parameters and the statistics related to the Gompertz model are shown

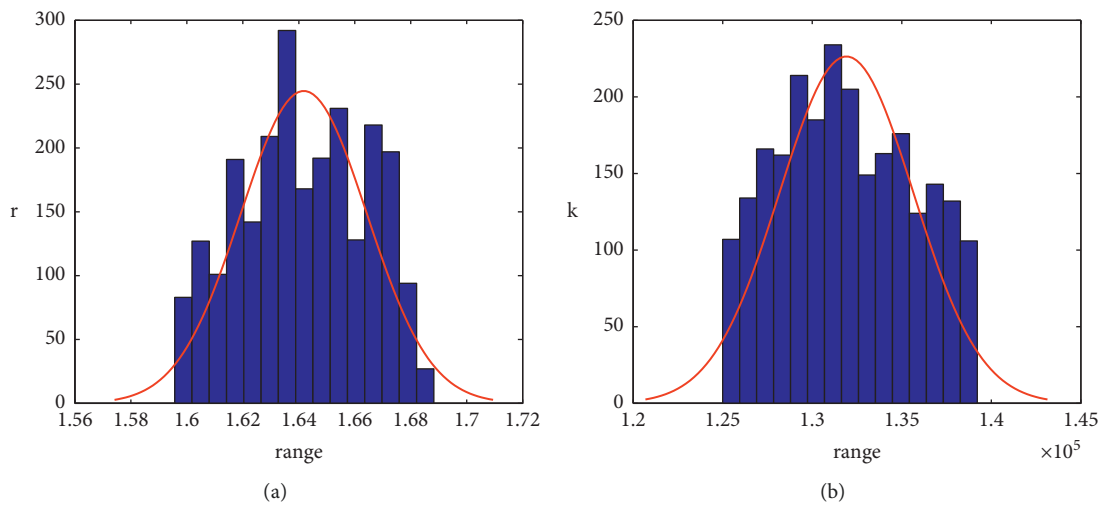

Figure 6: Parameter histograms of logistic model of the IABC-SMC algorithm. (a) Estimation of r. (b) Estimation of K. Here, the initial states are $n = 6000, x_0 = 22, a = 0.4, T = 6$, and $t = 12$.

Table 7: Parameter ranges and statistics of logistic model.

Parameter	Lower bound	Upper bound	Mean	Std.	[2.5th, 97.5th] percentiles
r	1.5983	1.6889	1.6442	6.7627×10^{-5}	[1.6022, 1.6833]
K	125130	139520	132460	93.6276	[125730, 138640]

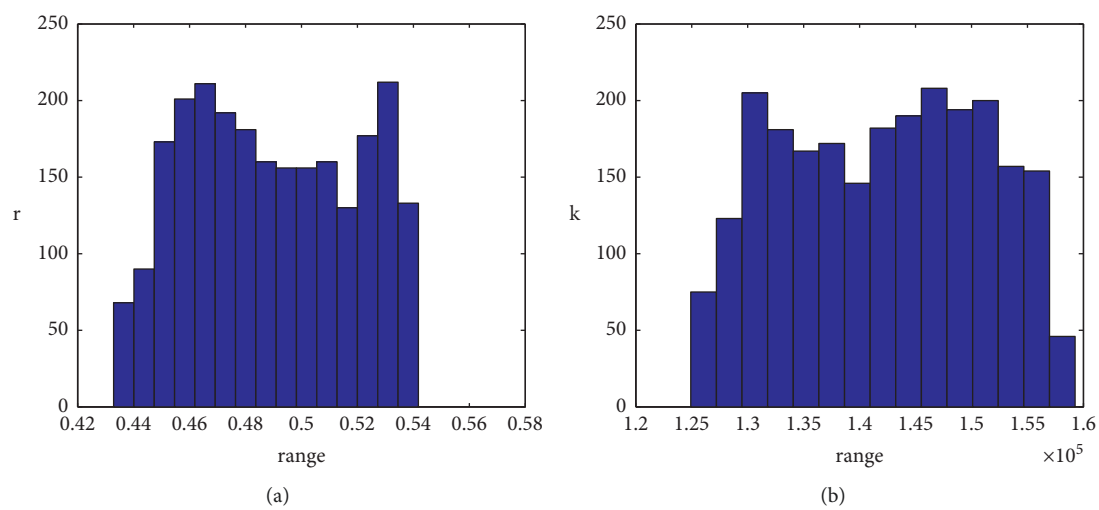

Figure 7: Parameter histograms of Gompertz model of the IABC-SMC algorithm. (a) Estimation of r. (b) Estimation of K. Here, the initial states are $n = 6000, x_0 = 22, a = 0.4, T = 6$, and $t = 12$.

Table 8: Parameter ranges and the statistics of the Gompertz model.

Parameter	Lower bound	Upper bound	Mean	Std.	[2.5th, 97.5th] percentiles
r	0.4336	0.5464	0.4971	6.4659×10^{-4}	[0.4417, 0.5421]
K	125050	161430	140430	95.3831	[127100, 158750]

in Table 8. We can see that the variances of these two parameters in Table 7 are smaller than that in Table 8, which indicates that the parameter range estimated by the logistic model is more accurate.

Similarly, to further verify the effects of the IABC-SMC algorithm, some calculations and simulations are carried out. According to the criteria presented in Table 9, the evidence for choosing logistic model is conclusive. The

Table 9: AIC, BIC, and operation time of two models.

Model	Logistic	Gompertz
AIC	4060	49816
BIC	4061	49817
Operation time (s)	209.6029	213.6122

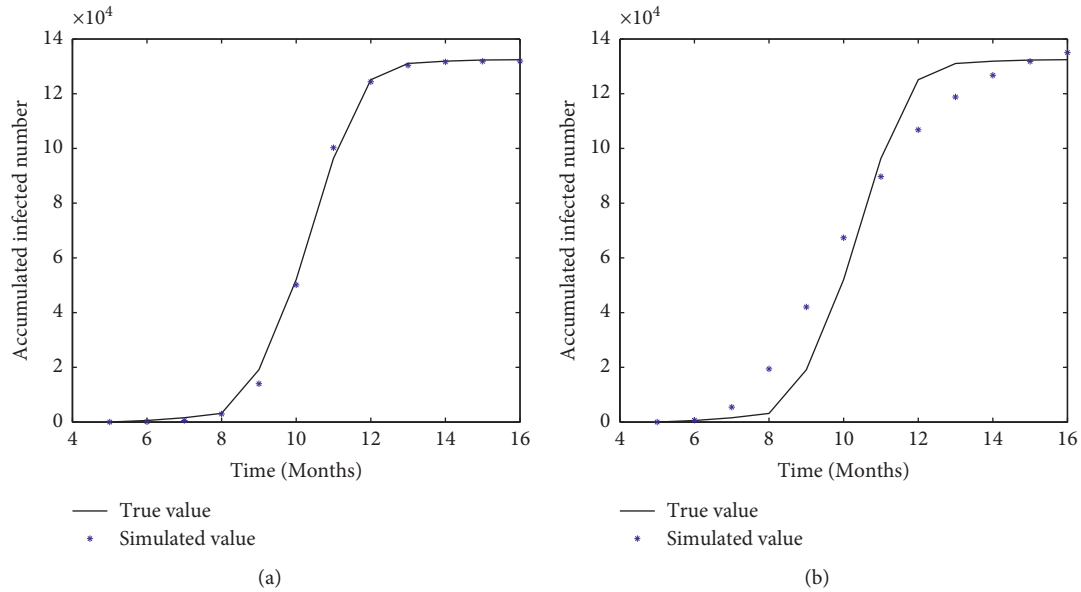

Figure 8: Comparison between the observed data and simulated data of the IABC-SMC algorithm. (a) Logistic model. (b) Gompertz model. Here, the initial states are $n = 6000, x_0 = 22, a = 0.4, T = 6$, and $t = 12$.

AIC values of $M1$ and $M2$ are calculated as 4060 and 49816, respectively. It is obvious that the AIC value of $M1$ is much smaller than that of $M2$, so the best model is the logistic model. The BIC values of $M1$ and $M2$ also support us to choose logistic model. Finally, we can use the model selection time to verify the above conclusions again. It is easy to notice that $M1$ saves more time than $M2$. So, the logistic model is the "best" model for us to fit the A/H1N1 data.

The fitting results of logistic model and Gompertz model in Figure 8 are plotted based on the observed data and the simulated data calculated using the average values of the estimated parameters. The X-coordinate shows the outbreak time of A/H1N1 disease from May 2009 to April 2010, and the Y-coordinate shows the cumulative number of infections. Obviously, the simulation data obtained by the logistic model and the A/H1N1 epidemic data have the best fitting effect. The result of model selection of A/H1N1 disease is also consistent with that of dengue disease.

(2) Simulation 2: Results of ABC-SMC Algorithm. To verify the efficiency of the IABC-SMC algorithm, the IABC-SMC algorithm is compared with ABC-SMC algorithm. Both algorithms used the same model, experimental data, parameter initial values, and threshold. The threshold set is selected manually and given as $\varepsilon = 168655, 106154, 78152, 64957, 59245$, and 41355. The prior probability of each model is equal; i.e., $p(M1) = p(M2) = 1/2$. Figure 9 is the fitting effect of the observed data and the simulated data obtained by the ABC-SMC algorithm. The black curve represents the number of confirmed cases with A/H1N1 from May 2009 to April 2010, and the blue dots represent the simulated data of the ABC-SMC algorithm. It is not difficult to see from the simulation results that the fitting effect of the observed data and the simulated data obtained by the logistic model is better than that of the Gompertz model. It is consistent with the results of the IABC-SMC algorithm and the results of model selection are all logistic model. Although the final results of model selection of the two algorithms are both logistic model, the simulation data obtained by the IABC-SMC algorithm fit the observed data better. The computation time of ABC-SMC algorithm is 3212 seconds, which is also much longer than that of the IABC-SMC algorithm.

Figure 10 shows the histograms of parameters r (Figure 10(a)) and K (Figure 10(b)) of the selected model obtained by the ABC-SMC algorithm. The X-axis is the range of the parameters, and the Y-axis is the total number of parameter. When r is 0.5, parameter r appears most frequently, which is about 2800 times. However, other values of r occur between 1.5 and 1.8. When the parameter K is between 115000 and 144000, the total number of K is about 200. When the value of K is between 144000 and 150000, the total number of K increases significantly. Table 10 represents the relevant statistical information of the unknown parameters estimated by the ABC-SMC

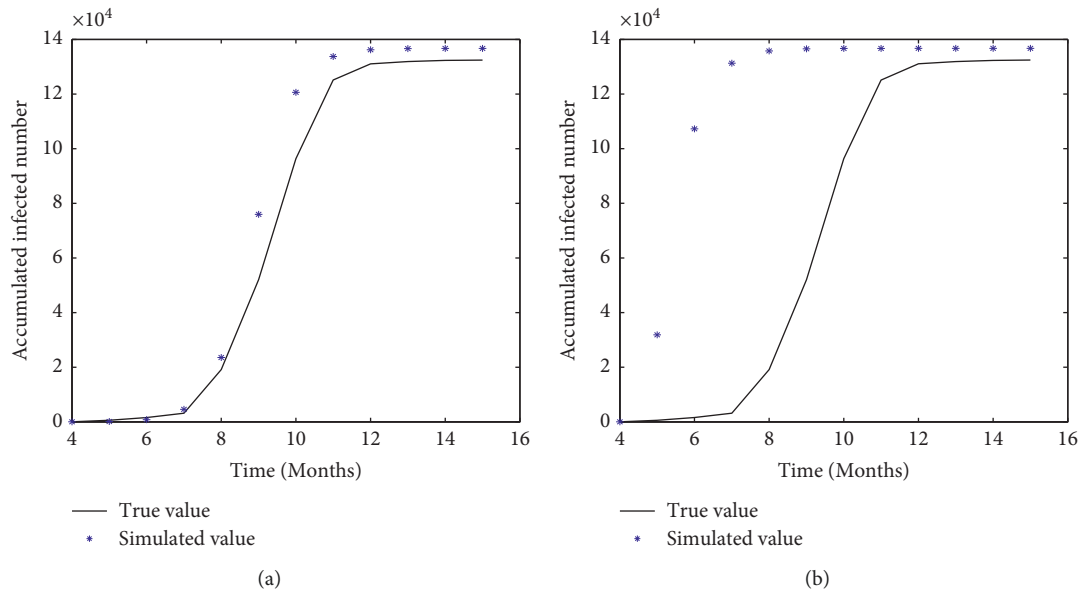

Figure 9: Fitting effect of simulated data and observed data of ABC-SMC algorithm. (a) Logistic model. (b) Gompertz model. Here, the initial states are $n = 6000, x_0 = 22, T = 6, t = 12, \varepsilon = 168655, 106154, 78152, 64957, 59245,$ and 41355, and $p(M1) = p(M2) = 1/2$.

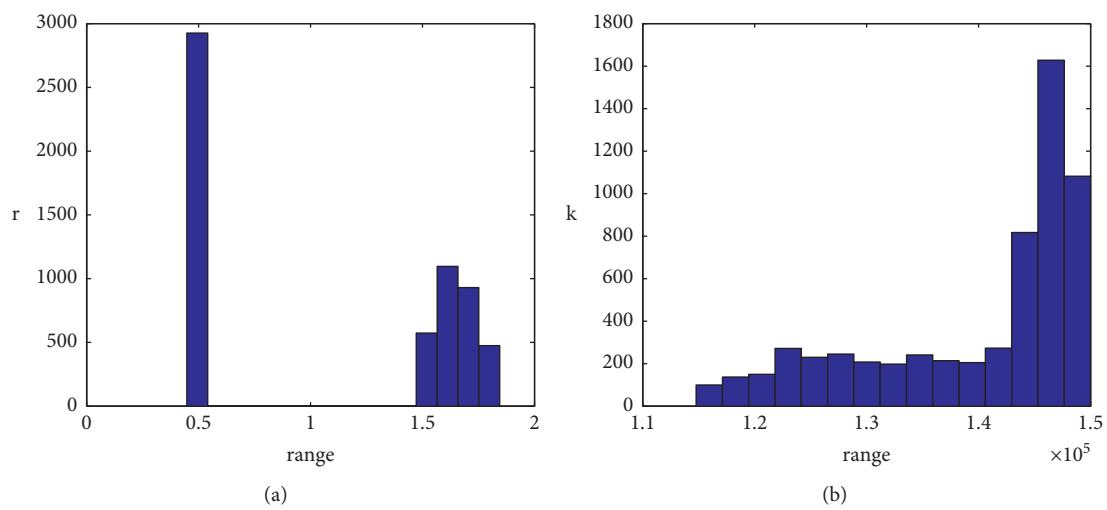

Figure 10: Model parameter histograms of ABC-SMC algorithm. (a) Estimation of r. (b) Estimation of K. Here, the initial states are $n = 6000, x_0 = 22, T = 6, t = 12,$ and $\varepsilon = 168655, 106154, 78152, 64957, 59245,$ and 41355.

Table 10: Parameter summary statistics of ABC-SMC algorithm.

Parameter	Lower bound	Upper bound	Mean	Std.	[2.5th, 97.5th] percentiles
r	0.4477	1.8446	1.0983	1.7324	[0.4556, 1.8013]
K	114780	150000	139490	29446	[118040, 149410]

algorithm. Although the ABC-SMC algorithm can also estimate the posterior information of the unknown parameters, it has a larger and more scattered parameter range than that of the IABC-SMC algorithm. These results confirm the advantages of IABC-SMC algorithm again.

4. Discussion

Many methods have various problems in the selection of models and parameter estimation, such as low efficiency in model selection and inaccuracy in parameter estima-

tion. These problems may lead to the selection of the wrong model and the inaccurate estimation of actual data scale. Our study proposed an IABC-SMC algorithm based on the ABC-SMC algorithm and recalibration post-processing method. We took the reported data of dengue epidemic and A/H1N1 epidemic in China as examples in our study.

We used the IABC-SMC algorithm and two simplest single-population models to analyze the results of model selection of the dengue epidemic data and the A/H1N1 epidemic data and the results of parameter estimation of the selected model. The selected model in two examples is consistent, and the model selected is the logistic model. Compared with the ABC-SMC algorithm, the IABC-SMC algorithm has the advantages of higher computational efficiency, lower time complexity, more fast and accurate model selection ability, and more accurate posterior distributions of parameters. The IABC-SMC algorithm avoids the problem of setting the threshold sequence of the ABC-SMC algorithm manually and the time-consuming problem and also avoids the shortage to find the optimal model and value of unknown parameters of model in each iteration in ABC-SMC algorithm.

Although the alternative model in this study is relatively simple, it demonstrates many promising aspects of the IABC-SMC algorithm, which can be extended to complex system models to deal with model selection and parameter estimation problems effectively in the future. It can be utilized not only for deterministic models but also for stochastic models in the physical, chemical, and biological sciences.

Data Availability

The underlying data supporting the results of the study are found in Tables 1 and 2.

Conflicts of Interest

The authors declare that they have no conflicts of interest.

Acknowledgments

The work was also supported by the National Natural Science Foundation of China (grant nos. 11471243 and 11971023).

References

[1] M. Muto and J. L. Beck, "Bayesian updating and model class selection for hysteretic structural models using stochastic simulation," *Journal of Vibration and Control*, vol. 14, no. 1C2, p. 7C34, 2008.

[2] B. A. Zrate, J. M. Caicedo, J. Yu, and P. Ziehl, "Bayesian model updating and prognosis of fatigue crack growth," *Engineering Structures*, vol. 45, Article ID 53C61, 2012.

[3] Ph. Bisaillon, R. Sandhu, M. Khalil, C. Pettit, D. Poirel, and A. Sarkar, "Bayesian parameter estimation and model selection for strongly nonlinear dynamical systems," *Nonlinear Dynamics*, vol. 82, no. 3, pp. 1061–1080, 2015.

[4] J. L. Beck and K. V. Yuen, "Model selection using response measurements: bayesian probabilistic approach," *Journal of Engineering Mechanics*, vol. 130, no. 2, pp. 192–203, 2004.

[5] R. Sandhu, M. Khalil, A. Sarkar, and D. Poirel, "Bayesian model selection for nonlinear aeroelastic systems using wind-tunnel data," *Computer Methods in Applied Mechanics and Engineering*, vol. 282, pp. 161–183, 2014.

[6] T. G. Ritto and L. C. S. Nunes, "Bayesian model selection of hyperelastic models for simple and pure shear at large deformations," *Computers & Structures*, vol. 156, pp. 101–109, 2015.

[7] W. Liu, S. Tang, and Y. Xiao, "Model selection and evaluation based on emerging infectious disease data sets including A/H1N1 and ebola," *Computational and Mathematical Methods in Medicine*, vol. 2015, Article ID 207105, 14 pages, 2015.

[8] F. Cadini, C. Sbarufatti, M. Corbetta, and M. Giglio, "A particle filter-based model selection algorithm for fatigue damage identification on aeronautical structures," *Structural Control and Health Monitoring*, vol. 24, no. 11, Article ID e2002, 2017.

[9] J. Skilling, *Nested Sampling*, R. Fischer, R. Preuss, and U. V. Toussaint, Eds., American Institute of Physics Conference Series, New York, NY, USA, Article ID 395C405, 2004.

[10] J. Skilling, "Nested sampling for general Bayesian computation," *Bayesian Anal*, vol. 1, no. 4, Article ID 833C860, 2006.

[11] J. K. Pritchard, M. T. Seielstad, A. Perez-Lezaun, and M. W. Feldman, "Population growth of human Y chromosomes: a study of Y chromosome microsatellites," *Molecular Biology and Evolution*, vol. 16, no. 12, pp. 1791–1798, 1999.

[12] A. Ben Abdessalem, N. Dervilis, D. Wagg, and K. Worden, "Model selection and parameter estimation in structural dynamics using approximate Bayesian computation," *Mechanical Systems and Signal Processing*, vol. 99, pp. 306–325, 2018.

[13] T. Toni, D. Welch, N. Strelkowa, A. Ipsen, and M. P. Stumpf, "Approximate bayesian computation scheme for parameter inference and model selection in dynamical systems," *Journal of The Royal Society Interface*, vol. 6, no. 31, pp. 187–202, 2009.

[14] G. S. Rodrigues, D. Prangle, and S. A. Sisson, "Recalibration: a post-processing method for approximate Bayesian computation," *Computational Statistics & Data Analysis*, vol. 126, pp. 53–66, 2018.

[15] D. J. Spiegelhalter, N. G. Best, B. P. Carlin, and A. van der Linde, "Bayesian measures of model complexity and fit," *Journal of the Royal Statistical Society: Series B*, vol. 64, no. 4, pp. 583–639, 2002.

[16] P. A. Stephens, S. W. Buskirk, G. D. Hayward, and C. M. Del Rio, "A call for statistical pluralism answered," *Journal of Applied Ecology*, vol. 44, no. 2, pp. 461–463, 2007.

[17] W. A. Link and R. J. Barker, "Model weights and the foundations of multimodel inference," *Ecology*, vol. 87, no. 10, pp. 2626–2635, 2006.

[18] P. Congdon, "Bayesian model choice based on Monte Carlo estimates of posterior model probabilities," *Computational Statistics & Data Analysis*, vol. 50, no. 2, pp. 346–357, 2006.

[19] F. Llorente, L. Martino, D. Delgado, and J. Lopez-Santiago, "Marginal Likelihood Computation for Model Selection and Hypothesis Testing: An Extensive Review," 2020, https://arxiv.org/abs/2005.08334, Article ID 08334.

[20] F. Llorente, L. Martino, E. Cuberlo, J. Lopez-Santiago, and D. Delgado, "On the safe use of prior densities for Bayesian model selection," *viXra*, vol. 2110, 2021.

[21] R. J. Boys, D. J. Wilkinson, and T. B. L. Kirkwood, "Bayesian inference for a discretely observed stochastic kinetic model," *Statistics and Computing*, vol. 18, no. 2, pp. 125–135, 2008.

[22] A. Golightly and D. J. Wilkinson, "Bayesian parameter inference for stochastic biochemical network models using particle Markov chain Monte Carlo," *Interface Focus*, vol. 1, no. 6, pp. 807–820, 2011.

[23] S. A. Sisson, Y. Fan, and M. M. Tanaka, "Sequential Monte Carlo without likelihoods," *Proceedings of the National Academy of Sciences*, vol. 104, no. 6, pp. 1760–1765, 2007.

[24] World Health Organization, *Accelerating Work to Overcome the Globalimpact of Neglected Tropical Diseases C a Roadmap for Implementation*, Geneva, Switzerland, 2012.

[25] H. Akaike, "Information theory as an extension of the maximum likelihood principle," *Second International Symposium on Information Theory*, Akademiai Kiado, Hungary, Europe, Article ID 267C281, 1973.

[26] K. P. Burnham and D. R. Anderson, *Model Selection and Multimodel Inference*, Springer, New York, NY, USA, 2002.

[27] L. Z. Garamszegi, "Information-theoretic approaches to statistical analysis in behavioural ecology: an introduction," *Behavioral Ecology and Sociobiology*, vol. 65, no. 1, pp. 1–11, 2010.

[28] P. F. Verhulst, "Notice sur la loi que la population suit dans son accroissement. correspondance mathematique et physique publiee par a quetelet, brussels," *Quetelet*, vol. 10, no. 10, Article ID 113C121, 1838.

[29] C. P. Winsor, "The gompertz curve as a growth curve," *Proceedings of the National Academy of Sciences*, vol. 18, no. 1, pp. 1–8, 1932.

Hindawi
Discrete Dynamics in Nature and Society
Volume 2022, Article ID 6317958, 13 pages
https://doi.org/10.1155/2022/6317958

Research Article

H^{∞} Filter for Discrete-Time Takagi–Sugeno Fuzzy Systems with Time-Varying Delays via a Novel Wirtinger-Based Inequality

Wanru Wang,[1,2] **Yonggang Wen**,[3] **Liankun Sun**,[1,2] **and Kaifan Ma**[1]

[1]*School of Software, Tiangong University, Tianjin 300387, China*
[2]*Tianjin Key Laboratory of Autonomous Intelligence Technology and Systems, Tianjin 300387, China*
[3]*Tianjin University of Commerce Boustead College, Tianjin 300384, China*

Correspondence should be addressed to Wanru Wang; tjpuwwr@126.com

Received 28 April 2022; Revised 2 June 2022; Accepted 3 June 2022; Published 29 June 2022

Academic Editor: Ya Jia

This paper is devoted to the analysis and design of H^{∞} filtering for discrete-time Takagi–Sugeno (TS) fuzzy systems with time-varying delays. By using the delay-partitioning method, more systematic information is introduced, which can reduce the conservatism of the conclusion. By constructing an appropriate Lyapunov functional and combining with a newly Wirtinger-based summation inequality, the existence condition of the H^{∞} filter is obtained. Thus, utilizing the contract matrix transformation method, the H^{∞} filter design for discrete-time TS fuzzy systems with time-varying delay based on LMI is proposed. Finally, a few numerical analysis results are given to prove the effectiveness of the method.

1. Introduction

In recent years, the analysis and synthesis of nonlinear systems has gradually become one of the research focuses in the domain of automatic control and automatic control technology. Nonlinearity is ubiquitous in chemical processes, robotic systems, automotive systems, and many manufacturing processes, which could introduce severe difficulties in the analysis and synthesis of control systems. Although nonlinearity is more accordant with people's actual production processes, nonlinear systems cannot be simply described by linear differential equations, and the stability of the system not only relies on the structural parameters of the system but also depends on the initial state of the system. These problems have caused considerable dilemmas for researchers to analyze and synthesize the stability of nonlinear systems. With the deepening of research, methods such as output control feedback [1–5], sliding mode control [6–8], optimal control [9, 10], and fuzzy control [11–20] have been proposed. Currently, the TS fuzzy system [21–24] is deemed to be one of the most effective methods for dealing with nonlinear systems.

In recent years, the TS fuzzy system has been widely used. The TS fuzzy model is a nonlinear model described by a series of if-then rules, which is arbitrarily smooth and nonlinear. The system can be approximated by the TS fuzzy model without constant term with any specified accuracy. Up to now, the strict LMI stability sufficient conditions for the robust stability of uncertain continuous TS fuzzy descriptor systems are given [25]. By constructing the augmented Lyapunov–Krasovskii functional and utilizing Wirtinger-based integral inequality, an improved condition for stability of the concerned systems was derived in terms of LMIs [26]. Li et al. [27] designed integral switching function to study the fault detection of sliding mode controller for a class of TS fuzzy singular systems. More research results can be found in [28–30] and the references therein.

Furthermore, time delays are common in any practical system, such as network systems, power systems, hydraulic systems, and so on. Thus, the problems such as poor system stability and degraded performance are unavoidable. Meanwhile, people have made a lot of analysis and research on the delay-dependent and delay-independent TS fuzzy

systems [31–33]. At present, delay-partitioning [34, 35] is considered as one of the most effective methods to process the time delay problems in control systems. By artificially dividing the lower bound d_m into m equal-length subintervals, the maximum time delay of the system's asymptotic stability in the guaranteed interval is obtained, thereby reducing the conservativeness of the stability conditions. Compared with the early Jensen inequality [47] and the free weight matrix method [48–50], the recently proposed Wirtinger-based inequality [36–38], Bessel–Legendre inequality [39–42], and reciprocal convex method [43–46] have many improvements in the derivation of quadratic terms. However, to our knowledge, few results can be found in the literature concerning with the discrete-time TS fuzzy delay systems by the delay-partitioning method and Wirtinger-based inequality. Thus, research on the filtering problem for discrete-time TS fuzzy systems with time-varying delay by employing the delay-partitioning method and Wirtinger-based inequality should be of both theoretical and practical importance, which motivates us to carry out this study.

As stated previously, in this paper, we consider the delay-dependent $H\infty$ filter for TS fuzzy discrete-time systems with time-varying delay. Firstly, we will utilize the delay-partitioning method to reduce the effect of system time-varying delays, and the quadratic accumulation term appearing in Lyapunov–Krasovskii function is processed by the improved Wirtinger-based inequality to ensure that the fuzzy system is asymptotically stable. Then, the contract matrix transformation is used to design the $H\infty$ filter. Finally, we will demonstrate the validity and low conservation of our experimental results through some simulation examples.

Notations. Throughout this paper, the superscript "T" represents the matrix transposition, $\mathbb{R}^n$ expresses the n-dimensional Euclidean space, I and 0 signify an identity matrix and a zero matrix with appropriate dimension, respectively, and $P>0$ is used to denote that the matrix P is positively defined and symmetric. Besides, sym {A} is equivalent to $A+A^T$, diag{...} is a block-diagonal matrix, and col$[A,B,C]=$, *that is*, $[A^T,B^T,C^T]^T$. It should be noted that in the symmetric block matrices, $*$ represent terms caused by symmetry, e.g.,

$$\begin{bmatrix} X_1 & X_2 \\ * & X_3 \end{bmatrix} = \begin{bmatrix} X_1 & X_2 \\ X_2^T & X_3 \end{bmatrix}. \tag{1}$$

2. Model Description and Problem Analysis

The description of the TS fuzzy model is represented by the fuzzy IF-THEN rule of the local linear input-output relationship of the nonlinear system. Then, consider a nonlinear system, which can be described as a discrete-time TS fuzzy time-varying delay model as follows.

Rule (i): IF $\vartheta_1(t)$ is F_{i1} and ... and $\vartheta_g(t)$ is F_{ig}, THEN

$$\begin{cases} x(t+1) = A_i x(t) + A_{di} x(t-\tau(t)) + B_i \omega(t), \\ y(t) = C_i x(t) + C_{di} x(t-\tau(t)) + D_i \omega(t), \\ z(t) = L_i x(t) + L_{di} x(t-\tau(t)) + F_i \omega(t), \\ x(t) = \varphi(t), t = -\tau_1, -\tau_1+1, \ldots, 0, i = 1, 2, \ldots r, \end{cases} \tag{2}$$

where $x(t) \in \mathbb{R}^n$ expresses the state vector, $y(t) \in \mathbb{R}^q$ denotes the measured output, $z(t) \in \mathbb{R}^p$ is the signal to be measured, $\omega(t) \in \mathbb{R}^l$ signifies the noise input vector, which belongs to $l_2[0,\infty)$, $t = -\tau_1, -\tau_1+1, \ldots, 0$ is given initial condition sequence, and $\tau(t)$ express the time-varying delays (we assume that it satisfies $1 \le \tau_2 \le \tau(t) \le \tau_1, t = 1, 2, \ldots$); besides, τ_2 and τ_1 indicate the known minimum and maximum bounds of delays, respectively. Meanwhile, F_{ij} is the fuzzy set, r represents the number of *IF-THEN* rule, and $\vartheta(t) = [\vartheta_1(t), \vartheta_2(t) \ldots \vartheta_g(t)]$ shows the premise variables vector. $A_i, A_{\mathrm{di}}, B_i, C_i, C_{\mathrm{di}}, D_i, L_i, L_{\mathrm{di}}$, and F_i are known constant systems matrices, and $x(t) = \varphi(t)$ refers to the initial condition.

Then, describe the normalized fuzzy-basis function as follows:

$$\hbar_i[\vartheta(t)] = \frac{\prod_{j=1}^{g} F_{ij}\left[\vartheta_j(t)\right]}{\sum_{i=1}^{r}\prod_{j=1}^{g} F_{ij}\left[\vartheta_j(t)\right]} \ge 0, \tag{3}$$

$$\sum_{i=1}^{r} \hbar_i[\vartheta(t)] = 1, \tag{4}$$

with $F_{ij}[\vartheta_j(t)]$ indicating the grade of membership of $\vartheta(t)$ in F_{ij}, and define $\hbar_i = [\hbar_1, \ldots, \hbar_r]$. Through product fuzzy inference and center-of-gravity defuzzification, the following discrete time-varying TS fuzzy dynamic model $\aleph$ can be obtained:

$$\begin{cases} x(t+1) = A(\hbar,t)x(t) + A_d(\hbar,t)x(t-\tau(t)) + B(\hbar,t)\omega(t) \\ y(t) = C(\hbar,t)x(t) + C_d(\hbar,t)x(t-\tau(t)) + D((\hbar,t))\omega(t) \\ z(t) = L(\hbar,t)x(t) + L_d(\hbar,t)x(t-\tau(t)) + F(\hbar,t)\omega(t) \\ x(t) = \varphi(t), t = -\tau_1, -\tau_1+1, \ldots, 0, \end{cases} \tag{5}$$

where

$$\begin{aligned} A(\hbar,t) &\triangleq \sum_{i=1}^{r} \hbar_i A_i(t), A_d(\hbar,t) \triangleq \sum_{i=1}^{r} \hbar_i A_{di}(t), B(\hbar,t) \\ &\triangleq \sum_{i=1}^{r} \hbar_i \mathrm{B}_i(t), \\ C(\hbar,t) &\triangleq \sum_{i=1}^{r} \hbar_i C_i(t), C_d(\hbar,t) \triangleq \sum_{i=1}^{r} \hbar_i C_{di}(t), D(\hbar,t) \\ &\triangleq \sum_{i=1}^{r} \hbar_i D_i(t), \\ L(\hbar,t) &\triangleq \sum_{i=1}^{r} \hbar_i L_i(t), L_d(\hbar,t) \triangleq \sum_{i=1}^{r} \hbar_i L_{di}(t), F(\hbar,t) \\ &\triangleq \sum_{i=1}^{r} \hbar_i F_i(t). \end{aligned} \tag{6}$$

Given system (1), we are committed to designing a full-order fuzzy filter for the estimation of $z(t)$ of general structure described by $\aleph_F$:

$$\begin{cases} x_F(t+1) = A_F(\hbar)x_F(t) + B_F(\hbar)y(t), \\ z_F(t) = L_F(\hbar)x_F(t) + D_F(\hbar)y(t), x_F(0) = 0, \end{cases} \tag{7}$$

where $x_F(t) \in \mathbb{R}^n$ is the filter state vector of the system $\aleph_F$ and $A_F(\hbar), B_F(\hbar), L_F(\hbar)$, and $D_F(\hbar)$ are filer matrices to be determined.

Next, define the augmented state vector $\zeta(t) := \mathrm{col}[x(t), x_F(t)]$ and the estimation error $e_t := z(t) - z_F(t)$. Thus, we could acquire the filtering error system $\aleph_e$ as follows:

$$\begin{cases} \zeta(t+1) = \overline{A}(\hbar,t)\zeta(t) + \overline{A}_d(\hbar,t)\zeta(t-\tau(t)) + \overline{B}(\hbar,t)\omega(t), \\ e(t) = \overline{L}(\hbar,t)\zeta(t) + \overline{L}_d(\hbar,t)\zeta(t-\tau(t)) + \overline{F}(\hbar,t)\omega(t), \\ \zeta(t) = \left[\phi^T(t), 0\right]^T, t = -\tau_1, -\tau_1+1, \ldots, 0, \end{cases} \tag{8}$$

where

$$\begin{aligned} \overline{A}(\hbar,t) &\triangleq \begin{bmatrix} A(\hbar,t) & 0 \\ B_F(\hbar)C(\hbar,t) & A_F(\hbar) \end{bmatrix}, \\ \overline{A}_d(\hbar,t) &\triangleq \begin{bmatrix} A_d(\hbar,t) \\ B_F(\hbar)C_d(\hbar,t) \end{bmatrix}, \\ \overline{B}(\hbar,t) &\triangleq \begin{bmatrix} B(\hbar,t) \\ B_F(\hbar)D(\hbar,t) \end{bmatrix}, \\ \overline{L}(\hbar,t) &\triangleq \left[L(\hbar,t) - D_F(\hbar)C(\hbar,t) \quad -C_F(\hbar)\right], \\ \overline{L}_d(\hbar,t) &\triangleq \left[L_d(\hbar,t) - D_F(\hbar)C_d(\hbar,t) 0\right], \\ \overline{F}(\hbar,t) &\triangleq F(\hbar,t) - D_F(\hbar)D(\hbar,t). \end{aligned} \tag{9}$$

Remark 1. The $H\infty$ filter is designed as follows. Given a fuzzy system (1), a fuzzy filter such as (6) with filter matrices $[A_F(\hbar), B_F(\hbar), L_F(\hbar), D_F(\hbar)]$ is designed to estimate the signal $z(t)$ to ensure that the filtering error system $\aleph_e$ in (7) is asymptotically stable, and $z_F(t)$ is a good estimate of $z(t)$ with the energy bounded disturbance $\omega(t)$. That means, for a given $\gamma > 0$, the filter error system $\aleph_e$ is asymptotically stable when the $H\infty$ performance index γ is asymptotically stable under the condition of $\omega = 0$, satisfying the following requirements: $\|e\|_2 < \gamma\|\omega\|_2$, for all nonzero $\omega \in l_2[0,\infty)$, where $\|e\|_2 \triangleq \sqrt{\sum_{t=0}^{\infty} e^T(t)e(t)}$.

Remark 2. Since the control input of the original fuzzy system model $\aleph$ is unknown and the system to be estimated must be asymptotically stable, which is also the precondition of asymptotically stable filter error system in $\aleph_e$, we assume that system $\aleph$ is asymptotically stable.

Before entering the main sections, a very vital lemma is introduced for the deduction of our conclusions.

Lemma 1 (see [51, 52]). *For a given symmetric positive definite matrix $\mathfrak{R} \in \mathbb{R}^{n\times n}$, matrices $L_p \in \mathbb{R}^{4n\times n}$, $p = 0, 1, 2$, and any differentiable function ϖ in $[\rho_0, \rho_1] \mapsto \mathbb{R}^n$, the following summation inequality holds:*

$$-\sum_{i=\rho_0}^{\rho_1-1} \varpi^T(i)\mathfrak{R}\varpi(i) \le \Delta, \tag{10}$$

where

$$\begin{aligned} \Delta &= \overline{\delta}^T\left[\Lambda_{(\ell,\mathfrak{R},L_p)} + sym\left\{\chi_{(L_p,I_p)}\right\}\right]\overline{\delta}, \\ \overline{\delta} &= col\left\{x(\rho_1), x(\rho_0), \frac{1}{\ell+1}\Sigma_0, \frac{2}{(\ell+1)(\ell+1)}\Sigma_1\right\}, \\ \ell &= \rho_1 - \rho_0, \Sigma_0 = \sum_{i=\rho_0}^{\rho_1} x(i), \Sigma_1 = \sum_{i=\rho_0}^{\rho_1}\sum_{j=i}^{\rho_1} x(j), \\ \Lambda_{(\ell,\mathfrak{R},L_p)} &= \ell L_0\mathfrak{R}^{-1}L_0^T + \frac{\ell(\ell-1)}{3(\ell+1)}L_1\mathfrak{R}^{-1}L_1^T + \frac{\ell(\ell-1)(\ell-2)}{5(\ell+1)(\ell+2)}L_2\mathfrak{R}^{-1}L_2^T, \\ \chi_{(L_p,I_p)} &= L_0I_0 + L_1I_1 + L_2I_2, \\ I_0 &= \left[1 \quad -1 \quad 0 \quad 0\right], \\ I_1 &= \left[1 \quad 1 \quad -2 \quad 0\right], \\ I_2 &= \left[1 \quad -1 \quad 6 \quad -6\right]. \end{aligned} \tag{11}$$

Remark 3. Introduced by Lemma 1, we can find that $\ell - 1/\ell + 1 < 1$ and $(\ell-1)(\ell-2)/(\ell+1)(\ell+2) < 1$, and inequality (10) could be abbreviated as follows:

$$\Lambda_{(\ell,\mathfrak{R},L_p)} = \ell\left(L_0\mathfrak{R}^{-1}L_0^T + \frac{1}{3}L_1\mathfrak{R}^{-1}L_1^T + \frac{1}{5}L_2\mathfrak{R}^{-1}L_2^T\right). \quad (12)$$

Furthermore, compared with previous Jensen's inequality, free-weighting matrices method, and Wirtinger-based inequality with single cumulative term, the new summation inequality reduces the conservativeness of the obtained results more effectively when dealing with the quadratic summation term.

3. H∞ Performance Analysis

In this section, based on the fuzzy-basis Lyapunov–Krasovskii function, delay-partitioning technique, and the improved Wirtinger-based inequality, novel delay-dependent stability and stabilization criteria for the fuzzy system $\aleph$ in (4) will be proposed to resolve the problem of robust $H\infty$ filter design mentioned in Section 2. Before beginning, here is an overview of several definitions that will be implemented in this article.

Before we start, in order to simplify, define it as follows:

$$\begin{aligned} &\tau_2 \triangleq m\mu\,(m = 1,\ldots,n),\ \tau_t \triangleq \tau(t),\ \overline{\tau} \triangleq \tau_2 - \tau_1, \\ &\xi(t) \triangleq \mathrm{col}\{x(t), x(t-\mu),\ldots,x(t-(m-1)\mu)\}. \end{aligned} \quad (13)$$

Theorem 1. *In consideration of system (1) and fuzzy filter $\aleph_F$ in (6), the filtering error system $\aleph_e$ in (7) is asymptotically stable with $H\infty$ performance γ, if there exist real symmetric positive-definite matrices $P(\hbar)_{(i,t)}, \alpha_{(1i,1l,2i,20)}, R_{(i,v,o)}, S_{(1z,2z)}, T_{(1i,2i)}$, constant matrices $N(\hbar)_j, M(\hbar)_j$, $(j = 0, 1, 2)$, such that for all i, l, o, t, v, z ∈ (1, 2, . . ., r), and scalar $\gamma > 0$. For given integers $m > 0$ and $\mu > 0$ with satisfying $\tau_2 = m\mu$, the following inequality holds*

$$\Upsilon_{(i,l,o,t,v,z)} < 0, i, l, o, t, v, z \in (1, 2, \ldots, r), \quad (14)$$

where

$$\begin{aligned}
\Upsilon_{(i,l,o,t,v,z)} &\triangleq \Upsilon_0 + \Upsilon_1 + \Upsilon_2, \\
\Upsilon_0 &\triangleq -\widetilde{\prod}_1^T P_i \widetilde{\prod}_1 + \widetilde{\prod}_2^T \alpha_{1i} \widetilde{\prod}_2 - \widetilde{\prod}_3^T \alpha_{1l} \widetilde{\prod}_3 + e_1^T \alpha_{2i} e_1 - e_{(2+m)+1}^T \alpha_{20} e_{(2+m)+1} + e_1^T(\overline{\tau}+1)R_i e_1 \\
&\quad - e_{2+m}^T R_v e_{2+m} - e_{(2+m)+1}^T R_0 e_{(2+m)+1} + \mathrm{sym}\left\{\widetilde{\prod}_4^T N(\hbar)_0 \widetilde{\prod}_5 + \widetilde{\prod}_4^T N(\hbar)_1 \widetilde{\prod}_6 + \widetilde{\prod}_4^T N(\hbar)_2 \widetilde{\prod}_7\right\} \\
&\quad + sym\left\{\widetilde{\prod}_8^T M(\hbar)_0 \widetilde{\prod}_9 + \widetilde{\prod}_8^T M(\hbar)_1 \widetilde{\prod}_{10} + \widetilde{\prod}_8^T M(\hbar)_2 \widetilde{\prod}_{11}\right\}, \\
\Upsilon_1 &\triangleq \Gamma_0^T P_t \Gamma_0 + \Gamma_1^T(\mu S_{1z} + \overline{\tau} S_{2z})\Gamma_1, \\
\Upsilon_2 &\triangleq \mu \widetilde{\Pi}_4^T N(\hbar)_j T_{1i}^{-1} N(\hbar)_j^T \widetilde{\Pi}4 + \overline{\tau}\widetilde{\Pi}_8^T M(\hbar)_j T_{2i}^{-1} M(\hbar)_j^T \widetilde{\Pi}8 \\
\Gamma_0 &\triangleq \left[\overline{A}(\hbar,t)\widetilde{\Pi}4, \overline{A}_d(\hbar,t)e_{2+m}, \overline{B}(\hbar,t)\right] \\
\Gamma_1 &\triangleq \left[\overline{A}(\hbar,t)e_1, A_d(\hbar,t)e_{2+m}, \overline{B}(\hbar,t)\right] \\
e_i &\triangleq \left\{0_{n\times(i-1)n} I_n 0_{n\times(9+m-i)n}\right\}, i \in \{1,\ldots,9+m\}, \\
\widetilde{\Pi}_1 &\triangleq \mathrm{col}\{e_1, e_2\}, \\
\widetilde{\Pi}_2 &\triangleq col\{e_1, e_3\}, \\
\widetilde{\Pi}_3 &\triangleq col\{e_{2+s}\}, s \in \{1,\ldots,m\}, \\
\widetilde{\Pi}_4 &\triangleq col\left\{e_1, e_3, e_{(2+m)+2}, e_{(2+m)+4}\right\}, \\
\widetilde{\Pi}_5 &\triangleq e_1 - e_3, \\
\widetilde{\Pi}_6 &\triangleq e_1 + e_3 - 2e_{(2+m)+1}, \\
\widetilde{\Pi}_7 &\triangleq e_1 - e_3 + 6e_{(2+m)+2} - 6e_{(2+m)+4}, \\
\widetilde{\Pi}_8 &\triangleq col\left\{e_{2+m}, e_{(2+m)+1}, e_{(2+m)+3}, e_{(2+m)+5}\right\}, \\
\widetilde{\Pi}_9 &\triangleq e_{2+m} - e_{(2+m)+1}, \\
\widetilde{\Pi}_{10} &\triangleq e_{2+m} + e_{(2+m)+1} - 2e_{(2+m)+3}, \\
\widetilde{\Pi}_{11} &\triangleq e_{2+m} - e_{(2+m)+1} + 6e_{(2+m)+3} - 6e_{(2+m)+5}.
\end{aligned} \quad (15)$$

Proof. Considering the idea of slack variable, now we construct the following fuzzy L-K candidate functions with time-varying delay-partitioning terms:

$$V(t) \triangleq V_0(t) + V_1(t) + V_2(t) + V_3(t), \tag{16}$$

with

$$\begin{aligned} V_0(t) &\triangleq \zeta^T(t)P(\hbar)\zeta(t), \\ V_1(t) &\triangleq \sum_{i=t-\mu}^{t-1} \xi^T(i)\alpha_1(i)\xi(i) + \sum_{i=t-\tau_1}^{t-1} x^T(i)\alpha_2(i)x(i), \\ V_2(t) &\triangleq \sum_{i=-\tau_1+1}^{-m\mu} \sum_{j=t-1+i}^{t-1} x^T(j)R(j)x(j), \\ V_3(t) &\triangleq \sum_{i=-\mu+1}^{-1} \sum_{j=t+i}^{t-1} \varsigma_d^T(j)S(j)_{1z}\varsigma_d(j) + \sum_{i=-\tau_1}^{-m\mu-1} \sum_{j=t+i}^{t-1} \varsigma_d^T(j)S(j)_{2z}\varsigma_d(j), \end{aligned} \tag{17}$$

where $\varsigma_d(t) \triangleq x(t+1) - x(t)$ and matrices $P > 0, \alpha_{(1,2)} > 0, R > 0, S > 0$. Then, we can define $\Delta V(t) \triangleq V(t+1) - V(t)$, and along the trajectory of fuzzy error system (7), we have

$$\Delta V_0(t) = \zeta^T(t+1)P(t+1)\zeta(t+1) - \zeta^T(t)P(t)\zeta(t) = \delta^T(t)\left[\Gamma_0^T P_t \Gamma_0 - \widetilde{\prod}_1^T P_t \widetilde{\prod}_1\right]\delta^T, \tag{18}$$

$$\begin{aligned} \Delta V_1(t) &= \xi^T(t)\alpha_1(t)\xi(t) - \xi^T(t-\mu)\alpha_1(t-\mu)\xi(t-\mu) + x(t)^T\alpha_2(t)x(t) - x^T(t-\tau_1)\alpha_2(t-\tau_1)x(t-\tau_1) \\ &= \delta^T(t)\left[\widetilde{\prod}_2^T \alpha_{1i}\widetilde{\prod}_2 - \widetilde{\prod}_3^T \alpha_{1l}\widetilde{\prod}_3 + e_1^T\alpha_{2i}e_1 - e_5^T\alpha_{2o}\right]\delta(t), \end{aligned} \tag{19}$$

$$\begin{aligned} \Delta V_2(t) &= (\tau_1 - m\mu + 1)x^T(t)R(t)x(t) - x^T(t-m\mu)R(t-m\mu)x(t-m\mu) - x^T(t-\tau_1)R(t-\tau_1)x(t-\tau_1) \\ &= \delta^T(t)\left[e_1^T(\tau_1 - m\mu + 1)R_i e_1 - e_4^T R_v e_4 - e_5^T R_o e_5\right]\delta(t), \end{aligned} \tag{20}$$

$$\begin{aligned} \Delta V_3(t) &= \varsigma_d^T(t)\left[(\mu S_1(t)) + (\tau_1 - m\mu)S_2(t)\right]\varsigma_d(t) - \sum_{i=t-\mu}^{t-1} \varsigma_d^T(i)S_1(i)\varsigma_d(t) - \sum_{i=t-\tau_1}^{t-m\mu-1} \varsigma_d^T(i)S_2(i)\varsigma_d(i) \\ &= \delta^T(t)\left\{\Gamma_1^T\left[\mu S_{1z} + (\tau_1 - m\mu)S_{2z}\right]\Gamma_1\right\}\delta(t) - \sum_{i=t-\mu}^{t-1} \varsigma_d^T(i)S_1(i)\varsigma_d(i) - \sum_{i=t-\tau_1}^{t-m\mu-1} \varsigma_d^T(i)S_2(i)\varsigma_d(i), \end{aligned} \tag{21}$$

where $\delta(t) \triangleq col\{\zeta(t), \xi(t-\mu), 1/\mu + 1\sum_{i=t-\mu}^{t} x(i), 1/\overline{\tau} + 1\sum_{i=t-\tau_1}^{t-m\mu} x(i), 2/(\mu+1)(\mu+2)\sum_{i=t-\mu}^{t}\sum_{j=i}^{t} x(j) 2/(\overline{\tau}+1)(\overline{\tau}+2)\sum_{i=t-\tau_1}^{t-m\mu}\sum_{j=i}^{t-m\mu} x(j)\}$, Here we set $\delta_0(t) = col\{x(t), x(t-\mu), 1/\mu + 1\sum_{i=t-\mu}^{t} x(i), 2/(\mu+1)(\mu+2)\sum_{i=t-\mu}^{t}\sum_{j=i}^{t} x(j)\}$. For the summation terms (16) and (17), utilizing (9) and (11) in Lemma 1 and Remark 3, respectively, the following inequality holds:

$$\begin{aligned} &-\sum_{i=t-\mu}^{t-1} \varsigma_d^T(i)S_1(i)\varsigma_d(i) \le \Delta_1 \\ &\Delta_1 \triangleq \delta^T(t)\widetilde{\Pi}_4^T\left[\Lambda_1 + sym\{\chi_1\}\right]\widetilde{\Pi}_4\delta(t), \\ &\Lambda_1 \triangleq \ell\left(M_0 S_1^{-1} M_0^T + \frac{1}{3}M_1 S_1^{-1} M_1^T + \frac{1}{5}M_2 S_1^{-1} M_2^T\right), \\ &\chi_1 \triangleq M_0 I_0 + M_1 I_1 + M_2 I_2. \end{aligned} \tag{22}$$

Similarly, applying (9) and (11) and setting $\delta(t)_1 = col\{x(t-m\mu), x(t-\tau_1), 1/\overline{\tau}+1\sum_{i=t-\tau_1}^{t-m\mu} x(i), 2/(\overline{\tau}+1)(\overline{\tau}+2)\sum_{i=t-\tau_1}^{t-m\mu}\sum_{j=i}^{t-m\mu} x(j)\}$, we have

$$-\sum_{i=t-\tau_1}^{t-m\mu-1} \varsigma_d^T(i) S_2(i) \varsigma_d(i) \le \Delta_2$$

$$\begin{aligned} \Delta_2 &\triangleq \delta^T(t)\widetilde{\Pi}_8^T[\Lambda_2 + sym\{\chi_2\}]\widetilde{\Pi}_8\delta(t), \\ \Lambda_2 &\triangleq \ell\left(N_0 S_2^{-1} N_0^T + \frac{1}{3} N_1 S_2^{-1} N_1^T + \frac{1}{5} N_2 S_2^{-1} N_2^T\right), \\ \chi_2 &\triangleq N_0 I_0 + N_1 I_1 + N_2 I_2. \end{aligned} \tag{23}$$

Afterwards, by combining (14)–(19), under the assumption that the input is zero noise, i.e., $\omega(t) = 0$, we can obtain the following conclusions:

$$\begin{aligned} \Delta V(t) &= \Delta V_0(t) + \Delta V_1(t) + \Delta V_2(t) + \Delta V_3(t) \\ &\le \delta^T(t)[\Upsilon_0 + \Upsilon_1 + \Upsilon_2]\delta(t) \\ &= \delta^T(t)\Upsilon_{(i,l,o,t,v,z)}\delta(t). \end{aligned} \tag{24}$$

According to Schur's complement theorem, for all nonzero $\delta(t)$, we have that $\Upsilon_0 + \Upsilon_1 + \Upsilon_2(\tau_t) < 0$ is equivalent to the LMI in (7), that is, $\Delta V(t) < 0$. This condition of the negative definite $\Delta V(t)$ guarantees that the filtering error system $\aleph$ is asymptotically stable.

Furthermore, in order to construct the $H\infty$ performance index, we define $J \triangleq \sum_{t=0}^{\infty}[e^T(t) - \gamma^2\omega^T(t)\omega(t)]$. Also, under zero initial condition $V(0) = 0$, $V(\infty) > 0$, and $\omega(k) \neq 0$, one obtains

$$\begin{aligned} J &\le \sum_{t=0}^{\infty}\left[e^T = \sum_{t=0}^{\infty}\left[e^T(t)e(t) - \gamma^2\omega^T(t)\omega(t)\right] + \Delta V(t)\right] \\ &\le \sum_{t=0}^{\infty}\delta_*^T(t)\left[\Gamma + \Gamma_0^T P_t \Gamma_0 + \Gamma_1^T\widetilde{\Omega}\Gamma_1 + \Gamma_2^T\Gamma_2 + \Gamma_*\right]\delta_*(t)(t)e(t) - \gamma^2\omega^T(t)\omega(t) + V(0) - V(\infty), \end{aligned} \tag{25}$$

where

$$\begin{aligned} \delta_*(t) &\triangleq col\{\delta(t), \omega(t)\}, \\ \Gamma &\triangleq \begin{bmatrix} \Upsilon_0 & 0 \\ * & -\gamma^2 I \end{bmatrix}, \widetilde{\Omega} = \mu S_{1z} + \overline{\tau} S_{2z}, \\ \Gamma_2 &\triangleq \left[\overline{L}(\hbar,t)\Pi_1, \overline{L}_d(\hbar,t)e_{(2+m)+1,}\overline{F}(\hbar,t)\right], \\ \Gamma_* &\triangleq \Gamma_M T_{1i}\Gamma_M^T + \Gamma_N T_{2i}\Gamma_N^T, \\ \Gamma_M &\triangleq \mu\widetilde{\Pi}_4^T\left[M_0(\hbar)_j \;\; M_1(\hbar)_j \;\; M_2(\hbar)_j\right], \\ \Gamma_N &\triangleq \overline{\tau}\widetilde{\Pi}_8^T\left[N_0(\hbar)_j \;\; N_1(\hbar)_j \;\; N_2(\hbar)_j\right]. \end{aligned} \tag{26}$$

Then, using the Schur complement for inequality (21), we can get the following formula:

$$\begin{bmatrix} \Gamma & \Gamma_0^T P_t & \Gamma_1^T\widetilde{\Omega} & \Gamma_2^T & \Gamma_M & \Gamma_N \\ * & -P_t & 0 & 0 & 0 & 0 \\ * & * & -\widetilde{\Omega} & 0 & 0 & 0 \\ * & * & * & -I & 0 & 0 \\ * & * & * & * & -T_{1i} & 0 \\ * & * & * & * & * & -T_{2i} \end{bmatrix} < 0, \tag{27}$$

where

$$\begin{aligned} T_{1i} &\triangleq \mathrm{diag}\{T_{1i}, 3T_{1i}, 5T_{1i}\}, \\ T_{2i} &\triangleq \mathrm{diag}\{T_{2i}, 3T_{2i}, 5T_{2i}\}. \end{aligned} \tag{28}$$

Inequality (20) indicates that $J < 0$, which is equivalent to the LMI (21). Besides, for all $\omega(t) \in l_2[0, +\infty)$, $||e||_2 < \gamma||\omega||_2$. Then, this completes the proof. □

Remark 4. In this section, the stability analysis method of discrete-time TS fuzzy systems with time-varying delay is mainly based on the TS fuzzy logic theory to model a given mathematical model of a linear system and transform complex martingale linear problems into linear problems. Thus, a bounded real lemma for a discrete-time linear system with time delay is proposed. In addition, in the selection of Lyapunov–Krasovskii functionals, we construct a term that includes time-partitioning division and a double summation term. The double summation term appears during the derivative of the Lyapunov–Krasovskii function, using the novel Wirtinger-based inequality for scaling. As for the common Jensen's inequality, the method of free-weighting matrix, and Wirtinger-based inequality with signal summation term, the system stability conditions obtained by this method are relatively conservative.

4. H_∞ Filter Design

In this section, we are committed to designing a full-order H_∞ fuzzy filter $\aleph_F$ for state delay in system (4).

Theorem 2. *Consider a discrete-time TS fuzzy system with time-varying delay from (4), and assume that the integers $m > 0$, $\mu > 0$ satisfy $\tau_2 = m\mu$. For a full-order filter of form (6), filter error system (7) is asymptotically stable, with H_∞ performance γ, if there exist matrices with appropriate dimensions $A, B, L, D, W_1, W_2, M_q, N_q$, $(q = 0, 1, 2)$, and the following inequalities hold*

$$\wp > 0, g > 0, Q_{1i} = \begin{bmatrix} \alpha_{1i1} & \alpha_{1i2} \\ * & \alpha_{1i3} \end{bmatrix} > 0, Q_{2ii} > 0,$$
$$S_{1z} = \begin{bmatrix} S_{1z1} & S_{1z2} \\ * & S_{1z3} \end{bmatrix} > 0, S_{2z} = \begin{bmatrix} S_{2z1} & S_{2z2} \\ * & S_{2z3} \end{bmatrix} > 0,$$
$$\chi = \begin{bmatrix} \chi_1 & \chi_2 \\ ast & \chi_3 \end{bmatrix} > 0, R_i > 0, \widetilde{T}_{1i} > 0, \widetilde{T}_{2i} > 0. \tag{29}$$

Thus, the following linear matrix inequality can be obtained:

$$\widetilde{\Upsilon}_{(i,l,o,t,v,z)} = \begin{bmatrix} \widetilde{\Gamma} & \Gamma_M & \Gamma_N \\ * & -\widetilde{T}_{1i} & 0 \\ * & * & -\widetilde{T}_{2i} \end{bmatrix} < 0, \tag{30}$$

where

$$\widetilde{\Gamma} = \begin{bmatrix} \widetilde{\Upsilon}_0 & 0 & \widetilde{\Xi}_1^1 \\ * & -\gamma^2 I & \widetilde{\Xi}_1^2 \\ * & * & \widetilde{\Xi}_1^3 \end{bmatrix}, \widetilde{\Upsilon}_0 = \begin{bmatrix} \Upsilon_0 & 0 \\ 0 & -\chi \end{bmatrix},$$
$$\widetilde{\Xi}_1^1 = col\left[\ \widetilde{\Theta}_0\ \ \widetilde{\Theta}_1\ \ 0_{2\times4}\ \ \widetilde{\Theta}_2\ \ \widetilde{\Theta}_3\ \ 0_{4\times4}\ \ \widetilde{\Theta}_4\ \ 0_{2\times4}\ \right],$$
$$\widetilde{\Theta}_0 = [\ L_0\ \ L_1\ \ L_2\ \ L_3\ \ L_4\ \ L_5\ \ L_6\ \ L_7\ \ L_8\ ], L_0 = A_i^T\wp^T + C_i^T B^T, L_1 = A_i^T g + C_i^T B^T, L_2 = A_i^T W_1 + C_i^T B^T - W_1,$$
$$L_3 = A_i^T W_2 + C_i^T B^T - W_2, L_4 = A_i^T W_1 + C_i^T B^T - W_1, L_5 = A_i^T W_2 + C_i^T B^T - W_2,$$
$$L_6 = A_i^T W_1 + C_i^T B^T - W_1, L_7 = A_i^T W_2 + C_i^T B^T - W_2, L_8 = L_i^T - C_i^T D^T,$$
$$\widetilde{\Theta}_1 = \left[\ A^T\ \ A^T\ \ A^T - g^T\ \ A^T - g^T\ \ A^T - g^T\ \ A^T - g^T\ \ A^T - g^T\ \ A^T - g^T\ \ -L^T\ \right],$$
$$\widetilde{\Theta}_2 = \frac{1}{2}[\ M_0\ \ M_1\ \ M_2\ \ M_3\ \ M_4\ \ M_5\ \ M_6\ \ M_7\ \ M_8\ ], M_0 = A_{di}^T\wp^T + C_{di}^T B^T, M_1 = A_{di}^T L + C_{di}^T B^T, M_2 = A_{di}^T W_1 + C_{di}^T B^T,$$
$$M_3 = A_{di}^T W_2 + C_{di}^T B^T, M_4 = A_{di}^T W_1 + C_{di}^T B^T, M_5 = A_{di}^T W_2 + C_{di}^T B^T, M_6 = A_{di}^T W_2 + C_{di}^T B^T, M_7 = A_{di}^T W_1 + C_{di}^T B^T, M_8 = A_{di}^T W_2 + C_{di}^T B^T,$$
$$\widetilde{\Theta}_3 = \frac{1}{2}[\ N_0\ \ N_1\ \ N_2\ \ N_3\ \ N_4\ \ N_5\ \ N_6\ \ N_7\ \ N_8\ ], N_0 = A_{di}^T\wp^T + C_{di}^T B^T, N_1 = A_{di}^T L + C_{di}^T B^T, N_2 = A_{di}^T W_1 + C_{di}^T B^T,$$
$$N_3 = A_{di}^T W_2 + C_{di}^T B^T, N_4 = A_{di}^T W_1 + C_{di}^T B^T, N_5 = A_{di}^T W_2 + C_{di}^T B^T, N_6 = A_{di}^T W_1 + C_{di}^T BD^T, N_7 = A_{di}^T W_2 + C_{di}^T B^T, N_8 = L_{di}^T - C_{di}^T D^T,$$
$$\widetilde{\Theta}_4 = \frac{\overline{\tau}}{2}[\ P_0\ \ P_1\ \ P_2\ \ P_3\ \ P_4\ \ P_5\ \ P_6\ \ P_7\ \ P_8\ ], P_0 = A_{di}^T\wp^T + C_{di}^T B^T, P_1 = A_{di}^T L + C_{di}^T B^T, P_2 = A_{di}^T W_1 + C_{di}^T B^T,$$
$$P_3 = A_{di}^T W_2 + C_{di}^T B^T, P_4 = A_{di}^T W_1 + C_{di}^T B^T, P_5 = A_{di}^T W_2 + C_{di}^T B^T, P_6 = A_{di}^T W_1 + C_{di}^T B^T, P_7 = A_{di}^T W_2 + C_{di}^T B^T, P_8 = L_{di}^T - C_{di}^T D^T,$$
$$\widetilde{\Xi}_1^2 = [\ Q_0\ \ Q_1\ \ Q_2\ \ Q_3\ \ Q_4\ \ Q_5\ \ Q_6\ \ Q_7\ \ Q_8\ ], Q_0 = B_i^T\wp^T + D_i^T B^T, Q_1 = B_i^T g^T + D_i^T B^T, Q_2 = B_i^T W_1 + D_i^T B^T,$$
$$Q_3 = B_i^T W_2 + D_i^T B^T, Q_4 = B_i^T W_1 + D_i^T B^T, Q_5 = B_i^T W_2 + D_i^T B^T,$$
$$Q_6 = B_i^T W_1 + D_i^T B^T, Q_7 = B_i^T W_2 + D_i^T B^T, Q_8 = F_i^T - D_i^T D^T,$$
$$\widetilde{\Xi}_1^3 = \begin{bmatrix} -\wp & -g & 0 & 0 & 0 & 0 & 0 & 0 \\ * & -g^T & 0 & 0 & 0 & 0 & 0 & 0 \\ * & * & \mu^{-1}S_1 & 0 & 0 & 0 & 0 & 0 \\ * & * & * & \overline{\tau}^{-1}S_2 & 0 & 0 & 0 & 0 \\ * & * & * & * & \Phi & 0 & 0 & 0 \\ * & * & * & * & * & -I & 0 & 0 \\ * & * & * & * & * & \∗ & -\widetilde{T}_{1i} & 0 \\ * & * & * & * & * & * & * & -\widetilde{T}_{2i} \end{bmatrix},$$
$$S_1 = \begin{bmatrix} S_{1z1} - W_1 - W_1^T & S_{1z2} - W_2 - g \\ * & S_{1z3} - g - g^T \end{bmatrix}, S_2 = \begin{bmatrix} S_{2z1} - W_1 - W_1^T & S_{2z2} - W_2 - g \\ * & S_{2z3} - g - g^T \end{bmatrix},$$
$$\Phi = \begin{bmatrix} \chi_1 - W_1 - W_1^T & \chi_2 - W_2 - g \\ * & \chi_3 - g - g^T \end{bmatrix},$$
$$\widetilde{T}_{1i} \triangleq diag\{\mu T_{1i}, 3\mu T_{1i}, 5\mu T_{1i}\}, \widetilde{T}_{2i} \triangleq diag\{\overline{\tau} T_{2i}, 3\overline{\tau} T_{2i}, 5\overline{\tau} T_{2i}\}. \tag{31}$$

Then, the fuzzy filter state space parameters can be implemented as

$$A_F(\hbar) = g^{-1}A, B_F(\hbar) = g^{-1}B, L_F(\hbar) = L, D_F(\hbar) = D. \tag{32}$$

Proof. First, define the matrix $V = \begin{bmatrix} V_1 & V_2 \\ * & V_3 \end{bmatrix}$, where $V_1 \in \mathbb{R}^{n\times n}, V_3 \in \mathbb{R}^{n\times n}$ are positive-definite symmetric matrices. Here, suppose $V_2 \in \mathbb{R}^{n\times n}$ is a nonsingular matrix, and define the following nonsingular matrix:

$$\begin{aligned} f &= \begin{bmatrix} I & 0 \\ 0 & V_3^{-1}V_2^T \end{bmatrix}, W = \begin{bmatrix} W_1 & W_2V_2^{-T}V_3 \\ V_2^T & V_3 \end{bmatrix}, \\ g &\triangleq V_2V_3^{-1}V_2^T, \wp \triangleq V_1, \\ Q_{1i} &\triangleq g^{-T}\widetilde{Q}_{1i}g^{-1}, Q_{2ii} \triangleq g^{-T}\widetilde{Q}_{2i}g^{-1}, \\ S_{1z} &\triangleq g^{-T}\widetilde{S}_{1z}g^{-1}, S_{2z} \triangleq g^{-T}\widetilde{S}_{2z}g^{-1}, \\ \widetilde{T}_{1i} &\triangleq g^{-T}\widetilde{T}_{1i}g^{-1}, \widetilde{T}_{2i} \triangleq g^{-T}\widetilde{T}_{2i}g^{-1}, \\ M_q &\triangleq g^{-T}\widetilde{M}\mathrm{q}_q g^{-1}, N_q \triangleq g^{-T}\widetilde{N}_q g^{-1}, \\ \chi &\triangleq g^{-T}\widetilde{\chi}\mathrm{q}_q g^{-1}. \end{aligned} \tag{33}$$

Given that $V > 0$, linear matrix inequality (22) can be obtained:

$$\begin{bmatrix} A_F(\hbar) & B_F(\hbar) \\ L_F(\hbar) & D_F(\hbar) \end{bmatrix} \triangleq \begin{bmatrix} V_2^{-1} & 0 \\ 0 & I \end{bmatrix} \begin{bmatrix} A_F(\hbar) & B_F(\hbar) \\ L_F(\hbar) & D_F(\hbar) \end{bmatrix} \begin{bmatrix} V_3^{-1}V_2^T & 0 \\ 0 & I \end{bmatrix}. \tag{34}$$

Then, perform contract matrix transformation on equation (12):

$$J_1^T \Upsilon_{(i,l,o,t,v,z)} J_1 > 0, \tag{35}$$

where $J_1 = diag\{f, f, f, f, I, f, f, f, f, I\}$, and by combining (24) and (25), we can get linear matrix inequality (22). Here, note that equation (22) can be equivalent to equation (27):

$$\begin{bmatrix} A_F(\hbar) & B_F(\hbar) \\ L_F(\hbar) & D_F(\hbar) \end{bmatrix} \triangleq \begin{bmatrix} V_2^{-1} & 0 \\ 0 & I \end{bmatrix} \begin{bmatrix} A & B \\ L & D \end{bmatrix} \begin{bmatrix} V_2^{-T}V_3 & 0 \\ 0 & I \end{bmatrix} \triangleq \begin{bmatrix} \left(V_2^{-T}V_3\right)^{-1} g^{-1} & 0 \\ 0 & I \end{bmatrix} \begin{bmatrix} A & B \\ L & D \end{bmatrix} \begin{bmatrix} V_2^{-T}V_3 & 0 \\ 0 & I \end{bmatrix}. \tag{36}$$

Therefore, the state space implementation $[A_F(\hbar), B_F(\hbar), L_F(\hbar), D_F(\hbar)]$ of the desired filter as defined in (6) can be obtained from (22). Then, this completes the proof. □

Remark 5. Regarding the design process of the $H\infty$ filter, first, expand (21) to form an augmented matrix in the form of an LMI. It is found here that the filter parameter matrices $[A_F(\hbar), B_F(\hbar), L_F(\hbar), D_F(\hbar)]$ can be written as (36),which implies that V2–T V3 can be viewed as a similarity transformation on the state-space realization of the filter. Therefore, the contract matrix transformation method is used to decouple the matrix to be sought from the Lyapunov–Krasovskii matrix, so that the filter parameter matrix can be systematically replaced and obtained.

5. Numerical Examples

Example 1 (see [21, 53]). Firstly, we consider discrete-time system (4) with time-varying delay:

$$A_1 = \begin{bmatrix} -0.291 & 1 \\ 0 & 0.95 \end{bmatrix}, A_{d1} = \begin{bmatrix} 0.012 & 0.014 \\ 0 & 0.015 \end{bmatrix},$$
$$A_2 = \begin{bmatrix} -0.1 & 0 \\ 1 & -0.2 \end{bmatrix}, A_{d2} = \begin{bmatrix} 0.01 & 0 \\ 0.01 & 0.015 \end{bmatrix}, \tag{37}$$

where τ_t represents time-varying delay and the number of delay-partitioning segment $m = 3$. Furthermore, the upper bound of the delay is given in combination with the method in Theorem 1. Table 1 shows a detailed comparison. It can be seen that the method proposed in this paper is superior to the results published in the literature [20, 22, 53].

Example 2 (see [21]). Then, we consider the following time-varying delay Henon mapping system:

$$\begin{cases} x_1(t+1) = -[Cx_1(t) + (1-C)x_1(t-\tau(t))]^2 + 0.3x_2 + \omega(t), \\ x_2(t+1) = Cx_1(t) + (1-C)x_1(t-\tau(t)), \\ y(t) = Cx_1(t) + (1-C)x_1(t-\tau(t)) + \omega(t), \\ z(t) = x_1(t), \end{cases} \tag{38}$$

where $\omega(t)$ is the disturbance input and $C \in [0, 1]$ is a constant representing the delay coefficient. Next, we define $\vartheta(t) = \lfloor x_1(t) + (1 - \lfloor)x_1(t-\tau)$, and suppose that $\vartheta(t) \in [-M, M], M > 0$. By utilizing the same procedure as in paper [54], the nonlinear term $\vartheta^2(t)$ could be expressed as $\vartheta^2(t) = h_1(\vartheta(t))(-M)\vartheta(t) + h_2(\vartheta(t))(M)\vartheta(t)$, where $h_1(\vartheta(t)), h_2(\vartheta(t)) \in [0, 1]$, and $h_1(\vartheta(t)) + h_2(\vartheta(t)) = 1$. Then, by solving the equations, the membership functions $h_1(\vartheta(t))$ and $h_2(\vartheta(t))$ can be obtained as

$$h_1(\vartheta(t)) = \frac{1}{2}\left(1 - \frac{\vartheta(t)}{M}\right),$$
$$h_2(\vartheta(t)) = \frac{1}{2}\left(1 + \frac{\vartheta(t)}{M}\right). \tag{39}$$

It can be concluded from the above expression that $h_1(\vartheta(t)) = 1$, $h_2(\vartheta(t)) = 0$ when $\vartheta(t) = -M$, and $h_1(\vartheta(t)) = 0$, $h_2(\vartheta(t)) = 1$ when $\vartheta(t) = M$. Thus, nonlinear system (30) can be expressed as the following approximate TS fuzzy model.

Plant From.

Rule 1. IF $\vartheta(t)$ is $-M$, THEN

$$\begin{cases} x(t+1) = A_1x(t) + A_{d1}x(t-\tau(t)) + B_1\omega(t), \\ y(t) = C_1x(t) + C_{d1}x(t-\tau(t)) + D_1\omega(t), \\ z(t) = C_1x(t). \end{cases} \tag{40}$$

Rule 2. IF $\vartheta(t)$ is M, THEN

$$\begin{cases} x(t+1) = A_2x(t) + A_{d2}x(t-\tau(t)) + B_2\omega(t), \\ y(t) = C_2x(t) + C_{d2}x(t-\tau(t)) + D_2\omega(t), \\ z(t) = L_2x(t), \end{cases} \tag{41}$$

where

$$A_1 = \begin{bmatrix} CM & 0.3 \\ C & 0 \end{bmatrix}, A_{d1} = \begin{bmatrix} (1-C)M & 0 \\ 1-C & 0 \end{bmatrix}, A_2 = \begin{bmatrix} -CM & 0.3 \\ C & 0 \end{bmatrix}, A_{d2} = \begin{bmatrix} -(1-C)M & 0 \\ 1-C & 0 \end{bmatrix},$$
$$B_1 = \begin{bmatrix} 1 \\ 0 \end{bmatrix}, B_2 = \begin{bmatrix} 1 \\ 0 \end{bmatrix}, C_1 = [\,C \;\; 0\,], C_{d1} = [\,1-C \;\; 0\,], C_2 = [\,C \;\; 0\,], C_{d2} = [\,1-C \;\; 0\,],$$
$$D_1 = 1, L_1 = [\,1 \;\; 0\,], D_2 = 0.5, L_2 = [\,1 \;\; 0\,]. \tag{42}$$

Here, $x(t) = \mathrm{col}\{x_1(t), \; x_2(t)\}$, $C = 0.8, M = 0.2, \mathrm{m} = 2$, and $1 \le \tau(t) \le 3$ means time-varying state delay. Then, by solving the conditions in Theorem 2, the minimum upper bound of the H^∞ performance level obtained is $\gamma = 0.04574$. It can be seen that the result obtained in this section is smaller than the result obtained in reference [53], $\gamma = 2.0403$. The parameters of the full-order fuzzy filter are as follows:

$$A_F(\hbar) = \begin{bmatrix} 0.7032 & 0.0516 \\ 0.0019 & 0.6709 \end{bmatrix}, B_F(\hbar) = \begin{bmatrix} -1.1930 \\ -0.0536 \end{bmatrix},$$
$$L_F(\hbar) = \begin{bmatrix} -2.0658 \times 10^{-5} & -2.5756 \times 10^{-5} \end{bmatrix},$$
$$D_F(\hbar) = -6.4756 \times 10^{-5}. \tag{43}$$

Then, in the case where the initial condition is zero, that is $x(0) = 0$, assume that the disturbance input $\omega(t)$ is

Table 1: The upper bound of τ_1 with various τ_2 (Example 1).

$\tau 2$	3	12
[20, Theorem 1]	14	21
[22,Theorem 3]	$23(m=3)$	$32(m=3)$
[53,Corollary 1]	$100(m=3)$	$109(m=3)$
Theorem 2	$110(m=3)$	$130(m=3)$

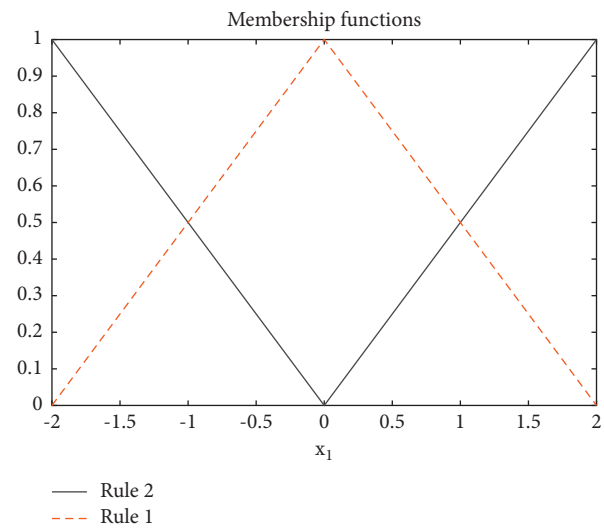

Figure 1: Membership functions (Example 2).

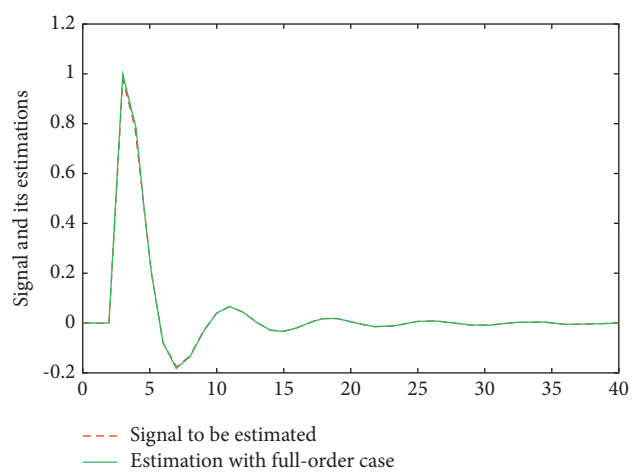

Figure 2: Signal $z(t)$ and its estimation $z_F(t)$ of the filter (Example 2).

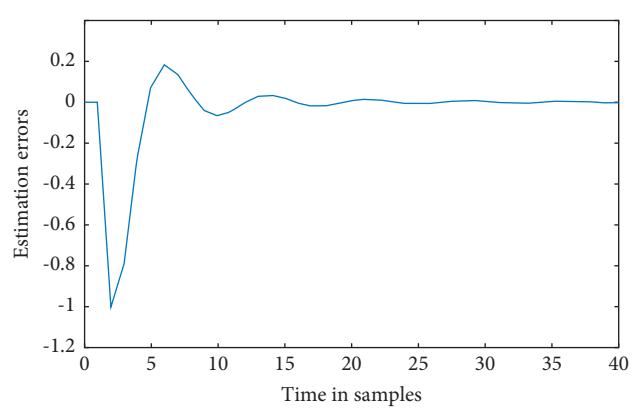

Figure 3: Estimation error $e(t)$ (Example 2).

$$\omega(t) = \frac{3\sin(0.85t)}{(0.55t)^2 + 1}. \tag{44}$$

Utilize the member function shown in Figure 1. Also, it can be concluded from the simulation results that Figures 2 and 3 reveal the signal $z(t)$ with its estimation $z_F(t)$ of the full-order filters and estimation error $e(t)$, respectively.

6. Conclusions

The main content of this paper is the analysis and design of $H\infty$ filter for discrete-time TS fuzzy systems with time-varying delay. In this paper, the bounded real lemma based on the improved Wirtinger-based inequality proposed in Section 3 is generalized and applied to the analysis and synthesis of nonlinear systems. For a given nonlinear system with time-varying delays and external disturbances, TS fuzzy logic is used to model it, and the nonlinear problem is transformed into a linear system analysis and synthesis problem. Based on the bounded real lemma and Wirtinger-based inequality with quadratic terms, $H\infty$ performance analysis is performed on the discrete-time TS fuzzy system with time-varying delay, and the coupling terms of the filter matrix and the Lyapunov matrix are uniformly replaced using the contract matrix transformation method. Furthermore, the design method of $H\infty$ filter for TS fuzzy system is given, and the bounded real lemma proposed in this paper is successfully extended to the analysis and synthesis of nonlinear systems. Finally, simulation examples are given to prove the validity and low conservativeness of the conclusion.

Data Availability

The data used to support the findings of this study are included within the article. Because it is a numerical simulation example, readers can get the same results as this article by using the LMI toolbox of Matlab and the theorem given in this article.

Conflicts of Interest

The authors declare that they have no conflicts of interest.

Acknowledgments

This study was supported by the National Natural Science Foundation of China (grant nos. 61403278 and 61503280).

References

[1] B. S. Chen, C. S. Tseng, and H. J. Uang, "Mixed H_2/H_∞ fuzzy out-put feedback control design for nonlinear dynamic systems: an LMI approach," *Fuzzy Systems IEEE Transactions*, vol. 8, no. 3, pp. 249–265, 2000.

[2] X. Su, L. Wu, P. Shi, and Y. D. Song, "A novel approach to output feed-back control of fuzzy stochastic systems," *Automatica*, vol. 50, no. 12, pp. 3268–3275, 2014.

[3] Z. W. Zheng, Y. T. Huang, L. H. Xie, and B. Zhu, "Adaptive trajectory tracking control of a fully actuated surface vessel with asymmetrically constrained input and output," *IEEE Transactions on Control Systems Technology*, vol. 26, no. 5, pp. 1851–1859, 2018.

[4] Y. X. Tian, H. C. Yan, H. Zhang, X. Zhan, and Y. Peng, "Resilient static output feedback control of linear semi-markov jump systems with incomplete semi-markov kernel," *IEEE Transactions on Automatic Control*, vol. 66, no. 9, pp. 4274–4281, 2021.

[5] H. C. Yan, C. Y. Hu, H. Zhang, H. R. Karimi, X. Jiang, and M Liu, "H_{∞} output tracking control for networked systems with adaptively adjusted event-triggered scheme," *IEEE Transactions on Systems, Man, and Cybernetics: Systems*, vol. 49, no. 10, pp. 2050–2058, 2019.

[6] P. V. Suryawanshi, P. D. Shendge, and S. B. Phadke, "Robust sliding mode control for a class of nonlinear systems using inertial delay control," *Nonlinear Dynamics*, vol. 78, no. 3, pp. 1921–1932, 2014.

[7] H. C. Yan, X. P. Zhou, H. Zhang, F. Yang, and Z. G Wu, "A novel sliding mode estimation for microgrid control with communication time delays," *IEEE Transactions on Smart Grid*, vol. 10, no. 2, pp. 1509–1520, 2019.

[8] K. D. Young, V. I. Utkin, and U. Ozguner, "A control engineer's guide to sliding mode control," *IEEE Transactions on Control Systems Technology*, vol. 7, no. 3, pp. 328–342, 1999.

[9] W. H. Chen, D. J. Ballance, and P. J. Gawthrop, "Optimal control of nonlinear systems: a predictive control approach," *Automatica*, vol. 39, no. 4, pp. 633–641, 2003.

[10] D. Vrabie and F. Lewis, "Neural network approach to continuous-time direct adaptive optimal control for partially unknown nonlinear systems," *Neural Networks*, vol. 22, no. 3, pp. 237–246, 2009.

[11] T. Yamakawa, "A fuzzy inference engine in nonlinear analog mode and its application to a fuzzy logic control," *IEEE Transactions on Neural Networks*, vol. 4, no. 3, pp. 496–522, 1993.

[12] H. Ma, Q. Zhou, L. Bai, and H. Liang, "Observer-based adaptive fuzzy fault-tolerant control for stochastic nonstrict-feedback nonlinear systems with input quantization," *IEEE Transactions on Systems Man, And Cybernetics Systems*, vol. 49, no. 2, pp. 287–298, 2019.

[13] W. Wang, H. J. Liang, Y. N. Pan, and T. Li, "Prescribed performance adaptive fuzzy containment control for nonlinear multi-agent systems using disturbance observer," *IEEE Transactions on Cybernetics*, vol. 50, no. 9, pp. 3879–3891, 2020.

[14] H. Zhang, W. X. Li, and C. Y. Zhang, "Intuitionistic fuzzy AHP and its application in evaluation of ecological architecture," *Advanced Materials Research*, vol. 518-523, pp. 4466–4472, 2012.

[15] J. X. Dong, Y. Y. Wang, and G. H. Yang, "And mixed control of discrete-time T–S fuzzy systems with local nonlinear models," *Fuzzy Sets and Systems*, vol. 164, no. 1, pp. 1–24, 2011.

[16] C. Lin, Q. G. Wang, and T. Heng Lee, "Delay-dependent LMI conditions for stability and stabilization of T-S fuzzy systems with bounded time-delay," *Fuzzy Sets and Systems*, vol. 157, no. 9, pp. 1229–1247, 2006.

[17] Y. Chen, Z. q. Pan, H. Peng, and L. Xu, "[Characteristics of staphylococcal enterotoxin B (SEB)-induced anergy in transplantation of allogeneic bone marrow cells]," *Fuzzy Sets and Systems*, vol. 21, no. 5, pp. 544–547, 2005.

[18] Y. Y. Cao and P. M. Frank, "Analysis and synthesis of nonlinear time-delay systems via fuzzy control approach," *IEEE Transactions on Fuzzy Systems*, vol. 8, no. 2, pp. 200–211, 2000.

[19] R. Bisdorff, "Logical foundation of fuzzy preferential systems with application to the electre decision aid methods," *Computers & Operations Research*, vol. 27, no. 7-8, pp. 673–687, 2000.

[20] H. Gao, X. Liu, and J. Lam, "Stability analysis and stabilization for discrete-time fuzzy systems with time-varying delay," *IEEE Transactions on Systems, Man, and Cybernetics, Part B (Cybernetics)*, vol. 39, no. 2, pp. 306–317, 2009.

[21] L. G. Wu, X. J. Su, P. Shi, and J. Qiu, "A new approach to stability analysis and stabilization of discrete-time T-S fuzzy time-varying delay systems," *IEEE Transactions on Systems, Man, and Cybernetics, Part B (Cybernetics)*, vol. 41, no. 1, pp. 273–286, 2011.

[22] Y. Wei, J. Qiu, P. Shi, and H. K. Lam, "A new design of H -infinity piecewise filtering for discrete-time nonlinear time-varying delay systems via T–S fuzzy affine models," *IEEE Transactions on Systems, Man, and Cybernetics: Systems*, vol. 47, no. 8, pp. 2034–2047, 2017.

[23] C. H. Liu, J. D. Hwang, and Z. R. Tsai, "An LMI-based stable T-S fuzzy model with parametric uncertainties using multiple Lyapunov function approach," in *Proceedings of the 2004 IEEE Conference on Cybernetics and Intelligent Systems*, pp. 514–519, Hague, Netherlands, October, 2005.

[24] B. J. Rhee and S. Won, "A new fuzzy Lyapunov function approach for a Takagi-Sugeno fuzzy control system design," *Fuzzy Sets and Systems*, vol. 157, no. 9, pp. 1211–1228, 2006.

[25] M. Chadli, H. R. Karimi, and P. Shi, "On stability and stabilization of singular uncertain Takagi -Sugeno fuzzy systems," *Journal of the Franklin Institute*, vol. 351, no. 3, pp. 1453–1463, 2014.

[26] O. M. Kwon, M. J. Park, J. H. Park, and S. Lee, "Stability and stabilization of T-S fuzzy systems with time-varying delays via augmented Lyapunov-Krasovskii functionals," *Information Sciences*, vol. 372, pp. 1–15, 2016.

[27] R. Li and Y. Yang, "Fault detection for TS fuzzy singular systems via integral sliding modes," *Journal of the Franklin Institute*, vol. 357, no. 17, pp. 13125–13143, 2020.

[28] X. R. Huang, A. L. Ralescu, H. L. Gao, and H. Huang, "A survey on the application of fuzzy systems for underactuated systems," *Proceedings of the Institution of Mechanical Engineers - Part I: Journal of Systems & Control Engineering*, vol. 233, no. 3, pp. 217–244, 2018.

[29] A. T. Nguyen, T. Taniguchi, L. Eciolaza, V. Campos, R. Palhares, and M. Sugeno, "Fuzzy control systems: past, present and future," *IEEE Computational Intelligence Magazine*, vol. 14, no. 1, pp. 56–68, 2019.

[30] Y. Z. Wang, L. Zou, L. F. Ma, Z. Zhao, and J. Guo, "A survey on control for Takagi-Sugeno fuzzy systems subject to engineering-oriented complexities," *Systems Science & Control Engineering*, vol. 9, no. 1, pp. 334–349, 2021.

[31] J. B. Qiu, G. Feng, and J. Yang, "A new design of delay-dependent robust H-infinity filtering for discrete-time T-S fuzzy systems with time-varying delay," *IEEE Transactions on Fuzzy Systems*, vol. 17, no. 5, pp. 1044–1058, 2009.

[32] D. Debeljkovic, S. Stojanovic, and N. Dimitrijevic, "Stability of time-delay systems in the sense of non-Lyapunov delay-independent and delay-dependent criteria," *Tehnika*, vol. 67, no. 3, pp. 385–393, 2012.

[33] H. Matsunaga, "Delay-dependent and delay-independent stability criteria for a delay differential system," *Proceedings of the American Mathematical Society*, vol. 136, no. 12, pp. 4305–4312, 2008.

[34] X. Meng, J. Lam, B. Du, and H. Gao, "A delay-partitioning approach to the stability analysis of discrete-time systems," *Automatica*, vol. 46, no. 3, pp. 610–614, 2010.

[35] S. Xu, J. Lam, B. Zhang, and Y. Zou, "New insight into delay-dependent stability of time-delay systems," *International Journal of Robust and Nonlinear Control*, vol. 25, no. 7, pp. 961–970, 2015.

[36] P. T. Nam, P. N. Pathirana, and H. Trinh, "Discrete wirtinger-based in-equality and its application," *Journal of the Franklin Institute*, vol. 352, no. 5, pp. 1893–1905, 2015.

[37] X. M. Li, Q. Zhou, P. S. Li, H. Li, and R. Lu, "Event-triggered consensus control for multi-agent systems against false data-injection attacks," *IEEE Transactions on Cybernetics*, vol. 50, no. 5, pp. 1856–1866, 2020.

[38] A. Seuret, F. Gouaisbaut, and E. Fridman, "Stability of discrete-time systems with time-varying delays via a novel summation inequality," *IEEE Transactions on Automatic Control*, vol. 60, no. 10, pp. 2740–2745, 2015.

[39] Z. Lian, Y. He, C. K. Zhang, and M. Wu, "Further robust stability analysis for uncertain takagi-sugeno fuzzy systems with time-varying delay via relaxed integral inequality," *Information Sciences*, vol. 409-410, no. 10, pp. 139–150, 2017.

[40] A. Seuret and F. Gouaisbaut, "Stability of linear systems with time-varying delays using bessel–legendre inequalities," *IEEE Transactions on Automatic Control*, vol. 63, no. 1, pp. 225–232, 2018.

[41] S. Y. Lee, J. Park, and P. Park, "Bessel summation inequalities for stability analysis of discrete-time systems with time-varying delays," *International Journal of Robust and Nonlinear Control*, vol. 29, no. 2, pp. 473–491, 2019.

[42] Z. Lian, Y. He, C. K. Zhang, and M. Wu, "Stability and stabilization of T-S fuzzy systems with time-varying delays via delay-product-type functional method," *IEEE Transactions on Cybernetics*, vol. 50, no. 6, pp. 2580–2589, 2020.

[43] P. Park, J. W. Ko, and C. Jeong, "Reciprocally convex approach to stability of systems with time-varying delays," *Automatica*, vol. 47, no. 1, pp. 235–238, 2011.

[44] A. Seuret and F. Gouaisbaut, "Delay-dependent reciprocally convex combination lemma," *Rapport LAAS*, vol. 16006, 2016.

[45] X. M. Zhang, Q. L. Han, A. Seuret, and F. Gouaisbaut, "An improved reciprocally convex inequality and an augmented Lyapunov-Krasovskii functional for stability of linear systems with time-varying delay," *Automatica*, vol. 84, pp. 221–226, 2017.

[46] A. Seuret, K. Liu, and F. Gouaisbaut, "Generalized reciprocally convex combination lemmas and its application to time-delay systems," *Automatica*, vol. 95, pp. 488–493, 2018.

[47] C. Briat, "Convergence and Equivalence results for the Jensen's inequality Application to time-delay and sampled-data systems," *IEEE Transactions on Automatic Control*, vol. 56, no. 7, pp. 1660–1665, 2011.

[48] Y. He, Q. G. Wang, L. Xie, and C. Lin, "Further improvement of free-weighting matrices technique for systems with time-varying delay," *IEEE Transactions on Automatic Control*, vol. 52, no. 2, pp. 293–299, 2007.

[49] Q. Zhu and J. Cao, "Stability of Markovian jump neural networks with impulse control and time varying delays," *Nonlinear Analysis: Real World Applications*, vol. 13, no. 5, pp. 2259–2270, 2012.

[50] L. Cao, H. Y. Li, G. Dong, and R. Lu, "Event-Triggered control for multi-agent systems with sensor faults and input saturation," *IEEE Transactions on Systems, Man, and Cybernetics: Systems*, vol. 51, no. 6, pp. 3855–3866, 2021.

[51] J. Chen, S. Y. Xu, X. L. Jia, and B. Zhang, "Novel summation inequalities and their applications to stability analysis for systems with time-varying delay," *IEEE Transactions on Automatic Control*, vol. 62, no. 5, pp. 2470–2475, 2017.

[52] S. P. Xiao, L. X. Xu, H. B. Zeng, and K. L. Teo, "Improved stability criteria for discrete-time delay systems via novel summation inequalities," *International Journal of Control, Automation and Systems*, vol. 16, no. 4, pp. 1592–1602, 2018.

[53] X. J. Su, P. Shi, and L. G. Wu, "A novel approach to filter design for T-S fuzzy discrete-time systems with time-varying delay," *IEEE Transactions on Fuzzy Systems*, vol. 20, no. 6, pp. 1114–1129, 2012.

[54] K. Tanaka and H. O. Wang, *Fuzzy Control Systems Design and Analysis: A Linear Matrix Inequality Approach*, pp. 2011–2013, Wiley, New York, NY, USA, 2001.

Hindawi
Discrete Dynamics in Nature and Society
Volume 2022, Article ID 7848008, 7 pages
https://doi.org/10.1155/2022/7848008

Research Article

Signal Analysis of Characteristics Using Passive Acoustic Emission Technique in Gas-Solid Pipeline Flows

Weigang Qin

School of Electronic and Information Engineering, Tiangong University, Tianjin 300387, China

Correspondence should be addressed to Weigang Qin; qinweigang@tiangong.edu.cn

Received 25 April 2022; Accepted 7 June 2022; Published 29 June 2022

Academic Editor: Zi-Peng Wang

This paper investigates a case study of the use of a passive acoustic sensor for online measurement of the dilute phase gas-solid pipeline flows. The acoustic emission sensor is mounted externally on a stainless steel line conveying silica powders. For different experimental conditions, including the solid to air mass ratios from 0.6 to 1.4 and the gas volume flows from 160 to 240 m^3/h, the sound signals in the pipeline are discussed using the wavelet transform technique. The measured values of transmission mechanism of two different lengths, 25 mm and 35 mm, are analyzed. The results show that the variation tendency of standard deviations is consistent and that the noninvasive, online acoustic detect technique can be regarded as a satisfactory tool in gas-solid flows.

1. Introduction

Pneumatic conveying is commonly referred to wind power transport of granular materials with a certain air pressure and speed in industry. Pneumatic conveying is widely used in different fields, such as grain, cement, coal, chemical materials, powder, salt, flour, and other industrial processes.

There are many methods to measure gas-solid two-phase flow, such as the microwave method [1], electrostatic method [2], electrical tomography [3], optical method [4], and acoustic method [5]. Previous work is encountered in the technique using acoustic signals to measure particle size and other characteristics in dilute phase pneumatic conveying lines. The electrostatic method and image method are conducted in gas-solid flow regimes. For instance, the electrostatic method is adapted for electrostatic correlation velocimetry, while the image method is used in the movement of particles and flames imaging. The work has also demonstrated the feasibility of using acoustic measurement of particle size by Yan [6]. The active acoustic technique in gas-solid two-phase flows has been studied in different locations near the pipeline bends to measure the flow velocity and particle concentration. The results show that the speed near the elbow is divergent from one of the straight pipes and that the concentration at the elbow is approximately twice in the straight pipe [7]. Dilute phase flow has been observed in the pneumatic transport of fine powders. As the gas flow rate is reduced or the solids flow rate increased, particles may settle on the bottle of the horizontal sections, forming a stagnant layer, and affecting the stability of the fluid. Therefore, the work is to develop reliable flow regime detection through the online analysis of signals reflecting the solid phase velocity from nonintrusive acoustic sensors [8, 9]. Particle size is inferred from measurement of the peak compression of a specially designed ultrasonic transducer subject to the impact of the particles using a noninvasive acoustic sensor. In the laboratory, the impact size monitor (ISM) has demonstrated the ability to discriminate between powders with a difference in peak particle size of 2% at an approximate peak size of 150 microns [10]. Acoustic method, determining the pipeline leak location, also shows that the technique can achieve the online measurements [11]. With discussing the relationship between acoustic signals and particle size distribution, signal processing technique based on acoustic emission is used to extract the sound signal through the wavelet transform, thus multivariate dimension is reduced through component analysis. Finally, particle size distribution is obtained in terms of

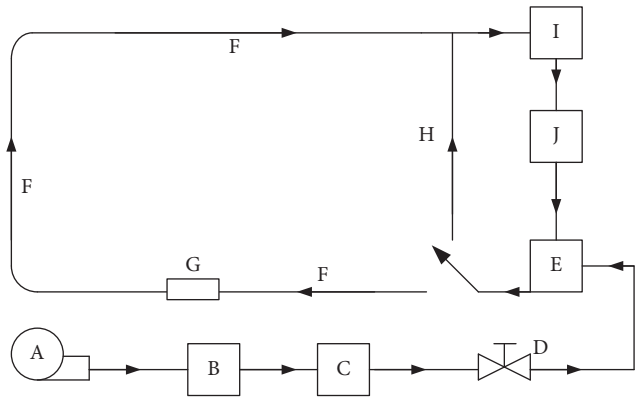

Figure 1: Schematic diagram of the experimental system: A: air compressor, B: gas tank, C: air dryer, D: regulating valve, E: screw feeder, F: transport pipeline, G: acoustic sensor, H: removing blockage pipeline, I: solid storage silo, and J: weighing device.

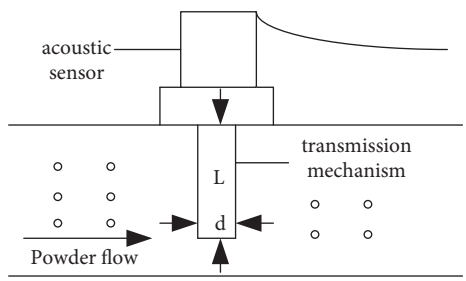

Figure 2: Schematic diagram showing the layout of acoustic sensor.

neural networks [12]. A quantitative model is established to detect related process parameters, including particle concentration, volume flow, and mass flow using passive acoustic sensors [13, 14]. Online measurement signals are achieved through passive acoustic emission sensors used in chemical process. Because of the particle collision, sound frequency between 15 kHz and 200 kHz is described [15]. Combined with the particle temperature and particle collision mechanism, the quality of the gas-solid fluidized bed is judged by signal analysis [16]. Ultrasonic waves are applied to improve the gas-solid flow homogeneity in CFB risers. The best geometrical configuration of an ultrasonic device with a frequency of 40 kHz applied to a lab-scale CFB riser is defined with a design of experiments [17].

The mechanism of acoustic emission in gas-solid flows mainly comes from three aspects: collision between the particles the wall or pipeline, and fluid turbulence. Since the frequency below 20 kHz is difficultly absorbed into the solid, internal ultrasonic sound generated by particles' friction and collision with the wall is detected through the passive acoustic detection systems. The acoustic method combined with principal component analysis, neural network analysis, and wavelet analysis, is widely used in the measurement of gas-solid two-phase flow parameters [18, 19].

2. Basic Principles

When extracting the spectrum of the signal, the Fourier transform needs to use the time-domain information of the signal. The time when the frequency component

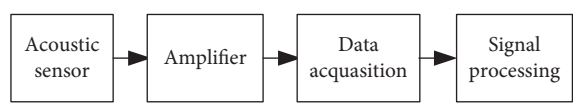

Figure 3: Whole signal processing system.

contained in the signal appears is uncertain. Compared with Fourier transform, wavelet transform converts the infinite trigonometric function basis in Fourier transform into a finite attenuated wavelet basis and analyzes the signal with a set of basic functions with changing width. Therefore, wavelet transform can not only obtain the frequency but also locate the time. Wavelet analysis is also a rapidly developing new field in signal analysis and has been widely used.

2.1. Continuous Wavelet Transform in Time Domain. For function,

$$W_s(t) = a^{-1/2} \int_{-\infty}^{+\infty} s(t) \psi_{a,b}^{*}\left(\frac{t-b}{a}\right) \mathrm{d}t, \tag{1}$$

we further obtain

$$W_s(t) = \int_{-\infty}^{+\infty} s(t) \psi_{a,b}^{*}(t) \mathrm{d}t = \langle s(t), \psi_{a,b}(t) \rangle, \tag{2}$$

where $s(t)$ represents the signal, $\varphi_{a,b}(t) = \psi_{a,b}(t) = a^{-1/2}\varphi_{a,b}(t-b/a)$ is the kernel function, which is the result of the scaling a and time translation b of the window function. The window function $\psi(t)$ is called the

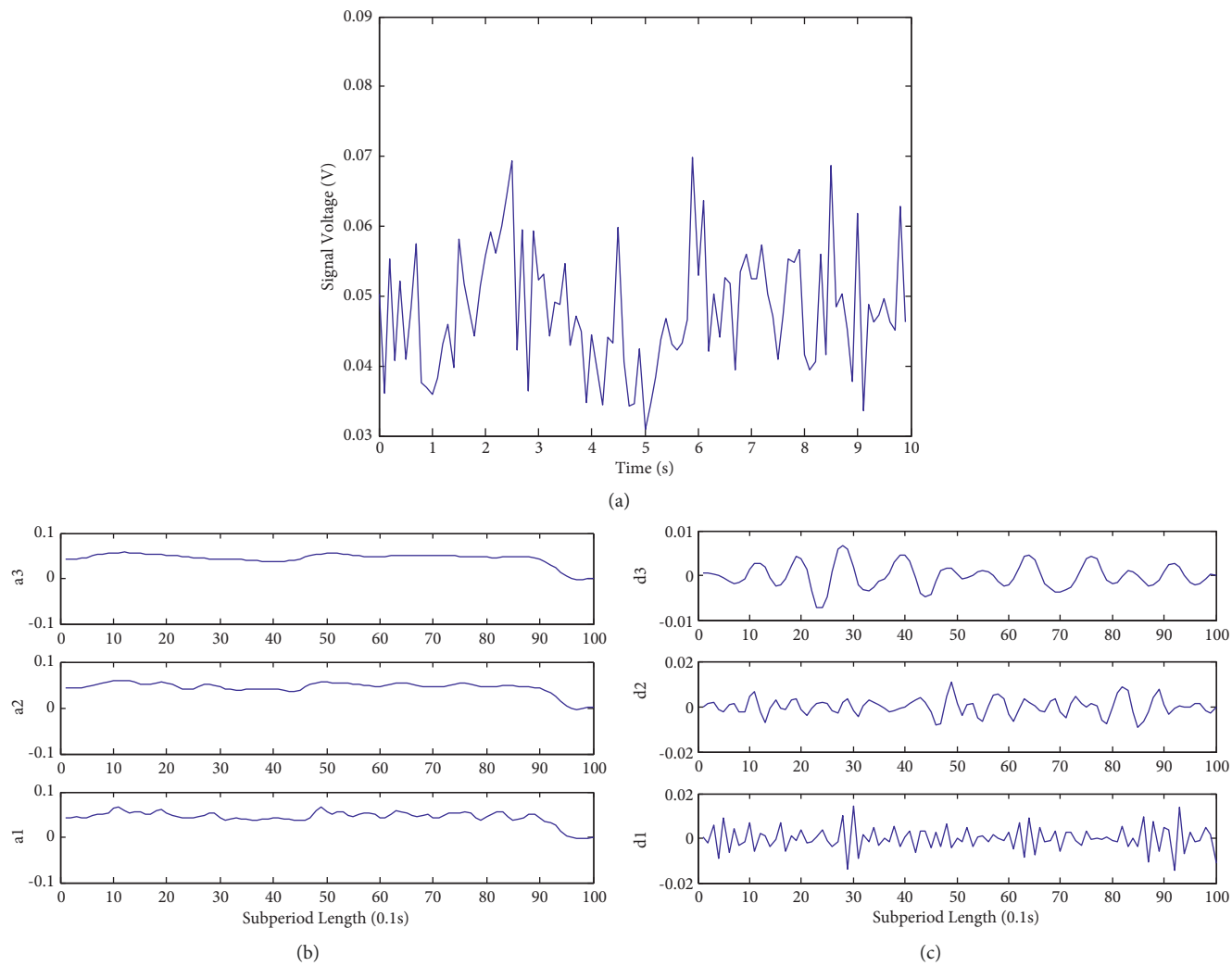

Figure 4: (a) FFT signal with solid to air mass ratio 0.6 and gas flow of 160 m^3/h; (b) wavelet transform approximation signal; (c) wavelet transform detail signal.

mother wavelet, where $a > 0$ is the scaling of the basic wavelet. $B \in R$ is the time position of the analysis signal, that is, the time center. It is to ensure that the energy of the function and the mother wavelet is the same under different scales [20–22].

2.2. Wavelet Transform in Frequency Domain. For function,

$$W_s(\omega) = \frac{a^{1/2}\int_{-\infty}^{+\infty} S(\omega)\widehat{\psi}^*(a\omega)e^{j\omega b}\mathrm{d}\omega}{2\pi} = \frac{\langle S(\omega), \widehat{\psi}_{a,b}(\omega)\rangle}{2\pi},$$
$$\widehat{\psi}_{a,b}(\omega) = a^{-1/2}\widehat{\psi}(a\omega)e^{-j\omega b}, \tag{3}$$

where $S(\omega)$ represents the frequency domain transformation of $s(t)$ and $\widehat{\psi}(\omega)$ is the frequency transformation of $\psi(t)$.

3. Experimental System

3.1. Pneumatic Transport System. The pneumatic transport circuit is shown schematically in Figure 1. The loop consists of 0.5 m inside diameter stainless steel pipeline. Air is supplied by two compressors, regulated using a valve and monitored by several pressure gauges. Air flows through a horizontal pipeline located underneath a gas-solid mixer from which particles are fed into the pipeline with a weighing device. After the powder feeds point, the gas-solid mixture flows through a 6 m horizontal line with five 6 m horizontal sections and a 3 m vertical line into powder hopper and a cyclone where particles are separated from the air. The gas stream is controlled by a regulating valve. The amount of particles in the loop is determined by a weighing device. In order to avoid solid blockage, it is necessary to use a removing blockage pipeline connecting a cyclone.

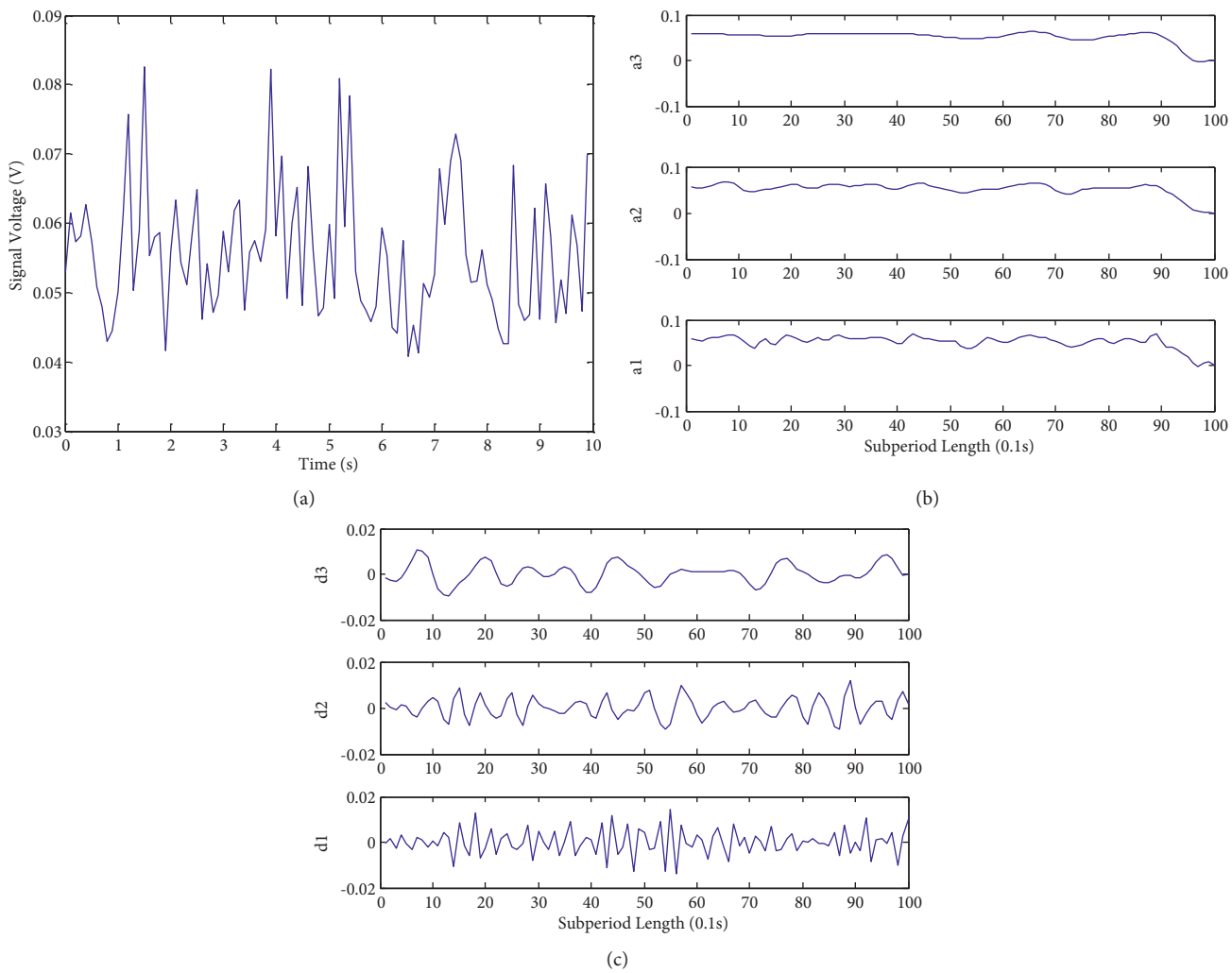

Figure 5: (a) FFT signal with solid to air mass ratio 1.0 and gas flow of 160 m^3/h; (b) wavelet transform approximation signal; (c) wavelet transform detail signal.

3.2. Particle Properties. Silica particles with white powder, the density of 2.65 g/cm^3, the diameter of 100 um, are used in the whole experiment. Its physical properties cannot be changed with high hardness, moisture-proof performance, and easily saving under experimental conditions.

3.3. Measurement System. Acoustic sensors can provide a reliable, online, and nonintrusive monitoring. There are two acoustic monitoring methods, that is, active acoustics and passive acoustics [8].

As we all know, the direct impact of particles on the object's surface will cause the rebound of particles, and the rebound particles and subsequent particles will cause secondary or multiple impacts. To reduce multiple bounce caused by particle collision, as shown in Figure 2, the sound transmission device is a stainless steel rod with the particles hitting its diamond-shaped surface. The d is the diagonal of the diamond-shaped surface and L is the length of the device. The diagonal width d with 10 mm and two kinds of length L with 25 mm and 35 mm are selected here. The acoustic emission sensor is installed externally on a horizontal pipe (shown in Figure 1). This position is also where the particles are fully mixed. In order to better measure the sound of particles, the viscous couplant is located between the sound transmission device and the acoustic sensor.

4. Experimental Results and Discussion

For each experiment, the different solid to air mass ratios depending on the motor speed are 0.6, 1.0, and 1.4. Whereas for air, the stable gas fluxes are 160, 200, and 240 m^3/h. The measuring signals are acquired from the rod of two different lengths of 25 mm and 35 mm.

Firstly, solids are not added to the pneumatic pipeline until the gas flow into the line reaches a stable condition for some time. Once the air flow stabilized, acoustic measurements are recorded right away. After each measurement, the powder hopper is stopped and the gas maintained in the process until the line is completely cleared of solids.

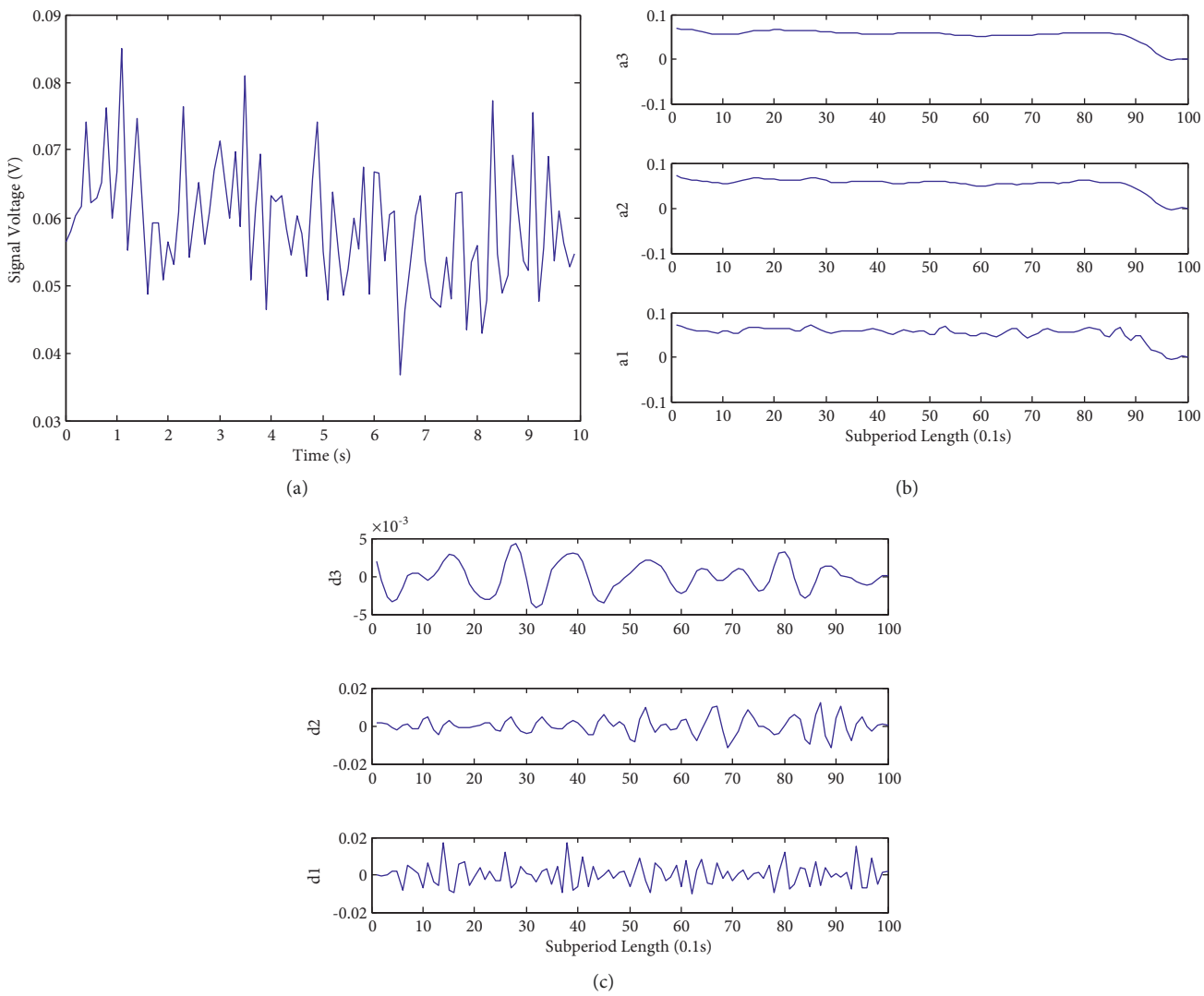

Figure 6: (a) FFT signal with solid to air mass ratio 1.4 and gas flow of 160 m^3/h; (b) wavelet transform approximation signal; (c) wavelet transform detail signal.

All measurements in the laboratory are performed with commercially available instrumentation and sensors. The whole signal processing system is given in Figure 3. The signal of acoustic emission sensor manufactured by the PengXiang Technology Co., Ltd. is collected and then magnified in the experiment. Finally, the signal is fed into the personal computer using NI Labview USB6259 acquisition card. In addition, according to Shannon sampling theorem, if the maximum signal frequency is f_m, then the sampling frequency f must meet $f \geq 2\ f_m$. As the frequency band of the acoustic sensor in the work is 15–165 kHz, the sampling rate of 1 MHz and the acquisition time of 10 s are set to record detail spectral characteristics of the signal in frequency domain.

Figures 4(a), 5(a), and 6(a) show that the 105 acquisition points within every 0.1 s for the fast Fourier transform (FFT) are carried out 100 times for the rod of length 35 mm. The Daubechies3 wavelet approximation signals are obtained in Figures 4(b), 5(b), and 6(b). Figures 4(c), 5(c), and 6(c) represent the Daubechies3 wavelet detail signals, respectively.

Figures 4(a), 5(a), and 6(a) show the signal voltage of acoustic measurement recorded at the different solid to air mass ratios: 0.6, 1.0, and 1.4, after the FFT, filtered to eliminate the 50 Hz electrical noise. With the solid to air mass ratio increasing, the signal voltage magnitude is significantly strengthened. The wavelet transform approximation signals and detail signals are demonstrated in figures 4(b), 4(c), 5(b), 5(c), 6(b), and 6(c).

With the solid to air mass ratio increasing, under the different gas volume flows, the standard deviation of measurement signal is summarized in Figure 7. Under the same gas volume flow and the different solid to air mass ratios, the standard deviation is increased. Meanwhile, under the different gas volume flows and the same solid to air mass ratio, the standard deviation is also increased. Whether the rod length is 25 mm or 35 mm, the trend of standard deviation is

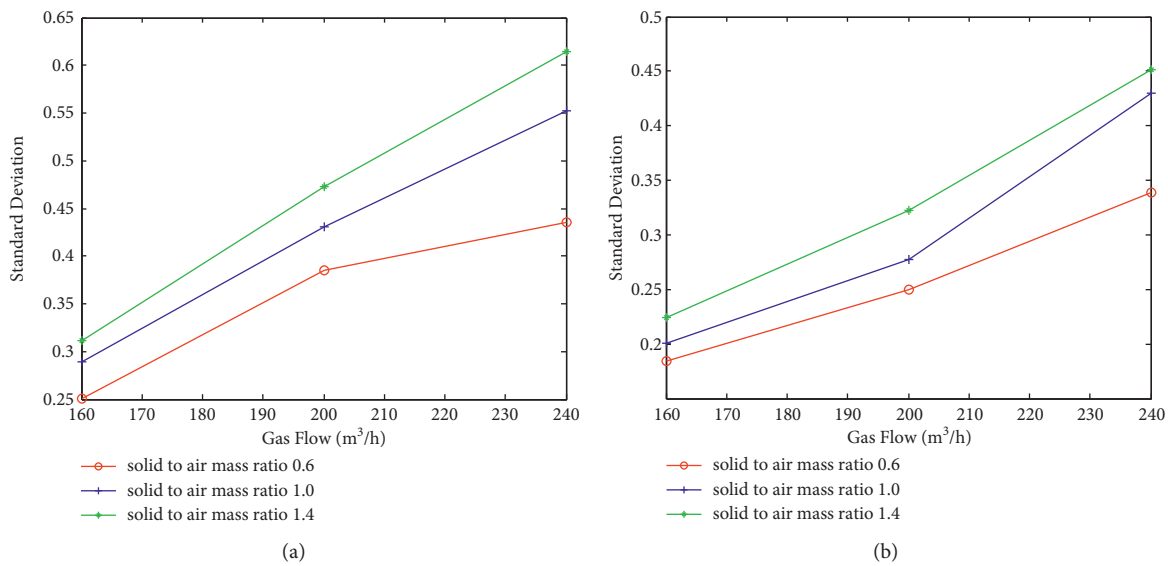

Figure 7: (a) Standard deviation of rod length 25 mm for different gas volume flows and different solid to air mass ratios; (b) standard deviation of rod length 35 mm for different gas volume flows and different solid to air mass ratios.

Table 1: Standard deviation of different lengths.

Length of rod (mm)	Solid to air mass ratio	Gas volume flow (m^3/h)	Standard deviation
25	0.6	160	0.1838
		200	0.2495
		240	0.3385
	1.0	160	0.2010
		200	0.2775
		240	0.4300
	1.4	160	0.2242
		200	0.3222
		240	0.4510
35	0.6	160	0.2501
		200	0.3855
		240	0.4350
	1.0	160	0.2891
		200	0.4305
		240	0.5523
	1.4	160	0.3114
		200	0.4732
		240	0.6142

basically consistent. The standard deviation for every case is shown in Table 1.

5. Conclusions

The passive acoustic measurement apparatus described in this experiment operates in the dilute phase gas-solid flows following the horizontal pipeline. The acquisition points are analyzed to obtain approximation signals and detail signals using wavelet transform method. The results present that the collision chance is increased by the different solid to air mass ratios from 0.6 to 1.4 and the same gas volume flow. However, under the same solid to air mass ratio and the different gas volume flows from 160 to 240 m^3/h, the signals obtained from the acoustic sensor are enhanced as the more impact between the particles and sound transmission device in the pipeline. At the same time, the standard deviation is obviously increased under the different gas volume flow and the different solid to air mass ratios. The longer the length of the transmission mechanism is, the bigger the standard deviation is. The standard deviation is roughly proportional to the solid to air mass ratio and the gas volume flow, but their value can be acceptable. It is confident that the passive acoustic measurement will bring major improvements to gather the characteristics of gas-solid regime in this study. The relationship between gas flow rate and particle size concentration is established. The advantage of acoustic method is that it is not affected by static electricity. This method is suitable for the measurement of gas-solid two-phase flow. At the same time, a lot of work needs to be done in the future, such as multisensor data fusion technology.

Data Availability

The data used to support the findings of this study are available from the author upon request.

Conflicts of Interest

The author declares that there are no conflicts of interest.

Acknowledgments

The work was supported by the collaborative education project of industry university cooperation of the Ministry of Education (201901138036).

References

[1] J. Zou, C. Liu, H. Wang, and Z. Wu, "Mass flow rate measurement of bulk solids based on microwave tomography and microwave Doppler methods," *Powder Technology*, vol. 360, pp. 112–119, 2020.

[2] M. Manafi, R. Zarghami, and N. Mostoufi, "Effect of electrostatic charge of particles on hydrodynamics of gas-solid fluidized beds," *Advanced Powder Technology*, vol. 30, no. 4, pp. 815–828, 2019.

[3] C. Chinedu Anyaoku, S. N. Bhattacharya, and R. Parthasarathy, "A novel methodology for measuring batch settling velocities of particles using Electrical Resistance Tomography," *Chemical Engineering Science*, vol. 250117364 pages, 2022.

[4] M. Mokhtari and J. Chaouki, "New technique for simultaneous measurement of the local solid and gas holdup by using optical fiber probes in the slurry bubble column," *Chemical Engineering Journal*, vol. 358, pp. 831–841, 2019.

[5] K. T. Aminu, D. McGlinchey, and A. Cowell, "Acoustic signal processing with robust machine learning algorithm for improved monitoring of particulate solid materials in a gas flowline," *Flow Measurement and Instrumentation*, vol. 65, pp. 33–44, 2019.

[6] Y. Yan, "Mass flow measurement of bulk solids in pneumatic pipelines," *Measurement Science and Technology*, vol. 7, no. 12, pp. 1687–1706, 1996.

[7] S. J. Tallon and C. E. Davies, "The effect of pipeline location on acoustic measurement of gas–solid pipeline flow," *Flow Measurement and Instrumentation*, vol. 11, no. 3, pp. 165–169, 2000.

[8] K. Albion, L. Briens, C. Briens, and F. Berruti, "Flow regime determination in horizontal pneumatic transport of fine powders using non-intrusive acoustic probes," *Powder Technology*, vol. 172, no. 3, pp. 157–166, 2007.

[9] Y. Zhou, L. Yang, Y. Lu, X. Hu, X. Luo, and H. Chen, "Flow regime identification in gas-solid two-phase fluidization via acoustic emission technique," *Chemical Engineering Journal*, vol. 334, pp. 1484–1492, 2018.

[10] P. J. Coghill, "Particle size determination by impact measurement in pneumatically conveyed solids," *Particle & Particle Systems Characterization*, vol. 18, no. 3, p. 114, 2001.

[11] R. K. Miller, A. A. Pollock, D. J. Watts, J. M. Carlyle, A. N. Tafuri, and J. J. Yezzi Jr, "A reference standard for the development of acoustic emission pipeline leak detection techniques," *NDT&E International*, vol. 32, pp. 1–8, 1999.

[12] A. Bastari, C. Cristalli, R. Morlacchi, and E. Pomponi, "Acoustic emissions for particle sizing of powders through signal processing techniques," *Mechanical Systems and Signal Processing*, vol. 25, no. 3, pp. 901–916, 2011.

[13] R. Hou, A. Hunt, R. A. Williams, and A. Hunt, "Acoustic monitoring of pipeline flows: particulate slurries," *Powder Technology*, vol. 106, no. 1-2, pp. 30–36, 1999.

[14] P. Zhang, Y. Yang, Z. Huang et al., "Machine learning assisted measurement of solid mass flow rate in horizontal pneumatic conveying by acoustic emission detection," *Chemical Engineering Science*, vol. 229116083 pages, 2021.

[15] J. W. R. oyd and J. Varley, "The uses of passive measuremen of acoustic emissions from chemical engineering processes," *Chemical Engineering Science*, vol. 56, pp. 1749–1767, 2001.

[16] C. Ren, J. Wang, and Y. Yang, "Signal analysis and judgement of acoustic emission of particle motion in gas-solid fluidized bed," *Science in China, Series B: Chemistry*, vol. 38, pp. 645–651, 2008.

[17] V. Rossbach, N. Padoin, H. F. Meier, and C. Soares, "Influence of acoustic waves on the solids dispersion in a gas-solid CFB riser: numerical analysis," *Powder Technology*, vol. 359, pp. 292–304, 2020.

[18] H. Sadegh, A. N. Mehdi, and A. Mehdi, "Classification of acoustic emission signals generated from journal bearing at different lubrication conditions based on wavelet analysis in combination with artificial neural network and genetic algorithm," *Tribology International*, vol. 95, pp. 426–434, 2016.

[19] E. M. Hansuld, L. Briens, A. Sayani, and J. A McCann, "An investigation of the relationship between acoustic emissions and particle size," *Powder Technology*, vol. 219, no. 3, pp. 111–117, 2012.

[20] A. Chakravarty and S. Misra, "Hydraulic fracture mapping using wavelet-based fusion of wave transmission and emission measurements," *Journal of Natural Gas Science and Engineering*, vol. 96, p. 104274, 2021.

[21] A. Mostafapour, S. Davoodi, and M. Ghareaghaji, "Acoustic emission source location in plates using wavelet analysis and cross time frequency spectrum," *Ultrasonics*, vol. 54, no. 8, pp. 2055–2062, 2014.

[22] O. Stankevych, V. Skalskyi, B. Klym, and P. Velykyi, "Identification of fracture mechanisms in cementitious composites using wavelet transform of acoustic emission signals," *Procedia Structural Integrity*, vol. 36, pp. 114–121, 2022.

Hindawi
Discrete Dynamics in Nature and Society
Volume 2022, Article ID 8372291, 12 pages
https://doi.org/10.1155/2022/8372291

Research Article

Fall Detection and Direction Judgment Based on Posture Estimation

Chunmiao Yuan,[1] **Pengju Zhang**,[2] **Qingyong Yang**,[3] **and Jianming Wang**[2]

[1]*School of Software, Tiangong University, Tianjin 300387, China*
[2]*School of Computer Science and Technology, Tiangong University, Tianjin 300387, China*
[3]*School of Software and Communication, Tianjin Sino-German University of Applied Sciences, Tianjin 300350, China*

Correspondence should be addressed to Jianming Wang; wangjianming@tiangong.edu.cn

Received 22 April 2022; Accepted 18 May 2022; Published 15 June 2022

Academic Editor: Chun Wei

For the problem of elderly people falling easily, it is very necessary to correctly detect the occurrence of falls and provide early warning, which can greatly reduce the injury caused by falls. Most of the existing fall detection algorithms require the monitored persons to carry wearable devices, which will bring inconvenience to their lives and few algorithms pay attention to the direction of the fall. Therefore, we propose a video-based fall detection and direction judgment method based on human posture estimation for the first time. We predict the joint point coordinates of each human body through the posture estimation network, and then use the SVM classifier to detect falls. Next, we will use the three-dimensional human posture information to judge the direction of the fall. Compared to the existing methods, our method has a great improvement in sensitivity, specificity, and accuracy which reaches 95.86, 99.5, and 97.52 on the Le2i fall dataset, respectively, whereas on the UR fall dataset, they are 95.45, 100, and 97.43, respectively.

1. Introduction

According to statistical information, accidental fall is a phenomenon with a high frequency among the elderly population [1, 2]. Even for people living independently, falls are common occurrences. At the same time, the injury of falling to the elderly is also extremely serious, which is the main factor causing the death of the elderly [3]. It will take a lot of time and energy if unexpected fall activities are monitored manually. Therefore, it is very important to realize a platform that can monitor people's activity status, detect the occurrence of falls and other unexpected behaviors in real time, and give a timely early warning of falls.

In recent years, the researches on fall detection have achieved remarkable results and have a wide application prospect [4, 5]. However, many existing studies are based on wearing wearable devices [6–8]; these approaches have led to the appearance of smart environments for elderly assistance, which had been traditionally limited to home settings. And most strategies often only focus on detecting whether the falling behavior occurs, but pay little attention to the direction of the fall and the degree of injury caused by the fall. Actually, the extent of injury caused by a fall is largely affected by the direction of the human body fall, and different fall directions will cause different intensities of injury to the human body. The injury caused by a human body falling forward is generally smaller than that caused by falling back. Therefore, a perfect and practical fall prediction system should not bring a burden to the monitored person and it can not only accurately detect falls but also classify the risk of falls.

As a result of the research carried out, this study presents the following main contributions:

(1) A vision-based fall detection algorithm is proposed which extracts human features directly from video through posture analysis and does not need the observed person to carry any wearable devices.

(2) By using 3D spatial coordinates containing depth information, the fall direction of the human body can be judged so as to estimate the risk degree of fall and make accurate early warning.

2. Related Works

With the in-depth study of fall detection, a large number of schemes have been proposed and great achievements have been made. According to different research methods and experimental equipment, fall detection can be divided into two classifications: wearable sensor-based and vision-based.

The wearable sensor-based collects motion and other parameter signals through relevant sensor devices and then uses the calculation formula to convert the collected signals into information that can represent the motion state, such as acceleration information [9]. According to this information, the real state of the current target can be judged. Sensors are usually placed on the waist, legs, or near the neck. The commonly used equipment is an accelerometer, three-axis gyroscope, magnetometer, and barometer. Zerrouki et al. [10] used an accelerometer to get the motion state to detect falls. Chen et al. [11] proposed a fall detection system that integrated a three-axis gyroscope, a three-axis accelerometer, and a Bluetooth module for wireless communication to design a waist-attached, miniature fall detection device. The device collected information from the gyroscope and accelerometer for analysis to deduce continuous signals representing the human body postures. According to the posture and signal relationship, artificial intelligence was used to construct a highly accurate model. Alarifi and Alwadain [12] used the wearable sensor device composed of a magnetometer, gyroscope, and accelerometer which was placed in six different positions on the subject's body, then they used the intelligent AlexNet convolution network for fall detection. A waist-mounted device was presented to detect possible falls in elderly people [13] through data coming from a three-axis accelerometer, a three-axis gyroscope, a three-axis magnetometer, and a barometer sensor integrated into the device. Built-in smartphone sensors can be utilized to detect falls [14]. Built-in smart helmets are also wearable sensors [15] to detect falls for ease of use. After getting the angular motion or trunk inclination by sensors, machine learning or deep learning methods are often used to judge the fall. The wearable sensor-based method has high recognition accuracy, but is less convenient because sensor devices need to be carried by the monitored person.

The vision-based method records the activities of people in the scene by using different types of cameras, such as ordinary cameras and depth cameras. According to the changes in human characteristics in each frame, the target people are analyzed by image processing or neural network. The human body silhouettes or bounding boxes can be extracted by traditional computer vision methods, such as the frame difference method, background subtraction, or foreground segmentation, then the methods use those features as input for a classifier (e.g., Gaussian mixture model (GMM), SVM, and MLP) to automatically detect if a fall has occurred. For example, Sehairi et al. [16] obtained human contour from a series of video frames through background subtraction, extracted the change of aspect ratio according to the difference of contour, calculated the vertical velocity of the head using a finite state machine, and inferred the state of target by synthesizing these features. Zerrouki et al. [17] computed occupancy areas around the body's gravity center, extracted their angles, and fed them into various classifiers; the SVM being the one that obtained the best results. The same authors extended their previous work by adding curvelet coefficients as extra features and applying a hidden Markov model (HMM) to model the different body poses [18]. A less frequent technique was used by Harrou et al. [19], who applied multivariate exponentially weighted moving average (MEWMA) charts. Rougier et al. [20] detected whether fall behavior occurred by quantifying the change of human body shape in the video sequence. For these solutions, the shape of the human body will produce different results due to different camera positions, at the same time, carrying backpacks, crutches, and other objects will also affect the detection results.

Another vision-based method judges according to the joint information of pose estimation. The pose estimation method can accurately predict the position of each joint of the body and represent the abstract human body information with a set of 2D or 3D joint points. Asif et al. [21] obtained the feature information of the human body represented by human joint point information through a stacked hourglass network, inputted the features into a CNN model with modal-specific layer and multimodal embedding layer, and learned high-level feature embedding to distinguish fall posture and non-fall posture. Chen et al. [22] used OpenPose [23] to get the data of human joint points and then identified whether the falling behavior occurred by calculating the falling speed of the hip joint center, the angle between the human body centerline and the ground, and the width-height ratio of the rectangle outside the human body. At the same time, whether the person stood up independently after falling was considered, and the state of the target was judged by combining the above conditions. Compared with contour information, using the human bone joint feature is easier for action recognition and is less affected by external factors. Therefore, this study selects a pose estimation method to extract human features. The injury caused by falling is largely affected by the direction of the human body falling when the falling action occurs; however, most of these studies pay no attention to the direction of the fall, which is a major issue that is taken into account in our solution.

3. Proposed Method

3.1. Overview of Our Method. Our method is divided into two modules: fall detection and direction judgment. In the fall detection module, the videos captured by an ordinary camera are analyzed frame by frame and then sent to the fall detection network to detect whether there are accidents such as falls in the current scene. After the fall action is detected, the 2D joint feature will be sent to the direction judgment module: first the dimension transformation network will

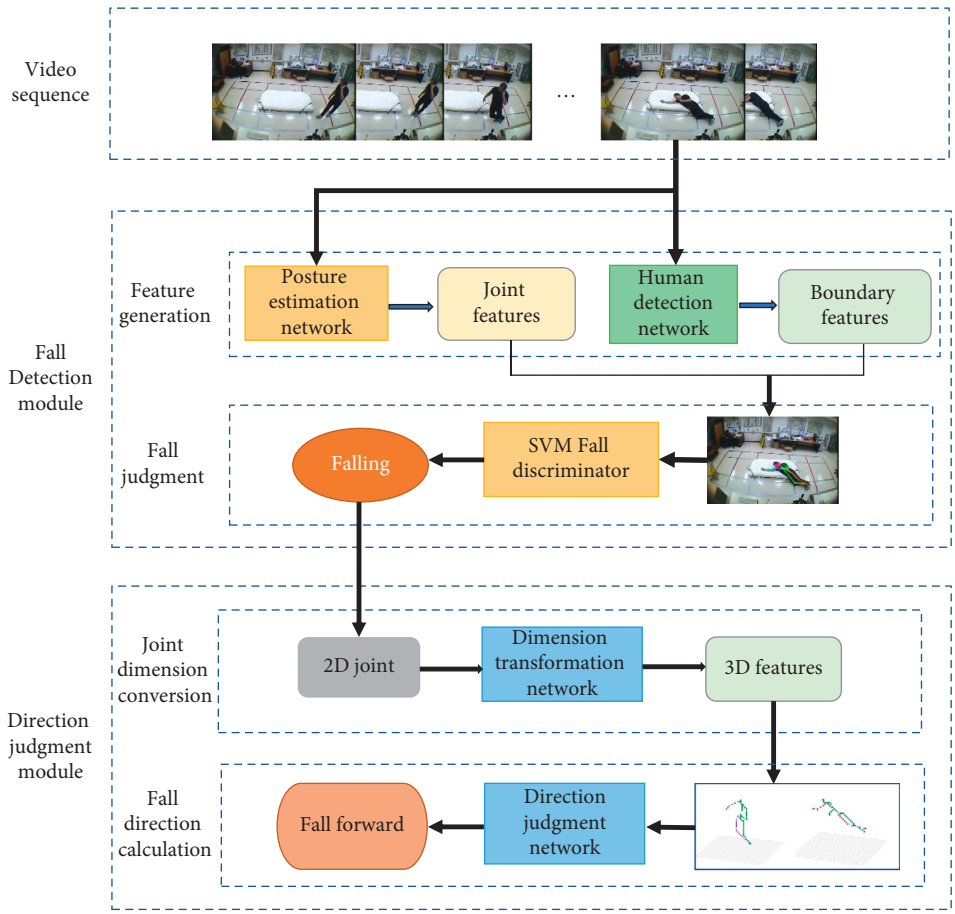

Figure 1: Overview of fall detection and direction recognition method.

transform the 2D feature into 3D joint points with depth information, and then the direction judgment network will estimate the specific fall direction by calculating 3D joint set, so as to give appropriate early warning for the fall event. The overview of this method is shown in Figure 1.

3.2. Fall Detection Module

3.2.1. Human Posture Extraction. In order to realize fall detection, we used the joint point information as the feature. We first extracted the relevant joint point information from the video frame through the posture estimation method, screened the bone points with high correlation as the feature input into the classification network, and then trained and learned a group of fall and non-fall data by support vector machine, so as to judge whether the human body is in a fall state.

Through the comprehensive analysis and comparison of current posture estimation algorithms, the OpenPose algorithm with better real-time performance was finally selected to realize posture estimation to obtain joint point parameters. When using the OpenPose algorithm to test our dataset, it was found that there was misjudgment in some data, such as identifying background or objects similar to the human body as a part of the body, which greatly affected the final recognition effect. After analysis, the reason for this is that OpenPose is a bottom-up method that first predicts all possible joint points from the picture, and then clusters these points according to the dependency relationship to form an independent skeleton. In this process, it is impossible to ensure whether the predicted points belong to a part of the human body which results in some points offset from the human body area being predicted.

In order to solve the above problems and accurately obtain the joint point coordinates within the human body area, we proposed a top-down posture estimation network, which took the OpenPose network as the baseline, and added a layer of human body detection network to detect the human body and determine the regional range of each person. Through the combination of human body boundary features and joint features, the final joint information was more accurate.

The human detection network uses Fast R-CNN to detect boundary features of the human body and these features will be used to screen the false human joint points. The posture estimation network puts the human picture into a 10-layer VGG19 convolution network and extracts a set of feature map F after a series of convolution pooling operations. Next, F is sent to a two-branch structure to predict the confidence S of body joint points and affinity vector L between the inter joints, respectively. S represents the possibility of a joint at the pixel position, and L is used to determine the position and direction of the body part. In order to improve the

accuracy of prediction, an iterative architecture is used to establish a multilevel two-branch structure. Each time, the prediction results and image features of the previous stage are inputted to the next two-branch structure for prediction. After continuous iteration, a more accurate S and L are finally generated. A candidate body joint point set D_J of multiple persons is obtained.

$$D_J = \left\{ d_j^m : \ j \in \{1 \ldots J\}, m \in \left\{1 \ldots N_j\right\}\right\}, \tag{1}$$

where d_j^m represents the coordinate of the mth joint point of body part j.

In the process of posture estimation, some structures are often judged as human joint points because they are very similar to human parts. At the same time, they have high confidence, which will produce errors in the final joint set and affect the accuracy of recognition results. In order to ensure that the obtained joint point set is a real human joint and is located within the contour of the human body, we screened and judged the boundary features and joint features extracted earlier to obtain a more accurate joint set. By means of traversal screening, for each set of joint points in the joint features, we compared each joint coordinate with all the bounding box features to judge whether the current joint coordinate was within one of the bounding boxes and selected all the qualified joint points as the final joint feature output.

3.2.2. Fall Detection by SVM. After optimizing the joint points combined with the human body boundary box, the misidentified and out-of-range joints are screened out, and the joint points are input into the SVM classifier for fall and non-fall classification training. Then, according to the trained model, the input human joint points coordinate parameters are directly used to predict the fall of the target person. But it is found that because the accuracy of each pose estimation is different, for the pictures with unclear human structure, many joint points will not be recognized, resulting in the loss of features, which will affect the final fall classification results. Furthermore, different camera shooting angles will affect the height and body shape of the human body and even lead to deformation, which will also affect the results of fall classification.

Therefore, in order to eliminate these factors that may cause deviation results, this study uses also a direction vector instead of a direct coordinate as the input of SVM. The process of fall detection using SVM is shown in Figure 2. By comparing and observing the changes in joint points before and after falling and the division relationship of body parts, three joint points with significant changes in the shoulder, hip, and ankle are selected, and a directed vector is formed according to their coordinates; and finally, the calculated vector set is inputted into the fall classification network as features for training and learning, so as to judge whether the current person is in a fall state.

3.2.3. Pseudocode of Fall Detection. The pseudocode of fall detection is described as Algorithm 1.

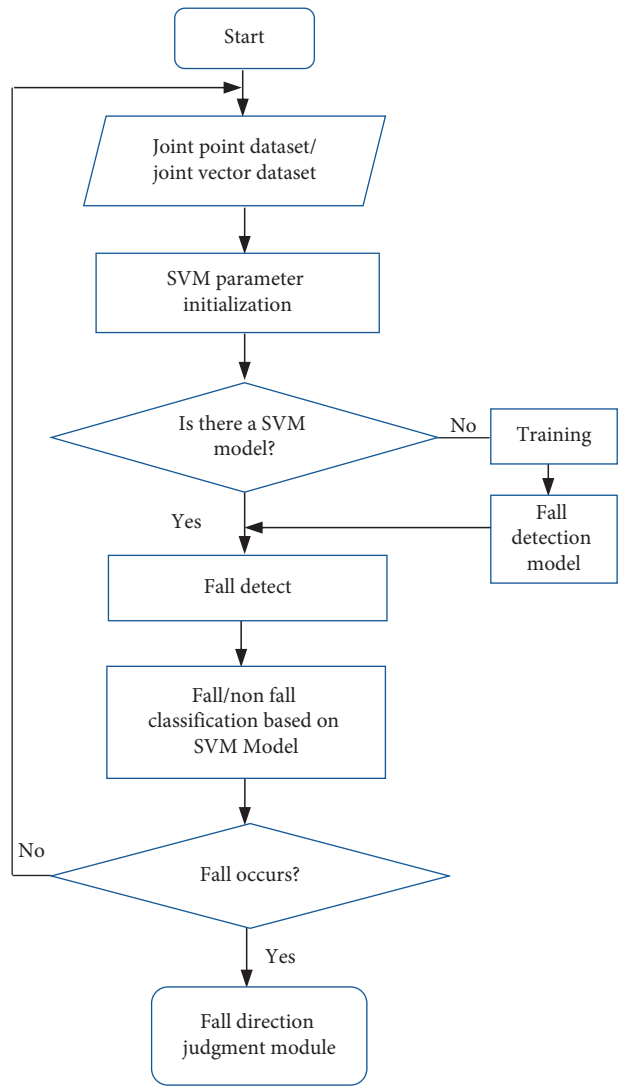

Figure 2: Flowchart of fall detection by SVM.

3.3. Fall Direction Judgment Module

3.3.1. Feature Dimension Transformation. After the human joint features are obtained through the fall detection module, the next work is to deeply analyze and calculate these features, so as to obtain the specific fall direction information. Because the characteristics of human joints are 2D information, in 2D plane space, we can only simply distinguish the left and right, and there is no way to judge other directions. Therefore, we transformed the 2D parameters into 3D parameters and then used the 3D coordinates with depth information as the parameters to construct the 3D coordinate system, selected specific joint points to form the 3D vector, and calculated the spatial transformation angle according to the change of the vector, so as to obtain more detailed direction change information. At the same time, we calculated the change range and direction of specific joint points in space, so as to accurately calculate the direction of the fall. The process of the fall direction module is shown in Figure 3.

Input: A group of image sequence or video frame sequence $\{X\}_{i=1}^{t}$
Output: If a fall occurs, the corresponding joint point set is output; otherwise, the output is null.
While $X_i <$ total sequence length do:
  Extract feature maps from X_i;
  Judge the category of anchors through softmax;
  Regression proposal;
  Unifying feature shapes through ROI pooling;
  Get bounding box BBX = $[t_x, t_y, t_w, t_h]$;
  Calculate the joint confidence: $S_{j,k}^{*}(p) = \exp(-\|p - x_{j,k}\|_2^2/\sigma^2)$;
  Calculate the joint point affinity vector;
  Calculation sequence Xi coordinate positions of each joint point, Positions = $[x_i, y]_{i=1}^{18}$;
  Filter out the qualified coordinates: Position = $[x_i, y]_{i=1}^{18} \in$ BBX;
  If SVM(Position) = = "fall"
    When the human body is in a falling state, return the predicted position;
  End if
  Else
    Next frame;
End while

Algorithm 1: Fall detection.

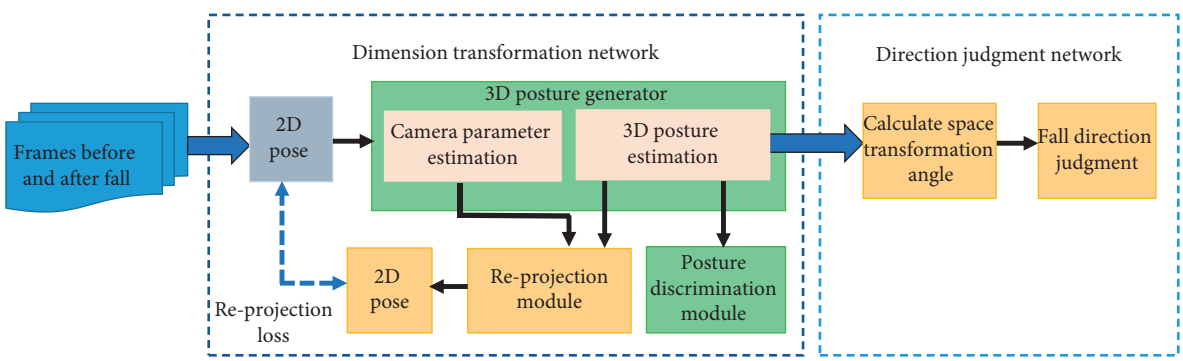

Figure 3: Flowchart of fall direction judgment module.

Dimension transformation network adopts the idea of Wandt and Rosenhahn [24] to convert 2D parameters into 3D parameters which uses the idea of generative adversarial networks (GANs) consisting of three modules, namely generator module, discriminator module, and re-projection module.

The input 2D human pose is first processed by the 3D generator, which is composed of two branches: 3D pose estimation and camera parameter estimation, which are used to generate a preliminary estimation of 3D human coordinates and internal parameters of the camera. The 3D pose estimation branch continuously learns the mapping from 2D pose to 3D coordinates to obtain a better representation. It is composed of two continuous residual blocks, and each block contains a fully connected network of two 1000 neurons. After full connection, leaky ReLU is used as the activation function; and finally, a set of vectors are outputted as 3D estimated coordinates. The camera parameter estimation branch adopts the same network structure to learn the camera parameters and outputs it as a 6D camera parameter vector.

In order to match the 3D pose estimation branch generation with the real pose, in the re-projection module, the camera parameters obtained from the camera parameter estimation branch are used to convert the predicted 3D coordinate results into 2D pose representation, so as to compare the deviation between the predicted results and the originally inputted 2D pose, so as to realize weak supervision. The loss function of the camera parameter estimation branch is as follows:

$$L_{\text{rep}}(X, K) = \|W - \text{KX}\|_F, \tag{2}$$

where W is the original input 2D posture matrix, K represents the camera parameter matrix, X represents the estimated 3D posture matrix, and KX is the result of projecting the estimated 3D posture into 2D space by re-projection.

The posture discrimination module is the same as the discriminator in GAN to judge whether the picture generated by the generator is correct. For the 3D posture predicted above, it is necessary to determine whether the prediction is accurate by comparing the discrimination model with the real 3D coordinates. The discrimination network model is also composed of two branches. The first branch introduces the kinematic chain space layer, transforms the generated 3D posture into the kinematic chain

space matrix, and then feeds them into the full connection layer containing 100 neurons. The kinematic space matrix is a match matrix, which introduces the symmetry of human body structure. The elements on the diagonal of the kinematic chain space matrix represent the length of each bone, which ensures the size of the generated posture. Elements outside the diagonal actually represent the angle information of bone motion, because they can actually be regarded as the cosine of the included angle. The calculation formula of the motion chain space matrix is as follows:

$$B = \mathrm{XC};$$
$$\Psi = B^T B = \begin{pmatrix} l_1^2 & \cdot & \cdot & \cdot \\ \cdot & l_2^2 & \cdot & \cdot \\ \cdot & \cdot & \ddots & \cdot \\ \cdot & \cdot & \cdot & l_b^2 \end{pmatrix}, \tag{3}$$

where X represents the estimated 3D posture matrix, C is an adjacency matrix, and the non-zero elements of each column are composed of 1 and −1.

The other branch is the pure fully connected layer, which is directly represented by the coordinate of 3D posture. After two-branch processing, the features of the two parts are spliced, and finally inputted into a full connection layer. Finally, combined with the real 3D coordinates, Wasserstein is used as the loss function to calculate the loss.

In the training process, the discrimination module and generator are trained in turn, so that the discriminator can effectively judge the authenticity of the current generator input. After continuous learning, the generator gradually improves the reliability of the generated samples to pass the authentication of the discrimination module. In this way, through mutual training and learning, the loss between the two parts converges to the lowest. Finally, the input 2D human posture can be used to obtain the corresponding precise joint coordinates in 3D space to achieve the transformation of coordinate feature dimension. The converted 3D space coordinates are shown in Figure 4.

3.3.2. Calculating the Angle of the Fall. After obtaining the 3D joint coordinates of the human body at the timing of falling, and before/after falling, the specific fall direction can be calculated from the perspective of 3D space.

Fall direction is a broad concept, which includes both angle size and direction. In a 3D space, for the human body represented by different coordinate points, calculating the angle of a human fall is to find the included angle between the plane composed of human joint points when falling and the plane composed of human joint points before/after falling. Because the human body in this article is composed of 18 joint points, if all points are used to form a complex irregular graph rather than a plane, it is impossible to calculate the angle of human falling by calculating the included angle of the two planes. We used the vector as input to solve this problem. According to the relationship between joints, we selected specific joint points to form a vector. By calculating the included angle between the vector composed of the same group of joints when falling and before/after falling, we could get the

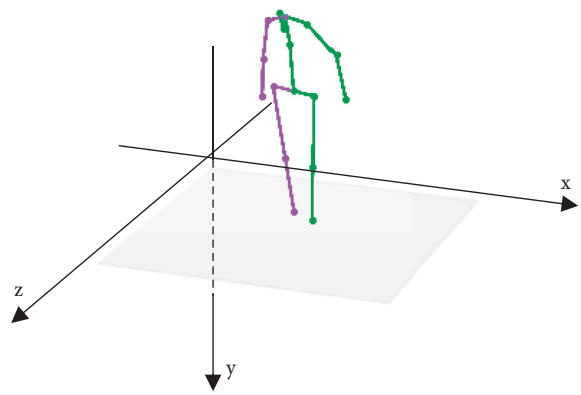

Figure 4: Schematic diagram of a human posture in 3D space.

fall angle of the human body. Therefore, the problem of calculating the fall angle of the human body in 3D space can be transformed into the problem of calculating the included angle between vectors composed of specific joint points.

As for the selection of vectors, when the body is blocked or blurred, some joints will not be recognized, resulting in the problem that vectors cannot be formed. In order to prevent the nonexistence of joint points when calculating the included angle with only one vector, we selected four easily identifiable joint points from the joint set, combined them in pairs to form four vectors, and calculated the included angle by transformation, respectively, and finally synthesized the results to reduce the probability of errors. According to the observation, the occurrence probability and recognition accuracy of joint points of the left shoulder, left hip, right shoulder, and right hip are higher than other joint points. Therefore, these four points are combined in pairs to form feature vectors.

Vectors $\vec{a}$ and $\vec{b}$ are, respectively, composed of the same group of joints before and after the fall in 3D space. The angle θ between two vectors can be calculated as follows:

$$\theta = \arccos \frac{\vec{a} \cdot \vec{b}}{|\vec{a}| \cdot |\vec{b}|} \cdot \frac{180}{\pi}. \tag{4}$$

If the coordinates of the vectors $\vec{a}$, $\vec{b}$ are (x_1, y_1, z_1) and (x_2, y_2, z_2), then angle θ is as follows:

$$\theta = \arccos \frac{x_1 x_2 + y_1 y_2 + z_1 z_2}{\sqrt{x_1^2 + y_1^2 + z_1^2} \cdot \sqrt{x_2^2 + y_2^2 + z_2^2}} \cdot \frac{180}{\pi}. \tag{5}$$

3.3.3. Calculating the Direction of the Fall. Through the above method, the angle of the fall is calculated, and the specific direction of the fall also needs to be calculated. In this study, the direction of the human fall is divided into four kinds: forward, backward, left, and right. Next, the method of calculating the direction of falling will be introduced.

When we analyze the human body in the video frame, the fall direction is compared with the original position of the human body, not from the perspective of the observer. Therefore, when estimating the direction of a human falling, it is first necessary to determine whether the human body is facing the surveillance camera or back to the camera before

Input: The 2D joint features obtained by the fall detection module;
Output: Specific direction of fall;
If fall detection $(P) = =$ "fall":
  Building 3D coordinate system: {
    The generator maps 2D feature p to 3D; Feature $X \in\in R^{3n}$;
    The discriminator judges the generated 3D feature X;
    The re-projection module calculates the deviation of the estimation result;
    }
  Select a group of joint points from X to form vector set L
  Calculate the included angle θ of the same vector before and after the fall;
  Determine the orientation of human body according to the position relationship of joint points;
  Calculate the changes of X and Z coordinates of head joint points;
  Estimate the specific direction of the fall;
  Next frame;
End if

Algorithm 2: Fall direction judgment.

falling. To solve this problem, we determine the orientation of the human body in the frame by comparing the position relationship of some joints in the 3D joint points.

According to experience, when the front of the human body faces the camera, the left and right of the body are just opposite to the left and right of the camera. In the previously established 3D coordinate system of the human body, we selected two joint points of the left shoulder and right shoulder to compare their positional relationship. For the human body in 3D space, if the coordinate of the left shoulder joint point in the x-axis direction is greater than that of the right shoulder joint point in the x-axis direction, it indicates that the human body faces the camera, otherwise it indicates that the human body faces away from the camera. After determining the orientation of the human body, these two situations are discussed, respectively:

(1) When the human body faces the camera, we supervise the changes in the human head joint points in 3D space. For the same joint point, if the coordinate of the joint point in the depth z-axis direction is greater than the original coordinate and exceeds a certain range after falling, it can be judged as falling backward. If the coordinate of the joint point in the z-axis direction is lesser than the original coordinate and exceeds a certain range after falling, it can be judged as falling forward. If the coordinate of the joint point in the horizontal x-axis direction is greater than the original coordinate and exceeds a certain range after falling, it can be judged as falling to the left. If the coordinate of the joint point in the x-axis direction is lesser than the original coordinate and exceeds a certain range after falling, it can be judged as falling to the right. The calculation formula of the fall direction is as follows:

$$\text{Direction} = \begin{cases} \text{left}; C \leq \text{Position 1}(x) - \text{Position}(x) \\ \text{right}; C < \text{Position}(x) - \text{Position 1}(x) \\ \text{backward}; C \leq \text{Position 1}(z) - \text{Position}(z) \\ \text{forward}; C < \text{Position}(z) - \text{Position 1}(z) \end{cases}, \tag{6}$$

Position (x) and *Position* (z) refer to the original coordinates of the joint point on the x-axis and z-axis; *Position1* (x) and *Position1* (z) refer to the coordinates of the same point on the x-axis and z-axis after falling; and C is the threshold.

(2) If the human body is facing away from the camera, it shall be calculated according to the reverse rule.

According to the above discussion, the direction judgment of the fall is divided into two scenarios and eight possibilities. Finally, it is necessary to comprehensively match all conditions to estimate the specific direction of falling. According to the observation, different fall directions of the human body will cause different degrees of injury. When falling backward, the protection ability of the human body is the worst and the probability of head injury is the largest, so the injury of falling backward is much greater than that of falling in other directions. Therefore, we classify the risk level of the previously estimated human fall direction: when the human body falls backward, the corresponding risk level is very dangerous, and the risk level of falls in other directions is general.

3.3.4. Pseudocode of Fall Direction Judgment. The pseudocode of fall direction judgment is described as Algorithm 2.

4. Main Results

4.1. Dataset. At present, the datasets mainly used for fall detection include the Multiple Cameras Fall Dataset (Multicam) [25], Le2i fall dataset (Le2i) [26], and the UR Fall Dataset (URFD) [27], which contain a large number of scenes of normal human movement and fall action. For our study, in addition to detecting whether the fall event occurs, we will estimate the direction of the fall. Each dataset above only contains the fall action in partial directions, which cannot completely cover the fall events in each direction. Therefore, we screened the above datasets to form a new fall dataset, in which we selected some videos containing fall events, and some videos of normal daily activities as a comparison. In our fall dataset, the fall direction of the human body includes forward, backward, left, and right.

4.2. Evaluation Metrics. In fall detection, all samples are classified by the fall detection algorithm, and the classification results can be divided into the following four categories: TP (true positive) indicates that there is a fall event in the samples, and the fall detection algorithm correctly identifies it as a fall; TN (true negative) indicates that there is no fall event in the samples, and the fall detection algorithm correctly identifies it as non-fall; FP (false positive) indicates that there is no fall event in the samples, but the fall detection algorithm incorrectly identifies it as a fall; and FN (false negative) indicates that there is a fall event in the samples, but the fall detection algorithm incorrectly identifies it as a non-fall.

In order to measure the performance of the fall detection algorithm, the existing evaluation standards such as precision, accuracy, specificity, sensitivity, and $F1$ score are used generally [28]. The values of the above standards are calculated from the classification results of the algorithm. The higher the value, the better the performance of the method. The evaluation metrics we used are defined as follows:

The accuracy represents the ratio of the number of samples correctly identified by the fall detection algorithm to all samples.

$$\text{Accuracy} = \frac{\text{TP} + \text{TN}}{\text{TP} + \text{TN} + \text{FP} + \text{FN}}. \tag{7}$$

The precision represents the ratio of the samples accurately judged as fall to all the samples judged as fall:

$$\text{Precision} = \frac{\text{TP}}{\text{TP} + \text{FP}}. \tag{8}$$

Sensitivity refers to the ratio of the samples correctly identified as falls to all fall samples. The higher its value in fall detection, the better the recognition performance of fall events. Here, the sensitivity is the same as the recall rate.

$$\text{Sensitivity} = \text{Recall} = \frac{\text{TP}}{\text{TP} + \text{FN}}. \tag{9}$$

Table 1: Fall detection results on URFD.

Detection methods	Sensitivity (%)	Specificity (%)	Accuracy (%)
Ali et al. [29]	99.3–99.13	99.03	—
Kwolek and Kepski [30]	100	96.67	95.71
Bourke et al. [31]	100	90	—
Kwolek and Kepski [27]	100	92.5	95
Yun and Gu [32]	96.77	89.74	—
Alaoui et al. [33]	100	95	97.5
Our method 1	95	96.47	95.64
Our method 2	95.45	100	97.43

Specificity refers to the ratio of correctly identified non-fall samples to all non-fall samples. The higher its value in fall detection, the better the recognition performance of non-fall events.

$$\text{Specificity} = \frac{\text{TN}}{\text{TN} + \text{FP}}. \tag{10}$$

$F1$ score is the harmonic average of precision and recall to punish extreme cases.

$$F1\ \text{Score} = \frac{2 * \text{Precision} * \text{Recall}}{\text{Precision} + \text{Recall}}. \tag{11}$$

For the performance of the fall direction estimation algorithm, we also use the above evaluation criteria to calculate.

4.3. Results of Fall Detection. Our proposed algorithms are compared with other fall detection algorithms in different literatures. According to the classification of fall detection results above, we calculated different fall detection evaluation standard values, and the results are shown in Table 1.

In the above table, our method 1 and our method 2 represent the fall detection results obtained by using human body coordinates directly and using direction vectors, respectively.

It can be seen from Table 1 that the experimental results of all methods are relatively good in URFD. The effect of using coordinates in our method 1 is lower than that of using direction vectors in our method 2. For the standard of accuracy, although our methods are not the highest, our method 2 has only a little difference from the first place and is higher than other methods. For the sensitivity standard, our methods are lower than that of other methods, because ours depend on the joint points identified by posture estimation. In some cases, the positions of joint points estimated are not accurate enough, which cause the failure of fall detection.

As shown in Figure 5, the first row of pictures is the result of behavior detection as a fall, and the second row of pictures is the result of non-fall caused by inaccurate joint point recognition due to occlusion, incomplete human body, or other reasons.

For the standard of specificity, our methods are higher than other methods, which shows that our methods are very accurate in judging non-fall behaviors.

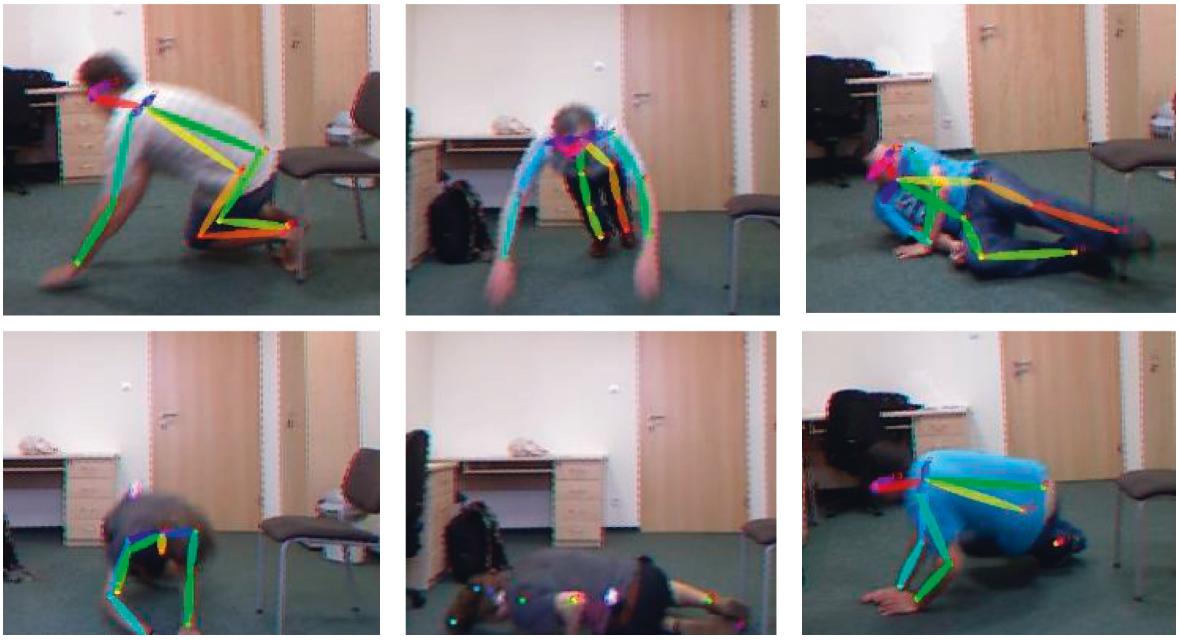

Figure 5: Fall detection results.

Table 2: Fall detection results on Le2i.

Detection methods	Sensitivity (%)	Specificity (%)	Accuracy (%)	Precision (%)
Charfi et al. [34]	73	97.7	—	—
Chamle et al. [35]	83.47	73.07	79.31	—
Poonsri and Chiracharit [36]	93	64.29	86.21	—
Alaoui et al. [37]	94.55	90.84	90.9	—
Alaoui et al. [33]	95	100	97.5	—
Asif et al. [21]	92.44	—	—	92.45
Asif et al. [38]	89.92	—	—	90.08
Our method 1	91.73	98.5	94.79	98.66
Our method 2	95.86	99.5	97.52	99.57

It can be seen from Table 2 that compared with other methods, our methods have better results on the Le2i dataset. Our method 2 of using direction vector has higher sensitivity, accuracy, and precision than other methods, but for the specificity standard, it is slightly lower than the method of Alaoui et al. [33]. Overall, our methods have a good recognition effect for fall detection.

It can be seen from Table 3 that in the MultiCam dataset, our method 1 of using coordinate features for fall detection is higher than the other two methods in terms of accuracy and F1 score, and slightly lower than the method of Asif et al. [21] in terms of recall rate. Overall, the performance of our methods is slightly better than other methods.

Table 3: Fall detection results on MultiCam.

Detection methods	F1 score (%)	Precision (%)	Recall (%)
Asif et al. [21]	87.08	87.03	87.05
Asif et al. [38]	86.38	86.28	86.58
Our method 1	87.38	88.13	86.66

4.4. Results of Fall Direction Judgment. The direction judgment module will be executed only after the human body is detected as in a fall state. In order to verify the performance of fall direction judgment, it needs to be tested in the dataset containing only fall events. Therefore, the direction judgment experiments are carried out on our fall dataset. Results of converting to a 3D posture by our method are shown in Figure 6.

It can be seen from Table 4 that the method in this article has the highest recognition accuracy for humans falling forward and low recognition accuracy for falling backward. The main reason for this phenomenon is that the direction judgment module in this article depends on the 3D joint points obtained by the dimension transformation network. For the complex 2D human posture, the 3D joint coordinates obtained by the dimension transformation network are not accurate enough, which affects the final direction judgment.

When the human body falls, the fall direction is usually either forward or backward, either left or right. Therefore, this article divides the fall dataset into forward-backward and left-right groups to verify our fall direction method. For the parameters in the evaluation criteria, TP in the forward-backward fall dataset represents the samples that are correctly judged as falling forward; TN represents the samples

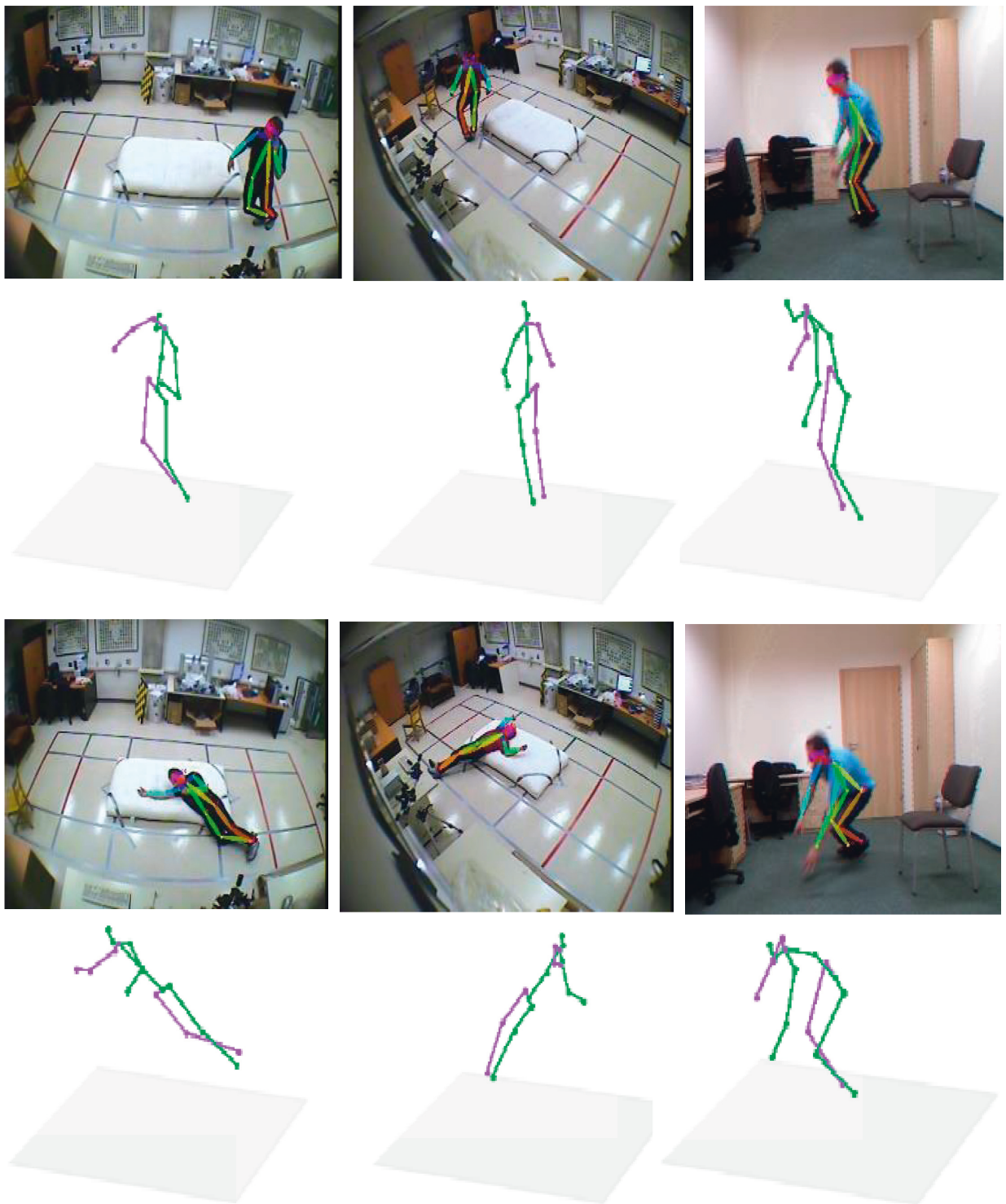

Figure 6: Dimension conversion results.

Table 4: Accuracy of different fall directions.

Fall direction	Precision (%)
Forward	82.5
Backward	70.37
Left	72.22
Right	75

Table 5: Fall direction judgment results on our forward-backward and left-right datasets.

	Sensitivity (%)	Specificity (%)	Accuracy (%)
Forward-backward	80.48	73.07	77.61
Left-right	78.26	68.42	73.81

that are correctly judged as falling backward; FP refers to the samples whose direction of falling are wrongly judged to be forward; and FN refers to the samples whose fall direction are wrongly judged to be backward. For the left-right fall dataset, the parameters are also selected according to the corresponding rules. The experimental results are shown in Table 5.

5. Conclusion

In this article, a fall detection algorithm based on human posture analysis is proposed. Different situations of falling are studied from the perspective of posture analysis, the timing of fall behavior is detected, and the direction of fall is judged, so as to make an accurate early warning. Human body detection and joint point estimation are combined to screen and calculate the 2D joint information according to the human body boundary box and confidence, and the wrong joint points and redundant information are eliminated to obtain a more accurate set of human joints. Next, the limited 2D joint point information is promoted to 3D spatial coordinates containing depth information; and finally, the 3D coordinates are used to judge the fall direction of the human body.

Although the method proposed in this article has certain advantages in the human fall detection tasks, there are still defects to be improved in the following aspects: (1) this method is only applicable to some simple fall movements, and the judgment of fall direction is not ideal for complex fall movements; (2) the method consists of multiple modules. Each module needs less time to run alone, but it needs more time to realize the whole process. Therefore, in the future, it is necessary to improve the adaptability of the dimension transformation network to the complex fall movements and generate a more accurate 3D human posture, so as to realize more accurate fall direction judgment; at the same time, it is necessary to improve the real-time performance of the method.

Data Availability

The data that are used to support the findings of this study are included within the article.

Conflicts of Interest

The authors declare that they have no conflicts of interest.

Acknowledgments

This work was supported by the Tianjin Science and Technology Program (19PTZWHZ00020).

References

[1] D. Mrozek, A. Koczur, and B. Maysiak-Mrozek, "Fall detection in older adults with mobile IoT devices and machine learning in the cloud and on the edge," *Information Sciences*, vol. 537, no. 5, 2020.

[2] V. Kumar, N. Badal, and R. Mishra, "Elderly Fall Due to Drowsiness: Detection and Prevention Using Machine Learning and IOT," *Modern Physics Letters B*, vol. 35, 2021.

[3] M. Suh and I. Cho, "Effectiveness of Nursing Care provided for Fall Prevention: Survival Analysis of Nursing Records in a Tertiary hospital," *Japan Journal of Nursing Science*, vol. 18, 2021.

[4] S. Usmani, A. Saboor, and M. Haris, "Latest research trends in fall detection and prevention using machine learning: a systematic review," *Sensors*, vol. 21, no. 15, p. 5134, 2021.

[5] N. Mozaffari, J. Rezazadeh, and R. Farahbakhsh, "Practical fall detection based on IoT technologies: a survey," *Internet of Things*, vol. 8, Article ID 100124, 2019.

[6] Y. Nizam and M. Jamil, "Classification of Daily Life Activities for Human Fall Detection: A Systematic Review of the Techniques and Approaches," *Studies in Systems, Decision and Control*, vol. 273, 2020.

[7] V. R. Xefteris, A. Tsanousa, G. Meditskos, S. Vrochidis, and I. Kompatsiaris, "Performance, challenges, and limitations in multimodal fall detection systems: a review," *IEEE Sensors Journal*, no. 99, p. 1, 2021.

[8] P. Bet, P. C. Castro, and M. A. Ponti, "Fall detection and fall risk assessment in older person using wearable sensors: a systematic review," *International Journal of Medical Informatics*, vol. 130, Article ID 103946, 2019.

[9] A. Ramachandran and A. Karuppiah, "A survey on recent advances in wearable fall detection systems," *BioMed Research International*, vol. 2020, pp. 1–17, 2020.

[10] N. Zerrouki, F. Harrou, Y. Sun, and A. Houacine, "Accelerometer and camera-based strategy for improved human fall detection," *Journal of Medical Systems*, vol. 40, p. 284, 2016.

[11] M. C. Chen, Y. T. Cheng, and R. W. Chen, "Improve the accuracy of fall detection based on artificial intelligence algorithm," *Computer Modeling in Engineering and Sciences*, vol. 128, no. 3, pp. 1103–1119, 2021.

[12] A. Alarifi and A. Alwadain, "Killer heuristic optimized convolution neural network-based fall detection with wearable IoT sensor devices," *Measurement*, vol. 167, Article ID 108258, 2020.

[13] P. Pierleoni, A. Belli, L. Maurizi, and S. Valenti, "A wearable fall detector for elderly people based on AHRS and barometric sensor," *IEEE Sensors Journal*, vol. 16, no. 17, pp. 6733–6744, 2016.

[14] X. Li, L. Nie, H. Xu, and W. Xianzhi, "Collaborative Fall Detection Using Smart Phone and Kinect," *Mobile Networks & Applications*, vol. 23, pp. 4775–788, 2018.

[15] K. M. Shahiduzzaman, X. Hei, C. Guo, and W. Cheng, "Enhancing fall detection for elderly with smart helmet in a cloud-network-edge architecture," in *Proceedings of the 2019 IEEE International Conference on Consumer Electronics - Taiwan (ICCE-TW)*, May 2020.

[16] K. Sehairi, F. Chouireb, and J. Meunier, "Elderly Fall Detection System Based on Multiple Shape Features and Motion analysis," in *Proceedings of the 2018 International Conference on Intelligent Systems and Computer Vision (ISCV)*, pp. 1–8, IEEE, Fez, Morocco, May 2018.

[17] Zerrouki, N. Harrou, and F. Houacine, "Fall Detection Using Supervised Machine Learning Algorithms: A Comparative study," in *Proceedings of the 2016 8th International Conference on Modelling, Identification and Control (ICMIC)*, Nov 2017.

[18] N. Zerrouki and A. Houacine, "Combined curvelets and hidden Markov models for human fall detection," *Multimedia Tools and Applications*, vol. 77, no. 5, pp. 6405–6424, 2017.

[19] F. Harrou, N. Zerrouki, S. Ying, and A. Houacine, "A simple strategy for fall events detection," in *Proceedings of the 2016 IEEE 14th International Conference on Industrial Informatics (INDIN)*, July 2017.

[20] C. Rougier, J. Meunier, A. St-Arnaud, and J. Rousseau, "Robust video surveillance for fall detection based on human shape deformation," *IEEE Transactions on Circuits and Systems for Video Technology*, vol. 21, no. 5, pp. 611–622, 2011.

[21] U. Asif, B. Mashford, and S. Von Cavallar, "Privacy Preserving Human Fall Detection Using Video Data," *Machine Learning for Health Workshop*, vol. 116, pp. 39–51, 2020.

[22] W. Chen, Z. Jiang, and H. Guo, "Fall detection based on key points of human-skeleton using OpenPose," *Symmetry*, vol. 12, no. 5, p. 744, 2020.

[23] Z. Cao, T. Simon, and S. E. Wei, "Realtime multi-person 2d pose estimation using part affinity fields," in *Proceedings of the IEEE Conference on Computer Vision and Pattern Recognition*, pp. 7291–7299, IEE, San Juan, PR, USA, June 2017.

[24] B. Wandt and B. Rosenhahn, "RepNet: weakly supervised training of an adversarial reprojection network for 3D human pose estimation," in *Proceedings of the 2019 IEEE/CVF Conference on Computer Vision and Pattern Recognition (CVPR)*, June 2020.

[25] E. Auvinet, C. Rougier, J. Meunier, and A. St-Arnaud, "Multiple cameras fall dataset," DIRO-Université de Montréal, Technical Report D, p. 1350, 2010.

[26] I. Charfi, J. Miteran, J. Dubois, and M. Atri, "Optimized spatio-temporal descriptors for real-time fall detection: comparison of support vector machine and Adaboost-based classification," *Journal of Electronic Imaging*, vol. 22, no. 4, Article ID 041106, 2013.

[27] B. Kwolek and M. Kepski, "Human fall detection on embedded platform using depth maps and wireless accelerometer," *Computer Methods and Programs in Biomedicine*, vol. 117, no. 3, pp. 489–501, 2014.

[28] S. K. Gharghan, S. L. Mohammed, and H. A. Hashim, "Accurate fall detection for patients with Parkinson's disease based on a data event algorithm and wireless sensor nodes," *Measurement*, vol. 156, Article ID 107573, 2020.

[29] S. F. Ali, R. Khan, A. Mahmood, and T. Hassan, "Using temporal covariance of motion and geometric features via boosting for human fall detection," *Sensors*, vol. 18, no. 6, p. 1918, 2018.

[30] B. Kwolek and M. Kepski, "Improving fall detection by the use of depth sensor and accelerometer," *Neurocomputing*, vol. 168, pp. 637–645, 2015.

[31] A. K. Bourke, J. V. O'brien, and G. M. Lyons, "Evaluation of a threshold-based tri-axial accelerometer fall detection algorithm," *Gait & Posture*, vol. 26, no. 2, pp. 194–199, 2007.

[32] Y. Yun and I. Y. H. Gu, "Human Fall Detection via Shape Analysis on Riemannian Manifolds with Applications to Elderly care," in *Proceedings of the 2015 IEEE International Conference on Image Processing (ICIP)*, pp. 3280–3284, IEEE, Quebec City, QC, Canada, 27 September 2015.

[33] A. Y. Alaoui, S. El Fkihi, and R. O. H. Thami, "Fall detection for elderly people using the variation of key points of human skeleton," *IEEE Access*, vol. 7, pp. 154786–154795, 2019.

[34] I. Charfi, J. Miteran, J. Dubois, M. Atr, and R. Tourki, "Definition and Performance Evaluation of a Robust SVM Based Fall Detection solution," in *Proceedings of the 2012 Eighth International Conference on Signal Image Technology and Internet Based Systems*, pp. 218–224, IEEE, Sorrento, Italy, Nov 2012.

[35] M. Chamle, K. G. Gunale, and K. K. Warhade, "Automated unusual event detection in video surveillance,"vol. 2, pp. 1–4, in *Proceedings of the 2016 international conference on inventive computation technologies (ICICT)*, vol. 2, IEEE, Coimbatore, India, Aug 2016.

[36] A. Poonsri and W. Chiracharit, "Fall Detection Using Gaussian Mixture Model and Principle Component analysis," in *Proceedings of the 2017 9th International Conference on Information Technology and Electrical Engineering (ICITEE)*, pp. 1–4, IEEE, Phuket, Thailand, Oct 2017.

[37] A. Y. Alaoui, A. El Hassouny, R. O. H. Thami, and H. Tairi, "Human fall detection using von Mises distribution and motion vectors of interest points," in *Proceedings of the 2nd international Conference on Big Data, Cloud and Applications*, pp. 1–5, ACM, Tetuan, Morocco, 29 March 2017.

[38] U. Asif, S. Von Cavallar, J. Tang, and S. Harrer, "SSHFD: Single Shot Human Fall Detection with Occluded Joints Resilience," vol. 20, 2020, https://arxiv.org/abs/2004.00797.

Hindawi
Discrete Dynamics in Nature and Society
Volume 2022, Article ID 7167821, 8 pages
https://doi.org/10.1155/2022/7167821

Research Article

Bearing Fault Diagnosis of End-to-End Model Design Based on 1DCNN-GRU Network

Liu Zhiwei

Dean's Office of IT Center and Educational Affairs Office, Tianjin University of Commerce Boustead College, Tianjin 300384, China

Correspondence should be addressed to Liu Zhiwei; liuzhiwei_2008@126.com

Received 23 April 2022; Accepted 25 May 2022; Published 9 June 2022

Academic Editor: Zi-Peng Wang

At present, the complex and varying operating conditions of bearings make the feature extraction become difficult and lack adaptability. An end-to-end fault diagnosis is proposed. A convolutional neural network (CNN) is good at mining spatial features of samples and has the advantage of "end-to-end." Gates recurrent neural (GRU) network has good performance in processing time-dependent characteristics of signals. We design an end-to-end adaptive 1DCNN-GRU model (i.e., one-dimensional neural network and gated recurrent unit) which combines the advantages of CNN's spatial processing capability and GRU's time-sequence processing capability. CNN is applied instead of manual feature extraction to extract effective features adaptively. Moreover, GRU can learn further the features processed through the CNN and achieve the fault diagnosis. It was shown that the proposed model could adaptively extract spatial and time-dependent features from the raw vibration signal to achieve an "end-to-end" fault diagnosis. The performance of the proposed method is validated using the bearing data collected by Case Western Reserve University (CWRU), and the results showed that the proposed model had recognition accuracy higher than 99%.

1. Introduction

Bearings are vital machine components that appear in almost all rotating machinery, and the health status of bearings plays a vital role in the effective operation of the mechanical system [1]. Bearings in the mechanical equipment must undergo lousy environments, such as high speed, complicated structure, and high failure rate. Bearings are also one of the vulnerable parts of rotating machinery. Most mechanical equipment failure is caused by bearing failure; once the bearing fails, a series of failures will be triggered, which will directly affect the operation safety of the whole equipment [2]. Therefore, real-time monitoring of the state and diagnosing the bearing fault have a significant meaning.

With the development of machine learning, intelligent fault diagnosis methods have become the main approaches in mechanical diagnosis. Traditional intelligent fault diagnosis methods mainly contain feature extraction, feature selection, and fault classification [3]. The raw vibration signal sampled by the sensor contains much fault information. Extracting features related to faults from the raw signal to diagnose bearing faults is a crucial step that affects fault classification directly. Some methods of feature extraction include frequency domain analysis and time-frequency analysis [4], Fast Fourier Transform [5], wavelet transform [6], wavelet packet transform [7], empirical mode decomposition [8], and so on. However, these conventional methods have the disadvantage of relying on handcrafted features and signal processing technologies. The robustness and extensibility of models need to be improved.

Recently, deep learning [9] and solutions to extract features from raw signals have been widely paid attention to, that combines multiple nonlinear learning layers to process raw data layer by layer and mine the association between data adaptively. Thus, this approach possesses the capacity to extract features end-to-end and avoids the complexity and uncertainty often observed in traditional feature extraction processes. That is an end-to-end algorithm structure makes the whole process without manual feature extraction. Hoang et al. transform one-dimensional vibration signals into two-dimensional images without noise reduction as the input data of CNN to diagnosis fault, which achieves very high

accuracy and has a strong character of robustness [10]. Chen et al. fused the vibration signals from the horizontal and vertical into a two-dimensional matrix and proposed a deep CNN for extracting features automatically to identify the health status of gearboxes [11]. All the above studies use CNN to extract features from vibration signals, which shows that it has excellent performance. However, vibration, pressure and other state signals gathered during machine operation are usually one-dimensional vectors [12, 13]. Therefore, some researchers seek to construct a 1DCNN model for faults diagnosis. For example, Peng et al. [14] proposed a novel deeper 1DCNN for fault diagnosis of wheel set bearings and gained good effects. Wu et al. present a method based on 1DCNN to realize fault diagnosis of rotating machinery [15]. You et al. proposed an improved ReLU-CNN model based on CNN to diagnosis mechanical faults, whose model has good performance and fast convergence rate [16]. Zhang et al. proposed an end-to-end model for bearing fault diagnosis, that extracts features with 6-layer TICNN. High accuracy is achieved in a noisy environment and even under different load by this model [17]. Guo et al. built a deep convolutional transfer learning model to diagnose bearings faults, which learns invariant features by the 1DCNN network. The proposed model was verified through six transfer experiments [18].

Compared with CNN, 1DCNN uses the raw data as input directly without processing, thus avoiding features loss or distortion. In addition, the vibration signal is time-series and contains abundant time-dependent properties. RNN (recurrent neural network) has good performance in processing time-dependent characteristics of signals. For the networks based on RNN, LSTM (long short-term memory network) and GRU(gated recurrent unit) have applied to fault diagnosis. Yu et al. proposed a novel algorithm based on stacked LSTM for bearing fault diagnosis, features extracted automatically by LSTM. Experimental results show that the accuracy is up to 99% [19]. Hinchi et al. constructed lifetime a prediction model of rolling bearing, which can reflect the degradation trend of the rolling bearing well [20]. Rui et al. designed an enhanced GRU network and applied it on the generated sequence of local features to learn the representation. Experiments on tool wear prediction, gearbox fault diagnosis, and incipient bearing fault detection verify the effectiveness of this model [21].

This paper presents an end-to-end adaptive framework named 1DCNN-GRU for bearing fault diagnosis. Combine advantages of CNN and GRU to extract features from raw data and achieve end-to-end fault diagnosis. Extract features by CNN to replace manual screening and characterization and then input the features into GRU to extract temporal characteristics further. The features extracted jointly are used for fault diagnosis. A series of experiments with the rolling bearing dataset from CWRU demonstrate that the proposed method has high accuracy, practicability, and feasibility.

2. Related Theories

2.1. Convolutional Neural Network (CNN). CNN is a typical feed forward neural network inspired by biological neural processes, which is powerful for processing spatial data. The network is structured by a convolutional layer and a pooling layer. The topological features embedded in the input data are extracted, through convoluting and pooling the input data layer by layer. A typical convolutional neural network structure is shown in Figure 1, which can mainly divide into five steps: input layer, convolutional layer, pooling layer, full-connected layer, and output layer.

Generally, the convolutional layer contains a set of filters. We can combine with each filter using the input volume to extract the local l function from the local input area. The convolutional layer convolutes the input volume by the kernel, to generate the characters of input data. We can express the output of convolution as follows:

$$x_j^l = f\left(\sum_{i\in M_j} x_i^{l-1} \times k_{\mathrm{ij}}^l + b_j^l\right), \tag{1}$$

where f is an activation function, M_j is an input, x_i^{l-1} is the input to layer l, x_j^l is the output of layer l, k is the kernel, and b is the bias.

The pooling layer is followed behind the convolutional layer, also named the subsampling layer. The feature extraction is obtained by the convolution layer as the input of the pooling layer. It is not modified by back propagation. The max-pooling mathematics model is described as follows:

$$\begin{aligned} P_i^{l+1}(j) &= \max\left\{Q_i^l(t)\right\} \\ (j-1)W + 1 &< t_x \le jW. \end{aligned} \tag{2}$$

Here, $(j-1)H + 1 < t_y \le jH$ $P_i^{l+1}(j)$ is the corresponding to the neuron in layer $l+1$, $Q_i^l(t)$ is the corresponding in the i_{th} frame of a layer to the t_{th} activations, W denotes width, and H denotes height.

2.2. 1D Convolutional Neural Network. The kernel of a typical convolutional neural network is usually two-dimensional. Convolution operates a feature graph through a sliding window in the width and height directions; multiply and sum the corresponding positions. Operate a feature signal through a sliding window in one (width or height) direction while performing one-dimensional convolution. The input of one-dimensional CNN is one-dimensional data, like some text and time series data samples usually, the kernel is one dimensional, and the output of convolution and pooling is also one-dimensional data. The structure of one-dimensional CNN is shown in Figure 1.

2.3. Gate Recurrent Unit Network. The recurrent neural network is a special network, which is proposed based on the view that "human cognition is based on experiences and memories." Compared with CNN, there is an association between each time step calculation in RNN, which not only considers the input of the previous moment but also gives the network "memory" of the previous content. So RNN is good at capturing the long-term dependence of input sequences. GRU is an improved version of RNN by the gates, which can overcome the vanishing gradient problem of

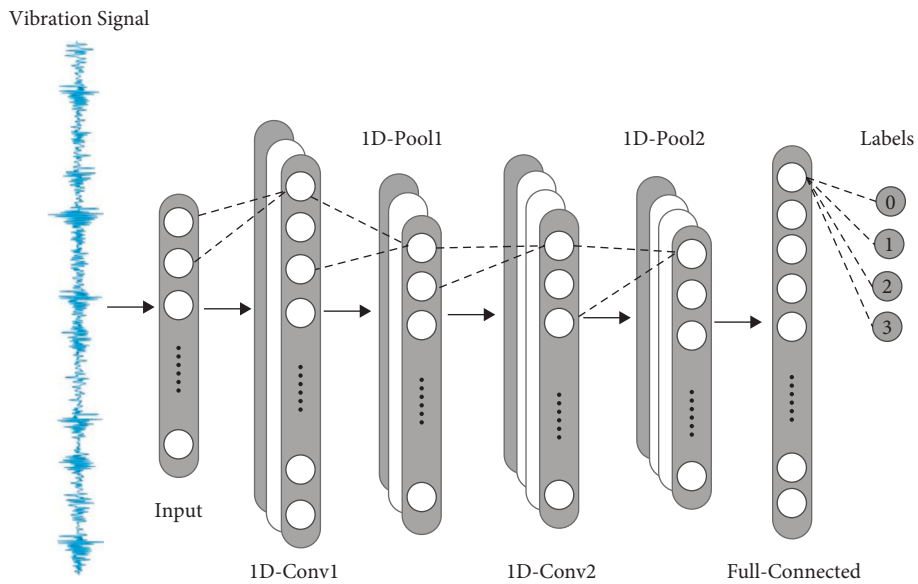

Figure 1: The structure of one-dimensional convolution.

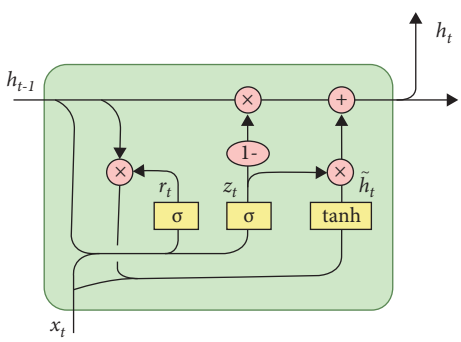

Figure 2: The internal structure diagram of GRU.

RNN. A typical GRU consists of a hidden state, reset gate, and update gate, and the basic structure is shown in Figure 2.

The basic GRU process is as follows: update gate z_t. The update gate acts on the output of the hidden layer at the previous time h^{t-1} and the input of the current time x^t, and the logical value is the state of the gate. The calculation process is as follows:

$$z_t = \sigma\left(W_z x_t + U_z h_{t-1} + b_z\right), \tag{3}$$

where W_z and U_z are all the weight matrices which can be obtained through learning. σ is an activation function and b_z is the bias weight.

Reset gate is r_t . Similarly, reset gate r_t acts on the output of the hidden layer at the previous time h^{t-1} and the input of the current time x^t, and the logical value is the state of the gate. The calculation process is as follows:

$$r_t = \sigma\left(W_r x_t + U_r h_{t-1} + b_r\right), \tag{4}$$

where W_r and U_r are the weight matrices, b_r and σ are similar with (3) and instant information of the current time $\tilde{h}_t$. After getting the state of the gate, the reset gate judges the importance of current input and previous output, then decides the proportion of past activation to realize information reset. Updating the $\tilde{h}_t$ with the activation function $\tan h$.

$$\tilde{h}_t = \tanh\left(W_h x_t + r_t \odot \left(U_h h_{t-1}\right) + b_h\right). \tag{5}$$

Here, W_h and U_h are the weight matrices, $\odot$ denotes an elementwise multiplication, and b_h is the bias.

The output of the current hidden layer is controlled by the update gate, which can perform two operations: forgetting and selective memory; forgetting the output of the previous moment; and selecting memory of instant information of the current time. Finally, the current activation is computed as follows:

$$h_t = z_t \odot h_{t-1} + \left(1 - z_t\right) \odot \tilde{h}_t. \tag{6}$$

3. The Proposed 1DCNN-GRU Network

The main framework of the proposed 1DCNN-GRU model for bearing fault diagnosis is shown in Figure 3. The model which we design mainly includes four parts: data processing with a nonoverlap sliding window; data input based on the raw processed data; feature extraction based on 1DCNN and GRU; faults classifier based on GRU, and sigmoid is the activation function of the probability of classifying output. In order to improve the adaptability and accuracy of bearing fault diagnosis, the proposed model is designed by 1DCNN and GRU. The main effect of 1DCNN is to perform preliminary feature extraction on the raw signal, training to fitting, and preliminary screening score is high, so effective features can be quickly screened from the raw signal.

The data training process of the model is shown in Figure 3. First, the raw signal data is obtained from the drive end accelerometer, and then we analyzed the vibration frequency, fluctuation amplitude, and vibration amplitude period of the signal to acquire the ideal truncated sampling

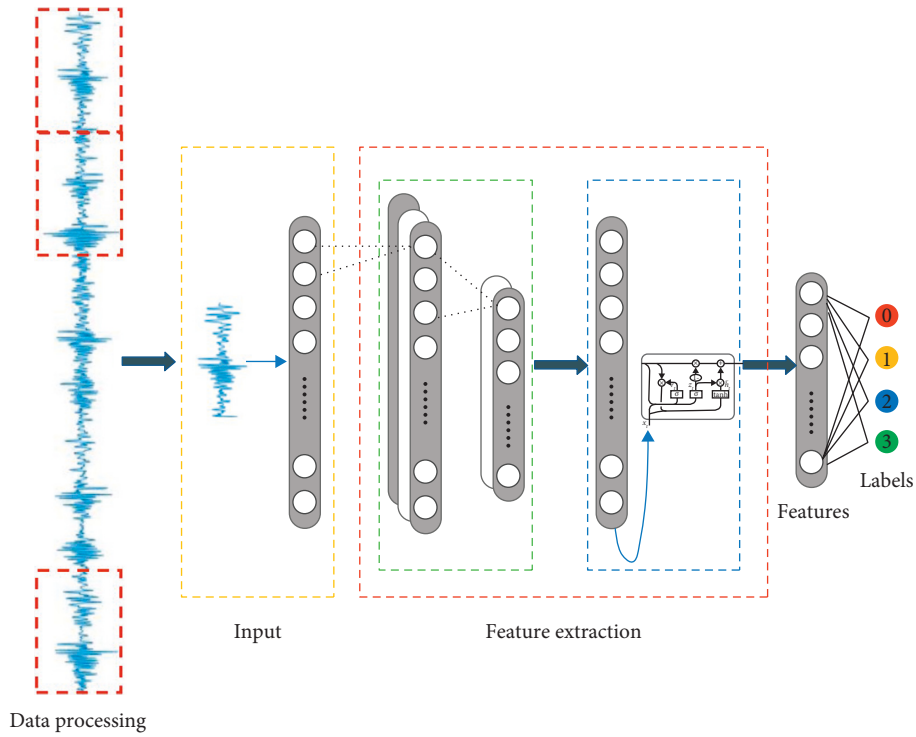

Figure 3: The structure of the proposed 1DCNN-GRU model.

window size. Through the mechanism of the sliding window to intercept raw acceleration signal sequence to generate preliminary characteristics as the input of the neural network. Next, the CNN network extract features from the input data automatically without any handcrafted features, which has the advantages of high efficiency. However, the CNN network has a poor ability to obtain the temporal correlation features. Then, the GRU network was subsequently designed to overcome the disadvantages of the CNN network, and the high-weight features learned by CNN as the input of the GRU network for learning and training. The features with correlation among vibration signal were further learned and then perform better correlation explanation. Finally, output the probability of the category through the sigmoid function to diagnosis the health status.

In order to solve the optimization problem of the proposed model, PMSprop, Adam, and Adadelta are used. The classification loss function used mean-squared-logarithmic-error (MSLE). The proposed 1DCNN-GRU model predicts $\hat{y}$, and the loss function is defined as follows:

$$L(y, \hat{y}) = \frac{1}{N} \sum_{i=0}^{N} \left(\log(y_i + 1) - \log(\hat{y}_i + 1)\right)^2. \quad (7)$$

3.1. Validation of the Proposed 1DCNN-GRU Network

3.1.1. Data Description. We can obtain the raw fault data of rolling bearing through Case Western Reserve University (CWRU). There are four health types as follows: respectively, normal (NO), rolling ball fault (BF), inner fault (IF), and outer fault (OF). We select the raw vibration signals from the load of 1, 2, and 3 horsepower randomly. Then, nonoverlapping sampling was used to process the original signals, and samples of each type are obtained, Table 1 shows some of the experimental samples and the each health vibration signal is shown in Figure 4. The dataset contains 500 samples of each type, of which 60% are randomly selected for training, 20% for verification, and 20% for testing.

Table 1: Description of the experimental samples.

Fault type	Load (horsepower)	Sample length	Number of samples	Label
NO	1/2/3	1024	500	0
IF	1/2/3	1024	500	1
OF	1/2/3	1024	500	2
BF	1/2/3	1024	500	3

3.1.2. Model Training and Testing

(1) Optimizer and Learning Rate. Selecting different optimizers and learning rates plays a vital role in improving the training speed and classification accuracy for different models and classification tasks. Therefore, for the model in this paper, the alternative optimizers include RMSprop, Adam, and Adadelta, meanwhile considering the influence of different learning rates on the actual rate of convergence, different learning rates are applied for model training. To test the performance of the proposed model, each group of optimizers and learning rates used in training is independent. The accuracy with different groups is shown in Table 2. The loss change of different optimizers and learning rates is shown in Figure 5.

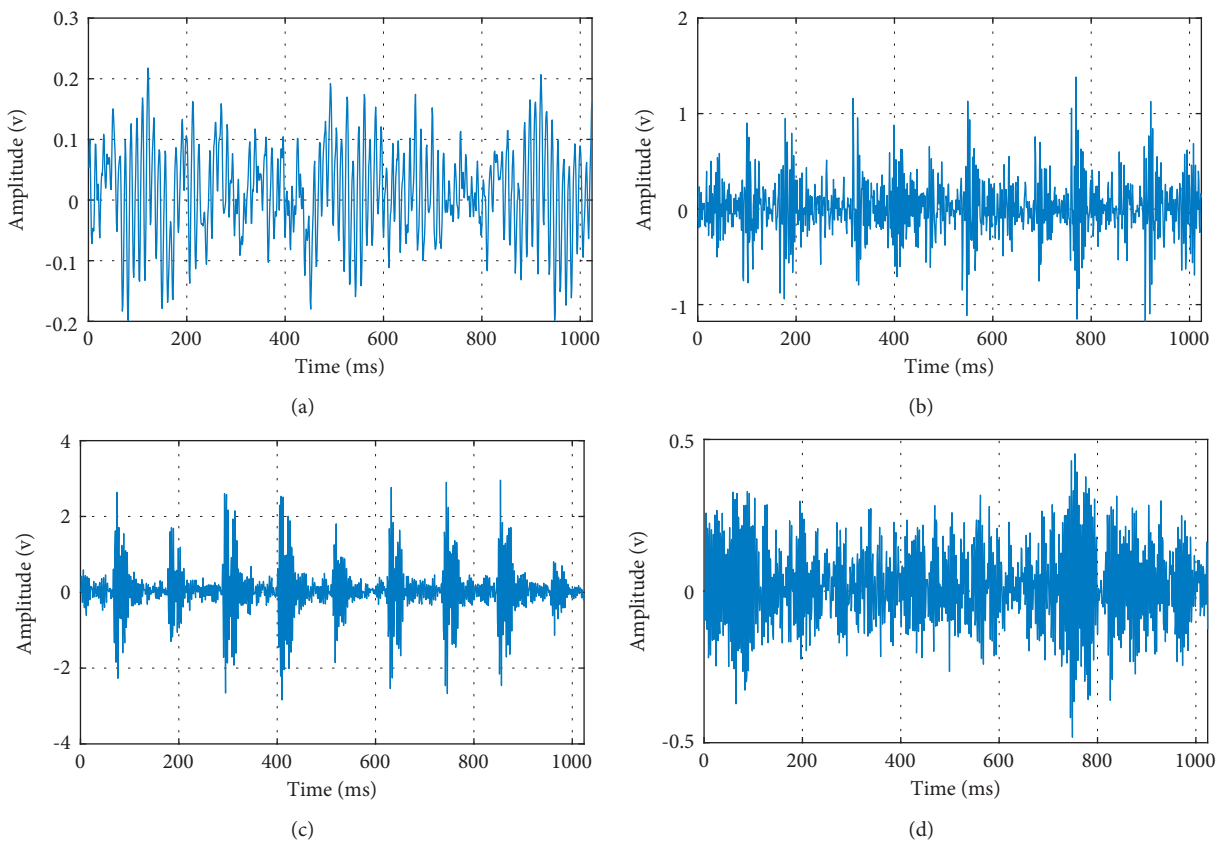

Figure 4: Vibration signals of bearings with different types. (a) NO. (b) IF. (c) OF. (d) BF.

Table 2: Accuracy of different optimizers and learning rates.

Learning rates	0.001		0.01		0.1	
Optimizers	Train	Test	Train	Test	Train	Test
			Accuracy (%)			
RMSprop	0.998	0.992	0.987	0.965	0.241	0.237
Adam	0.993	0.992	0.995	0.985	0.432	0.487
Adadelta	0.312	0.237	0.723	0.715	0.992	0.986

Table 2 shows that the experimental results of RMSprop and Adam optimizer are similar, and the best classification results appear when the learning rate is 0.001. With the increase of learning rate, the classification results decreased seriously. It is the direct opposite of the Adadelta optimizer, and the best classification effect is achieved when the learning rate is equal to 1. Considering the accuracy and loss, the RMSprop optimizer is finally selected, and the learning rate is set to 0.001.

(2) Batch Size. Before the optimizer performs a weight update, we can obtain the batch size which is the number of training instances through observing, which can affect the model's generalization performance. Compared with the learning rate, the batch size is less sensitive to the model, but the batch size is also a critical parameter to further improve the performance of the model. Increasing the batch size in an appropriate range can reduce the training time and contribute to the stability of model convergence. However, performance appears to have a downward trend when the batch size is too large. Table 3 shows that the model which we

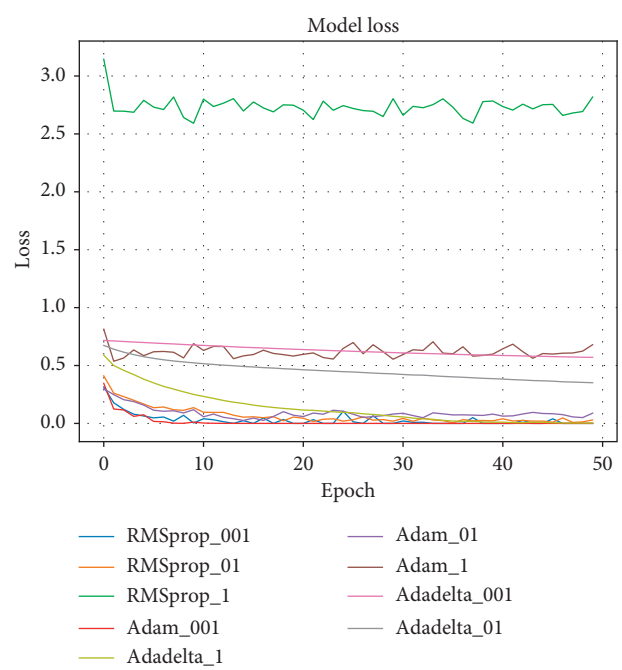

Figure 5: Loss change of different optimizers and learning rates.

Table 3: Performance of model w.r.t different batch size.

Batch size	Converge time (s)	Training accuracy	Testing accuracy
50	41.9s	1	0.9850
100	29.3	1	0.9775
200	24.9	1	0.9850
300	25.9	0.9987	0.9725

Table 4: Performance of model w.r.t different dropout value.

Dropout	Converge time (s)	Training accuracy	Testing accuracy
0.1	25.5	0.9981	0.9775
0.2	24.9	0.9981	0.9700
0.3	25.4	0.9956	0.9750
0.4	25	0.9987	0.9825
0.5	25.4	0.9987	0.9850

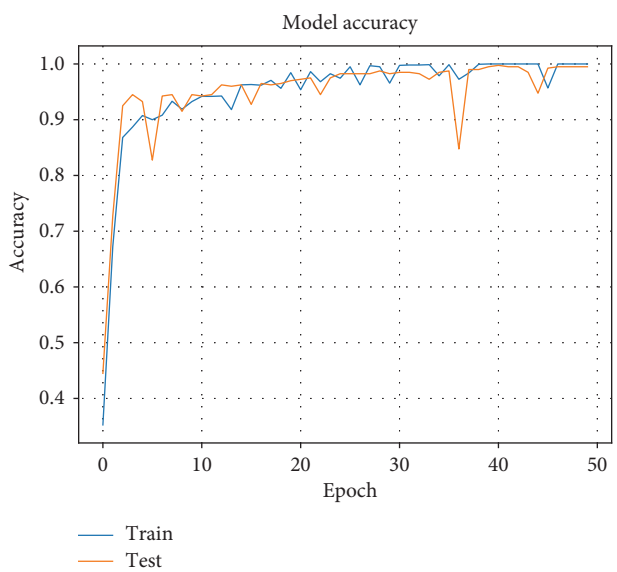

Figure 6: Accuracy change of training and testing data.

design can achieve the best classification and the shortest training time when batch size equals 200.

(3) Dropout. Dropout is one of the forms for regularization. We can verify the influence in the different dropout values; we further experiment on the bearing data. Table 4 shows that the different dropout values have a weakly influence on the converge time and accuracy of the proposed model. Finally, the dropout value is set to 0.5, because the model has the highest accuracy when dropout equals to 0.5.

3.1.3. Results Analysis. Keras framework is selected to train the data after building the fault diagnosis model using 1DCNN-GRU. The iterations, batch size, learning rate of the PMSprop algorithm, and dropout value are set at 50, 200, and 0.01 to training. The accuracy and loss of training set and testing set change with training epochs are shown in Figures 6 and 7.

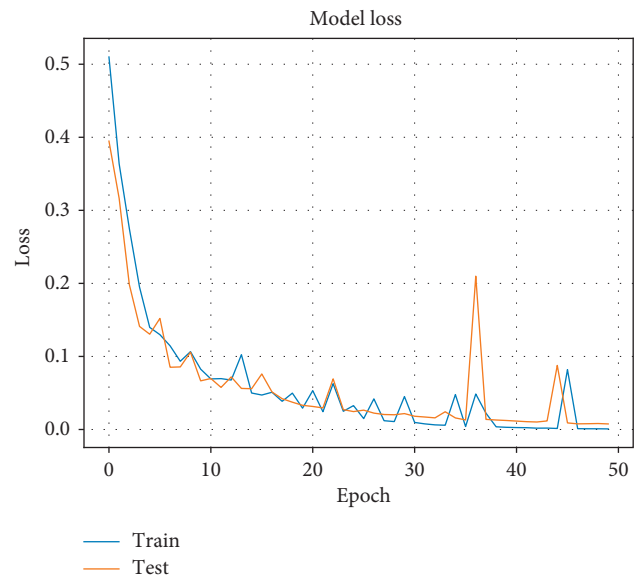

Figure 7: Loss change of training and testing data.

Table 5: Accuracy of classification models.

Methods	Average training accuracy (%)	Average testing accuracy (%)
SVM	79.61	69.29
Bayesian	68.93	70.10
CNN	97.86	95.76
LSTM	98.35	96.67
1DCNN-GRU	99.98	98.96

According to Figures 6 and 7, the proposed model has high accuracy stability. After the first eight training epochs, the loss value of the testing data decreased rapidly, and the model fitted quickly. After the 8th training, the loss value decreased slowly, the slope of the losing curve was close to 0, and the model can complete convergence. The accuracy of the training set and testing set increased rapidly in the first four training epochs, which reached 1.0 nearly after the 30th training iteration. With increasing the number of epochs, the accuracy curve is very smooth, and the curves of the training set and testing set tend to coincide.

In order to compare the diagnosis results of the proposed model with the current mainstream intelligent fault diagnosis algorithms, this paper experimented based on the representative traditional machine learning methods SVM and Bayesian and the deep learning methods CNN and LSTM. The time and frequency domain feature parameters include mean, variance, standard deviation, maximum, minimum, RMS, absolute mean, root mean square, waveform factor, kurtosis factor, pulse factor, margin factor, skewness, and kurtosis as the input of SVM and Bayesian for fault diagnosis. The input of CNN and LSTM is the same as the proposed method to perform the end-to-end fault diagnosis. The accuracy of different methods is presented in Table 5. The accuracy of 1DCNN-GRU is higher than other methods.

4. Conclusions

In this paper, an end-to-end bearing diagnosis classification model based on 1DCNN and GRU are proposed. We test and verify the following four types of faults experiments:

(1) The proposed model avoided the dependence of traditional feature extraction methods on professional knowledge and realized the end-to-end bearing fault diagnosis, which reduced the complexity of the diagnosis process.

(2) GRU was applied in tandem with 1DCNN, it can not only extract spatial features of vibration signal but also further learn the characteristics of time-sequenced, so that have better data expression ability. Meanwhile, it avoids the dependence of traditional feature extraction methods on professional knowledge and reduces the complexity of the diagnosis process.

(3) The experiments on the CWRU dataset show that the average diagnosis accuracy of the proposed model is higher than SVM, Bayesian, CNN, and LSTM, and it is suitable for the accurate diagnosis of rolling bearing faults.

In future work, in order to avoid the influence of the overfitting phenomenon on the accuracy of fault diagnosis, we will study the optimization of model parameters.

Data Availability

The data used to support the findings of this study are included within the article. Because it is a numerical simulation example, readers can get the same results as this article by using the LMI toolbox of Matlab and the theorem given in this article.

Conflicts of Interest

The author declares that there are no conflicts of interest regarding the publication of this paper.

Acknowledgments

This study was supported by the Tianjin Municipal Education Commission, Social Science Major Project of Tianjin Municipal Education Commission, under Grant No. 2017JW2D28, Education Informatization Development Strategy Research in Tianjin under "China's Education Modernization 2030," 2017-10 to 2020-12, 80,000 yuan.

References

[1] Q. T. Tran, S. D. Nguyen, and T. I. Seo, "Algorithm for estimating online bearing fault upon the ability to extract meaningful information from big data of intelligent structures," *IEEE Transactions on Industrial Electronics*, vol. 66, no. 5, pp. 3804–3813, 2019.

[2] A. Rai and S. H. Upadhyay, "A review on signal processing techniques utilized in the fault diagnosis of rollingelement bearings," *Tribology International*, vol. 96, pp. 289–306, 2016.

[3] H. D. Shao, H. K. Jiang, Y. Lin, and X. Li, "A novel method for intelligent fault diagnosis of rolling bearings using ensemble deep auto-encoders," *Mechanical Systems and Signal Processing*, vol. 102, pp. 278–297, 2018.

[4] J. H. Cai, W. W. Hu, and X. Ch Wang, "Rotor fault diagnosis based on Higher-order statistics," *Journal of Vibration, Measurement & Diagnosis*, vol. 33, no. 2, pp. 298–301, 2013.

[5] H. C. Lin and Y. C. Ye, "Reviews of bearing vibration measurement using fast Fourier transform and enhanced fast Fourier transform algorithms," *Advances in Mechanical Engineering*, vol. 11, no. 1, Article ID 168781401881675, 2019.

[6] N. BeSsous, S. E. Zouzou, W. Bentrah, S. Sbaa, and M. Sahraoui, "Diagnosis of bearing defects in induction motors using discrete wavelet transform," *International Journal of System Assurance Engineering and Management*, vol. 9, no. 2, pp. 335–343, 2018.

[7] S. Djaballah, K. Meftah, K. Khelil, M. Tedjini, and L. Sedira, "Detection and diagnosis of fault bearing using wavelet packet transform and neural network," *Frattura ed Integrità Strutturale*, vol. 13, no. 49, pp. 291–301, 2019.

[8] X. Zhang and J. Zhou, "Multi-fault diagnosis for rolling element bearings based on ensemble empirical mode decomposition and optimized support vector machines," *Mechanical Systems and Signal Processing*, vol. 41, no. 1-2, pp. 127–140, 2013.

[9] G. E. Hinton and R. R. Salakhutdinov, "Reducing the dimensionality of data with neural networks," *Science*, vol. 313, no. 5786, pp. 504–507, 2006.

[10] D. T. Hoang and H. J. Kang, "Rolling element bearing fault diagnosis using convolutional neural network and vibration image," *Cognitive Systems Research*, vol. 53, pp. 42–50, 2019.

[11] H. Chen, N. Hu, Z. Cheng, L. Zhang, and Y. Zhang, "A deep convolutional neural network based fusion method of two-direction vibration signal data for health state identification of planetary gearboxes," *Measurement*, vol. 146, pp. 268–278, 2019.

[12] Y. X. Chou, B. L. Xu, Y. Gu, R. L. Zhang, L. G. Wang, and Y. Jin, "A fast mathematical morphology filter on one dimensional sampled signal," in *Proceedings of the 2017 Int'l Conf. on Control, Automation and Information Sciences (ICCAIS)*, pp. 233–238, Chiang Mai, Thailand, November 2017.

[13] D. C. Yu, Z. G. Yu, X. C. Chen et al., "Compliance control with vector decomposer using one-dimensional pressure sensor for robotichand," in *Proceedings of the Chinese Automation Congress (CAC)*, pp. 445–450, Jinan, China, October 2017.

[14] D. D. Peng, Z. L. Liu, H. Wang, Y. Qin, and L. Jia, "A novel deeper one-dimensional CNN with residual learning for fault diagnosis of wheelset bearings in high-speed trains," *IEEE Access*, vol. 7, pp. 10278–10293, 2019.

[15] X. Wu, Z. K. Peng, J. Ren, C. Cheng, W. Zhang, and D. Wang, "Rub-impact fault diagnosis of rotating machinery based on 1-D convolutional neural networks," *IEEE Sensors Journal*, vol. 20, no. 15, pp. 8349–8363, 2020.

[16] W. You, C. Shen, D. Wang, L. Chen, X. Jiang, and Z. Zhu, "An intelligent deep feature learning method with improved activation functions for machine fault diagnosis," *IEEE Access*, vol. 8, pp. 1975–1985, 2020.

[17] W. Zhang, C. Li, Peng, Y. Chen, and Z Zhang, "A deep convolutional neural network with new training methods for bearing fault diagnosis under noisy environment and different working load," *Mechanical Systems and Signal Processing*, vol. 100, pp. 439–453, 2018.

[18] L. Guo, Y. Lei, S. Xing, T. Yan, and N. Li, "Deep convolutional transfer learning network: a new method for intelligent fault diagnosis of machines with unlabeled data," *IEEE Transactions on Industrial Electronics*, vol. 66, no. 9, pp. 7316–7325, 2019.

[19] L. Yu, J. Qu, F. Gao, and Y. Tian, "A novel hierarchical algorithm for bearing fault diagnosis based on stacked LSTM," *Shock and Vibration*, vol. 2019, Article ID 2756284, 2019.

[20] A. Z. Hinchi and M. Tkiouat, "Rolling element bearing-remaining useful life estimation based on a convolutional long-short-term memory network," *Procedia Computer Science*, vol. 127, pp. 123–132, 2018.

[21] R. Zhao, D. Wang, R. Yan, K. Mao, F. Shen, and J. Wang, "Machine health monitoring using local feature-based gated recurrent unit networks," *IEEE Transactions on Industrial Electronics*, vol. 65, no. 2, pp. 1539–1548, 2018.

Hindawi
Discrete Dynamics in Nature and Society
Volume 2022, Article ID 7119370, 11 pages
https://doi.org/10.1155/2022/7119370

Research Article

Finite-Time Pinning Synchronization Control for Coupled Complex Networks with Time-Varying Delays

Hebing Zhang,[1] **Xiaojing Zheng**,[2] **and Ning Li**[1]

[1]*School of Intelligent Manufacture, Taizhou University, Jiaojiang 318000, Zhejiang, China*
[2]*Weifang University of Science and Technology, Shouguang 262700, Shandong, China*

Correspondence should be addressed to Hebing Zhang; zhanghebing729@163.com

Received 2 April 2022; Revised 14 April 2022; Accepted 18 April 2022; Published 18 May 2022

Academic Editor: Giulio E. Cantarella

The finite-time pinning synchronization control problem is studied for coupled complex networks with time-varying delays. Based on the finite-time stability theorem, a finite-time tractive synchronous controller is designed. In addition, the selection process of tractive nodes is developed to control as few nodes as possible such that all nodes are synchronized in the network in finite time. At the same time, sufficient conditions of the finite-time constraint synchronization of the drive-response network are obtained using the Lyapunov stability theory and the matrix inequality method. The effectiveness of the proposed controller is verified by numerical simulation. This approach can be applied to large-scale complex networks with time-varying delays.

1. Introduction

Complex networks are ubiquitous, such as the Internet and biological neural, social, and supply chain networks. A large number of nodes, along with the complexity of structural links and temporal and spatial evolution, make these networks a hot research topic in nonlinear science. When some nodes or edges in a network fail, other nodes may fail through the coupling relationship between nodes and propagation dynamics, resulting in a chain reaction and the subsequent collapse of a large subset of nodes or possibly the whole network. For example, in a power network, faults in circuit breakers, transmission lines, and power generation units often lead to large-scale power outages, which can cause significant destruction. Within this propagation mechanism, the interactions between nodes shift the states of different complex dynamic systems slowly toward consistency under different initial conditions [1], which leads to the synchronization of complex networks.

The synchronization behavior of complex networks can explain many complex phenomena in the natural world, such as the resonance of a bridge caused by multiple people crossing, different routers sending messages at the same frequency, and communication satellites staying relatively stationary with respect to the Earth. In 1998, Pecora and Carroll, two scientists from the US naval laboratory, observed the synchronization of two chaotic systems for the first time and proposed a hybrid synchronization method [2]. At present, the synchronization control of coupled, orderless systems involves observations in the field of chaos and control, with practical applications in various fields, including secure communication, a multiagent network coordinated control, and unmanned aerial vehicle (UAV) cooperative operation. This control is especially beneficial in soft robotics, which requires more sensors than rigid robotics because this kind of sensor network presents challenges in cooperation to task completion.

However, the synchronous application of complex networks has disadvantages, such as packet transmission within the Internet. Researchers found that different routers eventually send data synchronously, resulting in network congestion. Therefore, detailed observations on the synchronous control of various natural and unnatural complex dynamic networks are necessary to finally promote the benign synchronization of complex networks in practical projects, establish the positive role of networks, inhibit the malignant synchronization of complex networks, and reduce the negative impact [3]. The challenges of network synchronization

reach mathematics, control, genetics, epidemiology and other disciplines [4–6].

The research on synchronization originated from the synchronization behavior of chaotic systems, mainly including internal and external synchronizations. Internal synchronization studies the internal dynamic characteristics of networks, and external synchronization considers multiple systems. Traditional approaches to synchronization use the main stability and Lyapunov functions, which focus on a network's coupling characteristics. When adjusting the coupling characteristics of the network does not improve the system synchronization ability, these methods are no longer applicable. Nishikawa et al. found no apparent relationship between the synchronization ability of complex networks and the average distance between networks. The authors also noted that the distribution of degrees and mediators in the networks could better characterize the synchronization ability of the system. A more uniform distribution results in a stronger synchronization ability of the system. Moreover, a less uniform distribution yields a worse synchronization ability [7]. As far as the problem of discontinuous inertial neural networks (DINNS) with time-varying delays is considered, the periodic solutions are synchronized with a fixed time [8]. Kong analyze the fixed-time synchronization of a class of discontinuous fuzzy inertial neural networks with time-varying delays based on the new improved fixed-time stability lemmas [9].

Many achievements were made in the research on synchronization modes of complex networks, including $H¥H_\infty$ [10], finite-time [11], exponential [12], complete [13], and generalized synchronizations [14]. More recently, scholars aimed to improve the synchronization ability of the network by designing a controller [15] and obtaining sufficient conditions using the Lyapunov method [16]. New techniques are developed in dealing with the stochastic Lyapunov functional, and sufficient conditions are gained to ensure that the resulting dynamics are stochastically stable [17]. Synchronous control methods of complex networks are also emerging, such as intermittent control [18], sampling data control [19], and pulse control [12]. A relatively new approach is to consider pulse synchronization based on an unknown bounded time-varying delay. Each node in the corresponding system can synchronize with the corresponding node in the driving system [15]. The number of nodes in the complex network is large, and the network structure presents different complex characteristics. In fact, the strength of inner link will also be changed under random disturbance [20], which makes all nodes in this networks not necessary to be controlled.

Wang and Chen first proposed the method of pinning control for the synchronization behavior of a scale-free network and achieved good experimental results [21]. Subsequently, boundary control [22] and pinning control [23] have aroused the interest of scholars. Boundary control only needs to select boundary nodes for control. Yang et al. [24] studied the juxtaposed boundary controller with boundary measurement, which solves the cluster synchronization control problem of nonlinear complex spatiotemporal dynamic networks with community structure by placing sensors and actuators at the spatial boundary. Similarly, the network synchronization is controlled through a few nodes. The node selection is more flexible than the boundary control and not limited to nodes along the boundary.

Most research on pinning synchronization control falls into one of two categories. One approach is to design the pinning cluster synchronization controller when the number of network nodes is small (generally less than ten nodes) to control only those directly connected to other clusters, reducing the number of controllers [25–27]. The design aims to provide appropriate pinning feedback controllers such that the nodes converge to a consistent state as well as the equilibrium, periodic orbit, or chaotic orbit of the nonlinear part of the node dynamics. In a simulation of this design [28], a network composed of six nodes is given, and three nodes are selected for control. The other approach assumes that the number of network nodes is large. Shi et al. [29] considered a complex network of 500 nodes, from which 50 nodes are randomly selected for containment control, and better results were obtained. While the pinning node is easier to determine for the network with fewer nodes, efforts to select the appropriate pinning node for a complex network with many nodes are meaningful.

Several achievements have emerged in the research of complex networks and their synchronous control, both in theory and application. The aim is for when time $t \longrightarrow \infty$, error $e(t) \longrightarrow 0$. However, to gain faster control, many scholars have carried out studies on limited-time synchronous control [30]. This approach not only saves significant time and cost but also yields other economic benefits, such as the cooperative work of a UAV network, the information transmission of a communication network, and the coordination between supply chain network enterprises. Traditional work included criteria for finite-time stability of nonlinear systems [31, 32]. Recently, a study [33] introduced combined synchronization in complex networks. Based on the synovial control principle and finite-time stability theory, the network synovial area control input was designed, and sufficient conditions for synchronization were obtained. In [34], an adaptive synchronization controller was designed to realize the finite-time stability of the error system when the network coupling weight was known and unknown. To realize the finite-time control of nonstrict feedback stochastic nonlinear systems with input quantization and full-state constraints, Zhu et al. [35] proposed a semiglobal finite-time uncertain control method in the sense of probability, which accelerated the convergence of the system. The research on single coupling and coupling weight in the above study obtained good results, while the problem of time-delay coupling needs further investigation. In addition, the coupling time delays of complex networks are inevitable phenomena, and especially for networks with many nodes, the time-delay coupling situation is more involved.

Based on actual engineering and management needs and the literature review, a finite-time pinning synchronization control is proposed to solve the synchronization problem of large-scale complex networks with time-varying delay couplings. This control is valuable for practical engineering applications. The main contributions of this paper are as follows:

(1) The designed controller realizes limited-time synchronization of multiple complex networks by controlling some nodes under the consideration of a coupling delay. In other words, the controller not only synchronizes in a limited time but also reduces the number of control nodes, which can present design challenges. The synchronization problem of large-scale time-varying coupled networks can be addressed with this controller, with significant economic benefits.

(2) The existing literature has not specified a method for pinning node selection. This paper is likely the first effort to determine the number of pinning nodes according to the coupling strength of the network and then select the corresponding pinning nodes through the arrangement of node degrees.

The remainder of this paper is organized as follows. Section 2 presents the node dynamics model of a complex network and related lemmas and assumptions. Section 3 describes the pinning controller design and the finite-time synchronization control theorem and proof. In addition, the procedure for pinning node selection is outlined. In Section 4, the numerical simulation is carried out. Finally, Section 5 concludes the study and briefly explains the application direction and future research.

2. Construction of a Complex Network

Consider the dynamic drive-response model of a complex network composed of N identical nodes, which is described as

$$\begin{aligned}\dot{x}_i(t) &= f(x_i(t)) + c_0\sum_{j=1}^{N} a_{ij}\Gamma x_j(t)\\ &\quad + c_1\sum_{j=1}^{N} b_{ij}\Gamma h\big(x_j(t-\tau(t))\big), \quad i = 1,2\ldots,N,\end{aligned} \tag{1}$$

$$\begin{aligned}\dot{y}_i(t) &= f(y_i(t)) + c_0\sum_{j=1}^{N} a_{ij}\Gamma y_j(t)\\ &\quad + c_1\sum_{j=1}^{N} b_{ij}\Gamma h\big(y_j(t-\tau(t))\big) + u_i(t), \quad i = 1,2\ldots,N,\end{aligned} \tag{2}$$

where $x_i(t) = (x_{i1}(t), x_{i2}(t), \ldots, x_{in}(t))^T \in R^n$ is the state variable of the first driving network node; $y_i(t) = (y_{i1}(t), y_{i2}(t), \ldots, y_{in}(t))^T \in R^n$ is the state variable of the first node of the response network; i is the network node label; c_0 and c_1 are the coupling strength of complex networks without delay and with delay, respectively; Γ is the internal coupling matrix of network nodes; and $A = (a_{ij}) \in \mathbf{R}^{N\times N}$ and $B = (b_{ij}) \in \mathbf{R}^{N\times N}$ are the delay-free and delay-coupled configuration matrices of the network, respectively. If an uncoupled delay edge exists between nodes i and j, then $a_{ij} > 0\,(i \neq j)$; otherwise, $a_{ij} = 0\,(i \neq j)$. If a coupled time-delay edge is between nodes i and j, then $b_{ij} > 0\,(i \neq j)$; otherwise, $b_{ij} = 0\,(i \neq j)$. Its diagonal elements satisfy $a_{ii} = -\sum_{j=1, j\neq i}^{N} a_{ij}$. Furthermore, $b_{ii} = -\sum_{j=1, j\neq i}^{N} b_{ij}$. $\tau(t)$ stands for coupled time-delay and continuously differentiable function. Thus, to satisfy $0 \le \tau(t) \le \tau < 1$, $u_i(t) \in \mathbf{R}^n$ is the synchronization controller to be designed.

Definition 1. For any initial condition, make $e_i(t) = y_i(t) - x_i(t)$, and there is a certain moment $t_1 > 0$. Under the action of the controller $u_i(t)$, $\lim_{t\longrightarrow t_1}\|e(t)\| = 0$; then, the drive-response network described by equations (1) and (2) realizes synchronization in a finite time t_1.

Remark 1. For the following expressions, symbolic definitions are given: $\|\Gamma\|_2 = \gamma$; $\rho_{\min}$ represents the minimum eigenvalue of matrix $(\Gamma + \Gamma^T)/2$, where $\rho_{\min} \neq 0$; $\widehat{A} = (\widetilde{A}^T + \widetilde{A})/2$ is a symmetric matrix; matrix $\widetilde{A}$ transforms the diagonal element a_{ii} into $(\rho_{\min}/\gamma)a_{ii}$ based on matrix A; $\widehat{A}_l$ is the submatrix of l rows and l columns before $\widehat{A}$ is deleted; l is the number of pinning nodes in the article; and $\lambda_{\max}(A)$ is the maximum eigenvalue of matrix A.

Lemma 1. *(see [11]). Assume that function $V(t)$ is continuous positive definite. If a continuous function $\gamma(\cdot)$ exists, $\gamma(\sigma) > 0, \sigma \in (0, +\infty)$ satisfying $V(t) \le -\gamma(V(t))$, $\int_0^{V(0)} 1/\gamma(\sigma)\mathrm{d}\sigma = t^* < \infty$; then, $V(t) \equiv 0, \forall t \ge t^*$. If $\gamma(\sigma) = d\sigma^q$ and $d > 0, 0 < q < 1$, then the transient synchronization time is formulated as*

$$t^* = \frac{V^{1-q}(0)}{d(1-q)}. \tag{3}$$

Lemma 2. *(see [36]). Given a symmetric matrix $M = \begin{pmatrix} X & Y \\ Y^T & M_l\end{pmatrix} \in \mathbf{R}^{N\times N}$, $D = \begin{pmatrix} D_1 & 0 \\ 0 & 0\end{pmatrix} \in \mathbf{R}^{N\times N}$, where $X, D_1 \in \mathbf{R}^{r\times r}\,(1 \le r \le N)$, and matrix $D_1 = \mathrm{diag}\{d_1, d_2, \ldots, d_r\}$ is diagonal positive definite, then $M - D < 0$ hold if and only if $M_l < 0, d_i \ge \lambda_{\max}(X - YM_l^{-1}Y^T)$, where $(1 \le i \le r)$.*

Lemma 3. *(see [37]). Assume X and Y are arbitrary n-dimensional vectors and $\varepsilon > 0$; the following inequality holds: $2X^TY \le \varepsilon X^TX + 1/\varepsilon Y^TY$.*

Lemma 4. *(adjoint inequality of Minkowski inequality). If $r > 0$ and $r \neq 1$, then*

$$\begin{aligned}&\sum(a + b + \cdots + l)^r > \sum a^r + \sum b^r + \cdots + \sum l^r, \quad r > 1,\\ &\sum(a + b + \cdots + l)^r < \sum a^r + \sum b^r + \cdots + \sum l^r, \quad 0 < r < 1,\end{aligned} \tag{4}$$

unless all the numbers in each set $a_v, b_v, \ldots, l_v\,(v = 1, 2, \ldots, n)$ except one are zero.

Assumption 1. For arbitrary $x, y \in \mathrm{R}^n$ and the existence constant $L_1 > 0$, the following inequality is true:

$$(y - x)^T(f(y) - f(x)) \le L_1(y - x)^T(y - x). \tag{5}$$

Assumption 2. Assume that f satisfies the Lipschitz condition, i.e., for any scalars $x, y \in R^n$, $\xi > 0$, there exist scalars $L_2 > 0$ such that

$$\|f(y) - f(x)\| \le L_2 \|y - x\|. \tag{6}$$

Remark 2. The above assumptions are common Lipschitz conditions in dynamic system research and are widely used in synchronization research. Our assumptions are easy to verify. Most chaotic systems satisfy the above assumptions.

3. Pinning Controller

3.1. Controller Design. Without losing generality, select the first l nodes in the drive-response models (1) and (2) as the constraint nodes. At this time, equation (2) can be further described as

$$\begin{cases} \dot{y}_i(t) = f(y_i(t)) + c_0 \sum_{j=1}^{N} a_{ij} \Gamma y_j(t) + c_1 \sum_{j=1}^{N} b_{ij} \Gamma h\big(y_j(t - \tau(t))\big) + u_i(t), \quad i = 1, 2, \ldots, l, \\ \dot{y}_i(t) = f(y_i(t)) + c_0 \sum_{j=1}^{N} a_{ij} \Gamma y_j(t) + c_1 \sum_{j=1}^{N} b_{ij} \Gamma h\big(y_j(t - \tau(t))\big), \quad i = l+1, l+2, \ldots, N. \end{cases} \tag{7}$$

Remark 3. The first l nodes selected here only describe the current complex network dynamic model and do not represent the subsequent selection method of nodes in containment control. The determination method of l is given later in this section.

Design the following controllers, where α, k, and λ are control gains with $\alpha > 0, k > 0$, and $\lambda > 0$. Especially, if $e_i(t) = 0$, then $u_i(t) = 0$.

$$u_i(t) = \begin{cases} -k e_i(t) - \alpha \left(\dfrac{\lambda}{1-\tau} \sum_{i=1}^{l} \int_{t-\tau(t)}^{t} e_i^T(s) e_i(s) \mathrm{d}s \right)^{1+\mu/2} \dfrac{e_i(t)}{\|e(t)\|^2} - \alpha \operatorname{sign}(e_i(t)) |e_i(t)|^{\mu}, \quad i = 1, 2, \ldots, l \\ 0, \quad i = l+1, l+2, \ldots, N. \end{cases} \tag{8}$$

Remark 4. In the controller design process, we need to consider both finite-time synchronization and containment control, which presents a significant challenge. Moulay et al. [38] proposed a new approach to achieving finite-time stability. However, the Lyapunov function satisfying the assumptions is difficult to find, limiting the practical application of this method. Many controller designs involve symbolic functions, which can cause system state and signal chattering, serious damage, and other impacts on the system [39, 40]. This paper avoids symbolic functions by using the quantitative controller in [41], but containing nodes is difficult. Therefore, weighing the advantages and disadvantages, a controller of equation (7) is designed.

The dynamic equation of the synchronization error can be obtained from equations (1) and (7):

$$\dot{e}_i(t) = \begin{cases} f(y_i(t)) - f(x_i(t)) + c_0 \sum_{j=1}^{N} a_{ij} \Gamma\big(y_j(t) - x_j(t)\big) + c_1 \sum_{j=1}^{N} b_{ij} \Gamma\big[h\big(y_j(t-\tau(t)) - x_j(t-\tau(t))\big)\big] + u_i(t), \quad i = 1, 2, \ldots, l \\ f(y_i(t)) - f(x_i(t)) + c_0 \sum_{j=1}^{N} a_{ij} \Gamma\big(y_j(t) - x_j(t)\big) + c_1 \sum_{j=1}^{N} b_{ij} \Gamma\big[h\big(y_j(t-\tau(t)) - x_j(t-\tau(t))\big)\big], \quad i = l+1, l+2, \ldots, N. \end{cases} \tag{9}$$

Theorem 1. *Under Assumptions 1 and 2, the pinning controller equation (8), and the drive of complex network equation (1), the finite time synchronizes the response of the complex network of equation (2). Thus, the synchronization transition time is*

$$t^* = \frac{V^{1-\mu/2}(0)}{\alpha(1-\mu)}, \quad x \in \Omega. \tag{10}$$

If $p + 2\gamma c_0 \lambda_{\max}(\widehat{A}_l) < 0$, where $l (1 \le l < N)$, then $p = 2L_1 + \lambda/1 - \tau + \varepsilon c_1/2\lambda_{\max}(AA^T)\lambda_{\max}(\Gamma\Gamma^T)$, $\lambda > \max\{L_2^2/2\varepsilon, \lambda_{\max}(E - \overline{AQ}_1^{-1}\overline{A}^T)\}$, and L_1 and L_2 are positive constant.

Proof. Construct the Lyapunov functional candidate as

$$V(t) = \sum_{i=1}^{N} e_i^T(t) e_i(t) + \frac{\lambda}{1-\tau} \sum_{i=1}^{l} \int_{t-\tau(t)}^{t} e_i^T(s) e_i(s) \mathrm{d}s. \tag{11}$$

Substituting equation (9) into the time derivative of $V(t)$,

$$\begin{aligned}\dot{V}(t) &= 2\sum_{i=1}^{N} e_i^T(t)\dot{e}_i(t) + \frac{\lambda}{1-\tau}\sum_{i=1}^{l} e_i^T(t)e_i(t) \\ &\quad - \frac{\lambda}{1-\tau}\sum_{i=1}^{l} e_i^T(t-\tau(t))e_i(t-\tau(t))(1-\dot{\tau}(t)) \\ &\le 2\sum_{i=1}^{N} e_i^T(t)[f(y_i(t)) - f(x_i(t)) + c_0\sum_{j=1}^{N} a_{ij}\Gamma e_j(t) \\ &\quad + c_1\sum_{j=1}^{N} b_{ij}\Gamma e_j h(t-\tau(t))] + 2\sum_{i=1}^{l} e_i^T(t)[-ke_i(t) \\ &\quad - \alpha\left(\frac{\lambda}{1-\tau}\sum_{i=1}^{l}\int_{t-\tau(t)}^{t} e_i^T(s)e_i(s)\mathrm{d}s\right)^{1+\mu/2}\frac{e_i(t)}{\|e(t)\|^2} \\ &\quad - \alpha\,\mathrm{sign}(e_i(t))|e_i(t)|^{\mu}] \\ &\quad + \frac{\lambda}{1-\tau}\sum_{i=1}^{l} e_i^T(t)e_i(t) - \lambda\sum_{i=1}^{l} e_i^T(t-\tau(t))e_i(t-\tau(t)).\end{aligned} \tag{12}$$

According to the characteristics of coupling matrix $\mathbf{A}$,

$$\begin{aligned}\sum_{i=1}^{N}\sum_{j=1}^{N} e_i^T(t)a_{ij}\Gamma e_j(t) &\le \sum_{i=1}^{N}\sum_{j=1}^{N}\gamma a_{ij}\|e_i(t)\|_2\|e_j(t)\|_2 \\ &\quad + \sum_{i=1}^{N} a_{ii}\rho_{\min}e_i^T(t)e_i(t) = e^T(t)(\gamma\widehat{A})e(t).\end{aligned} \tag{13}$$

From Lemma 3 and the properties of the Kronecker product,

$$\begin{aligned}&\sum_{i=1}^{N}\sum_{j=1}^{N} e_i^T(t)b_{ij}\Gamma h(e_j(t-\tau(t))) \\ &\quad = e^T(t)(B\otimes\Gamma)H(e(t-\tau(t))) \\ &\quad \le \frac{1}{2}\varepsilon e^T(t)(BB^T\otimes\Gamma\Gamma^T)e(t) \\ &\qquad + \frac{1}{2\varepsilon}H^T(e(t-\tau(t)))H(e(t-\tau(t))) \\ &\quad \le \frac{\varepsilon}{2}\lambda_{\max}(BB^T)\lambda_{\max}(\Gamma\Gamma^T)\sum_{i=1}^{N} e_i^T(t)e_i(t) \\ &\qquad + \frac{1}{2\varepsilon}L_2^2\sum_{i=1}^{N} e_i^T(t-\tau(t))e_i(t-\tau(t)),\end{aligned} \tag{14}$$

where L_2 is positive constant, and

$$\begin{aligned}&H(e(t-\tau(t))) \\ &= \left(h^T(e_1(t-\tau(t))), h^T(e_2(t-\tau(t))), \ldots, h^T(e_N(t-\tau(t)))\right)^T.\end{aligned} \tag{15}$$

Substituting equations (13) and (14) into the time derivative of equation (12),

$$\begin{aligned}\dot{V}(t) &\le e^T(t)\left[\left(2L_1 + \frac{\lambda}{1-\tau} + \frac{\varepsilon c_1}{2}\lambda_{\max}(BB^T)\cdot\lambda_{\max}(\Gamma\Gamma^T)I_N\right) + 2\gamma c_0\widehat{A} - 2K\right]e(t) \\ &\quad + e^T(t-\tau(t))\left(\frac{1}{2\varepsilon}L_2^2 - \lambda\right)I_N e(t-\tau(t)) - 2\alpha\left(\frac{\lambda}{1-\tau}\sum_{i=1}^{l}\int_{t-\tau(t)}^{t} e_i^T(s)e_i(s)\mathrm{d}s\right)^{1+\mu/2} \\ &\quad - 2\alpha\sum_{i=1}^{l} e_i^T(t)\mathrm{sign}(e_i(t))|e_i(t)|^{\mu},\end{aligned} \tag{16}$$

where $e(t) = (e_1(t), e_2(t), \ldots, e_N(t))^T$ and $K = \mathrm{diag}(\underbrace{k, \ldots, k}_{l}, \underbrace{0, \ldots, 0}_{N-l})$. Let

$$Q_1 = \left(2L_1 + \frac{\lambda}{1-\tau}\right)I_N + \frac{\varepsilon c_1}{2}(BB^T\otimes\Gamma\Gamma^T) + 2\gamma c_0\widehat{A} - 2K. \tag{17}$$

Note that Q_1 is symmetric and can be decomposed into $Q_1 = \begin{bmatrix} E-\overline{K} & \overline{B} \\ \overline{B}^T & \overline{Q}_1 \end{bmatrix}$, where $\overline{K} = \mathrm{diag}[\underbrace{k, \ldots, k}_{l}]$ and $\overline{Q}_1 = (2L_1 + \lambda/1-\tau + \varepsilon c_1/2\lambda_{\max}(BB^T)\lambda_{\max}(\Gamma\Gamma^T))I_{N-l} + 2\gamma c_0\widehat{A}_{N-l}$ is the minor matrix of Q_1 by removing its first $l\,(1 \le l < N)$ row-column pairs. Take appropriate parameters to make $2L_1 + \lambda/1-\tau + \varepsilon c_1/\ 2\lambda_{\max}(BB^T)\lambda_{\max}(\Gamma\Gamma^T) + 2\gamma c_0\lambda_{\max}(\widehat{A}_{N-l}) < 0$.

That is, $\overline{Q}_1 < 0$. At the same time, take $\lambda > \lambda_{\max}(E - \overline{B}\overline{Q}_1^{-1}\overline{B}^T)$, which can be known according to Lemma 2, where $\overline{Q}_1 < 0$ is equivalent to $Q_1 < 0$. For $Q_2 = (1/2\varepsilon L_2^2 - \lambda)I_N$, take $\lambda > L_2^2/2\varepsilon$ to satisfy $Q_2 < 0$. Thus, $\lambda > \max\{L_2^2/2\varepsilon, \lambda_{\max}(E - \overline{B}\overline{Q}_1^{-1}\overline{B}^T)\}$ shows that both Q_1 and Q_2 are less than zero, so we have

$$\begin{aligned}\dot{V}(t) &\le -2\alpha\left(\frac{\lambda}{1-\tau}\sum_{i=1}^{l}\int_{t-\tau(t)}^{t} e_i^T(s)e_i(s)\mathrm{d}s\right)^{1+\mu/2} \\ &\quad - 2\alpha\sum_{i=1}^{l} e_i^T(t)\mathrm{sign}(e_i(t))|e_i(t)|^{\mu},\end{aligned} \tag{18}$$

where

$$
\begin{aligned}
&-2\alpha\sum_{i=1}^{l} e_i^T(t)\operatorname{sign}(e_i(t))\left|e_i(t)\right|^{\mu} \\
&\le -2\alpha\sum_{i=1}^{N}\left|e_i(t)\right|^{1+\mu} \le -2\alpha\left(\sum_{i=1}^{N}\left|e_i(t)\right|^2\right)^{1+\mu/2} \\
&= -2\alpha\left(\sum_{i=1}^{N} e_i^T(t)e_i(t)\right)^{1+\mu/2}.
\end{aligned}
\tag{19}
$$

Substituting equation (20) into the time derivative of equation (17), along with Lemma 4,

$$
\begin{aligned}
\dot{V}(t) &\le -2\alpha\left(\frac{\lambda}{1-\tau}\sum_{i=1}^{l}\int_{t-\tau(t)}^{t} e_i^T(s)e_i(s)\mathrm{d}s\right)^{1+\mu/2} \\
&\quad -2\alpha\left(\sum_{i=1}^{N} e_i^T(t)e_i(t)\right)^{1+\mu/2} \\
&\le -2\alpha\left(\frac{\lambda}{1-\tau}\sum_{i=1}^{l}\int_{t-\tau(t)}^{t} e_i^T(s)e_i(s)\mathrm{d}s + \sum_{i=1}^{N} e_i^T(t)e_i(t)\right)^{1+\mu/2} \\
&= -2\alpha V^{1+\mu/2}(t).
\end{aligned}
\tag{20}
$$

□

Remark 5. Theorem 1 gives sufficient conditions for the drive-response complex network to realize the pinning synchronization in a finite time. In addition, we can calculate the synchronization time. Clearly, the synchronization time is closely related to parameters α and μ in the controller. Therefore, selecting appropriate values α and μ is crucial to the synchronization time, and the ideal parameter values can be determined through multiple calculations.

Remark 6. For complex networks with large-scale node books, a controller on each node is unrealistic to apply. Only some network nodes are selected to achieve network synchronization, which is essential to containment control and applicable to practical problems. Therefore, this paper adopts the containment control scheme, which has strong economic benefits. Note that the condition $p + 2\gamma c_0\lambda_{\max}(\widehat{A}_l) < 0$ in the theorem can only determine the number of pinned nodes and not which node. However, the selection of appropriate nodes is of more significance to the synchronization efficiency. The specific node selection method will be given in Section 3.2.

3.2. Selection Scheme for Pinning Node. Considering the sufficient condition of synchronization in Theorem 1 and giving priority to nodes with high control degrees [23], the procedure for the selection of restraining nodes is as follows.

Step 1. Determine the appropriate parameters to meet the sufficient conditions in Theorem 1.

Step 2. Similar to [23], take the degree of nodes in the network as the reference standard for the selection of pinning nodes. When the network is undirected, prioritize the nodes with high degrees; when the network is directed, calculate the ratio of outgoing and incoming degrees of each point, sort the ratio, and prioritize the nodes with high ratios.

Step 3. Let $l = 1$ and check whether the sufficient condition in Theorem 1 is satisfied. If so, the number of pinning nodes is one. If not, increase the number of pinning nodes one by one until the sufficient condition is satisfied.

Remark 7. The pinning node can be selected in two ways. One is to select according to the node degree. For strongly connected networks, select nodes with large degrees as containment nodes [23]. Low-degree nodes should be selected as the pinning node in the weakly connected network, which has better synchronization efficiency [42]. The second approach is to arbitrarily select the pinning node [25]. Although network synchronization is possible as long as the number of pinning nodes meets the sufficient conditions in Theorem 1, in practical applications, the connection mechanism between network nodes affects the transmission efficiency of network information. Therefore, the selection of appropriate nodes can achieve network synchronization faster. After determining the number of pinning nodes, the selection of the control node is critical.

4. Numerical Simulation

A coupled time-delay complex network with 50 identical nodes is considered, and its driving system is as follows:

$$
\begin{aligned}
\dot{x}_i(t) &= f(x_i(t)) + c_0\sum_{j=1}^{50} a_{ij}\Gamma x_j(t) \\
&\quad + c_1\sum_{j=1}^{50} b_{ij}\Gamma h\big(x_j(t-\tau(t))\big), \quad 1 \le i \le 50.
\end{aligned}
\tag{21}
$$

The response system is as follows:

$$
\dot{y}_i(t) = \begin{cases}
f(y_i(t)) + c_0\sum_{j=1}^{50} a_{ij}\Gamma y_j(t) + c_1\sum_{j=1}^{50} b_{ij}\Gamma h\big(y_j(t-\tau(t))\big) + u_i(t), & 1 \le i \le l, \\
f(y_i(t)) + c_0\sum_{j=1}^{50} a_{ij}\Gamma y_j(t) + c_1\sum_{j=1}^{50} b_{ij}\Gamma h\big(y_j(t-\tau(t))\big), & l+1 \le i \le 50,
\end{cases}
\tag{22}
$$

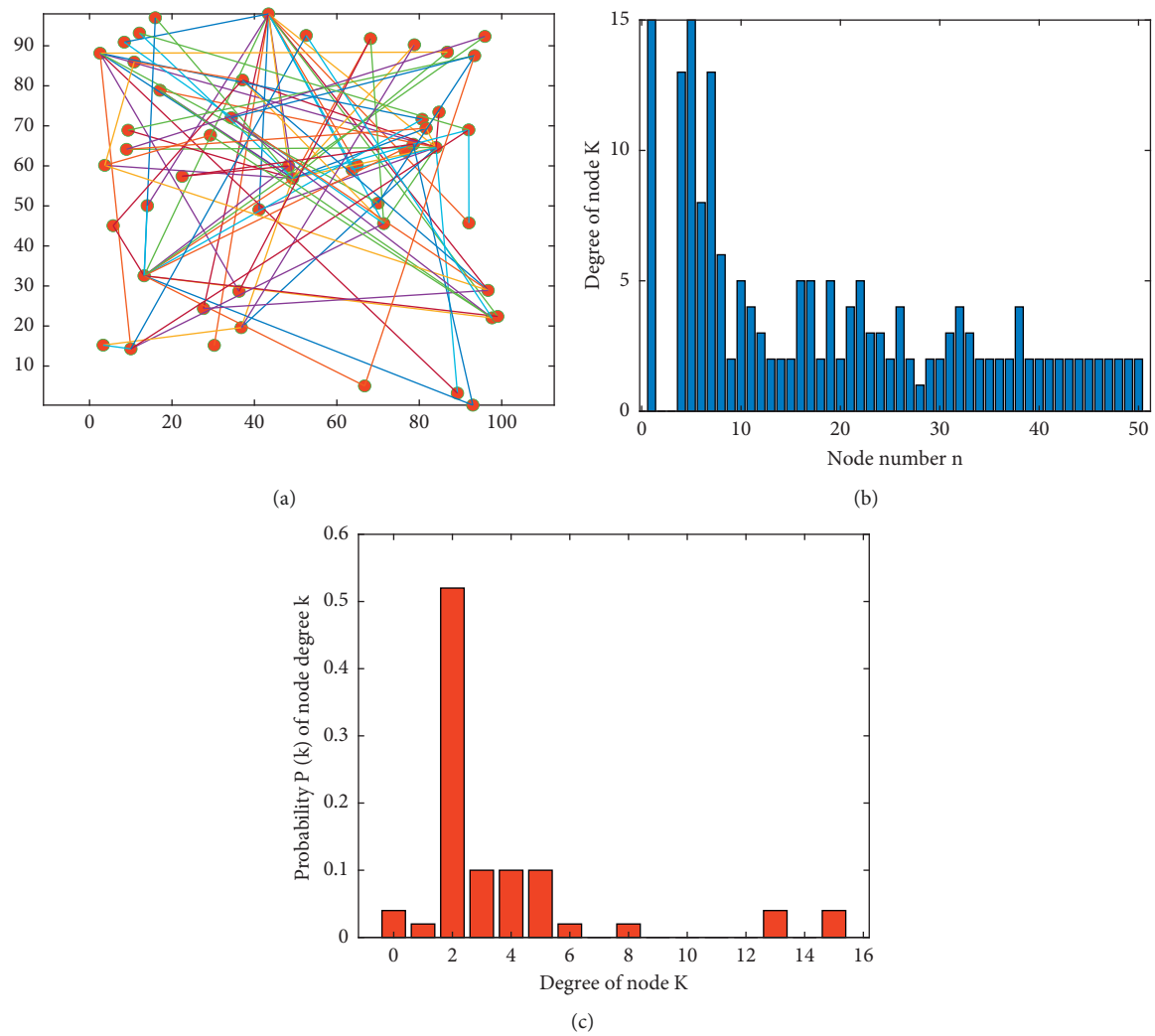

Figure 1: Scale-free network and related statistics. (a) Scale-free network topology. (b) Distribution diagram of node degree. (c) Probability distribution of node degree in the network.

where $x_i(t) = (x_{i1}(t), x_{i2}(t), x_{i3}(t))^T$, $y_i(t) = (y_{i1}(t), y_{i2}(t), y_{i3}(t))^T$ and $\Gamma = \mathrm{diag}\{1, 1.2, 1\}$. The coupling configuration $A = (a_{ij})_{50\times 50}$ is a network that conforms to scale-free characteristics. The number of nodes in the initial state of the network is set to $m_0 = 3$. Each time a new node is introduced, the number of newly generated edges is $m = 2$. Using the roulette algorithm, m nodes are selected from the existing nodes to connect with the newly added nodes to obtain a scale-free network and further generate matrix $\mathbf{A}$, as shown in Figure 1(a). The sufficient conditions of Theorem 1 are obtained as $\lambda_{\max}(AA^T) = 31.4537$; let $B = 0.1A$, coupling strength of edges $c_0 = 0.2$, $c_1 = 0.1$, and the nonlinear term

$$\begin{aligned} h\left(x_j(t-\tau(t))\right) = \Big(& x_{j1}(t-\tau(t)) \\ &+ \sin\left(x_{j1}(t-\tau(t))\right), x_{j2}(t-\tau(t)) \\ &+ \sin\left(x_{j2}(t-\tau(t))\right), x_{j3}(t-\tau(t)) \\ &+ \sin\left(x_{j3}(t-\tau(t))\right)\Big), \end{aligned} \tag{23}$$

where $\tau(t) = e^t/1 + e^t$.

Assuming that the nodes of the driving network and the response network are Lorenz systems, we write the node dynamic equations to unify the representation of network nodes as follows:

$$\begin{cases} \dot{x}_{i1} = 10\left(x_{i2} - x_{i1}\right), \\ \dot{x}_{i2} = 28x_{i1} - x_{i2} - x_{i1}x_{i3}, \\ \dot{x}_{i3} = -\dfrac{8}{3}x_{i3} + x_{i1}x_{i2}. \end{cases} \tag{24}$$

Set the initial conditions of each node of the drive and response system, respectively: $x_i(0) = (7.5 + 0.6i, 0.2 + 0.1i, 3 + 0.1i)^T$, $y_i(0) = (0.5 + 0.6i, 3.2 + 0.1i, 7 + 0.2i)^T$, $i = 1, 2, \ldots, 50$. Figures 2 and 3 show the attractor and time series of a Lorenz system of the first node of the driving system and the response system, respectively.

Here, we only show the trajectory of one node for the driving network and the response network, and the other trajectories will not be repeated.

Based on the parameter design of Li et al. [43], set $\tau = 1/4$, $\beta = 1$, $\alpha = 8$, $\lambda = 2$, and $\mu = 1/2$ in controller $u_i(t)$.

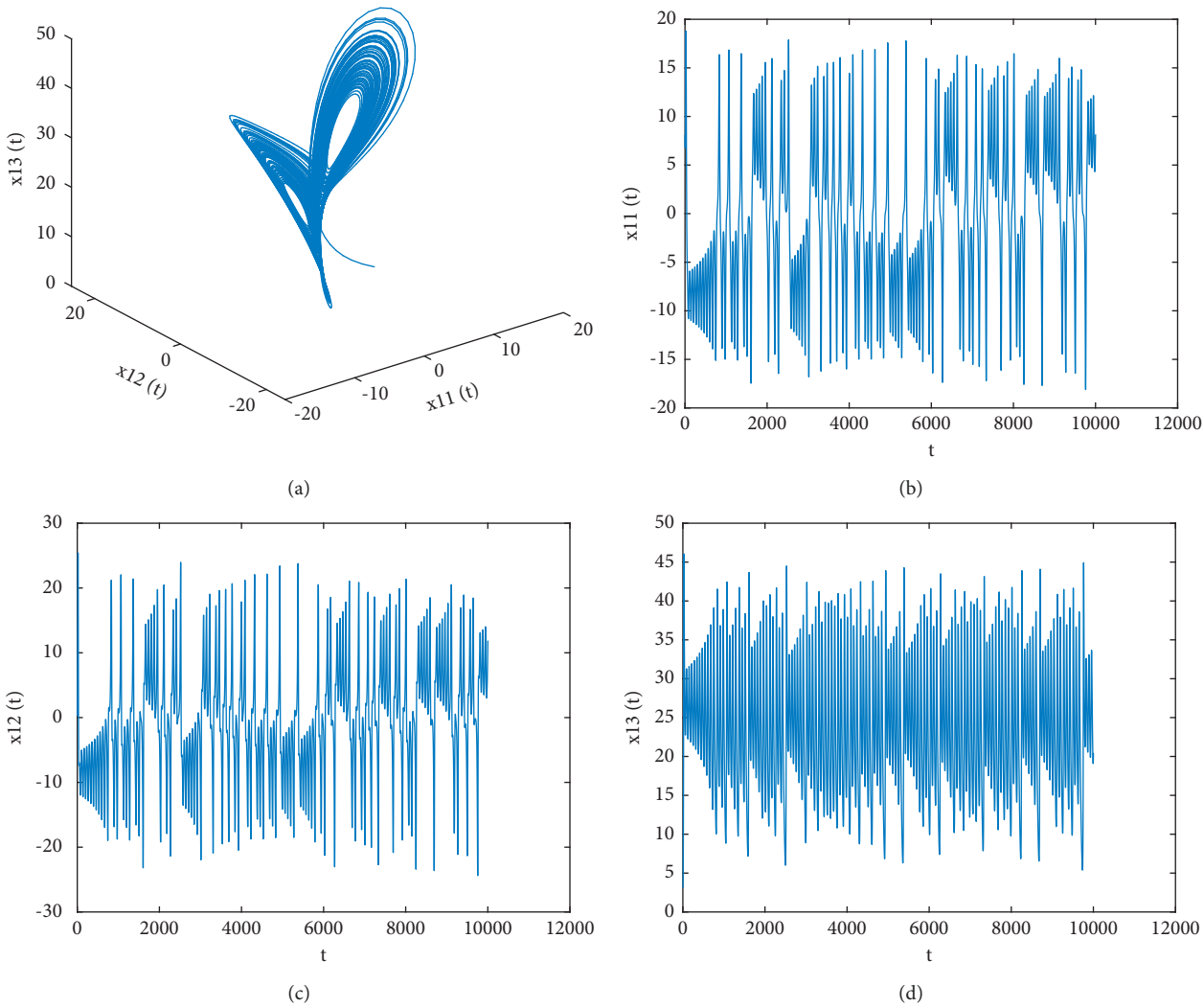

Figure 2: Attractor and time series of the first node of the driving system. (a) Lorenz attractor. (b) x time series. (c) y time series. (d) z time series.

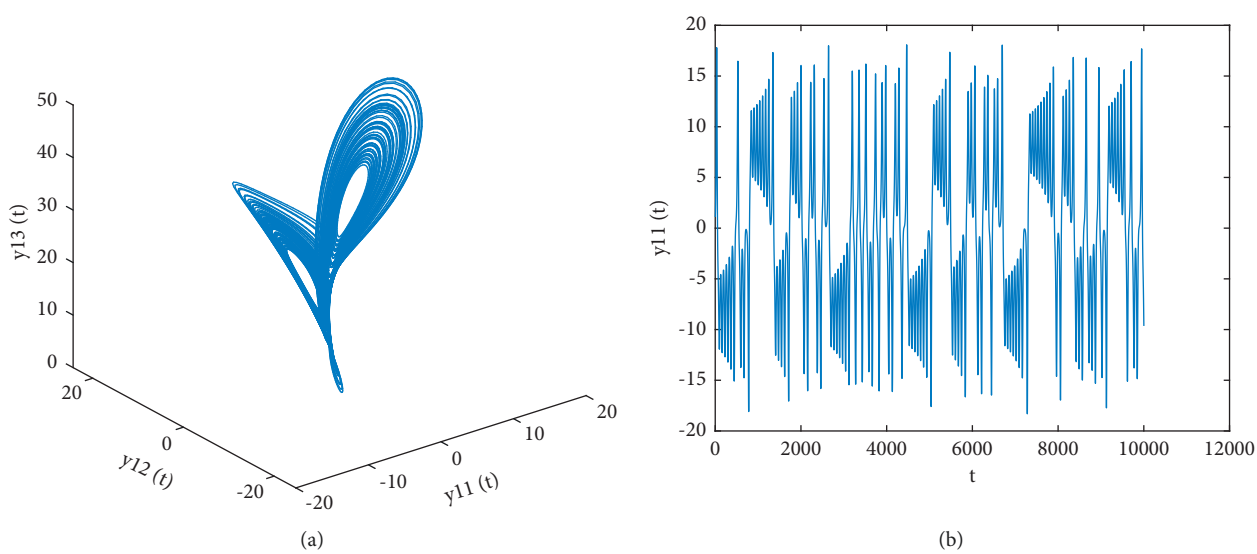

Figure 3: Continued.

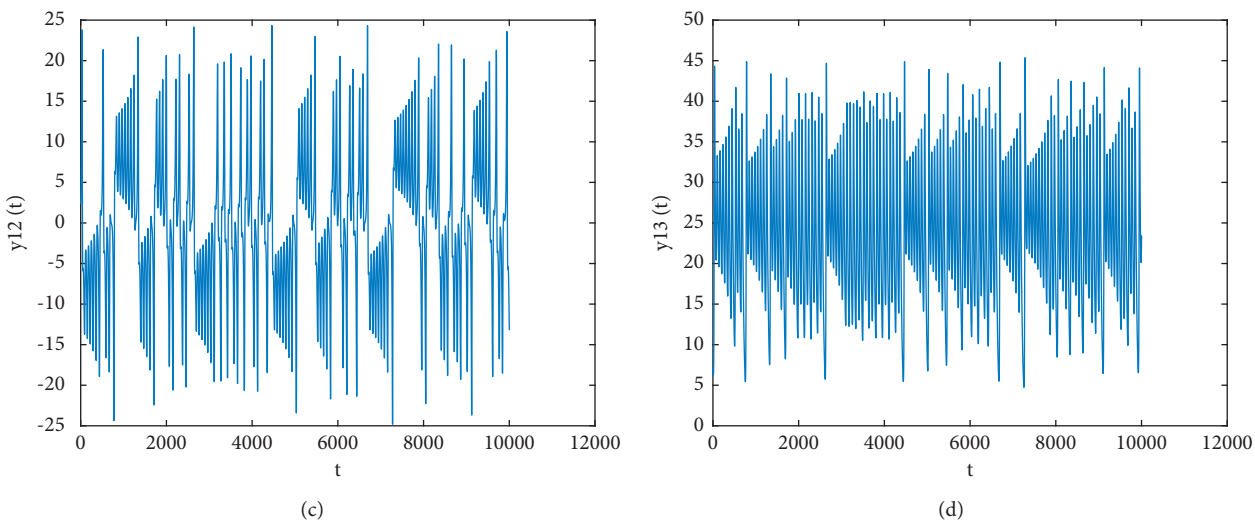

Figure 3: Attractor and time series of the first node of the response system. (a) Lorenz attractor. (b) x time series. (c) y time series. (d) z time series.

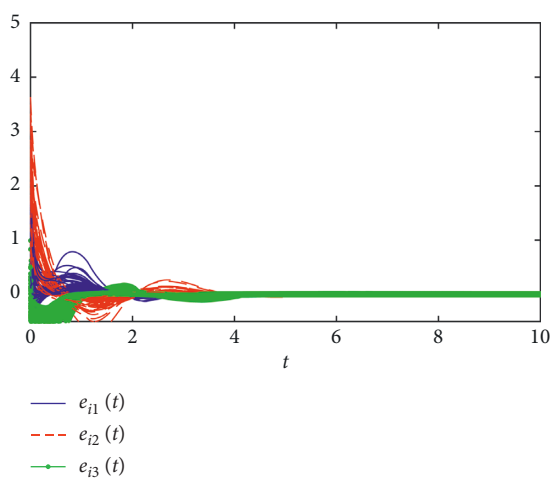

Figure 4: Synchronization error of 13 node networks controlled according to the node selection rules in this paper.

From Assumption 1, we can verify that $L_1 = 1.7342$ and $L_2 = 1.0225$. For the sufficient condition $\lambda > L_2^2/2\varepsilon$ of Theorem 1, set $\varepsilon = 0.3$, and $\gamma = 1.2$ can be obtained from $\|\Gamma\|_2 = \gamma$. Input parameters into sufficient conditions $p + 2\gamma c_0 \lambda_{\max}(\widehat{A}_l) < 0$ to obtain $\lambda_{\max}(\widehat{A}_l) < -0.8077$. Arrange the nodes according to the degree and the selection procedure of the pinning nodes: $\lambda_{\max}(\widehat{A}_{13}) = -0.8176$, $\lambda_{\max}(\widehat{A}_{12}) = -0.7869$. The first 13 nodes can synchronize the drive network and the response network, as shown in Figure 4.

Remark 8. The coupling strength of the network is closely related to the network synchronization ability. In this paper, the value $\lambda_{\max}(\widehat{A})$ also depends on the coupling strengths c_0 and c_1 of the network. In other words, the coupling strength of the network determines the number of pinning nodes. Therefore, in some studies of random pinning node selections (e.g., [25]), the effect of synchronous control can continue to be optimized.

From the above calculation and simulation results, we conclude that the finite-time pinning synchronization control of time-delay coupled complex networks is realized.

5. Conclusions

The effectiveness of this method, which focuses on the selection of pinning nodes, is verified by numerical simulation. This paper attempts to select pinning nodes based on the degree to which sufficient conditions are met. Research results on the identification of key nodes and edges in complex networks are available [44]. Following this, we aim to control the synchronization of complex networks, defining key nodes as pinning nodes.

The relevant research results can be applied to the synchronous control of a supply chain network. For example, the change of products promotes the evolution of a supply chain network and affects the coupling relationship between companies within the network. In particular, the coupling time delay problem greatly impacts the efficiency of the supply chain. Currently, we choose "degree" when considering the time-delay coupling problem among companies in a supply chain network, connect larger enterprises as the nodes of containment control, and finally realize a smooth synchronous evolution path of the supply chain. Our approach can also be applied to UAV clusters to achieve synergy, providing the ability to perform complex, changeable, and dangerous tasks; improve the overall load capacity, information perception, and processing ability; and avoid attacks or low efficiency when a single UAV performs tasks. However, it is precise because we consider the containment control through some nodes, which is conservative compared with controlling all nodes to achieve synchronization. Therefore, reducing conservatism is also an important direction for future research.

In practical applications, the number of pinning nodes and time limitations are significant issues. Therefore, the selection of fewer pinning nodes in a strict, limited time is a necessary research direction for the future.

Data Availability

The data used to support the findings of this study are included within the article.

Conflicts of Interest

The authors declare that they have no conflicts of interest.

Acknowledgments

This research was sponsored by the Natural Science Foundation of Zhejiang Province under grant no. LQ20E050011 and the Science and Technology Plan of Taizhou City under grant no. 2003gy10.

References

[1] V. Afraimovich, A. Cordonet, and N. F. Rulkov, "Generalized synchronization of chaos in noninvertible maps," *Physical Review A*, vol. 66, no. 1, Article ID 016208, 2002.

[2] L. M. Pecora and T. L. Carroll, "Master stability functions for synchronized coupled systems," *Physical Review Letters*, vol. 80, no. 10, pp. 2109–2112, 1998.

[3] D. J. Watts and S. H. Strogatz, "Collective dynamics of "small-world" networks," *Nature*, vol. 393, no. 6684, pp. 440–442, 1998.

[4] Z.-G. Wu, P. Shi, H. Su, and J. Chu, "Stochastic synchronization of markovian jump neural networks with time-varying delay using sampled data," *IEEE Transactions on Cybernetics*, vol. 43, no. 6, pp. 1796–1806, 2013.

[5] J. Mason, P. S. Linsay, J. J. Collins, and L. Glass, "Evolving complex dynamics in electronic models of genetic networks," *Chaos: An Interdisciplinary Journal of Nonlinear Science*, vol. 14, no. 3, pp. 707–715, 2004.

[6] A. Arenas, A. Díaz-Guilera, J. Kurths, Y. Moreno, and C. Zhou, "Synchronization in complex networks," *Physics Reports*, vol. 469, no. 3, pp. 93–153, 2008.

[7] T. Nishikawa, A. E. Motter, Y.-C. Lai, and F. C. Hoppensteadt, "Heterogeneity in oscillator networks: are smaller worlds easier to synchronize?" *Physical Review Letters*, vol. 91, no. 1, Article ID 014101, 2003.

[8] F. Kong and Q. Zhu, "New fixed-time synchronization control of discontinuous inertial neural networks via indefinite Lyapunov-Krasovskii functional method," *International Journal of Robust and Nonlinear Control*, vol. 31, no. 2, pp. 471–495, 2021.

[9] F. Kong, Q. Zhu, and T. Huang, "New fixed-time stability lemmas and applications to the discontinuous fuzzy inertial neural networks," *IEEE Transactions on Fuzzy Systems*, vol. 29, no. 12, pp. 3711–3722, 2021.

[10] W. Chen, Z. X. Jiang, and S. Luo, "Synchronization for complex dynamical networks with coupling delays using distributed impulsive control," *Nonlinear Analysis: Hybrid Systems*, vol. 17, pp. 111–127, 2015.

[11] S. P. Bhat and D. S. Bernstein, "Finite-time stability of continuous autonomous systems," *SIAM Journal on Control and Optimization*, vol. 38, no. 3, pp. 751–766, 2000.

[12] W. He, F. Qian, and J. Cao, "Pinning-controlled synchronization of delayed neural networks with distributed-delay coupling via impulsive control," *Neural Networks*, vol. 85, pp. 1–9, 2017.

[13] H. Sun and H. Cao, "Complete synchronization of coupled Rulkov neuron networks," *Nonlinear Dynamics*, vol. 84, no. 4, pp. 2423–2434, 2016.

[14] H. Liu, J. Chen, J.-a. Lu, and M. Cao, "Generalized synchronization in complex dynamical networks via adaptive couplings," *Physica A: Statistical Mechanics and Its Applications*, vol. 389, no. 8, pp. 1759–1770, 2010.

[15] Z. Xu, X. Li, and P. Duan, "Synchronization of complex networks with time-varying delay of unknown bound via delayed impulsive control," *Neural Networks*, vol. 125, pp. 224–232, 2020.

[16] A. Lin, J. Cheng, L. Rutkowski, and S. P. Wen, "Asynchronous fault detection for memristive neural networks with dwell-time-based communication protocol," *IEEE Transactions on Neural Networks and Learning Systems(Early Access)*, 2022.

[17] J. Cheng, J. H. Park, and Z.-G. Wu, "A hidden Markov model based control for periodic systems subject to singular perturbations," *Systems & Control Letters*, vol. 157, no. 157, Article ID 105059, 2021.

[18] X. Tan and J. Cao, "Intermittent control with double event-driven for leader-following synchronization in complex networks," *Applied Mathematical Modelling*, vol. 64, pp. 372–385, 2018.

[19] S. H. Lee, M. J. Park, O. M. Kwon, R. Sakthivel, and R. Sakthivel, "Advanced sampled-data synchronization control for complex dynamical networks with coupling time-varying delays," *Information Sciences*, vol. 420, pp. 454–465, 2017.

[20] L. Liang, J. Cheng, J. Cao, W.-H. Wu, and W. H. Chen, "Proportional-integral observer-based state estimation for singularly perturbed complex networks with cyberattacks," *IEEE Transactions on Neural Networks and Learning Systems*, pp. 1–11, 2022.

[21] X. F. Wang and G. R. Chen, "Pinning control of scale-free dynamical networks," *Physica A: Statistical Mechanics and Its Applications*, vol. 310, no. 3-4, pp. 521–531, 2002.

[22] A. Baccoli, A. Pisano, and Y. Orlov, "Boundary control of coupled reaction-diffusion processes with constant parameters," *Automatica*, vol. 54, pp. 80–90, 2015.

[23] Q. Song, F. Liu, J. Cao, and J. Lu, "Some simple criteria for pinning a Lur'e network with directed topology," *IET Control Theory & Applications*, vol. 8, no. 2, pp. 131–138, 2014.

[24] C. Yang, J. Cao, T. Huang, J. Zhang, and J. Qiu, "Guaranteed cost boundary control for cluster synchronization of complex spatio-temporal dynamical networks with community structure," *Science China Information Sciences*, vol. 61, no. 5, 13 pages, Article ID 052203, 2018.

[25] C. Yang, T. Huang, Z. Li, J. Zhang, J. Qiu, and F. E. Alsaadi, "Synchronization of nonlinear complex spatio-temporal networks using adaptive boundary control and pinning adaptive boundary control," *IEEE Access*, vol. 6, Article ID 38216, 2018.

[26] Z. Tang, D. L. Xuan, Y. Wang, and Z. C. Ji, "Cluster synchronization of heterogeneous Lur'e networks via pinning adaptive control," *Control Theory & Applications*, vol. 37, no. 10, pp. 2107–2114, 2020.

[27] X.-G. Guo, P.-M. Liu, H.-J. Li, J.-L. Wang, and C. K. Ahn, "Cluster synchronization of heterogeneous nonlinear multi-agent systems with actuator faults and IQCs through adaptive

fault-tolerant pinning control," *Information Sciences*, vol. 575, pp. 289–305, 2021.

[28] H. Lin and J. Wang, "Pinning synchronization of complex networks with time-varying outer coupling and nonlinear multiple time-varying delay coupling," *Physica A: Statistical Mechanics and Its Applications*, vol. 588, no. 588, p. 126564, 2022.

[29] L. Shi, C. Zhang, and S. Zhong, "Synchronization of singular complex networks with time-varying delay via pinning control and linear feedback control," *Chaos, Solitons & Fractals*, vol. 145, Article ID 110805, 2021.

[30] F. Kong, Q. Zhu, R. Sakthivel, and A. Mohammadzadeh, "Fixed-time synchronization analysis for discontinuous fuzzy inertial neural networks with parameter uncertainties," *Neurocomputing*, vol. 422, no. 422, pp. 295–313, 2021.

[31] S. P. Bhat and D. S. Bernstein, "Lyapunov analysis of finite-time differential equations," in *Proceedings of the American Control Conference*, pp. 1831-1832, IEEE, Washington,USA, August, 1995.

[32] H. Wang, B. Chen, C. Lin, Y. Sun, and F. Wang, "Adaptive finite-time control for a class of uncertain high-order nonlinear systems based on fuzzy approximation," *IET Control Theory & Applications*, vol. 11, no. 5, pp. 677–684, 2017.

[33] M. Zhang and M. Han, "Finite-time combination synvhronization of uncertain complex networks based on sliding mode control method," *Conrtol and Decision*, vol. 32, no. 8, pp. 1533–1536, 2017.

[34] Y. J. Shi and Q. Li, "Adaptlve finite-time synchronization of complex dynamical networks," *Control Theory & Applications*, vol. 37, no. 1, pp. 147–154, 2020.

[35] X. F. Zhu, W. W. Ding, and T. P. Zhang, "Finite-time dynamic surface control for nonstrict-feedback stochastic nonlinear systems with input quantization and full-state constraints," *Control and Decision*, vol. 34, 2021.

[36] Q. Song and J. Cao, "On pinning synchronization of directed and undirected complex dynamical networks," *IEEE Transactions on Circuits and Systems I: Regular Papers*, vol. 57, no. 3, pp. 672–680, 2010.

[37] C. Jian-Rui, J. Li-Cheng, W. Jian-She, and W. Xiao-Hua, "Adaptive synchronization between two different complex networks with time-varying delay coupling," *Chinese Physics Letters*, vol. 26, no. 6, Article ID 060505, 2009.

[38] E. Moulay, M. Dambrine, N. Yeganefar, and W. Perruquetti, "Finite-time stability and stabilization of time-delay systems," *Systems & Control Letters*, vol. 57, no. 7, pp. 561–566, 2008.

[39] X. Yang, D. W. C. Ho, J. Lu, and Q. Song, "Finite-time cluster synchronization of T-S fuzzy complex networks with discontinuous subsystems and random coupling delays," *IEEE Transactions on Fuzzy Systems*, vol. 23, no. 6, pp. 2302–2316, 2015.

[40] X. Yang, J. Lam, D. W. C. Ho, and Z. Feng, "Fixed-time synchronization of complex networks with impulsive effects via nonchattering control," *IEEE Transactions on Automatic Control*, vol. 62, no. 11, pp. 5511–5521, 2017.

[41] Y. Xu, C. Chu, and W. Li, "Quantized feedback control scheme on coupled systems with time delay and distributed delay: a finite-time inner synchronization analysis," *Applied Mathematics and Computation*, vol. 337, no. 337, pp. 315–328, 2018.

[42] W. Yu, G. Chen, and J. Lü, "On pinning synchronization of complex dynamical networks," *Automatica*, vol. 45, no. 2, pp. 429–435, 2009.

[43] J. Li, H. Jiang, C. Hu, and J. Yu, "Analysis and discontinuous control for finite-time synchronization of delayed complex dynamical networks," *Chaos, Solitons & Fractals*, vol. 114, pp. 291–305, 2018.

[44] J. W. Li, M. G. Wu, X. X. Wen, and F. Liu, "Identifying key nodes and edges of complex networks based on the minimum connected dominating set," *Systems Engineering and Electronics*, vol. 41, no. 11, pp. 2541–2549, 2019.

Hindawi
Discrete Dynamics in Nature and Society
Volume 2022, Article ID 4798415, 17 pages
https://doi.org/10.1155/2022/4798415

Research Article

Further Improvement on Stability Results for Delayed Load Frequency Control System via Novel LKFs and Proportional-Integral Control Strategy

Xingyue Liu,[1] Kaibo Shi,[1,2,3] Lin Tang,[1] and Yiqian Tang[1]

[1]*School of Electronic Information and Electrical Engineering, Chengdu University, Chengdu 610106, China*
[2]*Engineering Research Center of Power Quality of Ministry of Education, Anhui University, Hefei 230601, China*
[3]*Institute of Electronic and Information Engineering of University of Electronic Science and Technology of China, Guangdong 523808, China*

Correspondence should be addressed to Kaibo Shi; skbs111@163.com

Received 6 March 2022; Accepted 24 March 2022; Published 9 May 2022

Academic Editor: Zi-Peng Wang

In this work, novel stability results for load frequency control (LFC) system considering time-varying delays, nonlinearly perturbed load, and time-varying disturbance of system parameters are proposed by using proportional-integral control strategy. Considering the nonlinearly exogenous load disturbance and system parameters disturbance, an improved stability criterion in the form of linear matrix inequalities (LMIs) is derived by novel simple Lyapunov–Krasovskii functionals (LKFs). The delay-dependent matrix in quadratic term, cross terms of variables, and quadratic terms multiplied by 1st, 2nd, and 3rd degrees of scalar functions are included in the new simple LKF. Taking the single-area and two-area LFC system installed with proportional-integral (PI) controller as example, our results surpass the previous maximum allowable size of time delay. Meanwhile, the relationship between time delay varying rate, load disturbance degree, gains of PI controller, and delay margin of the LFC system is researched separately. The results can provide guidance to tune the PI controller for achieving maximum delay margin, in which the LFC system can withstand without losing stability. At last, the simulation results verify the effectiveness and superiority of the proposed stability criterion.

1. Introduction

The usage of load frequency control (LFC) is widely in the power system, which restores the balance of the power system between load demand and generation supply [1–3]. The sudden change of load can bring threaten to the safe and economic operation of the power system. Thus, the analysis and research about LFC scheme of the power system are considered to be essential and important segment to guarantee the safe operation of the power system. The LFC scheme is also effectively applied in smart grid [4, 5].

A wide and dedicated open communication network is needed to transmit control signals, measurements between remote RTUs, and the control center in the conventional LFC system [3, 6]. The usage of the communication network leads to a series of inevitable problems, like time delays [7–11], packet losses, and so on. Hence, many researchers focus on the time delay phenomenon of the power control system and the impact of network delay on the communication-based power system [12–16]. From the perspective of stability analysis, it is of significant to seek the maximum allowable network delay that the power system with LFC scheme can withstand without losing sable.

Generally speaking, there are mainly two approaches to seek the upper bound of the time delay system, which have different restriction and conservatism. One is the direct approach, which is frequency domain method, such as tracing eigenvalue [17, 18], or cluster treatment of characteristic roots [19–21]. The advantage of these direct methods is that the accurate delay margin can be derived by

calculating eigenvalues of the whole system. However, the disadvantage of direct methods is that they can only be applied to constant time delays situation. The other is time domain method, which is based on Lyapunov stability theory and linear matrix inequalities (LMIs) techniques [22–26]. Though the time domain methods are more conservatism than the frequency domain methods, the time domain methods can be applied in both constant and time-varying delays situation. So, the time domain methods based on Lyapunov stability theory are abroad exploited.

The main effort to diminish the conservatism of time domain methods has focused on two aspects, methods of constructing L-K functional and analyzing techniques for bounding the derivatives of L-K functional with regard to time. The former includes delay-division functional, functional with matrices dependent on the time delays [27], functional with two-integral or triple-integral terms [28], and so on. The latter techniques include improved majorization technique, free weighting matrix method [29], integral inequality including Jesen inequality [23], Wirtinger inequality [30], auxiliary function-based integral inequality [31], and reciprocal convex technique [32]. More and more researchers focus on the delay-dependent criteria for stability of the power system because the delay-dependent criteria have less conservatism than delay-independent criteria [22, 33].

Until now, there are a few excellent research studies about stability analysis of the delayed LFC systems. Ramakrishnan and Ray [34] focused on the delay-dependent robust stability problem for the LFC system with multiple time-invariant delays in H_∞ framework. The model of the LFC system with both sampling and transmission delay was proposed in [35]. The stability analysis problem was considered in [3], which focused on the LFC system with electric vehicles and time delays. The novel linear operator inequality approach was proposed, and a delay-dependent stability criterion with less conservative was obtained. Unfortunately, the load disturbance and random disturbance of system parameters were not considered either in the stability analysis or simulation in the above literatures. It is worth noting that the bounded nonlinear load perturbation model was built without considering random disturbance of system parameters in literatures [22, 36, 37]. The augmented L-K functional including single and double integral terms was developed to analyze stability of the LFC system in these literatures. The novel LKF with delay-dependent matrix in quadratic term, cross terms of variables, and quadratic terms multiple by a higher degrees of scalar function proposed by this paper contains more information about state variables than the routine L-K functional adopted in [22, 36, 37], and the results in this paper are less conservative than those of [22, 36, 37].

This work proposes a novel stability criterion for the time-varying delay LFC power system considering nonlinearly perturbed and random disturbance of system parameters. Considering unknown exogenous load disturbance and random disturbance of system parameters as constrained time-varying nonlinear function related to current and delayed state vectors, the delayed LFC system with PI controller can be described as a time-varying delay system. Then, the novel stability criterion of the LFC power system is expressed in the form of LMIs by a simple LKF and integral inequalities. The main opinion of constructing the new LKF is the application of delay-dependent matrix, cross terms of variables, and quadratic terms multiplied by 1st, 2nd, and 3rd degrees of scalar function. Moreover, the case studies are carried out taking the single-area and two-area LFC system installed with PI controller as example with simulation examples to verify the effectiveness and superiority of the proposed stability criteria.

2. System Description and Problem Formulation

The notations of jth area for the LFC system are given in Table 1. The subscript j should be omitted for the single-area LFC system. For example, K_{Pi} can be changed to K_P in the single-area LFC system. It is worth noting that $\Delta P_{tie} = 0$ in the single-area LFC system.

Consider the uncertainties in the power parameters of the actual LFC system. The state-space model with disturbance parameters and load disturbance of the multiarea LFC system (N area) is presented as follows:

$$\begin{cases} \dot{x}(t) = (A + \Delta A(t))x(t) + \sum_{j=1}^{N}\left(B_j + \Delta B_j(t)\right)x\left(t - h_j(t)\right) + C\Delta L_{\mathrm{d}}(t), \\ x(t) = \phi(t),\ t \in \left[-\max\left(h_j(t)\right), 0\right], \end{cases} \tag{1}$$

where $x(t)$ represents state vector. A and B represent the system matrices related to the current state and delayed state vectors. $\Delta A(t) = \mathrm{N}F(t)D_1$ and $\Delta B(t) = \mathrm{N}F(t)D_2$ represent perturbation parameters. $F(t)$ is a time-varying matrix, which satisfies $F^T(t)F(t) \le I$. N, D_1, and D_2 are the constant matrix. $h_j(t)$ represents the network time-varying delay in j th area. C represents the known matrix related to the disturbance vector. The initial state can be described by a continuous function defined in $t \in [-\max(h_j(t)), 0]$.

2.1. LFC Modeling. In order to simplify the calculation, it supposes that $h_j(t) = h(t)$, which means the multiple delays are supposed to be equal and shown as a unified time-

Table 1: Notations.

Δf_j	Deviation of frequency	K_{Pj}	Proportional gain	K_{Ij}	Integral gain
ACE_j	Area control error	ΔL_{dj}	Disturbance of load	D_j	Damping constant
M_j	Generator inertia moment	T_{tj}	Turbine time constant	T_{gj}	Time-constant
γ_j	Frequency bias factor	ΔP_{tie}	Tie-line power transfer	ΔP_{mj}	Generator output
ΔP_{vj}	Generator valve position	$\hat{v}_j$	Speed drop	R_{ij}	Synchronize coefficient

varying delay $h(t)$. So, the state-space model of multiple-area can be presented as follows:

$$\begin{cases} \dot{x}(t) = (A + \Delta A(t))x(t) + (B + \Delta B(t))x(t - h(t)) + C\Delta L_d(t)\,(0 \le h(t) \le h, -\mu \le \dot{h}(t) \le \mu), \\ x(t) = \phi(t), \quad t \in [-h, 0], \end{cases} \tag{2}$$

where $B = \sum_{i=1}^{n} B_i$ and $\Delta B(t) = \sum_{i=1}^{n} \Delta B_i(t)$. h and μ represent the upper bound of time-varying delay and the delay derivative separately. The constraints of $h > 0$ and $0 < \mu < 1$ can make time-varying delay systems well-posed because the fast time-varying delay will cause a series of problems, like causality, minimality, inconsistency, and so on.

Furthermore, considering $\Delta A(t) = \mathrm{NF}(t)D_1$ and $\Delta B(t) = \mathrm{NF}(t)D_2$, the state-space model of multiple-area can be rewritten as follows:

$$\begin{cases} \dot{x}(t) = Ax(t) + Bx(t - h(t)) + C\Delta L_d(t) + \mathrm{NF}(t)\big(D_1 x(t) + D_2 x(t - h(t))\big)\,(0 \le h(t) \le h, -\mu \le \dot{h}(t) \le \mu), \\ x(t) = \phi(t), \quad t \in [-h, 0]. \end{cases} \tag{3}$$

For a typical two-area LFC system, the dynamic model is shown in Figure 1. $e^{-sh(t)}$ is network time-varying delay notation. The state vectors, load disturbance vectors, and system matrices are presented as follows:

$$x(t) = \left[\Delta f_1(t)\ \ \Delta P_{m1}(t)\ \ \Delta P_{v1}(t)\ \ \int \mathrm{ACE}_1(t)\mathrm{d}t\ \ \Delta P_{12}(t)\ \ \Delta f_2(t)\ \ \Delta P_{m2}(t)\ \ \Delta P_{v2}(t)\ \ \int \mathrm{ACE}_2(t)\mathrm{d}t\right]^T,$$

$$A = \begin{bmatrix} -\frac{D_1}{M_1} & \frac{1}{M_1} & 0 & 0 & -\frac{1}{M_1} & 0 & 0 & 0 & 0 \\ 0 & -\frac{1}{T_{t1}} & \frac{1}{T_{t1}} & 0 & 0 & 0 & 0 & 0 & 0 \\ -\frac{1}{\hat{v}_1 T_{t1}} & 0 & -\frac{1}{T_{t1}} & 0 & 0 & 0 & 0 & 0 & 0 \\ \gamma_1 & 0 & 0 & 0 & 1 & 0 & 0 & 0 & 0 \\ 2\pi R_{12} & 0 & 0 & 0 & 0 & -2\pi R_{12} & 0 & 0 & 0 \\ 0 & 0 & 0 & 0 & \frac{1}{M_2} & \frac{-D_2}{M_2} & \frac{1}{M_2} & 0 & 0 \\ 0 & 0 & 0 & 0 & 0 & 0 & -\frac{1}{T_{t2}} & \frac{1}{T_{t2}} & 0 \\ 0 & 0 & 0 & 0 & 0 & -\frac{1}{\hat{v}_2 T_{t2}} & 0 & -\frac{1}{T_{t2}} & 0 \\ 0 & 0 & 0 & 0 & -1 & \gamma_2 & 0 & 0 & 0 \end{bmatrix},$$

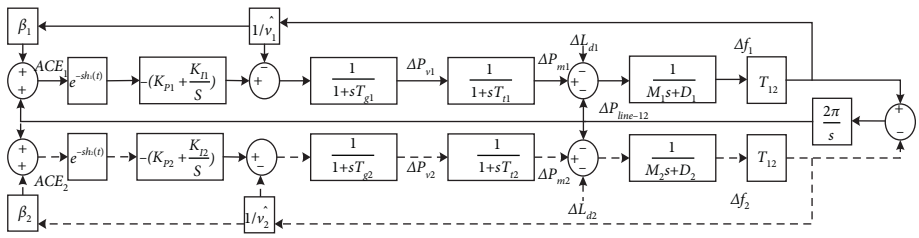

Figure 1: Dynamic model of two-areas LFC scheme and single-area without dotted lines.

$$B=\begin{bmatrix} 0 & 0 & 0 & 0 & 0 & 0 & 0 & 0 & 0 \\ 0 & 0 & 0 & 0 & 0 & 0 & 0 & 0 & 0 \\ -\frac{\gamma_1 K_{P1}}{T_{g1}} & 0 & 0 & -\frac{K_{I1}}{T_{g1}} & -\frac{K_{P1}}{T_{g1}} & 0 & 0 & 0 & 0 \\ 0 & 0 & 0 & 0 & 0 & 0 & 0 & 0 & 0 \\ 0 & 0 & 0 & 0 & 0 & 0 & 0 & 0 & 0 \\ 0 & 0 & 0 & 0 & 0 & 0 & 0 & 0 & 0 \\ 0 & 0 & 0 & 0 & 0 & 0 & 0 & 0 & 0 \\ 0 & 0 & 0 & 0 & \frac{K_{P2}}{T_{g2}} & -\frac{\gamma_2 K_{P2}}{T_{g2}} & 0 & 0 & -\frac{K_{I2}}{T_{g2}} \\ 0 & 0 & 0 & 0 & 0 & 0 & 0 & 0 & 0 \end{bmatrix},$$

$$C=\begin{bmatrix} -\frac{1}{M_1} & 0 & 0 & 0 & 0 & 0 & 0 & 0 & 0 \\ 0 & 0 & 0 & 0 & -\frac{1}{M_2} & 0 & 0 & 0 & 0 \end{bmatrix}^T \quad \Delta L_{\mathrm{d}}(t)=\left[\Delta L_{\mathrm{d1}}(t)\ \ \Delta L_{\mathrm{d2}}(t)\right]^T F(t) \quad =\left[F_1(t)\ \ F_2(t)\right]^T. \tag{4}$$

For the j th area, $j=1,2$, the notations are presented in Table 1.

The dynamic model of the single-area LFC system is shown in Figure 1 without dotted lines. The state vector, disturbance vector, and system matrices of the single-area LFC system are reduced as follows:

$$x(t)=\left[\Delta f(t)\ \ \Delta P_m(t)\ \ \Delta P_v(t)\ \ \int \mathrm{ACE}(t)\mathrm{d}s\right]^T,$$

$$A=\begin{bmatrix} -\frac{D}{M} & \frac{1}{M} & 0 & 0 \\ 0 & -\frac{1}{T_t} & \frac{1}{T_t} & 0 \\ -\frac{1}{\hat{v}T_g} & 0 & -\frac{1}{T_g} & 0 \\ \gamma & 0 & 0 & 0 \end{bmatrix},$$

$$B=\begin{bmatrix} 0 & 0 & 0 & 0 \\ 0 & 0 & 0 & 0 \\ -\frac{\gamma K_P}{T_g} & 0 & 0 & -\frac{K_I}{T_g} \\ 0 & 0 & 0 & 0 \end{bmatrix},$$

$$\Delta L_d(t)=\left[\Delta L_d(t)\right]^T F(t)=\left[F(t)\right]^T,$$

$$C=\left[-\frac{1}{M}\ \ 0\ \ 0\ \ 0\right]^T. \tag{5}$$

Remark 1. When there are $N\,(N>1)$ subareas connected by tie-lines forming a multiarea power system, the dotted line will be copied by N times. The decentralized control strategy is applied in the multiarea power system, which means every control area is independent and has its own LFC center to maintain the balance of generation and load. As a result, the interactions between i th area and other areas,

$\sum_{j=1,j\neq i}^{N} T_{ij}\Delta f_j$, are treated as disturbances for i th area. Then, define $x_i(t) = \mathrm{col}\{\Delta f^T \Delta P_{mi}^T \Delta P_{vi} \int \mathrm{ACE}_i^T \Delta P_{\mathrm{line}-i}^T\}$, where (4) is the expanded form of $x_i(t)$ in two-area power system. And the system matrices of multiareas are listed as follows:

$$A = \begin{bmatrix} A_{11} & A_{12} & \dots & A_{1N} \\ A_{21} & A_{22} & \dots & A_{2N} \\ \vdots & \vdots & \ddots & \vdots \\ A_{N1} & A_{N2} & \dots & A_{NN} \end{bmatrix},$$

$$A_{ii} = \begin{bmatrix} -\frac{D_i}{M_i} & \frac{1}{M_i} & 0 & 0 & -\frac{1}{M_i} \\ 0 & -\frac{1}{T_{chi}} & \frac{1}{T_{chi}} & 0 & 0 \\ -\frac{1}{R_i T_{gi}} & 0 & -\frac{1}{T_{gi}} & 0 & 0 \\ \beta_i & 0 & 0 & 0 & 1 \\ 2\pi\Sigma_{k=1,k\neq i}^{N} T_{ik} & 0 & 0 & 0 & 0 \end{bmatrix},$$

$$A_{ik} = \begin{bmatrix} 0 & 0 & 0 & 0 & 0 \\ 0 & 0 & 0 & 0 & 0 \\ 0 & 0 & 0 & 0 & 0 \\ 0 & 0 & 0 & 0 & 0 \\ 2\pi T_{ik} & 0 & 0 & 0 & 0 \end{bmatrix},$$

$$\begin{aligned} B &= \mathrm{diag}\{B_1, B_2, \dots, B_N\}, \\ B_i &= \begin{bmatrix} 0 & 0 & \frac{1}{T_{gi}} & 0 & 0 \end{bmatrix}^T, \\ C &= \mathrm{diag}\{C_1, C_2, \dots, C_N\}, \\ C_i &= \begin{bmatrix} \beta_i & 0 & 0 & 0 & 1 \\ 0 & 0 & 0 & 1 & 0 \end{bmatrix}, \\ F &= \mathrm{diag}\{F_1, F_2, \dots, F_N\}, \\ F_i &= \begin{bmatrix} -\frac{1}{M_i} & 0 & 0 & 0 & 0 \end{bmatrix}^T, \\ \Delta L_{\mathrm{d}}(t) &= \mathrm{dig}\{\Delta L_{\mathrm{d}1}(t) \dots \Delta L_{\mathrm{d}i}(t)\}. \end{aligned} \tag{6}$$

2.2. Disturbance Parameters and Load Disturbance Model of LFC System. This paper models the unknown disturbance of power system parameters as $\mathrm{NF}(t)(D_1 x(t) + D_2 x(t-h(t))) = Np(t, x(t), x(t-h(t)))$, which is nonlinear function related to current and delayed state vector. Owing to the restriction of $F(t)^T F(t) \leq I$, the following inequalities can be obtained:

$$\begin{aligned} p^T(t, x(t), x(t-h(t)) p(t, x(t), x(t-h(t)))) &= [D_1 x(t) + D_2 x(t-h(t))]^T F^T(t) F(t) [D_1 x(t) + D_2 x(t-h(t))] \\ &\leq [D_1 x(t) + D_2 x(t-h(t))]^T [D_1 x(t) + D_2 x(t-h(t))]. \end{aligned} \tag{7}$$

Similarly, the load disturbance is considered as time-varying nonlinear function with current and delayed state vector as $C\Delta L_d(t) = g(t, x(t), x(t-h(t)))$, which satisfy the following norm-bounded constraints:

$$\|g(t, x(t), x(t-h(t)))\|\| \leq \rho\|\|x(t)\|\| + \tau\|\|x(t-h(t))\|, \tag{8}$$

$$\begin{aligned} &g^T(t, x(t), x(t-h(t))) g(t, x(t), x((t-h(t))) \\ &\quad \leq \rho^2 x^T(t) G^T G x(t) + \tau^2 x^T(t-h(t)) H^T H x(t-h(t)). \end{aligned} \tag{9}$$

where $\rho \geq 0$ and $\tau \geq 0$ represent known scalars. G and H represent known constant matrices with appropriate dimensions. ρ, τ, G, and H bound the magnitude of time-varying load disturbance of power system together.

3. Main Results

Before deriving the main results, Lemma 1 should be introduced. Lemma 1 bounds the integral of quadratic function multiplied by a 1st/2nd degree scalar function [26].

Lemma 1. *For a positive definite matrix M with appropriate dimensions and a vector $f(s)$, the following inequalities can be obtained for all scalar valued function $\kappa(s) \geq 0, s \in [t_1, t_2]$:*

$$-\int_{t_1}^{t_2} \kappa(s) f^T(s) M f(s) \mathrm{d}s \leq \alpha_1 \varepsilon_t^T F_1^T M^{-1} F_1 \varepsilon_t + 2\varepsilon_t^T F_1^T \int_{t_1}^{t_2} \kappa(s) f(s) \mathrm{d}s,$$
$$-\int_{t_1}^{t_2} \kappa^2(s) f^T(s) M f(s) \mathrm{d}s \leq \alpha_2 \varepsilon_t^T F_2^T M^{-1} F_2 \varepsilon_t + 2\varepsilon_t^T F_2^T \int_{t_1}^{t_2} \kappa(s) f(s) \mathrm{d}s. \tag{10}$$

where $\alpha_1 = \int_{t_1}^{t_2} \kappa(s)$ and $\alpha_2 = t_2 - t_1$. And F_1 and F_2 represent appropriate dimensional matrices and ε_t represents arbitrary vector. Then, we can obtain the delay-dependent robust stability criterion of system (3).

Theorem 1. *Given constants h and μ, the considered system (3) is asymptotically stable if there exist positive matrices $P_1, P_2 \in \mathbb{R}^{4n\times 4n}$, $Q_1, Q_2, Q_3 \in \mathbb{R}_+^{2n\times 2n}$, $L_1, L_2 \in \mathbb{R}_+^{n\times n}$, and any matrices $K_1, K_4 \in \mathbb{R}^{2n\times 9n}$ and $K_2, K_3, K_5, K_6 \in \mathbb{R}^{n\times 9n}$ satisfying the following LMIs:*

$$P_1 + h(t)P_2 > 0$$

$$\begin{bmatrix} \Omega_{\beta_1} & hK_1^T & hK_2^T & hK_3^T \\ \star & -hQ_3 & 0 & 0 \\ \star & \star & -L_1 & 0 \\ \star & \star & \star & -\frac{h}{3}L_2 \end{bmatrix} < 0,$$

$$\begin{bmatrix} \Omega_{\beta_2} & hK_1^T & hK_2^T & hK_3^T \\ \star & -hQ_3 & 0 & 0 \\ \star & \star & -L_1 & 0 \\ \star & \star & \star & -\frac{h}{3}L_2 \end{bmatrix} < 0,$$

$$\begin{bmatrix} \Omega_{\beta_3} & hK_3^T & hK_4^T & hK_5^T \\ \star & -hQ_3 & 0 & 0 \\ \star & \star & -L_1 & 0 \\ \star & \star & \star & -\frac{h}{3}L_2 \end{bmatrix} < 0, \tag{11}$$

$$\begin{bmatrix} \Omega_{\beta_4} & hK_3^T & hK_4^T & hK_5^T \\ \star & -hQ_3 & 0 & 0 \\ \star & \star & -L_1 & 0 \\ \star & \star & \star & -\frac{h}{3}L_2 \end{bmatrix} < 0,$$

where $\beta_1, \beta_2, \beta_3$, and β_4 represent $h(t) = 0$ and $\dot{h}(t) = -\mu$, $h(t) = 0$ and $\dot{h}(t) = \mu$, $h(t) = h$ and $\dot{h}(t) = -\mu$, and $h(t) = h$ and $\dot{h}(t) = \mu$, the four situations, respectively. Moreover, the details about other notations are listed in Appendix.

Proof. The Lyapunov functionals are adopted as follows:

$$\begin{aligned} V(t) = &\int_{t-h(t)}^{t} \left[\Xi_1^T(t,s) Q_1 \Xi_1(t,s) + \Xi_2^T(s) Q_1 \Xi_2(s)\right] \mathrm{d}s + \int_{t-h}^{t-h(t)} \left[\Xi_1^T(t,s) Q_2 \Xi_1(t,s) + \Xi_2^T(s) Q_2 \Xi_2(s)\right] \mathrm{d}s \\ &+ \xi^T(t)\left(P_1 + h(t)P_2\right)\xi(t) + \int_{t-h}^{t} \left[(h-t+s)\Xi_2^T(s) Q_3 \Xi_2(s) + \dot{x}^T(s)\left((h-t+s)^2 L_1 + (h-t+s)^3 L_2\right)\dot{x}(s)\right] \mathrm{d}s, \end{aligned} \tag{12}$$

where $\xi(t) = [x^T(t), x^T(t-h(t)), x^T(t-h), \int_{t-h}^{t} x^T(s)\mathrm{d}s]^T$, $\Xi_1(t,s) = [x^T(t), x^T(s)]^T$, $\Xi_2(s) = [x^T(s), \dot{x}^T(s)]^T$.

Then, define $\zeta(t) \in \mathbb{R}^{9n\times 1}$ as $\zeta(t) = [x^T(t) x^T(t-h(t)) x^T(t-h) \int_{t-h}^{t-h(t)} x^T(s)\mathrm{d}s \int_{t-h(t)}^{t} x^T(s)\mathrm{d}s \quad \dot{x}^T(t-h(t)) \dot{x}^T(t-h),\ g^T(t, x(t), x((t-h(t)))p^T\ (t, x(t), x\ (t-h(t)))]^T$; $\zeta^T(t) e_k^T$ represents the k th vector of $\zeta(t)$, e.g., $\zeta^T(t) e_1^T = x^T(t)$.

Computing the derivative of $V(t)$ along the trajectories of system (3):

$$\begin{aligned} \dot{V}(t) = &2\xi^T(t)\left(P_1 + h(t)P_2\right)\dot{\xi}(t) + 2\int_{t-h(t)}^{t} \Xi_1^T(t,s) Q_1 \dot{\Xi}_1^T(t,s)\mathrm{d}s + 2\int_{t-h}^{t-h(t)} \Xi_1^T(t,s) Q_2 \dot{\Xi}_1(t,s)\mathrm{d}s + \dot{h}(t)\xi^T(t) P_2 \xi(t) \\ &+ \Xi_1^T(t,t) Q_1 \Xi_1(t,t) + (1-\dot{h}(t))\Xi_1^T(t, t-h(t))\left[Q_2 - Q_1\right]\Xi_1(t, t-h(t)) + \Xi_2^T(t)\left[Q_1 + hQ_3\right]\Xi_2(t) + h^2 \dot{x}^T(t) L_1 \dot{x}(t) \\ &+ (1-\dot{h}(t))\Xi_2^T(t-h(t))\left[Q_2 - Q_1\right]\Xi_2(t-h(t)) - \Xi_1^T(t, t-h) Q_2 \Xi_1(t, t-h) - \Xi_2^T(t-h) Q_2 \Xi_2(t-h) + h^3 \dot{x}^T(t) L_3 \dot{x}(t) \end{aligned}$$

$$\begin{aligned}&-\int_{t-h}^{t}\Xi_2^T(s)Q_3\Xi_2(s)\mathrm{d}s-2\int_{t-h}^{t}(h-t+s)\dot{x}^T(s)L_1\dot{x}(s)\mathrm{d}s-3\int_{t-h}^{t}(h-t+s)^2\dot{x}^T(s)L_2\dot{x}(s)\mathrm{d}s\\&=\zeta^T(t)\Big(He\Big(G_1^T[P_1+h(t)P_2]G_2+G_3^TQ_1G_4+G_5^TQ_2G_6\Big)+\Pi\Big)\zeta(t)+f_a(t).\end{aligned}\tag{13}$$

The sum of all integral terms is expressed by $f_a(t)$:

$$f_a(t)=-\int_{t-h}^{t}\Big\{\Xi_2^T(s)Q_3\Xi_2(s)+2(h-t+s)\dot{x}^T(s)L_1\dot{x}(s)+3(h-t+s)^2\dot{x}^T(s)L_2\dot{x}(s)\Big\}\mathrm{d}s.\tag{14}$$

Owing to $-(h-t+s)\leq-(h(t)-t+s),\forall s\in[t-h(t),t]$, the following inequalities can be obtained:

$$\begin{aligned}f_a(t)\leq&-\int_{t-h}^{t-h(t)}\Big\{\Xi_2^T(s)Q_3\Xi_2(s)+2(h(t)-t+s)\dot{x}^T(s)L_1\dot{x}(s)+3(h(t)-t+s)^2\dot{x}^T(s)L_2\dot{x}(s)\Big\}\mathrm{d}s\\&-\int_{t-h(t)}^{t}\Big\{\Xi_2^T(s)Q_3\Xi_2(s)+2(h(t)-t+s)\dot{x}^T(s)L_1\dot{x}(s)+3(h(t)-t+s)^2\dot{x}^T(s)L_2\dot{x}(s)\Big\}\mathrm{d}s\\=&\,\Upsilon(t).\end{aligned}\tag{15}$$

Using Lemma 1 to estimate $\Upsilon(t)$:

$$\Upsilon(t)\leq\zeta^T(t)\left\{\begin{array}{c}(h-h(t))K_1^TQ_3^{-1}K_1+2K_1^T(e_4,e_2-e_3)^T+(h-h(t))^2K_2^TL_1^{-1}K_2+4K_2^T[(h-h(t))e_2-e_4]^T\\+3(h-h(t))K_3^TL_2^{-1}K_3+6K_3^T[(h-h(t))e_2-e_4]^T+h(t)K_4^TQ_3^{-1}K_4+2K_4^T[e_5,e_1-e_2]^T\\+h^2(t)K_5^TL_1^{-1}K_5+4K_5^T[h(t)e_1-e_5]^T+3h(t)K_6^TL_2^{-1}K_6+6K_6^T(h(t)e_1-e_5)^T\end{array}\right\}\zeta(t).\tag{16}$$

The following inequality holds for any $\varsigma\geq0$ from (9) and (7), respectively:

$$\begin{aligned}-\varsigma g(.)^Tg(.)+\varsigma\rho^2x^T(t)G^TGx(t)+\varsigma\tau^2x^T(t-h(t))H^THx(t-h(t))\geq0,\\-p(.)^Tp+[D_1x(t)+D_2x(t-h(t))]^T[D_1x(t)+D_2x(t-h(t))]\geq0.\end{aligned}\tag{17}$$

They can be expressed by the augmented state vector $\zeta(t)$, respectively:

$$\begin{aligned}\zeta^T(t)\Big(e_8^T(-\varsigma I)e_8+e_1^T\Big(\varsigma\rho^2G^TG\Big)e_1+e_2^T\Big(\varsigma\tau^2H^TH\Big)e_2\Big)\zeta(t)\geq0,\\\zeta^T(t)e_9^T(-I)e_9+e_1^T\Big(D_1^TD_1\Big)e_1+e_1^T\Big(D_1^TD_2\Big)e_2+e_2^T\Big(D_2^TD_1\Big)e_1+e_2^T\Big(D_2^TD_2\Big)e_2\Big)\zeta(t)\geq0.\end{aligned}\tag{18}$$

By substituting (16) into (13) and adding the inequality (18), the following inequality can be obtained:

$$\dot{V}(t) \le \zeta^T(t)\left\{He\left(G_1^T P G_2 + G_3^T Q_1 G_4 + G_5^T Q_2 G_6 + H_1 + H_2 + H_3\right) + \Pi + \Lambda + \Psi\right\}\zeta(t), \tag{19}$$

where $G_1, G_2, G_3, G_4, G_5, G_6, H_1, H_2, H_3, \Lambda, \Pi$ have been defined in Appendix, and

$$\begin{aligned}\Psi = {} & (h - h(t))K_1^T Q_3^{-1} K_1 + (h - h(t))^2 K_2^T L_1^{-1} K_2 + 3(h - h(t))K_3^T L_2^{-1} K_3 \\ & + h(t)K_4^T Q_3^{-1} K_4 + h(t)H_5^T L_1^{-1} K_5 + 3h(t)K_6^T L_2^{-1} K_6.\end{aligned} \tag{20}$$

Finally, considering $0 \le h(t) \le h$ and $-\mu < \dot{h}(t) < \mu$, inequality (9) is obtained by Schur complement, which ensures the following inequality:

$$\begin{aligned}\dot{V}(t) & \le \zeta^T(t)\left\{He\left(G_1^T P G_2 + G_3^T Q_1 G_4 + G_5^T Q_2 G_6 + H_1 + H_2 + H_3\right) + \Pi + \Lambda + \Psi\right\}\zeta(t), \\ & < -\epsilon\|\zeta(t)\|^2. \exists \epsilon > 0, \\ & \le -\hat{\epsilon}\|x(t)\|^2. \exists \hat{\epsilon} > 0.\end{aligned} \tag{21}$$

Hence, the system is asymptotically stable. The proof is finished. □

Remark 2. The condition of positive matrices $P_1, P_2 \in \mathbb{R}^{4n\times 4n}$, $Q_1, Q_2, Q_3 \in \mathbb{R}_+^{2n\times 2n}$, and $L_1, L_2 \in \mathbb{R}_+^{n\times n}$ in Theorem 1 can guarantee the adopted Lyapunov functionals $V(t)$ being positive. Thus, the positive definite of $V(t)$ and negative definite of $V(t)$ in time domain $[-h, 0]$ can guarantee the asymptotic stability of system (3) in $[-h, 0]$.

Remark 3. Our work has investigated the stability condition of LFC system (3) under the limitation $0 \le h(t) \le h$ and $-\mu \le \dot{h}(t) \le \mu$. The limitation conditions are $0 < h(t) < h, -\mu < \dot{h}(t) < \mu$. That is to say, the stability condition should be satisfied under the four situations, β_1: $h(t) = h_1, \dot{h}(t) = -\mu$, β_2: $h(t) = h_1, \dot{h}(t) = \mu$, β_3: $h(t) = h_2, \dot{h}(t) = -\mu$, and β_4: $h(t) = h_2, \dot{h}(t) = \mu$. $\dot{V}(t) < 0$ must be guaranteed under the four situations. Thus, inequality (9) under $\beta_1 - \beta_4$ in Theorem 1 must be satisfied simultaneously for system asymptotic stability.

Remark 4. The main contribution of this section is to propose a novel Theorem 1 in the form of LMIs which can derive a less conservative result of maximum allowable network delay for LFC system (3). The LKF constructed by literature [36] is $V(t) = x^T(t)Px(t) + \int_{t-\tau(t)}^{t} x^T(s)Q_1 x(s)\mathrm{d}s + \int_{t-\tau}^{t} x^T(s)Q_2 x(s)\mathrm{d}s + \tau\int_{-\tau}^{0}\int_{t+\theta}^{t} \dot{x}^T(s)R\dot{x}(s)\mathrm{d}s\mathrm{d}\theta$. Compared with that, the LKF proposed by this paper has four improvement points. (i) The augmented variable $[x^T(t), x^T(t-h(t)), x^T(t-h), \int_{t-h}^{t} x^T(s)\mathrm{d}s]^T$, rather than $x(t)$ in [36], which can reduce the conservatism by increasing the link between variables. (ii) The time-delay dependent matrix $P_1 + h(t)P_2$ is introduced in quadratic term, rather than constant matrix P in [36], which can reduce the conservatism by introducing more messages about time-varying delay. (iii) The cross terms of variable $\{x(t), x(s)\}, \{x(s), \dot{x}(s)\}$ in $\Xi_1(t,s), \Xi_2(t,s)$ also can reduce the conservatism by increasing the link between variables. (iv) The 4th, 5th, and 6th terms of the novel LKF multiplied by 1st, 2nd, and 3rd degrees of a scalar function $(h - t + s)$. The increasing of $(h - t + s)$ by one signifies the increasing the number of integral by one. Compared with the LKF of literatures [22, 36, 37], we increase the quadratic terms multiplied by 2nd and 3rd degrees of the scalar function $(h - t + s)$, which may reduce the conservatism compared with literatures [22, 36, 37].

Remark 5. If there is a small disturbance or no disturbed load in the LFC system, the delay-dependent robust stability criterion can be developed from Theorem 1 by setting $\rho = 0, \tau = 0$. If there is no or very small disturbance in LFC system parameters, set $N = 0$.

4. Case Studies

In this section, the typical single-area and two-area LFC systems are carried out to analyze the delay margins based on Theorem 1. The parameters of the real two-area LFC system are listed as Table 2. For verifying the less conservatism of our proposed method, the parameters of the two-area LFC system given in [37] are presented in Table 2 for comparison purposes. M, D, γ, T_g, T_t, and $\hat{\nu}$ represent the

Table 2: Parameters of two-area LFC systems.

Parameter	T_t/s	T_g/s	$\hat{v}$	D	γ	M/s	T_{12}
Area 1	0.3	0.1	0.05	1.0	21	10	0.1986
Area 2	0.4	0.17	0.05	1.5	21.5	12	

inertia moments of generator, the generator damping coefficient, the frequency bias factor, time constant of the governor, the turbine time constant, and the speed drop separately. Delay margins with respect to different value of ρ, τ, gains of PI controller are calculated for constant and time-varying time delays. Then, simulation studies based on MATLAB/Simulink are shown to investigate the effect of time delay on control performance and verify the improvement and effectiveness of the Theorem 1 proposed by this paper.

4.1. Theoretical Delay Margins

4.1.1. Single-Area LFC System. The parameters of Area 1 in Table 2 are adopted as single-area LFC system parameters.

Setting K_P as very small, we investigate the effect of Integral (I) controller on delay margin under three situations of load disturbance ($\rho = 0, \tau = 0$; $\rho = 0, \tau = 0.025$; and $\rho = 0.025, \tau = 0.025$) for both constant and time-varying delays. Suppose G and H in (9) and D_1 and D_2 in (8) as $0.1I_n$, where n represents the dimension of the system state vector $x(t)$. It can be seen that $n = 4$ in the single-area LFC system from (5). Theorem 1 is adopted to calculate the delay margins. The results are shown in Table 3 and Figures 2–4.

The following conclusions can be obtained from Table 3 and Figures 2–4:

(i) The increasing of ρ and τ represents that the load fluctuation becomes more pronounced. With the increase in ρ and τ, the delay margin that PI controller can withstand without decrease in losing stability under the same value of μ and K_I. The effect of load disturbance on delay-dependent stability of the LFC system can be obtained.

(ii) It can be seen from Figures 2–4 that the increasing of μ causes the decreasing of delay margin h with the same value of K_I under the three situations of load disturbance ($\rho = 0, \tau = 0$; $\rho = 0, \tau = 0.025$; $\rho = 0.025, \tau = 0.025$). The effect of time delay changing rate on delay-dependent stability of the LFC system can be obtained.

(iii) Simultaneously, it can be seen from Figures 2–4 that maximum allowable network delay decreases with the increasing of K_I with the same value of μ under the three situations of load fluctuation.

As for the nominal system condition ($\rho = 0, \tau = 0$) with constant ($\mu = 0$) and time-varying delay ($\mu = 0.9$), the maximum allowable network delays are listed in Table 4 compared with the other results from literatures [22, 36, 37]. It can be seen that the results calculated by Theorem 1 are less conservative than those of [22, 36, 37], owing to the progressiveness of Lyapunov functional and Lemma 1 adopted by this paper. Therefore, when compared with [22, 36, 37], the results proposed by this paper are more realistic.

Results of the maximum allowable network delays with regard to gains of PI controller (K_P, K_I) are listed in Table 5 and Figure 5 with constant delays ($\mu = 0$) and no load disturbance ($\rho = 0, \tau = 0$) and in Table 6 and Figure 6 with time-varying delays ($\mu = 0.9$) and load disturbance ($\rho = 0.025$, $\tau = 0.025$), separately. Results demonstrate that smaller h is obtained under the bigger K_P, K_I, and a relatively larger h is acquired for the smaller K_P, K_I. h is reduced with the increasing of K_P when $K_I \leq 0.05$. For $K_I \geq 0.1$, h increases at first and then decreases with the increasing of K_P. This results implies that for a given K_I, there is a optimal value of K_P which can acquire the maximum h, which can give guidance to tune PI controller to achieve maximum delay margins. Moreover, it can be found that h of the time-varying delays is smaller and decreases faster than that of constant delays.

4.1.2. Two-Area LFC System. Maximum allowable network delay (h) is calculated by Theorem 1 for the two-area LFC system listed in Table 2 by simplifying the multiple delay as a single delay like (3) and gains of PI controller for two areas as same ($K_{Pi} = K_P$, $K_{Ii} = K_I$). In the two-area LFC system, both the values of G, H, D_1, and D_2 are taken as $0.1I_n$, where $n = 9$.

In two-area LFC system case, for more clearly comparisons with literatures [22, 36, 37], the results are summarized in Table 7 with the condition of ($\rho = 0, \tau = 0$) under constant ($\mu = 0$) and time-varying delay ($\mu = 0.5$). Similarity, the listed results are less conservative than those of [22, 36, 37]. Also, the results of Table 7 show the effect of PI controller gains on the delay margins.

Also, the results of delay margin with respect to gains of PI controller are listed in Table 8 and Figure 7 with constant delay ($\mu = 0$) and no load fluctuation ($\rho = 0, \tau = 0$) and in Table 9 and Figure 8 with time-varying delay ($\mu = 0.9$) and load fluctuation ($\rho = 0.025, \tau = 0.025$), respectively. The delay margin changing trend with regard to gains of PI controller of the two-area LFC system is consistent with that of the single-area LFC system. Hence, the details can be omitted here.

4.2. Simulation Verification. The models of the single-area and two-area LFC system are built in MATLAB/Simulink separately. The simulation results verify the above calculation results. The state vectors (Δf) are selected as the observation since the load fluctuation directly affects the frequency of the LFC system.

Table 3: Delay margin $h \propto K_I$ under three situations of load disturbance (single-area LFC).

K_I		0.05	0.1	0.2	0.4	0.6	1
$\rho = 0 \quad \tau = 0$	$\mu = 0$	32.89	15.752	7.82	3.8213	2.214	0.9824
	$\mu = 0.5$	25.178	10.818	5.812	2.813	1.5123	0.5812
$\rho = 0, \tau = 0.025$	$\mu = 0$	26.124	12.453	6.512	3.541	2.112	0.8721
	$\mu = 0.5$	24.981	9.718	4.774	2.572	1.417	0.4882
$\rho = 0.025, \tau = 0.025$	$\mu = 0$	25.516	12.011	5.918	3.211	1.812	0.743
	$\mu = 0.5$	23.828	7.521	3.514	2.012	1.228	0.334

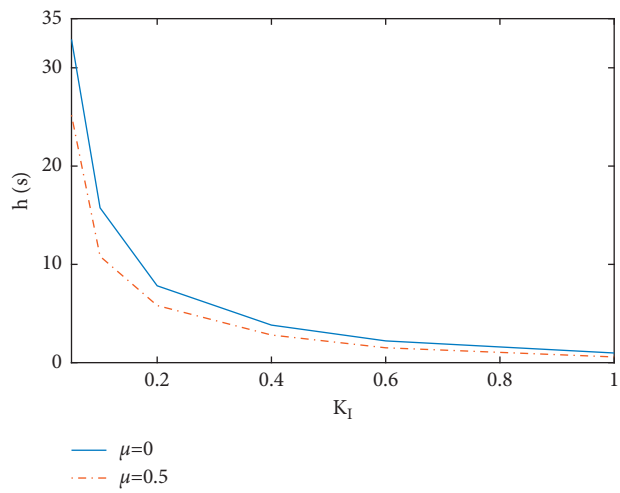

Figure 2: Delay margin $h \propto K_I$ for single-area with $(\rho = 0, \tau = 0)$.

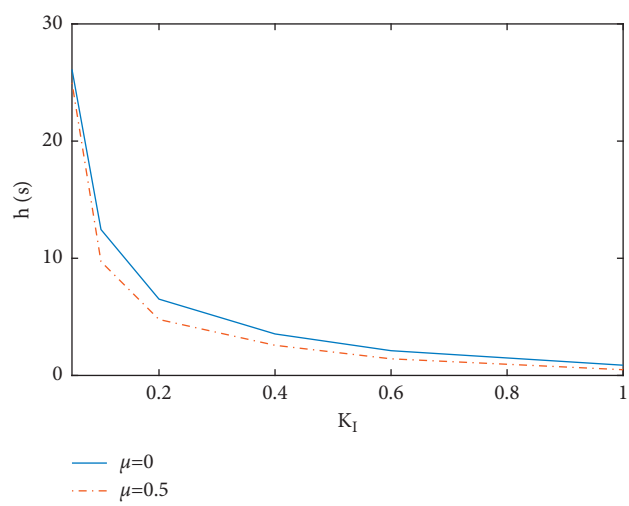

Figure 3: Delay margin $h \propto K_I$ for single-area with $(\rho = 0, \tau = 0.025)$.

4.2.1. Single-Area LFC System. It can be seen from Table 4 that the maximum allowable network delay calculated by Theorem 1 is $h = 6.64$ under the condition of $\rho = \tau = 0, \mu = 0.9, K_P = 0.1, K_I = 0.2$. The time-varying delay $h(t)$ is supposed to be a sine function $h(t) = 3.32 + 3.32\sin(0.27t)$. Figure 9 shows that the state vector Δf converges asymptotically to stable point for $h = 6.64$; however, the delay margin calculated by [22] is 4.67, calculated by [36] is 5.94, and calculated by [37] is 6.59. Moreover, if h exceeds beyond 6.64, the system becomes unstable as shown in Figure 10 for $h = 7s$.

4.2.2. Two-Area LFC System. At first, when $h(t) = 0$, the state-space model of two-area LFC system becomes $\dot{x}(t) = (A + \Delta A + B + \Delta B)x(t) + C\Delta L_d(t)$. Figure 11 shows that the delay-free system is asymptotically stable. It can be seen from Table 9 that the maximum allowable delay

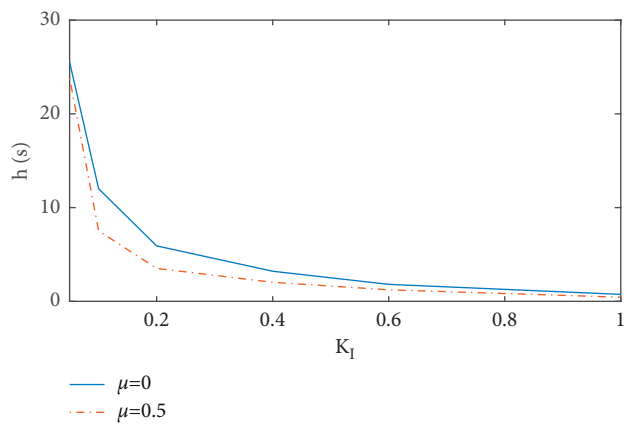

Figure 4: Delay margin $h \propto K_I$ for single-area with $(\rho = 0.025, \tau = 0.025)$.

Table 4: Delay margin h by Theorem 1 for single-area LFC with $\varrho = 0, \tau = 0$.

K_P		0	0	0	0	0	0.1	0.1	0.1	0.1	0.1
K_I		0.05	0.2	0.4	0.6	1	0.05	0.2	0.4	0.6	1
$\mu = 0$	Theorem 1	32.89	7.82	3.8213	2.214	0.9824	32.98	7.89	3.83	2.29	1.12
	[22]	27.92	6.69	3.12	1.91	0.88	27.03	6.94	3.29	2.02	0.96
	[36]	27.92	6.69	3.12	1.91	0.88	27.05	6.94	3.29	2.02	0.96
	[37]	30.91	7.33	3.38	2.04	0.92	31.61	7.79	3.61	2.19	1.01
$\mu = 0.9$	Theorem 1	27.87	6.54	3.02	1.82	0.78	22.84	6.64	3.14	1.86	0.79
	[22]	20.45	4.59	1.81	1.011	0.48	17.39	4.67	1.85	1.05	0.48
	[36]	26.37	6.25	2.85	1.68	0.74	20.25	5.94	2.87	1.75	0.74
	[37]	27.26	6.43	2.91	1.71	0.75	22	6.59	3.11	1.84	0.75

Table 5: Delay margin $h \propto (K_P, K_I)$ for single-area LFC with $\mu = 0, \rho = 0, \tau = 0$.

h	K_P						
K_I	0	0.05	0.1	0.2	0.4	0.6	1
0.05	32.89	31.72	30.98	28.312	26.424	25.124	20.818
0.1	16.43	14.34	16.89	15.24	10.24	5.71	2.14
0.15	9.23	8.82	9.51	8.92	4.14	1.56	0.75
0.2	7.82	6.23	7.89	7.899	3.12	1.52	0.54
0.4	3.8213	2.413	3.83	4.21	3.02	1.42	0.32
0.6	2.214	1.812	2.29	3.31	3.01	1.02	0.12
1	0.9824	0.813	1.12	2.32	2.48	0.83	0.08

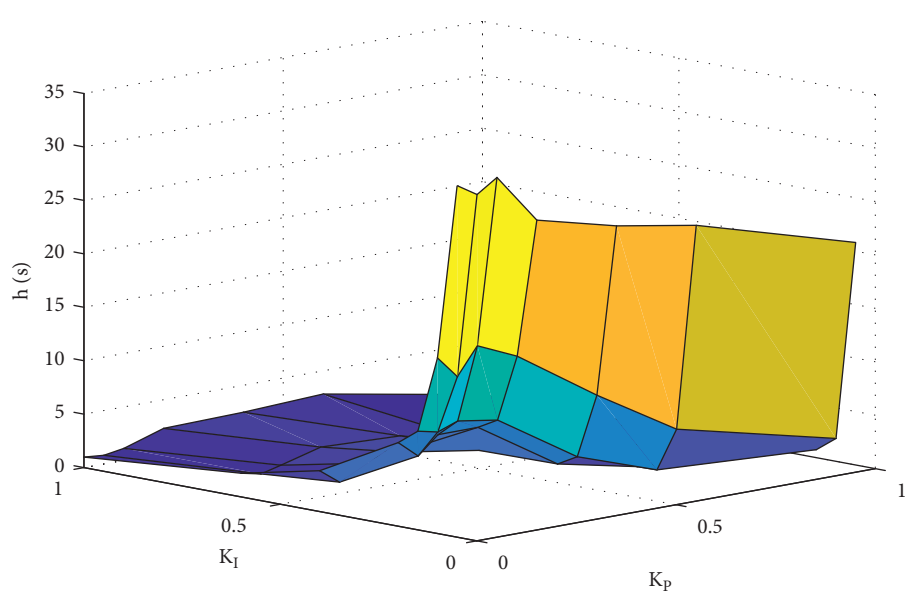

Figure 5: $h \propto (K_P, K_I)$ (single-area with $\mu = 0, \rho = 0, \tau = 0$).

Table 6: Delay margin $h \propto (K_P, K_I)$ for single-area LFC with $\mu = 0.9, \rho = 0.025, \tau = 0.025$.

h	K_P						
K_I	0	0.05	0.1	0.2	0.4	0.6	1
0.05	22.541	21.031	19.383	12.541	2.84	2.6	0.531
0.1	11.830	12.163	11.164	7.802	2.823	2.54	0.527
0.15	8.13	8.153	8.063	6.142	2.804	2.52	0.519
0.2	6.584	7.702	6.472	5.234	2.784	2.11	0.511
0.4	3.612	3.923	3.842	3.436	2.684	2.01	0.5
0.6	2.011	2.048	2.052	1.943	1.67	0.98	0.48
1.0	0.821	0.727	0.741	0.799	0.68	0.54	0.44

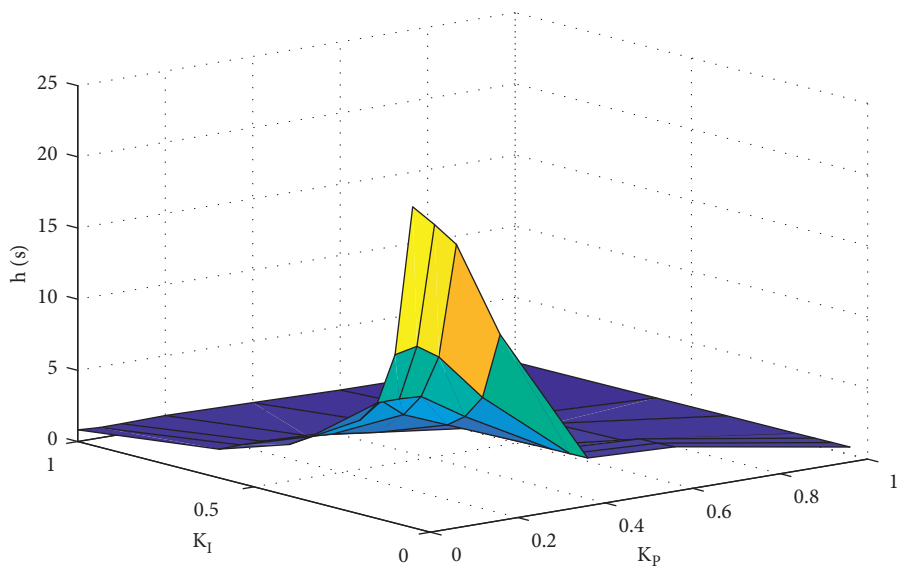

Figure 6: $h \propto (K_P, K_I)$ (single-area with $\mu = 0.9, \rho = 0.025, \tau = 0.025$).

Table 7: Delay margin h by Theorem 1 for two-area LFC with $\varrho = 0, \tau = 0$.

K_P		0	0	0	0	0.1	0.1	0.1
K_I		0.2	0.4	0.6	1	0.2	0.4	0.6
$\mu = 0$	Theorem 1	7.51	3.54	2.1	0.82	7.81	3.52	2.31
	[22]	6.6	3	1.74	0.57	6.88	3.17	1.86
	[36]	6.6	3	1.74	0.57	6.88	3.17	1.86
	[37]	7.23	3.24	1.86	0.58	7.67	3.47	2.01
$\mu = 0.5$	Theorem 1	6.52	2.92	1.84	0.52	6.81	2.92	1.82
	[22]	5.55	2.36	1.18	0.22	5.35	2.55	1.3
	[36]	6.14	2.68	1.4	0.35	6.34	2.83	1.51
	[37]	6.41	2.81	1.54	0.41	6.75	2.84	1.53

Table 8: Delay margin $h \propto (K_P, K_I)$ for two-area LFC with $\mu = 0, \varrho = 0, \tau = 0$.

h	K_P						
K_I	0	0.05	0.1	0.2	0.4	0.6	1
0.05	28.442	28.387	27.521	26.19	21.012	15.328	0.564
0.1	14.699	14.821	14.250	13.782	11.012	8.332	0.464
0.15	9.234	9.524	9.262	8.772	8.014	5.021	0.444
0.2	7.51	7.82	7.93	6.872	5.823	4.621	0.433
0.4	3.54	3.72	3.81	3.92	2.92	2.01	0.384
0.6	2.1	2.24	2.41	2.58	2.24	1.89	0.342
1	0.81	0.92	0.98	1.02	0.92	0.81	0.227

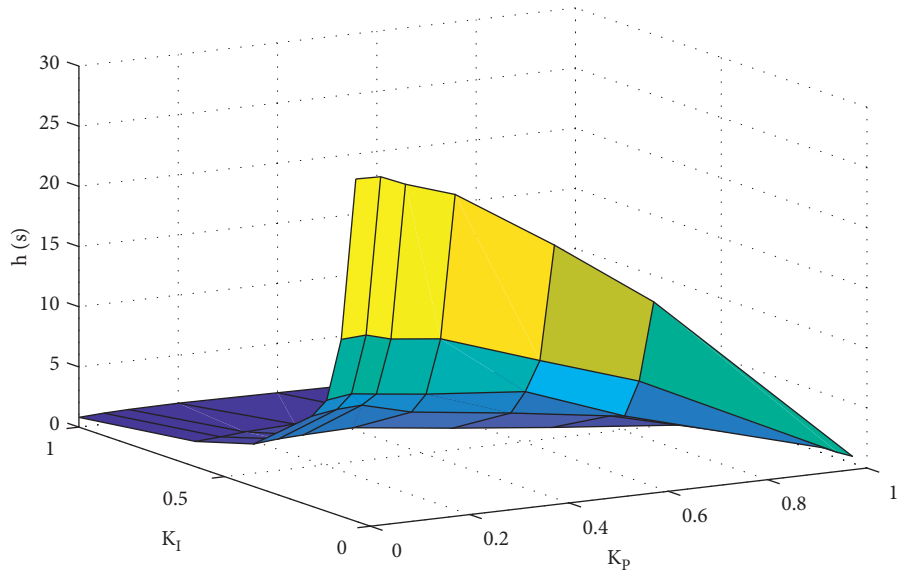

Figure 7: $h \propto (K_P, K_I)$ (two-area LFC with $\mu = 0, \rho = 0, \tau = 0$).

Table 9: Delay margin $h \propto (K_P, K_I)$ for two-area LFC with $\mu = 0.9, \varrho = 0.025, \tau = 0.025$.

h	K_P						
K_I	0	0.05	0.1	0.2	0.4	0.6	1
0.05	24.982	23.982	23.012	21.475	14.464	0.924	0.328
0.1	12.754	13.071	12.63	11.421	7.745	0.912	0.32
0.15	7.917	8.27	8.012	7.259	4.905	0.823	0.312
0.2	6.55	6.97	7.02	6.78	4.62	0.79	0.304
0.4	2.472	2.672	2.854	2.541	1.824	0.62	0.272
0.6	1.92	2.01	2.34	2.48	1.02	0.52	0.24
1	0.32	0.34	0.38	0.4	0.41	0.25	0.172

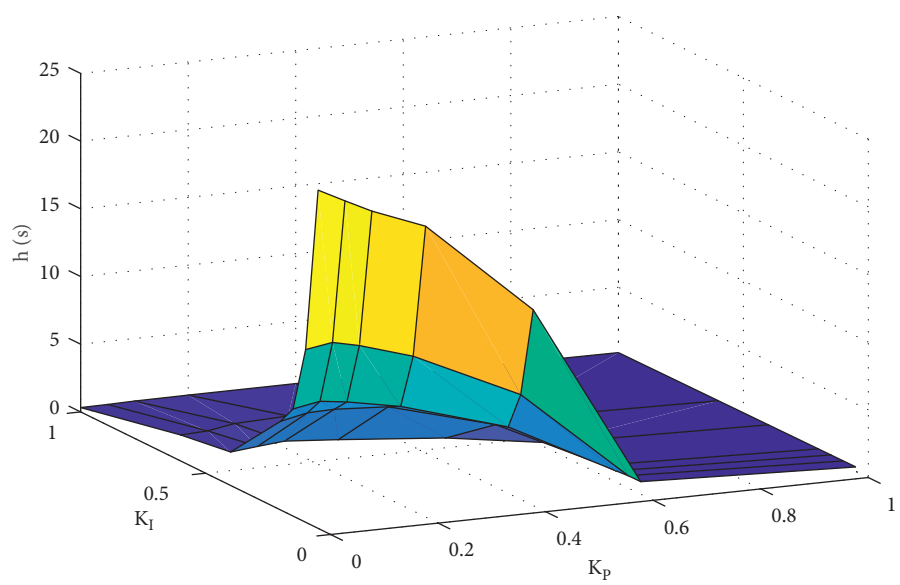

Figure 8: $h \propto (K_P, K_I)$ (two-area LFC with $\mu = 0.9, \rho = 0.025, \tau = 0.025$).

calculated by Theorem 1 is $h = 6.78$ under the condition of $\rho = \tau = 0.025, \mu = 0.9, K_P = K_I = 0.2$. Then, it can be seen from Figure 11 that the two-area LFC system is asymptotically stable under $h = 6.78$. Moreover, if h exceeds beyond 6.78, the system becomes unstable as shown in Figure 12 for $h = 7s$.

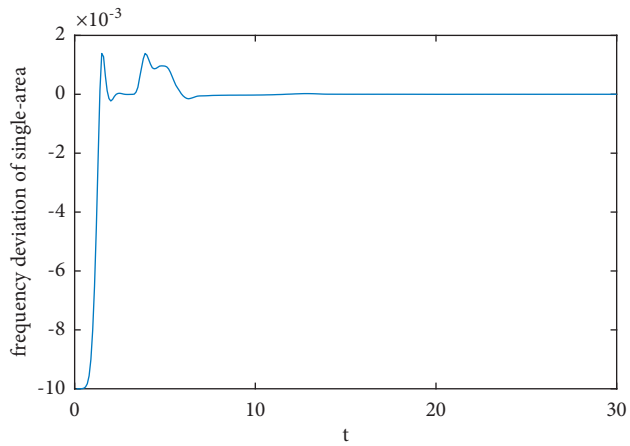

Figure 9: Frequency responses with $h = 6.64\,(\mu = 0.9)$ of single-area.

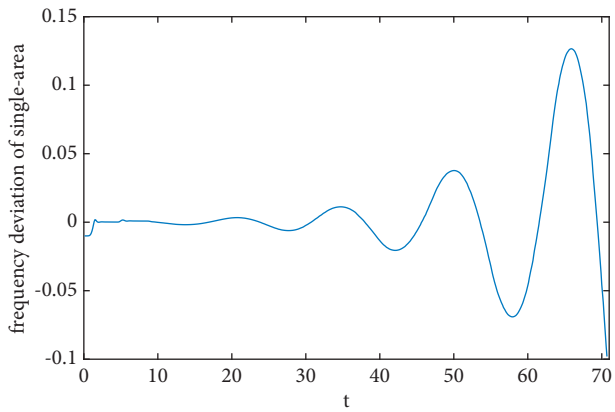

Figure 10: Frequency responses with $h = 7$ of single-area.

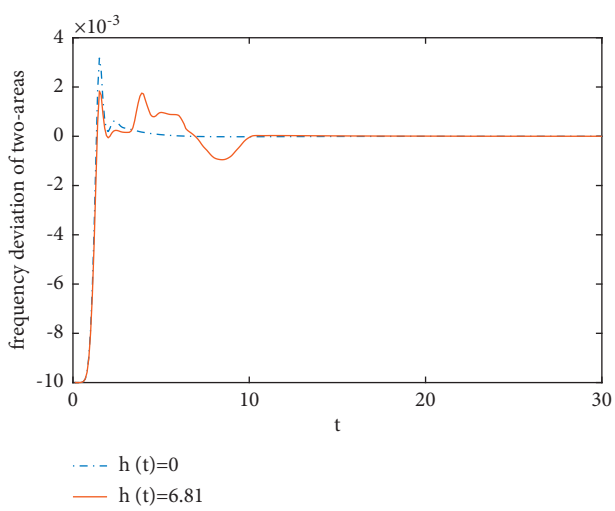

Figure 11: Frequency responses with $h = 6.81\,(\mu = 0.5)$ and without delay of two areas.

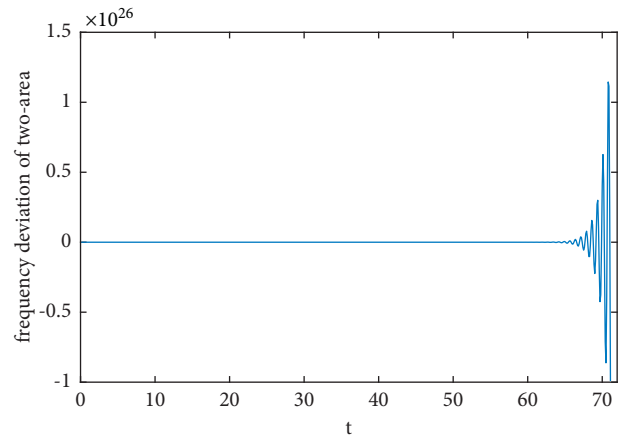

Figure 12: Frequency responses with $h = 7$ of two areas.

5. Conclusion

The stability criterion for the time-varying delay LFC system with nonlinearly load disturbance and random disturbance of system parameters has been investigated by adopting a novel simple LKF and integral inequality (Lemma 1). Considering the exogenous load disturbance and random disturbance of system parameters as constrained nonlinearly function, a time-varying delay system is modeled to describe the delayed LFC system. The novel simple LKF includes delay-dependent matrix in quadratic term, cross terms of variables, and quadratic terms multiplied by 1st, 2nd, and 3rd degrees of scalar function. Lemma 1 is adopted to bound the quadratic terms multiplied 1st and 2nd degrees of scalar function emerging in the derivative of LKF. The results of the novel simple LKF contributing to reduce conservatism and the relationships between the time delay varying rate, load disturbance degree, the gains of PI controller, and delay

margins are derived by the case studied. Meanwhile, simulation verifies the effectiveness and superiority of our results. Nevertheless, the security threats in actual communication network such as denial of service (DOS) attacks and deception attacks are not considered in our work. In the future, how to analyze the stability of the LFC system under the simultaneous existence of various network attack, such as DOS and deception attacks, will be the focus of our following work.

Appendix

$$
\begin{aligned}
\Omega &= He\left(G_1^T\left(P_1 + h(t)P_2\right)G_2 + G_3^T Q_1 G_4 + G_5^T Q_2 G_6 + H_1 + H_2 + H_3\right) + \Pi + \Lambda,\\
G_1 &= \left[e_1^T e_2^T e_3^T e_4^T + e_5^T\right]^T,\\
G_2 &= \left[A_c^T e_6^T e_7^T e_1^T - e_3^T\right]^T,\\
G_3 &= \left[h(t)e_1^T e_5^T\right]^T,\\
G_4 &= \left[A_c^T e_0^T\right]^T,\\
G_5 &= \left[(h - h(t))e_1^T e_4^T\right]^T,\\
G_6 &= \left[A_c^T e_0^T\right]^T,\\
H_1 &= \left[e_4^T e_2^T - e_3^T\right]K_1 + \left[e_5^T e_1^T - e_2^T\right]K_4,\\
H_2 &= 2\left((h - h(t))e_2^T - e_4^T\right)K_2 + 2\left(h(t)e_1^T - e_5^T\right)K_5,\\
H_3 &= 3\left((h - h(t))e_2^T - e_4^T\right)K_3 + 3\left(h(t)e_1^T - e_5^T\right)K_6,\\
\Pi &= \dot{h}(t)\left[e_1^T e_2^T e_3^T e_4^T + e_5^T\right]P_2\left[e_1^T e_2^T e_3^T e_4^T + e_5^T\right]^T + \left[e_1^T e_1^T\right]Q_1\left[e_1^T e_1^T\right]^T - (1 - \dot{h}(t))\left[e_1^T e_2^T\right]Q_1\left[e_1^T e_2^T\right]^T\\
&\quad + \left[e_1^T A_c^T\right]Q_1\left[e_1^T A_c^T\right]^T - (1 - \dot{h}(t))\left[e_2^T e_6^T\right]Q_1\left[e_2^T e_6^T\right]^T + (1 - \dot{h}(t))\left[e_1^T e_2^T\right]Q_2\left[e_1^T e_2^T\right]^T - \left[e_1^T e_3^T\right]Q_2\left[e_1^T e_3^T\right]^T\\
&\quad + (1 - \dot{h}(t))\left[e_2^T e_6^T\right]Q_2\left[e_2^T e_6^T\right]^T - \left[e_3^T e_7^T\right]Q_2\left[e_3^T e_7^T\right]^T + h\left[e_1^T A_c^T\right]Q_3\left[e_1^T A_c^T\right]^T + A_c^T\left(h^2 L_1 + h^3 L_2\right)A_c,\\
\Lambda &= -e_8^T(\varsigma I)e_8 + e_1^T\left(\varsigma\rho^2 G^T G\right)e_1 + e_2^T\left(\varsigma\tau^2 H^T H\right)e_2 - e_9^T(I)e_9 + e_1^T\left(D_1^T D_1\right)e_1 + e_1^T\left(D_1^T D_2\right)e_2 + e_2^T\left(D_2^T D_1\right)e_1 + e_2^T\left(D_2^T D_2\right)e_2,\\
e_i &= \left[0_{n\times(i-1)n}\, I_n\, 0_{n\times(9-i)n}\right] \quad i = 1, 2, \ldots, 9,\\
e_0 &= 0_{n\times 9n},\\
A_C &= \left[\mathrm{AB}0_{n\times 5n} I_n N\right].
\end{aligned}
\tag{A.1}
$$

Data Availability

The raw/processed data required to reproduce these findings cannot be shared at this time as the data also form part of an ongoing study.

Conflicts of Interest

The authors declare that there are no conflicts of interest.

Authors' Contributions

The manuscript was approved by all authors for publication.

Acknowledgments

This work was supported by the National Natural Science Foundation of China under Grant Nos. 61703060, 12061088, 61802036, and 61873305, the Sichuan Science and Technology Program under Grant No. 21YYJC0469, the project funded by China Postdoctoral Science Foundation under Grant Nos. 2020M683274 and 2021T140092, the Open Research Project of the State Key Laboratory of Industrial Control Technology, Zhejiang University, China, under Grant No. ICT2021B38, the Guangdong Basic and Applied Basic Research Foundation under Grant No. 2021A1515011692, and the Central Government Funds of Guiding Local Scientific and Technological Development for Sichuan Province of China under Grant No. 2021ZYD0012.

References

[1] A. Naveed, Ş. Sönmez, and S. Ayasun, "Impact of electric vehicle aggregator with communication time delay on stability regions and stability delay margins in load frequency

control system," *Journal of Modern Power Systems and Clean Energy*, vol. 9, no. 3, pp. 595–601, 2021.

[2] H. Bevrani, A. Ghosh, and G. Ledwich, "Renewable energy sources and frequency regulation: survey and new perspectives," *IET Renewable Power Generation*, vol. 4, no. 5, pp. 438–457, 2010.

[3] I. P. Kumar and D. P. Kothari, "Recent philosophies of automatic generation control strategies in power system," *IEEE Transactions on Power Systems*, vol. 20, pp. 346–357, 2005.

[4] P. S. Kundur, *Power System Stability and Control*, McGraw-Hill, New York, USA, 1994.

[5] H. Bevrani, *Robust Power System Frequency Control*, Springer, New York, USA, 2009.

[6] F. W, K. Moslehi, and A. Bose, "Power system control centers: past, present, and future," *Proceedings of the IEEE*, vol. 93, no. 11, pp. 1890–1908, 2005.

[7] K. Shi, Y. Tang, X. Liu, and S. Zhong, "Secondary delay-partition approach on robust performance analysis for uncertain time-varying Lurie nonlinear control system," *Optimal Control Applications and Methods*, vol. 38, no. 6, pp. 1208–1226, 2017.

[8] K. Shi, Y. Tang, X. Liu, and S. Zhong, "Non-fragile sampled-data robust synchronization of uncertain delayed chaotic Lurie systems with randomly occurring controller gain fluctuation," *ISA Transactions*, vol. 66, pp. 185–199, 2017.

[9] K. Shi, Y. Tang, S. Zhong, C. Yin, X. G. Huang, and W. Wang, "Nonfragile asynchronous control for uncertain chaotic Lurie network systems with Bernoulli stochastic process," *International Journal of Robust and Nonlinear Control*, vol. 28, no. 5, pp. 1693–1714, 2018.

[10] K. Shi, J. Wang, Y. Tang, and S. Zhong, "Reliable asynchronous sampled-data filtering of T-S fuzzy uncertain delayed neural networks with stochastic switched topologies," *Fuzzy Sets and Systems*, vol. 381, no. 15, pp. 1–25, 2020.

[11] K. Shi, J. wang, S. Zhong, Y. Tang, and J. Cheng, "Non-fragile memory filtering of T-S fuzzy delayed neural networks based on switched fuzzy sampled-data control," *Fuzzy Sets and Systems*, vol. 394, pp. 40–64, 2020.

[12] F. Milano and M. Anghel, "Impact of time delays on power system stability," *IEEE Transactions on Circuits and Systems I: Regular Papers*, vol. 59, no. 4, pp. 889–900, 2012.

[13] S. Wang, X. Meng, and T. Chen, "Wide-area control of power systems through delayed network communication," *IEEE Transactions on Control Systems Technology*, vol. 20, no. 2, pp. 495–503, 2012.

[14] A. Sargolzaei, K. K. Yen, and M. N. Abdelghani, "Preventing time-delay switch attack on load frequency control in distributed power systems," *IEEE Transactions on Smart Grid*, vol. 7, pp. 1–10, 2015.

[15] S. Wen, X. Yu. Z. Zeng, and J. Wang, "Event-triggering load frequency control for multi area power systems with communication delays," *IEEE Transactions on Industrial Electronics*, vol. 63, no. 2, pp. 1308–1317, 2016.

[16] V. P. Singh and N Kishor, "Load frequency control with communication topology changes in smart grid," *IEEE Transactions on Industrial Informatics*, vol. 12, no. 5, pp. 1943–1952, 2016.

[17] S. Sonmez, S. Ayasun, and C. O. Nwankpa, "An exact method for computing delay margin for stability of load frequency control systems with constant communication delays," *IEEE Transactions on Power Systems*, vol. 31, no. 1, pp. 370–377, 2016.

[18] H. J. Jia and X. D. Yu, "A simple method for power system stability analysis with multiple time delays," in *Proceedings of the 2008 IEEE Power and Energy Society General Meeting - Conversion and Delivery of Electrical Energy in the 21st Century*, pp. 20–24, Pittsburgh, PA, USA, July 2008.

[19] N. Olgac and R. Sipahi, "An exact method for the stability analysis of time-delayed linear time-invariant (LTI) systems," *IEEE Transactions on Automatic Control*, vol. 47, no. 5, pp. 793–797, 2002.

[20] R. Sipahi and N. Olgac, "Complete stability robustness of third-order LTI multiple time-delay systems," *Automatica*, vol. 41, no. 8, pp. 1413–1422, 2005.

[21] Z. Y. Liu, C. Z. Zhu, and Q. Y. Jiang, "Stability analysis of time delayed power system based on cluster treatment of characteristic roots method," in *Proceedings of the 2008 IEEE Power and Energy Society General Meeting - Conversion and Delivery of Electrical Energy in the 21st Century*, pp. 20–24, Pittsburgh, PA, USA, July 2008.

[22] L. Jiang, W. Yao, Wu, Wen, and Cheng, "Delay-dependent stability for load frequency control with constant and time-varying delays," *IEEE Transactions on Power Systems*, vol. 27, no. 2, pp. 932–941, 2012.

[23] C. K. Zhang, L. Jiang, Wu, Y. He, and M. Wu, "Further results on delay-dependent stability of multi-area load frequency control," *IEEE Transactions on Power Systems*, vol. 28, no. 4, pp. 4465–4474, 2013.

[24] F. Yang, J. He, and Q. Pan, "Further improvement on delay-dependent load frequency control of power systems via truncated B-L inequality," *IEEE Transactions on Power Systems*, vol. 33, no. 5, pp. 5062–5071, 2018.

[25] K. S. Ko and D. K. Sung, "The effect of EV aggregators with time-varying delays on the stability of a load frequency control system," *IEEE Transactions on Power Systems*, vol. 33, no. 1, pp. 669–680, 2018.

[26] J. H. Kim, "Note on stability of linear systems with time-varying delay," *Automatica*, vol. 47, pp. 2118–2121, 2011.

[27] E. Fridman, U. Shaked, and K. Liu, "New conditions for delay-derivative-dependent stability," *Automatica*, vol. 45, no. 11, pp. 2723–2727, 2009.

[28] J. Sun, G. Liu, J. Chen, and D. Rees, "Improved delay-range-dependent stability criteria for linear systems with time-varying delays," *Automatica*, vol. 46, no. 2, pp. 466–470, 2010.

[29] Y. He, Q. G. Wang, L. H. Xie, and C. Lin, "Further improvement of free-weighting matrices technique for systems with time-varying delay," *IEEE Transactions on Automatic Control*, vol. 52, no. 2, pp. 293–299, 2007.

[30] A. Seuret and F. Gouaisbaut, "Wirtinger-based integral inequality: application to time-delay systems," *Automatica*, vol. 49, no. 9, pp. 2860–2866, 2013.

[31] P. G. Park, W. I. Lee, and S. Y. Lee, "Auxiliary function-based integral inequalities for quadratic functions and their applications to time-delay systems," *Journal of the Franklin Institute*, vol. 352, no. 4, pp. 1378–1396, 2015.

[32] F. Yang and H. Zhang, "T-S model-based relaxed reliable stabilization of networked control systems with time-varying delays under variable sampling," *International Journal of Fuzzy Systems*, vol. 13, pp. 260–269, 2011.

[33] C. K. Zhang, L. Jiang, Q. H. Wu, Y. He, and M. Wu, "Delay-dependent robust load frequency control for time-delay power systems," *IEEE Transactions on Power Systems*, vol. 28, no. 3, pp. 2192–2201, 2013.

[34] K. Ramakrishnan, "Improved results on delay-dependent stability of LFC systems with multiple time-delays," *Journal of Control, Automation and Electrical Systems*, vol. 26, no. 3, pp. 235–240, 2015.

[35] H. C. Luo, I. A. Hiskens, and Z. Hu, "Stability analysis of load frequency control systems with sampling and transmission delay," *IEEE Transactions on Power Systems*, vol. 35, no. 5, pp. 3603–3615, 2020.

[36] K. Ramakrishnan and G. Ray, "Stability criteria for nonlinearly perturbed load frequency systems with time-delay," *IEEE Journal on Emerging and Selected Topics in Circuits and Systems*, vol. 5, no. 3, pp. 383–392, 2015.

[37] F. S. Yang, J. He, and D. H. Wang, "New stability criteria of delayed load frequency control systems via infinite-series-based inequality," *IEEE Transactions on Industrial Informatics*, vol. 14, no. 1, pp. 231–240, 2018.

Hindawi
Discrete Dynamics in Nature and Society
Volume 2022, Article ID 4494411, 12 pages
https://doi.org/10.1155/2022/4494411

Research Article

Cerebral Arterial Stenosis Detection Based on a Retained Two-Stage Detection Algorithm

Hanqing Liu,[1] **Xiaojun Li**,[1,2] **Jin Wei**,[3] **and Xiaodong Kang**[1]

[1]*School of Medical Technology, Tianjin Medical University, Tianjin 300202, China*
[2]*Chongqing Qianjiang Center Hospital, Chongqing 409000, China*
[3]*Tianjin Third Central Hospital, Tianjin 300171, China*

Correspondence should be addressed to Jin Wei; wj9717@sina.com and Xiaodong Kang; kxd2004@126.com

Received 28 January 2022; Accepted 17 March 2022; Published 26 April 2022

Academic Editor: Jinliang Wang

Stroke is one of the fatal diseases worldwide, and its primary mechanism is produced by cerebrovascular stenosis, blockages, or embolisms. Computer-aided diagnosis can assist clinical practitioners in identifying cerebrovascular anomalies, elucidating the precise lesions' location in the patients, and providing guidance for clinical therapy. Due to different portions of the cerebrovascular possessing diverse morphological properties and the limited narrow area, the detection effect is unsatisfactory. A retrained two-stage algorithm for detecting cerebral arterial stenosis in CTA images is proposed to solve these problems by further fusing image features and improving the quality of regions of interest. In Faster R-CNN and Libra R-CNN, the backbone network was Resnet50, with deformable convolutional and nonlocal neural networks introduced in the third, fourth, and fifth stages of the backbone network. Deformable convolutional networks learned offsets to extract morphological features of blood vessels in different tomographic planes. Nonlocal neural networks fused global information and extracted global features from location information of feature maps. A cascade detector refined object classification and bounding box regression before prediction. The experimental results show that the retained algorithm increases mAP by 7.3% and 7.5%, respectively, compared with Faster R-CNN and Libra R-CNN. Deformable convolutional networks, nonlocal neural networks, and cascade detectors are incorporated into further feature fusion; thus, semantic information about the cerebrovascular structure is learned, demonstrating more accurate stenotic region detection and demonstrating generalizability across different two-stage algorithms.

1. Introduction

Cerebrovascular disease is currently the world's second leading cause of mortality [1], with ischemic stroke being the most common type. As the primary pathogenesis of ischemic stroke, the atherosclerotic plaques cling to the vessel wall over time, restricting the lumen. Plaques can easily account for embolism, and prolonged ischemia develops as ischemic stroke [2]. Due to its speed, low physical trauma, and cost, computed tomography angiography (CTA) is frequently the first-choice radiological assessment approach for cerebrovascular disorders. Therefore, computer-aided detection (CAD) as liaison with CTA images to identify cerebrovascular stenosis can automatically assist clinicians in diagnosing abnormalities and pinpointing the precise site of lesions.

Traditional detection approaches for vascular stenosis mainly employ machine learning algorithms [3–6], which heavily rely on handcrafted features. Designing and extracting features is time-consuming and prone to human mistakes. Furthermore, traditional machine learning approaches are not competent for local and global encoding information in which they lack the semantic content of vascular image characteristics.

The advent of the convolutional neural network (CNN) has substantially increased object identification accuracy and delivered significant advances to the field of computer vision in recent years. The real-time application of a deep neural network is achievable. It attributes to the rapid growth of hardware technologies, massive data, structured information, and image processors, in which accuracy exceeds that

of many other advanced methods. The two-stage detection algorithm, which combines the proposal detector and region classifier, has gradually become prevalent because of the success of R-CNN (Region-Convolution Neural Network). Previously, the idea of region feature extraction was proposed by SPP-Net (Spatial Pyramid Pooling-Net) [7] and Fast R-CNN [8] to decrease redundant calculations in R-CNN and enhance response speed. Faster R-CNN [9] followed, achieving further acceleration by introducing a regional proposal network (RPN). The shallow layers typically learn location information, while the deep layers are responsible for semantic information. Faster R-CNN only employs the last layer (i.e., high-dimensional features) for object detection and top layer for feature prediction. It neglects feature information from other layers, resulting in a clear lack of detection capabilities for small objects. Feature pyramid networks (FPN) [10] integrate high- and low-dimensional feature information to produce fused features extracted for prediction and then provide a more substantial detection effect.

Lesion detection methods combined with deep learning also perform well in medical image processing. For example, Joo et al. [11] employed a 3D residual network combined with magnetic resonance imaging (MRI) images of the brain to the detection of aneurysms; high sensitivity and positive predictive specificity were obtained through internal and external dataset verification; Fast R-CNN was used by Smistad and Løvstakken [12] to detect deep venous thrombosis in ultrasonography, cross validation was carried out in the femoral regional dataset, and the average accuracy was 94.5%, while the accuracy was 96% in the carotid data set. Stib et al. [13] located cerebral vascular embolism sites by using DenseNet in multiphase CTA images with an AUC of 0.89, sensitivity of 100%, and specificity of 77%. De et al. [14] employed a residual encoder-decoder convolutional neural network to determine the core position of the coronary artery and a fully connected neural network to estimate the lumen cross-sectional area and demonstrated the method's viability in CT image analysis. Dai et al. [15] extracted 2D neighborhood projection images from 3D CTA images and combined them with Faster R-CNN to complete the detection of cerebral aneurysms, which was better for detecting aneurysms larger than 3 mm with a sensitivity of 96.7%. Yang et al. [16] incorporated a convolutional block attention module to Resnet18, which uses dense, atrous convolution and residual multikernel pooling blocks between encoding and decoding stages to perform intracranial aneurysm risk assessment. The algorithm detected cerebral aneurysms on CTA images with a sensitivity of 97.5%. Shinohara et al. [17] employed deep convolutional neural networks to detect hyperdense middle cerebral artery sign (HMCAS) in CT for the identification of acute cerebral infarction in the supply region. The approach effectively detects acute ischemic stroke by identifying HMCAS on noncontrast CT, with cross-validation sensitivity, specificity, accuracy, and AUC area of 82.9%, 89.7%, 86.5%, and 0.947, respectively. Hong et al. [18] fed coronary CTA dataset into CNN to quantify stenosis, and it was no significant differences between expert practitioners and the deep learning (DL) method. Chen et al. [19] assessed coronary artery stenosis with the DL method; diagnostic performances from three aspects showed that DL could take a faster and more precise response.

Although CTA plays a role as the convenient radiologic modality for cerebral arterial stenosis, the lesion location is usually not visible, and clinicians must still be strongly reliant on their discipline. Meanwhile, prolonged diagnosis raises the risk of misdiagnosis or missed diagnosis. Cerebral arteries can exhibit different shapes depending on the tomographic level, such as round, oval, shuttle, or irregular shapes. Due to individual differences among patients, feature maps are required to obtain more semantic information to detect the condition of the arteries to the greatest extent possible. The small stenosis area will lead to problems, such as sample imbalance when sampling positive and negative samples.

This paper proposes a retrained two-stage detection algorithm to identify the qualities of cerebrovascular stenosis in CTA images, improving the lesion detection performance, especially for small vessels. Faster R-CNN, classical two-stage detection neural network, and Libra R-CNN, which can effectively solve sampling imbalance, are utilized in lesion detection. Deformable convolutional networks and nonlocal neural networks were incorporated into the backbone in turn, and a cascade detector refines object classification and bounding box regression to solve the following three problems:

(1) Deformational characteristics of cerebral arteries and lesions with different tomographic levels

(2) Integrating semantic features on the lesions' global location information

(3) Optimizing the detection performance by increasing the threshold value of (intersection over union) IoU in stages

2. Libra R-CNN

An object detection network is trained in the following three stages: candidate region generation and selection, feature extraction, and category classification and bounding box regression, among others. In the detection task, the networks' performance is frequently limited by the imbalance of sample, feature, and object levels. Therefore, Libra R-CNN recommends IoU balanced sampling, a balance feature pyramid (BFP), and a balanced L1 loss function [21].

2.1. IoU Balance Sample. Difficult samples have larger loss functions, while easy samples have smaller ones. Difficult samples are essential during sampling because they are more effective at improving detection performance. A random method of selecting positive and negative samples after training the detector and generating certain boxes may result in most candidate boxes with negative samples lying in a smaller region with the IoU of the ground truth. Assume that N negative samples are drawn from a sample of M matching

candidates and that the probability of each sample being chosen at random is

$$p = \frac{N}{M}. \tag{1}$$

The IoU threshold interval is divided into K copies to increase the probability of difficult negative samples being selected. The same quantity of negative samples are sampled in each subinterval (if the average number is not reached, all samples in that subinterval are obtained), ensuring that the sampled negative samples reach as balanced a state as possible in the different IoU subintervals, and the IoU balanced sampling probability is

$$p_k = \frac{N}{K} * \frac{1}{M_k},\ k \in [0, K). \tag{2}$$

The quantity of sampling candidates in the corresponding interval K is M_k in equation (2). The default value in this study is 2, which means that the negative samples are divided into two parts according to IoU. The samples larger than the threshold are bucketed according to IoU to calculate the quantity of samples that should fall in each bucket. Finally, the negative samples with uniform IoU distribution are obtained, and the samples below the threshold are randomly sampled.

2.2. Balanced Feature Pyramid. Features' output from the backbone is fused in the FPN with the lateral connections. The feature maps of the enhanced FPN structure's output are completed in the BFP for the four-ordered steps: rescale, integrate, refine, and strengthen. The BFP is shown in Figure 1.

(1) Rescale: network proposes to obtain balanced semantic features, the semantic features of each layer must first be rescaled, and the feature maps output from the $\{C2, C3, C4, C5\}$ layers must then be unified in the $C4$ layer via interpolation and downsampling.

(2) Integrate: after unification, the feature maps are fused, and different levels of features are integrated with expressions such as

$$C = \frac{1}{L} \sum_{l=l_{\min}}^{l_{\max}} C_l, \tag{3}$$

where C_l denotes the feature at resolution level l, L the number of multilevel features, and $l_{\max}$ and $l_{\min}$ the highest and lowest level indices, respectively.

(3) Refine: it provided that convolutional kernels or nonlocal neural networks refine balanced semantic features, making more discriminators. The convolutional kernels typically have a smaller receptive field and learn local features, whereas the nonlocal neural network can incorporate more spatial location information and use the difference between local and global features to find more salient parts of the image, acquiring richer semantic features.

(4) Strengthen: the feature maps after being strengthened are added to the original feature maps of different layers to produce the enhanced FPN output $\{P2, P3, P4, P5\}$.

2.3. Balanced L1 Loss. The loss function in the object detection tasks is the sum of the classification and regression. Provided that the classification score is high, the final prediction result will have higher accuracy even if the regression is poor, so the weight of the regression loss function should be increased. In PRN, the smooth L1 loss function is frequently used to calculate the regression, the gradient corresponding to the difficult samples. In smooth L1, the gradient of the difficult samples is greater than that of the easy samples, resulting in an imbalance in the learning ability of the different samples. By smoothing the gradient at the boundary between the difficult and easy samples in the balanced L1 loss function, the balanced L1 loss function improves smooth L1:

$$\begin{aligned} &\frac{a}{b}(b|x| + 1)\ln(b|x| + 1) - \alpha|x|, \text{if } |x| < 1, \\ &\gamma|x| + C, \quad \text{otherwise}, \end{aligned} \tag{4}$$

where $\gamma = \alpha\ln(b+1)$ is defined, and the balance of loss functions between classification and regression is achieved by adjusting values of α and γ.

3. Related Work

A retrained two-stage object detection algorithm is presented in this section. Figure 2 depicts the flowchart of this study, which includes deformable convolutional networks and nonlocal networks in the backbone, as well as a cascade detector in the final prediction.

3.1. Deformable Convolutional Network. Stacking multiple convolutional layers, CNN can learn high-dimension semantic features automatically. Nevertheless, the convolutional kernels and pooling layers cannot adapt to spatial features. In a standard convolutional kernel, convolutional units sample the input feature map at a fixed position, and typical pooling layers (e.g., the average or maximum pooling layer) are fixed as well. They cannot be adaptively learned for feature downsampling, making it difficult to adapt to objects of various scales or shapes.

Standard convolutional operations, in which the activation units of the same convolutional layer all have the same receptive field, are not desirable for shallow networks encoding location information because of the complexity of the vascular structure. Different locations may correspond to objects of different geometries, and these layers require methods to adjust the scale or receptive field automatically. Deformable convolutional networks [22] learn offsets in the receptive fields to approximate the vessel shapes.

Precisely, a two-dimensional offset is calculated for inputted image pixels to construct deformable sampling point locations. The sampled position of each pixel with the

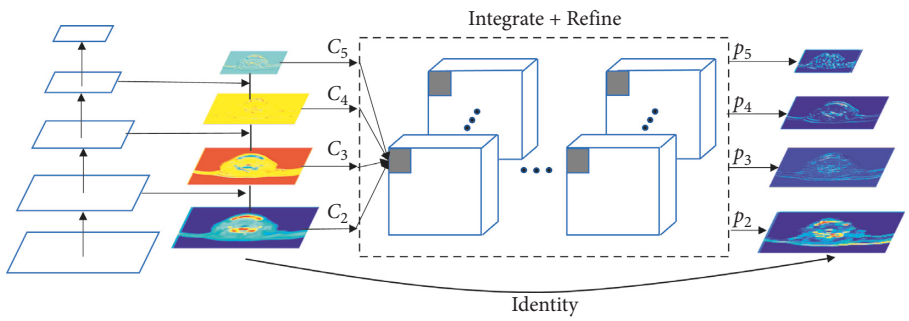

Figure 1: Visualization of balanced feature pyramid.

determined offset can override the locations of other surrounding pixels with similar features. Second, the identical structural information of neighboring pixels is compressed into a fixed grid using the deformable sampling points, and finally, the deformable feature image is formed. Therefore, a deformable convolutional network can describe the sophisticated structure, as indicated in Figure 3.

Assume that the regular convolution acts on a regular lattice R as

$$y(p_0) = \sum_{p_n \in R} w(p_n) \cdot x(p_0 + p_n). \tag{5}$$

A deformable convolutional operation is performed on R, but each point is given a learnable offset Δp_n, and the operation is described as

$$y(p_0) = \sum_{p_n \in R} w(p_n) \cdot x(p_0 + p_n + \Delta p_n). \tag{6}$$

A deformable convolutional network generates $2N$ feature maps corresponding to N 2D offsets Δp_n (each offset corresponding to having x- and y-directions).

3.2. Nonlocal Neural Network. CNNs are implemented as convolutional kernel windows that slide through the connections of neurons to perceive the local semantic information of an image and then integrate the local information at a higher dimension to obtain the global information. Wang et al. [23] and Shokri et al. [24] combined CNN with traditional nonlocal means to form a network structure of nonlocal blocks (shown in Figure 4), using the location information of feature maps to fuse global information and extract global features that traditional models cannot capture through repetitive convolutional operations. Furthermore, affluent global features help to find more significant parts of the image by exploiting the disparities between local features, bringing richer semantic representations to higher levels and improving the performance of existing methods. The representation of the nonlocal block is shown as

$$y_{i,j} = \frac{1}{C(x)} \sum_{\forall k,l} f\left(x_{i,j}, x_{k,l}\right) g\left(x_{k,l}\right), \tag{7}$$

where (i, j) are the position coordinates of the response to be computed and (k, l) are the coordinates of all possible positions in the input images. x denotes the input image or feature maps, and y denotes the output signal in the same dimension as x. The function $f(\cdot)$ calculates the scalar between (i, j) and (k, l), and the function $g(\cdot)$ represents the unary function of the input signal at position (k, l). $C(x)$ represents the response factor normalized to the output value. The expression for the one-dimensional function $g(\cdot)$ is

$$g\left(x_j\right) = W_g x_j, \tag{8}$$

where W_g is the weight matrix and the implementation of $g(\cdot)$ uses 2D convolutional kernels of size 1×1.

3.3. Cascade Detector. A positive sample in the detection network is larger than the IoU threshold; otherwise, it is a negative sample. A lower IoU threshold causes more background information in the extracted positive samples, making false detection more likely. A higher IoU threshold can reduce faults, but the quantity of selected positive samples will fall and then result in overfitting as the IoU threshold rises. A network predefines threshold u (assuming $u = 0.5$) to identify positive and negative samples. When the IoU of the input candidate regions is around this threshold, it frequently outperforms networks trained with alternative thresholds.

The core of Cascade R-CNN is the cascade detector [25] (shown in Figure 5), which is composed of a sequence of detection heads, each of which is trained with a dynamic threshold. The Cascade R-CNN improves on the Faster R-CNN by fine-tuning the region of interest (RoI) of the RPN output three times. The offset of each detection head's output and RoI decoding is fed into the next stage of RoI. A later detection head requires a higher IoU threshold that separates positive and negative samples. The cascade detector allows each stage of the detection head to focus on detecting the region proposals within a certain range of IoU and achieve the best results. Continuously improving the quality of the prediction frame to saturate the variation of the RoI inputs at different stages and improving the quality of the RoI ensures that each detection head has enough training samples to circumvent overfitting problems. The two components that make up the cascade detector are as follows.

(1) Multilevel bounding box regression: the regression branch calculates the offset from the candidate boxes to the ground truth. The vector of the candidate box

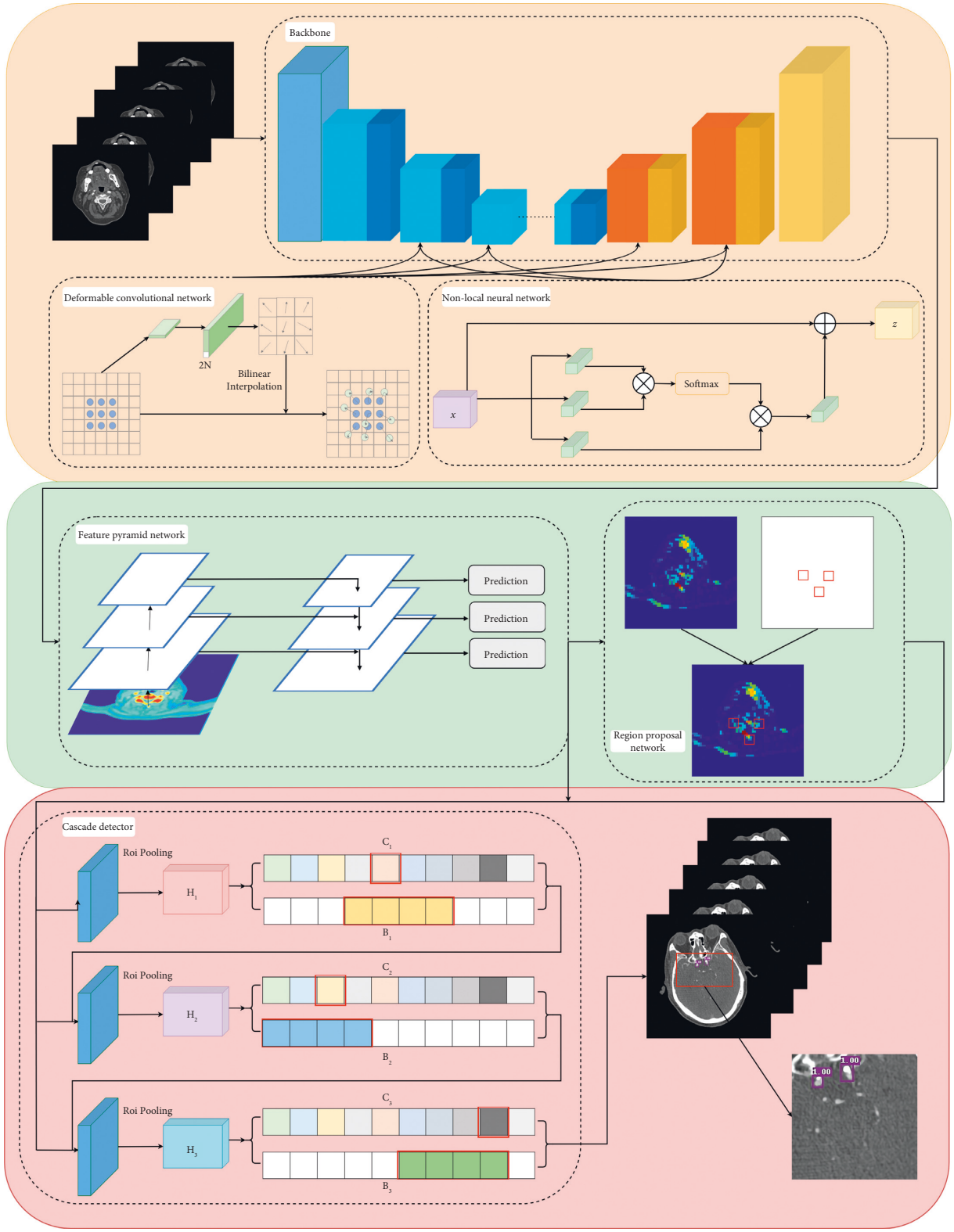

Figure 2: Flowchart of the retrained algorithm in this study. CTA images are fed into the backbone, consisting of Resnet50, deformable convolutional networks, and nonlocal neural networks incorporated in the third, fourth, and fifth stages of Resnet50. Feature maps from feature pyramid network and region proposal network with multiscale and proposal region information are integrated and then input to the cascade detector to refine the classification and regression by increasing the IoU thresholds in stages.

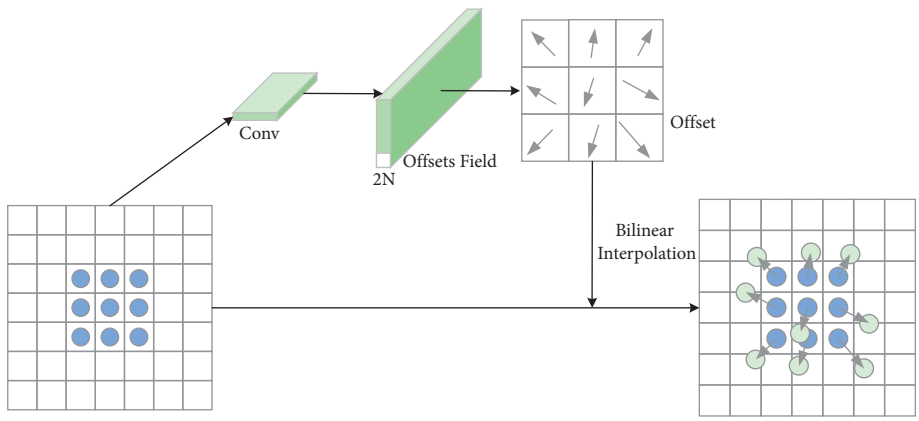

Figure 3: Structure of deformable convolutional network. The deformable convolutional layers were represented in this study by adding 18 output channels to a 2D convolution layer with a convolution kernel size of 3×3, a convolution step of 2×2, and a feature map padding of 1 as offsets before a 2D convolution layer with a convolution kernel size of 3×3, a convolution step of 2×2, and a feature map padding of 1.

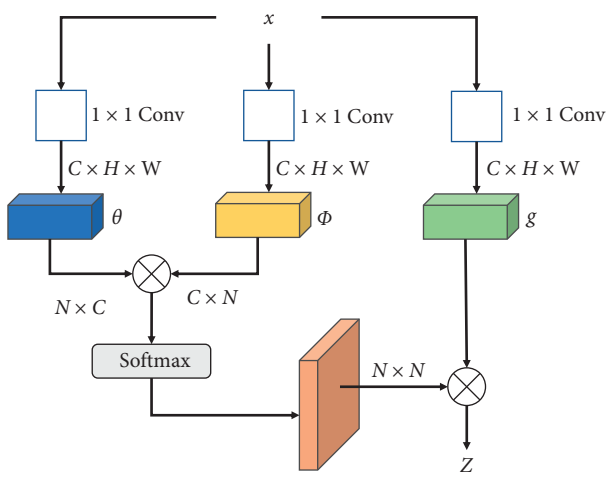

Figure 4: Structure of nonlocal neural network. C, H, and W correspond to dimensions, where $N = H \times W$.

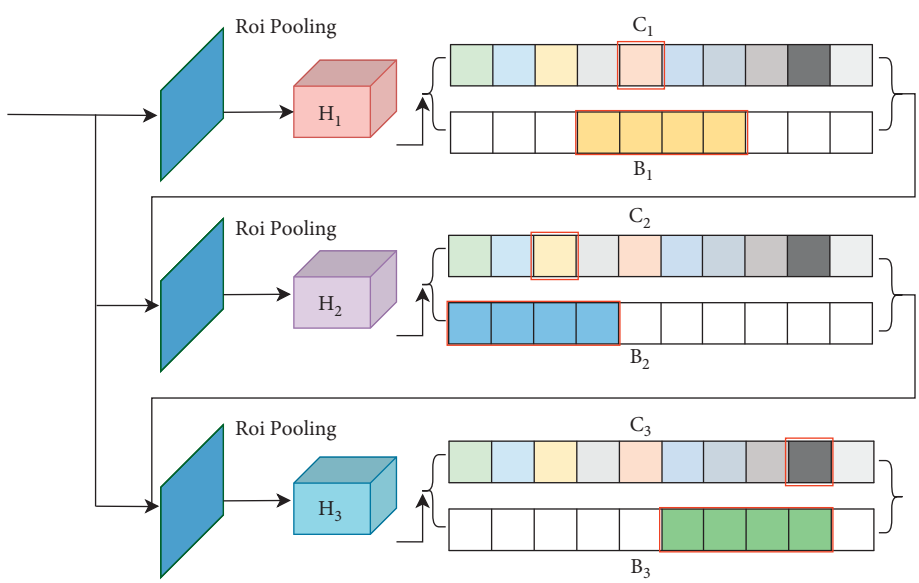

Figure 5: Structure of the cascade detector. Feature maps are fed into the cascade detector, and classification and bounding box regression are refined to optimize prediction, in which C_n and B_n represent classification and bounding box regression in n stage, respectively.

is represented by $b = (x_b, y_b, w_b, h_b)$, where x_b and y_b denote the central point position of the candidate box and w_b and h_b denote the width and height, respectively; the vector of the ground truth is represented by $b = (x^*, y^*, w^*, h^*)$, where x^* and y^* denote the central point position and w^* and h^* denote the width and height, respectively. The expression for the offset t^* from the candidate box to the ground truth is given as

$$\begin{cases} t_x^* = \dfrac{(x^* - x_b)}{w_b}, \\ t_y^* = \dfrac{h_b}{(y^* - y_b)}, \\ t_w^* = \log\left(\dfrac{w^*}{w_b}\right), \\ t_h^* = \log\left(\dfrac{h^*}{h_b}\right). \end{cases} \tag{9}$$

The candidate box is regressed towards the ground truth b^* using the regressor $f(x, b)$, where the expression for the loss function is

$$\begin{aligned} R_{\text{loc}}[f] &= \sum_{i=1}^{N} L_{\text{loc}}\left(f(x_i, b_i), b_i^*\right), \\ L_{\text{loc}}\left(y_i, b_i^*\right) &= \text{blance}_{L_1}\left(y_i - b_i^*\right). \end{aligned} \tag{10}$$

Cascade regression with a series of specific regression quantities is implemented with the following formula:

$$f(x, b) = f_T \circ f_{T-1} \circ \cdots \circ f_1(x, b), \tag{11}$$

where T denotes the total cascade stages and f_T denotes the regression corresponding to stage a.

(2) Classification: the classification function is defined as $h(x)$. The classifier divides the samples into $K+1$ classes, where class 0 contains the background information as well as the target to be detected. The given training sample set (x_i, y_i) is minimized by learning the classification risk as follows:

$$L_{cls}(h(x), y) = \sum_{i \in I} L_{cls}(h_i(x), y_i), \tag{12}$$

where L_{cls} is the cross-entropy loss function and y_i is the class label to which the corresponding image x_i belongs.

The cascade detector minimizes the multitasking loss function in each stage t by taking the output of the previous stage as the input of the next stage, the classifier h_t and the regressor f_t are used to optimize the threshold u_t $(u_t > u_t - 1)$ of the IoU, and the multitasking loss function expression is shown as.

$$L\left(x^t, g\right) = L_{\text{cls}}\left(h_t\left(x^t\right), y^t\right) + \lambda\left[y^t \geq 1\right] L_{\text{loc}}\left(f_t\left(x^t, b^t\right), g\right), \tag{13}$$

where $b_t = f_t - 1(x_t - 1, b_t - 1)$, g denotes the ground truth of the target x_t, y_t is the predicted label of x_t, and λ is the trade-off factor.

4. Materials and Parameters

The Qianjiang District Central Hospital in Chongqing provided the CTA dataset for cerebral arterial stenosis, including 109 patients. The data were desensitized and labelled in Pascal VOC2012 data format using Labelme by qualified radiologists with more than five years of experience. The data were then converted into COCO data format. The dataset was divided into a training set with 1645 images and a test set with 410 images.

The PaddlePaddle framework was used to create the experimental environment, which included an Ubuntu 18.04, a Tesla V100 graphics card, 32 GB of RAM, and a Resnet50 backbone network. With a total training epoch = 20, the initial learning rate was 0.00125, and with batch size = 2, the learning rate was reduced to 0.1 times the initial learning rate at epoch = 12 and epoch = 19, respectively. The size of the input image was 512×512 pixels.

5. Results

The experiment's metrics were conducted using mAPbest (mean average precision), mAP50, mAP75, and APS, where mAPbest represents the best mean average precision in the test set, AP50, AP75, and APS denote the average precision at IoU = 0.50, 0.75 and small objects (area $< 32 \times 32$). For objects in category C, the mAP is calculated as shown in equations (14) and (15):

$$\text{Precision}_C = \frac{\text{N}(\text{True Positives})_C}{\text{N}(\text{Total Objects})_C}, \tag{14}$$

$$\text{Average Precision}_C = \frac{\sum \text{Precision}_C}{N(\text{Total Images})_C}. \tag{15}$$

5.1. One-Stage and Two-Stage Algorithm Comparison. The results of one-stage detection Yolov3, as well as two-stage detection Faster R-CNN, Libra R-CNN, and Cascade R-CNN, are shown in Table 1. A training and testing strategy was employed in this experiment simultaneously. Figure 6 depicts the curve of mAPbest over time for each epoch, and Figure 7 depicts the visualization result of the above four basic algorithms.

5.2. Retrained Faster R-CNN Comparison. The experimental result, presented in Table 2, indicates that by adding deformable convolutional networks, nonlocal neural networks in the backbone network in Faster R-CNN, and the cascade detector added in the classification and regression branch

Table 1: Results of basic object detection algorithms.

Method	mAPbest	mAP0.5 : 0.95	mAP0.5	mAP0.75	mAPs
Yolov3 [26]	44.9	44.9	94.5	28.3	44.9
Faster R-CNN [9]	45.7	45.2	94.0	29.6	45.2
Libra R-CNN [21]	45.9	45.8	96.6	29.6	45.8
Cascade Libra R-CNN [25]	48.5	48.1	97.1	33.1	48.1

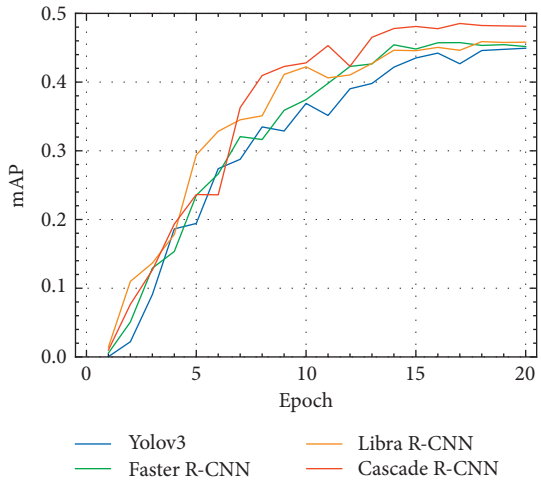

Figure 6: Visualization of the one-stage and two-stage algorithm comparison curve in mAPbest.

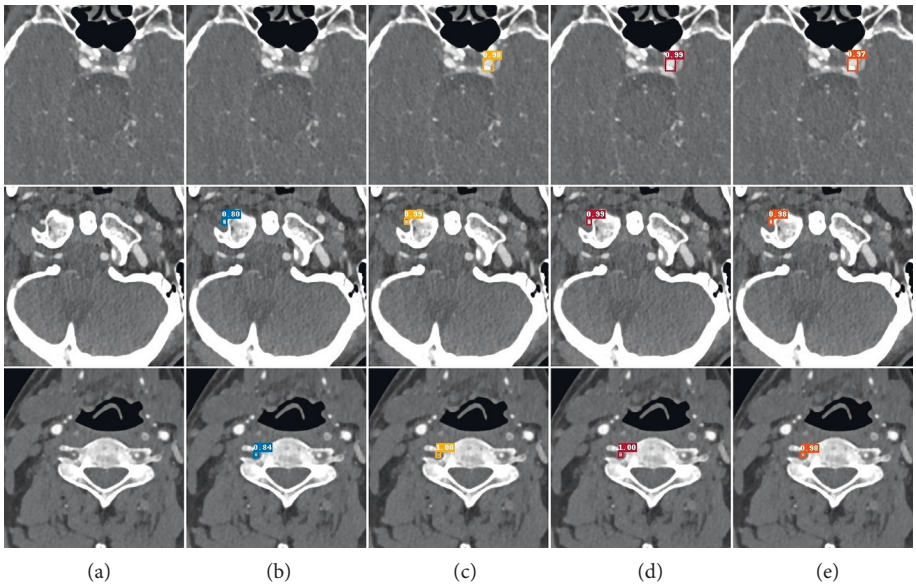

Figure 7: (a–e) Comparison between one-stage and two-stage algorithm prediction. (a) Raw image, (b) Yolov3, (c) Faster R-CNN, (d) Libra R-CNN, and (e) Cascade R-CNN.

refinement, metrics (in terms of mAP) are improved. The curve in mAPbest and the visualization are shown in Figures 8 and 9.

5.3. Retrained Libra R-CNN Comparison. The experimental result, presented in Table 3, indicates that, by gradually adding the above three modules to Libra R-CNN, all the

Table 2: Ablation comparison experiment of retrained Faster R-CNN.

Faster R-CNN	Dcn	Nonlocal	Cascade detector	mAPbest	mAP0.5 : 0.95	mAP0.5	mAP0.75	mAPs
✓				45.7	45.2	94.0	29.6	45.2
✓	✓			46.3	46.1	96.9	35.3	46.1
✓	✓	✓	✓	47.3	47.2	95.9	37.7	47.2
✓	✓	✓	✓	53.0	52.5	97.1	45.7	52.5

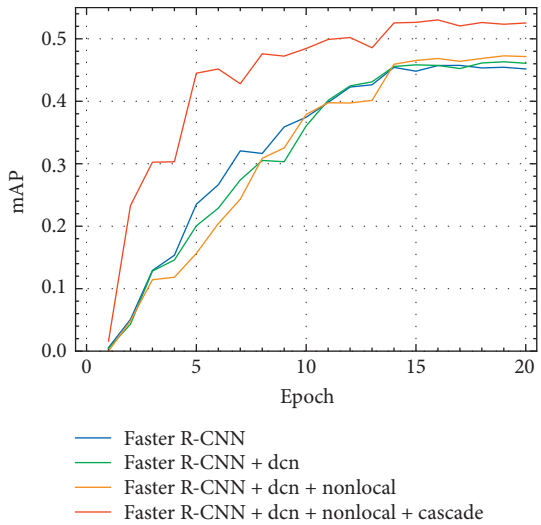

Figure 8: Visualization of the retrained Faster R-CNN curve in mAPbest.

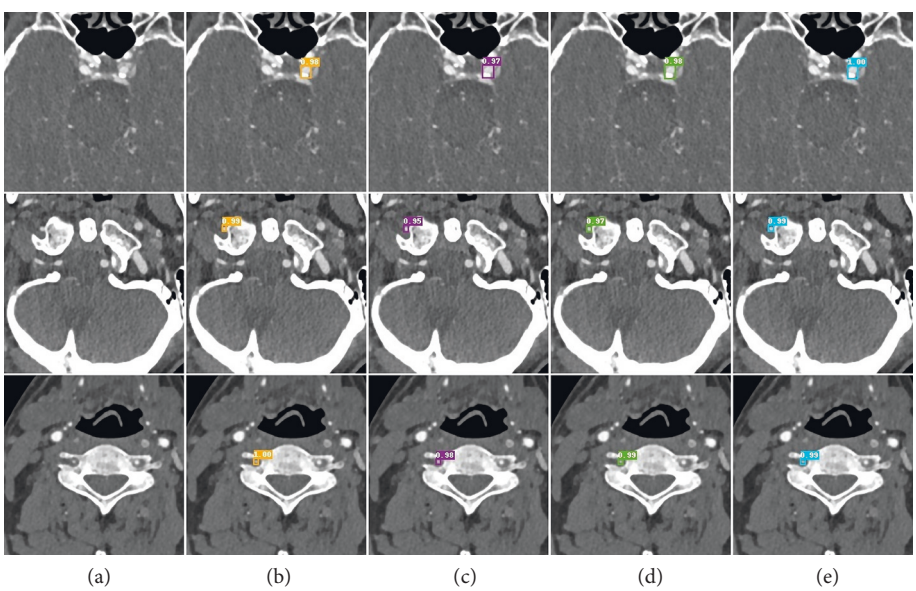

Figure 9: Prediction of retrained Faster R-CNN. (a) Raw image, (b) Faster R-CNN, (c) Faster R-CNN + dcn, (d) Faster R-CNN + dcn + nonlocal, and (e) Faster R-CNN + dcn + nonlocal + cascade detector.

Table 3: Ablation comparison experiment of retrained Libra R-CNN.

Libra R–CNN	DCN	Nonlocal	Cascade detector	mAP (best)	mAP0.5 : 0.95	mAP0.5	mAP0.75	mAPs
✓				45.9	45.8	96.6	29.6	45.8
✓	✓			48.6	47.6	96.9	34.3	47.6
✓	✓	✓	✓	48.1	48.1	95.7	40.1	48.1
✓	✓	✓	✓	53.4	53.1	97.0	50.7	53.1

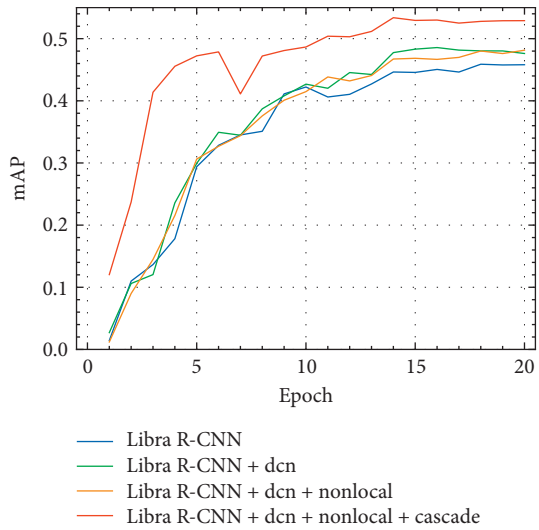

Figure 10: Visualization of the retrained Libra R-CNN curve in mAPbest.

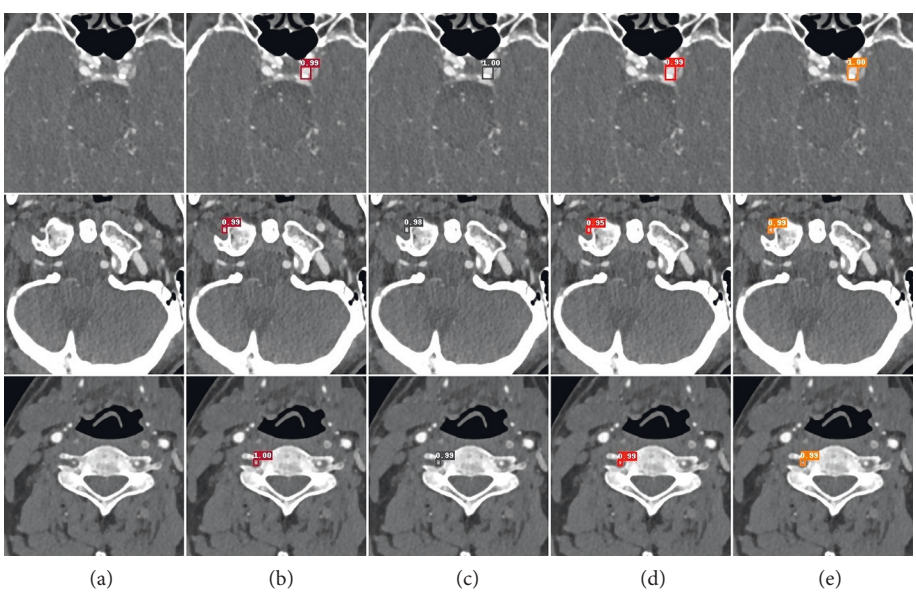

Figure 11: Prediction of retrained Libra R-CNN. (a) Raw image, (b) Libra R-CNN, (c) Libra R-CNN + dcn, (d) Libra R-CNN + dcn + nonlocal, and (e) Libra R–CNN + dcn + nonlocal + cascade detector.

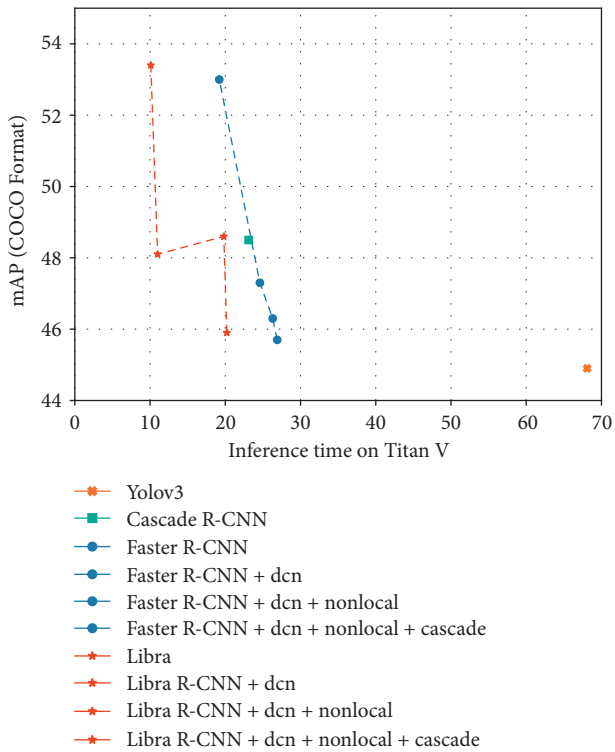

Figure 12: Visualization between inference time and mAPbest. It shows that the one-stage algorithm has its advantage in speed. The mAP of the two-stage algorithm rises as the above modules are added, but the computational complexity grows as well.

metrics of mAP are also improved. However, in Libra R-CNN + dcn + nonlocal, its mAPbest and mAP0.5 are decreased by 0.5% and 1.2%, respectively, compared to Libra R-CNN + dcn. The curve in mAPbest and the visualization are shown in Figures 10 and 11, respectively.

6. Discussion and Conclusions

This study proposed multiple modules as part of a two-stage algorithm for detecting cerebral arterial stenosis. The retrained networks employed deformable convolutional networks in backbone networks to learn offsets to extract morphological features of vessels in different tomographic planes, while nonlocal neural networks were incorporated into the backbone with the deformable convolutional networks at the same stages to learn deeper semantic representations by fusing global information with the location information of the features maps. Finally, a cascade detector optimizes the prediction performances by increasing the threshold value of IoU in stages.

The proposed methods outperform the above mainstream object detection algorithms in the CTA dataset of cerebral arterial stenosis, with considerable improvements in both objective metrics (mAP, mAP50, and mAP75) and prediction visualization. The methods' accuracy for small objects is also increased by optimizing the network structure.

Although the proposed algorithm is superior to baseline approaches such as Faster R-CNN and Cascade R-CNN, multiple modules are layered on top of each other with redundant network topologies. They increased the parameter quantity, which may cause a slower detection speed (shown in Figure 12) and higher cost. Stenosis is not presented in only one tomographic plane for a patient whose images are regarded as independent samples in this study, and liaison between two continuous levels is not well established. Furthermore, the proposed method does not effectively solve the problems that outline the lesion area and classify the stenosis grading which can provide more precise guidance for subsequent clinical treatment. In our subsequent work, we plan to investigate ways to simplify the network structure, minimize the parameters, increase detection accuracy and speed, and calculate the lesion area and its grading.

Data Availability

The data used to support the findings of this study are available from the corresponding author upon request.

Conflicts of Interest

The authors declare that there are no conflicts of interest.

Authors' Contributions

Hanqing Liu and Xiaojun Li contributed equally to this work.

Acknowledgments

This work was supported by the Beijing-Tianjin-Hebei Collaborative Innovation Project (17YEXTZC00020).

References

[1] Y.-Z. Hsieh, Y.-C. Luo, C. Pan, M.-C. Su, C.-J. Chen, and K. L.-C. Hsieh, "Cerebral small vessel disease biomarkers detection on MRI-sensor-based image and deep learning," *Sensors*, vol. 19, no. 11, p. 2573, 2019.

[2] S. Bash, J. P. Villablanca, R. Jahan et al., "Intracranial vascular stenosis and occlusive disease: evaluation with CT angiography, MR angiography, and digital subtraction angiography," *American Journal of Neuroradiology*, vol. 26, no. 5, pp. 1012–1021, 2005.

[3] K.-C. Hsu, C.-H. Lin, K. R. Johnson et al., "Autodetect extracranial and intracranial artery stenosis by machine learning using ultrasound," *Computers in Biology and Medicine*, vol. 116, Article ID 103569, 2020.

[4] T. Araki, P. K. Jain, H. S. Suri et al., "Stroke risk stratification and its validation using ultrasonic echolucent carotid wall plaque morphology: a machine learning paradigm," *Computers in Biology and Medicine*, vol. 80, pp. 77–96, 2017.

[5] L. Saba, P. K. Jain, H. S. Suri et al., "Plaque tissue morphology-based stroke risk stratification using carotid ultrasound: a polling-based pca learning paradigm," *Journal of Medical Systems*, vol. 41, no. 6, p. 98, 2017.

[6] S. L. Waddle, M. R. Juttukonda, S. K. Lants et al., "Classifying intracranial stenosis disease severity from functional MRI data using machine learning," *Journal of Cerebral Blood Flow and Metabolism*, vol. 40, no. 4, pp. 705–719, 2020.

[7] K. He, X. Zhang, S. Ren, and J. Sun, "Spatial pyramid pooling in deep convolutional networks for visual recognition," *IEEE Transactions on Pattern Analysis and Machine Intelligence*, vol. 37, no. 9, pp. 1904–1916, 2015.

[8] R. Girshick, "Fast R-CNN," in *Proceedings of the 2015 IEEE International Conference on Computer Vision*, pp. 1440–1448, IEEE, Santiago Chile, December 2015.

[9] S. Ren, K. He, R. Girshick, and J. Sun, "Faster R-CNN: towards real-time object detection with region proposal networks," *IEEE Transactions on Pattern Analysis and Machine Intelligence*, vol. 39, no. 6, pp. 1137–1149, 2017.

[10] T.-Y. Lin, P. Dollár, R. Girshick, K. He, B. Hariharan, and S. Belongie, "Feature pyramid networks for object detection," *2017 IEEE Conference on Computer Vision and Pattern Recognition (CVPR)* in *Proceedings of the 2017 IEEE Conference on Computer Vision and Pattern Recognition*, vol. 10949, pp. 2117–2125, IEEE, Honolulu, HI, USA, July 2017.

[11] B. Joo, S. S. Ahn, P. H. Yoon et al., "A deep learning algorithm may automate intracranial aneurysm detection on MR angiography with high diagnostic performance," *European Radiology*, vol. 30, no. 11, pp. 5785–5793, 2020.

[12] E. Smistad and L. Løvstakken, "Vessel detection in ultrasound images using deep convolutional neural networks," *Deep Learning and Data Labeling for Medical Applications*, Springer, Cham, pp. 30–38, 2016.

[13] M. T. Stib, J. Vasquez, M. P. Dong et al., "Detecting large vessel occlusion at multiphase CT angiography by using a deep convolutional neural network," *Radiology*, vol. 297, no. 3, pp. 640–649, 2020.

[14] Q. De Man, E. Haneda, B. Claus et al., "A two-dimensional feasibility study of deep learning-based feature detection and characterization directly from CT sinograms," *Medical Physics*, vol. 46, no. 12, pp. e790–e800, 2019.

[15] X. Dai, L. Huang, Y. Qian et al., "Deep learning for automated cerebral aneurysm detection on computed tomography images," *International Journal of Computer Assisted Radiology and Surgery*, vol. 15, no. 4, pp. 715–723, 2020.

[16] J. Yang, M. Xie, C. Hu et al., "Deep learning for detecting cerebral aneurysms with CT angiography," *Radiology*, vol. 298, no. 1, pp. 155–163, 2021.

[17] Y. Shinohara, N. Takahashi, Y. Lee, T. Ohmura, and T. Kinoshita, "Development of a deep learning model to identify hyperdense MCA sign in patients with acute ischemic stroke," *Japanese Journal of Radiology*, vol. 38, no. 2, pp. 112–117, 2020.

[18] Y. Hong, F. Commandeur, and S. Cadet, "Deep learning-based stenosis quantification from coronary CT angiography," in *Proceedings of the Medical Imaging 2019: Image Processing. SPIE*, vol. 10949, pp. 643–651, CF, USA, March 2019.

[19] M. Chen, X. Wang, G. Hao et al., "Diagnostic performance of deep learning-based vascular extraction and stenosis detection technique for coronary artery disease," *British Journal of Radiology*, vol. 93, no. 1113, Article ID 20191028, 2020.

[20] K. Han, L. Chen, and D. B. Geleri, "Deep-learning based significant stenosis detection from multiplanar reformatted Images of traced Intracranial arteries," *In: American Society of Neuroradiology 58th Annual Meeting.*, 2020.

[21] J. Pang, K. Chen, J. Shi, H. Feng, W. Ouyang, and D. Lin, "Libra R-CNN: towards balanced learning for object detection," in *Proceedings of the 2019 IEEE/CVF Conference on Computer Vision and Pattern Recognition (CVPR)*, pp. 821–830, IEEE, Long Beach, CA, USA, June 2019.

[22] J. Dai, H. Qi, and Y. Xiong, "Deformable Convolutional Networks," in *Proceedings of the 2017 IEEE International Conference on Computer Vision*, pp. 764–773, IEEE, Venice, Italy, October 2017.

[23] X. Wang, R. Girshick, A. Gupta, and K. He, "Non-local Neural Networks," in *Proceedings of the 2018 IEEE Conference on Computer Vision and Pattern recognition*, June 2018.

[24] M. Shokri, A. Harati, and K. Taba, "Salient object detection in video using deep non-local neural networks," *Journal of Visual Communication and Image Representation*, vol. 68, Article ID 102769, 2020.

[25] Z. Cai and N. Vasconcelos, "Cascade R-CNN: delving into high quality object detection," in *Proceedings of the 2018 IEEE/CVF Conference on Computer Vision and Pattern Recognition*, pp. 6154–6162, IEEE, Salt Lake City, UT, USA, June 2018.

[26] J. Redmon and A. Farhadi, "Yolov3: An Incremental Improvement [EB/OL]," 2021, https://arxiv.org/pdf/1804.02767.pdf.

Hindawi
Discrete Dynamics in Nature and Society
Volume 2022, Article ID 4167304, 10 pages
https://doi.org/10.1155/2022/4167304

Research Article

Secure Event-Triggered Mechanism for Networked Control Systems under Injection Cyber-Attacks

Xiao Cai,[1] **Jian Kang**,[2] **and Kaibo Shi**[3]

[1]*School of Information and Software Engineering, University of Electronic Science and Technology of China, Chengdu, Sichuan 611731, China*
[2]*Sichuan Provincial Big Data Technology Services Center, Chengdu, Sichuan 610041, China*
[3]*School of Information Science and Engineering, Chengdu University, Chengdu, Sichuan 611731, China*

Correspondence should be addressed to Jian Kang; kangjian_spbdtsc@sina.com

Received 17 February 2022; Revised 14 March 2022; Accepted 19 March 2022; Published 25 April 2022

Academic Editor: Zi-Peng Wang

This study focuses on the secure stability issue of networked control systems (NCSs) under injection cyber-attacks (ICAs), which have important research value of applications for network security. Firstly, a more general Lyapunov–Krasovskii functional (LKF) is constructed based on the time-delay phenomenon in systems. Secondly, a novel boundary looped function (BLF) is developed depending on the sampling period, fully considering delay and sampling information, and the initial constraints of the criteria on the matrices are effectively relaxed. In addition, appropriate integral inequalities are used, making the obtained criteria less conservative in this paper. Then, a new event-trigger mechanism (ETM) controller under ICAs is designed to control the asymptotical stability (AS) of NCSs. Finally, a numerical experiment verifies the correctness and feasibility of the theory.

1. Introduction

As one of the greatest inventions in the 21st century, the popularity of the Internet has brought significant changes and influences on people's production and lives. With the further development of the Internet, the emergence of big data better reflects the advantages of the Internet. Better handling of big data and better transmission of data have become a hot direction for future research [1, 2]. Data transmission is ultimately reflected in network communication applications (see Figure 1). Thus, network communication technology has been widely used in industrial and military fields. It is a current trend to add components of control systems to these applications through the Internet [3–5].

However, in control theory, signal transmission usually relies on network communication techniques. Therefore, this brings the control system into contact with the Internet [6, 7]. Signal transmission between the components of NCSs can be carried out through the network. When we design and implement the corresponding control system, we can reduce the influence of the signal transmission between the components of NCSs through the network [8]. This approach allows NCSs to reduce their complexity and overall cost-effectiveness. Unnecessary wiring between components is eliminated, which effectively reduces the NCS complexity and overall cost. Therefore, NCSs have become one of the hot issues of current research [9, 10]. In [8], Zhang proposed a novel robust event-triggered fault-tolerant automatic steering control strategy for autonomous land vehicles to achieve path tracking and vehicle lateral motion control under in-vehicle network delay. In [9], the problem of fault-tolerant sampled-data control for an NCS with random time delays and actuator faults was investigated. In [10], the authors studied the application of NCSs to high-speed trains.

On the one hand, the data on the NCS can be effectively shared, which facilitates the fusion of all the information in an ample actual physical space. This way, if the system needs to be upgraded or changed, sensors, controllers, and actuators will need to be added or removed without significant changes to the system architecture [11]. Most importantly, connecting cyber-space to physical space makes real-time control feasible. Therefore, this makes the NCSs gradually

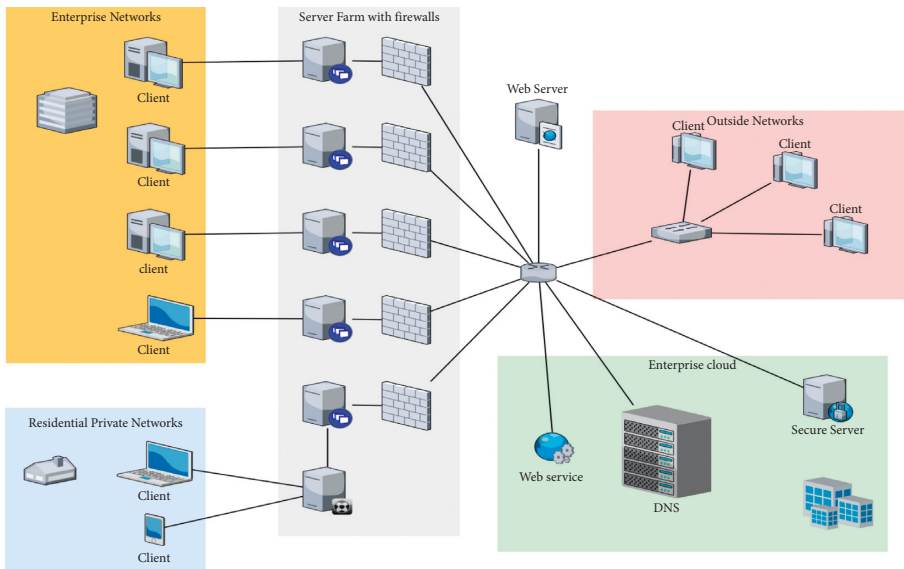

Figure 1: Internet communication topology.

tend to control artificial intelligence and the arrival of the era when everything is connected [12]. On the other hand, the transmission of signals in the communication process of the network is not always secure. Normal loss or delay of signals in network communications is a common phenomenon. We think this phenomenon is acceptable and can be controlled. There has been a malicious attack or sabotage of communication equipment or control systems. We believe this behavior is a cyber-attack, and the person that launched the cyber-attack is a hacker [13]. At present, common cyber-attacks are mainly divided into the following categories: random cyber-attacks [14–16], deception cyber-attacks [17–19], jamming attacks [20, 21], and DoS attacks [22–24]. Thus, effectively countering and defending against hacker attacks is also one of the hot topics. In [15], Liu focused on the controller design problem of NCSs, and a hybrid-triggering communication strategy was employed to save the limited communication resources. In [18], the authors investigated the H_∞ memory sample-data control issue of the T-S fuzzy NCSs with multiple asynchronous deception attacks. In [21], the event-based controller synthesis problem of NCSs under resilient event-triggering communication schemes and periodic DoS jamming attacks was studied. In [24], Feng aimed to explore the tradeoffs between system resilience and network bandwidth capacity.

Based on the above discussion, this paper mainly studies the security issues of NCSs. When hackers attack the system, the ETM controller we designed can effectively ensure the stability of the system. Compared with existing works [25–27], the main contributions of this paper are as follows:

(1) According to the advent of the Internet and the big data era, the security issues of NCSs are being studied. A new ICA is proposed to study the communication security of the system.

(2) A more general LKF is constructed by utilizing the time-delay phenomenon inside the system. According to the characteristics of the sampling period, the constructed LKF contains more sampling information. In addition, the positive definiteness constraint on the initial matrices is further relaxed.

(3) For ICAs launched by hackers, we designed an ETM controller to ensure the AS of the NCS.

2. Preliminaries

In this article, we research the following NCSs:

$$\dot{x}(t) = Ax(t) + B\tilde{u}(t), \tag{1}$$

where $x(t) \in \mathbb{R}^n$ is the current state vector of the system; $\tilde{u}(t) \in \mathbb{R}^m$ is the signal to control the input; and A and B are constant matrices.

The control signals are represented as follows:

$$\tilde{u}(t) = u(t) + f(t), \tag{2}$$

where $f(t)$ is the injection attack function.

Remark 1. The popularity of the Internet has made the processing of big data more efficient and faster. Therefore, studying the control of the system based on network communication has become a hot topic of research. There are always some signal fluctuations in the communication process of the control signal. Normal signal fluctuations of the control signal are acceptable. However, some abnormal signals are often injected into the system to destroy the systems' performance, which we call ICAs. As shown in Figure 2, the sensor communicates with the actuator through network communication with signal transmission. During this process, the system may be maliciously attacked by hackers. Therefore, this paper designs a suitable ETM controller for the communication security of NCSs to ensure the system's regular operation.

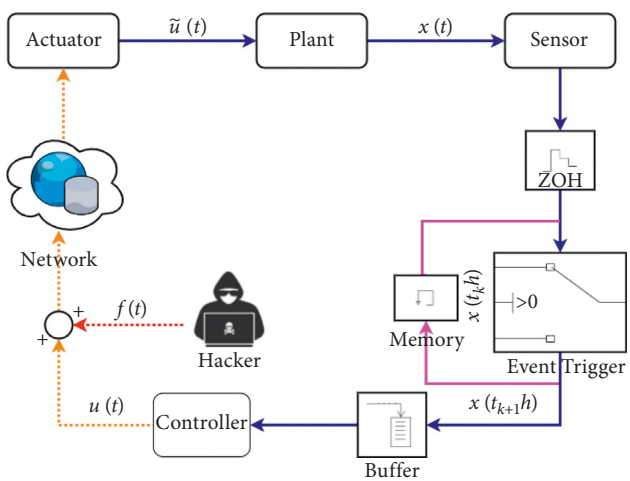

Figure 2: Networked control system under injection attack.

Then, the controller can be designed as

$$u(t) = Kx(t_k h), \quad t \in (t_k h, t_{k+1} h], \tag{3}$$

where K is a controller gain matrix.

In this framework, the sensor is time-triggered while the controller, the zero-order hold (ZOH), and the actuator are event-triggered.

We will illustrate our proposed security-orient resilient triggering strategy as follows:

$$t_{k+1}h = t_k h + \min_{\ell}\left\{\ell h | e(t_k)\Phi e(t_k) - \delta x^T(t_k h)\Phi x(t_k h) > 0\right\}, \tag{4}$$

where $e(t_k) = x(t_k h + \ell h) - x(t_k h)$ and $\Phi > 0$. $x(t_k h)$ is the latest transmitted signal at the latest triggering time $t_k h$. The sampling interval is divided into $[t_k h + \eta_{t_k}, t_{k+1}h + \eta_{t_{k+1}})$. η satisfies $[t_k h + \eta_{t_k}, t_{k+1}h + \eta_{t_{k+1}}) = \cup_{\ell=0}^{\eta}\Omega_\ell$, where $\Omega_\ell = [t_k h + \ell h + \eta_{t_{k+\ell}}, t_k h + \ell h + h + \eta_{t_k} + \ell + 1]$, $\ell = 0, 1, \ldots, \eta$, and $\eta = t_{k+1} - t_k - 1$. We define $d(t) = t - t_k h - \ell h$ and $0 \le \eta_{t_k+\ell} \le \rho(t) \le \rho$, in which $\rho \triangleq h + \eta_{t_k+\ell+1}$. From the definitions of $\rho(t)$ and $e(t_k)$, we can obtain $x(t_k h) = x(t - \rho(t)) + e(t_k)$.

Then, we can obtain

$$\tilde{u}(t) = K[x(t - \rho(t)) - e(t_k) + f(t)]. \tag{5}$$

From equations (1) and (5), the closed-loop system as follows:

$$\dot{x}(t) = Ax(t) + BK[x(t - \rho(t)) - e(t_k) + f(t)]. \tag{6}$$

Assumption 1. ([19]). Any $u_1(t)$ and $u_2(t) \in \mathbb{R}^{n_2}$ meets the Lipschitz condition with the following form:

$$f^T(t)f(t) \le x^T(t)F^T F x(t), \tag{7}$$

where F is the upper bound of $f(\cdot)$.

Lemma 1 (see [28]). *Given $\Omega > 0$ and integrate $e(s)$ over the interval $[a, b] \longrightarrow \mathbb{R}^{n\times n}$, we know the matrix inequality holds:*

$$-(b-a)\int_a^b \dot{e}(s)\Omega\dot{e}(s)\mathrm{d}s \ge -\zeta^T\Omega\zeta - 3\varpi^T\Omega\varpi, \tag{8}$$

where $\zeta = x(b) - x(a)$ and $\varpi = x(b) + x(a) - 2\int_a^b x(s)/b - a$.

3. Main Results

Theorem 1. *Given positive scalars ε, ν, α, h_m, and h_M, system (6) is AS; if there exist symmetric matrices P_1, $P_2 > 0$ and $M_1 > 0$, M_2, then any matrices R_1, R_2, and Y_i $(i = 1, 2, 3)$ with appropriate dimensions satisfy the following LMIs:*

$$\begin{aligned} P_1 + \rho P_2 > 0, \\ M_1 + \rho M_2 > 0, \end{aligned} \tag{9}$$

$$\begin{bmatrix} \Xi_{\rho(t)}^{h_k} & \Pi_1 & \Pi_2^T \\ * & -\varepsilon_1 I & 0 \\ * & * & -\varepsilon_2^{-1} I \end{bmatrix} < 0, \tag{10}$$

$$\begin{aligned} \rho(t) \in \{0, \rho\}, \\ h_k \in \{h_m, h_M\}, \end{aligned} \tag{11}$$

where other symbols and associated equations are expressed in Appendix B.

Proof. Construct a suitable LKF as follows:

$$V(x_t) = \sum_i^4 V_i(x_t), \quad t \in [t_k h, t_{k+1}h), \tag{12}$$

where

$V_1(x_t) = \alpha^T(t)P_{\rho(t)}\alpha(t)$,
$V_2(x_t) = \overline{h}_k \underline{h}_k \delta^T(t)M_{\rho(t)}\delta(t)$,
$V_3(x_t) = \overline{h}_k h_M \int_{t_k h-\rho}^{t-\rho} \dot{x}^T(s)R_1\dot{x}(s)\mathrm{d}s$,
$V_4(x_t) = \underline{h}_k h_M \int_{t-\rho}^{t_{k+1}h-\rho} \dot{x}^T(s)R_2\dot{x}(s)\mathrm{d}s$,
$P_{\rho(t)}$, $M_{\rho(t)}$, $\alpha(t)$, $\delta(t)$, $\overline{h}_k$, $\underline{h}_k$, and $\xi(t)$ are listed in Appendix A.

Then, we can obtain the derivative of $V(x_t)$ as follows:

$$\begin{aligned} \frac{\mathrm{d}V(x_t)}{\mathrm{d}t} &= \sum_i^4 \frac{\mathrm{d}V_i(x_t)}{\mathrm{d}t}, \quad t \in [t_k h, t_{k+1}h), \\ \frac{\mathrm{d}V(x_t)}{\mathrm{d}t} &= 2\alpha^T(t)P_{\rho(t)}\dot{\alpha}(t) - \dot{\rho}(t)\alpha^T(t)P_2\alpha(t), \\ &= -\dot{\rho}(t)\alpha^T(t)P_2\alpha(t) + 2\alpha^T(t)P_{\rho(t)}\begin{bmatrix} \dot{x}(t) \\ -x(t-\rho) \\ x(t-\rho) \end{bmatrix}, \\ &= \xi^T(t)\Xi_1\xi(t), \end{aligned} \tag{13}$$

$$\begin{aligned}\frac{\mathrm{d}V_2(x_t)}{\mathrm{d}t} &= \left(\overline{h}_k - \underline{h}_k\right)\delta^T(t)M_{\rho(t)}\delta(t) - \dot{\rho}(t)\overline{h}_k\underline{h}_k \\ &\quad \times \delta^T(t)M_2\delta(t) + 2\delta^T(t)M_{\rho(t)}\dot{\delta}(t), \\ &= \left(\overline{h}_k - \underline{h}_k\right)\delta^T(t)M_{\rho(t)}\delta(t) - \dot{\rho}(t)\overline{h}_k\underline{h}_k \\ &\quad \times \delta^T(t)M_2\delta(t) + 2\delta(t)M_{\rho(t)}\begin{bmatrix} x(t-\rho) \\ 0 \\ 0 \end{bmatrix}, \\ &= \xi^T(t)\Xi_2\xi(t),\end{aligned} \tag{14}$$

$$\begin{aligned}\frac{\mathrm{d}V_3(x_t)}{\mathrm{d}t} &= -\overline{h}_k h_M \dot{x}^T(t-\rho)R_1\dot{x}(t-\rho) \\ &\quad - h_M\int_{t_{k+1}h-\rho}^{t-\rho}\dot{x}(s)R_1\dot{x}(s)\mathrm{d}s,\end{aligned} \tag{15}$$

$$\begin{aligned}\frac{\mathrm{d}V_4(x_t)}{\mathrm{d}t} &= -\overline{h}_k h_M \dot{x}^T(t-\rho)R_1\dot{x}(t-\rho) \\ &\quad - h_M\int_{t_{k+1}h-\rho}^{t-\rho}\dot{x}(s)R_1\dot{x}(s)\mathrm{d}s.\end{aligned} \tag{16}$$

By using Lemma 1, we have

$$\begin{aligned}-h_M\int_{t-\rho}^{t_k h-\rho}\dot{x}^T(s)R_1x(s)\mathrm{d}s &\le \frac{h_M}{\underline{h}_k\left[x(t_kh-\rho) - x(t-\rho)/x(t_kh-\rho) + x(t-\rho) - 2\int_{t-\rho}^{t_{kh}h-\rho}x(s)/\underline{h}_k ds\right]^T} \\ &\quad \times \begin{bmatrix} R_1 & 0 \\ 0 & 3R_1 \end{bmatrix}\left[x(t_kh-\rho) - x(t-\rho)x(t_kh-\rho) + x(t-\rho) - 2\int_{t-\rho}^{t_{kh}h-\rho}x(s)/\underline{h}_k ds\right] \\ &\le \frac{h_M}{h_m\xi^T(t)\Omega_a^T\overline{R}\Omega_a\xi(t)},\end{aligned} \tag{17}$$

$$\begin{aligned}-h_M\int_{t-\rho}^{t_{k+1}h-\rho}\dot{x}^T(s)R_2x(s)\mathrm{d}s &\le \frac{h_M}{\overline{h}_k\left[x(t_{k+1}h-\rho) - x(t-\rho)/x(t_{k+1}h-\rho) + x(t-\rho) - 2\int_{t-\rho}^{t_{kh+1}h-\rho}x(s)/\overline{h}_k\mathrm{d}s\right]^T} \\ &\quad \times \begin{bmatrix} R_2 & 0 \\ 0 & 3R_2 \end{bmatrix}\left[x(t_{k+1}h-\rho) - x(t-\rho)x(t_{k+1}h-\rho) + x(t-\rho) - 2\int_{t-\rho}^{t_{kh+1}h-\rho}x(s)/\overline{h}_k\mathrm{d}s\right] \\ &\le \frac{h_M}{h_m\xi^T(t)\Omega_b^T\overline{R}\Omega_b\xi(t)}.\end{aligned} \tag{18}$$

Thus, we know that the following inequality holds:

$$\frac{\mathrm{d}V_3(x_t)}{\mathrm{d}t} + \frac{\mathrm{d}V_4(x_t)}{\mathrm{d}t} \le \xi^T(t)\left(h_Me^T\left(\underline{h}_kR_2 - \overline{h}_kR_1\right)e_7 + \frac{h_M}{\underline{h}_k\Omega_a\overline{R}_1\Omega_a} + \frac{h_M}{\overline{h}_k\Omega_b\overline{R}_2\Omega_b}\right)\xi(t) = \xi^T(t)\Xi_3\xi(t). \tag{19}$$

Based on system (6), for any matrices Y_1, Y_2, and Y_3, we have the following equation:

$$\begin{aligned}0 &= 2\left[e^T(t_k)Y_1 + x^T(t_kh)Y_2 + x^T(t-\rho(t))Y\right]_3 \\ &\quad \times [Ax(t) + BKx(t-\rho(t)) + BKf(t)], \\ &= \xi^T(t)\mathrm{Sym}\{L\phi\}\xi(t) + 2LBKf(t).\end{aligned} \tag{20}$$

According to Assumption 1, we have the following equation:

$$2LBKf(t) \le \xi^T(t)\left(\varepsilon\Pi_1\Pi_1^T + \varepsilon^{-1}\Pi_2^T\Pi_2\right)\xi(t). \tag{21}$$

Considering the rules of the designed event-triggered schemes, the following equation holds:

$$e(t_k)\Phi e(t_k) - \delta x^T(t_kh)\Phi x(t_kh) = \xi^T(t)\Theta\xi(t). \tag{22}$$

According to equations (13)–(22), the following equation hold:

$$\begin{aligned}&\frac{\mathrm{d}V(x_t)}{\mathrm{d}t} \\ &\le \xi^T(t)\left(\sum_{i=1}^{3}\Xi_i + \mathrm{Sym}\{L\phi\} + \varepsilon\times\Pi_1\Pi_1^T + \varepsilon^{-1}\Pi_2^T\Pi_2 + \Theta\right) \\ &\quad \cdot \xi(t).\end{aligned} \tag{23}$$

By using the LCCM, for all, $\mathrm{d}V(x_t)/\mathrm{d}t < 0$ are established. Then, using the Schur complement lemma, we know that (23) is equivalent to

$$\begin{bmatrix} \Xi_{\rho(t)}^{h_k} & \Pi_1 & \Pi_2^T \\ * & -\varepsilon_1 I & 0 \\ * & * & -\varepsilon_2^{-1} I \end{bmatrix} < 0. \tag{24}$$

Therefore, it follows $\sum_i^4 \mathrm{d}V_i(x_t)/\mathrm{d}t < 0$. Finally, system (6) tends to AS. □

Remark 2. Compared with existing works [26, 27, 29], this paper constructs a more general LKF for the time-delay phenomenon in systems: (1) when $\rho(t) = \rho$, the constructed LKF will degenerate into being independent of time delay and (2) when $\rho(t) = 0$, the LKF contains correct time-delay information and time-delay derivative information. This method can introduce more information storage and reduce the conservativeness of the criterion.

Remark 3. Different from the traditional BLFs, $V_2(x_t)$ constructed in this paper contains more sampling moments information $\overline{h}_k$ and $\underline{h}_k$. When $\lim_{t\longrightarrow t_{k+1}^+} \overline{h}_k = \lim_{t\longrightarrow t_k^+} \underline{h}_k = 0$ holds, there is no constraint on the matrices $M_{\rho(t)}$. The BLF constructed in this paper is a promotion and enhancement of the BLF in [30].

Remark 4. In this paper, we construct $V_3(x_t)$ and $V_4(x_t)$. Compared with the LKF in reference [30], $V_3(x_t)$ and $V_4(x_t)$ contain the sampling period h_M information and time-delay ρ information. Then, we obtain tighter upper bounds by scaling with appropriate integral inequalities, which ensures that the criterion is less conservative.

Remark 5. This paper analyzes the performance of the computer in the process of solving the LMIs. The computational complexity of Theorem 1 is $7n^2 + 2n$. Then, based on Intel(R) Core(TM) i7-8700 CPU@3.20 GHz 3.19 GHz, pairs of large-scale LMIs are calculated.

Theorem 2. *Given scalars ε, ν, α, ψ_1, ψ_2, h_m, and h_M, system (6) is AS; if there exist symmetric matrices P_1, $P_2 > 0$, $M_1 > 0$, and M_2, any matrices R_1, R_2, and N with appropriate dimensions satisfy the following LMIs:*

$$\begin{cases} \widetilde{P}_1 + \rho \widetilde{P}_2 > 0, \\ \widetilde{M}_1 + \rho \widetilde{M}_2 > 0, \end{cases} \tag{25}$$

$$\begin{bmatrix} \widetilde{\Xi}_{\rho(t)}^{h_k} & \widetilde{\Pi}_1 & \widetilde{\Pi}_2^T \\ * & -\varepsilon_1 I & 0 \\ * & * & -\varepsilon_2^{-1} I \end{bmatrix} < 0, \tag{26}$$

$$\begin{aligned} \rho(t) &\in \{0, \rho\}, \\ h_k &\in \{h_m, h_M\}, \end{aligned} \tag{27}$$

where other symbols and associated equations are expressed in Appendix C.

Table 1: MASPs h_M for different δ's.

δ	[25]	Theorem 2	Improvement (%)
0	1.6982	1.9601	13.3609
0.1	1.1596	1.4927	14.9496
0.2	0.9346	1.0854	13.8935
0.3	0.7621	1.0061	24.2521
0.4	0.6169	0.9592	35.6860
0.5	0.4894	0.6813	28.1667

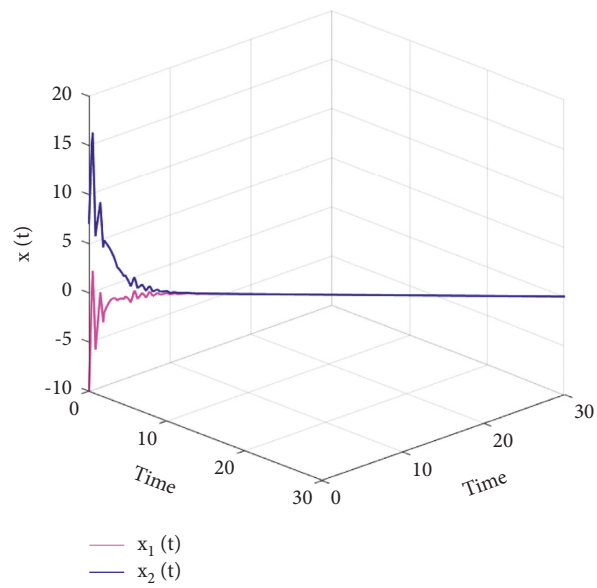

Figure 3: State responses of the original system with control.

Proof. the matrices are defined as $K = NX^{-1}$ and $\widetilde{\Phi} = X^{-T}\Phi X^{-1}$.

Then, other matrices are defined as follows:

$$\begin{aligned} Y_1 &= X^{-1}, \\ Y_2 &= \psi_1 X^{-1}, \\ Y_3 &= \psi_2 X^{-1}, \\ \widetilde{P}_{\delta(t)} &= \mathrm{diag}\{X^T, X^T, X^T\} P_{\delta(t)} \mathrm{diag}\{X, X, X\}, \\ \widetilde{M}_{\delta(t)} &= \mathrm{diag}\{X^T, X^T, X^T\} M_{\delta(t)} \mathrm{diag}\{X, X, X\}, \\ \widetilde{R}_1 &= X^T R_1 X, \\ \widetilde{R}_1 &= X^T R_1 X. \end{aligned} \tag{28}$$

Premultiplying and postmultiplying (9) and (10) by $\mathrm{diag}\{X^T, X^T, X^T\}$ and $\mathrm{diag}\{X, X, X\}$, then according to Schur complement, we can derive the LMIs (25) and (26). The proof process is consistent with Theorem 1. □

4. Illustrative Example

Example 1. Consider a NCS, the parameters are as follows [25]:

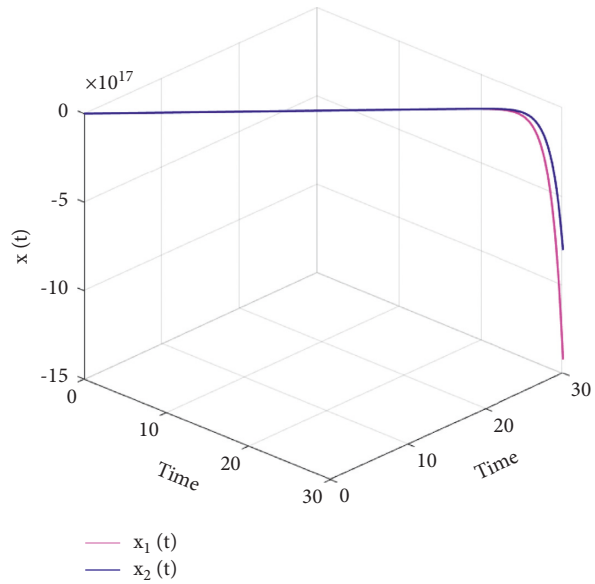

Figure 4: State responses of the original system without control.

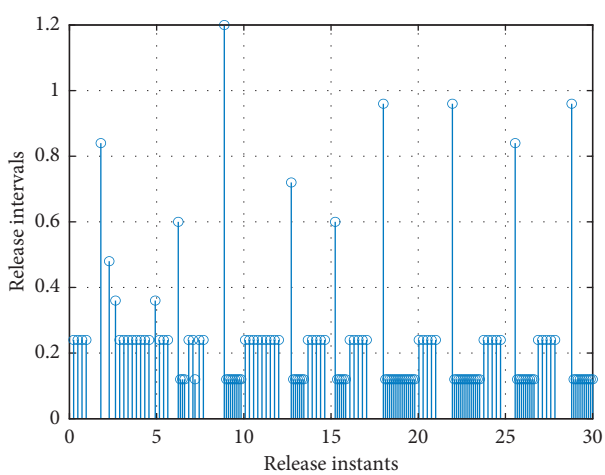

Figure 5: Release instants and time intervals.

$$A = \begin{bmatrix} 0 & 1 \\ 0 & -0.1 \end{bmatrix}, \quad B = \begin{bmatrix} 0 \\ 0.1 \end{bmatrix}. \tag{29}$$

4.1. Case A: The System Is in Normal State. In this case, our research system is operating normally in a safe state. When $\rho = 0$, $F = 0$, and $h_m = 0.1$, we solve for maximum acceptable sampling periods (MASPs) by using Theorem 2. It can be seen from Table 1 that the MASPs h_M under different δ are better than reference [25]. When $\delta = 0.3$, the $h_M = 1.0061$ solved in this paper is 24.2521% higher than the result of reference [25].

To verify the validity of the criterion, we solve the controller gain matrix is $K = [50.4168 - 17.8803]$ by using the Yalmip toolbox in Matlab. Then, we set $h_m = h_M = 0.01$, $\delta = 0.3$, and $x(0) = [-10, 7]^T$; furthermore, the stability of the system is verified by plotting the state trajectory images of the system.

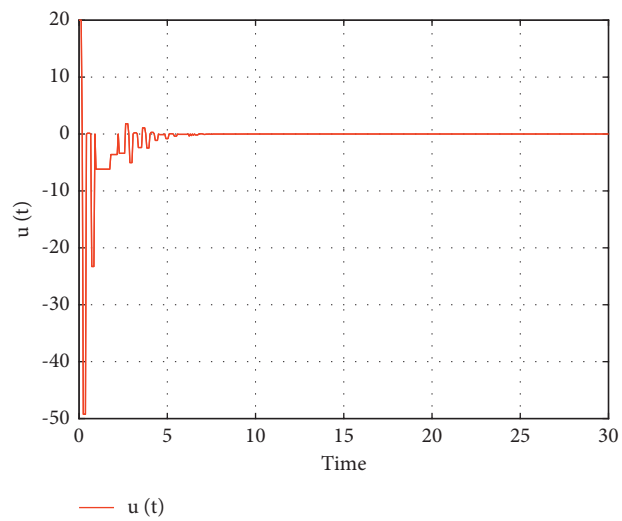

Figure 6: Control input signal $u(t)$.

Table 2: MASPs h_M for different δ's under ICA.

δ	[25]	Case A	Case B	Reduction (%)
0	1.6982	1.9601	1.5039	23.2743
0.1	1.1596	1.4927	1.1725	21.4511
0.2	0.9346	1.0854	0.9967	8.1721
0.3	0.7621	1.0061	0.8916	11.3806
0.4	0.6169	0.9592	0.7109	25.8861
0.5	0.4894	0.6813	0.4593	32.5845

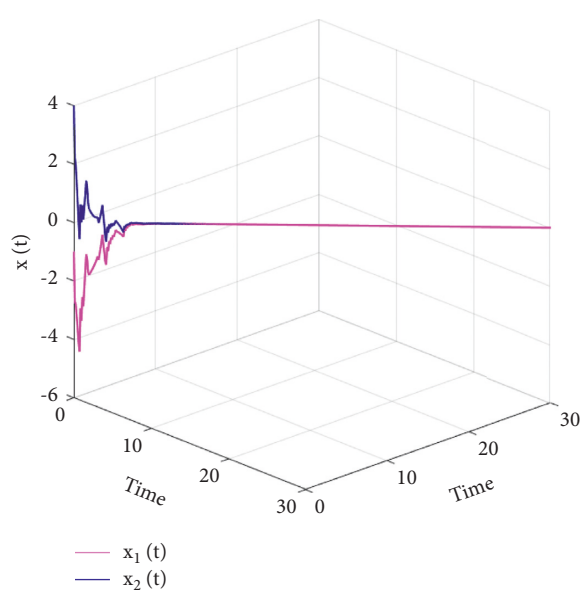

Figure 7: State responses of the original system with control.

In Figure 3, we can see that with the increase in time, the running trajectory of the system will fluctuate. But it eventually converges on a steady state. This means that the controller we designed is suitable. In order to more intuitively reflect the effect of the controller designed in this paper, we also draw Figure 4 of the running trajectory of the system when the controller fails.

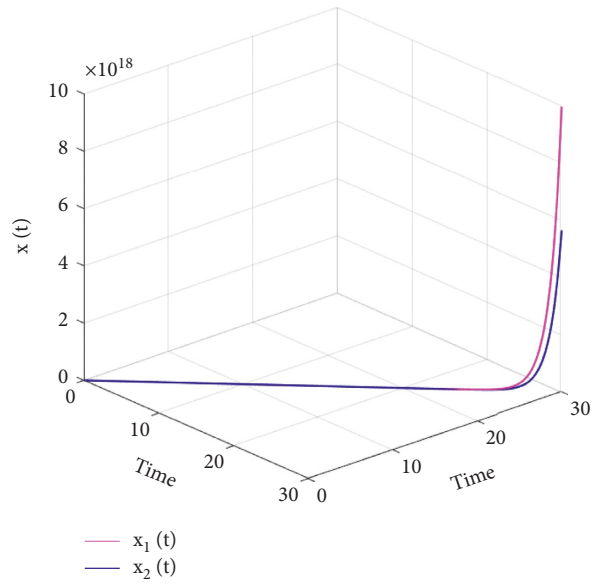

Figure 8: State responses of the original system without control.

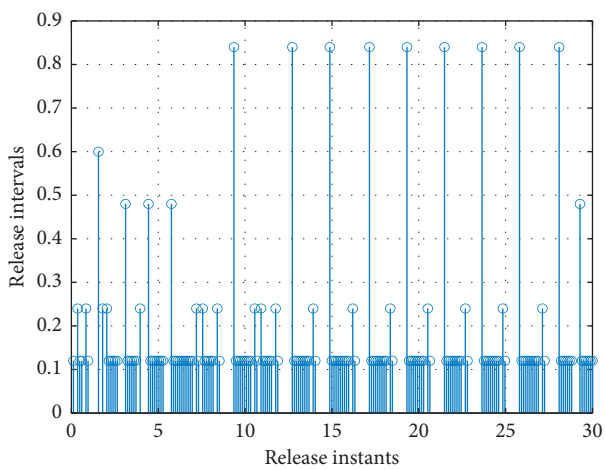

Figure 9: Release instants and time intervals.

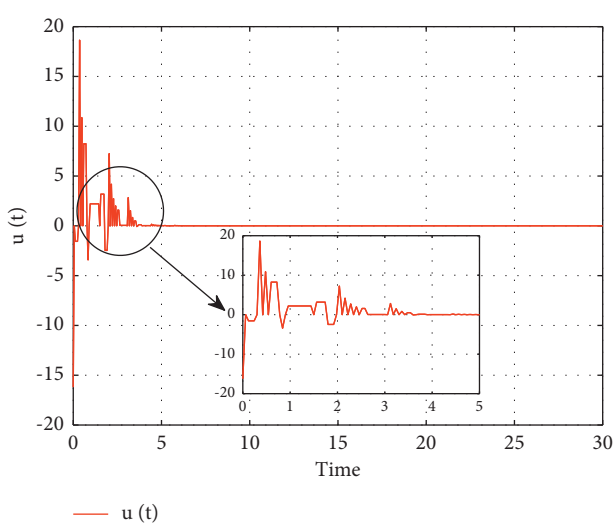

Figure 10: Control input signal $u(t)$.

In addition, the release time distribution and control signal input are shown in Figures 5 and 6, respectively.

4.2. Case B: The System Is in Abnormal State. In this case, we conducted a simulation experiment, as in Case A. When $\rho = 0$, $h_m = 0.1$, $F_1 = 0.1$, and $F_2 = 0.1$, the MASPs solved by using Matlab are shown in Table 2. Table 2 shows that the performance of the system is reduced when the system is attacked. However, the method proposed in this paper can still ensure the stability of the system. Assuming $\delta = 0.3$, we solve $h_M = 1.0061$ when the system is running normally. However, solve for $h_M = 0.8916$ when ICAs constrain the system. By comparing the results, we know that although 11.3806% reduces the performance, our criterion is still less conservative than the results in reference [25].

Then, when $\psi_1 = \psi_2 = 1$ the controller gain is $K = [27.8726 - 10.5776]$. Setting $\rho = 0$, $h_m = h_M = 0.01$, and $\delta = 0.3$, the initial condition is $x(0) = [4, -1]^T$. We assume that the attack function injected by the hacker is $f(t) = [-\tanh(0.5x(t)), -\tanh(0.25x(t))]^T$. When the system is subjected to ICAs, we plot the state trajectory of the system in Figure 7. Compared with the normal running trajectory in Figure 3, we can see that the system oscillates more obviously and can still reach a stable state eventually. Furthermore, the trajectory of the system in the case of controller failure is plotted in Figure 8.

Finally, we plot the release time distribution of the system in Figure 9 and the control signal input in Figure 10.

5. Conclusion

This paper has considered the secure stability issue of NCSs under ICAs, which have important research value of applications for network security. Firstly, a more general LKF has been constructed based on the time-delay phenomenon in the system. Secondly, a novel BLF has been developed depending on the sampling period, fully considering time delay and sampling information, and the initial constraints on the criterion on the matrices have been effectively relaxed. In addition, appropriate integral inequalities have been used, making the criteria less conservative in this paper. Then, a new ETM controller under ICAs has been designed to control the AS of NCSs. Finally, a numerical experiment has verified the correctness and feasibility of the theory. In the future, we extend this method and safety control strategy to T-S fuzzy systems, switching systems, Markov hopping systems, and some other systems.

Notations

R^n:	n-Dimensional Euclidean space
$\mathbf{Z}^{n\times n}$:	$n \times n$ real matrices
$\mathbf{I}$:	Identity matrix
$\mathbf{Q}^n$:	$n \times n$ real symmetric matrices
$\mathscr{H} > 0$:	Denote that $\mathscr{H}$ is a real positive definite matrix
Sym $= X^T + X$, and diag $\{\cdots\}$:	Block diagonal matrix.

Appendix

A

$$\alpha(t)=\mathrm{col}\left\{x(t),\int_{t-\rho}^{t_kh-\rho}x(s)\mathrm{d}s,\int_{t_{k+1}h-\rho}^{t-\rho}x(s)\mathrm{d}s\right\},$$

$$\delta(t)=\mathrm{col}\left\{x(t-\rho),x(t_kh-\rho),x\left(t_{k+1h-\rho}\right)\right\},$$

$$P_{\rho(t)}=P_1+(\rho-\rho(t))P_2,$$

$$M_{\rho(t)}=M_1+(\rho-\rho(t))M_2,$$

$$\overline{h}_k=t_{k+1}h-t,$$

$$\underline{h}_k=t-t_kh,$$

$$\xi(t)=\mathrm{col}\left\{\begin{array}{c} x(t),x(t-\rho), \\ x(t_kh-\rho),x(t_{k+1}h-\rho),x(t_kh),\dot{x}(t),\dot{x}(t-\rho) \\ \int_{t-\rho}^{t_kh-\rho}\frac{x(s)}{\underline{h}_k}\mathrm{d}s,\int_{t-\rho}^{t_{k+1}h-\rho}\frac{x(s)}{\overline{h}_k}\mathrm{d}s,x(t-\rho(t)),e(t_k) \end{array}\right\}. \tag{A.1}$$

B

$$\widetilde{\Xi}_{\rho(t)}^{h_k}=\sum_{i=1}^{3}\widetilde{\Xi}_i+\mathrm{Sym}\left\{\widetilde{L}\widetilde{\phi}\right\}+\widetilde{\Theta},$$

$$\widetilde{\Xi}_1=\mathrm{Sym}\left\{\Phi_1^T\widetilde{P}_{\rho(t)}\Phi_2\right\}-\mu_1\Phi_1^T\widetilde{P}_2\Phi_1,$$

$$\widetilde{\Xi}_2=-\underline{h}_k\Phi_3^T\widetilde{M}_{\rho(t)}\Phi_3+\overline{h}_k\Phi_3^T\widetilde{M}_{\rho(t)}\Phi_3-\mu_1\overline{h}_k\underline{h}_k\Phi_3^T\widetilde{M}_2\Phi_3,$$

$$\widetilde{\Xi}_3=h_Me_7^T\left(\underline{h}_k\widetilde{R}_2-\overline{h}_k\widetilde{R}_1\right)e_7+\frac{h_M}{h_m\Omega_a^T\widetilde{\overline{R}}_1\Omega_a}+\frac{h_M}{h_m\Omega_b^T\widetilde{\overline{R}}_2\Omega_b},$$

$$\widetilde{L}=e_{11}^T+\psi_1e_5^T+\psi_2e_{10}^T,$$

$$\widetilde{\varphi}=AXe_1+BNe_{10},$$

$$\Theta=e_{11}^T\Phi e_{11}-\delta e_5^T\Phi e_5,$$

$$\Pi_1=LBK,$$

$$\Pi_2=Fe_3,$$

$$\Omega_a=\mathrm{col}\{e_3-e_2,e_3+e_2-2e_8\},$$

(HTML translation failed)

$$\Phi_1=\mathrm{col}\left\{e_1,\underline{h}_ke_8,\overline{h}_ke_9\right\},$$

$$\Phi_2=\mathrm{col}\{e_6,-e_2,e_2\},$$

$$\Phi_3=\mathrm{col}\{e_2,e_3,e_4\},$$

$$\Phi_4=\mathrm{col}\{e_7,0,0\},$$

$$\overline{R}_1=\begin{bmatrix} R_1 & 0 \\ 0 & 3R_1 \end{bmatrix},$$

$$\overline{R}_2=\begin{bmatrix} R_2 & 0 \\ 0 & 3R_2 \end{bmatrix}, \tag{A.2}$$

C

$$\Xi_{\rho(t)}^{h_k}=\sum_{i=1}^{3}\Xi_i+\mathrm{Sym}\{L\phi\}+\Theta,$$

$$\Xi_1=\mathrm{Sym}\left\{\Phi_1^TP_{\rho(t)}\Phi_2\right\}-\mu_1\Phi_1^TP_2\Phi_1,$$

$$\Xi_2=-\underline{h}_k\Phi_3^TM_{\rho(t)}\Phi_3+\overline{h}_k\Phi_3^TM_{\rho(t)}\Phi_3-\mu_1\overline{h}_k\underline{h}_k\Phi_3^TM_2\Phi_3,$$

$$\Xi_3=h_Me_7^T\left(\underline{h}_kR_2-\overline{h}_kR_1\right)e_7+\frac{h_M}{h_m\Omega_a^T\overline{R}_1\Omega_a}+\frac{h_M}{h_m\Omega_b^T\overline{R}_2\Omega_b},$$

$$L=e_{11}^TY_1+e_5^TY_2+e_{10}^TN_3,$$

$$\varphi=Ae_1+BKe_{10},$$

$$\Theta=e_{11}^T\Phi e_{11}-\delta e_5^T\Phi e_5,$$

$$\Pi_1=LBK,$$

$$\Pi_2=Fe_3,$$

$$\Omega_a=\mathrm{col}\{e_3-e_2,e_3+e_2-2e_8\},$$

$$\Omega_b=\mathrm{col}\{e_4-e_2,e_4+e_2+2e_9\},$$

$$\Phi_1=\mathrm{col}\left\{e_1,\underline{h}_ke_8,\overline{h}_ke_9\right\},$$

$$\Phi_2=\mathrm{col}\{e_6,-e_2,e_2\},$$

$$\Phi_3=\mathrm{col}\{e_2,e_3,e_4\},$$

$$\Phi_4=\mathrm{col}\{e_7,0,0\},$$

$$\overline{R}_1=\begin{bmatrix} R_1 & 0 \\ 0 & 3R_1 \end{bmatrix},$$

$$\overline{R}_2=\begin{bmatrix} R_2 & 0 \\ 0 & 3R_2 \end{bmatrix}. \tag{A.3}$$

Data Availability

The data used to support this study are available from the corresponding author upon request.

Conflicts of Interest

The authors declare that there are no conflicts of interest.

Acknowledgments

This work was supported by the National Natural Science Foundation of China (n61703060, 12061088, 61802036, and 61873305), the Sichuan Science and Technology Program (21YYJC0469), the Project funded by the China Postdoctoral Science Foundation (2020M683274 and 2021T140092), the Open Research Project of the State Key Laboratory of Industrial Control Technology, Zhejiang University, China (ICT2021B38), and Guangdong Basic and Applied Basic Research Foundation (2021A1515011692). This study was supported by a grant from the Science and Technology Department of Sichuan Province (2020YFG0300) and an open project fund of Intelligent Terminal Key Laboratory of Sichuan Province (2019–2020)+SCITLAB-0002.

References

[1] M. G. H. Bangui and B. B. Uhnova, "Big data for Internet of things: a survey," *Future Generation Computer Systems*, vol. 87, pp. 601–614, 2018.

[2] S. Shadroo and A. M. Rahmani, "Systematic survey of big data and data mining in internet of things," *Computer Networks*, vol. 139, no. 5, pp. 19–47, 2018.

[3] R. M. Murray, "Future directions in control, dynamics, and systems: overview, grand challenges and new courses," *RM Murray European Journal of Control*, vol. 9, no. 2, pp. 144–158, 2003.

[4] L. Zhang, H. Gao, and O. Kaynak, "Network-induced constraints in networked control systems-A survey," *IEEE Transactions on Industrial Informatics*, vol. 9, no. 1, pp. 403–416, 2013.

[5] W. Zhang, M. S. Branicky, and S. M. Phillips, "Reachable set estimation for neural network control systems: a simulation-guided approach," *IEEE Transactions on Neural Networks and Learning Systems*, vol. 32, no. 5, pp. 1821–1830, 2021.

[6] A. L. S. N. Bharathi, A. B. Ganesh, and T. K. Radhakrishnan, "Particle swarm optimization tuned cascade control system in an Internet of Things (IoT) environment," *Measurement*, vol. 117, pp. 80–89, 2018.

[7] Z. L. Ning, K. Y. Zhang, X. J. Wang et al., "Joint computing and caching in 5G-envisioned Internet of vehicles: a deep reinforcement learning-based traffic control system," *IEEE Transactions on Intelligent Transportation Systems*, vol. 22, no. 5, pp. 5201–5212, 2021.

[8] J. Zhang, B. Zhang, N. Zhang, C. Wang, and Y. Chen, "A novel robust event-triggered fault tolerant automatic steering control approach of autonomous land vehicles under in-vehicle network delay," *International Journal of Robust and Nonlinear Control*, vol. 31, no. 7, pp. 2436–2464, 2021.

[9] F. Fang, H. Ding, Y. Liu, and J. H. Park, "Fault tolerant sampled-data H∞ control for networked control systems with probabilistic time-varying delay," *Information Sciences*, vol. 544, no. 12, pp. 395–414, 2021.

[10] X. Cai, K. Shi, S. Zhong, and X. Pang, "Dissipative sampled-data control for high-speed train systems with q_m," *IEEE Transactions on Intelligent Transportation Systems*, vol. 6, no. 429, pp. 1–12, 2021.

[11] Z. Zhang, S. Shu, F. Lin, and S. Li, "Online supervisory control of networked discrete-event systems with control delays," *IEEE Transactions on Automatic Control*, vol. 1, 2021.

[12] J. P. Farwell and R. Rohozinski, "Extended dissipative sliding mode control for nonlinear networked control systems via event-triggered mechanism with random uncertain measurement," *Applied Mathematics and Computation*, vol. 396, no. 1, Article ID 125901, 2021.

[13] X.-M. Zhang, Q.-L. Han, X. Ge, and L. Ding, "Resilient control design based on a sampled-data model for a class of networked control systems under denial-of-service attacks," *IEEE Transactions on Cybernetics*, vol. 50, no. 8, pp. 3616–3626, 2020.

[14] X. Cai, S. Zhong, J. Wang, and K. Shi, "Robust H∞ control for uncertain delayed T-S fuzzy systems with stochastic packet dropouts," *Applied Mathematics and Computation*, vol. 385, Article ID 125432, 2020.

[15] J. Liu, Z.-G. Wu, D. Yue, and J. H. Park, "Stabilization of networked control systems with hybrid-driven mechanism and probabilistic cyber attacks," *IEEE Transactions on Systems, Man, and Cybernetics: Systems*, vol. 51, no. 2, pp. 943–953, 2021.

[16] A. Y. Lu and G. H. Yang, "Hybrid-driven-based H_∞ control for networked cascade control systems with actuator saturations and stochastic cyber attacks," *IEEE Transactions on Systems, Man, and Cybernetics: Systems*, vol. 49, no. 12, pp. 2452–2463, 2019.

[17] K. Wang, E. Tian, J. Liu, L. Wei, and D. Yue, "Resilient control of networked control systems under deception attacks: a memory-event-triggered communication scheme," *International Journal of Robust and Nonlinear Control*, vol. 30, no. 4, pp. 1534–1548, 2020.

[18] X. Cai, K. Shi, K. She, and S. Zhong, "H_∞ memory sample-data control for T-S fuzzy network control system with multiple asynchronous deception attacks," in *Proceedings of the International Conference on Applied Nonlinear Dynamics*, pp. 801–811, Springer, Hong Kong, China, August 2021.

[19] Z. Gu, X. Zhou, T. Zhang, F. Yang, and M. Shen, "Event-triggered filter design for nonlinear cyber-physical systems subject to deception attacks," *ISA Transactions*, vol. 104, pp. 130–137, 2020.

[20] H. Yang, M. Shi, Y. Xia, and P. Zhang, "Security research on wireless networked control systems subject to jamming attacks," *IEEE Transactions on Cybernetics*, vol. 49, no. 6, pp. 2022–2031, 2019.

[21] S. Hu, D. Yue, X. Xie, X. Chen, and X. Yin, "Resilient event-triggered controller synthesis of networked control systems under periodic DoS jamming attacks," *IEEE Transactions on Cybernetics*, vol. 49, no. 12, pp. 4271–4281, 2019.

[22] Y. Deng, X. Yin, and S. Hu, "Event-triggered predictive control for networked control systems with DoS attacks," *Information Sciences*, vol. 542, no. 4, pp. 71–91, 2021.

[23] N. Zhao, P. Shi, W. Xing, and J. Chambers, "Observer-based event-triggered approach for stochastic networked control systems under denial of service attacks," *IEEE Transactions on Control of Network Systems*, vol. 8, no. 1, pp. 158–167, 2020.

[24] S. Feng, A. Cetinkaya, H. Ishii, P. Tesi, and C. D. Persis, "Networked control under DoS attacks: tradeoffs between resilience and data rate," *IEEE Transactions on Automatic Control*, vol. 66, no. 1, pp. 460–467, 2020.

[25] Y. Guan and C. Peng, "A hybrid transmission scheme for networked control systems," *ISA Transactions*, vol. 96, pp. 155–162, 2020.

[26] X. Cai, K. B. Shi, K. She, S. M. Zhong, J. Wang, and H. C. Yan, "New results for t-s fuzzy systems with hybrid communication delays," *Fuzzy Sets and Systems*, vol. 438, 2021.

[27] F. Long, C. K. Zhang, L. Jiang, Y. He, and M. Wu, "Stability analysis of systems with time-varying delay via improved Lyapunov-Krasovskii functional," *IEEE Transactions on Systems, Man, and Cybernetics: Systems*, vol. 51, no. 4, pp. 1–10, 2019.

[28] A. Seuret and F. Gouaisbaut, "Wirtinger-based integral inequality: application to time-delay systems," *Automatica*, vol. 49, no. 8, pp. 2860–2866, 2013.

[29] C.-K. Zhang, Y. He, L. Jiang, M. Wu, and Q.-G. Wang, "An extended reciprocally convex matrix inequality for stability analysis of systems with time-varying delay," *Automatica*, vol. 85, pp. 481–485, 2017.

[30] X. Cai, K. Shi, S. Zhong, and Y. Q. Tang, "Dissipative analysis for high speed train systems via looped-functional and relaxed condition methods," *Applied Mathematical Modelling*, vol. 96, pp. 570–583, 2021.

Hindawi
Discrete Dynamics in Nature and Society
Volume 2022, Article ID 5759152, 11 pages
https://doi.org/10.1155/2022/5759152

Research Article

Dynamics for a Type of Differential-Algebraic Complex-Valued Neural Networks with Delay

Han Yu[1] and Ailong Wu[1,2]

[1]*College of Mathematics and Statistics, Hubei Normal University, Huangshi 435002, China*
[2]*Institute for Information and System Science, Xi'an Jiaotong University, Xi'an 710049, China*

Correspondence should be addressed to Ailong Wu; hbnuwu@yeah.net

Received 21 February 2022; Accepted 14 March 2022; Published 16 April 2022

Academic Editor: Zi-Peng Wang

In the article, we apply complex-valued neural networks (CVNNs) to differential-algebraic neural networks (DANNs) and establish a new type of differential-algebraic complex-valued neural network (DACVNN) with delay (DDACVNN). First of all, the focus of existence and uniqueness of the solution to DDACVNN is addressed. Additionally, a theorem of global exponential stability (GES) of DDACVNN is investigated. In particular, in the discussion of this article, there is no restriction on whether the activation function requires that the real and imaginary parts can be dissociated. Finally, we will give two examples, namely, the activation function can separate the real and imaginary parts, and the activation function cannot separate the real and imaginary parts, both of which can confirm the truth of the effectiveness of theoretical results.

1. Introduction

Due to the various applications of artificial neural networks (ANNs) in graphics processing, combinatorial optimization, signal processing, and intelligent control, especially, in recently years, as artificial intelligence develops, the research on neural networks has received growing concern. When designing neural networks to solve application problems, it is crucial to guarantee the stability of the model under consideration. In the hardware implementation of neural networks, since the transmission of signals is delayed over time, delays inevitably occur, which may lead to network instability. Hence, the research on time-delay systems is meaningful and necessary. Also many research results can be seen in [1, 2] and its references.

During the past period, due to the diverse applications in multitudinous engineering and technical territories, such as pattern recognition, associative memory, and hole filling, complex-valued neural networks (CVNNs) are becoming increasingly needed in applications, as in [3]. Hence, it can be found initially from [4–6] that numerous CVNNs have been put forward and discussed.

As we all know, the state variables, activation functions, and connection weights of complex-valued systems are all defined in the complex number domain, and the analysis method is very different from that of real-valued systems. Actually, CVNNs have more superior characteristics than real-valued neural networks in complex signal processing and can solve more complex problems. For example, a single real-valued neuron cannot settle the XOR issue and the unearthing symmetry issue, and the application of complex-valued neurons can solve these problems (see [7]). For CVNNs, the staple difficulty is to look for an opposite activation function. Judging by Liouville's theorem, CVNNs cannot select a smooth and bounded function as the activation function, so how to choose a suitable activation function for research also needs to be paid attention to the problem. With the wide application of the neural network, the development of neural network models that can handle complex-valued problems is needed in sundry fields, so the research on CVNNs is meaningful. At present, many researchers have studied the stability of CVNNs, and a large number of related results have been reported (see [8]).

Differential-algebraic systems depend on a combination of differential equations and algebraic equations. Compared with the differential equation system, the differential-algebraic system, as a mathematical model, is more perfect in practical application, such as economic system, chemical process system, and robot system, all of which belong to differential-algebraic systems. Over the past two decades, it has been evidenced that the differential-algebraic (different from the accepted differential geometry) methods could lead to a clearer comprehension of some control concepts and their interrelationships, such as observability, reversibility, decoupling and controller specification form, and observability, existence, and uniqueness of minimal implementations. In [9], the control method problem of a nonlinear differential-algebraic system is considered. In [10], the stability analysis of nonlinear differential-algebraic systems is solved using tools from classical control theory. In [11], a new type of differential-algebraic neural network with delay (DDANN) is proposed. And, one kind of novel mathematical expression combining differential equation and algebraic equation is designed in [12]. In addition to a large number of differential-algebraic systems directly proposed in various disciplines and engineering practices, the theoretical study of differential-algebraic systems also provides new ideas and methods for the study of certain problems in normal systems. For example, optimal control of normal systems, control of specified outputs, and singular perturbations can all be reduced to problems in the theory of differential-algebraic systems. Therefore, the theoretical study of differential-algebraic systems has a wide range of practical engineering background and profound theoretical value. It is important to note that, however, the analysis of differential-algebraic neural networks (DANNs) is still in its early stages.

Based on the above-mentioned argumentation, the target of this article is to investigate a new type of differential-algebraic complex-valued neural network (DACVNN) with delay (DDACVNN). An essential consequent on the global existence and uniqueness of the solution is first proposed. It also shows that under some simple assumptions, we can obtain the unique solution of the system under the compatible initial-value problem. We then derive the global exponential stability of this system. Studying a complex differential-algebraic system has always been a more challenging subject. Approximately stated, the novelties of this article include as follows:

(1) Apply CVNNs to DANN and establish a new type of DDACVNN. In particular, in the discussion in this article, there is no restriction on whether the real and imaginary parts of the activation function are required to be clearly separated.

(2) The sufficient conditions to ensure the existence and uniqueness of DDACVNN solutions are expressed, in terms of Picard existence and uniqueness theorem.

(3) An innovative approach is offered to discuss the stability of DDACVNN; that is, under the present system, global exponential stability (GES) is equivalent to global exponential self-synchronization (GESS), which we also rigorously prove in Lemma 1. Thus, a theorem of GES of DDACVNN is investigated.

The structure of the article is as follows. Section 2 provides the preliminaries, the model description about a DACVNN model, a necessary assumption, and a useful lemma. The main results are given in Section 3. Two illustrative examples are discussed in Section 4 to show the feasibility of the results. At last, some conclusions are dedicated in Section 5.

2. Preliminaries, Model Description, and Hypothesis

2.1. Notation. In the whole article, i signifies the imaginary unit, which is $i = \sqrt{-1}$. For complex number $z = x + iy$, the notation $|z| = \sqrt{x^2 + y^2}$ means the module of z. $\mathbb{R}$ and $\mathbb{R}^n$ stand, respectively, the set of real numbers and all n-dimensional real-valued vectors. $\mathbb{C}$, $\mathbb{C}^n$, and $\mathbb{C}^{n\times m}$ represent, respectively, the set of all complex numbers, the set of all n-dimensional complex-valued vectors, and the set of all $n \times m$ complex-valued matrices. For $z = (z_1, z_2, \ldots z_n)^T \in \mathbb{C}^n$, let $|z| = (|z_1|, |z_2|, \cdots |z_n|)^T$ and $\|z(t)\| = \sqrt{\sum_{k=1}^{n} |z_k(t)|^2}$. For $A \in \mathbb{C}^{n\times n}$ or $\in \mathbb{R}^{n\times n}$, $A = (a_{ij})_{n\times n}$, we define $|A| = (|a_{ij}|)$. The matrix $A = (a_{ij})_{n\times n}$ is called a nonnegative matrix if $a_{ij} \geq 0$ for all i and j. We use $r_k(A)$ to denote k th row sum of $A = (a_{ij})_{n\times n}$ and let $\|A\|_\infty$ to be infinity norm of a matrix A with $\|A\|_\infty = \max_{1\leq k\leq n} r_k(|A|)$. We use $\lambda_{\max}(A)$ to denote the maximum eigenvalue of a $A \in \mathbb{R}^{n\times n}$. For $A \in \mathbb{C}^{n\times n}$, $\|A\|$ denotes a matrix norm defined by $\|A\| = \sqrt{A^* A}$, where A^* shows the conjugate transpose of complex-valued matrix A.

2.2. Model Description. This section presents a DACVNN model, introduces some functional conceptions, and concludes with a basic hypothesis and two lemmas.

In the first place, a complex-valued singular neural network with time delay can be considered as

$$A\frac{dv(t)}{dt} = -Bv(t) + DF(v(t)) + EG(v(t-\tau)) + I, \qquad (1)$$

where matrix $A \in \mathbb{R}^{n\times n}$ may be singular $(0 < \operatorname{rank}(A) = r < n)$; $\tau > 0$ is the time delay; $v(t) = (v_1(t), \ldots, v_n(t))^T \in \mathbb{C}^n$ stands for the complex-valued neuron state vector; $B = \operatorname{diag}\{b_1, \ldots b_n\}$ signifies state feedback coefficient matrix, which $b_k > 0 (k = 1, 2, \ldots, n)$; $D \in \mathbb{C}^{n\times n}$ and $E \in \mathbb{C}^{n\times n}$ correspond to, respectively, the complex-valued connection weight matrix and the complex-valued delayed connection weight matrix; $F(v)$ and $G(v)$ denote complex-valued neuron activation functions; $I \in \mathbb{C}^n$ infers an external complex-valued input signal.

More generally, let $A = \begin{pmatrix} I_r & 0 \\ 0 & 0 \end{pmatrix}$. Next, system (1) can compile a DDACVNN indicated as follows:

$$\begin{cases} \dfrac{dz(t)}{dt} = -B_1 z(t) + D_{11}F_1(z(t)) + D_{12}F_2(w(t)) \\ +E_{11}G_1(z(t-\tau)) + E_{12}G_2(w(t-\tau)) + I_1, \\ 0 = -B_2 w(t) + D_{21}F_1(z(t)) + D_{22}F_2(w(t)) \\ +E_{21}G_1(z(t-\tau)) + E_{22}G_2(w(t-\tau)) + I_2, \end{cases} \tag{2}$$

where $\tau > 0$ is the time delay; $z(t) = (z_1(t), \ldots, z_r(t))^T \in \mathbb{C}^r$ and $w(t) = (w_1(t), \ldots, w_{n-r}(t))^T \in \mathbb{C}^{n-r}$; $B_1 = \mathrm{diag}\{b_{11}, \ldots b_{1r}\}$, $B_2 = \mathrm{diag}\{b_{21}, \ldots b_{2r}\}$, b_{ij} are the positive constants; $D_{11} \in \mathbb{C}^{r\times r}$, $D_{12} \in \mathbb{C}^{r\times(n-r)}$, $D_{21} \in \mathbb{C}^{(n-r)\times r}$, and $D_{22} \in \mathbb{C}^{(n-r)\times(n-r)}$; $E_{11} \in \mathbb{C}^{r\times r}$, $E_{12} \in \mathbb{C}^{r\times(n-r)}$, $E_{21} \in \mathbb{C}^{(n-r)\times r}$, and $E_{22} \in \mathbb{C}^{(n-r)\times(n-r)}$; $F_1(z) = (F_{11}(z_1), \ldots, F_{1r}(z_r))^T$, and $F_2(w) = (F_{21}(w_1), \ldots, F_{2(n-r)}(w_{n-r}))^T$; $G_1(z) = (G_{11}(z_1), \ldots, G_{1r}(z_r))^T$, and $G_2(w) = (G_{21}(w_1), \ldots, G_{2(n-r)}(w_{n-r}))^T$; $I_1 = (I_{11}, \ldots, I_{1r})^T$ and $I_2 = (I_{21}, \ldots, I_{2(n-r)})^T$.

We define a Banach space $C_\tau^r = C([-\tau, 0], \mathbb{C}^r)$, which consists of all continuous complex-valued functions $\eta: [-\tau, 0] \longrightarrow \mathbb{C}^r$. $z_t \in C_\tau^r$ denotes $z_t(s) = z(t+s)$ with regard to $s \in [-\tau, 0]$. Towards $\gamma \in \mathbb{C}^r$, we donate $\gamma \in C_\tau^r$, which signifies $\gamma(s) \equiv \gamma$ in $[-\tau, 0]$. Let $\|\eta(s)\|_\tau = \sqrt{\sum_{k=1}^n |\eta_k(s)|_\tau^2}$ for $\eta \in C_\tau^r$, where $|\eta_k(s)|_\tau = \sup_{s\in[-\tau,0]}|\eta_k(s)|$.

Furthermore, we proceed to consider the initial conditions of DDACVNN (2) listed as follows:

$$z_{t_0} = \eta \in C_\tau^r, w_{t_0} = \theta \in C_\tau^{n-r}. \tag{3}$$

The initial conditions (3) of DDACVNN (2) are known as compatible; the necessary and sufficient condition is

$$\begin{aligned} 0 = &-B_2\theta(0) + D_{21}F_1(\eta(0)) + D_{22}F_2(\theta(0)) \\ &+ E_{21}G_1(\eta(-\tau)) + E_{22}G_2(\theta(-\tau)) + I_2, \end{aligned} \tag{4}$$

where $(\eta^T, \theta^T)^T \in C_\tau^r \times C_\tau^{n-r}$ is known as compatible initial value (CIV).

About CVNNs, the foremost difficulty is to look for an opposite activation function. Judging by Liouville's theorem, CVNNs cannot choose a smooth and bounded function as the activation function, so how to choose a suitable activation function for research also needs to pay attention to the problem. Therefore, in order for the following to proceed smoothly, we need to make the following hypothesis:

Hypothesis 1. $F_{1i}(z), F_{2j}(w), G_{1i}(z)$, and $G_{2j}(w)$ $(i = 1, \ldots, r;\ j = 1, \ldots, (n-r))$ satisfy the Lipschitz continuity condition in the complex domain, and there exist positive diagonal matrices $\widehat{F}_1 = \mathrm{diag}\{\widehat{F}_{11}, \ldots, \widehat{F}_{1r}\}$, $\widehat{F}_2 = \mathrm{diag}\{\widehat{F}_{21}, \ldots, \widehat{F}_{2n-r}\}$, $\widehat{G}_1 = \mathrm{diag}\{\widehat{G}_{11}, \ldots, \widehat{G}_{1r}\}$, and $\widehat{G}_2 = \mathrm{diag}\{\widehat{G}_{21}, \ldots, \widehat{G}_{2n-r}\}$ such that

$$\begin{cases} \left|F_{1i}(z) - F_{1i}(\overline{z})\right| \le \widehat{F}_{1i}|z - \overline{z}|, \\ \left|G_{1i}(z) - G_{1i}(\overline{z})\right| \le \widehat{G}_{1i}|z - \overline{z}|, \end{cases} \tag{5}$$

and

$$\begin{cases} \left|F_{2j}(w) - F_{2j}(\overline{w})\right| \le \widehat{F}_{2j}|w - \overline{w}|, \\ \left|G_{2j}(w) - G_{2j}(\overline{w})\right| \le \widehat{G}_{2j}|w - \overline{w}|, \end{cases} \tag{6}$$

for any $z, \overline{z} \in \mathbb{C}^r$ and $w, \overline{w} \in \mathbb{C}^{n-r}$.

Remark 1. In the discussion of the article, we merely require that the complex-valued activation functions globally Lipschitz.

It is worth noting that, in [13, 14], the activation function is required to be manifested by severing the real and imaginary parts as

$$f_j(z_j) = f_j{}^R(x_j, y_j) + i f_j{}^I(x_j, y_j), j = 1, \ldots, n, \tag{7}$$

where $z_j = x_j + iy_j$, $x_j, y_j \in \mathbb{R}$, $f_j{}^R(x_j, y_j)$ (or $f_j{}^R$) and $f_j{}^I(x_j, y_j)$ (or $f_j{}^I$) demonstrate, respectively, the real and imaginary parts of $f_j(z_j)(j = 1, \ldots, n)$. Hypothesis 1 indicates that the model discussed in this article is suitable for both the case where the activation function can separate the real and imaginary parts, and the case where it cannot be clearly separated. For instance, $f_j(z_j) = 1 - e^{-z_j}/1 + e^{-z_j}$, $j = 1, \ldots, n$.

Finally, an important lemma is offered, which will be applied in the following sections.

Lemma 1. *Let matrix $A = (a_{ij})_{n\times n}$ have nonpositive off-diagonal elements (i.e., $a_{ij} \le 0, i \ne j$); then, each of the following conditions is equivalent to the statement that A is a nonsingular M matrix.*

(1) All the leading principal minors of A are positive

(2) There are n positive constants $\xi_1, \xi_2, \ldots, \xi_n$ such that

$$\xi_i a_{ii} - \sum_{j=1, j\ne i}^n \xi_j \left|a_{ji}\right| > 0, 1 \le i \le n. \tag{8}$$

(3) There are n positive constants $\zeta_1, \zeta_2, \ldots, \zeta_n$ such that

$$\zeta_i a_{ii} - \sum_{j=1, j\ne i}^n \zeta_j \left|a_{ij}\right| > 0, 1 \le i \le n. \tag{9}$$

(4) The diagonal elements of A are all positive and there exists a positive vector θ such that $A\theta > 0$ or $A^T\theta > 0$.

3. Main Results

3.1. The Issue of Existence and Uniqueness of Solutions. The purpose of this subsection is to discuss the existence and uniqueness of the solution with the CIV problem (2) and (3).

First, we discuss the following DACVNN:

$$\begin{cases} \dfrac{dz(t)}{dt} = -B_1 z(t) + D_{11}F_1(z(t)) + D_{12}F_2(w(t)) + l_1(t), \\ 0 = -B_2 w(t) + D_{21}F_1(z(t)) + D_{22}F_2(w(t)) + l_2(t), \end{cases} \tag{10}$$

where the functions l_1: $[t_0, +\infty) \longrightarrow \mathbb{C}^r$ and l_2: $[t_0, +\infty) \longrightarrow \mathbb{C}^{n-r}$ are the continuous and differentiable functions.

We consider the initial conditions of DACVNN (10) as follows:

$$z(t_0) = z_0 \in \mathbb{C}^r, w(t_0) = w_0 \in \mathbb{C}^{n-r}. \tag{11}$$

The initial conditions (11) are considered to be compatible; the necessary and sufficient condition is

$$0 = -B_2 w_0 + D_{21} F_1(z_0) + D_{22} F_2(w_0) + l_2(t_0). \tag{12}$$

Theorem 1. *We assume that Hypothesis 1 is satisfied, and $B_2 - |D_{22}|\widehat{F}_2$ is a M matrix. Afterward, for every CIV condition (11) and (12), there is a unique solution $(z^T(t), w^T(t))^T$ on interval $[t_0, t_+)$ of DACVNN (10), where $t_0 < t_+ \leq +\infty$.*

Proof. First, we define a function g: $\mathbb{R} \times \mathbb{C}^n \longrightarrow \mathbb{C}^m$ such that

$$0 = -B_2 g(t, z) + D_{21} F_1(z) + D_{22} F_2(g(t, z)) + l_2(t), \tag{13}$$

for any $t \geq t_0$ and $z \in \mathbb{C}^r$.

In order to achieve the above effect, without loss of generality, we only need to show that, for every $\overline{t} \geq t_0$ and $\overline{z} \in \mathbb{C}^r$, there exists a $\overline{z} \in \mathbb{C}^{n-r}$, of (13) such that

$$0 = -B_2 \overline{w} + D_{21} F_1(\overline{z}) + D_{22} F_2(\overline{w}) + l_2(\overline{t}). \tag{14}$$

Let $D_{ij} = (d_{ijkl})$. On the basis of Lemma 1, there exist $\xi_s > 0 (s = 1, 2, \ldots, n-r)$ such that

$$\xi_k B_{2k} - \sum_{j=1}^{n-r} d_{22kj} \xi_j \widehat{F}_{2j} > 0, k = 1, \ldots, n-r, \tag{15}$$

as $B_2 - |D_{22}|\widehat{F}_2$ is a M matrix. Thus, we can get

$$r_{\max}\left(\Xi^{-1} B_2^{-1} |D_{22}| \widehat{F}_2 \Xi\right) < 1, \tag{16}$$

where $\Xi = \operatorname{diag}\{\xi_1, \xi_2, \ldots, \xi_{n-r}\}$.

We define an operator

$$T(\alpha) = \Xi^{-1} B_2^{-1} \left[D_{21} F_1(\overline{z}) + D_{22} F_2(\Xi\alpha) + l_2(\overline{t})\right], \tag{17}$$

where $\alpha \in \mathbb{C}^{n-r}$.

According to the definition of the operator $T(\alpha)$, we can get

$$|T(\beta) - T(\alpha)| \leq \Xi^{-1} B_2^{-1} |D_{22}| \widehat{F}_2 \Xi |\beta - \alpha|, \tag{18}$$

regarding whichever $\beta, \alpha \in \mathbb{C}^{n-r}$. By calculating the infinity norm in (18), we can get

$$\|T(\beta) - T(\alpha)\|_\infty \leq \nu \|\beta - \alpha\|_\infty, \tag{19}$$

where

$$\nu = r_{\max}\left(\Xi^{-1} B_2^{-1} |D_{22}| \widehat{F}_2 \Xi\right) < 1. \tag{20}$$

Through (19), we can readily find that T is a contraction operator on $\mathbb{C}^m$. Based on the contraction mapping principle, there exists a unique $\alpha^* \in \mathbb{C}^{n-r}$ so that $T(\alpha^*) = \alpha^*$, which is

$$B_2 \Xi \alpha^* = D_{21} F_1(\overline{z}) + D_{22} F_2(\Xi\alpha^*) + l_2(\overline{t}). \tag{21}$$

Let $\overline{w} = \Xi\alpha^*$, thus (14) satisfies. Therefore, there is a function $g(t, z)$ such that (14) satisfies.

According to (14) and Hypothesis 1, one has

$$\|g(t, \beta) - g(t, \alpha)\| \leq \left\| \left[B_2 - |D_{22}| \widehat{F}_2\right]^{-1} |D_{21}| \widehat{F}_1 \right\| \|\beta - \alpha\|, \tag{22}$$

which shows that the function $g(t, \beta)$ is continuous in $\mathbb{R} \times \mathbb{C}^{n-r}$.

Furthermore, from (14) and DACVNN (10), we see that

$$\frac{dz(t)}{dt} = -B_1 z(t) + D_{11} F_1(z(t)) + D_{12} F_2(g(t, z(t))) + l_1(t). \tag{23}$$

Picard existence and uniqueness theorem ensures existence and uniqueness of the solution $z(t)$ of system (23) considered on interval $[t_0, t_+)$ for any initial value $z_0 \in \mathbb{C}^n$. Furthermore, let $w(t) = g(t, z(t))$, and so there exists a unique solution $(z^T(t), w^T(t))^T$ on interval $[t_0, t_+)$ of the DACVNN (10), with the CIV $(z_0^T, g^T(t_0, z_0))^T$.

Furthermore, we consider the extension of t from $[t_0, t_+)$ to $[t_0, +\infty)$. □

Theorem 2. *We presume that Hypothesis 1 is satisfied, if $B_2 - |D_{22}|\widehat{F}_2$ is a M matrix; afterward, for every CIV $(\eta^T, \theta^T)^T$, DDACVNN (2) has a unique solution $(z^T(t), w^T(t))^T$ on $[t_0, +\infty)$.*

Proof. For $t \in [t_0, t_0 + \tau]$, DDACVNN (2) with CIV $(\eta^T, \theta^T)^T$ can be restated as DACVNN (10), in which

$$\begin{cases} l_1(t) = E_{11} G_1(\eta(t - \tau)) + E_{12} G_2(\theta(t - \tau)) + I_1, \\ l_2(t) = E_{21} G_1(\eta(t - \tau)) + E_{22} G_2(\theta(t - \tau)) + I_2. \end{cases} \tag{24}$$

Through Theorem 1, we can know that DDACVNN (2), which is DACVNN (10), has a unique solution on $[t_0, t_0 + \tau]$. Progressively, we are able to prove that there exists a unique solution on $[t_0, t_0 + k\tau]$ for any $k \geq 1$ of DDACVNN (2).

The existence and uniqueness of the solutions of complex-valued differential-algebraic systems is one of the most basic problems, and it is the premise and basis for discussing the system. Therefore, it is very important and necessary to study the existence and uniqueness of the solution of this system. For these reasons, this article considers the fundamental concepts of the solution of complex-valued differential-algebraic systems via Picard's theorem. □

3.2. Global Exponential Stability. We will consider the globally exponential stability (GES) and globally exponential self-synchronization (GESS) of DDACVNN (2) in this section.

The $(z^{*T}, w^{*T})^T \in \mathbb{C}^r \times \mathbb{C}^{n-r}$ is an equilibrium point of DDACVNN (2) if and only if

$$\begin{cases} 0 = -B_1 z^* + D_{11} F_1(z^*) + D_{12} F_2(w^*) \\ +E_{11} G_1(z^*) + E_{12} G_2(w^*) + I_1, \\ 0 = -B_2 w^* + D_{21} F_1(z^*) + D_{22} F_2(w^*) \\ +E_{21} G_1(z^*) + E_{22} G_2(w^*) + I_2. \end{cases} \tag{25}$$

Definition 1. If regarding any $t \geq t_0$, and regarding any solution $(z^T(t), w^T(t))^T$ of DDACVNN (2) corresponding to the CIV $(\eta^T, \theta^T)^T$, there exists an equilibrium point $(z^{*T}, w^{*T})^T \in \mathbb{C}^r \times \mathbb{C}^{n-r}$ satisfying

$$\|z(t) - z^*\| + \|w(t) - w^*\| \leq K\left[\|\eta - z^*\| + \|\theta - w^*\|\right] e^{-\rangle(t-t_0)}, \tag{26}$$

where $K \geq 1$ and $\varrho > 0$ are constants, then DDACVNN (2) is called GES.

Definition 2. If for any $t \geq t_0$, and for any solutions $(z^T(t), w^T(t))^T$ and $(\overline{z}^T(t), \overline{w}^T(t))^T$ of the DDACVNN (2) corresponding to the two CIVs $(\eta^T, \theta^T)^T$ and $(\overline{\eta}^T, \overline{\theta}^T)^T$, there are two constants $K \geq 1$ and $\varrho > 0$ satisfying

$$\|z(t) - \overline{z}(t)\| + \|w(t) - \overline{w}(t)\| \leq K[\|\eta - \overline{\eta}\| + \|\theta - \overline{\theta}\|] e^{-\rangle(t-t_0)}, \tag{27}$$

then DDACVNN (2) is called GESS.

Remark 2. Generally speaking, exponential stability and exponential self-synchronization are two completely different concepts. Evidently, exponential stability implies exponential self-synchronization but not vice versa. However, under DDACVNN (2), we have the following claim: GESS can deduce GES.

Lemma 2. *GESS is equivalent to GES in DDACVNN (2).*

Proof. We only need to show that GES can be deduced by GESS. Firstly, let $\Phi = (\eta^T, \theta^T)^T$, $u_t(\Phi) = (z^T(t), w^T(t))^T$ signify a solution of DDACVNN (2) with CIV $u_{t_0} = \Phi \in C_\tau^n$.

Suppose DDACVNN (2) is GESS, namely,

$$\|u_t(\Phi) - u_t(\Psi)\| \leq K\|\Phi - \Psi\| e^{-\rangle(t-t_0)}, \tag{28}$$

for any $\Phi, \Psi \in C_\tau^n$ and $t \geq t_0$, where $K \geq 1$ and $\varrho > 0$ are constants.

We define an operator Γ: $C_\tau^n \longrightarrow C_\tau^n$ with $\Gamma(\Phi) = u_s(\Phi)$, where $s \geq t_0$ so that $\sigma = Ke^{-\varrho(s-t_0)} < 1$. By (14), one has

$$\|\Gamma(\Phi) - \Gamma(\Psi)\| \leq \sigma\|\Phi - \Psi\|, \tag{29}$$

so we can get that Γ is a contraction. Then, through the Banach contraction principle, it can be obtained that Γ has a unique fixed point $\Phi^* \in C_\tau^n$, which is the equilibrium point of DDACVNN (2).

After giving the above lemma, we next introduce the following two lemmas. The introduction of these two lemmas plays a key role in the testimony of the next theorem. □

Lemma 3 (see [15]). *Let x: $[t_0 - \tau, +\infty) \longrightarrow [0, +\infty)$ and J: $[t_0, +\infty) \longrightarrow [0, +\infty)$ satisfying*

$$\frac{dx(t)}{dt} \leq -\gamma x(t) + \delta x(t-\tau) + J(t), \tag{30}$$

for $t \geq t_0$, where $\gamma, \delta, \tau > 0$, then

$$\tilde{x}(t) \leq \left(\tilde{x}(t_0) + \int_{t_0}^{t} e^{\alpha(s-t_0)} J(s) ds\right) e^{\alpha(t-t_0)}, \tag{31}$$

for $t \geq t_0$, where α is a constant sufficing $\alpha - \gamma_1 + \gamma_2 e^{\alpha\tau} \leq 0$ and $\tilde{x}(t) = sup_{\theta \in [-\tau, 0]} x(t+\theta)$.

Lemma 4 (see [11]). *Let x, y: $[t_0 - \tau, +\infty) \longrightarrow [0, +\infty)$. $x(t)$ and $y(t)$ are, respectively, continuously differentiable and continuous functions, sufficing*

$$\begin{cases} \dfrac{dx(t)}{dt} & \leq -\gamma_1 x(t) + \gamma_2 x(t-\tau) + \alpha_1 y(t-\tau), \\ y(t) & \leq \delta_1 x(t) + \delta_2 x(t-\tau) + \alpha_2 y(t-\tau). \end{cases} \tag{32}$$

For $t \geq t_0$, where there are positive real numbers $\gamma_1, \gamma_2, \delta_1, \delta_2, \alpha_1$, and α_2. And $x(t) \longrightarrow 0$ and $y(t) \longrightarrow 0$ as $t \longrightarrow \infty$ if $\lambda_{\max}(\Lambda) < 1$, where

$$\Lambda = \begin{pmatrix} e^{-\beta\tau} & \dfrac{\alpha_1}{\beta} \\ \delta_1 e^{-\beta\tau} + \delta_2 & \dfrac{\delta_1\alpha_1 + \beta\alpha_2}{\beta} \end{pmatrix}, \tag{33}$$

where $\beta > 0$ is a constant satisfying $\beta - \gamma_1 + \gamma_2 e^{\beta\tau} \leq 0$, $\tilde{x}(t) = \sup_{\theta \in [-\tau, 0]} x(t+\theta)$, and $\tilde{y}(t) = \sup_{\theta \in [-\tau, 0]} y(t+\theta)$. In addition, if there exists $\varphi > 0$ satisfying

$$\begin{cases} e^{-\beta\tau} + \varphi\left(\delta_1 e^{-\beta\tau} + \delta_2\right) = \sigma_1 < 1, \\ \dfrac{\alpha_1}{\beta\varphi} + \dfrac{\delta_1\alpha_1 + \beta\alpha_2}{\beta} = \sigma_2 < 1, \end{cases} \tag{34}$$

then

$$x(t) + y(t) \leq K\sigma_{\max}\left(\tilde{x}(t_0) + \tilde{y}(t_0)\right) e^{-\rangle(t-t_0)}, \tag{35}$$

for $t \geq t_0$, where $K = \max\{1, \varphi\}/\min\{1, \varphi\}$, $\sigma_{\max} = \max\{\sigma_1, \sigma_2\}$, and $\varrho = -1/\tau \ln\sigma_{\max}$.

Theorem 3. *We assume that hypothesis 1 holds and $B_2 - |D_{22}|\widehat{F}_2$ is a M matrix. Let*

$$\begin{aligned}
\delta_1 &= \max_{1\le l\le m} \frac{r_l\left(|D_{21}|\widehat{F}_1\right)}{r_l\left(B_2 - |D_{22}|\widehat{F}_2\right)},\\
\delta_2 &= \max_{1\le l\le m} \frac{r_l\left(|E_{21}|\widehat{G}_1\right)}{r_l\left(B_2 - |D_{22}|\widehat{F}_2\right)},\\
\alpha_2 &= \max_{1\le l\le m} \frac{r_l\left(|E_{22}|\widehat{G}_2\right)}{r_l\left(B_2 - |D_{22}|\widehat{F}_2\right)},\\
\gamma_1 &= r_{\min}\left(B_1 - |D_{11}|\widehat{F}_1\right) - r_{\max}\left(|D_{12}|\widehat{F}_2\right)\delta_1,\\
\gamma_2 &= r_{\max}\left(|E_{11}|\widehat{G}_1\right) + r_{\max}\left(|D_{12}|\widehat{F}_2\right)\delta_2,\\
\alpha_1 &= r_{\max}\left(|E_{12}|\widehat{G}_2\right) + r_{\max}\left(|D_{12}|\widehat{F}_2\right)\alpha_2,
\end{aligned} \tag{36}$$

and

$$\Lambda = \begin{pmatrix} e^{-\beta\tau} & \dfrac{\alpha_1}{\beta} \\ \delta_1 e^{-\beta\tau} + \delta_2 & \dfrac{\delta_1\alpha_1 + \beta\alpha_2}{\beta} \end{pmatrix}, \tag{37}$$

where $\beta > 0$ is a constant sufficing $\beta - \gamma_1 + \gamma_2 e^{\beta\tau} \le 0$. Then, if $\lambda_{\max}(\Lambda) < 1$, DDACVNN (2) is GES.

Proof. On the basis of Lemma 1, we only need to certify that DDACVNN (2) is able to achieve GESS.

For any two different solutions $(z^T(t), w^T(t))^T$ and $(\overline{z}^T(t), \overline{w}^T(t))^T$ of DDACVNN (2), let $Z(t) = z(t) - \overline{z}(t)$ and $W(t) = w(t) - \overline{w}(t)$. In line with DDACVNN (2), we can obtain that

$$\frac{d}{dt}\|Z(t)\| = \frac{d}{dt}\|z(t) - \overline{z}(t)\| = \frac{d}{dt}\sqrt{\sum_{k=1}^{n}\left|z_k(t) - \overline{z}_k(t)\right|^2}, \tag{38}$$

and

$$B_2\|W(t)\| = B_2\|w(t) - \overline{w}(t)\| = B_{2k}\sqrt{\sum_{k=1}^{m}\left|w_k(t) - \overline{w}_k(t)\right|^2}. \tag{39}$$

Let $|z_i(t) - \overline{z}_i(t)| = \max_{1\le k\le n}\{|z_k(t) - \overline{z}_k(t)|\}$ and $|w_l(t) - \overline{w}_l(t)| = \max_{1\le k\le n}\{|w_k(t) - \overline{w}_k(t)|\}$, then

$$\begin{aligned}
\frac{d}{dt}\|Z(t)\| &\le \sqrt{n}\,\frac{d}{dt}\left|z_i(t) - \overline{z}_i(t)\right|\\
&\le -\sqrt{n}\Bigg\{B_{1i}\left|Z_i(t)\right| + \sum_{j=1}^{m}\left|d_{11ij}\right|\left|F_{1j}\left(z_j(t)\right) - F_{1j}\left(\overline{z}_j(t)\right)\right|\\
&\quad + \sum_{j=1}^{m}\left|d_{12ij}\right|\left|F_{2j}\left(w_j(t)\right) - F_{2j}\left(\overline{w}_j(t)\right)\right|\\
&\quad + \sum_{j=1}^{n}\left|e_{11ij}\right|\left|G_{1j}\left(z_j(t-\tau)\right) - G_{1j}\left(\overline{z}_j(t-\tau)\right)\right|\Bigg\}\\
&\quad + \sqrt{n}\Bigg\{\sum_{j=1}^{m}\left|e_{12ij}\right|\left|G_{2j}\left(w_j(t-\tau)\right) - G_{2j}\left(\overline{w}_j(t-\tau)\right)\right|\\
&\le -B_{1i}\left|Z_i(t)\right| + \sum_{j=1}^{n}\left|d_{11ij}\right|\left|\widehat{F}_{1j}\right|\left|Z_j(t)\right|\\
&\quad + \sum_{j=1}^{m}\left|d_{12ij}\right|\left|\widehat{F}_{2j}\right|\left|W_j(t)\right| + \sum_{j=1}^{n}\left|e_{11ij}\right|\left|\widehat{G}_{1j}\right|\left|Z_j(t-\tau)\right|\\
&\quad + \sum_{j=1}^{m}\left|e_{12ij}\right|\left|\widehat{G}_{2j}\right|\left|W_j(t-\tau)\right|\Bigg\},
\end{aligned} \tag{40}$$

and

$$B_2\|W(t)\| \le \sqrt{m}B_{2l}|W_l(t)| \le \sqrt{m}\left\{\sum_{j=1}^{n}\left|d_{21lj}\right|\widehat{F}_{1j}\left|Z_j(t)\right| + \sum_{j=1}^{m}\left|d_{22lj}\right|\widehat{F}_{2j}\left|W_j(t)\right| + \sum_{j=1}^{n}\left|e_{21lj}\right|\widehat{G}_{1j}\left|Z_j(t-\tau)\right| + \sum_{j=1}^{m}\left|e_{22lj}\right|\widehat{G}_{2j}\left|W_j(t-\tau)\right|\right\}. \tag{41}$$

Let $x(t) = |z_i(t) - \overline{z}_i(t)|$ and $y(t) = |w_l(t) - \overline{w}_l(t)|$. Thus, one has

$$\begin{aligned}\frac{d}{dt}x(t) &\le \{-B_{1i} + \sum_{j=1}^{n}\left|d_{11ij}\right|\widehat{F}_{1j}\}x(t) + \sum_{j=1}^{m}\left|d_{12ij}\right|\widehat{F}_{2j}y(t) + \sum_{j=1}^{n}\left|e_{11ij}\right|\widehat{G}_{1j}x(t-\tau) + \sum_{j=1}^{m}\left|e_{12ij}\right|\widehat{G}_{2j}y(t-\tau)\\ &\le -r_{\min}\left(B_1 - |D_{11}|\widehat{F}_1\right)x(t) + r_{\max}\left(|D_{12}|\widehat{F}_2\right)y(t) + r_{\max}\left(|E_{11}|\widehat{G}_1\right)x(t-\tau) + r_{\max}\left(|E_{12}|\widehat{G}_2\right)y(t-\tau),\end{aligned} \tag{42}$$

and

$$\begin{aligned}y(t) &\le \frac{1}{b_{2l} - \sum_{j=1}^{m}\left|d_{22lj}\right|\widehat{F}_{2j}}\left\{\sum_{j=1}^{n}\left|d_{21lj}\right|\widehat{F}_{1j}x(t) + \sum_{j=1}^{n}\left|e_{21lj}\right|\widehat{G}_{1j}x(t-\tau) + \sum_{j=1}^{m}\left|e_{22lj}\right|\widehat{G}_{2j}y(t-\tau)\right\}\\ &\le \frac{r_l\left(|D_{21}|\widehat{F}_1\right)}{r_l\left(B_2 - |D_{22}|\widehat{F}_2\right)}x(t) + \frac{r_l\left(|E_{21}|\widehat{G}_1\right)}{r_l\left(B_2 - |D_{22}|\widehat{F}_2\right)}x(t-\tau) + \frac{r_l\left(|E_{22}|\widehat{G}_2\right)}{r_l\left(B_2 - |D_{22}|\widehat{F}_2\right)}y(t-\tau)\\ &\le \delta_1 x(t) + \delta_2 x(t-\tau) + \alpha_2 y(t-\tau).\end{aligned} \tag{43}$$

By (42) and (43), it follows that

$$\begin{cases}\dfrac{dx(t)}{dt} \le -\gamma_1 x(t) + \gamma_2 x(t-\tau) + \alpha_1 y(t-\tau),\\ y(t) \le \delta_1 x(t) + \delta_2 x(t-\tau) + \alpha_2 y(t-\tau).\end{cases} \tag{44}$$

According to Lemma 1 for the reason that $I_m - \Lambda$ is a M matrix since $\lambda_{\max}(\Lambda) < 1$. According to Lemma 2, we can deduce that there exists $\varphi > 0$ so that

$$\begin{cases}e^{-\beta\tau} + \varphi\left(\delta_1 e^{-\beta\tau} + \delta_2\right) = \sigma_1 < 1,\\ \dfrac{\alpha_1}{\beta\varphi} + \dfrac{\delta_1\alpha_1 + \beta\alpha_2}{\beta} = \sigma_2 < 1.\end{cases} \tag{45}$$

According to Lemma 2, and by (44) and (45), one has

$$x(t) + y(t) \le K\sigma_{\max}\widetilde{x}(t_0) + \widetilde{y}(t_0))e^{-\rangle(t-t_0)}, \tag{46}$$

for $t \ge t_0$, where $K = \max\{1, \varphi\}/\min\{1, \varphi\}, \sigma_{\max} = \max\{\sigma_1, \sigma_2\}$, and $\varrho = -(1/\tau)\ln\sigma_{\max}$. From (46), one has

$$\|z(t) - \overline{z}(t)\| + \|w(t) - \overline{w}(t)\| \le K'[\|\eta - \overline{\eta}\| + \|\theta - \overline{\theta}\|]e^{-\rangle(t-t_0)}, \tag{47}$$

where $K' = K\max\{\sqrt{n}, \sqrt{m}\}$, $\|\eta - \overline{\eta}\| \ge \widetilde{x}(t_0)$ and $\|\theta - \overline{\theta}\| \ge \widetilde{y}(t_0)$, which signifies that DDACVNN (2) is GESS. In accordance with Lemma 1, DDACVNN (2) is GES. □

Remark 3. In this article, we innovatively combine complex values with DANN and do not study complex-valued in real-valued methods (i.e., divide complex values into real and imaginary parts). And the requirements for the activation function are also reduced a lot (only the condition of global Lipschitz needs to be satisfied), so many restrictions on the activation function are eliminated, making the results of this article more effective.

Remark 4. Above, we propose a new paradigm and skill to discuss the stability of DDACVNN (2). It is strictly proved that, in Lemma 1, the DDACVNN (2) is GES if it can achieve GESS, which is able to reduce the argument of exponential stability in DDACVNN (2). Using a differential-algebraic inequality introduced, the GESS problem is studied, and the GES theorem of DDACVNN is given. Finally, in Theorem 1, it is successfully studied whether DDACVNN (2) can achieve GESS and thus achieve GES.

Remark 5. On the basis of this article, we can also discuss the case of time-varying delays. In fact, in the case where the time delays is time-varying delays, the results of this article still hold. We will continue to consider this issue in future research.

Remark 6. In addition, we can also consider nonlinear differential-algebraic systems. Objectively speaking, there are many essential differences between nonlinear differential-algebraic systems and ordinary differential equations and linear differential-algebraic systems. The most fundamental difference is that of nonzero exponents. In general, in an exponential sense, ordinary differential equations can be thought of as zero-exponential systems, a special case of differential-algebraic systems. The differential-algebraic system we mentioned, generally, refers to the nonzero exponential system, and the transition from the zero-exponential system to the nonzero exponential system is a leap, just like the transition from finite-dimensional space to infinite-dimensional space in mathematical analysis. Therefore, it will inevitably lead to qualitative changes in many issues. All the above have led to the very slow development of the research on nonlinear differential-algebraic systems.

4. Examples

At last, two numerical examples are proposed to demonstrate the above achievements in this section. Respectively, the activation function can separate the real and imaginary parts, and the other is that they cannot be clearly separated.

Example 1. We consider DDACVNN (2), taking $r = 1$ and $n = 3$. We allow $\tau = 0.1, I_1 = 1 + i$ and $I_2 = (0,0)^T$; $F_{1k}(\theta) = G_{1k}(\theta) = F_{2j}(\theta) = G_{2j}(\theta) = 0.5x + i0.5y$ where $\theta = x + iy$, for $k = 1$ and $j = 1, 2$,

$$\begin{aligned} &D_{11} = (1+i)_{1\times1}, E_{11} = (i)_{1\times1}, D_{12} = (-i,0)_{1\times2}, E_{12} = (0, 2+i)_{1\times2}, \\ &D_{21} = \begin{pmatrix} 1-i \\ 0 \end{pmatrix}_{2\times1}, E_{21} = \begin{pmatrix} 1-i \\ 2-i \end{pmatrix}_{2\times1}, \\ &D_{22} = \begin{pmatrix} 1-3i & 2+i \\ -1+i & 3+i \end{pmatrix}_{2\times2}, E_{22} = \begin{pmatrix} 1+2i & 0 \\ -1+i & 3-i \end{pmatrix}_{2\times2}. \end{aligned} \tag{48}$$

$B_1 = (10\sqrt{2})$ and $B_2 = \mathrm{diag}\{8\sqrt{10}, 8\sqrt{10}\}$.

We obviously see that Hypothesis 1 holds and $\widehat{F}_1 = \widehat{G}_1 = (0.5)$ and $\widehat{F}_2 = \widehat{G}_2 = \mathrm{diag}\{0.5, 0.5\}$. By calculation, we have

$$\begin{aligned} &|D_{11}| = (\sqrt{2}), |E_{11}| = (1), |D_{12}| = (1,0), |E_{12}| = (0, \sqrt{5}), \\ &|D_{21}| = \begin{pmatrix} \sqrt{2} \\ 0 \end{pmatrix}, |E_{21}| = \begin{pmatrix} \sqrt{2} \\ \sqrt{5} \end{pmatrix}, |D_{22}| = \begin{pmatrix} \sqrt{10} & \sqrt{5} \\ \sqrt{2} & \sqrt{10} \end{pmatrix}, |E_{22}| = \begin{pmatrix} \sqrt{5} & 0 \\ \sqrt{2} & \sqrt{10} \end{pmatrix}. \end{aligned} \tag{49}$$

And

$$B_2 - |D_{22}|\widehat{F}_2 = \begin{pmatrix} \frac{15\sqrt{10}}{2} & -\sqrt{5} \\ -\sqrt{2} & \frac{15\sqrt{10}}{2} \end{pmatrix}, \tag{50}$$

which is a M matrix. On the basis of Theorem 1, we can conclude that for any CIV $(\eta^T, \theta^T)^T \in C_\tau^1 \times C_\tau^2$, DDACVNN (2) has a unique solution.

Moreover, we can continue to calculate the following:

$$\begin{aligned} &\delta_1 = \max_{1\le l\le m} \frac{r_l(|D_{21}|\widehat{F}_1)}{r_l(B_2 - |D_{22}|\widehat{F}_2)} = 0.0317, \\ &\delta_2 = \max_{1\le l\le m} \frac{r_l(|E_{21}|\widehat{G}_1)}{r_l(B_2 - |D_{22}|\widehat{F}_2)} = 0.0501, \\ &\alpha_2 = \max_{1\le l\le m} \frac{r_l(|E_{22}|\widehat{G}_2)}{r_l(B_2 - |D_{22}|\widehat{F}_2)} = 0.1343, \\ &\gamma_1 = r_{\min}(B_1 - |D_{11}|\widehat{F}_1) - r_{\max}(|D_{12}|\widehat{F}_2)\delta_1 = 13.4192, \\ &\gamma_2 = r_{\max}(|E_{11}|\widehat{G}_1) + r_{\max}(|D_{12}|\widehat{F}_2)\delta_2 = 0.5159, \\ &\alpha_1 = r_{\max}(|E_{12}|\widehat{G}_2) + r_{\max}(|D_{12}|\widehat{F}_2)\alpha_2 = 1.6852, \end{aligned} \tag{51}$$

and

$$\Lambda = \begin{pmatrix} e^{-\beta\tau} & \dfrac{\alpha_1}{\beta} \\ \delta_1 e^{-\beta\tau} + \delta_2 & \dfrac{\delta_1\alpha_1 + \beta\alpha_2}{\beta} \end{pmatrix} = \begin{pmatrix} 0.3263 & 0.1505 \\ 0.0604 & 0.1391 \end{pmatrix}, \tag{52}$$

where $\beta = 11.2 > 0$ such that $\beta - \gamma_1 + \gamma_2 e^{\beta\tau} = -0.6380 < 0$; then, $\lambda(\Lambda) = 0.3663, 0.0991, \lambda_{\max}(\Lambda) = 0.3663 < 1$.

In the example, all the conditions of Theorem 2 are fully satisfied, so in the light of Theorem 2, DDACVNN (2) is GES.

Numerical simulations of Example 1 are exhibited in Figure 1.

Example 2. We consider DDACVNN (2), taking $r = 1$ and $n = 3$. We allow $\tau = 0.1, I_1 = 1 + i$ and $I_2 = (0,0)^T$; $F_{1k}(\theta) = G_{1k}(\theta) = F_{2j}(\theta) = G_{2j}(\theta) = 1 - e^{-|\theta|/1+|\theta|}/1 + e^{-|\theta|/1+|\theta|}$, for $k = 1$ and $j = 1, 2$,

$$\begin{aligned} &D_{11} = (1-i)_{1\times1}, E_{11} = (1-i)_{1\times1}, D_{12} = (i,0)_{1\times2}, E_{12} = (0, 2+i)_{1\times2}, \\ &D_{21} = \begin{pmatrix} 1+i \\ -i \end{pmatrix}_{2\times1}, E_{21} = \begin{pmatrix} 1+2i \\ 1-i \end{pmatrix}_{2\times1}, \\ &D_{22} = \begin{pmatrix} 3+i & 0 \\ -1+i & 1+3i \end{pmatrix}_{2\times2}, E_{22} = \begin{pmatrix} 1+3i & -1+i \\ 0 & 2-i \end{pmatrix}_{2\times2}. \end{aligned} \tag{53}$$

$B_1 = (10\sqrt{2})$ and $B_2 = \mathrm{diag}\{10\sqrt{10}, 9\sqrt{10}\}$.

We obviously see that hypothesis 1 holds and $\widehat{F}_1 = \widehat{G}_1 = (0.5)$ and $\widehat{F}_2 = \widehat{G}_2 = \mathrm{diag}\{0.5, 0.5\}$. By calculation, we have

$$\begin{aligned} &|D_{11}| = (\sqrt{2}), |E_{11}| = (\sqrt{2}), |D_{12}| = (1,0), |E_{12}| = (0, \sqrt{5}), \\ &|D_{21}| = \begin{pmatrix} \sqrt{2} \\ 1 \end{pmatrix}, |E_{21}| = \begin{pmatrix} \sqrt{5} \\ \sqrt{2} \end{pmatrix}, |D_{22}| = \begin{pmatrix} \sqrt{10} & 0 \\ \sqrt{2} & \sqrt{10} \end{pmatrix}, |E_{22}| = \begin{pmatrix} \sqrt{1}\,0 & \sqrt{2} \\ 0 & \sqrt{5} \end{pmatrix}. \end{aligned} \tag{54}$$

And

$$B_2 - |D_{22}|\widehat{F}_2 = \begin{pmatrix} \dfrac{19\sqrt{10}}{2} & 0 \\ -\sqrt{2} & \dfrac{17\sqrt{10}}{2} \end{pmatrix}, \tag{55}$$

which is a M matrix. On the basis of Theorem 1, we can conclude that for any CIV $(\eta^T, \theta^T)^T \in C_\tau^1 \times C_\tau^2$, DDACVNN (2) has a unique solution.

Moreover, we can continue to calculate the following:

$$\begin{aligned} \delta_1 &= \max_{1\le l\le m} \frac{r_l(|D_{21}|\widehat{F}_1)}{r_l(B_2 - |D_{22}|\widehat{F}_2)} = 0.1664, \\ \delta_2 &= \max_{1\le l\le m} \frac{r_l(|E_{21}|\widehat{G}_1)}{r_l(B_2 - |D_{22}|\widehat{F}_2)} = 0.0744, \\ \alpha_2 &= \max_{1\le l\le m} \frac{r_l(|E_{22}|\widehat{G}_2)}{r_l(B_2 - |D_{22}|\widehat{F}_2)} = 0.4985, \\ \gamma_1 &= r_{\min}(B_1 - |D_{11}|\widehat{F}_1) - r_{\max}(|D_{12}|\widehat{F}_2)\delta_1 = 13.3518, \\ \gamma_2 &= r_{\max}(|E_{11}|\widehat{G}_1) + r_{\max}(|D_{12}|\widehat{F}_2)\delta_2 = 0.7443, \\ \alpha_1 &= r_{\max}(|E_{12}|\widehat{G}_2) + r_{\max}(|D_{12}|\widehat{F}_2)\alpha_2 = 1.3673, \end{aligned} \tag{56}$$

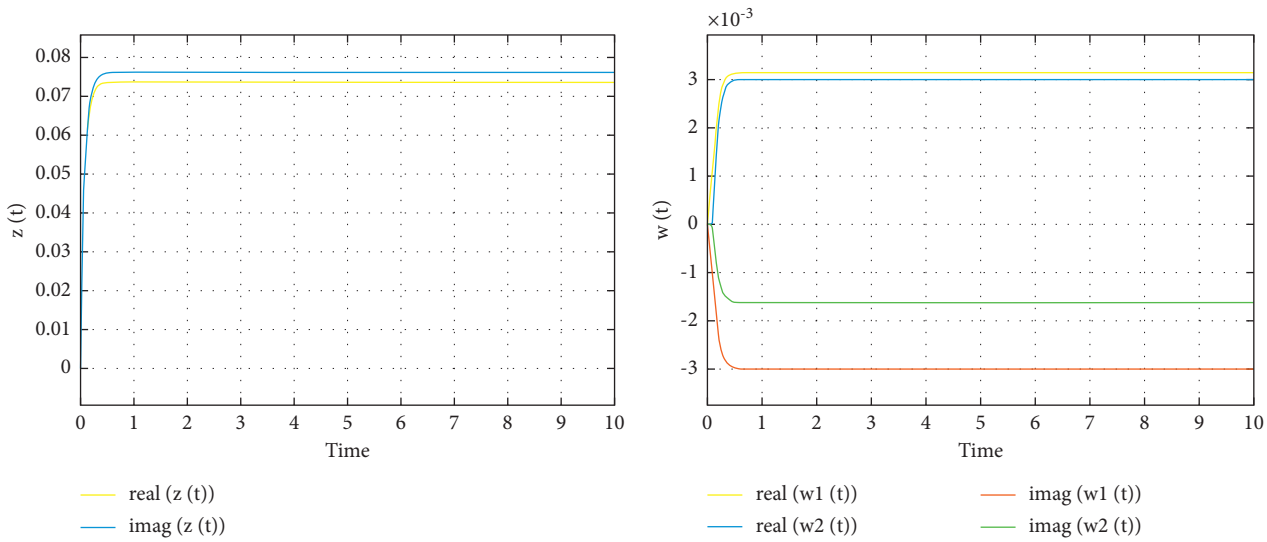

Figure 1: Curves of the real and imaginary parts of $z(t)$ and $w(t)$ in example 1.

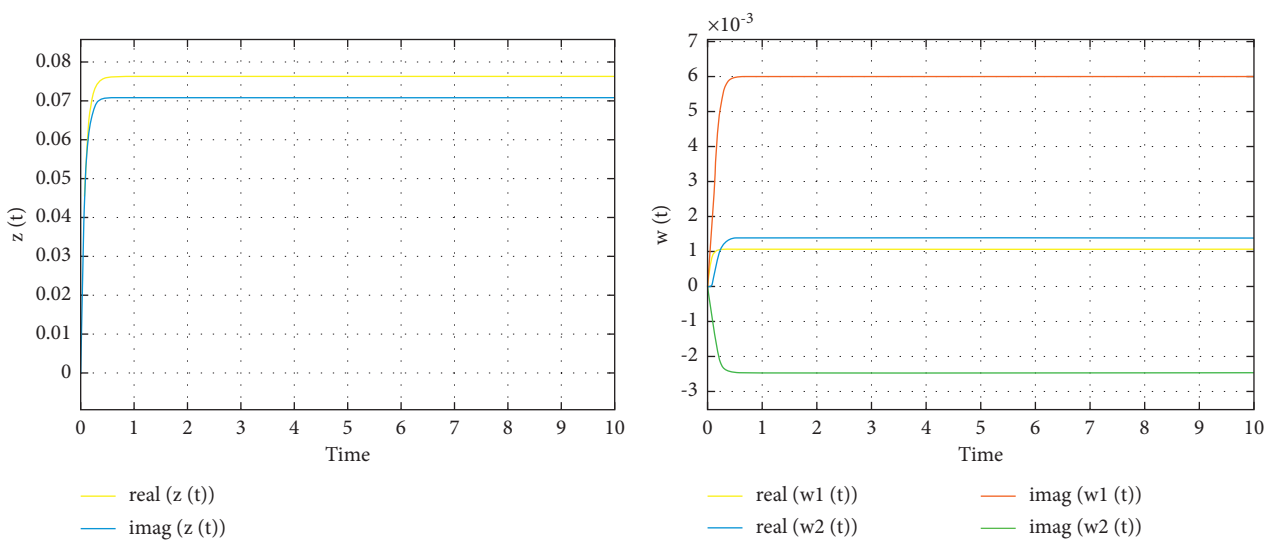

Figure 2: Curves of the real and imaginary parts of $z(t)$ and $w(t)$ in Example 2.

and

$$\Lambda = \begin{pmatrix} e^{-\beta\tau} & \dfrac{\alpha_1}{\beta} \\ \delta_1 e^{-\beta\tau} + \delta_2 & \dfrac{\delta_1\alpha_1 + \beta\alpha_2}{\beta} \end{pmatrix} = \begin{pmatrix} 0.3325 & 0.1242 \\ 0.1297 & 0.5192 \end{pmatrix}, \tag{57}$$

where $\beta = 11.01 > 0$ such that $\beta - \gamma_1 + \gamma_2 e^{\beta\tau} = -0.1036 < 0$; then, $\lambda(\Lambda) = 0.2683, 0.5834$, $\lambda_{\max}(\Lambda) = 0.5834 < 1$.

In the example, all the conditions of Theorem 2 are fully satisfied, so on the basis of Theorem 2, DDACVNN (2) is GES.

Numerical simulations of Example 2 are exhibited in Figure 2.

Remark 7. In the above, we have obtained that the activation function of the system considered in the article is feasible regardless of whether the real and imaginary parts can be departed, and the above two examples also prove the correctness of the derived conclusions.

5. Conclusion

Looked through the article, we establish a new type of DDACVNN. First, the existence and uniqueness of the DDACVNN solution is addressed. In addition, the GES theorem of DDACVNN is also studied. In particular, we verify that our activation function does not have the restriction that the real and imaginary parts must be separated. Finally, we also give two examples to confirm the validity of the theoretical results.

For the sake of simplicity, we only consider a simpler form of the differential-algebraic system. And studying a more complex differential-algebraic system has always been a more challenging subject. For example, we can conduct a series of studies similar to traditional neural networks on differential-algebraic systems, such as multiple stability, synchronicity, and periodic oscillations. At the same time, we can also study a differential-algebraic system with a high degree of exponential, or a differential-algebraic system with variable delays. In addition, we can also consider nonlinear differential-algebraic systems. And these issues will be considered in the future.

Data Availability

No data were used to support this study.

Conflicts of Interest

The authors declare that there are no conflicts of interest regarding the publication of this article.

Acknowledgments

This work was supported by the Natural Science Foundation of China under grant 61976084, the Natural Science Foundation of Hubei Province of China under grant 2021CFA080, and the Young Top-Notch Talent Cultivation Program of Hubei Province of China.

References

[1] P. Pepe, "Discrete-time systems with constrained time delays and delay-dependent Lyapunov functions," *IEEE Transactions on Automatic Control*, vol. 65, no. 4, pp. 1724–1730, 2020.

[2] D. Han, "Improved delay-derivative-dependent stability criteria for linear systems with time-varying delay," in *Proceedings of the 32nd Chinese Control Conference*, pp. 1374–1379, Xi'an, China, Oct. 2013.

[3] C. M. Marcus and R. M. Westervelt, "Stability of analog neural networks with delay," *Physical Review A*, vol. 39, no. 1, pp. 347–359, 1989.

[4] A. Hirose, "Complex-valued neural networks: theories and applications," *World Scientific Publishing Company*, vol. 5, 2003.

[5] T. Nitta, "Orthogonality of decision boundaries in complex-valued neural networks," *Neural Computation*, vol. 16, no. 1, pp. 73–97, 2004.

[6] M. F. Amin and K. Murase, "Single-layered complex-valued neural network for real-valued classification problems," *Neurocomputing*, vol. 72, no. 4-6, pp. 945–955, Jan. 2009.

[7] T. Nitta, "Solving the XOR problem and the detection of symmetry using a single complex-valued neuron," *Neural Networks*, vol. 16, no. 8, pp. 1101–1105, 2003.

[8] Q. Song, Z. Zhao, Y. Liu, and F. E. Alsaadi, "Mean-square input-to-state stability for stochastic complex-valued neural networks with neutral delay," *Neurocomputing*, vol. 470, pp. 269–277, 2022.

[9] W.-T. Wang and G.-M. Li, "Nonlinear control methods for a class of differential-algebraic systems," in *Proceedings of the 2009 Chinese Control and Decision Conference*, pp. 2900–2904, Guilin, China, Aug. 2009.

[10] P. Di Franco, G. Scarciotti, and A. Astolfi, "Stability of nonlinear differential-algebraic systems via additive identity," *IEEE/CAA Journal of Automatica Sinica*, vol. 7, no. 4, pp. 929–941, 2020.

[11] J. Chen, B. Chen, and Z. Zeng, "Basic theorem and global exponential stability of differential-algebraic neural networks with delay," *Neural Networks*, vol. 140, pp. 336–343, Aug. 2021.

[12] Q. Liu and J.-E. Zhang, "Evolution properties of complex-valued memristive differential-algebraic neural networks," in *Proceedings of the 2019 IEEE Symposium Series on Computational Intelligence (SSCI)*, pp. 1255–1262, Xiamen, China, Dec. 2019.

[13] J. Hu and J. Wang, "Global stability of complex-valued recurrent neural networks with time-delays," *IEEE Transactions on Neural Networks and Learning Systems*, vol. 23, no. 6, pp. 853–865, 2012.

[14] X.-H. Xu, J.-Y. Zhang, and J.-Z. Shi, "Exponential stability of complex-valued neural networks with mixed delays," *Neurocomputing*, vol. 128, pp. 483–490, 2014.

[15] J. Chen, B. Chen, Z. Zeng, and P. Jiang, "Event-based synchronization for multiple neural networks with time delay and switching disconnected topology," *IEEE Transactions on Cybernetics*, vol. 51, no. 12, pp. 5993–6003, 2021.

Hindawi
Discrete Dynamics in Nature and Society
Volume 2022, Article ID 8509213, 18 pages
https://doi.org/10.1155/2022/8509213

Research Article

Stabilization of Uncertain Switched Systems with Frequent Asynchronism via Event-Triggered Dynamic Output-Feedback Control

Jin-E Zhang[1] **and Xiangru Xing**[2]

[1]*College of Mathematics and Statistics, Hubei Normal University, Huangshi 435002, China*
[2]*Department of Applied Mathematics, Beijing Jiaotong University, Beijing 100044, China*

Correspondence should be addressed to Jin-E Zhang; zhang86021205@163.com

Received 19 January 2022; Accepted 22 February 2022; Published 15 April 2022

Academic Editor: Jinliang Wang

This article investigates stabilization for a group of uncertain switched systems with frequent asynchronism. Without the limitation of minimum residence time, the average dwell-time strategy makes it possible for switched systems with uncertain parameters to switch frequently over successive event intervals. Since it is highbrow and expensive to obtain the whole state information in practice, the dynamic output-feedback controller is applied. With the aid of a controller-pattern-related Lyapunov functional and an event-triggered dynamic output-feedback controller, sufficient conditions are established to ensure the stability of the resulting uncertain closed-loop system. To appropriately deal with the uncertain parameters, some inequalities of the linear matrix are tactfully utilized together with the Lyapunov functional and controller gains are constructed by the strategy of the block matrix. Furthermore, the presence of the lower boundary on adjacent event intervals is earnestly discussed to eliminate the Zeno behavior. Eventually, the feasibility and availability of the theoretical results are illuminated by a numerical simulation.

1. Introduction

As the control objects become more and more complex, the requirements for the control performance index become higher and higher. At the same time, the system's operation mechanism is restricted by many factors. Many practical control problems can be better solved through the switched system theory. The analysis and integration of switched systems have become a hot issue in the academic and engineering research fields. The concept of switched systems has been formally put forward in the earlier literature [1, 2]. Switched systems, in recent decades, have gained widespread attention in the field of control and have achieved plenteous accomplishments, such as [3–6] and its references. There are two leading reasons for the wide attention paid to switched system theory. On the one hand, switched systems have an extensive range of practical applications in numerous domains, such as transportation systems, robot control systems, power systems, and communication systems. On the other hand, the switched systems have a certain complicacy and idiosyncrasy in comparison with the traditional unitary mode control systems. Nonetheless, it enables the physical procedure and the considered control issues to be more accurate. Over the past decades, a number of achievements for multifarious switched systems have been made in stability analysis as well as control synthesis. The dynamic behavior of switched systems depends not only on each switching subsystem but also on switching rules. An average dwell-time-based switching rule is an effective tool for switched system analysis and synthesis. To name a few, a group of convex lifted conditions about the robust l_2 -stability of discrete-time switched linear systems is proposed by utilizing the switching characteristic of minimum residence time [7]. For the sake of stabilizing the switched systems that incorporate bounded additional perturbations, a quasi-time-varying Lyapunov function is constructed in [8]. And to

guarantee the exponential stabilization of switched systems in the presence of slow and fast switching restricted to unstable and stable subsystems severally, a multiple discontinuous Lyapunov functional technique is proposed in [9].

In the wake of the rapid development of the microelectronic technique, it has become feasible to implement wide-scale calculation in postmodern control theory, which boosts the dynamic analysis of control systems with information sampling [10, 11]. For time-triggered control and the traditional periodic sampling, the sensor sampling systems carry out states or measured outputs at a regular time interval. In spite of this sampling method being conducive to theoretical analysis and implementation, it generally produces vast data packets and results in the sending of redundant data. At this moment, if a state-feedback controller is utilized to feedback the system state, more resources will be wasted. An event-triggered mechanism has been proved to maintain the performance of a networked control system and reduce the number of data packets. However, there is still room for progress in reducing the number of data packets because most of the trigger parameters are static. Then how to further reduce the transmission rate and how to design an adaptive event-triggered mechanism are worth studying. Add in the fact that not all states are measurable in practice; therefore, event-triggered strategy and dynamic output-feedback controller attract considerable attention. For example, on the basis of introducing internal dynamic variables, the dynamic event-triggered approach for linear and nonlinear systems is proposed in [12]. It is testified that the method of dynamic event triggering has less data transmission than the conventional static one. Nevertheless, on account of the characteristics of switched systems, it is a great challenge to set up event-triggered control for system analysis and synthesis. The minimum commutative law is used to design the controller of switched systems so that system switching merely occurs at the triggered moments [13]. In the case of ignoring asynchrony between subsystems and their controllers and guaranteeing the Zeno behavior is eliminated during the event-triggered course, the event-triggered strategy-approved observer-based design of switched linear systems is investigated [14]. Equally, by supposing fully synchronism, the sampling time finiteness of the switched linear systems that incorporate switching signals of average dwell time is guaranteed by processing the event-triggered controller [15]. It is obvious that the assumption in [14, 15] is fairly strict. For the purpose of overcoming this weakness, asynchrony can be considered and event-triggered stability of switched linear neutral systems may be realized in virtue of introducing a maximum asynchrony interval and a minimum dwell time. Subsequently, a switched system with frequent switching between events is investigated in [16].

There are many key structured subsystems in mechanical systems, electronic circuits, robots, and other engineering fields. Meanwhile, these subsystems are mainly composed of core components with uncertainty. It is of great practical significance to study the control problem of complex uncertain dynamic systems and ensure the performance of the system under uncertain disturbances. As is known to all, uncertainty, one of the factors causing system instability, exists in almost all systems. It is inevitable for the existence of uncertainty in the model due to environmental noise, uncertain or slowly changing parameters, and other reasons. Without considering the uncertainty of the model, in practice, it seems preposterous to analyze the performance of a system like estimating the performance indexes in dynamic and steady state. Furthermore, there is usually uncertainty due to random disturbance, inherent variations, missing information, human error, or measurement inaccuracies for nonlinear and linear systems. The source of this uncertainty is known as parametric uncertainty, and parametric uncertainty is probably the most crucial source of model uncertainty [17]. Under the effect of certain factors, in other words, the switched systems with uncertain parameters can depict a broader range of the linear systems. Actually, it is still an unsolved problem to study uncertain switched systems with frequent asynchrony in event-triggered dynamic output-feedback control, and to our astonishment, the uncertainty of output parameters for switched linear systems has not yet received much attention from scholars. After all, in comparison with the traditional processing strategies, the robust treatment of many uncertain parameters in switched systems becomes exceedingly tricky. So far, there is no miraculous solution for detecting the error effects of parameter uncertainty.

In the light of the foregoing discussion, this article is devoted to investigating the exponential stabilization of a frequently switched system which is equipped with the uncertainty of state parameters, input parameters, and measured output parameters. Primarily, some uncertain parameters are inserted in the appropriate position according to the necessity of the model, and some ingenious ways of dealing with them are introduced. In addition, based on the logic mechanism triggered by events and the switching rules of the system and its controller, the matching situation of subsystems and controller could be categorized into synchronous and asynchronous to study the dynamic and steady state performance of the uncertain closed-loop system. The solution of the uncertain closed-loop system is globally exponential stable and no Zeno behavior occurs during the data sampling process, which proves that the selection of controller and problem-resolving method is valid and reasonable. Generally speaking, the primary contributions of this article could be summarized into three points:

(1) Switching linear system model with uncertain parameters is established. By making use of a few inequalities of linear matrix and the strategy of partitioned matrices, the values of parametric uncertainties are legitimately estimated.

(2) Based on the approach of the average dwell time, the co-designing of the event-triggered strategy and the dynamic output-feedback controller, and the construction of the controller-pattern-related Lyapunov functional by adopting block matrix method, the stability criterion of uncertain linear switching system with frequent asynchronism is guaranteed.

(3) In the uncertain switched system, the lower bound criterion of successive event intervals is established to avoid the Zeno behavior, which simultaneously suggests that it can be researched by more extensible frameworks with the methods exploited.

The remaining layout of this article is included as follows: Section 2 furnishes the uncertain system model and preparatory works. Section 3 puts forward the primary theorems for exponential stabilization analysis, controller device, and Zeno behavior elimination. Furthermore, in Section 4, a numerical simulation is added to corroborate the effectiveness of the derived results. Lastly, Section 5 draws a conclusion.

Notations: throughout this article, $\mathbb{R}^{p\times m}$ and $\mathbb{R}^p$ are severally the set of all $p\times m$ real matrices and p-dimensional Euclidean space. $\mathbb{N}$ means nonnegative set. $\mathbb{N}^+$ stands for the set of positive integers. I in matrices or matrix inequalities represents an identity matrix with matched dimensionality. 0 in matrices is a zero matrix of appropriate dimensions. The superscripts -1 and T of matrix $\mathfrak{G}$ represent the inverse and transposition of $\mathfrak{G}$, respectively. $He(\mathfrak{G})$ is defined as $He(\mathfrak{G}) = \mathfrak{G} + \mathfrak{G}^T$. $\mathfrak{G} > 0$ represents that matrix $\mathfrak{G}$ is positive definite and symmetric. $\lambda_{\max}(\mathfrak{G})$ and $\lambda_{\min}(\mathfrak{G})$ represent the maximum and minimum eigenvalue of matrix $\mathfrak{G}$ separately. We utilize $\star$ in a matrix to denote symmetry term. $\|\mathfrak{G}\|$ is defined as the 2-norm of matrix $\mathfrak{G}$.

2. Preliminaries

The switched linear system with parametric uncertainty is of the following form:

$$\begin{aligned}\dot{x}(t) &= \left(A_{\sigma(t)} + \Delta A_{\sigma(t)}\right)x(t) + \left(B_{\sigma(t)} + \Delta B_{\sigma(t)}\right)u(t),\\ y(t) &= \left(C_{\sigma(t)} + \Delta C_{\sigma(t)}\right)x(t),\end{aligned} \tag{1}$$

where $x(t)\in\mathbb{R}^n$, $u(t)\in\mathbb{R}^p$, and $y(t)\in\mathbb{R}^q$ are the system state, control input, and measured output, respectively. $A_{\sigma(t)}$, $B_{\sigma(t)}$, and $C_{\sigma(t)}$ are all known constant matrices, and $\Delta A_{\sigma(t)}$, $\Delta B_{\sigma(t)}$, and $\Delta C_{\sigma(t)}$ are the uncertain parameters. $\sigma(t)$: $[0,+\infty)\longrightarrow\mathscr{L}=\{1,2,\ldots,\mathfrak{n}\}$, signifying the switching signal, is a piecewise constant functional, where $\mathfrak{n}\in\mathbb{N}^+$ represents the quantity of subsystems. $\sigma(t)=j, j\in\mathscr{L}$ indicates the j-th subsystem is active. A chronological sequence $\{t_q, q\in\mathbb{N}\}$ is constructed to indicate that the switching instant is t_q.

For system (1) with parameter uncertainty and unknown nonlinearity, how to introduce an effective control mechanism and this control mechanism will ensure the stability of the closed-loop system and make the system state quickly converge to the ideal state is a difficult research problem.

An adaptive event-triggered precept is adopted to transmit the corresponding activated mode information and measurement output for the continuously updated controller at the instants $\{s_k, k\in\mathbb{N}\}$, which is governed as

$$s_{k+1} = \inf\left\{s_k < t \le s_k + T \mid e_{s_k}^T(t)\Omega_{\sigma(s_k)}e_{s_k}(t) \ge \epsilon y^T(t)\Omega_{\sigma(s_k)}y(t)\right\}, \tag{2}$$

where $e_{s_k}(t) = y(s_k) - y(t)$, $\epsilon>0, T>0$ are prescribed constants and $\Omega_{\sigma(s_k)}$ is a known positive definite matrix.

Remark 1. The argument T restricts the upper bound on each successive event interval and the overall asynchronous time. Not only is it beneficial to analyze and synthesize the problem, but it can also prevent the controller from not being updated for ages. One more point needs to be noted that when the foregoing mechanism is not triggered, according to its conditions, the inequation $e_{s_k}^T(t)\Omega_{\sigma(s_k)}e_{s_k}(t) < \epsilon y^T(t)\Omega_{\sigma(s_k)}y(t)$ holds. And we will employ it later in the proof of theorems.

For uncertain system (1), construct the following dynamic output-feedback control scheme:

$$\begin{aligned}\dot{\tilde{x}}(t) &= \tilde{A}_{\sigma(s_k)}\tilde{x}(t) + \tilde{B}_{\sigma(s_k)}y(s_k),\\ u(t) &= \tilde{C}_{\sigma(s_k)}\tilde{x}(t) + \tilde{D}_{\sigma(s_k)}y(s_k).\end{aligned} \tag{3}$$

For $t\in[s_k, s_{k+1})$, in which $\tilde{x}(t)\in\mathbb{R}^n$ is a controller state, $\tilde{A}_{\sigma(s_k)}$, $\tilde{B}_{\sigma(s_k)}$, $\tilde{C}_{\sigma(s_k)}$, and $\tilde{D}_{\sigma(s_k)}$, to be decided, are all constant matrices.

Substituting (3) into (1), the following augmented system is deduced:

$$\dot{\mathfrak{J}}(t) = \overline{A}_{\sigma(t)\sigma(s_k)}\mathfrak{J}(t) + \overline{B}_{\sigma(t)\sigma(s_k)}e_{s_k}(t), \tag{4}$$

for $t\in[s_k, s_{k+1})$, where $\mathfrak{J}(t) = [x^T(t), \tilde{x}^T(t)]^T$,

$$\begin{aligned}\overline{A}_{\sigma(t)\sigma(s_k)} &= \begin{bmatrix}\mathfrak{A}_{\sigma(t)} + \mathfrak{B}_{\sigma(t)}\tilde{D}_{\sigma(s_k)}\mathfrak{C}_{\sigma(t)} & \mathfrak{B}_{\sigma(t)}\tilde{C}_{\sigma(s_k)}\\ \tilde{B}_{\sigma(s_k)}\mathfrak{C}_{\sigma(t)} & \tilde{A}_{\sigma(s_k)}\end{bmatrix},\\ \overline{B}_{\sigma(t)\sigma(s_k)} &= \begin{bmatrix}\mathfrak{B}_{\sigma(t)}\tilde{D}_{\sigma(s_k)}\\ \tilde{B}_{\sigma(s_k)}\end{bmatrix},\\ \mathfrak{A}_{\sigma(t)} &= A_{\sigma(t)} + \Delta A_{\sigma(t)},\\ \mathfrak{B}_{\sigma(t)} &= B_{\sigma(t)} + \Delta B_{\sigma(t)},\\ \mathfrak{C}_{\sigma(\sigma(t)t)} &= C_{\sigma(t)} + \Delta C_{\sigma(t)}.\end{aligned} \tag{5}$$

In this article, the condition of the aforementioned adaptive event-triggered strategy relies on the error $e_{s_k}(t)$ between the recently updated sampling output and the current sampling output for transmission. When the condition of (2) holds $[s_k, s_k+T)$, the next event will be triggered at $t = s_{k+1}$; subsequently, the controller will update its mode based on the data collected and control system (1). The architecture diagram of the uncertain closed-loop system under event-triggered dynamic output-feedback control is presented in Figure 1.

Now, we hypothesize $\sigma(s_k) = i, \sigma(t_q) = j$ in the chronological sequence $s_k < t_q$ and focus attention on a running

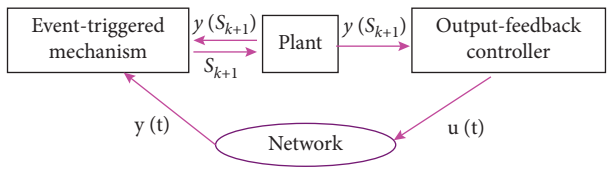

Figure 1: Diagram of the uncertain closed-loop system.

interval $[t_q, t_{q+1})$, which indicates $\sigma(t) = j$ for $\forall t \in [t_q, t_{q+1})$. Afterward, the system dynamics of (4) can be summarized as the following two cases:

Case (i): when mechanism (2) is not triggered in $[t_q, t_{q+1})$, i.e., $s_k < t_q < t_{q+1} \le s_{k+1}$, uncertain closed-loop system (4) is transformed into

$$\dot{\mathfrak{J}}(t) = \overline{A}_{ji}\mathfrak{J}(t) + \overline{B}_{ji}e(t), \tag{6}$$

where $e(t) \triangleq e_{s_k}(t), t \in [t_q, t_{q+1})$.

Case (ii): when mechanism (2) is triggered $m(\in \mathbb{N}^+)$ times in $[t_q, t_{q+1})$, i.e., $s_k < t_q \le s_{k+1} < \cdots < s_{k+m} \le t_{q+1} < s_{k+m+1}$, uncertain closed-loop system (4) is converted into

$$\dot{\mathfrak{J}}(t) = \begin{cases} \overline{A}_{ji}\mathfrak{J}(t) + \overline{B}_{ji}e(t), & t \in \left[t_q, s_{k+1}\right), \\ \overline{A}_{jj}\mathfrak{J}(t) + \overline{B}_{jj}e(t), & t \in [s_{k+1}, s_{k+2}), \\ \vdots \\ \overline{A}_{jj}\mathfrak{J}(t) + \overline{B}_{jj}e(t), & t \in \left[s_{k+m}, t_{q+1}\right), \end{cases} \tag{7}$$

where

$$e(t) \triangleq \begin{cases} e_{s_k}(t), & t \in \left[t_q, s_{k+1}\right), \\ e_{s_{k+1}}(t), & t \in [s_{k+1}, s_{k+2}), \\ \vdots \\ e_{s_{k+m}}(t), & t \in \left[s_{k+m}, t_{q+1}\right). \end{cases} \tag{8}$$

It is notable that the controller merely updates its state in contrast to the subsystem, in which both modes and states change in $[t_q, s_{k+1})$. Once (2) is triggered, (3) will receive both the activated mode information and the measured output, which will generate the synchronism with the corresponding subsystem for $t \in [s_{k+1}, s_{k+2}), \ldots, [s_{k+m}, t_{q+1})$ in Case (ii). Notations $T_\uparrow[t_q, t_{q+1})$ and $T_\downarrow[t_q, t_{q+1})$ are introduced to stand for the asynchronous and synchronous interval of $[t_q, t_{q+1})$ severally, where each subsystem does not match with their controller in interval $T_\uparrow[t_q, t_{q+1})$. After that, the aforementioned uncertain closed-loop system could be rewritten as

$$\dot{\mathfrak{J}}(t) = \begin{cases} \overline{A}_{ji}\mathfrak{J}(t) + \overline{B}_{ji}e(t), & t \in T_\uparrow\left[t_q, t_{q+1}\right), \\ \overline{A}_{jj}\mathfrak{J}(t) + \overline{B}_{jj}e(t), & t \in T_\downarrow\left[t_q, t_{q+1}\right). \end{cases} \tag{9}$$

As an assumption, several definitions and lemmas are given for employing in the sequel.

Assumption 1.

$$\left[\Delta A_{\sigma(t)} \;\; \Delta B_{\sigma(t)} \;\; \Delta C_{\sigma(t)}\right] = M_{\sigma(t)}E_{\sigma(t)}(t)\left[F_{\sigma(t)} \;\; F_{\sigma(t)}' \;\; F_{\sigma(t)}''\right], \tag{10}$$

where $E_{\sigma(t)}(t)$ is the unknown time-varying matrix with $E_{\sigma(t)}^T(t)E_{\sigma(t)}(t) \le I$, $F_{\sigma(t)}$ and $F_{\sigma(t)}'$ are constant matrices with applicable dimensionality and $M_{\sigma(t)}$ and $F_{\sigma(t)}'$ are nonsingular real matrices with appropriate dimensionality.

Remark 2. The uncertainties have a direct influence on the structure and stability of switched systems due to their own uncertainty. In order to avoid needlessly sophisticated notations and suppress parameter uncertainty, we only consider norm-bounded uncertainties. By utilizing subsequent Lemma 1, the effect of the uncertainty time-varying matrix $E_{\sigma(t)}(t)$ could be reasonably eliminated so that the uncertainties $\Delta A_{\sigma(t)}$, $\Delta B_{\sigma(t)}$, and $\Delta C_{\sigma(t)}$ could be tactfully estimated. However, when the uncertain terms also appear in other singular structures, the results obtained by the lemma could be extended to this case in parallel.

Definition 1. For any initial conditions and constants $k > 0$ and $\lambda > 0$, system (9) is said to be globally exponentially stable under some switching signals $\sigma(t)$, if the solution of system (9) satisfies $\|\mathfrak{J}(t)\| \le ke^{-\lambda(t-t_0)}\|\mathfrak{J}(t_0)\|$, $\forall t \ge t_0$.

Definition 2. For the switching signal $\sigma(t)$ and any $t_2 \ge t_1 \ge 0$, the switching number of $\sigma(t)$ labelled as $\mathfrak{n}_\sigma(t_1, t_2)$ during the interval (t_1, t_2). If there exist constants $\mathfrak{n}_0 > 0$ and $\tau_a > 0$ such that $\mathfrak{n}_\sigma(t_1, t_2) \le \mathfrak{n}_0 + t_2 - t_1/\tau_a$, then τ_a is called the average dwell time of $\sigma(t)$ and $\mathfrak{n}_0$ is called the chatter bound.

Lemma 1 (see [18]). *Let $\mathcal{G}$, $\mathcal{H}$, and $\mathcal{J}$ be constant matrices of suitable dimensionality and $\mathcal{F}(t)$ be a matrix function.*

(1) For any $\varepsilon > 0$ and $\mathcal{F}^T(t)\mathcal{F}(t) \le I$, then

$$\mathcal{H}\mathcal{F}(t)\mathcal{J} + \mathcal{J}^T\mathcal{F}^T(t)\mathcal{H}^T \le \frac{1}{\varepsilon}\mathcal{H}\mathcal{H}^T + \varepsilon\mathcal{J}^T\mathcal{J}. \quad (11)$$

(2) *For any $\varepsilon > 0$ such that $\varepsilon\mathcal{J}^T\mathcal{J} < I$ and $\mathcal{F}^T(t)\mathcal{F}(t) \le I$, then*

$$(\mathcal{G} + \mathcal{H}\mathcal{F}(t)\mathcal{J})(\mathcal{G} + \mathcal{H}\mathcal{F}(t)\mathcal{J})^T \le \mathcal{G}\left(I - \varepsilon\mathcal{J}^T\mathcal{J}\right)^{-1}\mathcal{G}^T + \frac{1}{\varepsilon}\mathcal{H}\mathcal{H}^T. \quad (12)$$

Especially, when $\mathcal{G} \equiv 0$, we get

$$\mathcal{H}\mathcal{F}(t)\mathcal{J}(\mathcal{H}\mathcal{F}(t)\mathcal{J})^T \le \frac{1}{\varepsilon}\mathcal{H}\mathcal{H}^T. \quad (13)$$

Lemma 2. *Given constant matrices $\mathcal{M}_1, \mathcal{M}_2, \mathcal{M}_3$, where $\mathcal{M}_1 = \mathcal{M}_1^T$ and $\mathcal{M}_2 > 0$, then*

$$\mathcal{M}_1 + \mathcal{M}_3^T\mathcal{M}_2^{-1}\mathcal{M}_3 < 0, \quad (14)$$

if

$$\begin{bmatrix} \mathcal{M}_1 & \mathcal{M}_3^T \\ \mathcal{M}_3 & -\mathcal{M}_2 \end{bmatrix} < 0 \quad \text{or} \begin{bmatrix} -\mathcal{M}_2 & \mathcal{M}_3 \\ \mathcal{M}_3^T & \mathcal{M}_1 \end{bmatrix} < 0. \quad (15)$$

Lemma 3 (see [19]). *The following representations are equivalent:*

(1) *There exist constant matrices $\mathcal{N}$, $\mathcal{V}$, $\mathcal{W}$, and $\mathcal{Z}$ and real scalar ς such that*

$$\begin{bmatrix} \mathcal{N} & \star \\ \mathcal{W} - \varsigma & \varsigma\mathcal{Z} + \varsigma\mathcal{Z}^T \end{bmatrix} < 0. \quad (16)$$

(2) *There exist constant matrices $\mathcal{N}$, $\mathcal{V}$, and $\mathcal{W}$ such that*

$$\begin{aligned} &\mathcal{N} < 0 \\ &\mathcal{N} + \mathcal{V}^T\mathcal{W} + \mathcal{W}^T\mathcal{V} < 0. \end{aligned} \quad (17)$$

Lemma 4 (see [16]). *Define $\mathcal{S}_1(t)$, $\mathcal{S}_2(t)$, and $\mathcal{G}(t,\cdot)$ as continuous functions for any $t \ge 0$; in particular, $\mathcal{G}(t,\cdot)$ is differentiable. If $\mathcal{S}_2(t_0) \le \mathcal{S}_1(t_0)$ and*

$$\begin{aligned} \dot{\mathcal{S}}_1(t) &= \mathcal{G}(t, \mathcal{S}_1(t)), \\ \dot{\mathcal{S}}_2(t) &\le \mathcal{G}(t, \mathcal{S}_2(t)), \end{aligned} \quad (18)$$

then $\mathcal{S}_2(t) \le \mathcal{S}_1(t)$, $\forall t \ge t_0$.

3. Main Results

In this section, the event-triggered mechanism and the dynamic output-feedback controller will be jointly devised to investigate the exponential stability of the switched linear system with uncertainties under the asynchrony phenomenon. In addition, we exclude Zeno's behavior by proving the existence of the lower boundary of the interevent intervals.

3.1. Stability Analysis. This section aims at the stability criterion for uncertain systems (9) with the adhibition of the average dwell-time switching approach and a controller-pattern-dependent Lyapunov functional.

Theorem 1. *With regard to given scalars $\gamma > 0$, $\delta > 0$, $\eta \ge 1$, $T > 0$, and $\epsilon > 0$, if Assumption 1 holds and there exist matrices $P_i > 0$, $\Omega_i > 0$, $\exists h_{iab} > 0$ $(a = 1, 2, \ldots, 7; b = 1, 2)$, $\exists h_{i8} > 0$, and $\forall i \in \mathcal{L}$ such that*

$$\Psi_{ji} = \begin{bmatrix} \Psi_{ji}^1 & P_i\overline{\overline{B}}_{ji}\mathcal{E}_i \end{bmatrix} < 0, \quad \forall i \ne j \in \mathcal{L}, \quad (19)$$

$$\Psi_{jj} = \begin{bmatrix} \Psi_{jj}^1 & P_j\overline{\overline{B}}_{jj}\mathcal{E}_j \end{bmatrix} < 0, \quad \forall j \in \mathcal{L}, \quad (20)$$

$$P_j \le \eta P_i, \quad \forall i \ne j \in \mathcal{L}, \quad (21)$$

$$\begin{bmatrix} I & F_j'\tilde{D}_iM_j \\ M_j^T\tilde{D}_i^TF_j'^T & \frac{1}{h_{i8}}I \end{bmatrix} > 0, \quad \forall i \ne j \in \mathcal{L}, \quad (22)$$

$$\begin{bmatrix} I & F_j'\tilde{D}_jM_j \\ M_j^T\tilde{D}_j^TF_j'^T & \frac{1}{h_{j8}}I \end{bmatrix} > 0, \quad \forall j \in \mathcal{L}, \quad (23)$$

where

$$
\begin{aligned}
\Psi_{ji}^{1} &= He\left(P_i\overline{\overline{A}}_{ji}\right) + \mathcal{Q}_i - \delta P_i,\\
\Psi_{jj}^{1} &= He\left(P_j\overline{\overline{A}}_{jj}\right) + \mathcal{Q}_j + \gamma P_j,\\
\widetilde{A}_i &= \begin{bmatrix} A_j + B_j\widetilde{D}_iC_j & B_j\widetilde{C}_i \\ \widetilde{B}_iC_j & \widetilde{A}_i \end{bmatrix},\\
\widetilde{B}_i &= \begin{bmatrix} B_j\widetilde{D}_i \\ \widetilde{B}_i \end{bmatrix},\\
\mathcal{Q}_i &= \begin{bmatrix} \mathcal{Q}_{i1} & \mathcal{Q}_{i2} \\ \mathcal{Q}_{i3} & \mathcal{Q}_{i4} \end{bmatrix},\\
P_i &= \begin{bmatrix} P_{i1} & P_{i2} \\ P_{i2}^T & P_{i3} \end{bmatrix},\\
\mathcal{Q}_{i1} &= (h_{i11} + h_{i21} + h_{i71} + h_{i41})P_{i1}M_jM_j^TP_{i1}\\
&\quad + h_{i31}P_{i1}B_j\widetilde{D}_iM_jM_j^T\widetilde{D}_i^TB_j^TP_{i1} + h_{i51}P_{i2}\widetilde{B}_iM_jM_j^T\widetilde{B}_i^TP_{i2}^T\\
&\quad + \frac{1}{h_{i11}}F_j^TF_j + \left(\frac{1}{h_{i31}} + \frac{1}{h_{i51}} + \frac{1}{h_{i41}h_{i8}}\right)F''^T_jF''_j\\
&\quad + \frac{1}{h_{i21}}C_j^T\widetilde{D}_i^TF'^T_jF'_j\widetilde{D}_iC_j + \epsilon C_j^T\Omega_iC_j,\\
\mathcal{Q}_{i3} &= (h_{i12} + h_{i22} + h_{i42})P_{i2}^TM_jM_j^TP_{i2} + h_{i32}P_{i2}^TB_j\widetilde{D}_iM_jM_j^T\widetilde{D}_i^TB_j^TP_{i2}\\
&\quad + h_{i52}P_{i3}\widetilde{B}_iM_jM_j^T\widetilde{B}_i^TP_{i3} + \frac{1}{h_{i12}}F_j^TF_j + \left(\frac{1}{h_{i32}} + \frac{1}{h_{i52}} + \frac{1}{h_{i42}h_{i8}}\right)F''^T_jF''_j\\
&\quad + \frac{1}{h_{i22}}C_j^T\widetilde{D}_i^TF'^T_jF'_j\widetilde{D}_iC_j,\\
\mathcal{Q}_{i2} &= \frac{1}{h_{i61}}\widetilde{C}_i^TF'^T_jF'_j\widetilde{C}_i + h_{i61}P_{i1}M_jM_j^TP_{i1},\\
\mathcal{Q}_{i4} &= \frac{1}{h_{i62}}\widetilde{C}_i^TF'^T_jF'_j\widetilde{C}_i + (h_{i62} + h_{i72})P_{i2}^TM_jM_j^TP_{i2},\\
\mathcal{X}_i &= \left(\frac{1}{h_{i71}} + \frac{1}{h_{i72}}\right)\widetilde{D}_i^TF'^T_jF'_j\widetilde{D}_i - \Omega_i,
\end{aligned}
\tag{24}
$$

then uncertain system (9) is globally exponentially stable with the average dwell time τ_a satisfying

$$\tau_a \geq \frac{\ln\eta + (\gamma + \delta)T}{\gamma}. \tag{25}$$

Proof. Construct the controller-pattern-related Lyapunov function $V(\mathfrak{J}(t))\mathfrak{J}^T(t)P_{\sigma(s_k)}\mathfrak{J}(t)$ by the strategy of the block matrix. It is evident that $V(\mathfrak{J}(t))$, except for a limited number of discontinuities, remains continuous. Then, in accordance with the cases in the hereinabove section, the stabilization analysis can be accordingly carried out from the two standpoints as follows:

Case (i): when mechanism (2) is not triggered during $[t_q, t_{q+1})$, the uncertain closed-loop system is $\overline{A}_{ji}\mathfrak{J}(t) + \overline{B}_{ji}e(t)$ with the Lyapunov function $V(\mathfrak{J}(t)) = \mathfrak{J}^T(t)P_i\mathfrak{J}(t)$.

By means of taking the derivative with respect to $V(\mathfrak{J}(t))$ along the system trajectory and exploiting the mechanism (2), we get

$$
\begin{aligned}
&\dot{V}(\mathfrak{J}(t)) - \delta V(\mathfrak{J}(t)) = 2\mathfrak{J}^T(t)P_i\dot{\mathfrak{J}}(t) - \delta\mathfrak{J}^T(t)P_i\mathfrak{J}(t)\\
&\leq 2\mathfrak{J}^T(t)P_i\left(\overline{A}_{ji}\mathfrak{J}(t) + \overline{B}_{ji}e(t)\right)\\
&- \delta\mathfrak{J}^T(t)P_i\mathfrak{J}(t) - e(t)^T\Omega_ie(t) + \varepsilon x^T(t)C_j^T\Omega_iC_jx(t).
\end{aligned}
\tag{26}
$$

On account of Lemma 1 (1), (2), Lemma 2, and (22), we get

$$
\begin{aligned}
He\left(\begin{bmatrix} P_{i1}\Delta A_j \\ P_{i2}^T\Delta A_j \end{bmatrix}\right) &\le \begin{bmatrix} \frac{1}{h_{i11}}F_j^T F_j + h_{i11}P_{i1}M_jM_j^TP_{i1} \\ \frac{1}{h_{i12}}F_j^T F_j + h_{i12}P_{i2}^TM_jM_j^TP_{i2} \end{bmatrix}, \\
He\left(\begin{bmatrix} P_{i1}\Delta B_j\tilde{D}_iC_j \\ P_{i2}^T\Delta B_j\tilde{D}_iC_j \end{bmatrix}\right) &\le \begin{bmatrix} \frac{1}{h_{i21}}C_j^T\tilde{D}_i^TF_j'^TF_j'\tilde{D}_iC_j + h_{i21}P_{i1}M_jM_j^TP_{i1} \\ \frac{1}{h_{i22}}C_j^T\tilde{D}_i^TF_j'^TF_j'\tilde{D}_iC_j + h_{i22}P_{i2}^TM_jM_j^TP_{i2} \end{bmatrix}, \\
He\left(\begin{bmatrix} P_{i1}B_j\tilde{D}_i\Delta C_j \\ P_{i2}^TB_j\tilde{D}_i\Delta C_j \end{bmatrix}\right) &\le \begin{bmatrix} \frac{1}{h_{i31}}F_j'^TF_j'h_{i31}P_{i1}B_j\tilde{D}_iM_jM_j^T\tilde{D}_i^TB_j^TP_{i1} \\ \frac{1}{h_{i32}}F_j'^TF_j' + h_{i32}P_{i2}^TB_j\tilde{D}_iM_jM_j^T\tilde{D}_i^TB_j^TP_{i2} \end{bmatrix}, \\
He\left(\begin{bmatrix} P_{i1}\Delta B_j\tilde{D}_i\Delta C_j \\ P_{i2}^T\Delta B_j\tilde{D}_i\Delta C_j \end{bmatrix}\right) &\le \begin{bmatrix} \frac{1}{h_{i41}}F_j''^TE_j^TM_j^T\tilde{D}_i^TF_j'^TF_j'\tilde{D}_iM_jE_jF_j'' \\ \frac{1}{h_{i42}}F_j''^TE_j^TM_j^T\tilde{D}_i^TF_j'^TF_j'\tilde{D}_iM_jE_jF_j'' \end{bmatrix} \\
&+ \begin{bmatrix} h_{i41}P_{i1}M_jM_j^TP_{i1} \\ h_{i42}P_{i2}^TM_jM_j^TP_{i2} \end{bmatrix} \le \begin{bmatrix} \frac{1}{h_{i41}\cdot h_{i8}}F_j''^TF_j'' + h_{i41}P_{i1}M_jM_j^TP_{i1} \\ \frac{1}{h_{i42}\cdot h_{i8}}F_j''^TF_j'' + h_{i42}P_{i2}^TM_jM_j^TP_{i2} \end{bmatrix}, \\
He\left(\begin{bmatrix} P_{i2}\tilde{B}_i\Delta C_j \\ P_{i3}\tilde{B}_i\Delta C_j \end{bmatrix}\right) &\le \begin{bmatrix} \frac{1}{h_{i51}}F_j''^TF_j'' + h_{i51}P_{i2}\tilde{B}_iM_jM_j^T\tilde{B}_i^TP_{i2}^T \\ \frac{1}{h_{i52}}F_j''^TF_j'' + h_{i52}P_{i3}\tilde{B}_iM_jM_j^T\tilde{B}_i^TP_{i3} \end{bmatrix}, \\
He\left(\begin{bmatrix} P_{i1}\Delta B_j\tilde{C}_i \\ P_{i2}^T\Delta B_j\tilde{C}_i \end{bmatrix}\right) &\le \begin{bmatrix} \frac{1}{h_{i61}}\tilde{C}_i^TF_j'^TF_j'\tilde{C}_i + h_{i61}P_{i1}M_jM_j^TP_{i1} \\ \frac{1}{h_{i62}}\tilde{C}_i^TF'^T_jF_j'\tilde{C}_i + h_{i62}P_{i2}^TM_jM_j^TP_{i2} \end{bmatrix}, \\
He\left(\begin{bmatrix} x^T(t)P_{i1}\Delta B_j\tilde{D}_ie(t) \\ \tilde{x}^T(t)P_{i2}^T\Delta B_j\tilde{D}_{ii}e(t) \end{bmatrix}\right) &\le \begin{bmatrix} \frac{1}{h_{i71}}e^T(t)\tilde{D}_{ii}^TF_j'^TF_j'\tilde{D}_ie(t) \\ \frac{1}{h_{i72}}e^T(t)\tilde{D}_{ii}^TF_j'^TF_j'\tilde{D}_{ii}e(t) \end{bmatrix} \\
&+ \begin{bmatrix} h_{i71}x^T(t)P_{i1}M_jM_j^TP_{i1}x(t) \\ h_{i72}\tilde{x}^T(t)P_{i2}^TM_jM_j^TP_{i2}\tilde{x}(t) \end{bmatrix}.
\end{aligned}
\tag{27}
$$

Then, it holds that

$$\dot{V}(\mathfrak{J}(t)) - \delta V(\mathfrak{J}(t)) = \mathfrak{J}_1^T(t)\Psi_{ji}\mathfrak{J}_1(t), \tag{28}$$

where $\mathfrak{J}_1(t) = [\mathfrak{J}^T(t), e^T(t)]^T$. It is apparent that $\dot{V}(\mathfrak{J}(t)) \le \delta V(\mathfrak{J}(t))$ from (19) for $\forall t \in [t_q, t_{q+1})$.

Combining the property of $V(\mathfrak{J}(t))$ at the instant $t = t_{q+1}$, it could be calculated that

$$V\left(\mathfrak{J}\left(t_{q+1}\right)\right) = V\left(\mathfrak{J}\left(t_{q+1}^-\right)\right) \le e^{\delta\left(t_{q+1}-t_q\right)}V\left(\mathfrak{J}\left(t_q\right)\right). \tag{29}$$

Case (ii): when mechanism (2) is triggered $m(\in \mathbb{N}^+)$ times during $[t_q, t_{q+1})$, the uncertain closed-loop system is converted into

$$\dot{\mathfrak{J}}(t) = \begin{cases} \overline{A}_{ji}\mathfrak{J}(t) + \overline{B}_{ji}e(t), & t \in \left[t_q, s_{k+1}\right), \\ \overline{A}_{jj}\mathfrak{J}(t) + \overline{B}_{jj}e(t), & t \in \left[s_{k+1}, t_{q+1}\right), \end{cases} \tag{30}$$

with the Lyapunov functional

$$V(\mathfrak{J}(t)) = \begin{cases} \mathfrak{J}^T(t)P_i\mathfrak{J}(t), & t \in \left[t_q, s_{k+1}\right), \\ \mathfrak{J}^T(t)P_j\mathfrak{J}(t), & t \in \left[t_q, s_{k+1}\right). \end{cases} \tag{31}$$

Executing the same procedure in Case (i) and employing condition (21), it could be obtained that

$$V(\mathfrak{J}(s_{k+1})) = V(\mathfrak{J}(s_{k+1}^-)) \le \eta e^{\delta\left(s_{k+1}-t_q\right)} V\left(\mathfrak{J}\left(t_q\right)\right). \tag{32}$$

For $t \in [s_{k+1}, t_{q+1})$, by virtue of Lemma 1 (1), (2), Lemma 2, and (23), we have

$$\begin{aligned}
He\left(\begin{bmatrix} P_{j1}\Delta A_j \\ P_{j2}^T\Delta A_j \end{bmatrix}\right) &\le \begin{bmatrix} \frac{1}{h_{j11}}F_j^TF_j + h_{j11}P_{j1}M_jM_j^TP_{j1} \\ \frac{1}{h_{j12}}F_j^TF_j + h_{j12}P_{j2}^TM_jM_j^TP_{j2} \end{bmatrix}, \\
He\left(\begin{bmatrix} P_{j1}\Delta B_j\tilde{D}_jC_j \\ P_{j2}^T\Delta B_j\tilde{D}_jC_j \end{bmatrix}\right) &\le \begin{bmatrix} \frac{1}{h_{j21}}C_j^T\tilde{D}_j^TF_j'^TF_j'\tilde{D}_jC_j + h_{j21}P_{j1}M_jM_j^TP_{j1} \\ \frac{1}{h_{j22}}C_j^T\tilde{D}_j^TF_j'^TF_j'\tilde{D}_jC_j + h_{j22}P_{j2}^TM_jM_j^TP_{j2} \end{bmatrix}, \\
He\left(\begin{bmatrix} P_{j1}B_j\tilde{D}_j\Delta C_j \\ P_{j2}^TB_j\tilde{D}_j\Delta C_j \end{bmatrix}\right) &\le \begin{bmatrix} \frac{1}{h_{j31}}F_j''^TF_j'' + h_{j31}P_{j1}B_j\tilde{D}_jM_jM_j^T\tilde{D}_j^TB_j^TP_{j1} \\ \frac{1}{h_{j32}}F_j''^TF_j'' + h_{j32}P_{j2}^TB_j\tilde{D}_jM_jM_j^T\tilde{D}_j^TB_j^TP_{j2} \end{bmatrix}, \\
He\left(\begin{bmatrix} P_{j1}\Delta B_j\tilde{D}_j\Delta C_j \\ P_{j2}^T\Delta B_j\tilde{D}_j\Delta C_j \end{bmatrix}\right) &\le \begin{bmatrix} \frac{1}{h_{j41}\cdot h_{j8}}F_j''^TF_j'' + h_{j41}P_{j1}M_jM_j^TP_{j1} \\ \frac{1}{h_{j42}\cdot h_{j8}}F_j''^TF_j'' + h_{j42}P_{j2}^TM_jM_j^TP_{j2} \end{bmatrix}, \\
He\left(\begin{bmatrix} P_{j2}\tilde{B}_j\Delta C_j \\ P_{j3}\tilde{B}_j\Delta C_j \end{bmatrix}\right) &\le \begin{bmatrix} \frac{1}{h_{j51}}F_j''^TF_j'' + h_{j51}P_{j2}\tilde{B}_jM_jM_j^T\tilde{B}_j^TP_{j2}^T \\ \frac{1}{h_{j52}}F_j''^TF_j'' + h_{j52}P_{j3}\tilde{B}_jM_jM_j^T\tilde{B}_j^TP_{j3} \end{bmatrix}, \\
He\left(\begin{bmatrix} P_{j1}\Delta B_j\tilde{C}_j \\ P_{j2}^T\Delta B_j\tilde{C}_j \end{bmatrix}\right) &\le \begin{bmatrix} \frac{1}{h_{j61}}\tilde{C}_j^TF_j'^TF_j'\tilde{C}_j + h_{i61}P_{j1}M_jM_j^TP_{j1} \\ \frac{1}{h_{j62}}\tilde{C}_j^TF_j'^TF_j'\tilde{C}_j + h_{j62}P_{j2}^TM_jM_j^TP_{j2} \end{bmatrix}, \\
He\left(\begin{bmatrix} x^T(t)P_{j1}\Delta B_j\tilde{D}_je(t) \\ \tilde{x}^T(t)P_{j2}^T\Delta B_j\tilde{D}_je(t) \end{bmatrix}\right) &\le \begin{bmatrix} \frac{1}{h_{j71}}e^T(t)\tilde{D}_j^TF_j'^TF_j'\tilde{D}_je(t) \\ \frac{1}{h_{j72}}e^T(t)\tilde{D}_j^TF_j'^TF_j'\tilde{D}_je(t) \end{bmatrix} \\
&\quad + \begin{bmatrix} h_{j71}x^T(t)P_{j1}M_jM_j^TP_{j1}x(t) \\ h_{j72}\tilde{x}^T(t)P_{j2}^TM_jM_j^TP_{j2}\tilde{x}(t) \end{bmatrix}.
\end{aligned} \tag{33}$$

Then, we derive

$$\begin{aligned}\dot{V}(\mathfrak{J}(t)) + \gamma V(\mathfrak{J}(t)) &= 2\mathfrak{J}^T(t)P_j\dot{\mathfrak{J}}(t) + \gamma\mathfrak{J}^T(t)P_j\mathfrak{J}(t)\\ &\le 2\mathfrak{J}^T(t)P_j\left(\overline{A}_{j,j}\mathfrak{J}(t) + \overline{B}_{j,j}e(t)\right) + \gamma\mathfrak{J}^T(t)P_j\mathfrak{J}(t)\\ &\quad - e(t)^T\Omega_j e(t) + \varepsilon x^T(t)C_j^T\Omega_j C_j x(t)\\ &= \mathfrak{J}_1^T(t)\Psi_{jj}\mathfrak{J}_1(t).\end{aligned} \tag{34}$$

This shadows

$$\dot{V}(\mathfrak{J}(t)) \le -\gamma V(\mathfrak{J}(t)), \quad \forall t \in [s_{k+1}, t_{q+1}), \tag{35}$$

because of (20). Then, the following inequation can be guaranteed with the nature of $V(\mathfrak{J}(t))$ at the instant $t = t_{q+1}$:

$$\begin{aligned}V\left(\mathfrak{J}\left(t_{q+1}\right)\right) &= V\left(\mathfrak{J}\left(t_{q+1}^-\right)\right)\\ &\le e^{-\gamma\left(t_{q+1}-s_{k+1}\right)}V(\mathfrak{J}(s_{k+1}))\\ &\le \eta e^{-\gamma\left(t_{q+1}-s_{k+1}\right)}V(\mathfrak{J}(s_{k+1}^-))\\ &\le \eta e^{-\gamma\left(t_{q+1}-s_{k+1}\right)+\delta\left(s_{k+1}-t_q\right)}V\left(\mathfrak{J}\left(t_q\right)\right).\end{aligned} \tag{36}$$

As a consequence, it can be summarized from (29) and (36) that

$$V\left(\mathfrak{J}\left(t_{q+1}\right)\right) \le \eta e^{-\gamma T_\downarrow\left(t_q,t_{q+1}\right)+\delta T_\uparrow\left(t_q,t_{q+1}\right)}V\left(\mathfrak{J}\left(t_q\right)\right). \tag{37}$$

Define $\widehat{\mathfrak{n}}_\sigma(0,t)$ as the switch time of controller in $[0,t)$, which is not more than the switch time of system $\mathfrak{n}_\sigma(0,t)$. Accordingly for $\forall t > 0$,

$$\begin{aligned}V(\mathfrak{J}(t)) &\le \eta^{\widehat{\mathfrak{n}}_\sigma(0,t)}e^{-\gamma T_\downarrow(0,t)+\delta T_\uparrow(0,t)}V(\mathfrak{J}(0))\\ &\le \eta^{\mathfrak{n}_\sigma(0,t)}e^{-\gamma t}e^{(\gamma+\delta)T\mathfrak{n}_\sigma(0,t)}V(\mathfrak{J}(0))\\ &\le \eta^{\left(\mathfrak{n}_0+t/\tau_a\right)}e^{-\gamma t}e^{(\gamma+\delta)T\left(\mathfrak{n}_0+t/\tau_a\right)}V(\mathfrak{J}(0))\\ &= \left(\eta e^{(\gamma+\delta)T}\right)^{\mathfrak{n}_0}e^{\left(\ln\mu+(\gamma+\delta)T/\tau_a-\gamma\right)t}V(\mathfrak{J}(0)).\end{aligned} \tag{38}$$

According to condition (25), there must exist a constant $\lambda > 0$ such that $V(\mathfrak{J}(t)) \le ce^{-2\lambda(t-0)}V(\mathfrak{J}(0))$. Considering inequalities $V(\mathfrak{J}(t)) \ge \lambda_1\|\mathfrak{J}(t)\|^2$ and $V(\mathfrak{J}(0)) \le \lambda_2\|\mathfrak{J}(0)\|^2$, we can derive $\|\mathfrak{J}(t)\| \le \kappa e^{-\lambda(t-0)}\|\mathfrak{J}(0)\|$, where $c = (\eta e^{(\gamma+\delta)T})^{\mathfrak{n}_0}$, $\lambda_1 = \min_{i\in\mathscr{L}}\lambda_{\min}(P_i)$, $\lambda_2 = \max_{i\in\mathscr{L}}\lambda_{\max}(P_i)$, and $\kappa = \sqrt{c\lambda_2/\lambda_1}$. Combined with Definition 1, system (9) is exponentially stable, which accomplishes the proof.

Remark 3. Motivated by the analysis of Case (ii), apart from a limited number of discontinuities, the error $e(t)$ remains continuous. To be specific, $e(t)$ could be piecewise continuous and bounded over a subinterval $[s_{k+1}, t_{q+1})$ provided that the lower bound exists on T, which would be clarified in Theorem 3. Furthermore, the Lyapunov function $V(\mathfrak{J}(t))$, whose structure determines that it has the property of global decay, is also continuous except for a limited number of discontinuities.

Remark 4. For $t \in (t_q^-, t_{q+1}^+)$, the inequality $\widehat{\mathfrak{n}}_\sigma(t_q^-, t_{q+1}^+) \le \mathfrak{n}_\sigma(t_q^-, t_{q+1}^+)$ can be illuminated in three cases as indicated in Figure 2. Case (a), Case (b), and Case (c) correspond to the above Case (i), Case (ii) with $m = 1$, and Case (ii) with $m > 1$, respectively. As for Case (i), it is obvious that $\widehat{\mathfrak{n}}_\sigma(t_q^-, t_{q+1}^+) = 0 \le \mathfrak{n}_\sigma(t_q^-, t_{q+1}^+) = 2$. Case (b) owns one triggered moment $s_{k+1} \in [t_q, t_{q+1})$, at which (3) receives the measurement date to change its pattern, meanwhile updating its input. Hence, $\widehat{\mathfrak{n}}_\sigma(t_q^-, t_{q+1}^+) = 1 \le \mathfrak{n}_\sigma(t_q^-, t_{q+1}^+) = 2$. Although m triggered moments in Case (c) over the interval $[t_q, t_{q+1})$, the controller pattern at the first triggered instant s_{k+1} is switched only once and the control input of the controller is only updated without switching its pattern at the other $m-1$ triggered moments. Thus, $\widehat{\mathfrak{n}}_\sigma(t_q^-, t_{q+1}^+) = 1 \le \mathfrak{n}_\sigma(t_q^-, t_{q+1}^+) = 2$ is still valid. In other words, the controller can be perceived as a postponed version of the uncertain system, more or less, in terms of switching. The switch time of the controller, consequently, will not surpass the switch time of the uncertain system.

3.2. Controller Design. In this section, the event-triggered scheme and the dynamic output-feedback controller for uncertain system (9) are codesigned by combining the above stability analysis. To calculate the control gains, we introduce notations as follows:

$$\begin{aligned}\mathscr{A}_j &= \begin{bmatrix} A_j & 0\\ 0 & 0\end{bmatrix},\\ \mathscr{B}_j &= \begin{bmatrix} 0 & B_j\\ I & 0\end{bmatrix},\\ \mathscr{C}_j &= \begin{bmatrix} 0 & I\\ C_j & 0\end{bmatrix},\\ \mathrm{E} &= \begin{bmatrix} 0\\ I\end{bmatrix},\\ \mathscr{K}_i &= \begin{bmatrix} \widetilde{A}_i & \widetilde{B}_i\\ \widetilde{C}_i & \widetilde{D}_i\end{bmatrix},\end{aligned} \tag{39}$$

which implies

$$\begin{aligned}\widetilde{A}_i &= \mathscr{A}_j + \mathscr{B}_j\mathscr{K}_i\mathscr{C}_j,\\ \widetilde{B}_i &= \mathscr{B}_j\mathscr{K}_i\mathscr{E}, \ \forall i, \quad j \in \mathscr{L}.\end{aligned} \tag{40}$$

Theorem 2. *Given scalars $\gamma > 0$, $\delta > 0$, $\eta \ge 1$, $T > 0$, $\epsilon > 0$, and $\varsigma > 0$, uncertain system (9) is globally exponentially stable for any $\sigma(t)$ if Assumption 1 holds and there exist matrices $P_i > 0$, $\Omega_i > 0$, R_i, S_i, $\mathscr{T}_{ic}$, $\exists h_{iab} > 0$ $(a = 1, 2, \ldots \infty, 7; b = 1, 2; c = 1, 2, 3, 4)$, $\exists h_{i8} > 0$, and $\forall i \in \mathscr{L}$ such that (21)–(25) and*

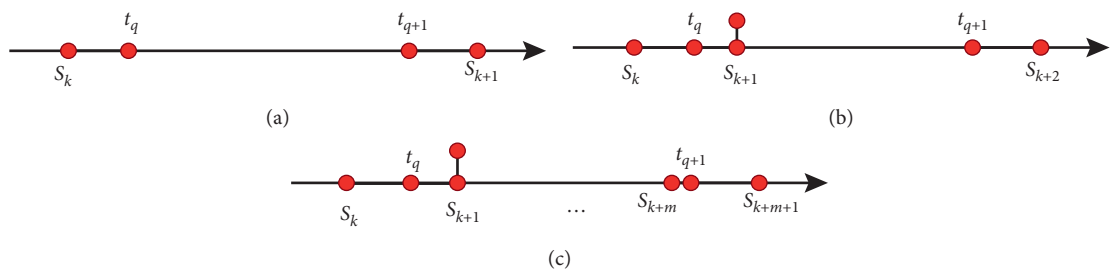

Figure 2: Moments of event triggering and system switching. (a) Case (i), (b) Case (ii), $m = 1$, (c) Case (ii), $m > 1$.

$$\Phi_{ji} = \begin{bmatrix} \Phi_{ji}^1 & \mathscr{B}_j S_i \mathscr{E} & 0 & P_j \mathscr{B}_j - \mathscr{B}_j R_i + \varsigma \mathscr{C}_j^T S_i^T \\ \star & -\Omega_i & \mathscr{T}_{i3}^T & \varsigma \mathscr{E}^T S_i^T \\ \star & \star & -\left(\dfrac{h_{i71} \cdot h_{i72}}{h_{i71} + h_{i72}}\right) I & 0 \\ \star & \star & \star & -\varsigma R_i - \varsigma R_i^T \end{bmatrix} < 0, \quad \forall i \neq j \in \mathscr{L}, \tag{41}$$

$$\Phi_{jj} = \begin{bmatrix} \Phi_{jj}^1 & \mathscr{B}_j S_j \mathscr{E} & 0 & P_j \mathscr{B}_j - \mathscr{B}_j R_j + \varsigma \mathscr{C}_j^T S_j^T \\ \star & -\Omega_j & \mathscr{T}_{j3}^T & \varsigma \mathscr{E}^T S_j^T \\ \star & \star & -\left(\dfrac{h_{j71} \cdot h_{j72}}{h_{j71} + h_{j72}}\right) I & 0 \\ \star & \star & \star & -\varsigma R_j - \varsigma R_j^T \end{bmatrix} < 0, \quad \forall j \in \mathscr{L}, \tag{42}$$

where

$$\begin{aligned}
\Phi_{ji}^1 &= \mathrm{He}\left(P_i \mathscr{A}_j + \mathscr{B}_j S_i \mathscr{C}_j\right) + \overline{\mathscr{Q}}_i - \delta P_i, \\
\Phi_{jj}^1 &= \mathrm{He}\left(P_i \mathscr{A}_j + \mathscr{B}_j S_i \mathscr{C}_j\right) + \overline{\mathscr{Q}}_j + \gamma P_j, \\
\overline{\mathscr{Q}}_i &= \begin{bmatrix} \overline{\mathscr{Q}}_{i1} & \overline{\mathscr{Q}}_{i2} \\ \overline{\mathscr{Q}}_{i3} & \overline{\mathscr{Q}}_{i4} \end{bmatrix}, \forall i \in \mathscr{L}, \\
\overline{\mathscr{Q}}_{i1} &= (h_{i11} + h_{i21} + h_{i71} + h_{i41}) P_{i1} M_j M_j^T P_{i1} + h_{i31} P_{i1} B_j \mathscr{T}_{i4} \mathscr{T}_{i4}^T B_j^T P_{i1} + h_{i51} P_{i2} \mathscr{T}_{i1} \mathscr{T}_{i1}^T P_{i2}^T \\
&\quad + \frac{1}{h_{i11}} F_j^T F_j + \left(\frac{1}{h_{i31}} + \frac{1}{h_{i51}} + \frac{1}{h_{i41} h_{i8}}\right) F_j''^T F_j'' + \frac{1}{h_{i21}} C_j^T \mathscr{T}_{i3}^T \mathscr{T}_{i3} C_j + \epsilon C_j^T \Omega_i C_j, \\
\overline{\mathscr{Q}}_{i3} &= (h_{i12} + h_{i22} + h_{i42}) P_{i2}^T M_j M_j^T P_{i2} + h_{i32} P_{i2}^T B_j \mathscr{T}_{i4} \mathscr{T}_{i4}^T B_j^T P_{i2} + h_{i52} P_{i3} \mathscr{T}_{i1} \mathscr{T}_{i1}^T P_{i3} \\
&\quad + \frac{1}{h_{i12}} F_j^T F_j + \left(\frac{1}{h_{i32}} + \frac{1}{h_{i52}} + \frac{1}{h_{i42} h_{i8}}\right) F_j''^T F_j'' + \frac{1}{h_{i22}} C_j^T \mathscr{T}_{i3}^T \mathscr{T}_{i3} C_j, \\
\overline{\mathscr{Q}}_{i2} &= \frac{1}{h_{i61}} \mathscr{T}_{i2}^T \mathscr{T}_{i2} + h_{i61} P_{i1} M_j M_j^T P_{i1}, \\
\overline{\mathscr{Q}}_{i4} &= \frac{1}{h_{i62}} \mathscr{T}_{i2}^T \mathscr{T}_{i2} + (h_{i62} + h_{i72}) P_{i2}^T M_j M_j^T P_{i2}.
\end{aligned} \tag{43}$$

Furthermore, the controller gain matrices are devised as $\mathscr{K}_i = R_i^{-1}S_i, \forall i \in \mathscr{L}$.

Proof. On the grounds of Theorem 1 and supposing that $\widetilde{B}_i = \mathscr{T}_{i1}M_j^{-1}, \widetilde{C}_i = F' j_{-1}\mathscr{T}_{i2}, \widetilde{D}_i = F' j_{-1}\mathscr{T}_{i3} = \mathscr{T}_{i4}M_j^{-1}$, such that the controller gains are presented as

$$\begin{aligned}\mathscr{K}_i &= R_i^{-1}S,\\ &= \begin{bmatrix} \widetilde{A}_i & \mathscr{T}_{i1}M_j^{-1} \\ F' j_{-1}\mathscr{T}_{i2} & F' j_{-1}\mathscr{T}_{i3} \end{bmatrix}, \quad \forall i \in \mathscr{L}.\end{aligned} \tag{44}$$

define

$$\begin{aligned} X_{ji} &= R_i^{-1}\left[\, S_i\mathscr{C}_j \;\; S_i\mathscr{E} \;\; 0 \,\right],\\ Y_{ji} &= \left[\, \mathscr{B}_j^T P_i - R_i^T\mathscr{B}_j^T \;\; 0 \;\; 0 \,\right]. \end{aligned} \tag{45}$$

Then,

$$\begin{aligned} X_{ji}^T Y_{ji} &= \begin{bmatrix} \left(R_i^{-1}S_i\mathscr{C}_j\right)^T\mathscr{B}_j^T P_i - \left(S_i\mathscr{C}_j\right)^T\mathscr{B}_j^T & 0 & 0 \\ \left(R_i^{-1}S_i\mathscr{E}\right)^T\mathscr{B}_j^T P_i - \left(S_i\mathscr{E}\right)^T\mathscr{B}_j^T & 0 & 0 \\ 0 & 0 & 0 \end{bmatrix},\\ Y_{ji}^T X_{ji} &= \begin{bmatrix} P_i\mathscr{B}_j R_i^{-1}S_i\mathscr{C}_j - \mathscr{B}_j S_i\mathscr{C}_j & P_i\mathscr{B}_j R_i^{-1}S_i\mathscr{E} - \mathscr{B}_j S_i\mathscr{E} & 0 \\ 0 & 0 & 0 \\ 0 & 0 & 0 \end{bmatrix}. \end{aligned} \tag{46}$$

Combining with Lemma 3 and (41), one derives

$$\begin{bmatrix} \Phi_{ji}^1 & \mathscr{B}_j S_i\mathscr{E} & 0 \\ \star & -\Omega_i & \mathscr{T}_{i3}^T \\ \star & \star & -\left(\dfrac{h_{i71}\cdot h_{i72}}{h_{i71}+h_{i72}}\right)I \end{bmatrix} + X_{ji}^T Y_{ji} + Y_{ji}^T X_{ji} < 0, \tag{47}$$

which is of equivalence to

$$\begin{bmatrix} He\left(P_i\mathscr{A}_j + \mathscr{B}_j\mathscr{K}_i\mathscr{C}_j\right) + \overline{\mathscr{Q}}_i - \delta P_i & P_i\mathscr{B}_j\mathscr{K}_i\mathscr{E} & 0 \\ \star & -\Omega_i & \mathscr{T}_{i3}^T \\ \star & \star & -\left(\dfrac{h_{i71}\cdot h_{i72}}{h_{i71}+h_{i72}}\right)I \end{bmatrix} < 0. \tag{48}$$

In accordance with (40) and above definition, one obtains

$$\begin{bmatrix} \Psi_{ji}^1 & P_i\overline{\overline{B}}_{ji} & 0 \\ \star & -\Omega_i & \widetilde{D}_i^T F_j'^T \\ \star & \star & -\left(\dfrac{h_{i71}\cdot h_{i72}}{h_{i71}+h_{i72}}\right)I \end{bmatrix} < 0. \tag{49}$$

On the basis of Lemma 2, one realizes that (41) ensures condition (19). Under the same technique as above, (20) is guaranteed by condition (42). In consequence, the conclusion can be obtained by Theorem 1.

Remark 5. By comparison with [14], the average dwell-time switching signals can be used to handle quick switching issues and are more widespread and pragmatic without minimum dwell-time restrictions [16]. And it is necessary to point out that the related works investigate the asynchronous stabilization via the strategy of multiple Lyapunov function. For instance, the Lyapunov function is delegated as $V(x(t)) = x^T(t)P_j x(t)$ for the synchronous course as well as $V(x(t)) = x^T(t)P_{ji}x(t)$ for the asynchronous period. The variable number deduced by the multiple Lyapunov functional matrices is $n(n+1)/2\mathfrak{n} + n(n+1)/2\mathfrak{n}(n-1)$, where $\mathfrak{n}$ represents the quantity of the Lyapunov functional matrix. Difference in these works, a piecewise Lyapunov functional, is constructed in this article, which only rests with the controller pattern. Under this choice, what delighted us is that the variable number is $n(n+1)/2\mathfrak{n}$. It is evident that the computation complexity can be effectually decreased, specifically for systems with a large dimensionality or plenty of modes. Most recently, great achievements have been dedicated to inquiry into the switched systems of state parameters uncertainty and input parameters uncertainty. However, as yet, little attention has been attracted to the

stabilization of frequently switched systems that are equipped with state, input, and especially measured output parameter uncertainties, which motivates this work.

In recent years, with the rise of large-scale networks, the calculation of performance criteria described by matrix equations or matrix inequalities has attracted much attention. In fact, in control systems, the investigation of many important characteristics such as stability and controllability can be transformed into the exploration of the constrained solution of the corresponding nonlinear matrix equation. The traditional method of solving matrix equations or matrix inequality is based on an iterative numerical algorithm. This kind of algorithm may meet the requirements of real-time for matrix equations or matrix inequality with small dimensions. Once the matrix dimension reaches a certain order of magnitude, it is generally difficult to find a solution method suitable for real-time large-scale applications. Theorems 1 and 2 in this paper are in the form of matrix inequalities, and how to systematically work out the problem of solving a high-dimensional matrix caused by the huge dimension of the network determines the scope of application of Theorems 1 and 2 to a certain extent.

3.3. Excluding the Zeno Behavior. In this section, the existence of T's lower definite bound is demonstrated, which thus eliminates Zeno behavior. Combining with (1) and (3) under event-triggered strategy (2), the uncertain closed-loop system is inferred as

$$\begin{aligned}\dot{x}(t) = &\left(A_{\sigma(t)} + \Delta A_{\sigma(t)}\right)x(t) + \left(B_{\sigma(t)} + \Delta B_{\sigma(t)}\right)\\ &\widetilde{D}_{\sigma(s_k)}\left(y(t) + e_{s_k}(t)\right)\\ &+\left(B_{\sigma(t)} + \Delta B_{\sigma(t)}\right)\widetilde{C}_{\sigma(s_k)}\widetilde{x}(t), \quad t \in [s_k, s_{k+1}).\end{aligned} \tag{50}$$

Theorem 3. *For system (50), suppose Assumption 1 holds. Given a scalar $\beta(>0)$ satisfying $\max\{\|x(t)\|, \|\widetilde{x}(t)\|\} \le \beta\|y(t)\|$, the adjacent event interval would be lower bounded via constant $T_1(>0)$ conforming to*

$$T_1 = \min\left\{T, \frac{1}{\overline{\Lambda} - \widehat{\Lambda}} \ln\left(1 + \frac{(\overline{\Lambda} - \widehat{\Lambda})\sqrt{\epsilon}}{\overline{\Lambda} + \widehat{\Lambda}\sqrt{\epsilon}}\right)\right\}, \tag{51}$$

where T and ϵ are specified in (2) and

$$\begin{aligned}\overline{\Lambda} = &\max_{i,j\in\mathscr{L}} \frac{1}{\lambda_{\min}\sqrt{\Omega_i}}\\ &\left[\begin{array}{c}\left(\begin{array}{c}\left\|\sqrt{\Omega_i}C_jA_j\right\| + \left\|\sqrt{\Omega_i}C_jM_j\right\|\cdot\left\|F_j\right\| + \left\|\sqrt{\Omega_i}M_j\right\|\cdot\left\|F_j''A_j\right\|\\ +\left\|\sqrt{\Omega_i}M_j\right\|\cdot\left\|F_j''M_j\right\|\cdot\left\|F_j\right\| + \left\|\sqrt{\Omega_i}C_jB_j\widetilde{C}_i\right\|\\ +\left\|\sqrt{\Omega_i}C_jM_j\right\|\cdot\left\|F_j'\widetilde{C}_i\right\| + \left\|\sqrt{\Omega_i}M_j\right\|\cdot\left\|F_j''B_j\widetilde{C}_i\right\|\\ +\left\|\sqrt{\Omega_i}M_j\right\|\cdot\left\|F_j''M_j\right\|\cdot\left\|F_j'\widetilde{C}_i\right\|\end{array}\right)\\ +\left\|\sqrt{\Omega_i}C_jB_j\widetilde{D}_i\right\| + \left\|\sqrt{\Omega_i}C_jM_j\right\|\cdot\left\|F_j'\widetilde{D}_i\right\| + \left\|\sqrt{\Omega_i}M_j\right\|\cdot\left\|F_j''B_j\widetilde{D}_i\right\|\\ +\left\|\sqrt{\Omega_i}M_j\right\|\cdot\left\|F_j''M_j\right\|\cdot\left\|F_j'D_j\right\|\end{array}\right]\beta,\\ \widehat{\Lambda} = &\max_{i,j\in\mathscr{L}}\left\|\sqrt{\Omega_i}C_jB_j\widetilde{D}_i\sqrt{\Omega_i}^{-1}\right\| + \left\|\sqrt{\Omega_i}C_jM_j\right\|\cdot\left\|F_j'\widetilde{D}_i\sqrt{\Omega_i}^{-1}\right\|\\ &+\left\|\sqrt{\Omega_i}M_j\right\|\cdot\left\|F_j''B_j\widetilde{D}_i\sqrt{\Omega_i}^{-1}\right\| + \left\|\sqrt{\Omega_i}M_j\right\|\cdot\left\|F_j''M_j\right\|\cdot\left\|F_j''B_j\widetilde{D}_i\sqrt{\Omega_i}^{-1}\right\|.\end{aligned} \tag{52}$$

Proof. Suppose that $\sigma(s_k) = i$, and construct an auxiliary function $\mathfrak{R}(t) = \|\sqrt{\Omega_i}e_{s_k}(t)\|/\|\sqrt{\Omega_i}y(t)\|$ for $t \in [s_k, s_{k+1})$. Event scheme (2) would be triggered only if $\mathfrak{R}(t) = \sqrt{\epsilon}$ or $t = s_k + T$. When the latter holds, $s_{k+1} - s_k = T \ge T_1$. Obviously, that is a bromidic case. Next, we will be dedicated to testify that $s_{k+1} - s_k \ge T_1$ holds when s_{k+1} meets regulation $\mathfrak{R}(t) = \sqrt{\epsilon}$. The proof is segmented into two steps as follows.

Step 1. When the system does not switch between the successive triggering moments s_k and s_{k+1}, $\sigma(t) = \sigma(s_k) = i$, $\forall t \in [s_k, s_{k+1})$, correspondingly, uncertain system (50) could be transformed into

$$\begin{aligned}\dot{x}(t) = &(A_i + \Delta A_i)x(t) + (B_i + \Delta B_i)\widetilde{D}_i\left(y(t) + e_{s_k}(t)\right)\\ &+ (B_i + \Delta B_i)\widetilde{C}_i\widetilde{x}(t),\ t \in [s_k, s_{k+1}).\end{aligned} \tag{53}$$

Differentiating the function $\mathfrak{R}(t)$, one gets

$$\dot{\mathfrak{R}}(t) \le \frac{\left\|\sqrt{\Omega_i}\,\dot{e}_{s_k}(t)\right\|}{\left\|\sqrt{\Omega_i}\,\dot{y}(t)\right\|} + \frac{\left\|\sqrt{\Omega_i}\,\dot{y}(t)\right\| \cdot \left\|\sqrt{\Omega_i}\,\dot{e}_{s_k}(t)\right\|}{\left\|\sqrt{\Omega_i}\,\dot{y}(t)\right\|^2}$$

$$= (1+\mathfrak{R}(t)) \frac{\left\|\sqrt{\Omega_i}\,(C_i+\Delta C_i)\dot{x}(t)\right\|}{\left\|\sqrt{\Omega_i}\,\dot{y}(t)\right\|} \le$$

$$\frac{1+\mathfrak{R}(t)}{\left\|\sqrt{\Omega_i}\,\dot{y}(t)\right\|} \begin{pmatrix} \left\|\sqrt{\Omega_i}\,(C_i+\Delta C_i)(A_i+\Delta A_i)\right\| \cdot \|x(t)\| \\ +\left\|\sqrt{\Omega_i}\,(C_i+\Delta C_i)(B_i+\Delta B_i)\widetilde{C}_i\right\| \cdot \|\widetilde{x}(t)\| \\ +\left\|\sqrt{\Omega_i}\,(C_i+\Delta C_i)(B_i+\Delta B_i)\widetilde{D}_i\right\| \cdot \|y(t)\| \\ +\left\|\sqrt{\Omega_i}\,(C_i+\Delta C_i)(B_i+\Delta B_i)\widetilde{D}_i e_{s_k}(t)\right\| \end{pmatrix}. \tag{54}$$

Since

$$\|E_i\| = \sqrt{\lambda_{\max}\left(E_i^T E_i\right)} \le \sqrt{\lambda_{\max}(I)} = 1 \tag{55}$$

$$\|x(t)\|, \|\widetilde{x}(t)\| \le \|\beta y(t)\|, \tag{56}$$

it satisfies

$$\dot{\mathfrak{R}}(t) \le (1+\mathfrak{R}(t)) \left\{ \frac{1}{\lambda_{\min}\sqrt{\Omega_i}} \begin{bmatrix} \begin{pmatrix} \left\|\sqrt{\Omega_i}\,C_iA_i\right\| + \left\|\sqrt{\Omega_i}\,C_iM_i\right\| \cdot \|F\|_i + \lfloor\sqrt{\Omega_i}\,M_i\rfloor \cdot \left\|F_j'A_i\right\| \\ +\left\|\sqrt{\Omega_i}\,M_i\right\| \cdot \left\|F_j''M_i\right\| \cdot \|F_i\| + \left\|\sqrt{\Omega_i}\,C_iB_i\widetilde{C}_i\right\| \\ +\left\|\sqrt{\Omega_i}\,C_iM_i\right\| \cdot \left\|F_j'\widetilde{C}_i\right\| + \left\|\sqrt{\Omega_i}\,M_i\right\| \cdot \left\|F_j''B_i\widetilde{C}_i\right\| + \left\|\sqrt{\Omega_i}\,M_i\right\| \cdot \left\|F_j''M_i\right\| \cdot \left\|F_j'\widetilde{C}_i\right\| \end{pmatrix}\beta \\ +\left\|\sqrt{\Omega_i}\,C_iB_i\widetilde{D}_i\right\| + \left\|\sqrt{\Omega_i}\,C_iM_i\right\| \cdot \left\|F_j'\widetilde{D}_i\right\| + \left\|\sqrt{\Omega_i}\,M_i\right\| \cdot \left\|F_j''B_i\widetilde{D}_i\right\| + \left\|\sqrt{\Omega_i}\,M_i\right\| \cdot \left\|F_j''M_i\right\| \cdot \left\|F_j'\widetilde{D}_i\right\| \end{bmatrix} \\ +\left\|\sqrt{\Omega_i}\,C_iB_i\widetilde{D}_i\sqrt{\Omega_i}^{-1}\right\| + \left\|\sqrt{\Omega_i}\,C_iM_i\right\| \cdot \left\|F_j'\widetilde{D}_i\sqrt{\Omega_i}^{-1}\right\| \\ +\left\|\sqrt{\Omega_i}\,M_i\right\| \cdot \left\|F_j''B_i\widetilde{D}_i\sqrt{\Omega_i}^{-1}\right\| + \left\|\sqrt{\Omega_i}\,M_i\right\| \cdot \left\|F_j''M_i\right\| \cdot \left\|F_j'\widetilde{D}_i\sqrt{\Omega_i}^{-1}\right\| \cdot \mathfrak{R}(t) \end{bmatrix} \right\} \tag{57}$$

$$\le (1+\mathfrak{R}(t))\left(\Lambda_a + \Lambda_b\mathfrak{R}(t)\right) \le (1+\mathfrak{R}(t))\left(\overline{\Lambda} + \widehat{\Lambda}\mathfrak{R}(t)\right),$$

where

$$\Lambda_a = \max_{i\in\mathscr{L}} \frac{1}{\lambda_{\min}\sqrt{\Omega_i}} \begin{bmatrix} \begin{pmatrix} \left\|\sqrt{\Omega_i}\,C_iA_i\right\| + \left\|\sqrt{\Omega_i}\,C_iM_i\right\| \cdot \|F\|_i + \left\|\sqrt{\Omega_i}\,C_iM_i\right\| \cdot \left\|F_j''A_i\right\| \\ +\left\|\sqrt{\Omega_i}\,M_i\right\| \cdot \left\|F_j''M_i\right\| \cdot \|F_i\| + \left\|\sqrt{\Omega_i}\,C_iB_i\widetilde{C}_i\right\| + \left\|\sqrt{\Omega_i}\,C_iM_i\right\| \cdot \left\|F_i'\widetilde{C}_i\right\| \\ +\left\|\sqrt{\Omega_i}\,M_i\right\| \cdot \left\|F_j''B_i\widetilde{C}_i\right\| + \left\|\sqrt{\Omega_i}\,M_i\right\| \cdot \left\|F_j''M_i\right\| \cdot \left\|F_i'\widetilde{C}_i\right\| \end{pmatrix}\beta \\ +\left\|\sqrt{\Omega_i}\,C_iB_i\widetilde{D}_i\right\| + \left\|\sqrt{\Omega_i}\,C_iM_i\right\| \cdot \left\|F_i'\widetilde{D}_i\right\| + \left\|\sqrt{\Omega_i}\,M_i\right\| \cdot \left\|F_j''B_i\widetilde{D}_i\right\| + \left\|\sqrt{\Omega_i}\,M_i\right\| \cdot \left\|F_j''M_i\right\| \cdot \left\|F_i'\widetilde{D}_i\right\| \end{bmatrix}, \tag{58}$$

$$\Lambda_b = \max_{i\in\mathscr{L}} = \left\|\sqrt{\Omega_i}\,C_iB_i\widetilde{D}_i\sqrt{\Omega_i}^{-1}\right\| + \left\|\sqrt{\Omega_i}\,C_iM_i\right\| \cdot \left\|F_i'\widetilde{D}_i\sqrt{\Omega_i}^{-1}\right\|$$

$$+\left\|\sqrt{\Omega_i}\,M_i\right\| \cdot \left\|F_j''B_i\widetilde{D}_i\sqrt{\Omega_i}^{-1}\right\| + \left\|\sqrt{\Omega_i}\,M_i\right\| \cdot \left\|F_i''M_i\right\| \cdot \left\|F_i'\widetilde{D}_i\sqrt{\Omega_i}^{-1}\right\|.$$

By introducing

$$\dot{\nu}(t) = (1 + \nu(t))(\overline{\Lambda} + \widehat{\Lambda}\nu(t)), \tag{59}$$

inequality $\mathfrak{R}(t) \le \nu(t)$ holds apparently for the initial value $\mathfrak{R}(s_k) = \nu(s_k) = 0$ from comparison Lemma 4.

As t adds from s_k to s_{k+1}, $\mathfrak{R}(t)$ varies and increases from 0 to $\sqrt{\epsilon}$. By integrating both sides of (59) and supposing (2) is triggered at $t = T_1 + s_k$, the inequality $\nu(T_1 + s_k) \ge \sqrt{\epsilon}$ can be derived. Subsequently, the lower bound of $s_{k+1} - s_k$ can be calculated to be $1/\overline{\Lambda} - \widehat{\Lambda}\ln(1 + ((\overline{\Lambda} - \widehat{\Lambda})\sqrt{\epsilon}/\overline{\Lambda} + \widehat{\Lambda}\sqrt{\epsilon}))$, which yields expressions (51).

Step 2. When the system switches $n(\in \mathbb{N}^+)$ between the successive triggering moments s_k and s_{k+1}, one could suppose that $s_k < t_{q+1} < \cdots < t_{q+n} \le s_{k+1}$. Considering the subinterval $[s_k, t_{q+1})$, system (50) has the identical form as (53); hence, the following inequality is deduced for $t \in [s_k, t_{q+1})$:

$$\dot{\nu}(t) \le (1 + \mathfrak{R}(t))(\overline{\Lambda} + \widehat{\Lambda}\mathfrak{R}(t)). \tag{60}$$

For the subinterval $[t_{q+1}, t_{q+2})$, uncertain system (50) could be expressed by

$$\begin{aligned}\dot{x}(t) = &\left(A_j + \Delta A_j\right)x(t) + \left(B_j + \Delta B_j\right)\widetilde{D}_i\left(y(t) + e_{s_k}(t)\right)\\ &+ (B_j + \Delta B_j)\widetilde{C}_i\widetilde{x}(t),\ t \in [t_{q+1}, t_{q+2}),\end{aligned} \tag{61}$$

with $\sigma(t_{q+1}) = j \in \mathscr{L}$. Parallelling to the deduction of Step 1, one derives

$$\begin{aligned}\dot{\mathfrak{R}}(t) \le &\frac{1 + \mathfrak{R}(t)}{\left\|\sqrt{\Omega_i}\, y(t)\right\|}\begin{pmatrix}\left\|\sqrt{\Omega_i}\left(C_j + \Delta C_j\right)\left(A_j + \Delta A_j\right)\right\| \cdot \|x(t)\|\\ +\left\|\sqrt{\Omega_i}\left(C_j + \Delta C_j\right)\left(B_j + \Delta B_j\right)\widetilde{C}_i\right\| \cdot \|\widetilde{x}(t)\|\\ +\left\|\sqrt{\Omega_i}\left(C_j + \Delta C_j\right)\left(B_j + \Delta B_j\right)\widetilde{D}_i\right\| \cdot \|y(t)\|\\ +\left\|\sqrt{\Omega_i}\left(C_j + \Delta C_j\right)\left(B_j + \Delta B_j\right)\widetilde{D}_i e_{s_k}(t)\right\|\end{pmatrix}\\ \le &(1 + \mathfrak{R}(t))\left(\Lambda_c + \Lambda_d\mathfrak{R}(t)\right) \le (1 + \mathfrak{R}(t))(\overline{\Lambda} + \widehat{\Lambda}\mathfrak{R}(t)),\end{aligned} \tag{62}$$

where

$$\begin{aligned}\Lambda_c = &\max_{i \ne j \in \mathscr{L}} \frac{1}{\lambda_{\min}\sqrt{\Omega_i}}\\ &\left[\begin{pmatrix}\left\|\sqrt{\Omega_i}C_jA_j\right\| + \left\|\sqrt{\Omega_i}C_jM_j\right\| \cdot \left\|F_j\right\| + \left\|\sqrt{\Omega_i}M_j\right\| \cdot \left\|F_j''A_j\right\|\\ +\left\|\sqrt{\Omega_i}M_j\right\| \cdot \left\|F_j''M_j\right\| \cdot \left\|F_j\right\| + \left\|\sqrt{\Omega_i}C_jB_j\widetilde{C}_i\right\| + \left\|\sqrt{\Omega_i}C_jM_j\right\| \cdot \left\|F_j'\widetilde{C}_i\right\|\\ +\left\|\sqrt{\Omega_i}M_j\right\| \cdot \left\|F_j''B_j\widetilde{C}_i\right\| + \left\|\sqrt{\Omega_i}M_j\right\| \cdot \left\|F_j''M_j\right\| \cdot \left\|F_j'\widetilde{C}_i\right\|\end{pmatrix}\beta\\ &+\left\|\sqrt{\Omega_i}C_jB_j\widetilde{D}_i\right\| + \left\|\sqrt{\Omega_i}C_jM_j\right\| \cdot \left\|F_j'\widetilde{D}_i\right\|\\ &+\left\|\sqrt{\Omega_i}M_j\right\| \cdot \left\|F_j''B_j\widetilde{D}_i\right\| + \left\|\sqrt{\Omega_i}M_j\right\| \cdot \left\|F_j''M_j\right\| \cdot \left\|F_j'\widetilde{D}_i\right\|\end{aligned}\Bigg],$$

$$\begin{aligned}\Lambda_d = &\max_{i \ne j \in \mathscr{L}}\left\|\sqrt{\Omega_i}C_jB_j\widetilde{D}_i\sqrt{\Omega_i}^{-1}\right\| + \left\|\sqrt{\Omega_i}C_jM_j\right\| \cdot \left\|F_j'\widetilde{D}_i\sqrt{\Omega_i}^{-1}\right\|\\ &+\left\|\sqrt{\Omega_i}M_j\right\| \cdot \left\|F_j''B_j\widetilde{D}_i\sqrt{\Omega_i}^{-1}\right\| + \left\|\sqrt{\Omega_i}M_j\right\| \cdot \left\|F_j''M_j\right\| \cdot \left\|F_j'\widetilde{D}_i\sqrt{\Omega_i}^{-1}\right\|.\end{aligned} \tag{63}$$

Based on the analysis above, inequality (60) is guaranteed for all subintervals $[s_k, t_{q+1})t, n[qt_{q+1}, t_{q+2}h), x \ldots 7, C[; t_{q+n}, s_{k+1})$. Defining $\varpi(t) = \dot{\nu}(t) = (1 + \nu(t))(\overline{\Lambda} + \widehat{\Lambda}\nu(t))$, we could derive from $\dot{\mathfrak{R}}(t) \le \varpi(t)$ and $\mathfrak{R}(s_k) = \nu(s_k) = 0$ that $\mathfrak{R}(t_{q+1}) \le \nu(t_{q+1})$. By repetitively applying Lemma 4, we deduce $\mathfrak{R}(t_{q+2}) \le \nu(t_{q+2}), \ldots, \mathfrak{R}(t_{q+n}) \le \nu(t_{q+n})$. Then, for $t \in [t_{q+n}, s_{k+1})$,

$$\begin{aligned}\mathfrak{R}(t) \le \nu(t) &= \int_{t_{q+n}}^{t} \varpi(\iota)\mathrm{d}\iota + \nu\left(t_{q+n}\right) \\ &= \int_{t_{q+n}}^{t} \varpi(\iota)d\iota + \int_{t_{q+n-1}}^{t_{q+n}} \varpi(\iota)\mathrm{d}\iota + \cdots + \int_{s_k}^{t_q} \varpi(\iota)\mathrm{d}\iota + \nu\left(s_k\right) \\ &= \int_{s_k}^{t} \varpi(\iota)\mathrm{d}\iota.\end{aligned} \tag{64}$$

Due to Step 1, the lower bound of $s_{k+1} - s_k$ can be deduced to be $1/\overline{\Lambda} - \widehat{\Lambda}\ln(1 + (\overline{\Lambda} - \widehat{\Lambda})\sqrt{\epsilon}/\overline{\Lambda} + \widehat{\Lambda}\sqrt{\epsilon})$. Consequently, the presence of the lower boundary on adjacent event intervals is ultimately demonstrated. Based on (51), we could reason out the following relationship:

$$\begin{aligned}\widehat{\Lambda} &= \left\|\max_{i,j\in\mathscr{L}} \sqrt{\Omega_i}\, C_j B_j \widetilde{D}_i \sqrt{\Omega_i}^{-1}\right\| + \left\|\sqrt{\Omega_i}\, C_j M_j\right\| \cdot \left\|F_j' \widetilde{D}_i \sqrt{\Omega_i}^{-1}\right\| \\ &\quad + \left\|\sqrt{\Omega_i}\, M_j\right\| \cdot \left\|F_j'' B_j \widetilde{D}_i \sqrt{\Omega_i}^{-1}\right\| + \left\|\sqrt{\Omega_i}\, M_j\right\| \left\|F_j'' M_j\right\| \cdot \left\|F_j' \widetilde{D}_i \sqrt{\Omega_i}^{-1}\right\| \\ &\le \max_{i,j\in\mathscr{L}} \left\|\sqrt{\Omega_i}\, C_j B_j \widetilde{D}_i\right\| \cdot \left\|\sqrt{\Omega_i}^{-1}\right\| + \left\|\sqrt{\Omega_i}\, C_j M_j\right\| \cdot \left\|F_j' \widetilde{D}_i\right\| \cdot \left\|\sqrt{\Omega_i}^{-1}\right\| \\ &\quad + \left\|\sqrt{\Omega_i}\, M_j\right\| \cdot \left\|F_j'' B_j \widetilde{D}_i\right\| \cdot \left\|\sqrt{\Omega_i}^{-1}\right\| + \left\|\sqrt{\Omega_i}\, M_j\right\| \cdot \left\|F_j'' M_j\right\| \cdot \left\|F_j' \widetilde{D}_i\right\| \cdot \left\|\sqrt{\Omega_i}^{-1}\right\| \\ &\le \max_{i,j\in\mathscr{L}} \frac{1}{\lambda_{\min}\sqrt{\Omega_i}} \begin{pmatrix} \left\|\sqrt{\Omega_i}\, C_j B_j \widetilde{D}_i\right\| + \left\|\sqrt{\Omega_i}\, C_j M_j\right\| \cdot \left\|F_j' \widetilde{D}_i\right\| \\ + \left\|\sqrt{\Omega_i}\, M_j\right\| \cdot \left\|F_j'' B_j \widetilde{D}_i\right\| + \left\|\sqrt{\Omega_i}\, M_j\right\| \cdot \left\|F_j'' M_j\right\| \cdot \left\|F_j'' \widetilde{D}_i\right\| \end{pmatrix} < \overline{\Lambda},\end{aligned} \tag{65}$$

which symbolizes that the lower boundary T_1 is positive invariably; therefore, the Zeno behavior could be eliminated.

The systems in the real world have more or less nonlinear characteristics, so the nonlinear switched systems have a wide range of practicability. However, due to the complexity of nonlinear systems, there are still many problems to be solved in the analysis and control of nonlinear switched systems. The system considered in this paper is a linear switched system, but the analysis framework and analytical method can be extended to the nonlinear switched system.

Time delay is a common phenomenon in the establishment of a mathematical model of control systems. It is one of the key factors leading to the performance degradation of the systems. Therefore, the analysis and design of time-delay switched systems are an important research field in control theory. How to extend the results of this paper to time-delayed switched systems is not only a more general problem but also a more complex problem.

4. Simulation Results

To verify the availability of the derived results, in this section, uncertain switched linear system (1) that incorporates two subsystems is considered, whose parameters are as follows:

$$\begin{aligned} A_1 &= \begin{bmatrix} -4.5 & 0 \\ 0 & -4.4 \end{bmatrix}, \\ A_2 &= \begin{bmatrix} -4 & 0 \\ 0 & -4 \end{bmatrix}, \\ B_1 &= \begin{bmatrix} -4.5 & -2 \\ 1.5 & 5 \end{bmatrix}, \\ B_2 &= \begin{bmatrix} -5 & -2 \\ 1 & 5 \end{bmatrix}, \\ C_1 &= \begin{bmatrix} -1.5 & 1.5 \end{bmatrix}, \\ C_2 &= \begin{bmatrix} -1 & 1 \end{bmatrix}, \\ M_1 &= M_2 = 0.05, \\ F_1 &= F_2 = \begin{bmatrix} -0.3 & 0 \\ 0 & 0.1 \end{bmatrix}, \\ F_1 &= F_2 = \begin{bmatrix} -0.3 & 0 \\ 0 & 0.1 \end{bmatrix}, \\ F_1' &= F_2' = \begin{bmatrix} -1 & 0.01 \\ 0 & -0.1 \end{bmatrix}, \\ F_1'' &= F_2'' = \begin{bmatrix} -1 & 1 \end{bmatrix}. \end{aligned} \tag{66}$$

The resultant uncertain closed-loop system form can be described by

$$\begin{aligned}
\widetilde{A}_1 &= \begin{bmatrix} -20 & -0.1 \\ 0.4 & -4 \end{bmatrix}, \\
\widetilde{A}_2 &= \begin{bmatrix} -15 & -0.01 \\ 0.3 & -4 \end{bmatrix}, \\
\mathscr{T}_{11} &= \begin{bmatrix} 0.001 \\ 0.0025 \end{bmatrix}, \\
\mathscr{T}_{21} &= \begin{bmatrix} 0.0015 \\ 0.002 \end{bmatrix}, \\
\mathscr{T}_{12} &= \begin{bmatrix} -0.1 & -0.4998 \\ 0 & -0.002 \end{bmatrix}, \\
\mathscr{T}_{22} &= \begin{bmatrix} -0.2 & -0.0496 \\ 0 & -0.004 \end{bmatrix}, \\
\mathscr{T}_{13} &= \begin{bmatrix} 0.003 \\ 0.002 \end{bmatrix}, \\
\mathscr{T}_{23} &= \begin{bmatrix} 0.004 \\ -0.002 \end{bmatrix}, \\
\mathscr{T}_{14} &= \begin{bmatrix} -0.00016 \\ -0.001 \end{bmatrix}, \\
\mathscr{T}_{24} &= \begin{bmatrix} -0.00019 \\ 0.001 \end{bmatrix}.
\end{aligned} \tag{67}$$

Obviously, the controller gains can be calculated as

Setting $\gamma = \delta = 0.1$, $\eta = 1.3$, $T = 4$, $\epsilon = 0.5$, $\varsigma = 1$,

$$\begin{aligned}
\mathscr{K}_1 &= \begin{bmatrix} -20 & -0.1 & 0.02 \\ 0.4 & -4 & 0.05 \\ 0.2 & 0.5 & -0.0032 \\ 0 & 0.02 & -0.02 \end{bmatrix}, \\
\mathscr{K}_2 &= \begin{bmatrix} -15 & -0.01 & 0.03 \\ 0.3 & -4 & 0.04 \\ 0.2 & 0.05 & -0.0038 \\ 0 & 0.04 & 0.02 \end{bmatrix}.
\end{aligned} \tag{68}$$

by employing the aforementioned event-triggered strategy and controller gains, the state trajectory of the resultant uncertain closed-loop system can be clearly portrayed in Figures 3-4. Since the system remains stable and converges to its original point, it follows that Theorem 2 is effective. Moreover, Figure 5 exhibits the dynamics of the corresponding controller. Some release instants and release intervals, which are yielded by the above-mentioned adaptive event generator, are illustrated in Figure 6. Meanwhile, viewed from the curve trend of Figure 5 and the triggered dynamics of Figure 6, the event-triggered dynamic output-feedback controller adopted by us can monitor the uncertain switched system in real time and reduce unnecessary data sampling, thus achieving the effect of resource-saving.

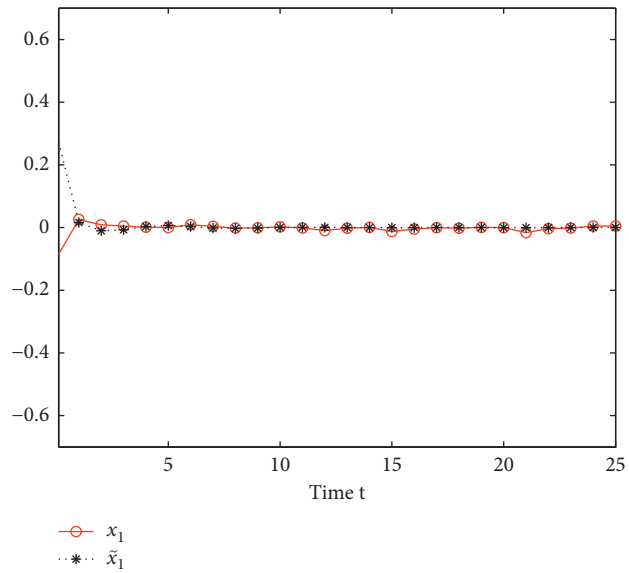

Figure 3: Responses of $x_1(t)$ and $\tilde{x}_1(t)$.

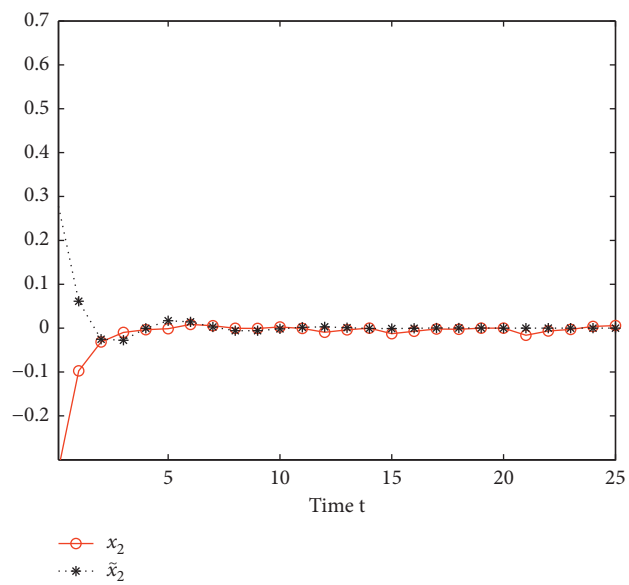

Figure 4: Responses of $x_2(t)$ and $\tilde{x}_2(t)$.

$$\begin{aligned}
h_{111} &= h_{121} = h_{131} = h_{141} = h_{151} = h_{161} = h_{211} = h_{221} \\
&= h_{231} = h_{241} = h_{251} = h_{261} = h_{112} = h_{122} = h_{132} \\
&= h_{142} = h_{152} = h_{162} = h_{212} = h_{222} = h_{232} = h_{242} \\
&= h_{252} = h_{262} = 20, \\
h_{271} &= h_{172} = h_{171} = h_{272} = 80, \\
h_{18} &= h_{28} = 30, \\
\Omega_1 &= 1, \\
\Omega_2 &= 0.5,
\end{aligned} \tag{69}$$

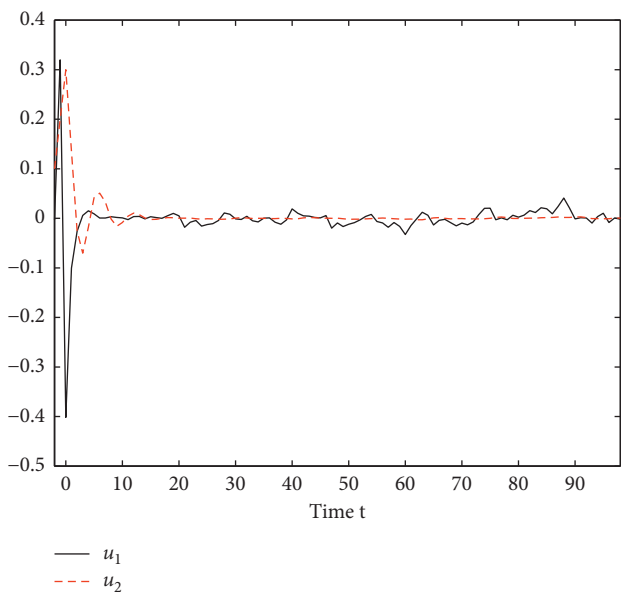

Figure 5: Responses of $u_1(t)$ and $u_2(t)$.

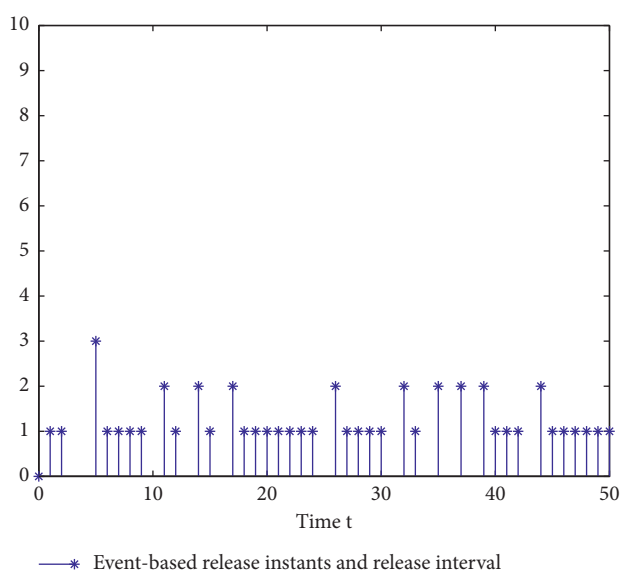

Figure 6: The dynamics of event-triggered mechanism.

5. Conclusion

In this article, we investigate innovatively the stabilization of an uncertain and frequently switched system that is equipped with an event-triggered dynamic output-feedback controller. By utilizing the average dwell-time strategy, the residence time of subsystems is arbitrarily small so that the uncertain system can be frequently switched. Moreover, we adopt dynamic output-feedback control for stabilization device, which replaces state-feedback control and is conducive to acquiring the whole information. Furthermore, a controller-pattern-related Lyapunov functional is constructed, and the pattern-related event-triggered scheme and the dynamic output-feedback controller are conjointly devised to guarantee the exponential stabilization of an uncertain closed-loop system. To reasonably deal with the uncertain parameters, the Lyapunov functional and controller gains are designed by the approach of a block matrix, as well as some linear matrix inequalities are exploited. Furthermore, the adopted event-triggered scheme can also avoid the Zeno phenomenon. Eventually, we provide a numerical simulation to confirm the availability of the derived results.

Data Availability

No data were used to support this study.

Conflicts of Interest

The authors declare that there are no conflicts of interest regarding the publication of this paper.

References

[1] P. J. Antsaklis and A. Nerode, "Hybrid control systems: an introductory discussion to the special issue," *IEEE Transactions on Automatic Control*, vol. 43, no. 4, pp. 457–460, 1998.

[2] D. Liberzon and A. S. Morse, "Basic problems in stability and design of switched systems," *IEEE Control Systems Magazine*, vol. 19, no. 5, pp. 59–70, 1999.

[3] P. Riedinger and J.-C. Vivalda, "Dynamic output feedback for switched linear systems based on a LQG design," *Automatica*, vol. 54, pp. 235–245, 2015.

[4] X.-Q. Zhao and J. Zhao, "Asynchronous fault detection for continuous-time switched delay systems," *Journal of the Franklin Institute*, vol. 352, no. 12, pp. 5915–5935, 2015.

[5] L. Sabattini, C. Secchi, and C. Fantuzzi, "Eigenvalue Placement for Asymptotic Stability in Piecewise Linear Switched Systems," in *Proceedings of the 54th IEEE Conference on Decision and Control*, pp. 4885–4890, Osaka, Japan, December 2015.

[6] W. Xu, Z. G. Feng, J. W. Peng, and K. F. C. Yiu, "Optimal switching for linear quadratic problem of switched systems in discrete time," *Automatica*, vol. 78, pp. 185–193, 2017.

[7] C. Briat, "Convex lifted conditions for robust l_2-stability analysis and l_2-stabilization of linear discrete-time switched systems with minimum dwell-time constraint," *Automatica*, vol. 50, no. 3, pp. 976–983, 2014.

[8] A. Mustafa, N. K. Dhar, and N. K. Verma, "Event-triggered sliding mode control for trajectory tracking of nonlinear systems," *IEEE/CAA Journal of Automatica Sinica*, vol. 7, no. 1, pp. 307–314, 2020.

[9] C. Zhang, M. Gan, and C. Xue, "Data-driven optimal switching and control of switched systems," *Control Theory and Technology*, vol. 19, no. 3, pp. 299–314, 2021.

[10] C. Tian, P. Yan, and Z. Zhang, "Sampled-data extended state observer for uncertain nonlinear systems," *Control Theory and Technology*, vol. 14, no. 3, pp. 189–198, 2016.

[11] Y.-F. Gao, X.-M. Sun, C. Wen, and W. Wang, "Estimation of sampling period for stochastic nonlinear sampled-data systems with emulated controllers," *IEEE Transactions on Automatic Control*, vol. 62, no. 9, pp. 4713–4718, 2017.

[12] A. Girard, "Dynamic triggering mechanisms for event-triggered control," *IEEE Transactions on Automatic Control*, vol. 60, no. 7, pp. 1992–1997, 2015.

[13] D. Zhao and M. M. Polycarpou, "Fault accommodation for a class of nonlinear uncertain systems with event-triggered input," *IEEE/CAA Journal of Automatica Sinica*, vol. 9, no. 2, pp. 235–245, 2022.

[14] X. Guo, D. Zhang, J. Wang, and C. K. Ahn, "Adaptive memory event-triggered observer-based control for nonlinear multi-agent systems under DoS attacks," *IEEE/CAA Journal of Automatica Sinica*, vol. 8, no. 10, pp. 1644–1656, 2021.

[15] Y. Qi and M. Cao, "Finite-time boundedness and stabilisation of switched linear systems using event-triggered controllers," *IET Control Theory & Applications*, vol. 11, no. 18, pp. 3240–3248, 2017.

[16] Z. Fei, C. Guan, and X. Zhao, "Event-triggered dynamic output feedback control for switched systems with frequent asynchronism," *IEEE Transactions on Automatic Control*, vol. 65, no. 7, pp. 3120–3127, 2020.

[17] A. Wu, H. Liu, and Z. Zeng, "Observer design and H∞ performance for discrete-time uncertain fuzzy-logic systems," *IEEE Transactions on Cybernetics*, vol. 51, no. 5, pp. 2398–2408, 2021.

[18] Y. Wang, L. Xie, and C. E. D. Souza, "Robust control of a class of uncertain nonlinear systems," *Systems & Control Letters*, vol. 19, no. 2, pp. 139–149, 1992.

[19] J. Zhou, J. H. Park, and H. Shen, "Non-fragile reduced-order dynamic output feedback $H\infty$ control for switched systems with average dwell-time switching," *International Journal of Control*, vol. 89, no. 2, pp. 281–296, 2016.

Hindawi
Discrete Dynamics in Nature and Society
Volume 2022, Article ID 4812018, 8 pages
https://doi.org/10.1155/2022/4812018

Research Article

Research on IQ Imbalance Error of Orthogonal Alternating Sampling

Junyi Luo [1] **and Tao Liu** [2]

[1] *School of Electronic Information and Electrical Engineering, Chengdu University, Chengdu 610106, China*
[2] *Chengdu Kinyea Technologies Co., Ltd, Chengdu 610106, China*

Correspondence should be addressed to Tao Liu; 179209457@qq.com

Received 13 January 2022; Accepted 11 February 2022; Published 4 March 2022

Academic Editor: Zi-Peng Wang

In the signal acquisition of complete orthogonal frequency alternating acquisition system, we need to transform the broadband input signal to baseband through analogue orthogonal demodulation. Thus, the IQ imbalance errors will inevitably exist, including amplitude imbalance error and phase imbalance error, resulting in distortion deterioration of reconstruction signals. This paper makes an in-depth study on such IQ imbalance errors and mathematically deduces the mathematical expressions of imbalance errors and the spurious frequency distribution caused by them, which shows that the positions where the spurious signals appear are closely related to the frequency of input signal and the tuning frequency of analogue quadrature demodulation. Meanwhile, the amplitude and phase imbalance parameters of the channels I and Q are also calculated. Finally, the spurious effects caused by imbalance errors are verified by simulation experiment, and the verification results are consistent with the theoretical derivation results.

1. Introduction

Sampling rate and bandwidth are two key indicators to evaluate the performance of a set of data acquisition systems, and the two indicators are also directly reflected in the performance of analogue-to-digital converter (ADC). At the current level of integrated circuit technology, the sampling rate and bandwidth of a single ADC is extremely limited; in order to build a wideband high-speed acquisition system, it can only be realized by combination sampling using several ADCs. One combination mode is time-interleaved sampling, namely, TIADC mode [1, 2], which can effectively break the limit of sampling rate, but the bandwidth is still limited; the other combination mode is frequency-interleaved sampling, namely, FIADC mode [3], also known as the HBF mode [4], which is the best means to effectively increase the sampling rate and bandwidth.

The structural forms of frequency-interleaved sampling technology mainly include two types, namely, traditional structure [5] and orthogonal structure [6, 7]. The orthogonal structure is an equivalent improvement of the traditional structure. Its concept is that the input signal is uniformly divided into several sub-bands in terms of frequency spectrum characteristics, each sub-band is moved to the baseband by analogue IQ quadrature demodulation, and then the various baseband signals are sampled using the ADC and the carrier frequency of these baseband signals is recovered with the help of the digital IQ quadrature modulation algorithm, so as to achieve the purpose of reproducing the characteristics of input signal. As this structure involves the two characteristic links of analogue IQ quadrature demodulation and digital IQ quadrature modulation, it is also known as a complete orthogonal frequency alternating acquisition structure. In this structure, it required to design only one analogue low-pass filter at the front end of the ADC array and one digital low-pass filter at the back end, which greatly reduces the design complexity and error sources of filters and is more conducive to engineering applications; moreover, the sampling rate and bandwidth of various ADCs are further reduced by a half compared to

those of the traditional structure, which is conducive to construction of higher speed and larger bandwidth acquisition systems.

The errors existing in both traditional and complete orthogonal frequency alternating acquisition systems include analogue device error, channel mismatch error, and signal reconstruction error. At present, a large number of literatures [8–11] have made an in-depth study on evaluation, compensation, calibration, etc. of these errors. However, due to the introduction of an analogue IQ quadrature demodulator at the front end of the ADC, the IQ imbalance errors will inevitably exist in the complete orthogonal frequency alternating structure [12, 13], including the two parts of IQ amplitude imbalance error and phase imbalance error, which directly leads to frequency spectrum deterioration and spurious cluttering of output signals. The study on IQ imbalance errors in such structures is still quite scarce and needs to be further developed. This paper focuses on studying the IQ imbalance errors in the complete orthogonal frequency alternating systems, progressively deduces the mathematical expression of the output spurious signals in the case of IQ imbalance, determines the frequency positions of various spurious signals and their correlations with input signal frequency, obtains the computation expressions of amplitude and phase imbalance parameters, and finally verifies the analysis by simulation experiment.

2. Principle of Complete Orthogonal Frequency Alternating Acquisition

Figure 1 shows the principle structure of complete orthogonal frequency alternating acquisition system, of which sampling period is T_s.

The analogue quadrature demodulator and analogue low-pass filter $\Phi(j\Omega)$ of M-channel are used to uniformly convert the input signals $\Phi(j\Omega)$ into M-channel baseband sub-signals of equal bandwidth, and thus the bandwidths of various sub-signals are reduced to $(1/2M)$ of the input signals; then, the base band signal can be digitized by M-channel ADC with sampling period of (1/2M), and then the carrier frequencies of various baseband sub-signals are, respectively, recovered to the tuning frequency points of analogue quadrature demodulator at the front end of corresponding channels using digital up-conversion (DUC) [14] and added together to obtain the full digital domain information of input analogue signals. The digital up-conversion (DUC) consists of three operations, namely, $2M$-fold interpolation, digital low-pass filtering with a frequency response of $\Psi(e^{j\omega})$, and digital quadrature modulation.

Full-domain processing is made for the signals in the first Nyquist domain, and then the tuning frequency of each channel analogue quadrature demodulator can be expressed as

$$\overrightarrow{\Omega} = \{\Omega_0, \ldots, \Omega_m, \ldots, \Omega_{M-1}\}, \quad m \in [0, M-1], \tag{1}$$

where $\Omega_m = (2m+1)\cdot(\pi/2M)$.

The time-domain expression of analogue quadrature demodulator is

$$OC_m = e^{-j\Omega_m t} = \cos(\Omega_m t) - j\sin(\Omega_m t). \tag{2}$$

According to Fourier transform characteristics, the signals $X_m(j\Omega)$ after analogue quadrature demodulation are as follows:

$$X_m(j\Omega) = X(j\Omega + j\Omega_m). \tag{3}$$

After sampling by analogue low-pass filter and ADC, the frequency characteristics of signals can be expressed as follows:

$$X_m(e^{j\omega}) = \frac{1}{2MT_s}\sum_{r=0}^{2M-1} \left[X\left(j\frac{\omega}{2MT_s} + j\Omega_m - j\frac{\pi r}{MT_s}\right) \times \Phi\left(j\frac{\omega}{2MT_s} - j\frac{\pi r}{MT_s}\right)\right]. \tag{4}$$

If ω_m is used to express the tuning frequency of subsequent digital quadrature modulator, then $\omega_m = \Omega_m T_s$ and the output signal $Y(e^{j\omega})$ is

$$Y(e^{j\omega}) = \sum_{r=0}^{2M-1} X\left(j\frac{\omega}{T_s} - j\frac{\pi r}{MT_s}\right)\cdot T_r(e^{j\omega}), \tag{5}$$

where

$$T_r(e^{j\omega}) = \frac{1}{2MT_s}\sum_{m=0}^{M-1}\Phi\left[j\frac{\omega}{T_s} - j\Omega_m - j\frac{\pi r}{MT_s}\right]\Psi\left(e^{j(\omega-\omega_m)}\right). \tag{6}$$

It expresses the transfer function of the system [15]. Assuming the output signal $Y(e^{j\omega})$ is reproduction of undistorted digital domain of the input signal $X(j\Omega)$, then $T_r(e^{j\omega})$ shall satisfy

$$T_r(e^{j\omega}) = \begin{cases} Ce^{-j\omega d}, & r = 0, \\ 0, & r \in [1, 2M-1]. \end{cases} \tag{7}$$

At this point, the output signal $Y(e^{j\omega}) = Ce^{-j\omega d} X(j(\omega/T_s))$ is only the result of grain and delay effects of the input signal and there are no other spurious or aliasing phenomena. However, in fact, when $r \neq 0$, $T_r(e^{j\omega})$ is impossible to be theoretically zero. This means that the reconstruction error exists objectively, which can only be reduced as far as possible to meet the signal-to-noise distortion ratio required by the intended design.

3. Analysis of Analogue IQ Imbalance Errors

This paper focuses on IQ imbalance analysis of analogue demodulation, so the effects of analogue device error, channel mismatch error, and signal reconstruction error are ignored for the time being.

Suppose the IQ imbalance errors are uncorrelated with the input signal's frequency; then, formula (2) is changed while the IQ imbalance errors are introduced:

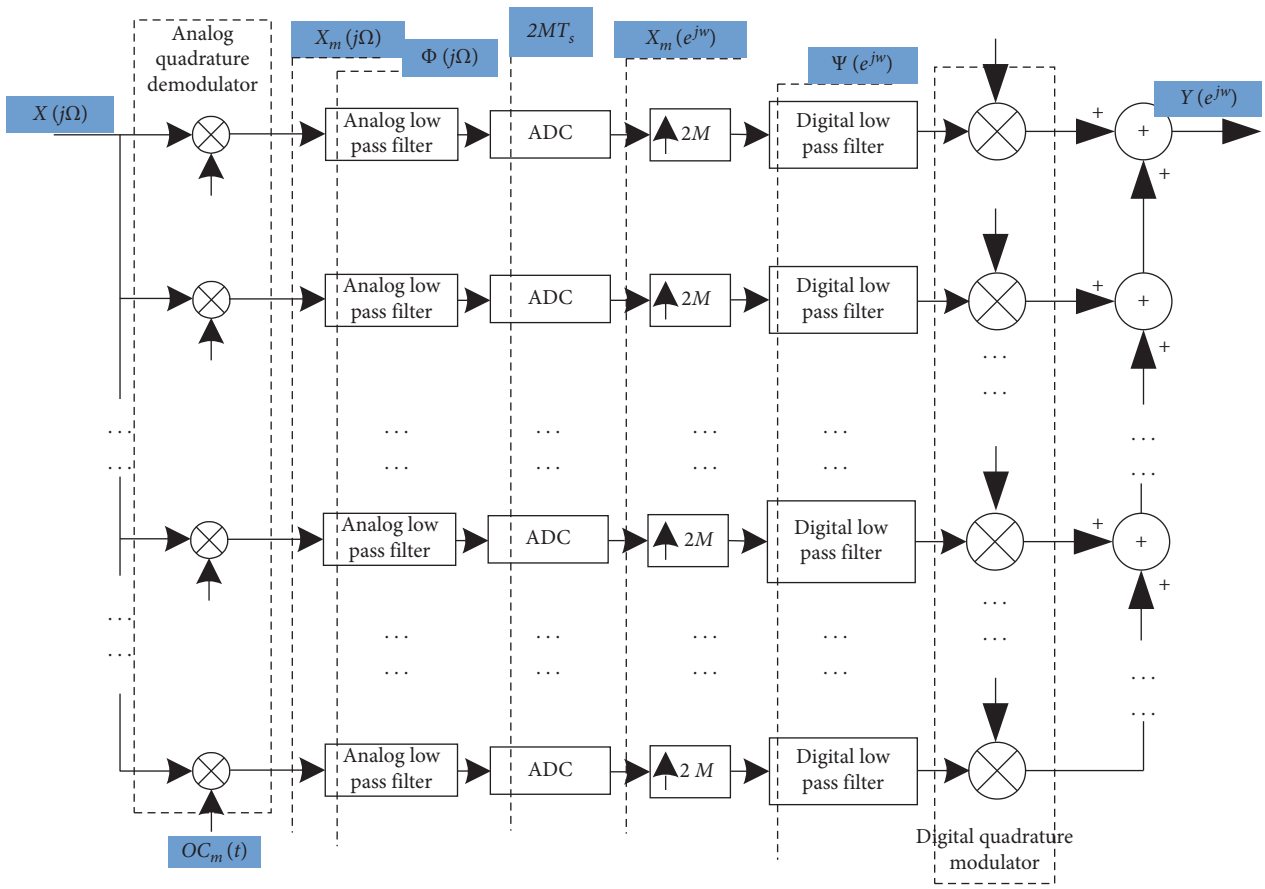

Figure 1: Principle of orthogonal frequency alternating acquisition systems.

$$OC_m^{\Delta} = \cos(\Omega_m t) - j(1+\alpha_m)\sin(\Omega_m t + \varphi_m), \tag{8}$$

where α_m and φ_m, respectively, express the magnitude imbalance parameter and phase imbalance parameter between the two channels I and Q in the mth channel analogue quadrature demodulator.

The Fourier transform expression of formula (8) is

$$\begin{aligned} F\left[OC_m^{\Delta}\right] = {} & 2\pi\delta(\Omega-\Omega_m) + \pi\left[1-(1+\alpha_m)\cos\varphi_m \right. \\ & \left. - j(1+\alpha_m)\sin\varphi_m\right]\delta(\Omega-\Omega_m) \\ & - \pi\left[1-(1+\alpha_m)\cos\varphi_m + j(1+\alpha_m)\sin\varphi_m\right]\delta \\ & \cdot(\Omega+\Omega_m), \end{aligned} \tag{9}$$

where $F[\cdot]$ represents Fourier operator. Then, in this case, the signal after analogue quadrature demodulation is updated as $X_m^{\Delta}(j\Omega)$, and

$$\begin{aligned} X_m^{\Delta}(j\Omega) = {} & X(j\Omega + j\Omega_m) + \frac{1-P_m}{2}X(j\Omega - j\Omega_m) \\ & + \frac{S_m - 1}{2}X(j\Omega + j\Omega_m), \end{aligned} \tag{10}$$

where $P_m = (1+\alpha_m)e^{j\varphi_m}$ and $S_m = (1+\alpha_m)e^{-j\varphi_m}$. The signal after sampling by analogue low-pass filter and ADC is updated as $X_m^{\Delta}(e^{j\omega})$ and

$$\begin{aligned} X_m^{\Delta}\left(e^{j\omega}\right) = {} & \frac{1}{2MT_s}\sum_{r=0}^{2M-1}\left[X\left(j\frac{\omega}{2MT_s} + j\Omega_m - j\frac{\pi r}{MT_s}\right) + \frac{1-P_m}{2}X\left(j\frac{\omega}{2MT_s} - j\Omega_m - j\frac{\pi r}{MT_s}\right)\right. \\ & \left. + \frac{S_m-1}{2}X\left(j\frac{\omega}{2MT_s} + j\Omega_m - j\frac{\pi r}{MT_s}\right)\right] \times \Phi\left(j\frac{\omega}{2MT_s} - j\frac{\pi r}{MT_s}\right). \end{aligned} \tag{11}$$

Then, the output signal is updated as $Y^{\Delta}(e^{j\omega})$ and satisfies

$$Y^{\Delta}\left(e^{j\omega}\right) = Y\left(e^{j\omega}\right) + \partial_m, \tag{12}$$

where ∂_m represents the error term of the system output signal with IQ imbalance compared with the output signal without IQ imbalance, and it meets

$$\begin{aligned}\partial_m = &\sum_{r=0}^{2M-1}\left[X\left(j\frac{\omega}{T_s} - j\frac{\pi r}{MT_s}\right) \times \frac{1}{2MT_s}\sum_{m=0}^{M-1}\frac{S_m - 1}{2}\Phi\left(j\frac{\omega}{T_s} - j\Omega_m - j\frac{\pi r}{MT_s}\right)\Psi\left(e^{j\omega - j\omega_m}\right)\right] \\ &+ \frac{1}{2MT_s}\sum_{r=0}^{2M-1}\sum_{m=0}^{M-1}\left[\frac{1 - P_m}{2}X\left(j\frac{\omega}{T_s} - j2\Omega_m - j\frac{\pi r}{MT_s}\right) \times \Phi\left(j\frac{\omega}{T_s} - j\Omega_m - j\frac{\pi r}{MT_s}\right)\Psi\left(e^{e^{j\omega - j\omega_m}}\right)\right].\end{aligned} \tag{13}$$

Obviously, ∂_m directly reflects the spurious situation in the case of IQ imbalance.

In order to further evaluate the specific impact of am, the input signal is loaded as a single tone sinusoidal signal. Suppose the amplitude is U_{IN}, and Ω_{IN} and ω_{IN} are the analogue and angular frequencies, respectively. At this point, formula (13) can be simplified into

$$\begin{aligned}\partial_m = &\sum_{r=0}^{2M-1}\left\{\pi U_{IN}\left[\delta\left(\omega + \omega_{IN} - \frac{\pi r}{M}\right) + \delta\left(\omega - \omega_{IN} - \frac{\pi r}{M}\right)\right] \times \sum_{m=0}^{M-1}\frac{S_m - 1}{2}\Phi\left(j\frac{\omega}{T_s} - j\Omega_m - j\frac{\pi r}{MT_s}\right)\Psi\left(e^{j\omega - j\omega_m}\right)\right\} \\ &+ \sum_{r=0}^{2M-1}\sum_{m=0}^{M-1}\left\{\frac{1 - P_m}{2}\pi U_{IN}\left[\delta\left(\omega + \omega_{IN} - 2\omega_m - \frac{\pi r}{M}\right) + \delta\left(\omega - \omega_{IN} - 2\omega_m - \frac{\pi r}{M}\right)\right]\right. \\ &\left.\times \Phi\left(j\frac{\omega}{T_s} - j\Omega_m - j\frac{\pi r}{MT_s}\right) \times \Psi\left(e^{j\omega - j\omega_m}\right)\right\}.\end{aligned} \tag{14}$$

In formula (14), according to the frequency response characteristics, the analogue low-pass filter and the digital low-pass filter should have

$$\Phi\left(j\frac{\omega}{T_s} - j\Omega_m - j\frac{\pi r}{MT_s}\right)\Psi\left(e^{j\omega - j\omega_m}\right)\Big|_{\omega = \pm\,\omega_{IN} + (\pi r/M)} = \Phi\left(\pm j\frac{\omega_{IN}}{T_s} - j\Omega_m\right)\Psi\left(e^{\pm j\omega_{IN} - j\omega_m + (j\pi r/M)}\right)\begin{cases}\neq 0, & r = 1, \\ \approx 0, & r > 1.\end{cases} \tag{15}$$

Therefore, analysis for ∂_m mainly focuses on the cases of $r = 0$ and $r = 1$. At this point,

$$\partial_m|_{r=0} = \pi U_{IN}\left[\delta(\omega+\omega_{IN})+\delta(\omega-\omega_{IN})\right]\times\sum_{m=0}^{M-1}\frac{S_m-1}{2}\Phi\left(j\frac{\omega}{T_s}-j\Omega_m\right)\Psi\left(e^{j\omega-j\omega_m}\right)$$
$$+\sum_{m=0}^{M-1}\left\{\frac{1-P_m}{2}\pi U_{IN}\left[\delta(\omega+\omega_{IN}-2\omega_m)+\delta(\omega-\omega_{IN}-2\omega_m)\right]\times\Phi\left(j\frac{\omega}{T_s}-j\Omega_m\right)\times\Psi\left(e^{j\omega-j\omega_m}\right)\right\}, \tag{16}$$

$$\partial_m|_{r=1} = \pi U_{IN}\left[\delta\left(\omega+\omega_{IN}-\frac{\pi}{M}\right)+\delta\left(\omega-\omega_{IN}-\frac{\pi}{M}\right)\right]\times\sum_{m=0}^{M-1}\frac{S_m-1}{2}\Phi\left(j\frac{\omega}{T_s}-j\Omega_m-j\frac{\pi}{MT_s}\right)\Psi\left(e^{j\omega-j\omega_m}\right)$$
$$+\sum_{m=0}^{M-1}\left\{\frac{1-P_m}{2}\pi U_{IN}\left[\delta\left(\omega+\omega_{IN}-2\omega_m-\frac{\pi}{M}\right)+\delta\left(\omega-\omega_{IN}-2\omega_m-\frac{\pi}{M}\right)\right]\times\Phi\left(j\frac{\omega}{T_s}-j\Omega_m-j\frac{\pi}{MT_s}\right)\times\Psi\left(e^{j\omega-j\omega_m}\right)\right\}. \tag{17}$$

According to formulas (16) and (17), it can be founded that ∂_m will produce excessive frequency spectrum signals at the frequency position $\overset{IQ}{\omega}$, and

$$\omega_{IQ} = \left\{\pm\omega_{IN}+\frac{\pi}{M}\right\}\cup\left\{\pm\omega_{IN}+2\omega_m\right\}\cup\left\{\pm\omega_{IN}+\frac{\pi}{M}+2\omega_m\right\}. \tag{18}$$

Formula (18) directly reflects the frequency distribution of spurious signals brought about by imbalance error, and the position where it appears is closely related to the input signal frequency and the tuning frequency of quadrature modulation and demodulation, and the number of spurious signals is obviously more than that of spurious signals caused by grain error, biased error, and time error of ADC acquisition channel. The reason mainly lies in that the IQ mismatch errors bring an additional impact factor (i.e., the tuning frequency of quadrature modulation) to the channel mismatch.

To further analyze the amplitude strength of spurious signals, now a uniform n-point discrete Fourier transform is made for formula (4) within the interval of $[0, 2\pi]$. At this point, $r = 0$; therefore,

$$X_m^{\Delta}\left(e^{j\omega}\right)|_{\omega=(2\pi k/N)} = \pi U_{IN}\left\{\begin{array}{l}\left[\left(1+\frac{S_m-1}{2}\right)\delta\left(\frac{2\pi k}{N}+2M\omega_{IN}+2M\omega_m\right)+\left(1+\frac{S_m-1}{2}\right)\delta\left(\frac{2\pi k}{N}-2M\omega_{IN}+2M\omega_m\right)\right]\\ +\frac{1-P_m}{2}\left[\left(\frac{2\pi k}{N}+2M\omega_{IN}-2M\omega_m\right)+\delta\left(\frac{2\pi k}{N}-2M\omega_{IN}-2M\omega_m\right)\right]\end{array}\right\}$$
$$\times\Phi\left(j\frac{\pi k}{MNT_s}\right). \tag{19}$$

In formula (19), $k \in [0, N-1]$. $X_m^{\Delta}(e^{j\omega})$ represents the frequency spectrum characteristics of signals after sampling by ADC, and the frequency spectrum value of each point is measurable and then the amplitude imbalance parameter α_m and phase imbalance parameter φ_m between the two analogue channels I and Q can be estimated in the inverse direction according to the number of frequency spectrum of signals after sampling by ADC. Details are as follows.

When $k = (\omega_{IN} - \omega_m/\pi)\cdot N\cdot M$, it can be obtained that

$$X_m^{\Delta}\left(e^{j\omega}\right)|_{\omega=(2\pi k/N)} = \pi U_{IN}\left(1+\frac{S_m-1}{2}\right)\Phi\left(j\Omega_{IN}-j\Omega_m\right). \tag{20}$$

When $k = (\omega_{IN} - \omega_m/\pi)\cdot N\cdot M$, it can be obtained that

$$X_m^{\Delta}\left(e^{j\omega}\right)|_{\omega=(2\pi k/N)} = \pi U_{IN}\left(1+\frac{1-P_m}{2}\right)\Phi\left(j\Omega_{IN}+j\Omega_m\right). \tag{21}$$

Then, combining formulas (20) and (21), it can be obtained that

$$\left\{\begin{array}{l}(1+\alpha_m)e^{-j\varphi_m} = \dfrac{2X_m^{\Delta}\left(e^{j\omega}\right)}{\pi U_{IN}\Phi\left(j\Omega_{IN}-j\Omega_m\right)}-1,\\ (1+\alpha_m)e^{j\varphi_m} = 3-\dfrac{2X_m^{\Delta}\left(e^{j\omega}\right)}{\pi U_{IN}\Phi\left(j\Omega_{IN}+j\Omega_m\right)}.\end{array}\right. \tag{22}$$

In formula (22), $\Phi(j\Omega_{IN}+j\Omega_m)$ can be obtained according to the designed analogue low-pass filter $\Phi(j\Omega)$. According to formula (22), the computation expressions of amplitude imbalance and phase imbalance parameters can be obtained as follows:

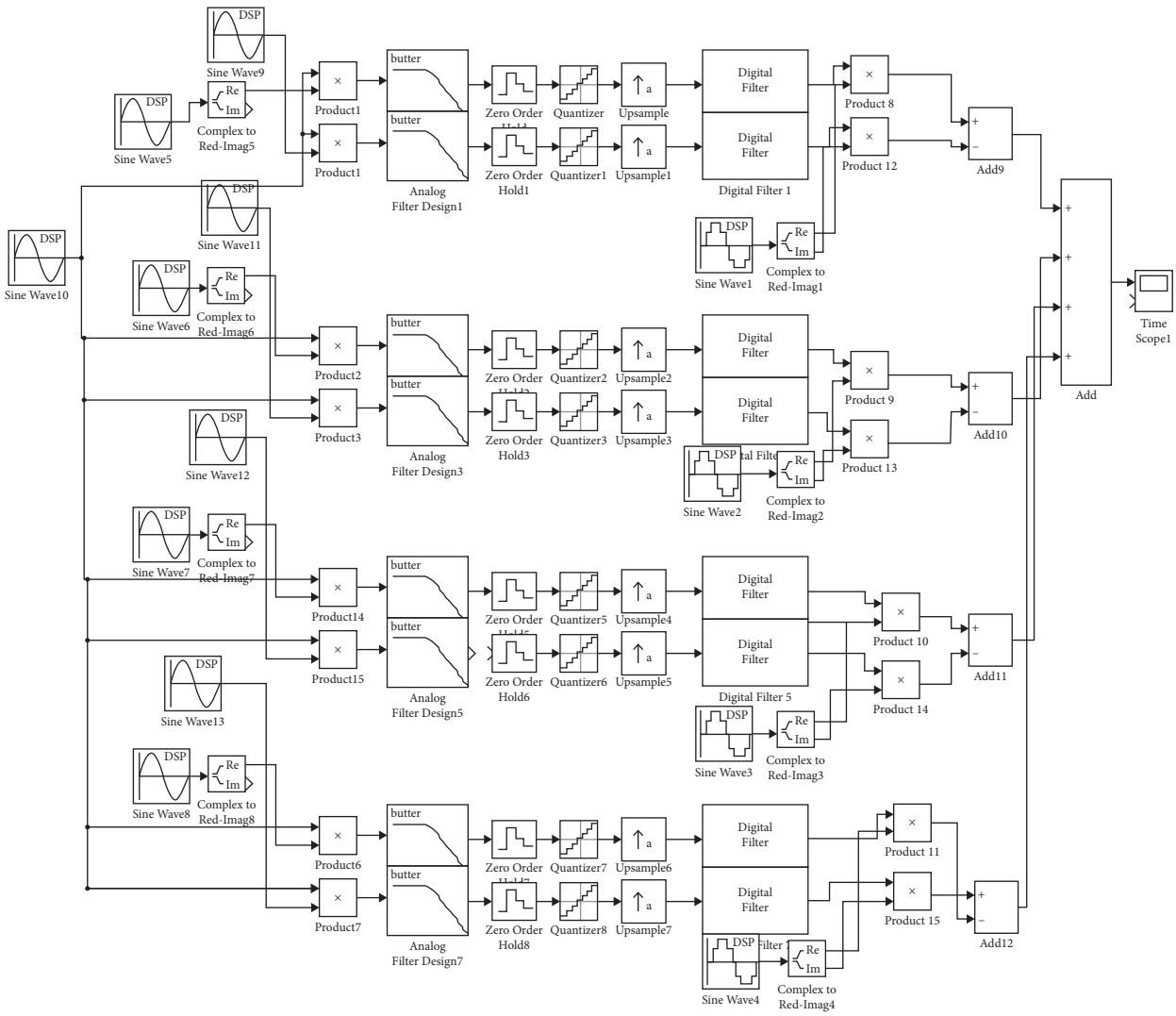

Figure 2: Simulink model of 4-channel high-speed system with IQ mismatch.

$$\begin{cases} \alpha_m = \sqrt{\Pi \times \coprod} - 1,\ \varphi_m = \dfrac{\Theta}{2\Gamma}, \\ \Pi = \dfrac{2\left|X_m^{\Delta}\left(e^{j\omega}\right)\right|}{\pi U_{IN}\left|\Phi\left(j\Omega_{IN} - j\Omega_m\right)\right|} - 1, \\ \coprod = 3 - \dfrac{2\left|X_m^{\Delta}\left(e^{j\omega}\right)\right|}{\pi U_{IN}\left|\Phi\left(j\Omega_{IN} - j\Omega_m\right)\right|}, \\ \Theta = \theta\left[3 - \dfrac{2X_m^{\Delta}\left(e^{j\omega}\right)}{\pi U_{IN}\Phi\left(j\Omega_{IN} - j\Omega_m\right)}\right], \\ \Gamma = \theta\left[\dfrac{2X_m^{\Delta}\left(e^{j\omega}\right)}{\pi U_{IN}\Phi\left(j\Omega_{IN} - j\Omega_m\right)} - 1\right]. \end{cases} \tag{23}$$

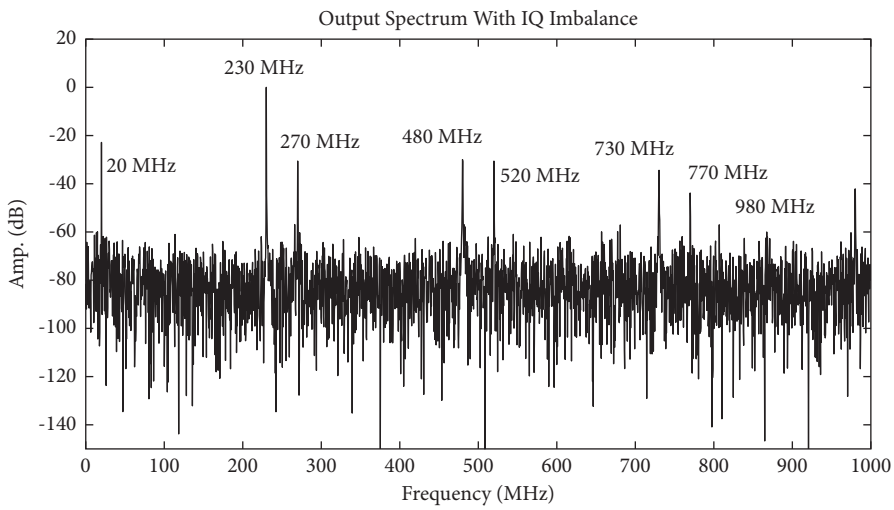

Figure 3: Output spectrum under the effect of IQ mismatch.

Table 1: Statistics of spurious source.

Spurious frequency point (MHz)	Spurious source
20	$-f_{IN} + (f_s/2M)$, $-f_{IN} + 2f_0$, $-f_{IN} + 2f_2$
270	$-f_{IN} + (f_s/2M) + 2f_0$, $-f_{IN} + (f_s/2M) + 2f_2$
480	$f_{IN} + (f_s/2M)$, $f_{IN} + 2f_0$, $f_{IN} + 2f_2$
520	$-f_{IN} + 2f_1$, $-f_{IN} + 2f_3$
730	$f_{IN} + (f_s/2M) + 2f_0$, $f_{IN} + (f_s/2M) + 2f_2$
770	$-f_{IN} + (f_s/2M) + 2f_1$, $-f_{IN} + (f_s/2M) + 2f_3$
980	$f_{IN} + 2f_1$, $f_{IN} + 2f_3$

4. Simulation Verification

To verify that the IQ imbalance error in the complete orthogonal frequency alternating acquisition system can bring about spurious effects on the output signal, experimental analysis is further made using the Simulink simulation tool. The Simulink model is shown in Figure 2. Here, the complete orthogonal frequency alternating acquisition system is instantiated as a four-channel ($M = 4$) high-speed acquisition system, with a total sampling rate of $f_s = 2GSPS$ ($f_s = (1/T_S)$), which totally requires eight low-speed ADCs operating at 250 MHz.

Then, the quadrature modulation and demodulation frequencies f_m ($f_m = \omega_m/2\pi = (\Omega_m T_s/2\pi)$) of various channels are $f_0 = 125$ MHz, $f_1 = 375$ MHz, $f_2 = 625$ MHz, and $f_3 = 875$ MHz, respectively.

Let the input signal be a cosine signal, and it is expressed as follows:

$$x(t) = \cos(2\pi f_{IN} t), \tag{24}$$

where $f_{IN} = (\omega_{IN}/2\pi) = (\Omega_{IN} T_s/2\pi)$. To significantly verify the spurious effects of amplitude imbalance and phase imbalance, the amplitude imbalance parameters of various channels are set as 8, 9, 10, and 11, respectively, and the phase imbalance parameters of various channels are set as $(\pi/6)$, $(\pi/8)$, $(\pi/10)$, and $(\pi/12)$, respectively. Meanwhile, set $f_{IN} = 230$ MHz. The frequency spectrum of the output signal is obtained as shown in Figure 3.

In the frequency spectrum information as shown in Figure 3, in addition to the input information including 230 MHz, there are also a total of seven spurious signals at 20 MHz, 270 MHz, 480 MHz, 520 MHz, 730 MHz, 770 MHz, and 980 MHz.

Here, formula (18) is rewritten as the frequency form:

$$f_{IQ} = \left\{\pm f_{IN} + \frac{f_s}{2M}\right\} \cup \{\pm f_{IN} + 2f_m\} \cup \left\{\pm f_{IN} + \frac{f_s}{2M} + 2f_m\right\}. \tag{25}$$

Calculation based on formula (25) and various setting parameters reveals that the spurious signals theoretically deduced are all reflected in these seven signals (see Table 1 for details).

Thus, it can be seen that the simulation verification results are consistent with the theoretical derivation, reflecting the objective existence of spurious effects caused by IQ imbalance.

5. Conclusion

The complete orthogonal frequency alternating acquisition systems are a kind of high-speed signal processing systems built based on low-speed narrowband analogue-to-digital converter devices, with the advantages of lower sampling rate of required devices, simpler filter design, and easier engineering application than the traditional frequency-interleaved acquisition systems. However, due to the different

analog quadrature demodulation operation of this kind of system, there are not only the same analog implementation error and channel mismatch error as the traditional system but also IQ imbalance error. In order to master the effects of IQ imbalance errors on such systems, this paper makes a detailed study and mathematically deduces the spurious effects of imbalance errors and verifies them combined with simulation experiments. As a whole, the IQ imbalance errors will bring several spurious signals to the output signals and cause frequency spectrum deterioration, and the frequency distribution of these spurious signals is directly influenced by the input signal frequency and the analogue quadrature demodulation frequency.

Data Availability

The data used to support the findings of this study are available from the corresponding author upon request.

Conflicts of Interest

The authors declare that they have no conflicts of interest.

Acknowledgments

This study was supported by the Chengdu Science and Technology Bureau Project (2019-YF05-02118-SN).

References

[1] E. J. Candes, J. Romberg, and T. Tao, "Robust uncertainty principles: exact signal reconstruction from highly incomplete frequency information," *IEEE Transactions on Information Theory*, vol. 52, no. 2, pp. 489–509, 2006.

[2] P. Yang and S. Su, "High speed high precision ADCsystem based on time interleaving technology," *Electron Device*, vol. 48, no. 39, pp. 1397–1401, 2016.

[3] L. Qiu, Y. Zheng, and L. Siek, "Analysis and design of high performance frequency-interleaved ADC," in *Proceedings of the IEEE International Symposium on Circuits & Systems*, pp. 2022–2025, Beijing, China, May 2013.

[4] Xu Liu and Y. Zhao, "A novel oversampling scheme for design of hybrid filter bank based ADCs," *IEICE Electronics Express*, vol. 15, Article ID 20180007, 2018.

[5] J. A. Tropp and A. C. Gilbert, "Signal recovery from random measurements via orthogonal matching pursuit," *IEEE Transactions on Information Theory*, vol. 53, no. 12, pp. 4655–4666, 2007.

[6] W. Wang and Z. Zhang, "Sampling technology of wide-band signals based on modulated hybrid filter banks," *Signal Processing*, vol. 30, no. 10, pp. 1185–1192, 2014.

[7] T. Liu, K. Lian, L. Ye, and S. Tian, "Research on an orthogonal frequency-interleaved sampling and reconstruction method," *Journal of University of Electronic Science and Technology of China*, vol. 48, no. 6, pp. 858–864, 2019.

[8] X. Peng, J. Li, X. Zhou, Q. Lin, and Z. Chen, "Analysis and design of M-channel hybrid filter bank with digital calibration," *IEEE Access*, vol. 6, Article ID 24606, 2018.

[9] E. J. Candès, J. K. Romberg, and T. Tao, "Stable signal recovery from incomplete and inaccurate measurements," *Communications on Pure and Applied Mathematics*, vol. 59, no. 8, pp. 1207–1223, 2006.

[10] S. L. Su, S. P. Hung, and J. Lin, "IQ imbalance compensation," *Journal of the Korean Society for Aeronautical & Space Sciences*, vol. 48, no. 11, pp. 861–871, 2020.

[11] T. Liu, S. Tian, Z. Wang, and L. Guo, "Analysis and design of *M*-channel frequency-interleaved ADC with analog filter estimation," *Analog Integrated Circuits and Signal Processing*, vol. 81, no. 1, pp. 173–180, 2014.

[12] H. Li and Y. Qian, "Influence of IQ channel imbalance on simultaneous transmission and reception based cognitive anti-jamming system," *Journal of Beijing University of Aeronautics and Astronautics*, vol. 43, no. 3, pp. 449–456, 2017.

[13] X. Zhan, P. Liu, S. Ren, and Y. Cheng, "IQ imbalance evaluation and compensation method of ultra-wideband receiver," *Chinese Journal of Scientific Instrument*, vol. 39, no. 6, pp. 157–163, 2018.

[14] H. Ye, K. Su, L. Wu, and Y. Weng, "Digital up-converter circuit for all-digital transmitter," *Journal of Fuzhou University (nature science version)*, vol. 44, no. 5, pp. 649–655, 2016.

[15] E. Nayebi, P. Dayal, and K. B. Song, "Adaptive IQ mismatch compensation in time-domain using frequency-domain observations," *IEEE Transactions on Signal Processing*, vol. 69, no. 99, p. 1, 2021.